

MASARYK UNIVERSITY

FACULTY OF MEDICINE

DEPARTMENT OF HISTOLOGY AND EMBRYOLOGY



TISSUE PLASTICITY IN CANCER, STRESS
AND AGING

HABILITATION THESIS

PETR VAŇHARA

BRNO 2018

ACKNOWLEDGEMENTS

Here I wish to thank to all my colleagues that guided my research career path. Especially, doc. MVDr. Aleš Hampl, CSc. and Dr. Karel Souček, PhD. for longstanding support and mentorship. I thank also Prof. MUDr. et RNDr. Svatopluk Čech, DrSc., doc. MUDr. Miroslava Sedláčková, CSc., and MUDr. Irena Lauschová, PhD., for revealing me the amazing world of human microscopic anatomy and guiding my steps in morphological disciplines, and prof. RNDr. Josef Havel, DrSc., and his MALDI team, namely Dr. Lenka Kolářová and Dr. Lubomír Prokeš, for ongoing superior cooperation and passion for analytical cell science. Ms. Dobromila Klemová and ing. Ladislav Ilkovic are acknowledged for their expert mastery of electron microscopy. I also wish to thank all my students and fellow colleagues for the enthusiasm and motivation. Last, but not least, I thank my family for their love and support.

FUNDING

This work was supported by the following grant projects.

- New tools for high throughput quality control of clinical grade pluripotent stem cells and progenitors (Czech Health Research Council, NV18-08-00299, Ministry of Health of the Czech Republic) (2018-2022, **PI**)
- Role of TUSC3-mediated ER stress response in dissemination of ovarian cancer, supported by the Czech-Biolmaging large RI project (LM2015062, Ministry of Education, Youth and Sports of the Czech Republic) (2017, **PI**)
- ER stress response in aging and regeneration, supported by the Czech-Biolmaging large RI project (LM2015062, Ministry of Education, Youth and Sports of the Czech Republic) (2017, **PI**)
- Centrosomal abnormalities in human pluripotent stem cells (GA15-11707S, Czech Science Foundation, 2015–2017, member of the team)
- Bioanalytical Cell and Tissue Authentication using Physical Chemistry Methods and Artificial Intelligence (MUNI/M/0041/2013, Grant Agency of Masaryk University, 2013–2015, member of the team)
- Junior researcher support (Faculty of Medicine, Masaryk University)
- HistoPARK - Centre for Analysis and Modeling of Tissues and organs (European Regional Fund, 2012–2015, researcher)
- Molecular mechanisms of novel tumor markers in ovarian and prostate cancers (7AMB12AT019, Ministry of Education, Youth and Sports of the Czech Republic, 2012–2013, **co-PI**)

The author declares no conflict of interest.

TABLE OF CONTENTS

I.	ABSTRACT	6
II.	INTRODUCTION	7
III.	AIMS	9
IV.	RESULTS AND DISCUSSION	10
	Research axis I: Epithelial plasticity in cancer, stress, and aging	10
	EMT and cell senescence	10
	Endoplasmic reticulum is linked to tissue morphology, development, and aging	14
	Epithelial plasticity: lessons from ovarian surface epithelium	20
	Alleviation of endoplasmic reticulum-stress in senescent epithelium delays onset of senescence	22
	TUSC3 is a novel genetic driver of ER-stress involved in ovarian cancer and aging	26
	Research axis II: New tools for determination of cell and tissue heterogeneity	31
	Mass spectrometry of cells and tissues	31
	Artificial intelligence-coupled mass spectrometry for analysis of cell heterogeneity	35
	Our relevant applications of ANN-coupled mass spectrometry biotyping in cell and tissue research	37
V.	CONCLUSIONS AND FUTURE PERSPECTIVES	42
VI.	REFERENCES	44
VII.	COMMENTED OVERVIEW OF SELECTED PUBLICATIONS	51
	1. Methylation status of TUSC3 is a prognostic factor in ovarian cancer	53
	2. Loss of the oligosaccharyl transferase subunit TUSC3 promotes proliferation and migration of ovarian cancer cells	63
	3. TUSC3 loss alters the ER stress response and accelerates prostate cancer growth <i>in vivo</i>	71

4.	Tumor Suppressor Candidate 3 (TUSC3) prevents the epithelial-to-mesenchymal transition and inhibits tumor growth by modulating the endoplasmic reticulum stress response in ovarian cancer cells	81
5.	The role of the endoplasmic reticulum stress in stemness, pluripotency and development	99
6.	TUSC3: functional duality of a cancer gene	109
7.	Formation of secretory senescent cells in prostate tumors: the role of androgen receptor activity and cell cycle regulation	118
8.	Growth/Differentiation Factor-15: prostate cancer suppressor or promoter?	135
9.	Coordination compounds in cancer: past, present and perspectives	145
10.	Alleviation of endoplasmic reticulum stress by tauroursodeoxycholic acid delays senescence of mouse ovarian surface epithelium	171
11.	Tissue visualization mediated by nanoparticles: from tissue staining to mass spectrometry tissue profiling and imaging	182
12.	Use of flower-like gold nanoparticles in time-of-flight mass spectrometry	205
13.	Clusters of monoisotopic elements for calibration in (TOF) mass spectrometry	217
14.	Artificial neural networks in medical diagnosis	227
15.	Tissue profiling by nanogold-mediated mass spectrometry and artificial neural networks in the mouse model of human primary hyperoxaluria 1	240
16.	Multivariate calibration approach for quantitative determination of cell-line cross contamination by intact cell mass spectrometry and artificial neural networks	248
17.	Intact cell mass spectrometry as a quality control tool for revealing minute phenotypic changes of cultured human embryonic stem cells	263
18.	Soluble Cripto-1 induces accumulation of supernumerary centrosomes and formation of aberrant mitoses in human embryonic stem cells	270
VIII.	FULL LIST OF PUBLICATIONS 2006-2018	279

LIST OF ABBREVIATIONS

AI	Artificial intelligence
ANN	Artificial neural networks
cGLP	Current good laboratory practice
ECM	Extracellular matrix
EMT	Epithelial-to-mesenchymal transition
ER	Endoplasmic reticulum
FIGO	International Federation of Gynecology and Obstetrics
hESCs	Human embryonic stem cells
MALDI-TOF MS	Matrix-assisted laser desorption/ionization Time-Of-Flight Mass Spectrometry
MET	Mesenchymal-to-epithelial transition
mOSE	Mouse ovarian surface epithelium
NPs	Nanoparticles
OC	Ovarian cancer
OST	Oligosaccharyl transferase
ROS	Reactive oxygen species
TEM	Transmission electron microscopy
TUSC3	Tumor suppressor candidate 3
UPR	Unfolded protein response

I. ABSTRACT

With prolonged life expectancy, aging and age-related disorders, such as cancer and degenerative diseases, become principal clinical as well as economic issues. Therefore, there is a compelling need to understand mechanisms altering cell and tissue morphology, to uncover the genetic background and function of individual genes associated with normal and abnormal histophysiology, and to develop novel methodological approaches revealing early alterations in cell and tissues. This habilitation thesis follows two research axes that aim to unravel the stress-induced alterations in normal and cancer epithelial cells and in parallel to introduce new tools applicable to modern state-of-the art histology and cell and tissue profiling. Using a broad spectrum of methods, ranging from classical immunohistochemistry to animal models, and deep molecular characterization of cell phenotypes, my research group identified a central role for endoplasmic reticulum in regulation of cell stress response during aging and/or cancer development, with the *TUSC3* gene involved. We discovered that *TUSC3* is a novel tumor suppressor gene in prostate and ovarian cancers and its loss evokes structural alterations within endoplasmic reticulum, enhanced cell survival and aggressive tumor growth. Moreover, epigenetic silencing of *TUSC3* predicts survival of cancer patients. Next, we addressed subtle alterations occurring in cells and tissues by the mass spectrometry coupled with artificial intelligence, and developed a powerful, robust and unbiased diagnostic tool for revealing unapparent patterns in cells and tissues. We validated this approach for identification of phenotypic shifts in cultured embryonic stem cells, and offered a promising quality-control tool for clinically oriented applications, contributing to development of personalized cell-based therapy in future.

II. INTRODUCTION

Virtually all higher multicellular organisms share the body plan composed of four principal tissue types, broadly categorized as epithelial, muscle, nerve and connective, that all have been traditionally considered as stable and determined. It was Xavier Bichat, a French anatomist, who for the first time recognized tissues as basic structural entities localized in body hierarchy between cells and organs, and classified them to more than twenty different types. His concept, however reflecting knowledge of the turn of the 19th century, complemented the theories of G.B. Morgagni and R. Virchow, and therefore laid the fundamentals for modern histology and pathology¹. The current understanding of structural organization of human body based on molecular and cell biology untied the four principal tissue categories and demonstrated that developmental potential of differentiated cells and their progenitors constituting individual tissue types can be altered in response to various developmental, physiological or even pathological stimuli. All cells of human body are exposed throughout their life to various sources of intrinsic and extrinsic stress, leading to accumulation of deleterious alterations of biomolecules, loss of cellular homeostasis and decay of tissue structures and functions. Abnormal changes at the cell and tissue levels are gradually followed by development of stress- or age-related disorders, like degenerative diseases or cancer².

Epithelial tissues emerged in metazoan evolution as remarkably organized structures, providing indispensable body barriers and functional interfaces. Major hallmarks of epithelial cytoarchitecture include defined morphology and distinct cell boundaries, presence of sophisticated intercellular junctions and adaptations of cell surfaces to various functions in tissues, such as transcellular transport, secretion, adhesion or sensing. Developmentally, epithelial surfaces convert to complex structures and their derivatives constitute fundamental organ systems. Moreover, differentiated epithelial tissues can rebuild their morphology and acquire new functional properties. This is most apparent during tissue regeneration or in pathological scenarios such as cancer,

when epithelial plasticity contributes to metastatic spreading or modifies a tumor niche towards immune escape and resistance to therapy³.

Molecular mechanisms that control cell biology and finally the tissue integrity, converge altogether to maintain lifelong homeostasis of different body systems. Deviations from tissue homeostasis in aging, injury or a general stress induced e.g. by viral infections, inflammation, hypoxia, oxidative stress, oncogene overexpression, telomere shortening, mechanical forces or cytotoxic compounds, are responded by virtually all types of mammalian cells by molecular events associated in broader context with the endoplasmic reticulum (ER). Molecular signaling initiated within ER then evokes an integrated response, leading to alterations of cell phenotype and effectual even beyond the scope of individual cells affecting tissue microenvironment, integrity, and function⁴.

While the last decades of cell research were dedicated to detailed description of genes and proteins within their individual structural, molecular and functional context, current understanding emphasizes their role within tissue morphology, histogenesis and histopathology, including development of techniques enabling novel and unbiased view on cell and tissue heterogeneity and variability. Research axes of the habilitation thesis are summarized in **Tab. 1** and defined in the following chapter.

Tab. 1. Research axes of the habilitation thesis

1. Investigation of the key molecular players that are involved in morphological and functional responses of epithelia in cancer, stress and aging.
2. Development of cell and tissue biotyping techniques based on mass spectrometry and machine-learning approaches.

III. AIMS

First, using ovarian cancer (OC) cell lines and the ovarian surface epithelium (OSE) as primary models, we investigate whether the alterations within the intrinsic molecular machinery associated with ER-stress response are capable of changing epithelial morphology or function (**Research axis I**), and second, we ask whether it is possible to reveal cell and tissue intrinsic heterogeneity and unambiguously distinguish morphologically uniform cells and tissues by mass spectrometry profiling (**Research axis II**).

Goals that are set up in this habilitation thesis and addressed in the accompanying set of publications, reveal the cell- and tissue plasticity driven by the ER-stress as a phenomenon deeply involved in alterations of tissue architecture in aging and cancer. In parallel, this habilitation thesis summarizes development of mass spectrometry-based profiling approaches, complementing the portfolio of classical histological approaches and cytometry methods for discrimination, classification and bio-typing of cells and tissues. Chemical composition of tissues traceable to individual molecular entities can provide a precise spectral fingerprint corresponding to cell phenotypes or states, including pathological scenarios. We demonstrated that multivariate datasets built on spectral fingerprints can serve as an input for sophisticated machine-learning tools that enable classification of non-linear data, and provide unbiased tool for cell and tissue authentication or diagnosis.

This habilitation thesis complements knowledge of classical morphology with molecular and cell biology, protein chemistry and analytical approaches, enabling better understanding of tissue structure and function.

The thesis represents a selected profile composed of eighteen author's publications elaborated between 2011-2018 at the Department of Histology and Embryology, Faculty of Medicine, Masaryk University. All the images, tables or research data presented here were acquired or designed by the author or members of his group, or obtained from author's publications. All details describing design of the research and experimental methods can be found in the attached publications. Quick references to author's publications are located next to the respective paragraph.

IV. RESULTS AND DISCUSSION

RESEARCH AXIS I

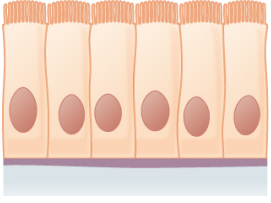
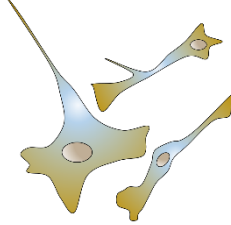
Epithelial plasticity in cancer, stress, and aging

EMT and cell senescence

In multicellular organisms including mammals, somatic cells exist in two principal morphological states, traditionally referred as “*epithelial*” and “*mesenchymal*”. Epithelial and mesenchymal phenotypes show distinct properties, including cell architecture, tissue morphology and variety of functional or molecular traits (**Tab. 2**).

These morphological and functional cell states are remarkably convertible, and mechanisms of epithelial-to-mesenchymal transition (EMT) drive crucial embryonic events, such as tissue morphogenesis and development, or tissue repair⁵. However, EMT is deeply involved also in organ fibrosis, cancer progression and development of distant metastases, organ failure or abnormal tissue repair, inflammation and scarification. Moreover, EMT is involved in remodeling of tissue microenvironment, mobilization of stem cells, regeneration, apoptosis and immunomodulation⁶⁻⁹. From a morphological point of view, EMT generally means conversion of adherent, *epithelial*, cells that are highly integrated in coherent tissue layers, to migratory, *mesenchymal*, state. In addition, EMT can be also reversed and cells of mesenchymal phenotype can acquire epithelial features, in the process of mesenchymal-to-epithelial-transition (MET). Molecularly, execution of EMT program is weaved into a signaling network interpreting various intrinsic and extrinsic stimuli. Cues that initiate EMT signaling include tissue-residing cytokines (e.g. TGF β ¹⁰), soluble molecules (Wnt, FGF^{11,12}), ECM- or cell-to-cell contacts (e.g. integrins, Rho-Rock pathway¹³, etc.) or numerous pro-inflammatory molecules⁹. There is substantial crosstalk of molecular signaling pathways in EMT making the conversion of the cell state tightly dependent on cell and tissue context¹⁴.

Tab. 2. Hallmarks of epithelial and mesenchymal phenotypes¹⁴

	<i>Epithelial</i>	<i>Mesenchymal (fibroblast-like)</i>
Cell type		
Localization in tissue	Adherent	Migratory
Tissue morphology	Coherent cell layers or cords	Individual, usually spindle-shape cells
Cell polarity	Apicobasal polarity	Non-polarized
Basement membrane	Yes	No
Intercellular junctions	Abundant	Absent
Cytoskeletal markers	Cytokeratins	Vimentin
Cell surface markers	E-cadherin, ZO-1	N-cadherin
Transcription factors	Tissue specific factors	Snail1/2, Twist, ZEB1
Extracellular proteins	Laminin 1, Collagen IV	Collagen I/III, Fibronectin
Anchorage-dependent survival	Yes	No
Typical functions	Barriers, transport, sensing, mechanical protection	Production of ECM, stromal cytokines and growth factors

Development of epithelial tissues can be traced back to embryoblast and bilaminar germ disc stages, where series of EMT ↔ MET represent a building principle that establishes the body plan during embryonic development of vertebrates, and probably all metazoans¹⁵. Embryonic EMT is induced even before implantation during formation of embryoblast, later during the germ disc differentiation, and even later in gastrulation and development of axial embryonic structures, such as primitive streak and axial mesoderm. EMT is also a driving mechanism of development of invasive extra-villous trophoblast and placenta formation¹⁶. In primary embryonic EMT, epiblast cells in epithelial state that form dorsal surface of bilaminar germ disc undergo conversion to mesenchymal state forming endoderm and mesoderm germ layers by subsequent MET steps. Next, as the mesodermal cells are exposed to varying morphogenetic signaling fields,

they form temporary embryonic epithelial structures, such as notochord, somites of paraxial mesoderm, mesodermal nephritic ducts or splanchnopleuric and somatopleuric lining that further undergo events of secondary EMT. By tertiary EMT, endocardial cushions develop e.g. into heart valves.

EMT is also tightly associated with tissue regeneration and aging. The embryonic genetic program of EMT can be recalled during wound healing and physiological tissue regeneration⁵. During tissue injury, EMT is transiently activated leading to epithelial migration from surrounding epithelial layers and differentiation of (myo)fibroblasts from progenitors residing in connective tissue. After re-epithelization and extracellular matrix (ECM) recovery, the EMT signaling is attenuated. However, this program can be hijacked in pathological scenarios, especially malignancy, and the EMT signaling is sustained typically by pro-inflammatory signaling. As a result, obstruction of re-epithelization and abnormal activity of fibroblasts lead to fibrogenesis and abnormal composition of tissue microenvironment⁸. The typical clinical example of failed control of EMT is the kidney fibrosis¹⁷. In cancer research, hints on development of tumors were inferred from abnormal tissue regeneration and cancerous tissues were described as “*wounds that do not heal*”, more than three decades ago¹⁸. Indeed, cancer cells are capable of multiple phenotype switches that involves molecular machinery similar or even identical to EMT resulting in the metastatic spreading¹⁹. The cancer EMT and the tumor invasion resulting in organ failure are then the cellular “*causa mortis*” of patients with advanced malignancy.

During aging, tissues and organs suffer from accumulation of deleterious changes on both the cellular and molecular levels, principally by losing balance between tissue damage and repair. Principally, tissues lose their integrity and functions by alterations of cellular and chemical composition, declining from original morphology, with EMT representing one of the mechanisms available even to clinical targeting²⁰. On cell level, the term “senescence” is linked to individual cell entities, and is defined as a state of permanent cell cycle arrest, originally described by Leonard Hayflick in early sixties of the 20th century^{21,22}. A somatic cell can quit cell cycle and become senescent by various intrinsic cues, including telomere shortening and limited replicative capacity, or by too excessive

damage caused by variety of extracellular factors, mostly chemical and physical stressors converging to the similar cell response. Generally, hallmarks of senescent cells include high expression of cell cycle inhibitors, formation of heterochromatin foci in nucleus and accumulation of gene expression changes, such as upregulation of the prototypical marker of senescent cells, the senescence-associated β galactosidase (SA- β Gal)²³ (**Fig. 1, Tab. 3**). In the tissue microenvironment, the induction of senescence represents a powerful tumor-suppressive mechanism preventing proliferation of aberrant cells. Importantly, senescent cells are not metabolically quiescent, and can acquire new capabilities, such as secretion of inflammatory cytokines, growth factors and neuro- and immune modulators. Collectively, this phenomenon called “senescence-associated secretory phenotype” (SASP), has been originally described by Krtolica et al in 2001²⁴ in

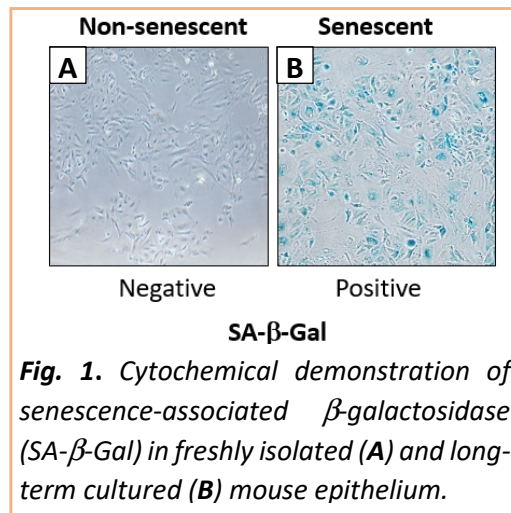


Fig. 1. Cytochemical demonstration of senescence-associated β -galactosidase (SA- β -Gal) in freshly isolated (A) and long-term cultured (B) mouse epithelium.

cancer context, documenting that senescent fibroblasts promote proliferation of cancer cells. SASP is also tightly associated with remodeling of tumor microenvironment by production of matrix-metalloproteases that facilitate tumor spreading through tissues. In prostate cancer, androgen depletion induces senescence of a minor population of neurosecretory cells that in response to the lack of androgen signaling acquire SASP and contribute to development of castration-resistant prostate cancer²⁵. In ovarian surface epithelium, estrogen deprivation in menopause alters the morphology and enhances permissibility to development of inclusion cysts or ovarian cancer. In connective tissue supporting epithelia (typically in *lamina propria mucosae*), senescent fibroblasts are potent inducers of EMT²⁶, while the senescence itself can be evoked by extrinsic stress, e.g. metabolite overload (e.g. abnormal glycemia)²⁷ or chemical compounds, including those used for the cytotoxic therapy^{28,29}. Cell stress signaling, induction of senescence and induction of EMT then integrate on cell phenotype altering tissue architecture and integrity.

Pernicová et al. 2013

Trudu et al. 2015

Tab 3. Hallmarks of cell senescence

Initiating event	Senescence-associated phenotype	Molecular signaling
<ul style="list-style-type: none"> • ROS damage • DNA damage • Telomere shortening • Alterations of ER and mitochondria • Stress signaling • Growth factor deprivation • Overexpression of oncogenes • Loss of tumor suppressors • Metabolic overload 	<ul style="list-style-type: none"> • Morphology alterations • Cell cycle arrest • Acquisition of SA-β-Gal • Secretory phenotype • Heterochromatin foci • Alteration of gene expression patterns • Tissue remodeling • Inflammation 	<ul style="list-style-type: none"> • γH2AX, ATM/ATR pathway • p38/JNK/SAPK, • Rb/E2F • p53/p21^{CIP1/WAF1} • CHK2 • p16^{INK4} • MMPs • PERK/IRE1α/ATF6 (UPR) pathway

Endoplasmic reticulum is linked to tissue morphology, development, and aging

Cues that change the cells states by induction of EMT can be evoked by the cell extrinsic or intrinsic sources¹⁴. Molecular signaling initiated from within the cell or from individual cell organelles, can induce gross changes of cell morphology or functions, having structural or functional effects also beyond the scope of individual cells towards the tissue microenvironment. One of these uniquely signaling organelles is the endoplasmic reticulum (ER). ER forms a complex system of flattened cisterns and tubules and represents a major membrane organelle within a eukaryotic cells (**Fig. 2**). ER is principally involved in synthesis of secreted and membranous proteins and their posttranslational modifications, calcium storage and biogenesis of cell membranes and many others cell tasks (**Tab. 4**). During proteosynthesis, nascent proteins are translated into the ER lumen where they are co-translationally and/or post-translationally modified with oligosaccharyl residues. Such glycosylated motifs are targets for intra-ER chaperones, such as Calnexin and Calreticulin. Properly folded proteins are then addressed to the Golgi apparatus and shipped to the extracellular surface by the secretory pathway or to other intracellular organelles^{30,31}.

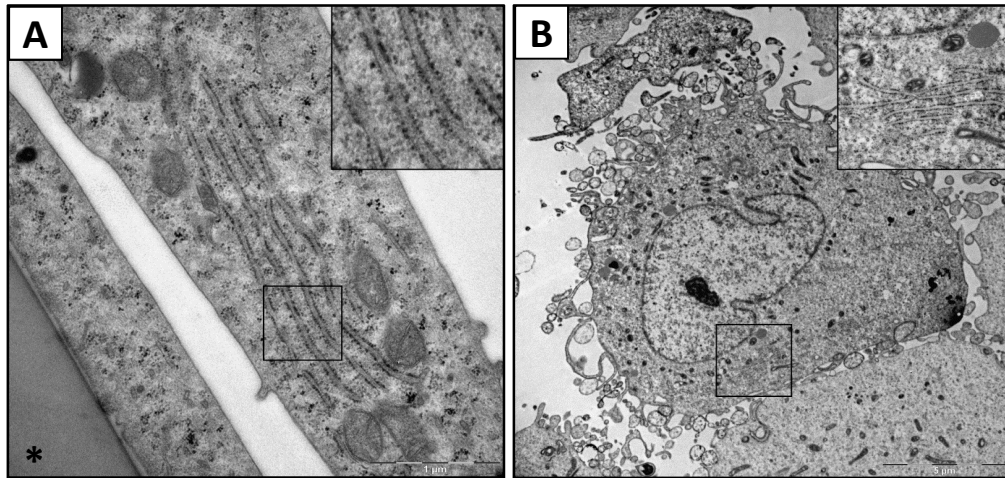


Fig. 2. Cisterns of rough ER form well-developed arrays in cultured ovarian cancer cell line SKOV-3, as revealed by transmission electron microscopy (TEM). **(A)** TEM of adherent cells. Asterisk indicates the culture surface. Scale bar 1 μm . **(B)** TEM of cells detached to suspension. Scale bar 5 μm . Both insets show magnified arrays of ER.

Tab. 4. Overview of essential functions of endoplasmic reticulum

- Synthesis, maturation, modifications, quality control, and degradation of proteins
- Biogenesis of cell membranes and lipid homeostasis
- Formation of intracellular vesicles and intracellular transport
- Hormone synthesis and other diverse anabolic and catabolic reactions
- Ion storage (e.g. Ca^{2+}) and dynamics of intracellular flow of ions
- Control of metabolism and cell cycle in response to intrinsic and extrinsic cues
- Cell stress response

Since the discovery of the ER by Albert Claude in the early forties of 20th century³² and a series of pioneering publications with George Palade that identified the fundamental structure of the ER and suggested the proteosynthetic function of the ER³³, and liver and pancreatic microsomal compartments³⁴⁻³⁶, the ER has been revealed as a complex organelle that regulates numerous aspects of cellular life. Recently, ER was established also as the important signaling hub integrating both cell-intrinsic (metabolic) and cell-extrinsic (environmental) stress signals including those evoked in aged or cancerous tissues, that agitate the cell homeostasis and compromise protein folding or trafficking, and thus inducing the ER-stress. Morphologically, ER-stress is pronounced by dilatations of ER cisterns **(Fig. 3)**^{4,37}.

Kratochvílová
et al. 2015

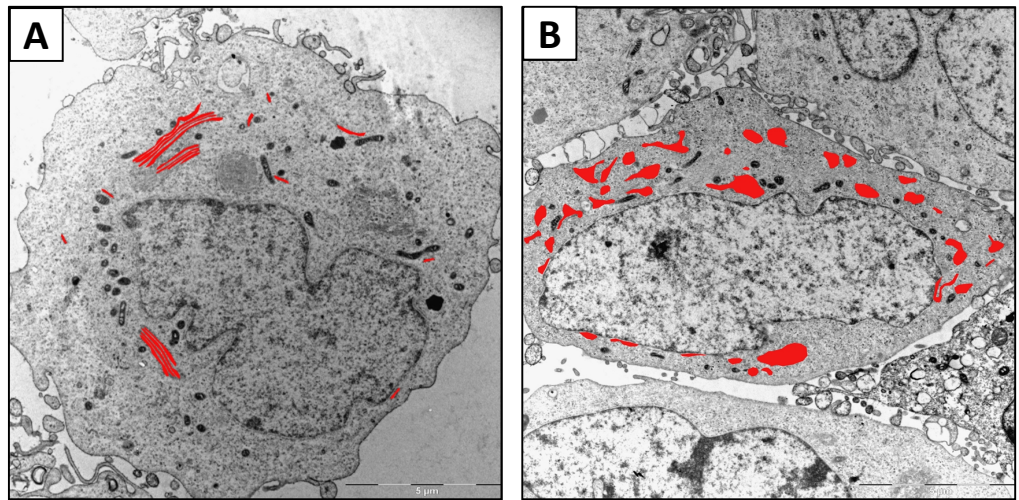


Fig. 3. ER cisterns dilate upon ER-stress. When the cells of the ovarian cancer cell line SKOV-3 were exposed to tunicamycin, a compound inducing ER-stress, cisterns of rough ER lost their regular arrangement and become strongly dilated (TEM). ER cisterns visualized in red. Scale bar 5 μ m. (A) control, (B) tunicamycin 0.5 μ M/24 hrs.

On the molecular level, accumulation of abnormal, misfolded or underglycosylated proteins in ER cisterns initiates a global signaling response termed Unfolded Protein Response (UPR). The UPR is composed of three sensor proteins embedded in ER membrane, PERK, IRE1 and ATF6 that link the ER both to the nucleus and cytoplasm, controlling transcription machinery and ribosomal assembly, respectively. Numerous extracellular or intracellular cues cause accumulation of abnormal proteins in ER or evoke UPR directly. Typically, abnormal proteins expose unusual glycan motifs and sequester the ER chaperon GRP78 and dissociate it from ER-membrane sensors: PERK phosphorylates translation initiation factor eIF2 α that results in attenuation of proteosynthesis but enhanced translation of ATF4 and transcription of ATF4-controlled promoters. IRE1 alternatively splices mRNA of Xbp-1 transcription factor and induces expression from promoters containing ER-stress elements (ER SE). Cleavage of transcription factor ATF6^{p50} by Golgi proteases produces the transcriptionally active form of ATF6^{p50} (Fig. 4). Crosstalk of these prototypical signaling pathways then determines the cell fate towards adaptation to ER-stress or to cell death³⁸.

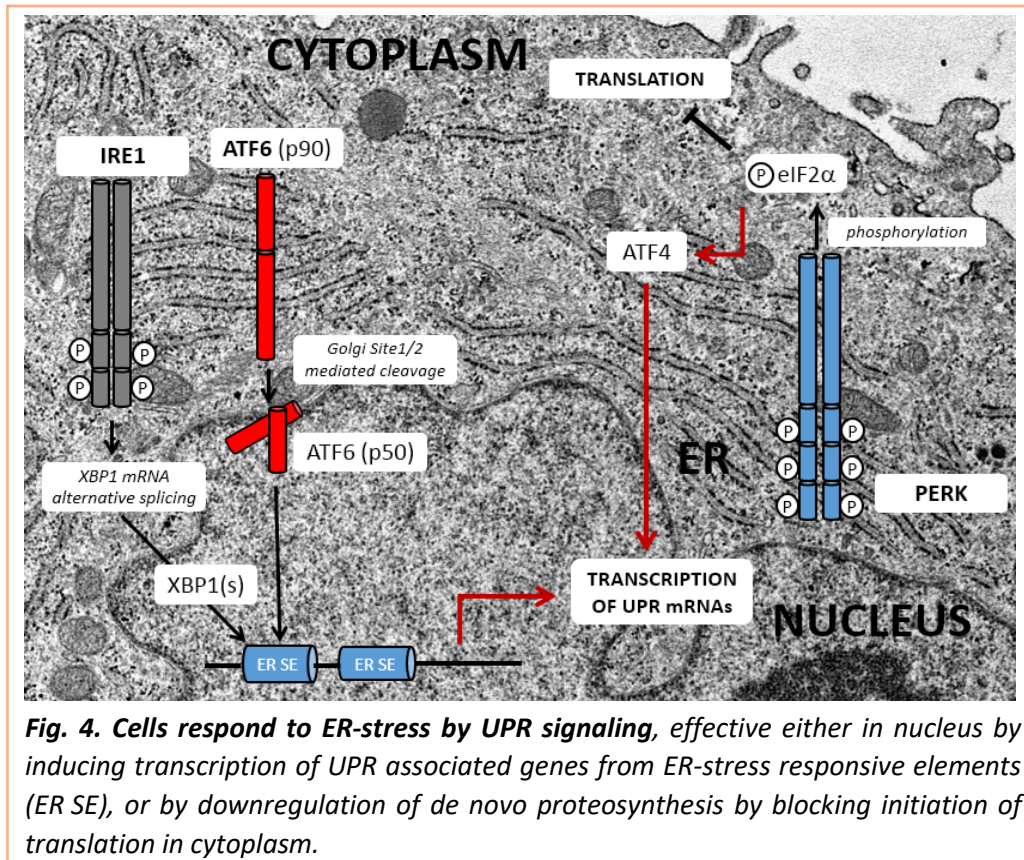
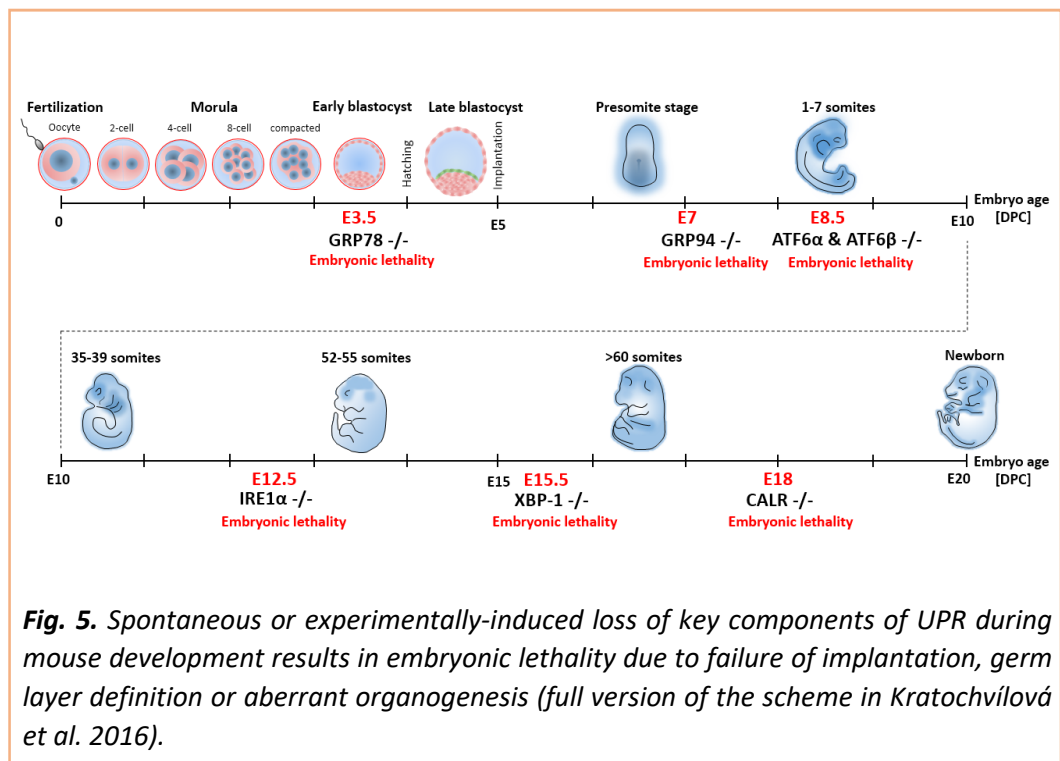


Fig. 4. Cells respond to ER-stress by UPR signaling, effective either in nucleus by inducing transcription of UPR associated genes from ER-stress responsive elements (ER SE), or by downregulation of de novo proteosynthesis by blocking initiation of translation in cytoplasm.

Individual components of ER-stress response machinery are in most cases indispensable during mammalian embryonic development. Mammalian zygotes and early embryos are exposed to various intrinsic or extrinsic stressors in their surrounding microenvironments, e.g., mechanical, oxidative, osmotic, and pH stress, as well as immunological and direct embryo-endometrium interactions. All these signals, together with a high rate of embryonic proteosynthesis, integrate at the ER and induce UPR in exposed cells^{39,40}. To compensate the ER-stress, embryonic cells recruit a wide range of ER chaperones and elements of the UPR network. In fact, homozygous deletions of ER-stress and UPR effectors, such as GRP78, GRP94, GRP58/ERp57, Ire1 α , XBP-1, Calreticulin, and double deletion of both ATF6 α and ATF6 β , result in embryonic lethality in mice. Mouse blastocysts lacking BiP (GRP78/HSPA5) or GRP94 chaperons fail to initiate EMT and hatch from *zona pellucida* or to develop the primitive streak, respectively. The absence of sensors (ATF6 or IRE1) or effectors (Xbp-1, CALR) then prevents proper establishment of fetoplacental unit or restrains development of organs, suggesting alterations in tissue-specific stem cell pools due to abnormal UPR signaling (Fig. 5).

Kratochvílová
et al. 2016



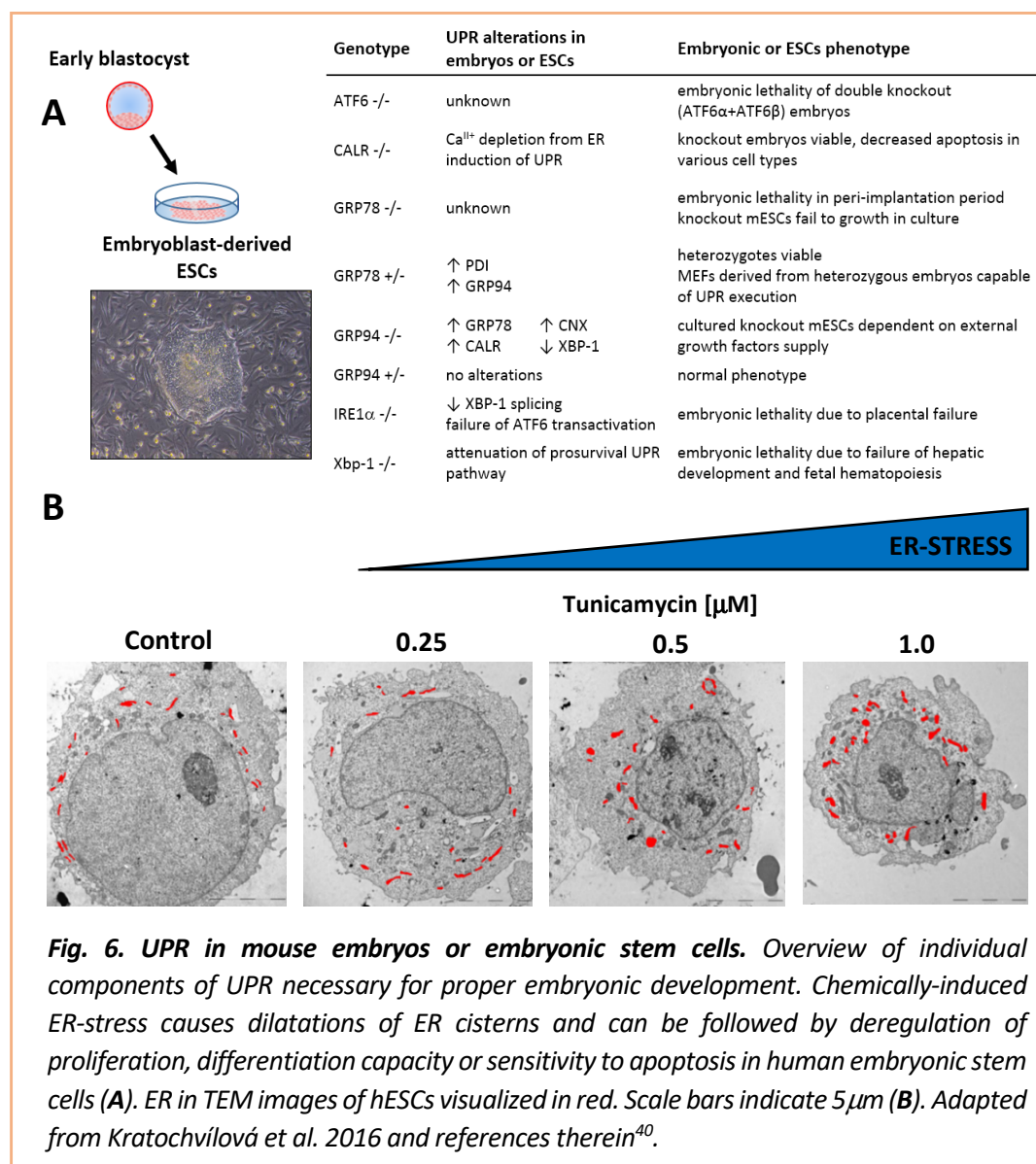
The cultured embryonic stem cells (ESCs) are, similarly to developing embryos, exposed to numerous stress factors coming from the culture microenvironment. ESCs are then exposed to Darwinian selection of successful clones, contributing to development of culture adaptation phenomena. Moreover, the method of culturing ESCs aims to preserve pluripotency and self-renewal, both contributing to proteosynthesis overload. Blanco-Gelaz et al.⁴¹ reported in 2010 a culture-dependent activation of UPR in the human ESC (hESC) lines HS181 and SHEF-1 when they were cultured on a feeder composed of human embryonic fibroblasts and in a feeder-free system composed of a mixture of extracellular matrix proteins (e.g. Matrigel™). In our experiments, we have also documented that human ESCs suffer from ER-stress in culture (Fig. 6) and eliciting of UPR contributes to general stress response that can include alterations in proteome, metabolome or secretome^{40,42,43}. Such global events occurring in cultures are then accessible by bioanalytical methods (see **Research axis II**). Thus, the knowledge obtained from embryonic development can be directly translated into research-oriented or clinical-grade long term cultures of pluripotent stem cells⁴ and tissue engineering.

Kratochvílová et al. 2016

Stress conditions evoked in responsive cells can propagate to the surrounding tissue microenvironment and affect other cell populations or tissue structures. In our models, we documented altered expression of TGF- β cytokines³⁷ capable of induction of EMT and tissue remodeling, and other works demonstrated cascade-propagation of molecular patterns associated with ER-stress through immune cells residing in the tissue and altering the tissue homeostasis. These findings underline the significance of stress-induced signaling that is associated with etiology of various pathologies and normal tissue homeostasis. For in-depth reviews see^{38,44-45}.

Kratochvílová et al. 2015

Vaňhara et al. 2012



Kratochvílová et al. 2016

Epithelial plasticity: lessons from ovarian surface epithelium

In many tissues morphological changes and molecular phenotypes associated with aging are hidden. Currently, majority of cell and tissue models are derived from tumors or are inevitably biased to cancer. A suitable tissue model that enables addressing molecular and cellular cues associated with cell stress and aging, has to meet stringent requirements and generally not present abnormal outputs (e.g. isolation- or culture-induced artifacts).

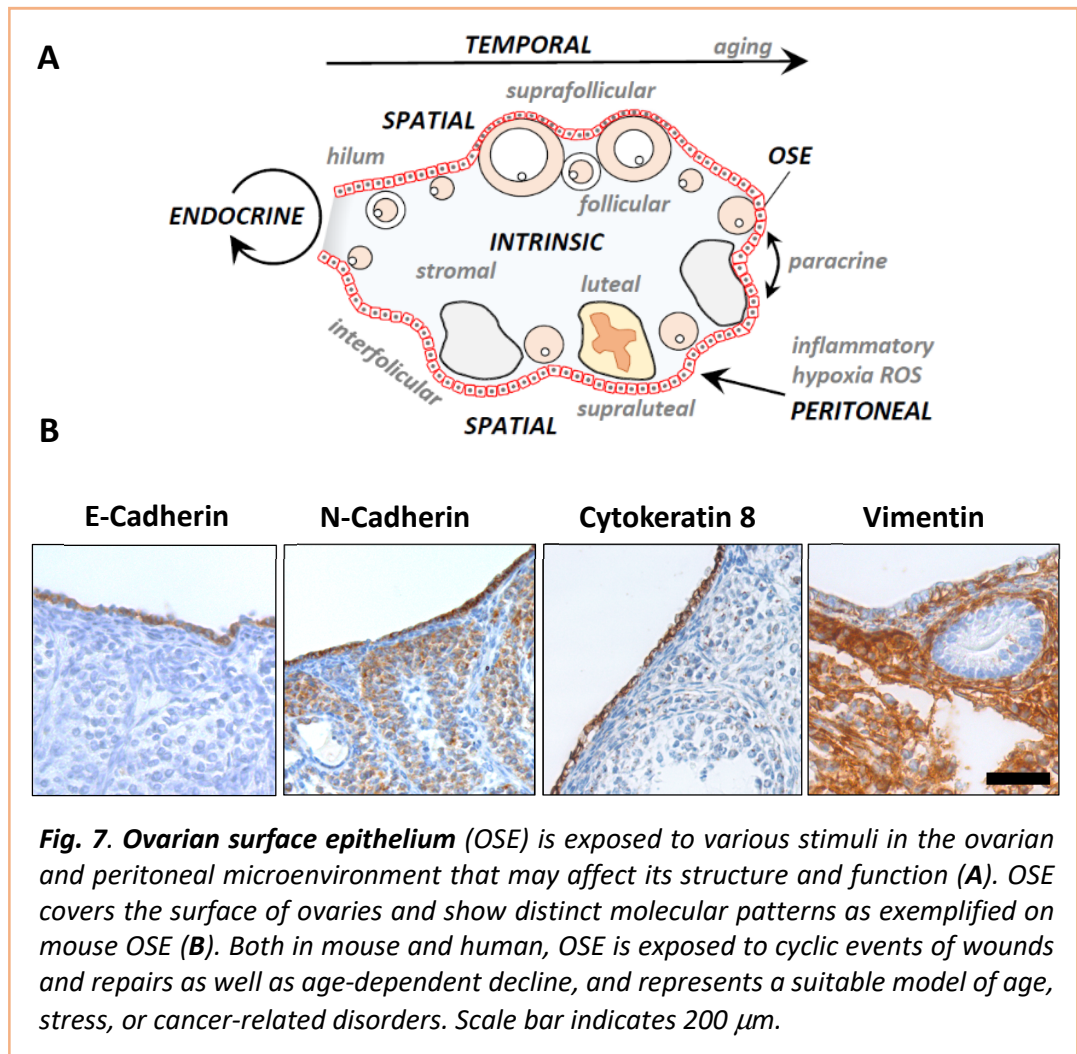
*Vašíčková
et al. 2018*

Mammalian ovaries and especially their superficial epithelial lining (ovarian surface epithelium, OSE) are easily accessible and allow clinically highly relevant modelling of morphological and functional alterations⁴⁶ (**Tab. 5**).

Tab. 5. Advantages of OSE for modelling tissue plasticity associated with aging, stress and cancer

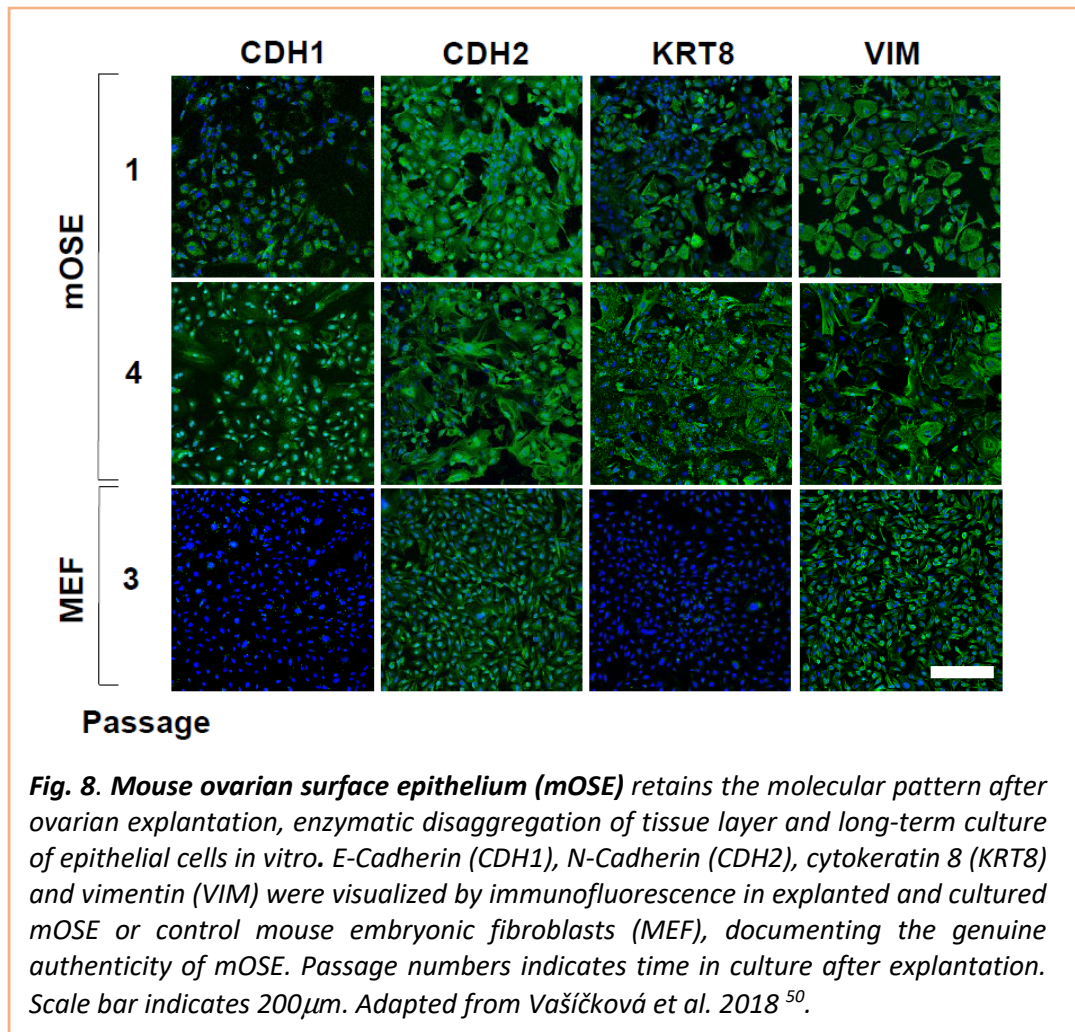
- High intrinsic morphological plasticity
- Physiological cycles of wounding and repair
- Apparent age-dependent cytological changes
- Hormonal sensitivity
- Easy isolation and culture
- High clinical relevance

Ovarian surface epithelium is a highly dynamic tissue structure, developmentally enabling formation of ovarian follicles, then during the fertile period undergoing regular cyclic reparations of ovulatory ruptures to decline finally both functionally and structurally after the menopause. Depending on the phase of the ovulatory/menstrual cycle, OSE forms a simple layer of squamous-to-cubic cells that express markers of both epithelial and mesenchymal phenotypes⁴⁷. OSE is physiologically exposed to stress events in ovulatory cycles of wounding and regeneration (**Fig. 7**). Repeated ovulations or ovarian stimulation were described to increase the risk of cancer, by disturbing mitochondrial metabolism and cell response to reactive oxygen species (ROS) stress or importantly, senescence and EMT-associated events⁶.



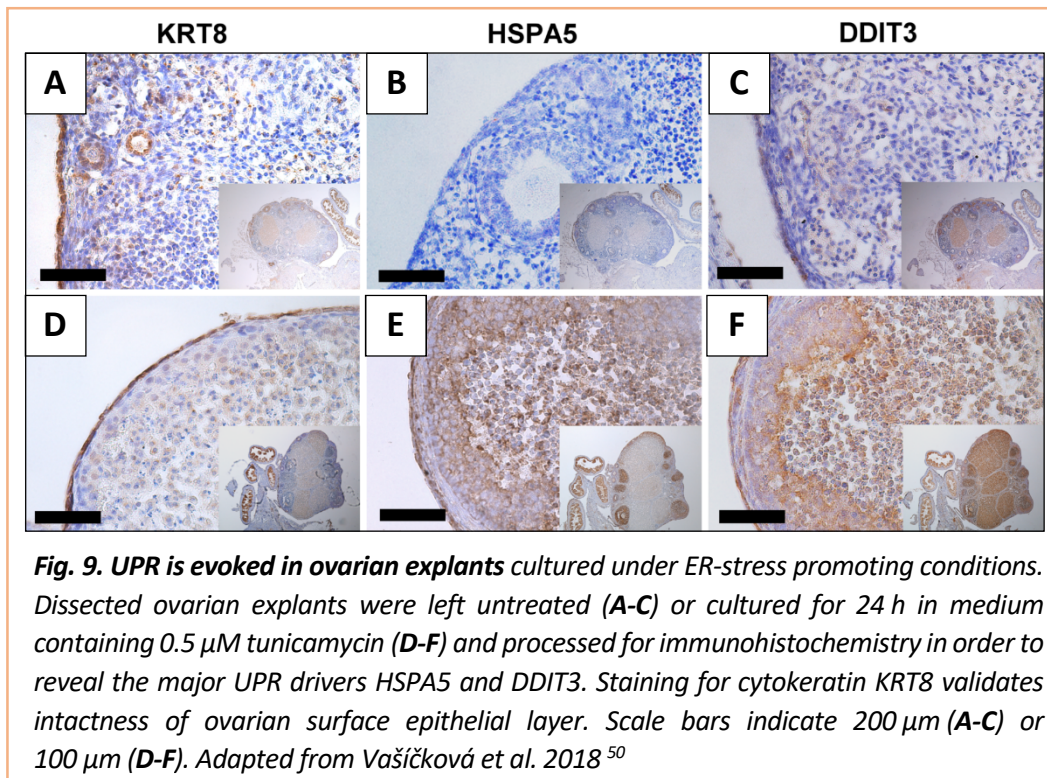
In aged, post-menopausal ovaries, the OSE proliferation and regeneration are uncoupled from the endocrine control and declines, epithelial lining flattens, but cancer-prone inclusion cysts and epithelial invaginations often develop in the stroma, representing a potentially hazardous precancerous condition. During menopause, imbalance of the microenvironment towards increased cells stress is evoked; mostly by estrogen loss, increased ROS and DNA damage or alterations of soluble endocrine, growth, or inflammatory factors and cytokines⁴⁷⁻⁴⁹. In summary, OSE is an easily accessible, morphologically well-defined and clinically highly relevant model for addressing questions related to cell stress, tissue aging and cancer. We adapted *ex vivo* explantation of delicate mouse OSE cells to preserve their phenotype and molecular patterns in long-term culture⁵⁰. Cells of OSE can be easily distinguished from stromal mesenchymal carryovers, e.g. fibroblasts (Fig. 8).

Vašíčková et al. 2018



Alleviation of ER-stress in senescent epithelium delays onset of senescence

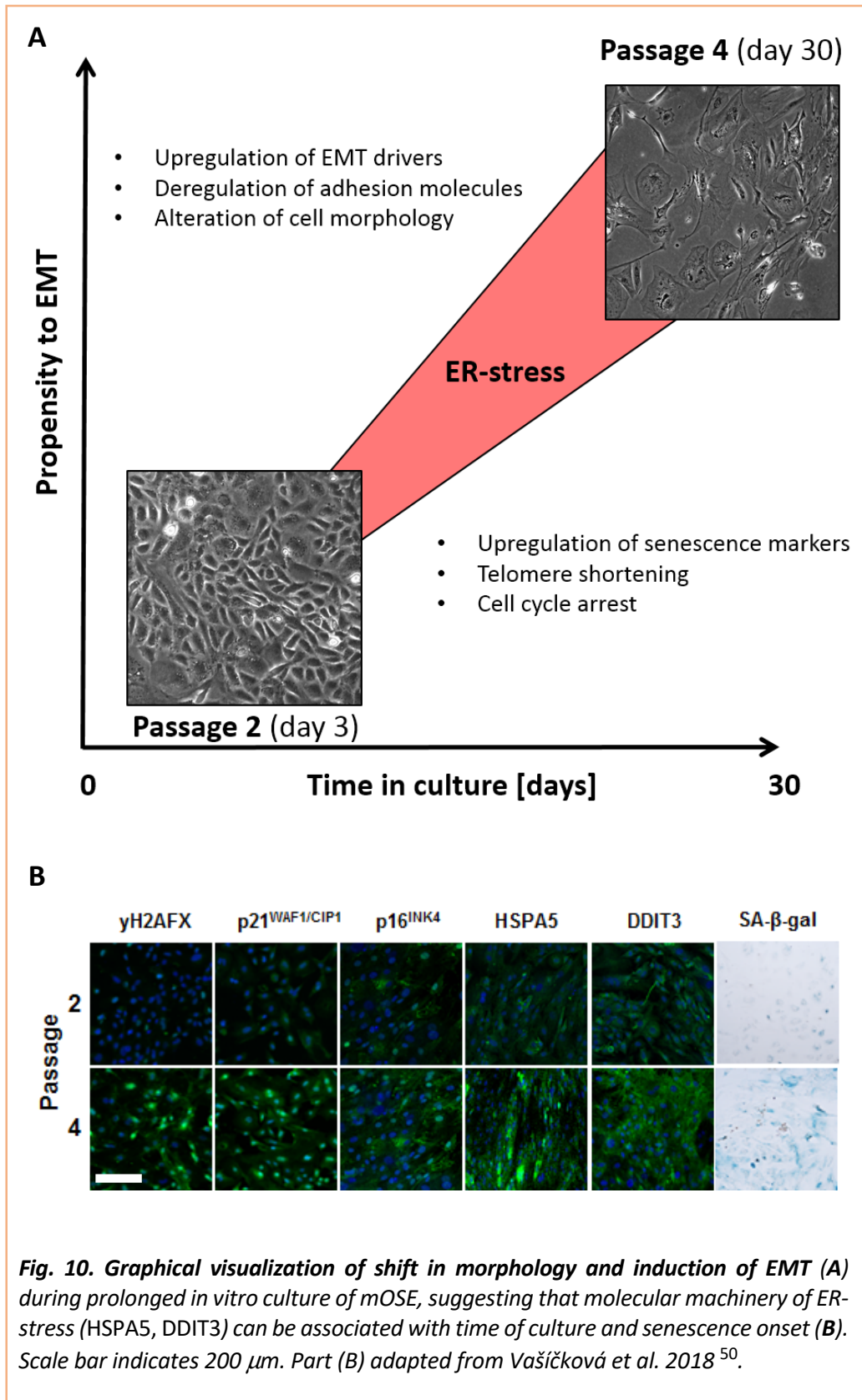
Learnt from the importance of ER-stress during embryonic development and histogenesis, we were curious, if the ER-stress can represent a factor altering morphology of normal epithelium and enhance the propensity towards senescence or cancer initiation and progression. The mouse OSE cells (mOSE) represent a unique model allowing addressing morphological as well as molecular questions with factual clinical significance. First, we validated that mOSE localized *in situ* still possess the necessary molecular machinery and can execute UPR under ER-stress evoking conditions. Indeed, the mOSE layer in explanted ovaries shows the genuine pattern of ER-stress drivers, and this molecular profile is not altered during organ explantation and enzymatic detachment of the epithelial lining (Fig. 9). This allowed us to study epithelial responses in a scenario that is physiologically close to the state *in vivo*⁵⁰.

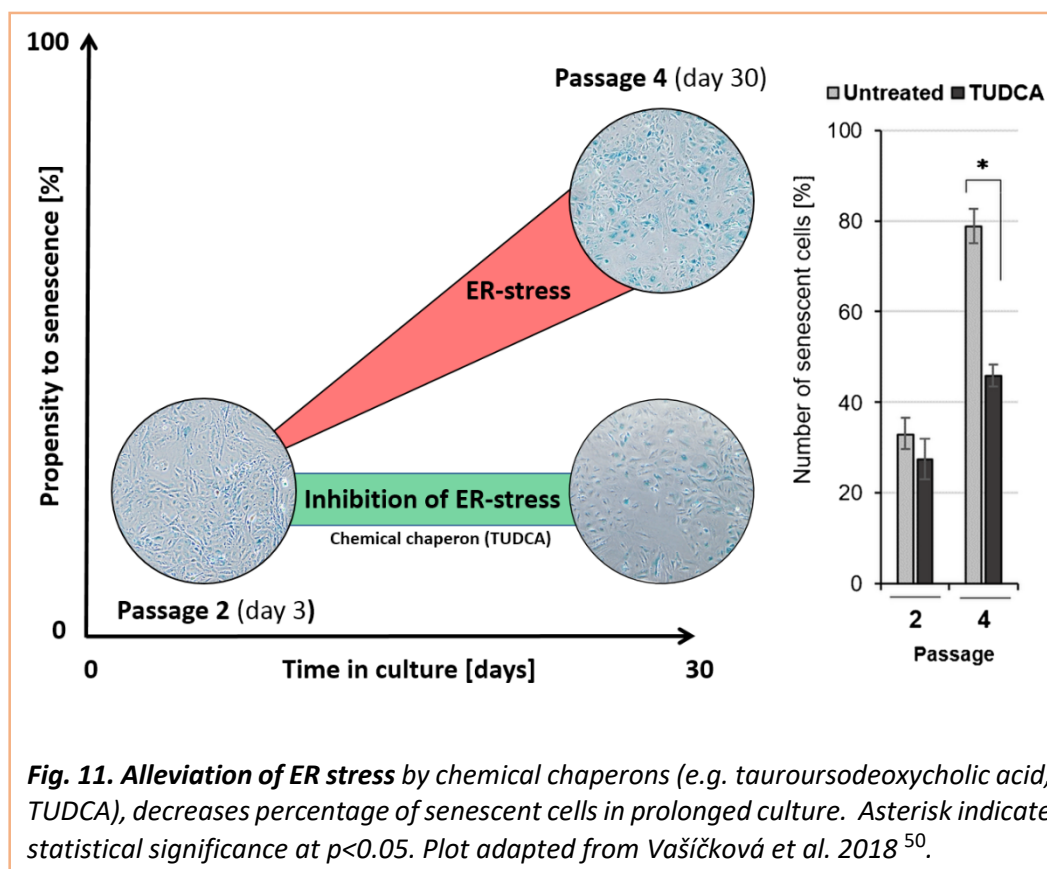


To reveal a link between the ER and cell senescence, we cultured explanted mOSE cells and assessed their morphology, ultrastructural abnormalities, functional responses and molecular patterns. Indeed, the cell morphology shifted towards mesenchymal appearance during the long-term culture, and in parallel markers of senescence, EMT and key components of UPR were upregulated. Therefore we got an initial mechanistic insight about the connection of ER-stress and EMT in ovarian epithelial lining (**Fig. 10**).

Speculating that ER-stress evoked during replicative senescence can be a causative mechanism affecting both the senescence and EMT, we investigated whether alteration of UPR machinery by chemical compounds leads to phenotypic changes. We alleviated load of misfolded nascent proteins in ER by chemical chaperons (TUDCA), and interestingly, number of senescence cells significantly decreased (**Fig. 11**), while their morphology remained rather unchanged. Thus, as we demonstrated by experimental attenuation of pro-apoptotic UPR branch, the permanent pro-survival signaling from the ER resulted in delayed onset of senescence, override of cell cycle arrest and alterations in EMT machinery⁵⁰.

Vašíčková
et al. 2018





In summary, deregulation of OSE under stress or senescence conditions could represent a potentially hazardous event that may form a permissive microenvironment for direct malignant transformation of OSE or the colonization of ovarian surface by cancers cells from extra-ovarian sources, and eventually development of ovarian cancer. Taken together, we revealed for the first time a direct predisposition to pro-survival UPR signaling in ageing OSE, which can represent a risk factor contributing to senescence override and malignant transformation⁵⁰.

Vašíčková et al. 2018

TUSC3 is a novel genetic driver of ER-stress involved in ovarian cancer and aging

According to the American Cancer Society, ovarian cancer (OC) is one of the most common malignancies and the fifth leading cause of cancer-related death in women⁵¹. Despite the recent progress in OC diagnosis and therapy, its overall prognosis remains unfavorable. The heterogeneity of its clinical display reflects the diverse molecular mechanisms contributing to malignant transformation and dissemination of the primary cancer. The origin of OC has traditionally been assigned to OSE, as the likely source of transformed cells, but recently, the extra-ovarian sources were suggested, such as endometrium of fallopian tube lining⁵². The permissivity of OSE to harbor disseminated cancer cells, however, appear to be a substantial condition for cancer spreading on the ovary, as we demonstrated in the mouse model⁵⁰. The molecular mechanism driving OSE either to malignant transformation or altering its phenotype towards permissive microenvironment, are despite the great progress in recent years still unclear.

Vašíčková et al. 2018

We have identified, by previous systematic screenings of the 8p22 chromosomal region of ovarian cancer (OC) patients, a novel, highly conserved tumor suppressor candidate 3 (*TUSC3*) gene affecting survival of OC patients⁵³. Expression of *TUSC3* was epigenetically silenced in high frequency of malignant cases and its loss correlated significantly with shortened disease-free or overall survival of OC patients. Methylation of *TUSC3* promotor provided a significant prognostic information comparable with FIGO staging, residual disease or response to the therapy (**Fig. 12**).

Pils et al. 2012

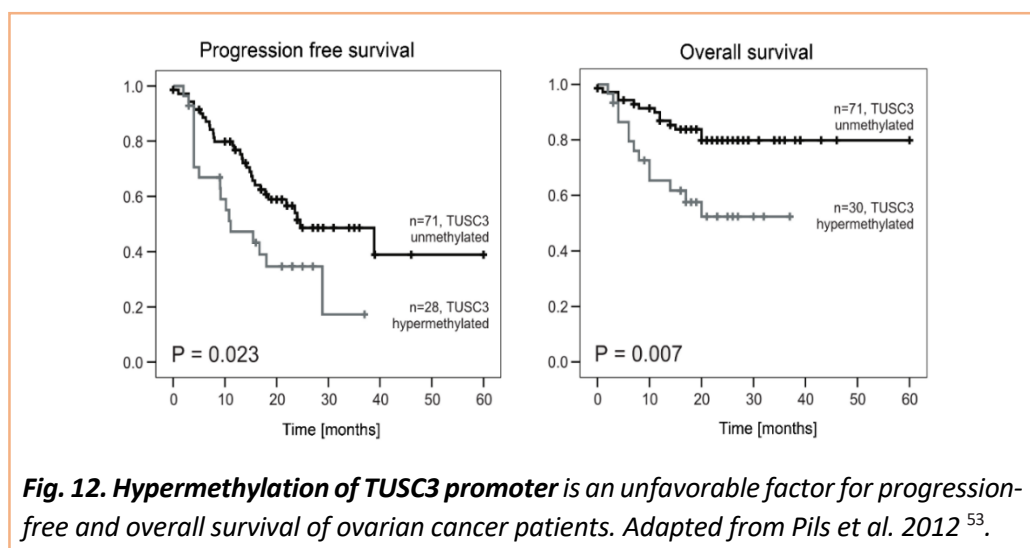


Fig. 12. Hypermethylation of *TUSC3* promoter is an unfavorable factor for progression-free and overall survival of ovarian cancer patients. Adapted from Pils et al. 2012⁵³.

However, no information on molecular function of *TUSC3* within cells and tissues explaining the observed phenomena was available at that time. Until recently, the molecular function of *TUSC3* protein was only inferred from its partial sequence homology to the yeast protein Ost3p, which forms a subunit of the oligosaccharyl transferase (OST) complex responsible for post- and co-translational N-glycosylation of proteins in the ER. OST is part of translocation channel in ER membrane and catalyzes transfer of nascent oligosaccharide from lipid carrier onto amino acid except proline. OST complex selects proteins for N-glycosylation and defines also the pattern of oligosaccharides on secreted proteins that enable entry into the secretory pathway from the ER towards the cell surface⁵⁴.

Thus we focused on intracellular localization of *TUSC3* first, and indeed, we revealed that *TUSC3*, the predicted subunit of OST, localizes directly to ER and physically interacts with catalytic core of OST, the STT3A/B proteins^{55,56}. Localization *TUSC3* was recently validated as the genuine part of the OST complex by crystallography and a role for *TUSC3* in selection of protein substrates to N-glycosylation by OST was suggested⁵⁷.

Vañhara et al. 2013

Horak et al. 2014

Observation that loss of *TUSC3* expression affects clinical parameters of OC patients, prompted us further to reveal its function in ovarian cancer cells. When we analyzed phenotype of cancer cells lacking or overexpressing *TUSC3* gene, we demonstrated that cells with silenced expression of *TUSC3* showed strong and stable hallmarks of invasive cancer phenotype, such as propensity to EMT, reduced doubling-time and massive growth of xenografted tumors in experimental mice followed by metastatic spreading^{37,58}. All these cues prompted us to investigate alterations within ER machinery and the cellular response to ER-stress associated with N-glycosylation. To mimic accumulation of abnormal proteins in ER, we used again tunicamycin, the well-established inhibitor of early steps of N-glycosylation. When we analyzed the UPR activity of OC cells cultured under tunicamycin induced ER-stress conditions, we showed that the siRNA-mediated downregulation of *TUSC3* expression, surprisingly switched the UPR signaling from *pro-apoptotic* to *pro-survival* pathway³⁷.

Kratochvilová et al. 2015

Moreover, *TUSC3*-downregulated OC cells altered expression of N-glycosylated adhesion molecules (e.g. E-cadherin, ZO-1) and were more resistant to exogenous inducers of ER-stress both in two-dimensional (2D) and three-dimensional (3D) *in vitro* cultures. This effect can possess a significant clinical relevance, as ovarian cancer cells typically delaminate from the primary tumor site and spread throughout the peritoneal cavity in the form of multicellular aggregates, adhering to the mesothelium and extracellular matrix (ECM)⁵⁸. Thus, to gain further insight into the role of *TUSC3* in the dissemination of ovarian cancer or tissue stability, 3D spheroids from control and *TUSC3*-manipulated OC cells were generated. Using time-lapse microscopy, we revealed that *TUSC3*-expressing cells assembled into compact clusters within 8–10 hours. Interestingly, *TUSC3*-silenced cells assembled into 3D aggregates in a significantly shorter time than controls, however, no significant difference in spheroid size or frequency of cell death was observed. Next, we were curious if induction of ER-stress would affect formation of such multicellular aggregates. Ovarian cancer cells were specifically exposed to ER-stress conditions and monitored using time-lapse microscopy. Surprisingly, ER-stress resulted in massive disintegration of spheroids derived from cells that physiologically or ectopically expressed *TUSC3* protein. This was not observed in spheroids generated from cells lacking *TUSC3*, as downregulation of *TUSC3* enhanced the formation of 3D spheroids and also attenuated the effect of ER-stress on intercellular interactions without directly affecting cell viability. We thus determined for the first time the *TUSC3* protein acts a genuine regulator of ER homeostasis that if lost, induces significant alterations of epithelial cells towards invasive OC phenotype. Indeed, when introduced *in vivo*, xenografts derived from *TUSC3*-silenced cells grew faster than controls and also disseminated massively through peritoneal cavity of experimental mice³⁷. Very similar phenotype was observed in prostate cancer. Here *TUSC3* preferentially localizes to epithelial lining of prostate glands rather than to fibromuscular stroma (**Fig. 13**) and its loss evokes massive abnormalities within ER and enhanced tumor growth in mouse models. Also, in prostate cancer, *TUSC3* was downregulated in tumors of higher stages, and its expression correlated with promoter hypermethylation. Taken together, we identified for

Kratochvílová
et al. 2015

the first time *TUSC3* as a novel tumor suppressor gene with a direct impact on cell ultrastructure and cell survival with significant clinical importance.

Horak et al. 2014

In consonance with our observations³⁷, other groups recently confirmed *TUSC3* as the tumor suppressor also in other cancers, such as lung and pancreatic cancer or glioblastoma, with impact on the clinical outcome of cancer patients. In other types of malignancies, e.g. colon cancer or particular types of lung cancer, *TUSC3* was shown to be acting rather as an oncogene than tumor-

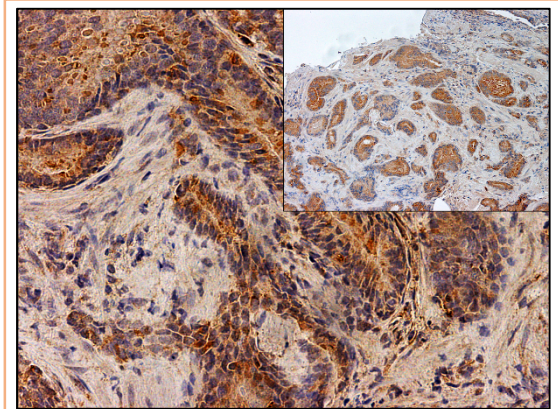


Fig. 13. Immunohistochemical localization of *TUSC3* in prostate adenocarcinoma. *TUSC3* preferentially localizes to prostate glandular epithelium rather than to the stroma. Magnification 200 \times . Inset shows a representative overview (100 \times).

Kratochvílová et al. 2015

suppressor and when lost, stimulated cancer growth. Based on the spectrum of molecules affected by *TUSC3* status, and knowledge based on our results, we propose that *TUSC3* can be involved in cancer immunoediting and cell response to altered tissue microenvironment⁵⁹. Cancer immunoediting is a multistep process that selects non-immunogenic cells from primary tumor and enables escape from immunosurveillance. In *TUSC3*-deficient tumors, the available portfolio of N-glycosylated proteins can enable cancer cells to avoid targeting by immune system. We identified that integrin β 1 is differentially N-glycosylated in *TUSC3* deficient cells⁵⁵, however, the identity of other proteins affected by *TUSC3* within the OST complex remains so far largely unknown.

Vašíčková et al. 2017

Interestingly, the *TUSC3* gene is upregulated also in non-cancerous epithelium during acquisition of senescent phenotype, together with other hallmark regulators of UPR and EMT. When the ovarian explants were exposed to conditions evoking ER-stress in vitro, *TUSC3* was specifically induced in OSE. Moreover, downregulation of *TUSC3* in senescent mOSE also increases cell survival, confirming the tumor suppressive role of *TUSC3* in normal, non-malignant ovarian surface epithelium in addition to ovarian cancer (**Fig. 14**, 2018, unpublished data).

Vaňhara et al. 2013

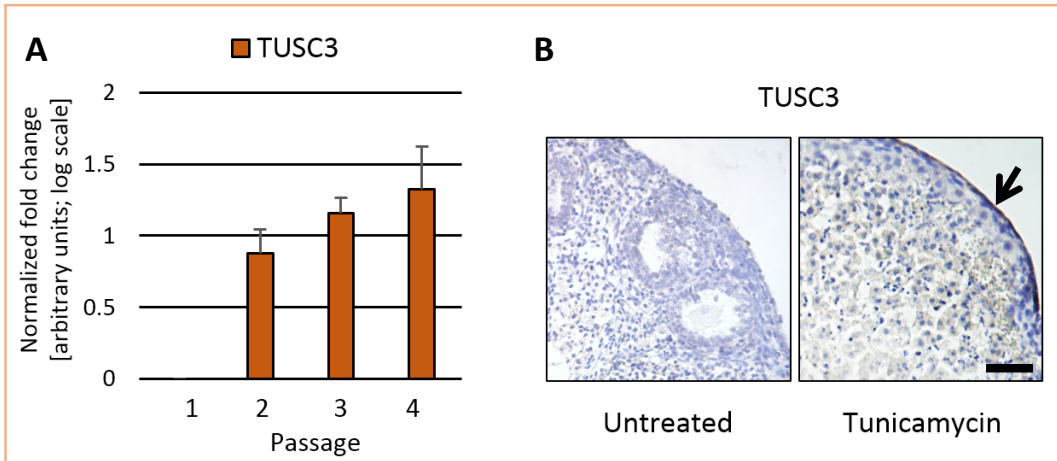
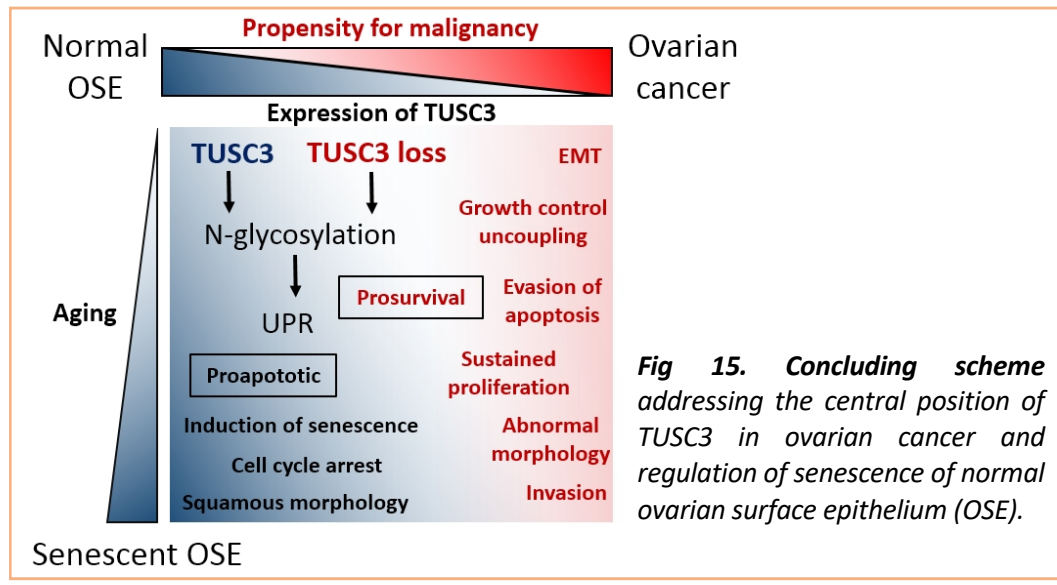


Fig 14. TUSC3 is upregulated in senescent mOSE cultured in vitro as documented by quantitative PCR (A). ER-stress conditions evoked by tunicamycin selectively upregulate TUSC3 in mOSE (arrow). Mouse whole ovaries were explanted, cultured in vitro and analyzed by immunohistochemistry same as in Fig. 9. Scale bar indicates 100µm (B). (2018, unpublished data)

In summary, we identified that induction of pro-survival UPR pathway by TUSC3 downregulation, results in enhanced proliferation of cancer cells, induction of EMT, and a massive tumor growth (Fig. 15). Our work on aged and cancerous ovarian surface epithelium showed that deregulation of a single gene can thus alter not only the cell phenotype, but pronounce to tissue context and even affect the systemic responses.



Taken together, we show that ER machinery stands in the midpoint of cellular decisions towards restoration of cell homeostasis and normal tissue morphology, or deleterious alterations, such as prostate and ovarian cancers, with TUSC3 gene playing a key role.

RESEARCH AXIS II

New tools for determination of cell and tissue heterogeneity

Mass spectrometry of cells and tissues

As documented in previous chapters, phenotypic shifts in tissues, induced either by cell stress, senescence, or metabolic deviations from homeostasis, can stay unapparent, but still determine substantial changes in cell and tissue structures and functions. For decades, determination of physiological and functional states of cells and tissues was based on qualified morphological assessment by light microscopy, followed later by chemical characterization, either by specific histochemical staining or antibody-based probing. Assuming that any stress or abnormal condition will be reflected in chemical composition of a cell, including small metabolites, peptides and proteins, one can distinguish a change by a sufficiently sensitive technique. Such methods are offered by analytical chemistry, especially by mass spectrometry and its derivatives.

Matrix-assisted laser desorption/ionization–time-of-flight mass spectrometry (MALDI-TOF MS) and its derivatives have manifold applications in classic analytical and structural chemistry and, thanks to their universality, have been adapted for analysis and determination of complex biological samples, including bacteria, yeasts or mammalian cells. Principally, laser beam of defined energy desorbs the molecules of sample (analyte) embedded in a matrix consisting of compounds enhancing analyte ionization. Molecules are then separated in electric field according to their mass to charge ratio, providing a precise simultaneous information on a number of ion species occurring in a sample (**Fig. 16**). Such spectrum composed of values of m/z assigned with the respective intensities (counts of ions of the same m/z hitting the detector in the same time) then enters statistical or chemometric evaluation leading usually to identification of individual molecules, their quantification or elucidating their structure⁶⁰.

Kolářová et al. 2014

In cells and tissues, MS reveals a unique chemical pattern covering small metabolites up to 1-2kDa, peptides and proteins, and MS-based proteomics becomes a fundamental method for revealing cell complexity on the biomolecular

level. The further innovation came with including the spatial resolution and development of mass spectrometry imaging that enhanced the histological image with multiple dimensions reflecting chemical composition of tissues (for in-depth review see ⁶⁰).

Kolářová et al. 2014

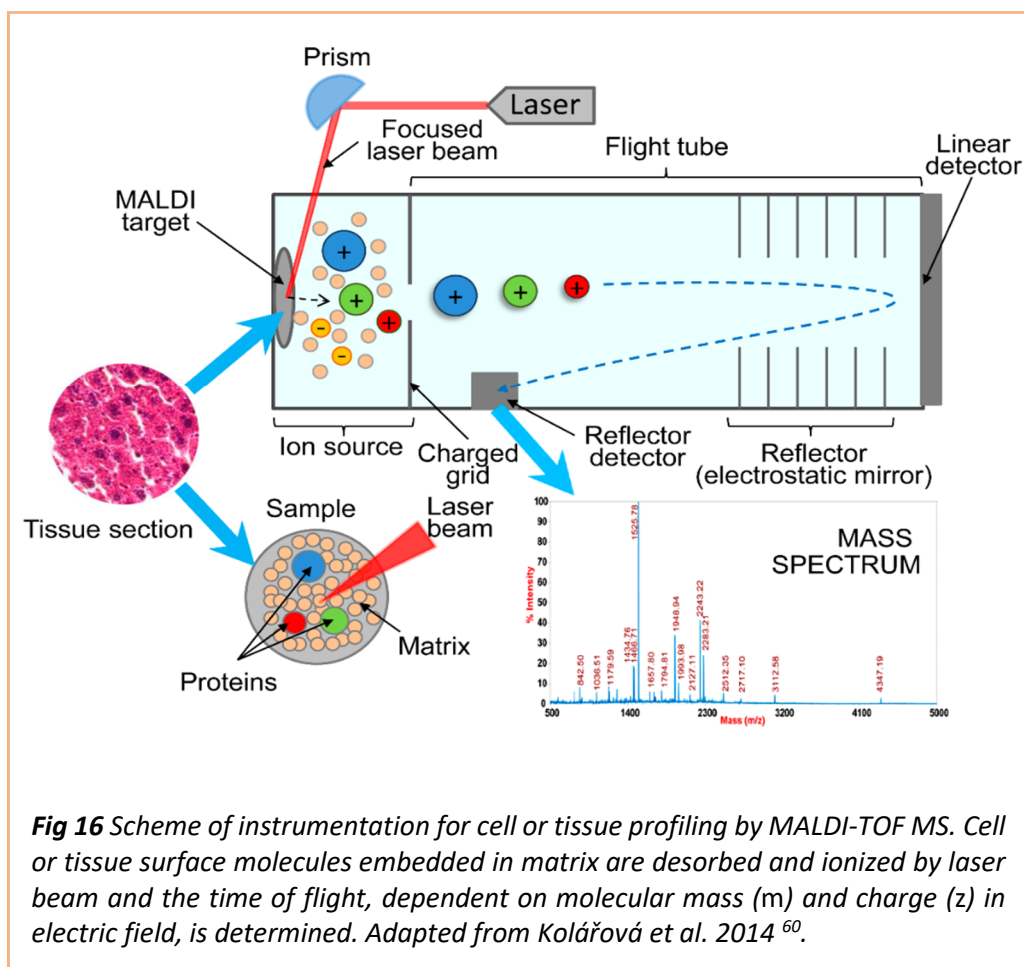


Fig 16 Scheme of instrumentation for cell or tissue profiling by MALDI-TOF MS. Cell or tissue surface molecules embedded in matrix are desorbed and ionized by laser beam and the time of flight, dependent on molecular mass (m) and charge (z) in electric field, is determined. Adapted from Kolářová et al. 2014 ⁶⁰.

Most of the matrices used for safe ionization of molecules in analytical chemistry were designed for relatively simple and non-complex analytes. However, MS analysis of cell extracts, intact cells and tissues is much more demanding in terms of non-linear or random “MALDI” effects (e.g. ionization quenching, technical reproducibility or mass calibration)^{61,62}. To reduce the unwanted variability, we introduced intact-cell MALDI-TOF MS that allows precise measurements without cell fractionation. In addition we demonstrated use of novel nanomaterials, e.g. phosphorus clusters or gold nano-particles (NPs) with defined spatial geometry as matrices or calibrants^{63,64} (**Fig. 17**). The gold NPs

Kolářová et al. 2015

enhance ionization of peptides and during desorption decompose to clusters of defined size, suitable as precise calibrants over a range of masses up to ca. 15kDa.

Similarly, phosphorus clusters provide extended mass range, suitable for calibration of biological samples. These technological innovations allowed us to obtain informative spectral datasets from various cell or tissue sources and use them for further analyses⁶³⁻⁶⁴.

For monitoring of cell cultures by MS, two principal approaches are available. The “top-down” approach is

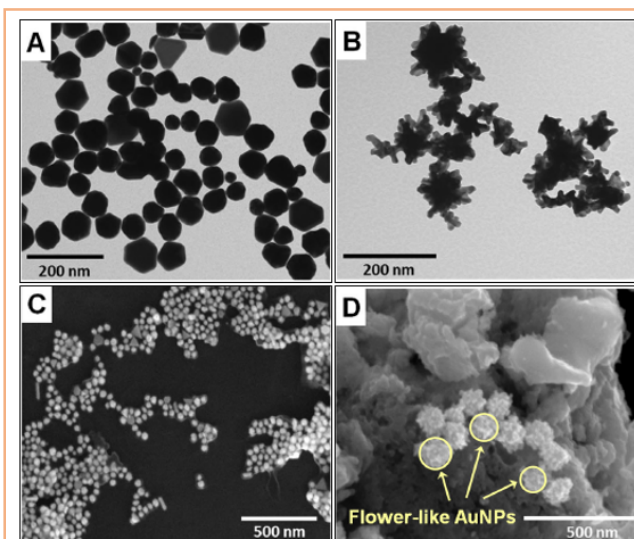


Fig 17. Examples of gold nanoparticles used in intact-cell and tissue MS. Uniform, polyhedral red gold nanoparticles (A, C) and flower-like gold nanoparticles (B, D) with fractal-like geometry. Both types of gold NP form stable clusters allowing for internal calibration of the mass spectra. Adapted from Kolářová et al. 2015.

based on revealing and identifying individual unique peaks and their use as biomarkers that are correlated with phenotypes or cell states, such as pluripotency, response to cell stress or cues in the culture microenvironment, reprogramming events, or differentiation. Intact-cell MS prevents a theoretical bias introduced by cell fractionation or too complex sample processing, and reduces the overall technical and experimental variability (Fig. 18).

However, despite the precise identification of specific biomarkers that could be statistically associated with cell parameters, their applicability is often based on a random correlation among myriads of other dynamically changing molecules in a cell- or culture-dependent context. Also, we have recently documented that using one or two dominant peaks for quantitative analysis of cell type reveals non-linear relationships that can be easily influenced by the technical or biological variability in the measurement or the sample itself⁶⁵. The alternative approach assumes that a full spectral fingerprint is sufficiently robust to eliminate any undesired variability but contains enough information to discriminate species, cell types, or even cell states differing in chemical

Kolářová et al. 2016

Valletta et al. 2015

composition, even without the identification of individual molecules. Thus, the analysis without a preceding subjective reduction to several major peaks and their identification can eliminate the bias of the random correlation of individual molecules to a phenotypic change or a cell status and avoid potential misinterpretation. Avoiding the fractionation of cells also helps to reduce the unwanted variability while improving the overall consistency of the mass spectra and their reproducibility^{65,66}.

Valletta et al.
2015

Vañhara et al.
2018

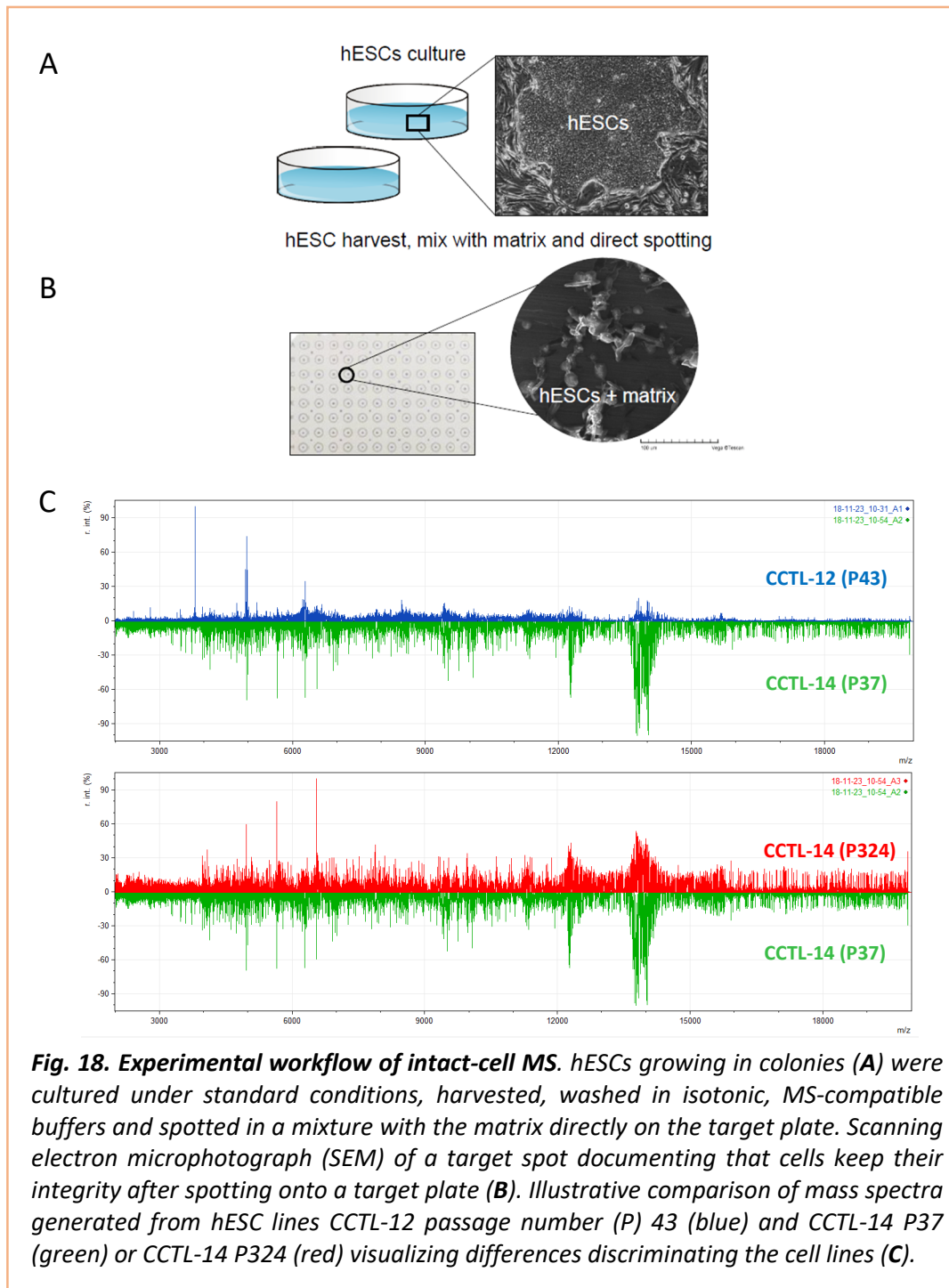


Fig. 18. Experimental workflow of intact-cell MS. hESCs growing in colonies (A) were cultured under standard conditions, harvested, washed in isotonic, MS-compatible buffers and spotted in a mixture with the matrix directly on the target plate. Scanning electron microphotograph (SEM) of a target spot documenting that cells keep their integrity after spotting onto a target plate (B). Illustrative comparison of mass spectra generated from hESC lines CCTL-12 passage number (P) 43 (blue) and CCTL-14 P37 (green) or CCTL-14 P324 (red) visualizing differences discriminating the cell lines (C).

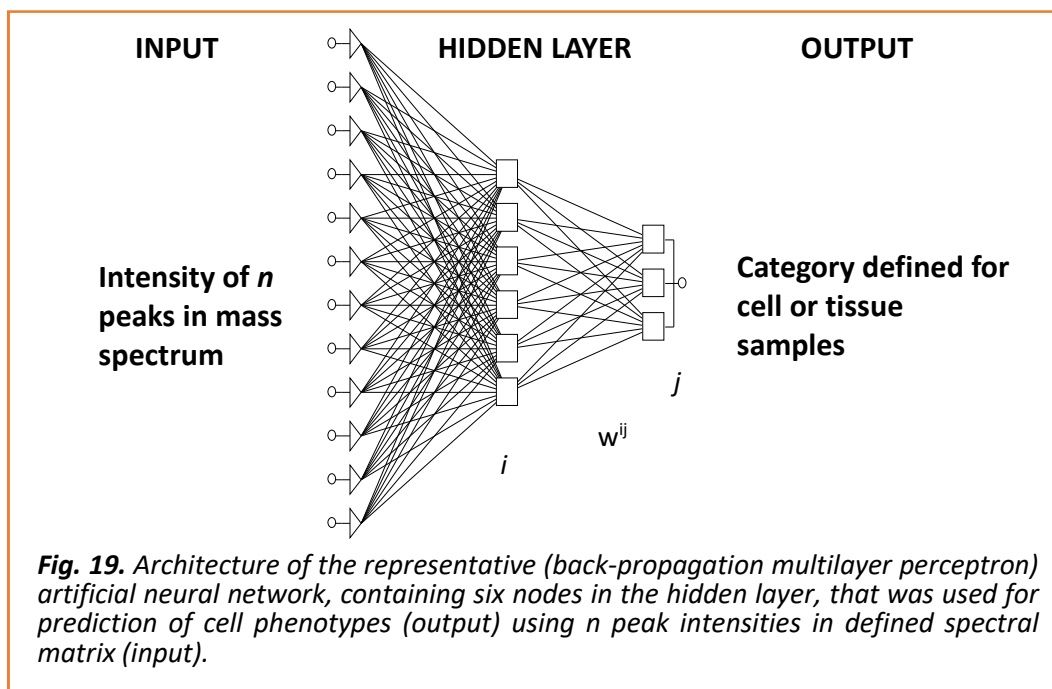
Artificial intelligence-coupled mass spectrometry for analysis of cell heterogeneity

Recognition of specific spectral patterns, however, can be extensively difficult due to inherent biological complexity of tissues, technical variability influencing outputs and also to the principles of MALDI analysis⁶⁷. Therefore, the post-measurement analysis has to cover all these issues to provide clear and confident decisions. While there is a number linear or non-linear statistical approaches available for biomarker recognition and spectral analysis, artificial intelligence (AI) and machine learning tools are straightforward and sufficiently sensitive and robust to discriminate very complex samples⁶⁸.

Amato et al.
2013

Artificial neural networks (ANN) represent a mathematical algorithm effective for processing of non-linear data. ANN were designed to follow the general structure of biological neural circuitry. Since the forties and fifties of the 20th century when first concepts and later definitions of processing units (perceptrons) capable of self-learning were suggested⁶⁹, AI entered divergent fields of computational industry and engineering, but also life-sciences, chemistry e.g. chemical kinetics or biomolecular engineering and structural computing, image analysis and pattern recognition. Recently the AI-based diagnostic tools were introduced to clinical medicine, to support decisions based in e.g. in diabetes, cardiovascular diseases, epilepsy or cancer^{68,70}. A typical ANN consists of nodes, or artificial “neurons”, assembled into layers of varying architecture. In the simplest form, the network is composed of a single unit - a perceptron. This unit is actually a classifier that assigns the input values (x) to the output values $f(x)$.

The limitations of single layer perceptrons to linear tasks only was overcome by introduction of multilayer perceptron networks with more complex topology and capabilities (for a review monograph see ref.⁷¹ and chapters therein). A typical structure of such network then consists of an input layer, one or more hidden layers and output layer, and its architecture reflects complexity of the analyzed system (**Fig. 19**). In our work, we have usually used a backpropagation multilayer perceptron ANN with number of nodes in the hidden layer ranging from 3 to 6.



All nodes in a network are interconnected by a weighed connections, or artificial “synapses”, where w indicates weight of connection i^{th} and j^{th} neurons in two adjacent layers. The input data are received in the input layer and processed to the hidden layer(s) through these weighted connections. During the ANN training, data are confronted with known data set and in the series of iterations the values of weights are adapted to fit the expected results. Then, the discriminative capability of the network is tested on validation data set that is independent on the training set. Simplified, the training process approximates a non-linear function between input and output datasets and defines values of weights connecting the nodes (**Tab. 5**).

The common limitation of ANNs is a phenomenon of overtraining, occurring in extensively complex networks or networks trained over too many iteration cycles. Such networks then fail to reveal a common trend in data and despite superior results in the training step, they fail in validation. Careful design and cross-validation may solve such problem. Currently, there are various network architectures and training approaches available in machine learning⁷¹ that can be suited for various tasks, including histopathological applications or cell phenotyping. In summary, ANN represent a universal approximator capable of discrimination and classification independently on the data distribution or complexity⁷⁰.

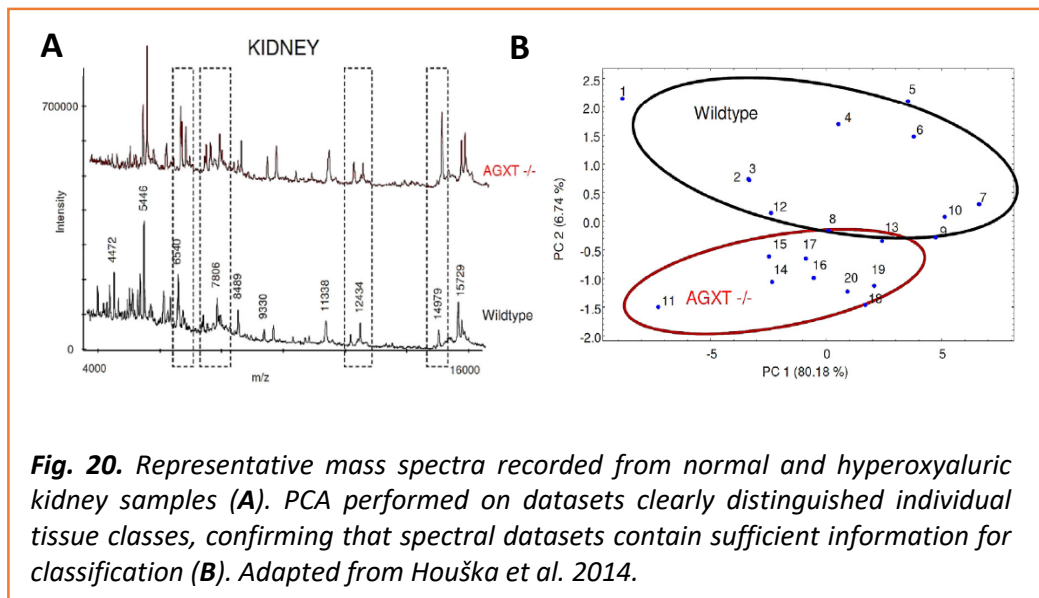
Tab. 5. Steps in a general ANN analysis	
1. Training	<ul style="list-style-type: none"> • Input of training data • Calculation of output • Comparing inputs and outputs • Modification of weights to minimize error <div style="text-align: right;">  Iterations </div>
2. Validation	<ul style="list-style-type: none"> • Input of validation data different to training set • Calculation of output based on weights obtained during training
3. Testing	<ul style="list-style-type: none"> • Input of unknown data • Calculation of outputs based on validated weights obtained during training

Our relevant applications of ANN-coupled mass-spectrometry biotyping in cell and tissue research

We tested the proof of concept using MS for discrimination of diseased and normal tissues in a specific mouse model of primary hyperoxaluria I, a rare disease with typical mineral depositions in liver and kidneys inducing tissue stress and organ failure⁷². Animals with serine—pyruvate aminotransferase (AGXT) knockout show symptoms of human disease and provide similar histopathologic display⁷³. We used cryo-cut sections of liver and kidney tissue obtained from healthy and AGXT -/- mice, and recorded mass spectra using MALDI-TOF MS. The unique chemical fingerprints allowed the principal component analysis to distinguish the samples according to peak/intensity matrix (**Fig. 20**)⁷⁴.

*Houška et al.
2014*

ANN then revealed patterns typical for altered chemical composition of the diseased tissue and classified the sample as normal or diseased with success rate >99%, even without preceding identification of relevant peaks.



Next, we were curious if we can use ANN-coupled MS to discriminate between distinct cell types and asked, whether it is possible to even (semi)-quantitate the classification. We developed a multivariate-calibration approach based on ANN analysis of MS fingerprints, and applied it in a model scenario of cultured human and mouse ESCs or mouse embryonic fibroblasts. To demonstrate the proof-of-principle, we designed a simple and straightforward experiment, and prepared defined binary mixtures composed of determined number of cells, and recorded mass spectra of these mixtures. We constructed an ANN and used a training dataset of spectral fingerprints specific for individual binary mixtures. Interestingly, the ANN was able to recognize presence of contaminating cell type in mixture and quantitatively estimate the approximate number of individual cell types. In well-defined experimental design we reached a limit of detection about 10^3 of contaminating cells in 10^6 of total number of cells⁶⁵ (Fig. 21). Based on our observation that well-trained ANN provides a precise quantitative determination of different cell types, we envisage that ANN-coupled MS can provide also sufficient information even for potential translation to routine cell cultures as a cell authentication tool.

Valletta et al.
2015

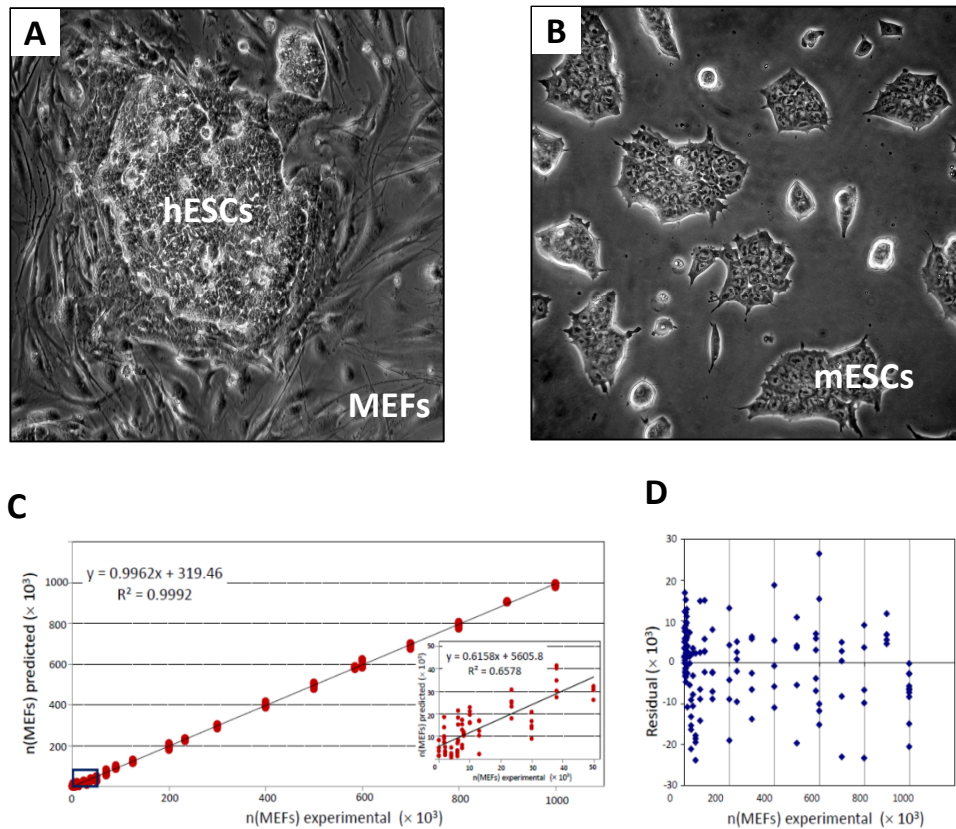


Fig. 21. A colony of human embryonic stem cells (hESCs) cultured on a layer of mouse embryonic fibroblasts (MEFs) (A), mouse embryonic stem cells (kind gift of J. Pachernik, Masaryk University) (B). Correlation plot between experimental (defined) number of cells in mixture and number of cells predicted by the ANN. Inset shows magnified region of the plot values up to ca 2×10^3 (C). Plot of root-mean-square errors showing random distribution of values, documenting absence of systematic trend in data (biased results) (D). Adapted from Valletta et al. 2016.

With the onset of large-scale, routine cell cultures for sophisticated bio-industrial applications, such quality control of cells and cell products becomes indeed a critical issue, concerning a variety of users from clinics, pharmacology and drug design or tissue engineering. The hESCs paved the road for the development of state-of-the-art cell technologies for such applications, especially in regenerative medicine. However, any cell-based application is dependent on rigorous conditions including predictable and stable cell culture, and moreover, hESCs are inherently unstable and prone to rapid, spontaneous differentiation *in vitro*.

Current culture protocols are focused on maintaining the pluripotent character of hESCs by repressing their differentiation and supporting sustained self-renewal. In routine cultures, hESCs cumulatively acquire various alterations on both the genetic and non-genetic levels⁷⁵, and despite sophisticated culture techniques, culture-adapted clones are inevitably selected during long-term *in vitro* cultures^{76,77} (**Tab. 6**).

Porokh et al.
2018

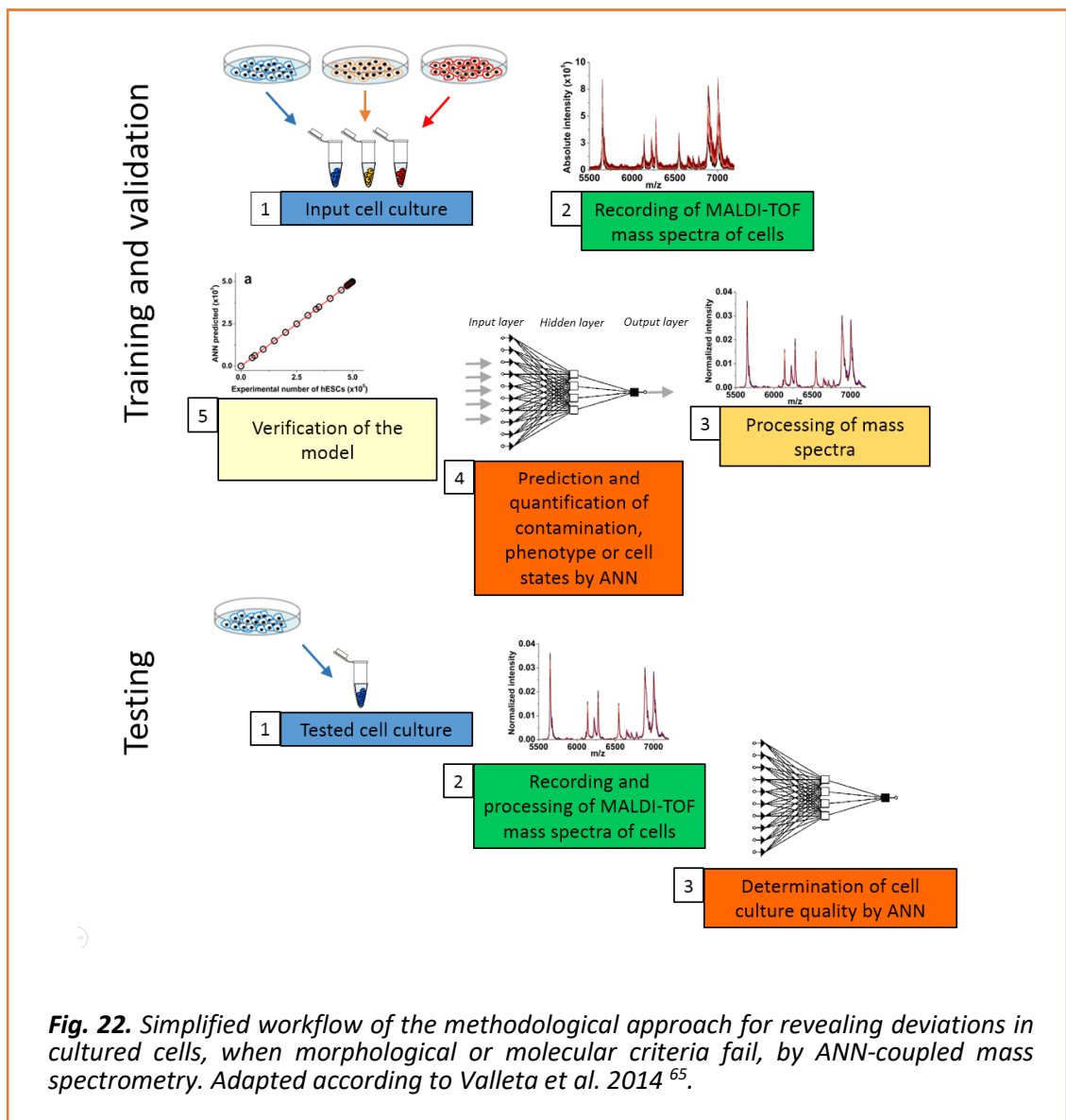
Tab. 6. Examples of phenotypic shifts of hESCs occurring during adaptation to long-term culture

- karyotype aberrations^{75-76,78}
- upregulation of surface markers, such CD30 and CD44⁷⁷
- deregulation of centrosomal metabolism⁷⁸ and cell cycle⁷⁹
- enhanced proliferation and altered differentiation potential⁸⁰
- altered sensitivity to apoptosis⁸¹
- alterations in secretome⁷⁷

However, these changes that regularly occurring in cultured pluripotent stem cells, could remain unnoticed until they substantially alter the karyotype or phenotype, even in case of the stable expression of stemness-associated transcription factors including c-Myc, Sox-2, Klf4, Nanog, or Oct3/4, or their differentiation capacity, or a typical morphology –parameters normally assessed by culture routine. Furthermore, molecular, genetic, and/or light-microscopy analyses can fail in the case of the genetically or karyotypically silent changes that arise in cultured cells. Thus, the MS-based methodological approach can be used for revealing of hidden patterns in mass spectra of cells divergent from their defined optima. Indeed, we identified gradual divergences emerging in long term cultured hESCs (cells of low vs. high passage number, or pluripotent cells vs. cells committed to differentiation) by mass spectrometry followed by linear statistics, such as PCA, or non-linear, artificial intelligence-based determination and classification (ANN)^{65,66}.

Vaňhara et al.
2018

In summary, we have documented that a whole mass spectrum without preceding peak identification can provide sufficient discrimination capacity due to high variability in molecular species, constituting the whole spectrum a multivariate biomarker. ANN-coupled MS can be widely applied in various other scenarios that require identification of hidden heterogeneity, ranging from intrinsic cell and tissue variability to systemic population divergences (Fig. 22). In our publications, we show the potential and real applications of ANN-coupled MS in characterization of cells and tissues.



V. CONCLUSIONS AND FUTURE PERSPECTIVES

This habilitation thesis integrates different approaches of tissue morphology, molecular and cell biology, analytical chemistry and chemometrics together aiming to extend understanding of structural and functional alterations in cells and tissues (**research axis I**), and to develop novel methods addressing the intrinsic cell and tissue heterogeneity (**research axis II**). In summary, my research group demonstrated for the first time that:

- Morphology of ovarian surface epithelium is shifted towards mesenchymal phenotype during replicative senescence *in vitro*
- Senescent ovarian epithelial cells develop ultrastructural abnormalities, especially in endoplasmic reticulum
- Stress of endoplasmic reticulum enhances propensity to senescence and changes of cell morphology
- Alleviation of endoplasmic reticulum stress overrides cell senescence
- *TUSC3* gene is a genuine tumor suppressor gene associated with endoplasmic reticulum and N-glycosylation machinery
- Silencing of *TUSC3* in ovarian and prostate cancer enhances cell survival by alleviation of endoplasmic reticulum stress
- Loss of *TUSC3* evokes aggressive cancer phenotype in mouse models
- Downregulation of *TUSC3* is associated with higher grade of prostate and ovarian tumors
- Hypermethylation of *TUSC3* promoter predicts poor prognosis of ovarian cancer patients
- Intact cell mass spectrometry allows unambiguous profiling and innovative characterization of cells and tissues, including discrimination of morphologically identical cell types
- Coupling of intact cell mass spectrometry with artificial intelligence allows quantitative estimations of stem cell heterogeneity in complex samples
- Intact cell mass spectrometry coupled with artificial neural networks reveals minute phenotypic changes and can provide robust and hypothesis-free tool for safe and effective quality control in stem cells-based therapy

My research group contributed to unraveling of the central role of the ER in maintenance of cell and tissue homeostasis. Identification of the ER-associated molecular players that change cell phenotype, such as TUSC3 protein, is critical for understanding of local regulations within tissues, as well as morphological aberrations, immunosurveillance, apoptosis, mobilization of tissue-residing stem cells or induction of senescence. Elucidation of this fine interplay offers various regulatory molecules that can be specifically monitored to improve diagnostics and follow-up, targeted to prevent cancer development or spreading, or to support stem cells-driven tissue regeneration. In summary, we identified endoplasmic reticulum as the driving organelle controlling structural, functional or molecular alterations in ovarian epithelium and epithelial cancer cells.

In parallel, we developed techniques revealing intrinsic heterogeneity in cells and tissues, globally aiming to provide a quality control tool for implementation of pluripotent stem cells into clinical trials. Cell-based technologies require stringent assurance of the quality and safety of the cell product, including development of formal methodology in every step of the production. Presence of an unwanted phenotype or deviation from the optimal state of cells in culture inevitably results in failure of the product and a potential harm to a patient. Current methods easily reveal microbial and viral contaminations, cell misidentifications or chromosomal aberrations occurring in the culture. However, subtle phenotypic shifts or unapparent alterations are not recognized by current conventional methods, such as microscopy or narrow focused screening for molecular markers. Here, we combined a state-of-the-art cell-directed mass spectrometry, and advanced analysis of specific molecular patterns stored in global mass spectra to reveal such alterations. Finally, we outlined and validated a diagnostic tool suitable for implementation into methodology of quality control in long-term clinical-grade stem cells cultures.

VI. REFERENCES

1. Shoja M, Tubbs R, Loukas M, Shokouhi G, Ardalan M. **Marie-François Xavier Bichat (1771–1802) and his contributions to the foundations of pathological anatomy and modern medicine.** *Annals of Anatomy - Anatomischer Anzeiger* 2008; **190**(5): 413-420.
2. Kourtis N, Tavernarakis N. **Cellular stress response pathways and ageing: intricate molecular relationships.** *Embo Journal* 2011; **30**(13): 2520-2531.
3. Del Pozo Martin Y, Park D, Ramachandran A, Ombrato L, Calvo F, Chakravarty P *et al.* **Mesenchymal cancer cell-stroma crosstalk promotes niche activation, epithelial reversion, and metastatic colonization.** *Cell Reports* 2015; **13**(11): 2456-2469.
4. Kratochvílová K, Moráň L, Paďourová S, Stejskal S, Tesařová L, Šimara P *et al.* **The role of the endoplasmic reticulum stress in stemness, pluripotency and development.** *European Journal of Cell Biology* 2016; **95**(3-5): 115-123.
5. Nieto MA. **Epithelial plasticity: a common theme in embryonic and cancer cells.** *Science* 2013; **342**(6159): 1234850.
6. Ahmed N, Thompson EW, Quinn MA. **Epithelial-mesenchymal interconversions in normal ovarian surface epithelium and ovarian carcinomas: an exception to the norm.** *Journal of Cellular Physiology* 2007; **213**(3): 581-588.
7. Goossens S, Janzen V, Bartunkova S, Yokomizo T, Drogat B, Crisan M *et al.* **The EMT regulator Zeb2/Sip1 is essential for murine embryonic hematopoietic stem/progenitor cell differentiation and mobilization.** *Blood* 2011; **117**(21): 5620-5630.
8. Stone RC, Pastar I, Ojeh N, Chen V, Liu S, Garzon KI *et al.* **Epithelial-mesenchymal transition in tissue repair and fibrosis.** *Cell and Tissue Research* 2016; **365**(3): 495-506.
9. Suarez-Carmona M, Lesage J, Cataldo D, Gilles C. **EMT and inflammation: inseparable actors of cancer progression.** *Molecular Oncology* 2017; **11**(7): 805-823.
10. Moustakas A, Heldin CH. **Mechanisms of TGFbeta-induced epithelial-mesenchymal transition.** *Journal of Clinical Medicine* 2016; **5**(7): 1-34.
11. Billottet C, Tuefferd M, Gentien D, Rapinat A, Thiery JP, Broet P *et al.* **Modulation of several waves of gene expression during FGF-1 induced epithelial-mesenchymal transition of carcinoma cells.** *Journal of Cellular Biochemistry* 2008; **104**(3): 826-839.
12. Liu PT, Wakamiya M, Shea MJ, Albrecht U, Behringer RR, Bradley A. **Requirement for Wnt3 in vertebrate axis formation.** *Nature Genetics* 1999; **22**(4): 361-365.

13. Fan L, Sebe A, Peterfi Z, Masszi A, Thirone AC, Rotstein OD, Nakano H, McCulloch CA, Szászi K, Mucsi I, Kapus A. **Cell contact-dependent regulation of epithelial-myofibroblast transition via the rho-rho kinase-phospho-myosin pathway.** *Molecular Biology of the Cell* 2007; **18**(3): 1083-1097.
14. Lamouille S, Xu J, Derynck R. **Molecular mechanisms of epithelial-mesenchymal transition.** *Nature Reviews Molecular Cell Biology* 2014; **15**(3): 178-196.
15. Gul IS, Hulpiau P, Saeys Y, van Roy F. **Evolution and diversity of cadherins and catenins.** *Experimental Cell Research* 2017; **358**(1): 3-9.
16. Knofler M, Pollheimer J. **Human placental trophoblast invasion and differentiation: a particular focus on Wnt signaling.** *Frontiers in Genetics* 2013; **4**: 190.
17. Cruz-Solbes AS, Youker K. **Epithelial to mesenchymal transition (emt) and endothelial to mesenchymal transition (EndMT): role and implications in kidney fibrosis.** *Results and Problems in Cell Differentiation* 2017; **60**: 345-372.
18. Dvorak HF. **Tumors: wounds that do not heal. Similarities between tumor stroma generation and wound healing.** *The New England Journal of Medicine* 1986; **315**(26): 1650-1659.
19. Tsai JH, Yang J. **Epithelial-mesenchymal plasticity in carcinoma metastasis.** *Genes & Development* 2013; **27**(20): 2192-2206.
20. Saraswat K, Rizvi SI. **Novel strategies for anti-aging drug discovery.** *Expert Opinion on Drug Discovery* 2017; **12**(9): 955-966.
21. Hayflick L. **The limited in vitro lifetime of human diploid cell strains.** *Experimental Cell Research* 1965; **37**: 614-636.
22. Hayflick L, Moorhead PS. **The serial cultivation of human diploid cell strains.** *Experimental Cell Research* 1961; **25**: 585-621.
23. Hornsby P. **Stress-Induced Senescence: Molecular Pathways.** In: Hayat MA (ed). *Tumor Dormancy, Quiescence, and Senescence, Volume 1: Aging, Cancer, and Noncancer Pathologies.* Springer Netherlands; 2013, pp 129-139.
24. Krtolica A, Parrinello S, Lockett S, Desprez PY, Campisi J. **Senescent fibroblasts promote epithelial cell growth and tumorigenesis: a link between cancer and aging.** *Proceedings of the National Academy of Sciences of the United States of America* 2001; **98**(21): 12072-12077.
25. Pernicová Z, Vaňhara P, Souček K. **Formation of Secretory Senescent Cells in Prostate Tumors: The Role of Androgen Receptor Activity and Cell Cycle Regulation.** In: Hayat MA (ed). *Tumor Dormancy, Quiescence, and Senescence, Volume 1: Aging, Cancer, and Noncancer Pathologies.* Springer Netherlands, 2013; pp 303-316.

26. Laberge RM, Awad P, Campisi J, Desprez PY. **Epithelial-mesenchymal transition induced by senescent fibroblasts.** *Cancer Microenvironment : official journal of the International Cancer Microenvironment Society* 2012; **5**(1): 39-44.
27. Dong D, Cai GY, Ning YC, Wang JC, Lv Y, Hong Q *et al.* **Alleviation of senescence and epithelial-mesenchymal transition in aging kidney by short-term caloric restriction and caloric restriction mimetics via modulation of AMPK/mTOR signaling.** *Oncotarget* 2017; **8**(10): 16109-16121.
28. Tato-Costa J, Casimiro S, Pacheco T, Pires R, Fernandes A, Alho I *et al.* **Therapy-induced cellular senescence induces epithelial-to-mesenchymal transition and increases invasiveness in rectal cancer.** *Clinical Colorectal Cancer* 2016; **15**(2): 170-178 e173.
29. Trudu F, Amato F, Vanhara P, Pivetta T, Pena-Mendez EM, Havel J. **Coordination compounds in cancer: past, present and perspectives.** *Journal of Applied Biomedicine* 2015; **13**(2): 79-103.
30. McCaffrey K, Braakman I. **Protein quality control at the endoplasmic reticulum.** *Essays in Biochemistry* 2016; **60**(2): 227-235.
31. Ogata M, Hino S, Saito A, Morikawa K, Kondo S, Kanemoto S *et al.* **Autophagy is activated for cell survival after endoplasmic reticulum stress.** *Molecular and Cellular Biology* 2006; **26**(24): 9220-9231.
32. Claude A. **The constitution of protoplasm.** *Science* 1943; **97**(2525): 451-456.
33. Porter KR, Claude A, Fullam EF. **A study of tissue culture cells by electron microscopy : methods and preliminary observations.** *The Journal of Experimental Medicine* 1945; **81**(3): 233-246.
34. Palade GE. **The endoplasmic reticulum.** *The Journal of Biophysical and Biochemical Cytology* 1956; **2**(4 Suppl): 85-98.
35. Palade GE, Siekevitz P. **Pancreatic microsomes; an integrated morphological and biochemical study.** *The Journal of Biophysical and Biochemical Cytology* 1956; **2**(6): 671-690.
36. Palade GE, Siekevitz P. **Liver microsomes; an integrated morphological and biochemical study.** *The Journal of Biophysical and Biochemical Cytology* 1956; **2**(2): 171-200.
37. Kratochvilova K, Horak P, Esner M, Soucek K, Pils D, Anees M, Tomasich E, Dráfi F, Jurtíková V, Hampl A, Krainer M, Vaňhara P. **Tumor suppressor candidate 3 (TUSC3) prevents the epithelial-to-mesenchymal transition and inhibits tumor growth by modulating the endoplasmic reticulum stress response in ovarian cancer cells.** *International Journal of Cancer* 2015; **137**(6): 1330-1340.

38. Wang M, Kaufman RJ. **The impact of the endoplasmic reticulum protein-folding environment on cancer development.** *Nature Reviews Cancer* 2014; **14**(9): 581-597.
39. Michalak M, Gye MC. **Endoplasmic reticulum stress in periimplantation embryos.** *Clinical and Experimental Reproductive Medicine* 2015; **42**(1): 1-7.
40. Kratochvílová K, Moráň L, Paďourová S, Stejskal S, Tesařová L, Šimara P, Hampl A, Koutná I, Vaňhara P. **The role of the endoplasmic reticulum stress in stemness, pluripotency and development.** *European Journal of Cell Biology* 2016; **95**(3-5): 115-123.
41. Blanco-Gelaz MA, Suarez-Alvarez B, Ligeró G, Sanchez L, Vidal-Castineira JR, Coto E, Moore H, Menendez P, Lopez-Larrea C. **Endoplasmic reticulum stress signals in defined human embryonic stem cell lines and culture conditions.** *Stem Cell Reviews and Reports* 2010; **6**(3): 462-472.
42. Moráň L, Vaňhara P, Kratochvílová K, Hampl A. **Mechanism of human embryonic stem cells response to alterations of endoplasmic reticulum homeostasis.** *Frontiers in Material and Life Sciences: Creating life in 3D 2015*; Conference proceedings. Brno, Czech Republic
43. Vaňhara P, Kratochvílová K, Bárta T., Hampl A. **Phenotypic plasticity of human embryonic stem cells induced by culture microenvironment.** *EMBO Conference: The molecular and cellular basis of regeneration and tissue repair 2014*; Conference proceedings. Saint Feliu de Guixols, Spain
44. Rufo N, Garg AD, Agostinis P. **The unfolded protein response in immunogenic cell death and cancer immunotherapy.** *Trends in Cancer* 2017; **3**(9): 643-658.
45. Vaňhara P, Hampl A, Kozubík A, Souček K. **Growth/differentiation factor-15: prostate cancer suppressor or promoter?** *Prostate cancer and prostatic diseases* 2012; **15**(4): 320-328.
46. Nelson SM, Telfer EE, Anderson RA. **The ageing ovary and uterus: new biological insights.** *Human Reproduction Update* 2013; **19**(1): 67-83.
47. Auersperg N, Wong AS, Choi KC, Kang SK, Leung PC. **Ovarian surface epithelium: biology, endocrinology, and pathology.** *Endocrine Reviews* 2001; **22**(2): 255-288.
48. King SM, Quartuccio SM, Vanderhyden BC, Burdette JE. **Early transformative changes in normal ovarian surface epithelium induced by oxidative stress require Akt upregulation, DNA damage and epithelial-stromal interaction.** *Carcinogenesis* 2013; **34**(5): 1125-1133.
49. McCluggage WG. **Morphological subtypes of ovarian carcinoma: a review with emphasis on new developments and pathogenesis.** *Pathology* 2011; **43**(5): 420-432.

50. Vašíčková K, Moráň L, Gurín D, Vaňhara P. **Alleviation of endoplasmic reticulum stress by tauroursodeoxycholic acid delays senescence of mouse ovarian surface epithelium.** *Cell and Tissue Research* 2018; **374**(3): 643-652.
51. Torre LA, Trabert B, DeSantis CE, Miller KD, Samimi G, Runowicz CD, Gaudet MM, Jemal A, Siegel RL. **Ovarian cancer statistics.** *CA: a Cancer Journal for Clinicians* 2018; **68**(4): 284-296.
52. Kurman RJ, Shih Ie M. **The Dualistic Model of Ovarian Carcinogenesis: Revisited, Revised, and Expanded.** *The American Journal of Pathology* 2016; **186**(4): 733-747.
53. Pils D, Horak P, Vaňhara P, Anees M, Petz M, Alfanž A, Gugerell A, Wittinger M, Gleiss A, Auner V, Tong D, Zeillinger R, Braicu Ei, Sehouli J, Krainer M. **Methylation status of TUSC3 is a prognostic factor in ovarian cancer.** *Cancer* 2013; **119**(5): 946-954.
54. Dempski RE, Jr., Imperiali B. **Oligosaccharyl transferase: gatekeeper to the secretory pathway.** *Current Opinion in Chemical Biology* 2002; **6**(6): 844-850.
55. Vaňhara P, Horak P, Pils D, Anees M, Petz M, Gregor W, Zeillinger R, Krainer M. **loss of the oligosaccharyl transferase subunit TUSC3 promotes proliferation and migration of ovarian cancer cells.** *International Journal of Oncology.* 2013; **42**(4): 1383-1389.
56. Horak P, Tomasich E, Vaňhara P, Kratochvílova K, Anees M, Marhold M, Lemberger CE, Gerschpacher M, Horvat R, Sibilia M, Pils D, Krainer M. **TUSC3 loss alters the er stress response and accelerates prostate cancer growth in vivo.** *Scientific Reports* 2014; **4**: 3739.
57. Mohorko E, Owen RL, Malojcic G, Brozzo MS, Aebi M, Glockshuber R. **Structural basis of substrate specificity of human oligosaccharyl transferase subunit N33/Tusc3 and its role in regulating protein N-glycosylation.** *Structure* 2014; **22**(4): 590-601.
58. Burleson KM, Casey RC, Skubitz KM, Pambuccian SE, Oegema TR, Jr., Skubitz AP. **Ovarian carcinoma ascites spheroids adhere to extracellular matrix components and mesothelial cell monolayers.** *Gynecologic Oncology* 2004; **93**(1): 170-181.
59. Vašíčková K, Horak P, Vaňhara P. **TUSC3: functional duality of a cancer gene.** *Cellular and Molecular Life Sciences* 2017; **75**(5): 849-857.
60. Kolářová L, Vaňhara P, Pena-Mendez EM, Hampl A, Havel J. **Tissue visualization mediated by nanoparticles: from tissue staining to mass spectrometry tissue profiling and imaging.** In: Seifalian A, Editor. *Nanomedicine.* Manchester, UK: One Central Press 2014; pp. 468-482.
61. Furey A, Moriarty M, Bane V, Kinsella B, Lehane M. **Ion suppression; a critical review on causes, evaluation, prevention and applications.** *Talanta* 2013; **115**: 104-122.

62. Strupat K. **Molecular weight determination of peptides and proteins by ESI and MALDI.** *Methods in Enzymology* 2005; **405**: 1-36.
63. Kolářová L, Prokeš L, Kučera L, Hampl A, Pena-Mendez E, Vaňhara P, Havel J. **Clusters of monoisotopic elements for calibration in (TOF) mass spectrometry.** *Journal of the American Society for Mass Spectrometry* 2017; **28**(3): 419-427.
64. Kolářová L, Kučera L, Vaňhara P, Hampl A, Havel J. **Use of flower-like gold nanoparticles in time-of-flight mass spectrometry.** *Rapid Communications in Mass Spectrometry* 2015; **29**(17): 1585-1595.
65. Valletta E, Kučera L, Prokeš L, Amato F, Pivetta T, Hampl A, Havel J, Vaňhara P. **Multivariate calibration approach for quantitative determination of cell-line cross contamination by intact cell mass spectrometry and artificial neural networks.** *PLoS One* 2016; **11**(1): e0147414.
66. Vaňhara P, Kučera L, Prokeš L, Jurečková L, Pena-Mendez EM, Havel J, Hampl A. **Intact cell mass spectrometry as a quality control tool for revealing minute phenotypic changes of cultured human embryonic stem cells.** *Stem Cells Translational Medicine* 2018; **7**(1): 109-114.
67. Duncan MW, Roder H, Hunsucker SW. **Quantitative matrix-assisted laser desorption/ionization mass spectrometry.** *Briefings in Functional Genomics & Proteomics* 2008; **7**(5): 355-370.
68. Amato F, Lopez A, Pena-Mendez E, Vanhara P, Hampl A, Havel J. **Artificial neural networks in medical diagnosis.** *Journal of Applied Biomedicine* 2013; **11**(2): 47-58.
69. Rosenblatt F. **The perceptron: a probabilistic model for information storage and organization in the brain.** *Psychological Review* 1958; **65**(6): 386-408.
70. Hornik K. **Approximation Capabilities of Multilayer Feedforward Networks.** *Neural Networks* 1991; **4**(2): 251-257.
71. da Silva IN, Spatti DH, Flauzino RA, Liboni LHB, dos Reis Alves SF. *Artificial Neural Networks: A Practical Course*, 1 edn. Springer International Publishing, 2017, 307pp.
72. Nishiyama K, Funai T, Katafuchi R, Hattori F, Onoyama K, Ichiyama A. **Primary hyperoxaluria type-I due to a point mutation of T to C in the coding region of the serine - pyruvate aminotransferase gene.** *Biochemical and Biophysical Research Communications* 1991; **176**(3): 1093-1099.
73. Salido EC, Li XM, Lu Y, Wang X, Santana A, Roy-Chowdhury N, Torres A, Shapiro LJ, Roy-Chowdhury J. **Alanine-glyoxylate aminotransferase-deficient mice, a model for primary hyperoxaluria that responds to adenoviral gene transfer.** *Proceedings of the National Academy of Sciences of the United States of America*. 2006; **103**: 18249-18254.

74. Houška J, Pena-Mendez EM, Hernandez-Fernaund JR, Salido E, Hampl A, Havel J, Vaňhara P. **Tissue profiling by nanogold-mediated mass spectrometry and artificial neural networks in the mouse model of human primary hyperoxaluria 1.** *Journal of Applied Biomedicine* 2014; **12**(2): 119-125.
75. Amps K, Andrews PW, Anyfantis G, Armstrong L, Avery S, Baharvand H *et al.* **Screening ethnically diverse human embryonic stem cells identifies a chromosome 20 minimal amplicon conferring growth advantage.** *Nature Biotechnology* 2011; **29**(12): 1132-U1113.
76. Harrison NJ, Baker D, Andrews PW. **The significance of culture adaptation of embryonic stem cells for regenerative medicine.** In: Baharvand H, Aghdami N (eds). *Advances in Stem Cell Research, Stem Cell Biology and Regenerative Medicine*. Springer Science + Bussines Media, LLC 2012, 2012, pp 17-27.
77. Porokh V, Vaňhara P, Bárta T, Jurečková L, Bohačiaková D, Pospíšilová V, Holubcová Z, Pelková V, Souček K, Hampl A. **Soluble Cripto-1 induces accumulation of supernumerary centrosomes and formation of aberrant mitoses in human embryonic stem cells.** *Stem Cells and Development* 2018; **27**(16): 1077-1084.
78. Catalina P, Montes R, Ligeró G, Sanchez L, de la Cueva T, Bueno C, Leone PE, Menendez P. **Human ESCs predisposition to karyotypic instability: Is a matter of culture adaptation or differential vulnerability among hESC lines due to inherent properties?** *Molecular Cancer* 2008; **7**: 76-84.
79. Bárta T, Vinarský V, Holubcová Z, Doležalová D, Verner J, Pospíšilová Š, Dvořák P, Hampl A. **Human embryonic stem cells are capable of executing G1/S checkpoint activation.** *Stem Cells* 2010; **28**(7): 1143-1152.
80. Park YB, Kim YY, Oh SK, Chung SG, Ku SY, Kim SH *et al.* **Alterations of proliferative and differentiation potentials of human embryonic stem cells during long-term culture.** *Experimental & Molecular Medicine* 2008; **40**(1): 98-108.
81. Vinarský V, Křivánek J, Rankel L, Nahacká Z, Bárta T, Jaroš J, Anděra L, Hampl A. **Human embryonic and induced pluripotent stem cells express TRAIL receptors and can be sensitized to TRAIL-induced apoptosis.** *Stem Cells and Development* 2013; **22**(22): 2964-2974.

VII. COMMENTED OVERVIEW OF SELECTED PUBLICATIONS

Eighteen publications elaborated 2011-2018 primarily at the Department of Histology and Embryology of the Faculty of Medicine, Masaryk University, are commented. Author contributed to the presented set of publications in five cases as the first-author, in seven cases as co-author and in six cases as the corresponding author of the multidisciplinary team.

Research axis I

1. Pils D, Horak P, Vaňhara P, Anees M, Petz M, Alfanž A, Gugerell A, Wittinger M, Gleiss A, Auner V, Tong D, Zeillinger R, Braicu Ei, Sehouli J, Krainer M. **Methylation status of TUSC3 is a prognostic factor in ovarian cancer.** *Cancer*. 2013; **119**(5): 946-954.
2. Vaňhara P, Horak P, Pils D, Anees M, Petz M, Gregor W, Zeillinger R, Krainer M. **Loss of the oligosaccharyl transferase subunit tusc3 promotes proliferation and migration of ovarian cancer cells.** *International Journal of Oncology*. 2013; **42**(4): 1383-1389.
3. Horak P, Tomasich E, Vaňhara P, Kratochvílová K, Anees M, Marhold M, Lemberger CE, Gerschpacher M, Horvat R, Sibilía M, Pils D, Krainer M. **TUSC3 loss alters the ER stress response and accelerates prostate cancer growth in vivo.** *Scientific Reports* 2014; **4**: 3739.
4. Kratochvílová K, Horak P, Ešner M, Souček K, Pils D, Anees M, Tomasich E, Dráfi F, Jurtíková V, Hampl A, Krainer M, Vaňhara P. **Tumor suppressor candidate 3 (TUSC3) prevents the epithelial-to-mesenchymal transition and inhibits tumor growth by modulating the endoplasmic reticulum stress response in ovarian cancer cells.** *International Journal of Cancer* 2015; **137**(6): 1330-1340.
5. Kratochvílová K, Moráň L, Paďourová S, Stejskal S, Tesařová L, Šimara P, Hampl A, Koutná I, Vaňhara P. **The role of the endoplasmic reticulum stress in stemness, pluripotency and development.** *European Journal of Cell Biology* 2016; **95**(3-5): 115-123.
6. Vašíčková K, Horak P, Vaňhara P. **TUSC3: functional duality of a cancer gene.** *Cellular and Molecular Life Sciences* 2017; **75**(5): 849-857.
7. Pernicová Z, Vaňhara P, Souček K. **Formation of secretory senescent cells in prostate tumors: the role of androgen receptor activity and cell cycle regulation.** In: Hayat MA (ed). *Tumor Dormancy, Quiescence, and Senescence, Volume 1: Aging, Cancer, and Noncancer Pathologies*. Springer Netherlands, 2013; pp 303-316.

8. Vaňhara P, Hampl A, Kozubík A, Souček K. **Growth/differentiation Factor-15: prostate cancer suppressor or promoter?** *Prostate Cancer and Prostatic Diseases* 2012; **15**(4): 320-328.
9. Trudu F, Amato F, Vaňhara P, Pivetta T, Pena-Mendez EM, Havel J. **Coordination compounds in cancer: past, present and perspectives.** *Journal of Applied Biomedicine* 2015; **13**(2): 79-103.
10. Vašíčková K, Moráň L, Gurín D, Vaňhara P. **Alleviation of endoplasmic reticulum stress by tauroursodeoxycholic acid delays senescence of mouse ovarian surface epithelium.** *Cell and Tissue Research* 2018; **374**(3): 643-652.

Research axis II

11. Kolářová L, Vaňhara P, Pena-Mendez EM, Hampl A, Havel J. **Tissue visualization mediated by nanoparticles: from tissue staining to mass spectrometry tissue profiling and imaging.** In: Seifalian A (ed). *Nanomedicine*. Manchester, UK: One Central Press; 2014; pp 468-82.
12. Kolářová L, Kučera L, Vaňhara P, Hampl A, Havel J. **Use of flower-like gold nanoparticles in time-of-flight mass spectrometry.** *Rapid Communications in Mass Spectrometry* 2015; **29**(17): 1585-1595.
13. Kolářová L, Prokeš L, Kučera L, Hampl A, Pena-Mendez EM, Vaňhara P, Havel J. **Clusters of monoisotopic elements for calibration in (TOF) mass spectrometry.** *Journal of the American Association for Mass Spectrometry* 2017; **28**(3): 419-47.
14. Amato F, Lopez A, Pena-Mendez E, Vaňhara P, Hampl A, Havel J. **Artificial neural networks in medical diagnosis.** *Journal of Applied Biomedicine*. 2013; **11**(2): 47-58.
15. Houška J, Pena-Mendez EM, Hernandez-Fernaund JR, Salido E, Hampl A, Havel J, Vaňhara P. **Tissue profiling by nanogold-mediated mass spectrometry and artificial neural networks in the mouse model of human primary hyperoxaluria 1.** *Journal of Applied Biomedicine* 2014; **12**(2): 119-125.
16. Valletta E, Kučera L, Prokeš L, Amato F, Pivetta T, Hampl A, Havel J, Vaňhara P. **Multivariate calibration approach for quantitative determination of cell-line cross contamination by intact cell mass spectrometry and artificial neural networks.** *PLoS One* 2016; **11**(1): E0147414.
17. Vaňhara P, Kučera L, Prokeš L, Jurečková L, Peña-Méndez EM, Havel J, Hampl A. **Intact cell mass spectrometry as a quality control tool for revealing minute phenotypic changes of cultured human embryonic stem cells.** *Stem Cells Translational Medicine* 2018; **7**(1): 109-114.
18. Porokh V, Vaňhara P, Bárta T, Jurečková L, Bohačiaková D, Pospíšilová V, Holubcová Z, Pelková V, Souček K, Hampl A. **Soluble Cripto-1 induces accumulation of supernumerary centrosomes and formation of aberrant mitoses in human embryonic stem cells.** *Stem Cells and Development* 2018; **27**(16): 1077-1084.

1. Pils D, Horak P, **Vanhara P**, Anees M, Petz M, Alfan A, Gugerell A, Wittinger M, Gleiss A, Auner V, Tong D, Zeillinger R, Braicu Ei, Sehouli J, Krainer M. **Methylation status of TUSC3 is a prognostic factor in ovarian cancer.** *Cancer* 2013; **119**(5): 946-54.

Commentary:

Despite the fact, that this publication was not carried out at the Faculty of Medicine MU but at the Medical University of Vienna, Austria, it is included here for the integrity of the habilitation thesis and setting up the clinical backgrounds. We demonstrated clinically-relevant effects of TUSC3 promoter hypermethylation on ovarian cancer patients' survival. The results indicated that TUSC3 expression is decreased significantly because of promoter methylation in malignant ovarian tumors compared with benign controls. TUSC3 hypermethylation predicted progression-free and overall survival in ovarian cancer. The current observations suggested a role for N-glycosylating events in ovarian cancer pathogenesis in general and identified the epigenetic silencing of TUSC3 as a prognostic factor in this disease.

DOI: 10.1002/cncr.27850
Journal: Cancer
Impact factor (WOS, 2013): 4.901
Number of citations (WOS, 2018): 32
Cited in: Molecular Cancer, Oncotarget, Seminars in Cancer biology, Journal of Pathology, etc.

Most important citation:

Oliveira-Ferrer L, Legler K, Milde-Langosch K. **Role of protein glycosylation in cancer metastasis.** *Seminars in Cancer Biology* 2017; **44**:141-152.
doi: 10.1016/j.semcancer.2017.03.002.
(IF 2016: 9.141)

Contribution of the author: Co-authorship. Collection and/or assembly of data, data analysis and interpretation, manuscript writing.

Methylation Status of TUSC3 Is a Prognostic Factor in Ovarian Cancer

Dietmar Pils, PhD¹; Peter Horak, MD²; Petr Vanhara, PhD²; Mariam Anees, PhD²; Michaela Petz²; Angela Alfanzi²; Alfred Gugerell, PhD²; Michael Wittinger, PhD²; Andreas Gleiss, PhD³; Veronika Auner¹; Dan Tong, PhD¹; Robert Zeillinger, PhD³; Elena-Ioana Braicu, MD⁴; Jalid Sehoul, MD⁴; and Michael Krainer, MD²

BACKGROUND. Current prognostic information in ovarian cancer is based on tumor stage, tumor grade, and postoperative tumor size. Reliable molecular prognostic markers are scarce. In this article, the authors describe epigenetic events in a frequently deleted region on chromosome 8p22 that influence the expression of tumor suppressor candidate 3 (*TUSC3*), a putative tumor suppressor gene in ovarian cancer. **METHODS.** Messenger RNA expression and promoter hypermethylation of *TUSC3* were studied in ovarian cancer cell lines and in tumor samples from 2 large, independent ovarian cancer cohorts using polymerase chain reaction-based methods. **RESULTS.** The results indicated that *TUSC3* expression is decreased significantly because of promoter methylation in malignant ovarian tumors compared with benign controls. Almost 33% of ovarian cancer samples had detectable *TUSC3* promoter methylation. Furthermore, methylation status of the *TUSC3* promoter had a significant and independent influence on progression-free and overall survival. **CONCLUSIONS.** *TUSC3* hypermethylation predicted progression-free and overall survival in ovarian cancer. The current observations suggested a role for N-glycosylating events in ovarian cancer pathogenesis in general and identified the epigenetic silencing of *TUSC3* as a prognostic factor in this disease. *Cancer* 2013;119:946-54. © 2012 American Cancer Society.

KEYWORDS: *TUSC3*, methylation, ovarian cancer, glycosylation, progression-free survival, overall survival, biomarker..

INTRODUCTION

Epithelial ovarian cancer is the most lethal gynecologic malignancy and the fourth most frequent cause of cancer-related death among women in industrialized countries.¹ Because >75% of women are diagnosed with advanced disease (International Federation of Gynecology and Obstetrics [FIGO] stages III and IV), an early diagnosis presents 1 of the challenges of this disease. Patients with advanced ovarian cancer undergo intensive multimodal therapy consisting of cytoreductive surgery and (neo)adjuvant platinum-based and taxane-based chemotherapy. Regardless of the progress made in surgical and medical therapies over recent decades, the outcome for women with advanced ovarian cancer remains grim. Innovative, hypothesis-driven approaches to biomarker development remain essential even in the era of high-throughput sequencing and various omics. Studies of promoter methylation patterns in tumor suppressor genes have yielded several promising methylated biomarker candidates.²⁻⁴ In contrast to a gene or protein expression analysis, methylation can easily be detected using polymerase chain reaction (PCR)-based methods in both tumor material and body fluids.⁵⁻⁷

TUSC3 (tumor suppressor candidate 3), originally named N33, was identified as a potential tumor suppressor gene in prostate cancer^{8,9} and is located on chromosome band 8p22. Known homozygous deletions of this region in pancreatic cell lines^{10,11} and prostate cancer cell lines^{12,13} contain no other cancer-related genes except *TUSC3*, although mutations of the *TUSC3* coding sequence have not been observed. Through a systematic screening of this region on 8p22, we recently observed that *TUSC3* is significantly down-regulated in high-grade ovarian cancer and may have prognostic significance.¹⁴ *TUSC3* deletions or mutations reportedly are frequently associated with mental retardation.^{15,16} *TUSC3* shares high sequence homology with Ost3p, a subunit of the oligosaccharyltransferase (OST) complex involved in N-glycosylation of proteins in *Saccharomyces cerevisiae*,¹⁷⁻¹⁹ suggesting an analogous function in mammalian cells. Alterations of protein N-glycosylation have been associated with some carcinogenic traits, such as invasiveness and metastatic potential.²⁰⁻²² Deregulated enzymatic activities of proteins directly involved in N-glycosylation or the availability of potential

Corresponding author: Michael Krainer, MD, Department of Internal Medicine I and Comprehensive Cancer Center, Medical University of Vienna, Waehringer Guertel 18-20, A-1090 Vienna, Austria; Fax: (011) 43 1-40400-1685; michael.krainer@meduniwien.ac.at

¹Department of Obstetrics and Gynecology, Division of Gynecology; Medical University of Vienna, Vienna, Austria; ²Department of Internal Medicine I and Comprehensive Cancer Center, Medical University of Vienna, Vienna, Austria; ³Center for Medical Statistics, Informatics and Intelligent Systems, Medical University of Vienna, Vienna, Austria; ⁴Department of Gynecology and Obstetrics, Virchow Clinic Campus, Charite Medical University of Berlin, Berlin, Germany.

The first 2 authors contributed equally to this article.

We thank Cornelia Sax, Dr. Brigitte Wolf and Andrea Schanzer for their excellent technical support, and Dr. Werner Aufsatz for providing the protocol for bisulfite treatment.

DOI: 10.1002/cncr.27850, **Received:** May 22, 2012; **Revised:** September 4, 2012; **Accepted:** September 5, 2012, **Published online** October 23, 2012 in Wiley Online Library (wileyonlinelibrary.com)

glycosylation sites determined by the branching of N-glycans are considered to be crucial for these effects.^{23–26} In the current report, we describe the epigenetic regulation of *TUSC3* expression through promoter methylation in ovarian cancer and define *TUSC3* as an independent prognostic factor in 2 large, independent cohorts of women with ovarian cancer.

MATERIALS AND METHODS

Patient Characteristics

A written informed consent form for the scientific use of biologic material was signed by all participating patients according to the requirements of the Institutional Ethics Committee of the Medical University of Vienna and the Ethics Committee of the Charite Hospital of Berlin. All patient-associated information was anonymized for further analysis.

Samples of ovarian tumors for establishing the test set were obtained between the years 2000 and 2003 from patients who underwent radical surgery with the primary objective of maximal tumor reduction at the Charite Hospital of Berlin. Normal ovaries (microdissected ovarian epithelium) and benign cyst samples came from patients who were diagnosed without malignant disease and underwent oophorectomy at the Medical University of Vienna. In total, 20 benign ovarian samples and 102 primary tumor samples were assessed, microdissected, and enriched for epithelial tissue (the clinicopathologic characteristics are provided in Table 1). The validation set included 97 ovarian tumor samples that were obtained between the years 2005 and 2008 (Table 2). The majority of patients in the test set (89%) and the validation set (92%) received a platinum-based first-line chemotherapy regimen (Tables 1 and 2). The study design adhered to Reporting Recommendations for Tumor Marker (REMARK) criteria, as applicable.²⁷

Cell Culture and Cloning

The ovarian cancer cell lines A2780, A2780 ADR, MDAH-2774, ES2, OVCAR-3, Caov-3, MIA PaCa-2, and SKOV3 were obtained from the European Collection of Cell Cultures (Health Protection Agency Culture Collections, Porton Down, United Kingdom) or the American Type Culture Collection (Manassas, Va). Cells were cultivated in medium (Caov-3 cells, Dulbecco modified Eagle medium; MIA PaCa-2 and OVCAR-3 cells, α -minimal essential medium; SKOV3 cells, McCoy medium; A2780, A2780 ADR, MDAH-2774, and ES2 cells, RPMI medium; H134 cells, Dulbecco modified Eagle medium with 25 mM HEPES, pH 8.0) enriched with

TABLE 1. Clinicopathologic Patient Characteristics: Test Set

Characteristic	No. of Patients (%)
Benign ovarian samples with corresponding mRNA samples	20 (20)
Age at operation: Mean \pm SD, y	49.9 \pm 11.8
7 Normal ovaries: Mean age, y	51.6
13 Benign cysts: Mean age, y	49.0
Tumor samples (corresponding mRNA samples)	102 (99)
Age at diagnosis: Mean \pm SD, y	58.3 \pm 11.0
Histology	
Serous	79 (77.4) ^a
Endometrioid	10 (9.8)
Mucinous	5 (4.9)
Clear cell	2 (2)
Other	5 (4.9)
Missing	1 (1)
FIGO stage	
I	17 (16.7)
II	10 (9.8)
III	51 (50)
IV	22 (21.6)
Missing	2 (2)
Tumor grade	
1	2 (2)
2	48 (46.1)
3	51 (50)
Missing	1 (1)
Residual disease after initial surgery	
\leq 1 cm	86 (84.3)
>1 cm	13 (12.7)
Missing	3 (2.9)
First-line chemotherapy	
Carboplatin and paclitaxel	66 (64.7)
Carboplatin, paclitaxel, and gemcitabine	17 (16.7)
Carboplatin and other	8 (7.8)
Other	3 (2.9)
None	5 (4.9)
Missing	3 (2.9)
Response to first-line chemotherapy	
NED ^b	6 (5.9)
NC ^c	3 (2.9)
PD ^c	12 (11.8)
PR ^c	5 (4.9)
CR ^b	43 (42.2)
Missing	16 (15.7)
Duration of response, mo	
0–6 ^b	6 (5.9)
6–12 ^b	5 (4.9)
>12 ^b	6 (5.9)
Remissions/PD	
Without remission	49 (48)
With remission	33 (32.4)
PD	17 (16.7)
Missing	3 (2.9)

Abbreviations: CR, complete response; FIGO, International Federation of Gynecology and Obstetrics; NC, no change; NED, no evidence of disease; PD, progressive disease;

PR, partial response; SD, standard deviation.

^aPercentages for histology were based on 102 tumor samples, because 1 patient (1%) was missing information on histology.

^bThese patients were responders to first-line chemotherapy.

^cThese patients were nonresponders to first-line chemotherapy.

TABLE 2. Clinicopathologic Patient Characteristics: Validation Set

Characteristic	No. of Patients (%)
No. of tumor samples	97
Age at diagnosis: Mean±SD, y	57.7 ± 10.7
Histology	
Serous	89 (91.7) ^a
Endometrioid	2 (2.1)
Mixed epithelial tumor	2 (2.1)
Other	4 (4.1)
FIGO stage	
II	2 (2.1)
III	82 (84.5)
IV	13 (13.4)
Tumor grade	
1	4 (4.1)
2	15 (15.5)
3	72 (74.2)
Missing	6 (6.2)
Residual disease after initial surgery	
≤1 cm	60 (61.9)
>1 cm	35 (36.1)
Missing	2 (2)
First-line chemotherapy	
Carboplatin and paclitaxel and other	78 (80.4)
Carboplatin and docetaxel	5 (5.2)
Cisplatin and paclitaxel/docetaxel	6 (6.2)
Other	4 (4.1)
Missing	4 (4.1)

Abbreviations: FIGO, International Federation of Gynecology and Obstetrics; SD, standard deviation.

^a Percentages for histology were based on 97 tumor samples.

10% fetal calf serum, 50 U/mL⁻¹ penicillin G, and 50 µg/mL⁻¹ streptomycin sulfate at 37°C in a humidified atmosphere with 5% CO₂. The 32 ovarian cancer cell lines that were used in our study were derived from patients and cultivated as described previously.¹⁴ For the reconstitution of *TUSC3* expression, the coding DNA sequence of the IMAGE clone (BC010370 in pDNR-LIB; Takara Bio Europe/Clontech, St. Germain-en-Laye, France) was cloned into the expression vector pLP-IRE-Sneo (Takara Bio Europe/Clontech). For the *TUSC3*-FLAG-tag (*TUSC3*-FLAG) fusion protein, the FLAG peptide was cloned in frame behind the C-terminus of *TUSC3*. The empty vector pLP-IRE-Sneo was used as a control. Transfections were performed using Lipofectamine 2000 (Invitrogen, Darmstadt, Germany), and stable clones were selected with G418 (Sigma-Aldrich, Munich, Germany) (H134 cells, 700 µg/mL⁻¹; MIA PaCa-2 cells, 800 µg/mL⁻¹) and subcultured with half of these concentrations. For the collagen I and bovine serum albumin adhesion assay, the cells were incubated on coated 96-well enzyme-linked immunosorbent assay plates for 30 minutes, washed, and the remaining cells

were quantified with the Cell Titer-Blue cell-viability assay (Promega, Madison, Wis).

DNA and RNA Isolation

Genomic DNA from approximately 15 mg of frozen tissue or cell lines was extracted using the DNeasy Tissue Kit (Qiagen, Hilden, Germany) and quantified with the PicoGreen dsDNA Quantitation Kit (Molecular Probes, Darmstadt, Germany). Total RNA from frozen tissues was extracted using the Agilent Total RNA Isolation Mini Kit (Agilent Technologies, Waldbronn, Germany). Total RNA from cancer cell lines was prepared using the RNeasy Mini Kit (Qiagen) and was quality/quantity assessed on RNA Nano Chips (Lab-on-a-Chip, Agilent Technologies).

Methylation-Specific Polymerase Chain Reaction and 5-Aza-2'-Deoxycytidine Treatment

Bisulfite treatment with 1 µg genomic DNA was done as described previously.²⁸ Methylation-specific PCR (MSP) was performed with 25 ng of bisulfite-treated DNA using previously published primers²⁹ for the test cohort and primers of our own design (methylated sequence: sense, 5'-GGTCGGGTAGGCGTGGTGCG-3'; antisense, 5'-CCGCCCCGCTTACCTACGACGT-3'; with amplification of a 122-base-pair product; unmethylated sequence: sense, 5'-GAGGTTGGTTGGGTA GGTGTGGTGG-3'; antisense, 5'-CACAACCACCACCCACTTACCTA-CAACAT-3'; with amplification of a 136-base-pair product) for the validation cohort with AmpliTaq Gold DNA polymerase (Applied Biosystems, Carlsbad, Calif). Bisulfite sequencing was performed directly with the PCR products purified with the QIAquick PCR Purification Kit (Qiagen). PCR products for the validation cohort were quantified using ALFexpress II (GE Healthcare, Madison, Wis). Because this method yielded continuous data in contrast to the binary results from the original MSP, we dichotomized it at the 29.4% level to match the distribution of *TUSC3* methylation negative and positive samples in the test cohort. DNA demethylation of the MZ6 cancer cell line was performed using a 72-hour treatment with 1 µM or 2.5 µM 5-aza-2'-deoxycytidine (Sigma-Aldrich) in cell culture medium, and relative *TUSC3* expression was evaluated by quantitative real-time reverse transcriptase (RT)-PCR.

cDNA Synthesis and Quantitative Real-Time Reverse Transcriptase-Polymerase Chain Reaction

cDNA was synthesized from 1 µg DNase I-digested total RNA using the DuraScript RT-PCR Kit (Sigma-Aldrich). Expression was relatively quantified using TaqMan probes specific for *TUSC3* Hs00185147_m1 and β2-

microglobulin Hs99999907_m1 (Applied Biosystems), as described elsewhere,^{14,30} and was expressed in relative ratio units. All PCR reactions were performed in at least 3 independent experiments, and RT-negative and template-negative controls were included.

Statistical Analysis

Continuous variables are expressed as means and standard deviations, and categorical variables are expressed as absolute and relative frequencies. To compare frequencies between 2 or more groups, we used Fisher exact tests or Fisher-Freeman-Halton tests, respectively. To compare *TUSC3* expression between 2 or more groups, a *t* test or a 1-way analysis of variance, respectively, was performed using the log-transformed expression as independent variable. Analogously, the potential influence of methylation on *TUSC3* expression was investigated using a *t* test on the logarithmic scale. The potential influence of *TUSC3* methylation on progression-free and overall survival is presented in plots of the corresponding Kaplan-Meier estimates and quantified using Cox proportional hazards regression models. Because of the restricted number of events, only *TUSC3* methylation and the most prominent predictor, FIGO stage, were forced into the model; whereas the remaining variables were selected in a stepwise manner. The date of documented first relapse or the first documentation of disease progression, starting from the time of the first diagnosis, was used as the time point for disease progression. Univariate Cox models were used to demonstrate the influence of known prognostic factors and the potential new prognostic factor. To externally validate our estimated Cox regression models, a risk score for progression-free and overall survival was calculated with the coefficients from the Cox regression models that we built from our test set and corresponding data from our validation set. A Cox regression model using this risk score as a single predictor was used to validate the model estimated from the test set. Coefficients close to 1.00 indicated satisfactory prediction based on the model. *P* values $\leq .05$ were considered statistically significant. All computations were performed using the SAS statistical software package (version 9.2; SAS Institute Inc., Cary, NC), and the graphics were produced using SPSS software (version 13.0; SPSS Inc., Chicago, Ill).

RESULTS

Loss of Expression and Increased *TUSC3* Promoter Methylation in Ovarian Cancer

Analyses of patient samples indicated that *TUSC3* messenger RNA (mRNA) expression was decreased signifi-

cantly in malignant ovarian tumors compared with benign ovarian tissues ($P < .001$) (Fig. 1A, Table 3). We did not observe any significant differences in *TUSC3* expression with regard to patient age, FIGO stage, or histologic grade.

To evaluate methylation status of the *TUSC3* promoter in ovarian cancer, we used methylation specific PCR. Hypermethylation of the *TUSC3* promoter was observed in 30 of 102 ovarian cancer tissues (29.4%), and it was not observed in controls ($P = .003$) (Fig. 1A, B). *TUSC3* promoter methylation in primary tumors was correlated significantly with decreased *TUSC3* mRNA expression ($P < .001$) (Fig. 1A), suggesting a mechanism of promoter methylation-dependent epigenetic silencing of *TUSC3* in ovarian tumors. The statistical analysis revealed no significant association between *TUSC3* promoter methylation and clinicopathologic parameters like tumor histology, tumor grade, FIGO stage, or patient age (Table 4). To validate the results from MSP-based methods, we determined the CpG methylation frequency within the *TUSC3* promoter region using bisulfite sequencing in 3 hypermethylated cell lines and 2 controls. In the hypermethylated cell lines, on average, 75% of CpG islands were methylated compared with 10% in controls (data now shown).

Next, we used a panel of 38 ovarian cancer cell lines that has been introduced and characterized previously.¹⁴ Expression and methylation analyses of ovarian cancer cell lines confirmed a highly significant correlation between *TUSC3* mRNA expression and *TUSC3* promoter methylation ($P < .001$) (Fig. 1A, C). We used MZ6 ovarian cancer cells, which demonstrated *TUSC3* promoter hypermethylation (Fig. 1B), and treated the cell line with the demethylating agent 5-aza-2'-deoxycytidine for 72 hours. Genome-wide demethylation led to a consequent increase in *TUSC3* mRNA expression in this ovarian cancer cell line (Fig. 1D). These results further illustrate the role of DNA methylation in the regulation of *TUSC3* expression.

TUSC3 Affects Cancer Cell Proliferation and Adhesion

We reconstituted *TUSC3* expression in a cancer cell line model using H134 cells (an ovarian cancer cell line with methylated *TUSC3*) and MIA PaCa-2 cells (a pancreatic carcinoma cell line with homozygous deletion of *TUSC3*). *TUSC3* expression was stably reconstituted with DNA constructs that coded for the *TUSC3*-FLAG fusion protein or full-length *TUSC3* cDNA (*TUSC3*), respectively. Reconstitution was confirmed quantitatively by mRNA expression (Fig. 1E). We also assessed the

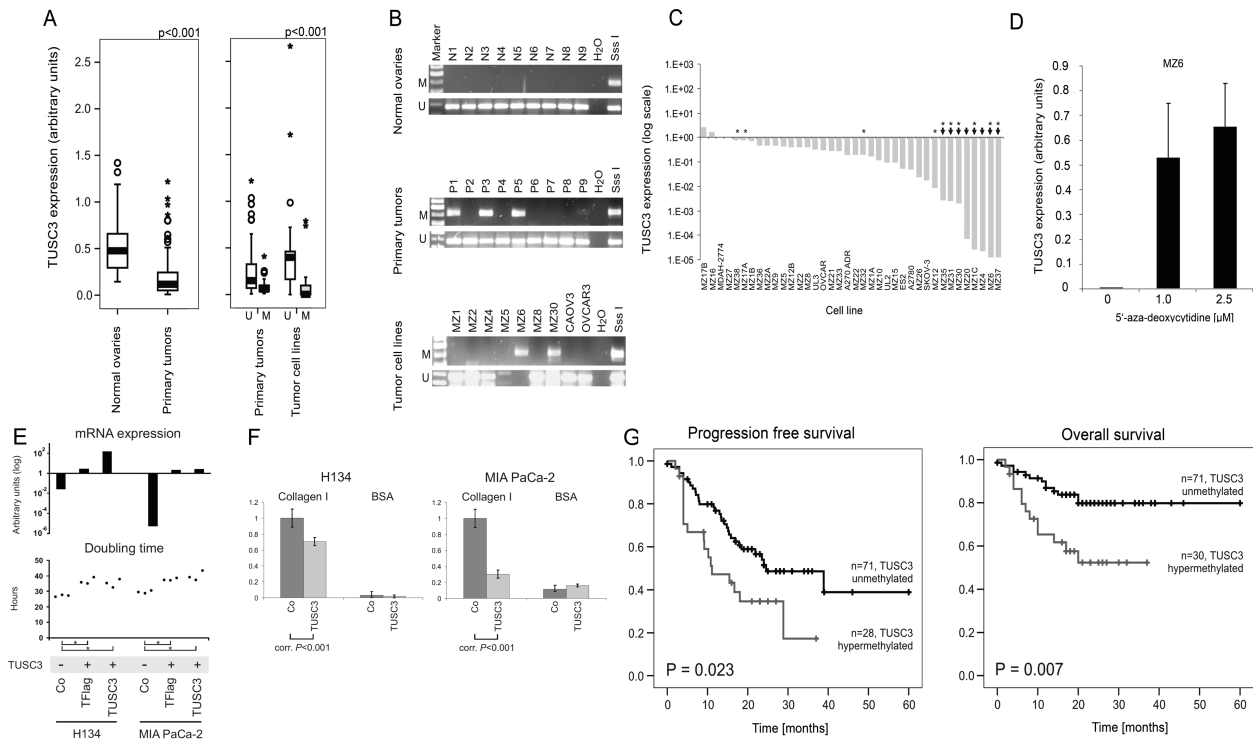


Figure 1. *TUSC3* expression in ovarian cancer and survival analysis. (A) These box plots illustrate (Left) median expression levels of the tumor suppressor candidate 3 (*TUSC3*) gene in benign ovarian tissue and ovarian tumors and (Right) the expression of *TUSC3* subdivided into unmethylated (U) and hypermethylated (M) fractions, including cell lines. (B) Representative ethidium bromide agarose gels reveal methylation-specific polymerase chain reaction (PCR) products from (Top) 9 benign ovarian tissue samples (N1-N9), (Middle) 9 ovarian tumor samples (P1-P9), and (Bottom) 9 ovarian cancer cell lines. Sss I (CpG methylase)-methylated human DNA was used as a positive control. (C) The expression of *TUSC3* is illustrated in 38 ovarian cancer cell lines (log scale). Arrows indicate cell lines that had silenced *TUSC3* expression, and asterisks indicate cell lines that had methylation-specific PCR products. The expression of *TUSC3* was determined by quantitative reverse transcriptase-PCR and was normalized to β -2 microglobulin. (D) The reconstitution of *TUSC3* expression in the MZ6 cell line is illustrated. Cells either were cultivated in the presence of 1.0 M or 2.5 M of the demethylating agent 5-aza-2'-deoxycytidine or were left untreated for 48 hours. *TUSC3* expression was determined as indicated in C. (E) This chart illustrates the in vitro characterization of cell line models that had reconstituted *TUSC3* expression (H134 cells and MIA PaCa-2 cells). Messenger RNA (mRNA) expression is illustrated in arbitrary units, and doubling time is illustrated in hours. Co indicates control; TFlag, *TUSC3*-FLAG fusion protein; +, *TUSC3* positive; – *TUSC3* negative. (F) The adhesion of cells to 96-well plates that were coated with collagen I and bovine serum albumin (BSA) (as a control) is illustrated. Binding of the control cells to collagen I was set arbitrarily to 1. All experiments were performed in triplicate, and significance was calculated using *t* tests. (G) These Kaplan-Meier survival curves illustrate progression-free and overall survival for patients who had tumor samples with hypermethylated or unmethylated *TUSC3*. The date of either the first documented relapse or the first documented disease progression, starting from the time of the first diagnosis, was used as the time point to define progression. *P* values indicate the statistical significance determined using univariate Cox regression analysis.

influence of *TUSC3* re-expression on cell proliferation and adhesion. In *TUSC3*-reconstituted H134 and MIA PaCa-2 cell lines, a significant decrease in cellular proliferation (expressed as increased doubling time) was observed (Fig. 1E). In addition to these findings, *TUSC3* re-expression significantly decreased the adhesion of cancer cells to collagen I, an extracellular matrix component (Fig. 1F).

***TUSC3* Promoter Methylation Predicts Survival in Patients With Ovarian Cancer**

We previously observed that *TUSC3* was down-regulated in high-grade ovarian cancer using a systematic approach

to analyze putative tumor suppressor genes on the short arm of chromosome 8.¹⁴ In the current analysis of a larger cohort, we observed that patients who had tumors with *TUSC3* promoter methylation had significantly shorter progression-free and overall survival rates, with a median progression-free survival of 11.1 months in the methylated group versus 24.6 months in the unmethylated group (Fig. 1G). In addition, a Cox proportional hazards analysis that included known risk factors (age, histologic subtype, FIGO stage, tumor grade, residual disease, and therapy response) and *TUSC3* methylation status revealed a significant association between *TUSC3* promoter

TABLE 3. TUSC3 Expression in Ovarian Cancer and Survival Analysis

Clinicopathologic Characteristic	Expression of TUSC3: Mean (95% CI), Arbitrary Units	P for Comparison
Benign ovarian samples	0.465 (0.347–0.623)	
Tumor samples vs benign ovarian samples	0.105 (0.082–0.135)	< .001 ^a
Age, y		
≤50	0.085	.299 ^a
>50	0.114	
Histology		
Serous	0.121	.037 ^a
Nonserous	0.064	
FIGO stage		
I	0.084	.764 ^b
II	0.124	
III	0.104	
IV	0.126	
Tumor grade		
1	0.068	.188 ^b
2	0.135	
3	0.086	

Abbreviations: CI, confidence interval; FIGO, International Federation of Gynecology and Obstetrics; TUSC3, tumor suppressor candidate 3.

^aAn analysis of variance was used to calculate *P* values after logarithmic transformation; means and CIs were calculated after back-transformation to the original scale.

^b*T* tests were used to calculate *P* values after logarithmic transformation; means and CIs were calculated after back-transformation to the original scale.

methylation and progression-free survival (relative risk [RR], 2.23; *P* = .012) as well as overall survival (RR, 5.14; *P* = .001). This association was independent of other risk factors, including FIGO stage and response to chemotherapy, which were the strongest predictive factors in our analysis (the interaction term was not significant) (Table 5). The hazard ratio of methylated versus unmethylated TUSC3 promoter status for progression-free survival was significant (RR, 1.97; *P* = .023) and was only slightly inferior to an increase of 1 FIGO stage (RR, 2.82; *P* < .001) and to the presence residual disease after surgery (RR, 3.04; *P* = .001). Similarly, the significant influence of TUSC3 methylation on overall survival (RR, 2.92; *P* = .007) was comparable to an increase of 1 FIGO stage (RR, 2.52; *P* = .002), to histologic subtype (serous vs nonserous: RR, 2.37; *P* = .037), and to residual disease after surgery (RR, 4.86; *P* < .001).

To validate our finding of TUSC3 hypermethylation in ovarian cancer and its prognostic significance, we determined TUSC3 methylation status in an independent cohort of 97 patients with late-stage ovarian cancer (FIGO stage ≥II) (Table 1) using a different MSP-based method. A second set of MSP primers targeting the same CpG island in the TUSC3 promoter was designed, and PCR

TABLE 4. TUSC3 Promoter Methylation and Clinicopathologic Characteristics

Clinicopathologic Characteristic	Methylation of TUSC3: No. of Patients/ Total No. (%)	P for Comparison ^a
Benign ovarian samples	0/20 (0)	
Primary tumor samples	30/102 (29.4)	.003
Age, y		.218
≤50	5/26 (19.2)	
>50	25/75 (33.3)	
Histology		.200
Serous	21/79 (26.6)	
Nonserous	9/22 (40.9)	
FIGO stage		.948
I	5/17 (29.4)	
II	2/10 (20)	
III	15/51 (29.4)	
IV	7/22 (31.8)	
Tumor grade		.102
1	2/2 (100)	
2	15/48 (31.2)	
3	13/51 (25.5)	

Abbreviations: FIGO, International Federation of Gynecology and Obstetrics; TUSC3, tumor suppressor candidate 3.

^aThe Fisher exact test and the Fisher-Freeman-Halton test were used to calculate *P* values.

products were quantified with a semiquantitative gel system and dichotomized at the 29.4% level, generating 29 positive samples (the rationale for this procedure is provided above; see Materials and Methods). The hazard ratio for TUSC3 was estimated from a multiple Cox model using validation data in the same manner that was used for the test set data (disease-free survival: RR, 1.40; 95% confidence interval, 0.77–2.52; *P* = .269; overall survival: RR, 6.34; 95% confidence interval, 1.95–20.62; *P* = .002).

To confirm that the Cox regression models from our test and validation cohorts were similar, given the slightly different patient characteristics, risk scores for progression-free survival ($0.83 \times \text{FIGO stage} + 1.09 \times \text{therapy response} + 0.80 \times \text{TUSC3 methylation}$) and overall survival ($0.76 \times \text{FIGO stage} + 1.80 \times \text{therapy response} + 1.64 \times \text{TUSC3 methylation}$) were calculated with the coefficients from the Cox regression models we built from our test set (Table 5) and with the corresponding values (FIGO stage, response to chemotherapy, and TUSC3 methylation status) from our validation set. Cox regression models using the respective risk score as a single predictor were used to validate the models estimated from the test set. The resulting regression coefficients were 1.05 (95% confidence interval, 0.67–1.42) for disease-free survival and 1.16 (95% confidence interval, 0.73–1.59) for overall survival, demonstrating a successful validation of

TABLE 5. Univariate and Multivariate Cox Proportional Hazards Analysis of Factors Affecting Progression-Free and Overall Survival in Ovarian Cancer

Variable	Univariate Analysis		Multivariate Analysis	
	RR (95% CI)	P	RR (95% CI)	P
Progression-free survival				
Age at diagnosis	1.02 (0.99–1.05)	.184	— ^a	
Histology: Nonserous vs serous ^b	1.16 (0.58–2.32)	.683	— ^a	
FIGO stage ^c	2.82 (1.87–4.26) ^d	< .001	2.30 (1.45–3.64) ^d	< .001
Tumor grade ^c	0.98 (0.58–1.65)	.933	— ^a	
Residual disease: >1 cm vs ≤1 cm ^b	3.04 (1.53–6.03) ^d	.001	— ^a	
Therapy response: No vs yes ^b	4.91 (2.64–9.10) ^d	< .001	2.97 (1.56–5.66) ^d	.001
Methylation of <i>TUSC3</i> : Yes vs no ^b	1.97 (1.10–3.53) ^d	.023	2.23 (1.19–4.17) ^d	fo.012
Overall survival				
Age at diagnosis	1.06 (1.02–1.10) ^d	.003	— ^a	
Histology: Nonserous vs serous ^b	2.37 (1.05–5.33) ^d	.037	— ^a	
FIGO stage ^c	2.52 (1.41–4.49) ^d	.002	2.14 (0.96–4.75)	.062
Tumor grade ^c	0.76 (0.38–1.53)	.446	— ^a	
Residual disease: >1 cm vs ≤1 cm ^b	4.86 (2.13–11.12) ^d	< .001	— ^a	
Therapy response: No vs yes ^b	9.56 (3.56–25.66) ^d	< .001	6.05 (2.06–17.73) ^d	.001
Methylation of <i>TUSC3</i> : Yes vs no ^b	2.92 (1.35–6.30) ^d	.007	5.14 (1.93–13.66) ^d	.001

Abbreviations: CI, confidence interval; FIGO, International Federation of Gynecology and Obstetrics; RR, relative risk; *TUSC3*, tumor suppressor candidate 3.

^aThis variable was not selected in the stepwise selection procedure.

^bThis was a categorical variable.

^cThis was an ordinal variable.

^dThis *P* value was statistically significant.

the regression model. Note that FIGO stage was incorporated into the risk score and, thus, was accounted for when transferring the coefficients estimated from the test set to the validation set.

DISCUSSION

Prognostic factors in ovarian cancer include disease stage, tumor grade, and size of the residual tumor after primary cytoreductive surgery.^{31,32} By using publicly available gene-expression profiling data, we have systematically screened the region on 8p22 for differentially regulated genes and identified *TUSC3* as a candidate tumor suppressor gene in ovarian cancer.¹⁴ In our current work, we validate our previous observations in a larger, completely independent patient population and demonstrate that the expression of *TUSC3* in ovarian cancer may be regulated by promoter methylation. We did not investigate other possible mechanisms for *TUSC3* down-regulation in ovarian cancer, which may include micro-RNA-mediated silencing, transcriptional regulation, or homozygous deletions of 8p22, as demonstrated in prostate and pancreatic cancers.^{11,13}

Some of our observations differ from the screening study, most probably because of the larger size of the cohorts. We can now observe a significant difference in *TUSC3* methylation and expression between ovarian cancer and controls, and we can confirm an impact of *TUSC3* on ovarian cancer survival, although we do not

observe differences between high-grade and low-grade tumors, as described previously.¹⁴ Our cohorts did not explicitly exclude patients with FIGO stage I and II disease, but the stepwise multivariate analysis did include FIGO staging, hinting at a FIGO-independent prognostic effect of *TUSC3* methylation. A recent paradigm shift points toward distinct tissues of origin in ovarian cancer that are responsible for its various histologic subtypes.³³ Because our study was designed to be exploratory, we deliberately included different histologic subtypes of ovarian cancer, because we were acutely aware of the recent controversy regarding their differing origin and pathogenesis.^{34,35} Nevertheless, the vast majority of our patients, particularly in the validation cohort, were diagnosed with advanced stage, high-grade, serous ovarian cancer. Hence, we propose the further evaluation of *TUSC3* as a prognostic factor primarily in this subset of patients with ovarian cancer.

TUSC3 is the human homologue to *S. cerevisiae* Ost3p, a noncatalytic subunit of the oligosaccharyltransferase complex.^{18,19} Analyses of the Ost3p and its yeast paralogue Ost6p (human MagT1/IAP) demonstrated their function in regulating glycosylation efficiency³⁶ and recently also uncovered their oxidoreductase activity as well as a possible role in magnesium transport.³⁷ Aberrant glycosylation of proteins can be observed in essentially all in vitro cancer models and human cancers, and many glycosylated epitopes constitute tumor-associated antigens,^{38,39}

sustaining a long-standing debate regarding whether and how protein glycosylation is involved in tumorigenesis. Recently, global DNA methylation changes in ovarian cancer cells were linked to significant alterations of protein glycosylation.⁴⁰ One possible explanation for this effect is the re-expression of epigenetically silenced key glycosyltransferase enzymes. Treatment with 5-aza-2'-deoxycytidine restores sensitivity to carboplatin in patients with advanced ovarian cancer.⁴¹ In addition, it has been demonstrated that defective multidrug resistance proteins lead to platinum resistance.⁴² Defects in N-glycosylation also may affect tumor growth in cells with deregulated phosphatidylinositol 3-kinase/v-Akt murine thymoma viral oncogene homolog (PI3K-Akt) pathway.²⁶ We have observed that reconstitution of TUSC3 in vitro decreases proliferation as well as binding of cancer cells to the extracellular matrix. Consequently, we propose that loss of TUSC3 not only may lead to ovarian cancer growth but also may facilitate the adhesion of cancer cells to the extracellular matrix caused by differential glycosylation of yet unknown adhesion molecules. In ovarian cancer in particular, loss of TUSC3 may promote intraperitoneal dissemination, which is generally associated with a poor prognosis. In light of these data, our results further add to the picture and emphasize the role of methylation and N-glycosylation in ovarian cancer tumorigenesis.

A deeper understanding of the role of *TUSC3* promoter methylation in the development of ovarian cancer may offer additional possibilities for therapeutic interventions in the future. Regardless of the molecular function of TUSC3 protein, the frequency of *TUSC3* promoter methylation in ovarian cancer deserves prospective evaluation either on its own or as a part of a larger prognostic biomarker panel.

FUNDING SOURCES

This work was supported by the Austrian Science Fund (FWF) (grant P17891), Initiative Krebsforschung, and the Center for International Cooperation and Mobility of the Austrian Agency for International Cooperation in Education and Research (Project CZ 04/2012).

CONFLICT OF INTEREST DISCLOSURES

The authors made no disclosures.

REFERENCES

- Jemal A, Bray F, Center MM, Ferlay J, Ward E, Forman D. Global cancer statistics. *CA Cancer J Clin*. 2011;61:69-90.
- Wei SH, Balch C, Paik HH, et al. Prognostic DNA methylation biomarkers in ovarian cancer. *Clin Cancer Res*. 2006;12:2788-2794.
- Campan M, Moffitt M, Houshdaran S, et al. Genome-scale screen for DNA methylation-based detection markers for ovarian cancer [serial online]. *PLoS One*. 2011;6:e28141.
- Gloss BS, Patterson KI, Barton CA, et al. Integrative genome-wide expression and promoter DNA methylation profiling identifies a potential novel panel of ovarian cancer epigenetic biomarkers. *Cancer Lett*. 2012;318:76-85.
- Das PM, Singal R. DNA methylation and cancer. *J Clin Oncol*. 2004;22:4632-4642.
- Jones PA, Baylin SB. The fundamental role of epigenetic events in cancer. *Nat Rev Genet*. 2002;3:415-428.
- Laird PW. The power and the promise of DNA methylation markers. *Nat Rev Cancer*. 2003;3:253-266.
- Bova GS, MacGrogan D, Levy A, Pin SS, Bookstein R, Isaacs WB. Physical mapping of chromosome 8p22 markers and their homozygous deletion in a metastatic prostate cancer. *Genomics*. 1996;35:46-54.
- MacGrogan D, Levy A, Bova GS, Isaacs WB, Bookstein R. Structure and methylation-associated silencing of a gene within a homozygously deleted region of human chromosome band 8p22. *Genomics*. 1996;35:55-65.
- Bashyam MD, Bair R, Kim YH, et al. Array-based comparative genomic hybridization identifies localized DNA amplifications and homozygous deletions in pancreatic cancer. *Neoplasia*. 2005;7:556-562.
- Levy A, Dang UC, Bookstein R. High-density screen of human tumor cell lines for homozygous deletions of loci on chromosome arm 8p. *Genes Chromosomes Cancer*. 1999;24:42-47.
- Arbieva ZH, Banerjee K, Kim SY, et al. High-resolution physical map and transcript identification of a prostate cancer deletion interval on 8p22. *Genome Res*. 2000;10:244-257.
- Bova GS, Carter BS, Bussemakers MJ, et al. Homozygous deletion and frequent allelic loss of chromosome 8p22 loci in human prostate cancer. *Cancer Res*. 1993;53:3869-3873.
- Pils D, Horak P, Gleiss A, et al. Five genes from chromosomal band 8p22 are significantly down-regulated in ovarian carcinoma: N33 and EFA6R have a potential impact on overall survival. *Cancer*. 2005;104:2417-2429.
- Garshabi M, Hadavi V, Habibi H, et al. A defect in the TUSC3 gene is associated with autosomal recessive mental retardation. *Am J Hum Genet*. 2008;82:1158-1164.
- Molinari F, Foulquier F, Tarpey PS, et al. Oligosaccharyltransferase-subunit mutations in nonsyndromic mental retardation. *Am J Hum Genet*. 2008;82:1150-1157.
- Kelleher DJ, Gilmore R. An evolving view of the eukaryotic oligosaccharyltransferase. *Glycobiology*. 2006;16:47R-62R.
- Kelleher DJ, Karaoglu D, Mandon EC, Gilmore R. Oligosaccharyltransferase isoforms that contain different catalytic STT3 subunits have distinct enzymatic properties. *Mol Cell*. 2003;12:101-111.
- Schulz BL, Stirnimann CU, Grimshaw JP, et al. Oxidoreductase activity of oligosaccharyltransferase subunits Ost3p and Ost6p defines site-specific glycosylation efficiency. *Proc Natl Acad Sci U S A*. 2009;106:11061-11066.
- Collard JG, Schijven JF, Bikker A, La Riviere G, Bolscher JG, Roos E. Cell surface sialic acid and the invasive and metastatic potential of T-cell hybridomas. *Cancer Res*. 1986;46:3521-3527.
- Dennis JW, Granovsky M, Warren CE. Glycoprotein glycosylation and cancer progression. *Biochim Biophys Acta*. 1999;1473:21-34.
- Yogeeswaran G, Salk PL. Metastatic potential is positively correlated with cell surface sialylation of cultured murine tumor cell lines. *Science*. 1981;212:1514-1516.
- Janik ME, Litynska A, Vereecken P. Cell migration—the role of integrin glycosylation. *Biochim Biophys Acta*. 2010;1800:545-555.
- Kakugawa Y, Wada T, Yamaguchi K, et al. Up-regulation of plasma membrane-associated ganglioside sialidase (Neu3) in human colon cancer and its involvement in apoptosis suppression. *Proc Natl Acad Sci U S A*. 2002;99:10718-10723.
- Lau KS, Partridge EA, Grigorian A, et al. Complex N-glycan number and degree of branching cooperate to regulate cell proliferation and differentiation. *Cell*. 2007;129:123-134.

26. Fang M, Shen Z, Huang S, et al. The ER UDPase ENTPD5 promotes protein N-glycosylation, the Warburg effect, and proliferation in the PTEN pathway. *Cell*. 2010;143:711-724.
27. McShane LM, Altman DG, Sauerbrei W, Taube SE, Gion M, Clark GM. REporting recommendations for tumour MARKer prognostic studies (REMARK). *Eur J Cancer*. 2005;41:1690-1696.
28. Horak P, Pils D, Haller G, et al. Contribution of epigenetic silencing of tumor necrosis factor-related apoptosis inducing ligand receptor 1 (DR4) to TRAIL resistance and ovarian cancer. *Mol Cancer Res*. 2005;3:335-343.
29. Xu XL, Yu J, Zhang HY, et al. Methylation profile of the promoter CpG islands of 31 genes that may contribute to colorectal carcinogenesis. *World J Gastroenterol*. 2004;10:3441-3454.
30. Pfaffl MW. A new mathematical model for relative quantification in real-time RT-PCR [serial online]. *Nucleic Acids Res*. 2001;29:e45.
31. Holschneider CH, Berek JS. Ovarian cancer: epidemiology, biology, and prognostic factors. *Semin Surg Oncol*. 2000;19:3-10.
32. van der Burg ME. Advanced ovarian cancer. *Curr Treat Options Oncol*. 2001;2:109-118.
33. Vaughan S, Coward JI, Bast RC Jr, et al. Rethinking ovarian cancer: recommendations for improving outcomes. *Nat Rev Cancer*. 2011;11:719-725.
34. Birrer MJ. The origin of ovarian cancer-is it getting clearer? *N Engl J Med*. 2010;363:1574-1575.
35. Ahmed A, Becker C, Bast R. Jr The origin of ovarian cancer. *BJOG*. 2012;119:134-136.
36. Karaoglu D, Kelleher DJ, Gilmore R. Functional characterization of Ost3p. Loss of the 34-kD subunit of the *Saccharomyces cerevisiae* oligosaccharyltransferase results in biased underglycosylation of acceptor substrates. *J Cell Biol*. 1995;130:567-577.
37. Zhou H, Clapham DE. Mammalian MagT1 and TUSC3 are required for cellular magnesium uptake and vertebrate embryonic development. *Proc Natl Acad Sci U S A*. 2009;106:15750-15755.
38. Hakomori S. Glycosylation defining cancer malignancy: new wine in an old bottle. *Proc Natl Acad Sci U S A*. 2002;99:10231-10233.
39. Kobata A, Amano J. Altered glycosylation of proteins produced by malignant cells, and application for the diagnosis and immunotherapy of tumours. *Immunol Cell Biol*. 2005;83:429-439.
40. Saldova R, Dempsey E, Perez-Garay M, et al. 5-AZA-2'-deoxycytidine induced demethylation influences N-glycosylation of secreted glycoproteins in ovarian cancer. *Epigenetics*. 2011;6:1362-1372.
41. Matei D, Fang F, Shen C, et al. Epigenetic resensitization to platinum in ovarian cancer. *Cancer Res*. 2012;72:2197-2205.
42. Beretta GL, Benedetti V, Cossa G, et al. Increased levels and defective glycosylation of MRPs in ovarian carcinoma cells resistant to oxaliplatin. *Biochem Pharmacol*. 2010;79:1108-1117.

2. Vaňhara P, Horak P, Pils D, Anees M, Petz M, Gregor W, Zeillinger R, Krainer M. **Loss of the oligosaccharyl transferase subunit TUSC3 promotes proliferation and migration of ovarian cancer cells.** *International Journal of Oncology* 2013; **42**(4):1383-9.

Commentary:

In this work, phenotypes associated with TUSC3 loss were for the first time described in ovarian cancer context. We demonstrated that TUSC3 is an integral protein of the endoplasmic reticulum constituting on several subunits of the oligosaccharyltransferase complex. Alterations in TUSC3 level affected glycosylation patterns in ovarian cancer cells. Downregulation of TUSC3 promoted proliferation and migration of ovarian cancer cells *in vitro*. In summary, reveal TUSC3 as a novel tumor suppressor gene in ovarian cancer, and the first tumor suppressor at all that directly affect N-glycosylation machinery.

DOI: 10.3892/ijo.2013.1824
Journal: International Journal of Oncology
Impact factor (WOS, 2013): 2.773
Number of citations (WOS, 2018): 18
Cited in: Nature Communications, Tumor biology, Seminars in Cancer biology, American Journal of Medical Genetics, Molecular Cancer, etc.

Most important citation:

Oliveira-Ferrer L, Legler K, Milde-Langosch K. **Role of protein glycosylation in cancer metastasis.** *Seminars in Cancer Biology* 2017; **44**:141-152.
doi: 10.1016/j.semcan.2017.03.002. (IF 2016: 9.141)

Contribution of the author: 1st author. Collection and/or assembly of data, data analysis and interpretation, manuscript writing.

Loss of the oligosaccharyl transferase subunit *TUSC3* promotes proliferation and migration of ovarian cancer cells

PETR VAŇHARA^{1*}, PETER HORAK^{2*}, DIETMAR PILS³, MARIAM ANEES², MICHAELA PETZ²,
WOLFGANG GREGOR⁴, ROBERT ZEILLINGER³ and MICHAEL KRAINER²

¹Department of Histology and Embryology, Faculty of Medicine, Masaryk University, Brno, Czech Republic; Departments of ²Internal Medicine I and Comprehensive Cancer Center and ³Obstetrics and Gynecology, Division of Gynecology, Medical University of Vienna; ⁴Research Group of Molecular Pharmacology and Toxicology, University of Veterinary Medicine Vienna, Vienna, Austria

Received November 18, 2012; Accepted January 8, 2013

DOI: 10.3892/ijo.2013.1824

Abstract. Consequences of deregulated protein N-glycosylation on cancer pathogenesis are poorly understood. *TUSC3* is a gene with a putative function in N-glycosylation, located on the short arm of chromosome 8. This is a chromosomal region of frequent genetic loss in ovarian cancer. We established recently that the expression of *TUSC3* is epigenetically decreased in epithelial ovarian cancer compared to benign controls and provides prognostic information on patient survival. Therefore, we analyzed the consequences of silenced *TUSC3* expression on proliferation, invasion and migration of ovarian cell lines. In addition, we performed subcellular fractionation, co-immunofluorescence and co-immunoprecipitation experiments to establish the molecular localization of *TUSC3* in ovarian cancer cells. We demonstrated that *TUSC3* is localized in the endoplasmic reticulum as a subunit of the oligosaccharyltransferase complex and is capable of modulation of glycosylation patterning of ovarian cancer cells. Most importantly, silencing of *TUSC3* enhances proliferation and migration of ovarian cancer cells *in vitro*. Our observations suggest a role for N-glycosylating events in ovarian cancer pathogenesis in general, and identify *TUSC3* as a tumor suppressor gene in ovarian cancer in particular.

Introduction

Epithelial ovarian cancer is the most lethal gynecologic malignancy and the fourth most frequent cause of cancer mortality in women in western industrialized countries (1). Early

detection and diagnosis of ovarian cancer presents one of the challenges of this entity and consequently a majority of cases are diagnosed in advanced stages (FIGO III and IV). The prognosis for women with advanced ovarian cancer remains bleak despite the advances of surgical and medical therapies in the last decades. A better understanding of the pathogenesis of ovarian cancer may lead to earlier diagnosis and novel therapies for this disease.

Tumor suppressor candidate 3 (*TUSC3*), originally named N33, was identified as a potential tumor suppressor gene in prostate cancer located on chromosome band 8p22 (2,3). Homozygous deletions of this chromosomal region have been detected in pancreatic (4,5) and prostate cancer cell lines (6,7), even though mutations of the *TUSC3* coding sequence are rare. Using a systematical screening approach, we recognized *TUSC3* as a significantly downregulated gene in ovarian cancer (8). Recently, we revealed a strong prognostic significance of epigenetic silencing of *TUSC3* on survival of ovarian cancer patients (9), however, the molecular mechanism of tumor-suppressor effect of *TUSC3* on cancer cells remained unclear. *TUSC3* deletions or mutations are frequently associated with familial mental retardation syndromes (10,11). *TUSC3* function in regulation of magnesium transport and embryonic development in vertebrates has been suggested (12). *TUSC3* shares a high sequence homology with Ost3p, a subunit of the oligosaccharyltransferase (OST) complex involved in N-glycosylation of proteins in *Saccharomyces cerevisiae* (13-15), implying an analogous function in mammalian cells. Alterations of protein N-glycosylation are associated with carcinogenic properties, such as invasion and metastasis (16-18). Deregulated enzymatic activities of proteins directly involved in N-glycosylation, or the availability of potential glycosylation sites determined by the branching of N-glycans are considered to be crucial for these effects (19-21). Well known targets for differential N-glycosylation in tumor cells or their microenvironment are, among others, growth factor receptors (21,22), immunomodulators (23) or extracellular matrix receptors, such as integrins (24).

In this study, we investigated the subcellular localization of *TUSC3* in human ovarian cancer cell lines and identified it as a binding partner of STT3A, a core protein of oligo-

Correspondence to: Dr Michael Krainer, Department of Internal Medicine I and Comprehensive Cancer Center, Medical University of Vienna, Währinger Gürtel 18-20, A-1090 Vienna, Austria
E-mail: michael.krainer@meduniwien.ac.at

*Contributed equally

Key words: *TUSC3*, ovarian cancer, glycosylation, proliferation

saccharyltransferase complex in endoplasmic reticulum *in vitro*. Additionally, we observed that silencing of *TUSC3* expression *in vitro* stimulates migration and proliferation of ovarian cancer cell lines, in particular under conditions of growth factor deprivation. Taken together, we present the first experimental evidence that a protein involved in N-glycosylation may act as a clinically-relevant tumor suppressor gene in ovarian cancer.

Materials and methods

Cell culture and lentiviral transduction. The cancer cell lines were obtained from American Type Culture Collection and cultured in medium (HEK293T, H134, DMEM; OVCAR-3, α -MEM; SKOV3, McCoy's 5A; TR-170, RPMI-1640) enriched with 10% FCS (fetal calf serum), 50 U/ml penicillin G and 50 μ g/ml streptomycin sulfate at 37°C in a humidified atmosphere with 5% CO₂. For the reconstitution of *TUSC3* expression in H134 cell line, the CDS of the IMAGE clone (BC010370 in pDNR-LIB) was cloned into the expression vector pLP-IRESneo. The FLAG peptide was cloned in frame behind the C-terminus of *TUSC3* to form a *TUSC3*-FLAG fusion protein. The empty vector pLP-IRESneo was used as a control. Transfection was performed with Lipofectamine 2000 (Invitrogen), stable clones were selected with G418 (700 μ g/ml). Downregulation of *TUSC3* in SKOV3 and TR-170 cell lines was performed by lentiviral transduction using a 4-plasmid system with pLKO.1 puro vector containing *TUSC3* shRNA or scrambled control (Open Biosystems, Thermo Fisher Scientific) and HEK-293T packaging cell line. To generate stable cell lines, cells were selected in media containing puromycin (3 μ g/ml). Prior to the proliferation, migration and invasion assays, cells were cultivated in the absence of selection antibiotics and the status of *TUSC3* silencing was assessed by qRT-PCR regularly.

RNA isolation, cDNA synthesis and quantitative real-time RT-PCR. Total RNA from cancer cell lines was prepared using the RNeasy Mini kit (Qiagen) and quality/quantity assessed on RNA Nano Chips (Lab-on-a-Chip, Agilent Technologies). cDNA was synthesized from 1 μ g DNase I-digested total RNA using the DuraScript RT-PCR kit (Sigma-Aldrich). Expression was relatively quantified using TaqMan probes specific for *TUSC3*, Hs00185147_m1 and β 2-microglobulin, Hs99999907_m1 (Applied Biosystems) as described elsewhere (8,25) and expressed in relative ratio units. All PCR reactions were performed from at least three independent experiments, and reverse transcriptase-negative and template-negative controls were included.

Proliferation, migration and invasion assays. Proliferation rates were determined in 96-well format using Cell Titer-Blue cell viability assay (Promega) according to the manufacturer's instructions. Migration and invasion abilities were measured using *in vitro* migration (8.0- μ m pore size control chambers) and invasion assays (BD Matrigel™ invasion chambers). Cells that penetrated the membrane were quantified after Calcein dye (BD Bioscience) uptake by fluorescence measurement at 435_{Ex}-538_{Em} nm. Each data point was calculated as mean of three technical replicates. Three independent experiments were

performed. For direct assessment of cell migration a wound healing assay in a confluent cell monolayer was performed. Wound closure was assessed after 18 h. Representative images out of three independent experiments are shown.

Subcellular fractionation and immunofluorescence. Subcellular fractionation (nuclei, mitochondria, lysosomes, microsomes, and cytoplasm) of H134-*TUSC3*-Flag cells were performed based on a differential centrifugation protocol (1,000, 9,700, 20,200 and 182,000 g_{max} for aforementioned organelles, respectively (26) after cell lysis with a Potter pestle. The purity of these fractions was analyzed by immunoblotting with antibodies against marker proteins for the respective fractions (nucleus, nucleoporin p62; mitochondria, cox 5a; lysosomes, none; microsomes, ribophorin I; and cytoplasm, β -actin; Sigma-Aldrich). A mouse monoclonal anti-FLAG M2 antibody (F3165, Sigma-Aldrich) primary antibody against FLAG and a goat secondary anti-mouse HRP-linked antibody (Calbiochem) were used.

Immunofluorescence staining was performed on formaldehyde-fixed H134-*TUSC3*-FLAG cells with antibodies against FLAG SIG1-25 (F2555, Sigma-Aldrich) and calnexin (polyclonal rabbit antibody, kind gift from E. Ivessa) and counterstained with phalloidin (F-actin). For a morphological overview, the whole cells were stained with hematoxylin/eosin or phalloidin (F-actin)/DAPI (nuclei).

Immunocytochemistry. For immunocytochemical staining, cells on Lab-Tek™ Chamber Slides™ (Nalge Nunc International, Rochester, NY) were formaldehyde-fixed and permeabilized with 0.5% Triton X-100. Endogenous peroxidase activity and slides were blocked with 3% H₂O₂/PBS and 0.2% fish gelatine, respectively. After incubation with polyclonal goat anti-integrin β 1 antibody (1:500, R&D, Minneapolis, MN) and biotinylated rabbit anti-goat antibody (1:200, Vector Laboratories, Burlingame, CA) or with the biotinylated sialic acid-specific lectin SNA (1:200, Vector Laboratories), the streptavidin ABCComplex-HRP (ABC-kit from Dako, Glostrup, Denmark) was employed and subsequently DAB⁺ (Dako) staining was performed. IgG-negative controls were included. Finally, cells were counterstained with hematoxyline/eosin and mounted in Eukitt (O. Kindler GmbH, Freiburg, Germany). Microscopy was performed on an Olympus BX50 upright light microscope (Olympus Europe, Hamburg, Germany) equipped with the Soft Imaging system CC12.

Western blotting and immunoprecipitation. Harvested cells were washed two times with 1X PBS and resuspended in the NP-40 lysis buffer containing 50 mM Tris-Cl (pH 7.4), 150 mM NaCl, 2 mM EDTA, 1% NP-40, 50 mM NaF and supplemented with phosphatase inhibitor cocktail (PhosStop, Roche) and protease inhibitor cocktail (Complete, Roche). Protein extracts (15 μ g) quantified by BCA protein assay (Pierce, Austria), were mixed with 2X Laemmli sample buffer (100 mM Tris pH 6.8, 4% SDS, 200 mM DTT, 20% glycerol and 0.1% bromophenol blue) boiled for 3 min and resolved by 10% sodium dodecyl-sulfate-polycrylamide gel electrophoresis (SDS-PAGE). For analysis of glycosylation of integrin β 1, the 7% SDS-PAGE was employed. The resolved proteins were then electroblotted to the 0.45- μ m PVDF membrane (Millipore) and incubated

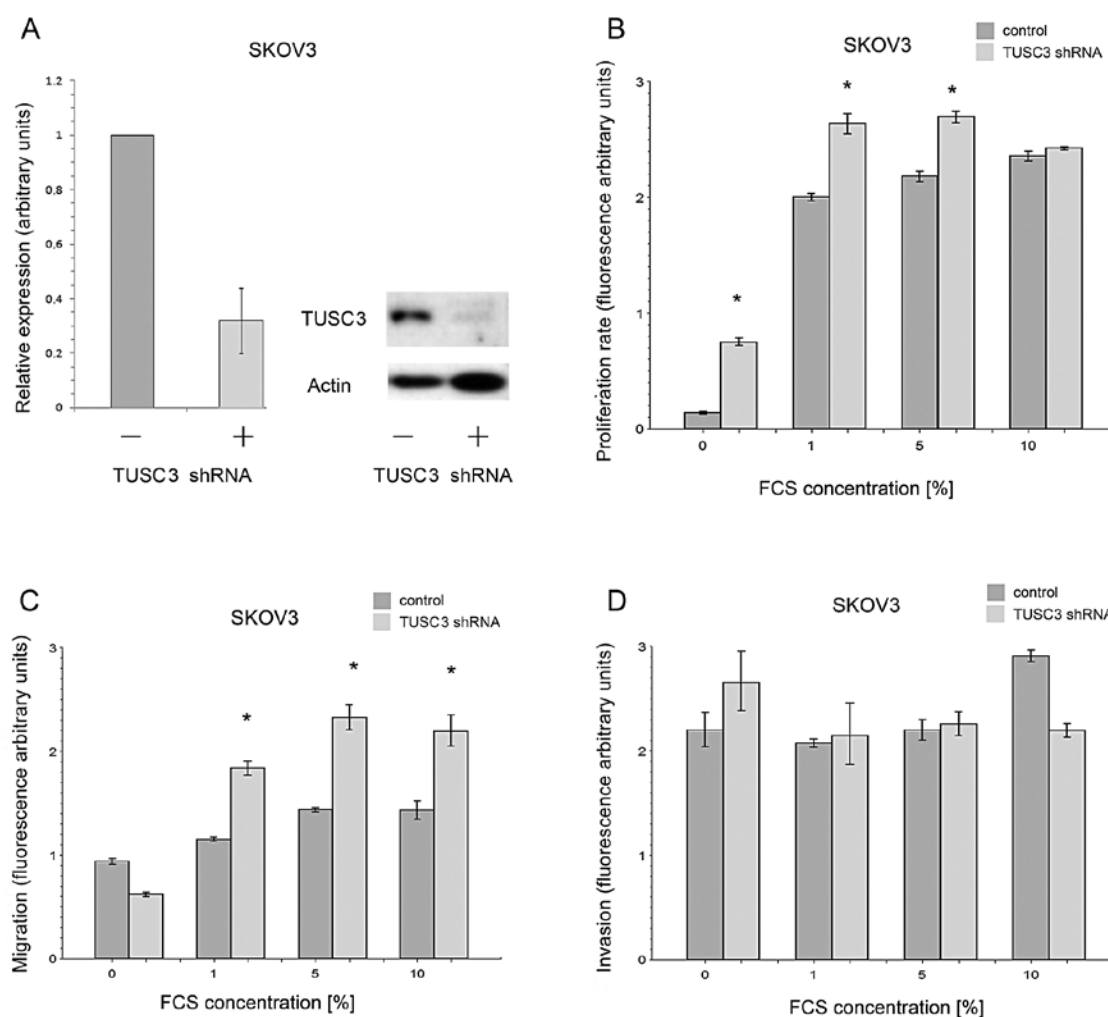


Figure 1. (A) Downregulation of TUSC3 in SKOV-3 cells. β 2-microglobulin-normalized expression of TUSC3 was determined by qRT-PCR and western blotting. (B) Silencing of TUSC3 stimulates metabolic activity/proliferation of SKOV-3 under conditions of serum deprivation. TUSC3-silenced and control SKOV-3 cells were cultivated in 96-well plate for 72 h in a medium supplemented with different concentration of FCS. Accumulation of fluorescent product (Cell Titer-Blue[®] cell viability assay) was then determined. Mean \pm SD of three independent experiments. Asterisks indicate statistical significance at $p \leq 0.001$. (C) Silencing of TUSC3 enhances migration of SKOV-3 cells through 8.0- μ m membrane. TUSC3-silenced and control SKOV-3 cells were seeded on BD transwell plate and cultivated for 24 h. Cells that penetrated the membrane to lower chamber were incubated with Calcein fluorescent dye and quantified by fluorescence measurement at 435_{Ex}, 538_{Em} nm. Mean \pm SD of three independent experiments. Asterisks indicate statistical significance at $p \leq 0.001$. (D) Silencing of TUSC3 does not enhance invasion of SKOV-3 cells through 8.0- μ m tumor invasion system. Quantity of cells penetrating through Matrigel was determined fluorometrically as described in (C). Mean \pm SD of three independent experiments. Asterisks indicate statistical significance at $p \leq 0.001$.

with the indicated primary antibodies diluted 1:500-1:1,000 at 4°C overnight. The blots were developed using horseradish peroxidase-conjugated secondary antibodies (anti-rabbit HRP no. 7074 (Cell Signaling) anti-mouse HRP Ab50043 (Abcam), both 1:4,000 and Immobilon Western HRP substrate (Millipore) according to the manufacturer's instructions.

For co-immunoprecipitation, 150 μ g of cell extracts were precleared using NP-40-washed G-protein beads (Sigma-Aldrich). Supernatants were incubated with 5 μ l of one of the following antibodies: anti-TUSC3 (Ab65213, Abcam), anti-STT3A (Ab55371, Abcam) or commercially available non-specific mouse or rabbit IgG antibody, at 4°C for 1 h. Then, 25 μ l of NP-40-washed G-proteins were added and incubated overnight at 4°C. Pellets were washed four times in NP-40 buffer and resolved by SDS-PAGE.

Statistical analysis. In order to compare the TUSC3 shRNA silenced ovarian cancer cell lines to controls at the specified

FCS concentrations, two-way ANOVA model with interaction was used. P-values for pairwise *post hoc* comparisons were corrected for multiple testing using the Holm-Bonferroni method. $P \leq 0.05$ were considered to be statistically significant. All calculations were performed using the SPSS software Version 13.0 (SPSS Inc.).

Results

Loss of TUSC3 promotes cell proliferation and migration in vitro. To investigate the tumor suppressive function of TUSC3 in an ovarian cancer model, we silenced the expression of TUSC3 in two serous ovarian cystadenocarcinoma cell lines (SKOV-3, TR-170) using shRNA. Efficiency of the knock-down was confirmed on both mRNA and protein levels (Figs. 1A and 2A). Consequently, we analyzed the effect of TUSC3 silencing on cell proliferation, migration and invasion conditions, however, we did not detect

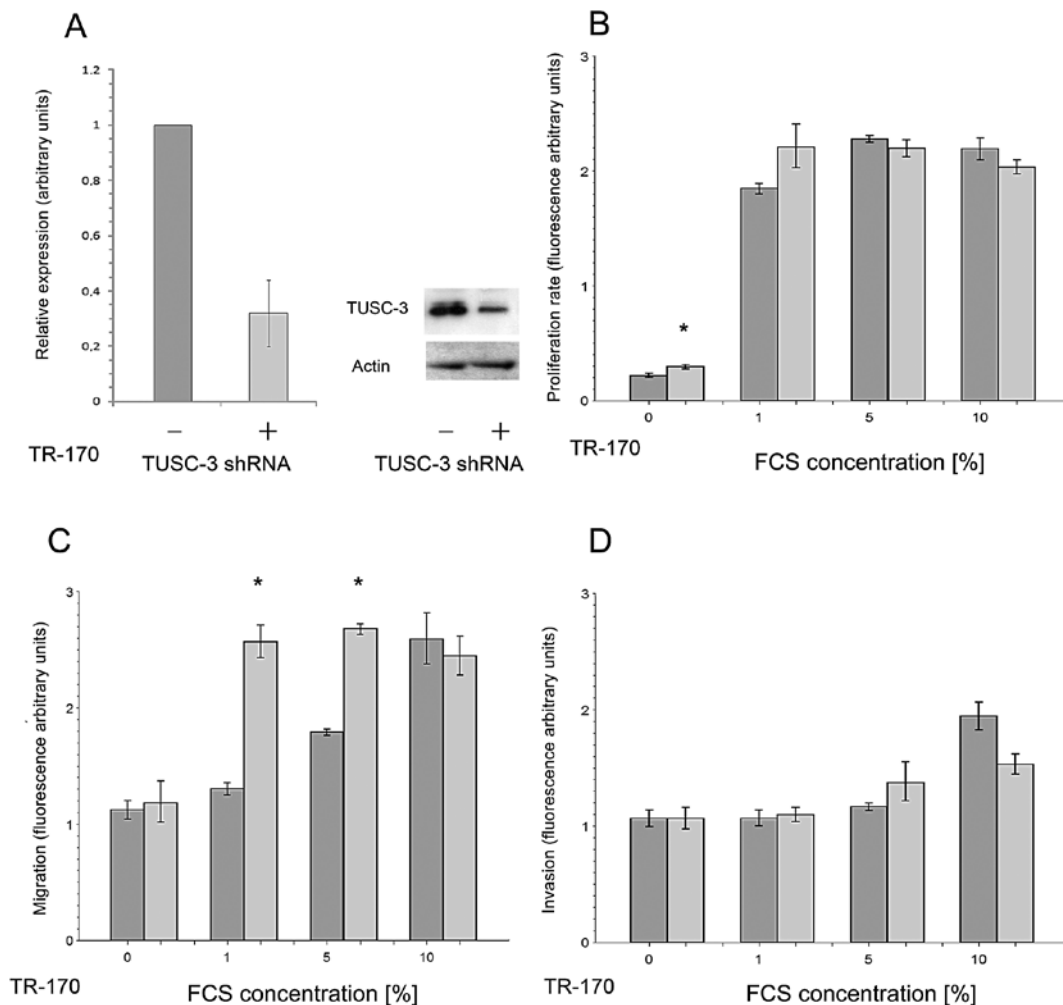


Figure 2. (A) Downregulation of TUSC3 in TR-170 cells. β 2-microglobulin-normalized expression of TUSC3 was determined by qRT-PCR and western blotting. (B) Silencing of TUSC3 stimulates proliferation of TR-170 cells under conditions of serum deprivation. TUSC3-silenced and control TR-170 cells were cultivated for 72 h in a medium supplemented with different concentrations of FCS and quantified as in Fig. 1B. Mean \pm SD of three independent experiments. Asterisks indicate statistical significance at $p \leq 0.001$. (C) Silencing of TUSC3 enhances migration of TR-170 cells through 8.0- μ m membrane. TUSC3-silenced and control TR-170 cells were seeded on BD transwell plate and cultivated for 24 h and quantified as in Fig. 1C. Mean \pm SD of three independent experiments. Asterisks indicate statistical significance at $p \leq 0.001$. (D) Silencing of TUSC3 does not enhance invasion of TR-170 cells through 8.0- μ m tumor invasion system was quantified as in Fig. 1C. Mean \pm SD of three independent experiments.

major differences in proliferation between TUSC3 silenced and control cells cultured under optimal conditions (10% FCS) (Fig. 1B and 2B). To assess their propensity for serum-independent growth, we exposed the cells to stress conditions using varying serum concentrations. Interestingly, the *TUSC3* silenced cells gained a significant survival advantage in contrast to controls after 72 h of cultivation in the absence of serum stimulation (Figs. 1B and 2B). This effect could also be observed to a lesser degree at different time intervals (data not shown). As a next step, we used a Matrigel™ based assay in order to assess effects of TUSC3 knock-down on migration and extracellular matrix (ECM) invasion of ovarian cancer cells. While we did not observe any differences in invasive properties of control ovarian cancer cells regardless of attractant concentration (Figs. 1D and 2D), *TUSC3* silenced cells displayed increased migration through the insert membrane in both cell lines studied (Figs. 1C and 2C). These results were further supported by a wound healing assay, showing increased migration and consequent enhanced closure of the epithelial

monolayer of SKOV-3 cells in no serum or low serum conditions after 18 h (Fig. 3).

TUSC3 is localized in the endoplasmic reticulum as a subunit of the OST complex. The largest part of the data on TUSC3 localization and function is derived from observations of its yeast homologue Ost3p. To determine the subcellular localization of TUSC3 in mammalian cells, we stably transfected the ovarian cancer cell line H134 with a TUSC3-FLAG fusion protein (Fig. 4A). The H134 cell line does not express *TUSC3* due to promoter hypermethylation (data not shown). We performed co-immunofluorescence labeling, which revealed a substantial overlap of the TUSC3-FLAG protein and calnexin, an integral protein of the endoplasmic reticulum (Fig. 4B). Further, subcellular fractions derived from the H134 cells (microsomes, soluble cytoplasm, mitochondria, lysosomes, and nuclei) were analyzed for the presence of exogenous TUSC3-FLAG expression and appropriate fraction markers. We observed TUSC3 enrichment in the microsomal fraction that comprises the endoplasmic

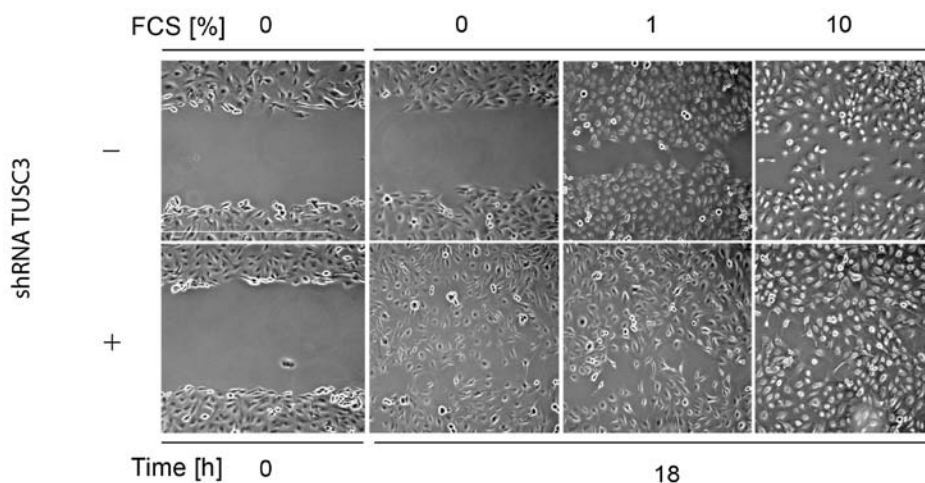


Figure 3. Silencing of TUSC3 stimulates migration of SKOV3 cells. Cells were cultivated at 6-well plates until they reached confluence. The surface was then scratched using sterile tip and cells were cultivated at indicated serum conditions for 18 h. Closing of the gap was assessed by light microscopy. Representative images of three independent experiments are shown.

reticulum (ER) and some minor amounts of cytoplasmic membranes (Fig. 4C). Levels of the endogenous TUSC3 protein in ovarian cancer cell lines were not sufficient for detection in the subcellular fractionation protocol. However, our data confirm the predicted subcellular localization of TUSC3 in the endoplasmic reticulum in ovarian cancer.

Within the endoplasmic reticulum, TUSC3 is supposed to function as a subunit of the OST complex. To determine whether TUSC3 indeed physically interacts with OST in human ovarian cancer cells, we performed co-immunoprecipitation experiments using antibodies specific to endogenous TUSC3 and STT3A, a core catalytic protein of the OST complex. We demonstrated a specific interaction between endogenous TUSC3 and STT3A proteins in TUSC3 expressing ovarian cancer cell lines SKOV-3, TR-170 and OVCAR-3 (Fig. 4D) and provided the evidence for TUSC3 localization in mammalian cells.

TUSC3 modulates glycosylation pattern in H134 ovarian cancer cell line. Next, we wanted to investigate whether there is a causative link between TUSC3 and glycosylation of putative molecular targets. As a model molecule we chose integrin $\beta 1$, a highly glycosylated membrane protein involved in cell adhesion and migration. We employed the H134 with almost null endogenous *TUSC3* gene expression and compared it with H134 cell line highly producing exogenous TUSC3 protein. Probing for integrin $\beta 1$ in H134 total cell extracts on 6% SDS-PAGE revealed bands between 110-150 kDa corresponding to glycosylated integrin $\beta 1$. As a control, a complete removal of N-glycosylated oligosaccharides was achieved by digestion with PNGase F, resulting in bands of equal mobility at ~80 kDa, consistent with the calculated molecular weight of roughly 85 kDa. Interestingly, H134 cells overexpressing TUSC3 showed a shift in bands intensity towards the higher molecular weight when compared to control H134 cells (Fig. 5). Accordingly, immunohistochemical staining of H134 cells for total sialylated proteins using the Sambucus nigra lectin (SNA) revealed an increase in sialylation in TUSC3-positive cells compared to TUSC3-negative cells (Fig. 6). Staining for integrin $\beta 1$ was used as a control.

Discussion

We previously identified *TUSC3* as a candidate tumor suppressor gene in ovarian cancer by systematically screening the chromosomal region 8p22 for differentially regulated genes (8). Nevertheless, mutational analysis performed in several tumor entities failed to reveal a significant rate of protein disruptive mutations and the interest in *TUSC3* gene consequently vanished. Recently, we documented epigenetic silencing of TUSC3 by promoter hypermethylation in various ovarian cell lines and independent cohorts of ovarian cancer patient samples, revealing a strong prognostic potential on survival and indicating a character of tumor-suppressor gene (9). Upregulation of TUSC3 in pancreatic carcinoma cell line MIA-PACA-2 lacking endogenous expression of TUSC3, decreased binding capacity of TUSC3 overexpressing cells to collagen I and prolonged the doubling time (9). However, molecular information on the role of TUSC3 in ovarian cancer is still insufficient.

TUSC3 is the human homologue to *S. cerevisiae* Ost3p, a non-catalytic subunit of the oligosaccharyltransferase complex (14,15). Analyses of the Ost3p and its yeast paralogue Ost6p (human MagT1/IAP) demonstrated their function in regulating glycosylation efficiency (27) and later also uncovered their oxidoreductase activity as well as a possible role in magnesium transport (12). Aberrant glycosylation of proteins can be found in essentially all *in vitro* cancer models and human cancers, and many glycosylated epitopes constitute tumor-associated antigens (28,29), sustaining a long-standing debate if and how protein glycosylation is involved in tumorigenesis. Recently, global DNA methylation changes in ovarian cancer cells were linked to significant alterations of protein glycosylation (30). Re-expression of epigenetically silenced glycosylation enzymes or their subunits, such as TUSC3, may provide a possible explanation for this effect. Our functional analysis builds upon this hypothesis and adds crucial data to the incremental understanding of the causal connection between TUSC3 expression and cancer. We were able to show the subcellular localization of TUSC3 in the endoplasmic

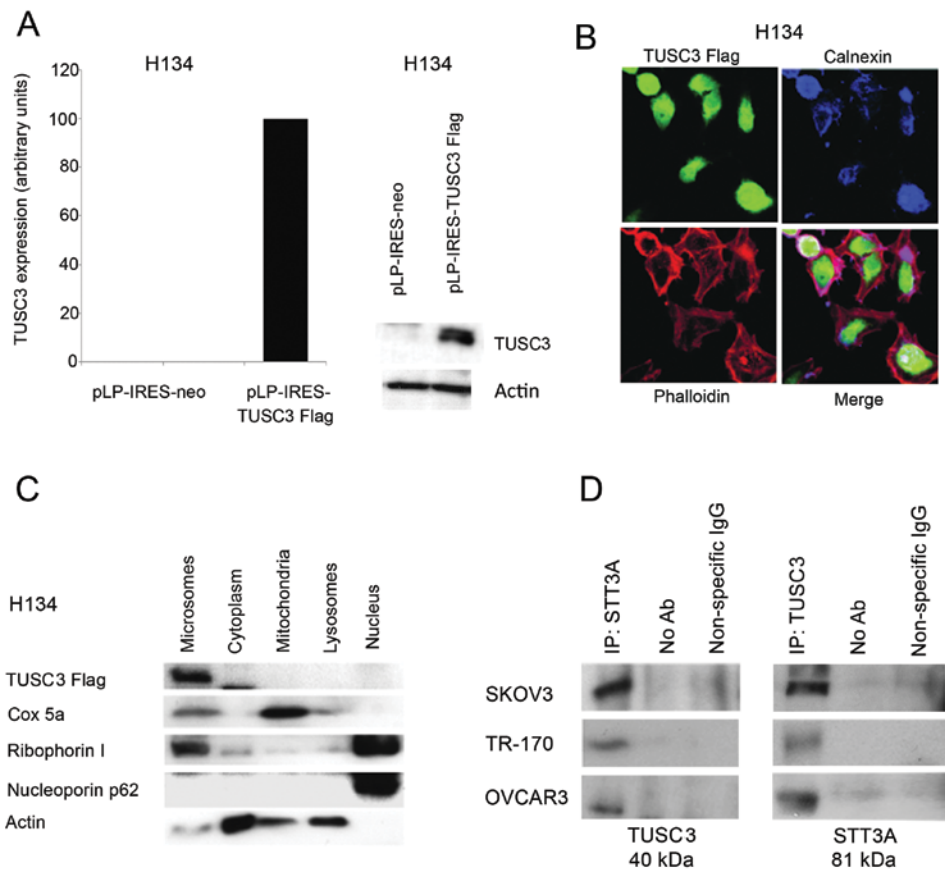


Figure 4. (A) *TUSC3* expression in H134 cell line. H134 cells were transfected with pLP-IRESneo or pLP-IRES-TUSC3-FLAG vectors or left untreated. Transfection was confirmed by *TUSC3*-specific qRT-PCR normalized to $\beta 2$ -microglobulin and western blotting. (B) *TUSC3* colocalizes with endoplasmic reticulum marker calnexin. Colocalization experiment of fixed H134 cells stained with the *TUSC3*-FLAG fusion protein with anti-FLAG antibody, with anti-calnexin for an integral endoplasmic reticulum protein and with phalloidin as a counterstain. (C) Western blot analysis of subcellular fractions for FLAG-tagged *TUSC3* (*TUSC3*-FLAG) in the ovarian cancer cell line H134. Individual fractions - microsomes, cytoplasm, mitochondria, lysosomes and nuclei - were probed with *TUSC3*-Flag and ribophorin I, β -actin, *cox 5a* and nucleoporin p62, respectively. (D) *TUSC3* co-immunoprecipitates with *STT3A*. Total proteins from SKOV-3, TR-170 and OVCAR3 cells were extracted and subjected to the co-immunoprecipitation analysis using antibodies specific against *TUSC3* or *STT3A*. Non-specific IgG was used as a control. Binding partner was visualized by western blotting specific either against *TUSC3* or *STT3A*.

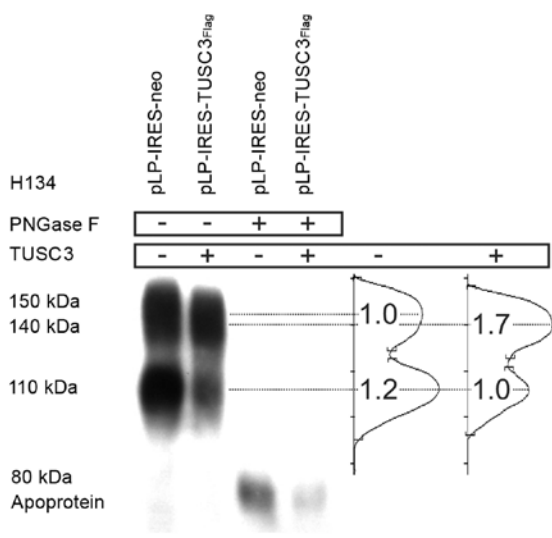


Figure 5. Western blot analysis of integrin $\beta 1$ in H134 cell line. Total cell extracts were resolved on 6% SDS-PAGE, electroblotted to PVDF membrane and probed for integrin $\beta 1$. The 110-kDa band represents the precursor $\beta 1$ -pool in the ER, the 140-150-kDa bands correspond to the mature integrin $\beta 1$ protein. Treatment of proteins with the PNGase F resulted in one band approximately at the position of the calculated apoprotein mass (~80 kDa). Adjacent to the blots, quantification curves and band density ratios according to β -actin are shown. Representative image is shown.

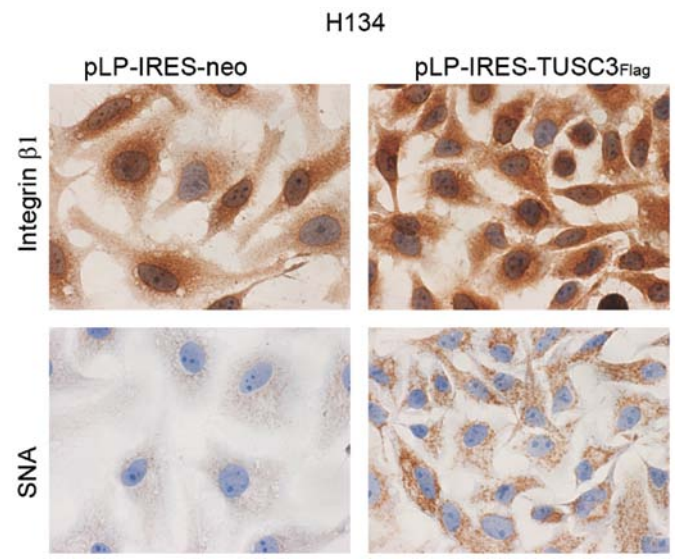


Figure 6. Immunocytochemical stains for sialylated proteins (*Sambucus nigra* lectin, SNA) and integrin $\beta 1$ in either *TUSC3*-overexpressing or control H134 ovarian cancer model cell line. Cells were formaldehyde-fixed, permeabilized and probed with anti-integrin $\beta 1$ antibody and biotinylated-SNA, respectively. The staining for integrin $\beta 1$ was used as an internal control. Cells were counterstained with hematoxylin/eosin. Representative images are shown.

reticulum of ovarian cancer cells, as predicted from its homology to Ost3p. Further, we demonstrate direct physical interaction between TUSC3 and the OST complex catalytic subunit STT3A. Experiments showing changes in overall or protein-specific glycosylation patterns suggest direct functional involvement of TUSC3 in N-glycosylation. In line with the putative function of TUSC3 as a tumor suppressor, we observed enhanced serum-independent cellular proliferation and migration after silencing of TUSC3 in ovarian cancer cell lines and similarly, a mild increase of the doubling time and reduced migration in H134 cell line overexpressing TUSC3 (data not shown). Although these *in vitro* effects remain relatively modest due to the limitations of a cell culture system, we believe that loss of TUSC3 and consequent aberrant N-glycosylation might have a much greater effect in ovarian cancer progression and metastasis. In light of recent data on N-glycosylation affecting tumor growth in cells with e.g., deregulated PI3K-Akt pathway (22), our results further add to the picture and highlight the possible role of N-glycosylation events in ovarian cancer tumorigenesis.

Taken together, our data are consistent with tumor-suppressive character of TUSC3 published previously (9), but provide the first evidence of a tumor suppressor gene in ovarian cancer involved in protein glycosylation. Although abnormal protein glycosylation is a common event in many cancers, the missing comprehension of its mechanisms and lack of any substantial evidence for causative genetic aberrations are obstructive to development of glycosylation targeted cancer therapies. Defining the molecular function of TUSC3 in ovarian cancer may contribute to understanding the role of N-glycosylation in ovarian cancer and possibly open the door for future drug development.

Acknowledgements

We thank Cornelia Sax, Dr Brigitte Wolf and Andrea Schanzer, for their excellent technical support, Dr Erwin Ivessa for providing the calnexin antibody. This study was supported by the Austrian Science Fund (FWF) grant no. P17891 and Oesterreichische Nationalbank (ONB) grant no. 14109, by the Initiative Krebsforschung and Centre for International Cooperation & Mobility of the Austrian Agency for International Cooperation in Education and Research (project no. CZ 04/2012) and by Ministry of Education, Youth and Sports of Czech Republic (project no. 7AMB12AT019 and CZ.1.07/2.3.00/20.0185).

References

- Jemal A, Bray F, Center MM, Ferlay J, Ward E and Forman D: Global cancer statistics. *CA Cancer J Clin* 61: 69-90, 2011.
- Bova GS, MacGrogan D, Levy A, Pin SS, Bookstein R and Isaacs WB: Physical mapping of chromosome 8p22 markers and their homozygous deletion in a metastatic prostate cancer. *Genomics* 35: 46-54, 1996.
- MacGrogan D, Levy A, Bova GS, Isaacs WB and Bookstein R: Structure and methylation-associated silencing of a gene within a homozygously deleted region of human chromosome band 8p22. *Genomics* 35: 55-65, 1996.
- Bashyam MD, Bair R, Kim YH, *et al*: Array-based comparative genomic hybridization identifies localized DNA amplifications and homozygous deletions in pancreatic cancer. *Neoplasia* 7: 556-562, 2005.
- Levy A, Dang UC and Bookstein R: High-density screen of human tumor cell lines for homozygous deletions of loci on chromosome arm 8p. *Genes Chromosomes Cancer* 24: 42-47, 1999.
- Arbieva ZH, Banerjee K, Kim SY, *et al*: High-resolution physical map and transcript identification of a prostate cancer deletion interval on 8p22. *Genome Res* 10: 244-257, 2000.
- Bova GS, Carter BS, Bussemakers MJ, *et al*: Homozygous deletion and frequent allelic loss of chromosome 8p22 loci in human prostate cancer. *Cancer Res* 53: 3869-3873, 1993.
- Pils D, Horak P, Gleiss A, *et al*: Five genes from chromosomal band 8p22 are significantly down-regulated in ovarian carcinoma: N33 and EFA6R have a potential impact on overall survival. *Cancer* 104: 2417-2429, 2005.
- Pils D, Horak P, Vanhara P, *et al*: Methylation status of TUSC3 is a prognostic factor in ovarian cancer. *Cancer Oct 23, 2012* (Epub ahead of print). doi: 10.1002/cncr.27850.
- Garshasbi M, Hadavi V, Habibi H, *et al*: A defect in the TUSC3 gene is associated with autosomal recessive mental retardation. *Am J Hum Genet* 82: 1158-1164, 2008.
- Molinari F, Foulquier F, Tarpey PS, *et al*: Oligosaccharyltransferase-subunit mutations in nonsyndromic mental retardation. *Am J Hum Genet* 82: 1150-1157, 2008.
- Zhou H and Clapham DE: Mammalian MagT1 and TUSC3 are required for cellular magnesium uptake and vertebrate embryonic development. *Proc Natl Acad Sci USA* 106: 15750-15755, 2009.
- Kelleher DJ and Gilmore R: An evolving view of the eukaryotic oligosaccharyltransferase. *Glycobiology* 16: R47-R62, 2006.
- Kelleher DJ, Karaoglu D, Mandon EC and Gilmore R: Oligosaccharyltransferase isoforms that contain different catalytic STT3 subunits have distinct enzymatic properties. *Mol Cell* 12: 101-111, 2003.
- Schulz BL, Stirnimann CU, Grimshaw JP, *et al*: Oxidoreductase activity of oligosaccharyltransferase subunits Ost3p and Ost6p defines site-specific glycosylation efficiency. *Proc Natl Acad Sci USA* 106: 11061-11066, 2009.
- Collard JG, Schijven JF, Bikker A, La Riviere G, Bolscher JG and Roos E: Cell surface sialic acid and the invasive and metastatic potential of T-cell hybridomas. *Cancer Res* 46: 3521-3527, 1986.
- Dennis JW, Granovsky M and Warren CE: Glycoprotein glycosylation and cancer progression. *Biochim Biophys Acta* 1473: 21-34, 1999.
- Yogeeswaran G and Salk PL: Metastatic potential is positively correlated with cell surface sialylation of cultured murine tumor cell lines. *Science* 212: 1514-1516, 1981.
- Janik ME, Litynska A and Vereecken P: Cell migration-the role of integrin glycosylation. *Biochim Biophys Acta* 1800: 545-555, 2010.
- Kakugawa Y, Wada T, Yamaguchi K, *et al*: Up-regulation of plasma membrane-associated ganglioside sialidase (Neu3) in human colon cancer and its involvement in apoptosis suppression. *Proc Natl Acad Sci USA* 99: 10718-10723, 2002.
- Lau KS, Partridge EA, Grigorian A, *et al*: Complex N-glycan number and degree of branching cooperate to regulate cell proliferation and differentiation. *Cell* 129: 123-134, 2007.
- Fang M, Shen Z, Huang S, *et al*: The ER UDPase ENTPD5 promotes protein N-glycosylation, the Warburg effect, and proliferation in the PTEN pathway. *Cell* 143: 711-724, 2010.
- Kuball J, Hauptrock B, Malina V, *et al*: Increasing functional avidity of TCR-redirectioned T cells by removing defined N-glycosylation sites in the TCR constant domain. *J Exp Med* 206: 463-475, 2009.
- Seales EC, Jurado GA, Singhal A and Bellis SL: Ras oncogene directs expression of a differentially sialylated, functionally altered beta1 integrin. *Oncogene* 22: 7137-7145, 2003.
- Pfaffl MW: A new mathematical model for relative quantification in real-time RT-PCR. *Nucleic Acids Res* 29: e45, 2001.
- Graham J and Rickwood D (eds): *Subcellular fractionation, a practical approach*. Oxford University Press, New York, 1997.
- Karaoglu D, Kelleher DJ and Gilmore R: Functional characterization of Ost3p. Loss of the 34-kD subunit of the *Saccharomyces cerevisiae* oligosaccharyltransferase results in biased underglycosylation of acceptor substrates. *J Cell Biol* 130: 567-577, 1995.
- Hakomori S: Glycosylation defining cancer malignancy: new wine in an old bottle. *Proc Natl Acad Sci USA* 99: 10231-10233, 2002.
- Kobata A and Amano J: Altered glycosylation of proteins produced by malignant cells, and application for the diagnosis and immunotherapy of tumours. *Immunol Cell Biol* 83: 429-439, 2005.
- Saldova R, Dempsey E, Perez-Garay M, *et al*: 5-AZA-2'-deoxycytidine induced demethylation influences N-glycosylation of secreted glycoproteins in ovarian cancer. *Epigenetics* 6: 1362-1372, 2011.

3. Horak P, Tomasich E, **Vaňhara P**, Kratochvílová K, Anees M, Marhold M, Lemberger Ce, Gerschpacher M, Horvat R, Sibilia M, Pils D, Krainer M. **TUSC3 loss alters the ER stress response and accelerates prostate cancer growth in vivo.** *Scientific Reports* 2014; **4**:3739.

Commentary:

In this work, phenotypes associated with TUSC3 loss were for the first time described in prostate cancer context. Silencing of TUSC3 expression in DU145 and PC3 prostate cancer cell lines resulted in enhanced proliferation, migration and invasion. Xenografts derived from TUSC3-silenced cells grew extensively when compared to controls in a PTEN negative background. Attenuation of TUSC3 disturbed endoplasmic reticulum (ER) architecture and altered the ER stress response. Moreover, alterations in UPR promoted the Akt signaling. Altogether, our findings provided first molecular mechanism associated with TUSC3 in prostate carcinogenesis that affect N-glycosylation and PTEN-Akt signaling.

DOI: 10.1038/srep03739
Journal: Scientific Reports
Impact factor (WOS, 2014): 5.578
Number of citations (WOS, 2018): 32
Cited in: Nature Reviews Cancer, Nature Communications, Tumor biology, Oncotarget, Seminars in Cancer biology, American Journal of Medical Genetics, Molecular Cancer, Current Opinion in Pediatrics, etc.

Most important citation:

Wang M, Kaufman RJ. **The impact of the endoplasmic reticulum protein-folding environment on cancer development.** *Nature Reviews Cancer* 2014; **14**(9):581-97. doi: 10.1038/nrc3800. (IF 2016: 37.147)

Contribution of the author:

Co-authorship. Collection and/or assembly of data, data analysis and interpretation, manuscript writing.



OPEN

TUSC3 Loss Alters the ER Stress Response and Accelerates Prostate Cancer Growth *in vivo*

SUBJECT AREAS:

PROSTATE CANCER

ONCOGENESIS

TUMOUR SUPPRESSORS

STRESS SIGNALLING

Peter Horak¹, Erwin Tomasich¹, Petr Vaňhara², Kateřina Kratochvílová², Mariam Anees¹, Maximilian Marhold¹, Christof E. Lemberger¹, Marion Gerschpacher¹, Reinhard Horvat³, Maria Sibilica⁴, Dietmar Pils⁵ & Michael Krainer¹

Received

24 June 2013

Accepted

18 December 2013

Published

17 January 2014

Correspondence and requests for materials should be addressed to M.K. (michael.krainer@meduniwien.ac.at)

¹Division of Oncology, Department of Internal Medicine I and Comprehensive Cancer Center Medical University of Vienna, Austria, ²Department of Histology and Embryology, Faculty of Medicine, Masaryk University Brno, Czech Republic, ³Clinical Institute of Pathology, Medical University of Vienna, Austria, ⁴Institute for Cancer Research, Department of Medicine I and Comprehensive Cancer Center, Medical University of Vienna, Austria, ⁵Department of Obstetrics and Gynecology, Molecular Oncology Group, Medical University of Vienna, Austria.

Prostate cancer is the most prevalent cancer in males in developed countries. Tumor suppressor candidate 3 (*TUSC3*) has been identified as a putative tumor suppressor gene in prostate cancer, though its function has not been characterized. *TUSC3* shares homologies with the yeast oligosaccharyltransferase (OST) complex subunit Ost3p, suggesting a role in protein glycosylation. We provide evidence that *TUSC3* is part of the OST complex and affects N-linked glycosylation in mammalian cells. Loss of *TUSC3* expression in DU145 and PC3 prostate cancer cell lines leads to increased proliferation, migration and invasion as well as accelerated xenograft growth in a PTEN negative background. *TUSC3* downregulation also affects endoplasmic reticulum (ER) structure and stress response, which results in increased Akt signaling. Together, our findings provide first mechanistic insight in *TUSC3* function in prostate carcinogenesis in general and N-glycosylation in particular.

In developed countries, prostate cancer is the most prevalent cancer in males and the second most common cause of cancer related death¹. Despite PSA screening and availability of multiple therapeutic options a number of patients experience relapse in the form of hormone-refractory or castration-resistant prostate cancer (CRPC). These patients constitute a heavily pretreated and highly heterogeneous population and despite current advances in treatment of CRPC patients, the 5-year survival rate remains less than 5%. Molecular factors for onset and development of prostate cancers are largely elusive, although their number and characterizations are growing rapidly. Most prostate cancers harbor mutations or deletions of tumor suppressor genes, such as *PTEN*, *SMAD4*, *MAGI2*, *CADM2* or *TP53*². Recently, a genome wide expression, mutation and copy number alteration analysis identified genomic loss on chromosome 8p as the most common genetic aberration in prostate cancers³, confirming earlier observations of chromosomal loss and loss of heterozygosity (LOH) in this region^{4,5}. These losses include large regions of this chromosomal arm encompassing a multitude of genes including prostate cancer tumor suppressors, such as the homeodomain-containing transcription factor NKX3-1. *TUSC3*, originally named *N33*, was identified as a potential tumor suppressor gene on the chromosomal band 8p22 in prostate cancer in the mid 1990's⁶⁻⁹. Our previous work described high frequency of LOH on the short arm of chromosome 8 in ovarian cancer¹⁰ and specifically defined the prognostic influence^{11,12} and carcinogenic effects¹³ of *TUSC3* loss in this cancer entity.

TUSC3 has been described and identified as a homologue of the yeast Ost3p subunit of the oligosaccharyltransferase (OST) complex^{14,15}. OST is an integral membrane protein complex that catalyzes N-linked glycosylation of proteins in the endoplasmic reticulum (ER)¹⁶. *TUSC3* mutations have been found in families with non-syndromic autosomal recessive mental retardation¹⁷⁻²⁰. In analogy to this observation, several congenital disorders of glycosylation present phenotypically with variable degrees of mental retardation. N-glycosylation is a ubiquitous posttranslational modification of eukaryotic proteins that modulates protein folding, protects them from degradation, and regulates their function as well as their immunogenicity²¹. In general, glycosylation is involved in biological processes such as intercellular or cell-matrix interactions, which play an important role in



cancer initiation and progression^{22–24}. In PTEN driven prostate cancer, increase in N-glycosylation results in increased tumorigenicity due to the activity of an endoplasmic reticulum UDPase ENTPD5²⁵. Changes in protein glycosylation patterns lead to accumulation of unfolded or misfolded proteins in the endoplasmic reticulum and induce the unfolded protein response (UPR)²⁶. UPR then facilitates cellular adaptation to ER stress by several distinct mechanisms in order to modulate the crosstalk between autophagy and apoptosis, and its deregulation might thus further contribute to carcinogenesis^{27,28}.

So far, function of TUSC3 in neither N-glycosylation nor ER stress has been well characterized. In our work we present the first evidence of TUSC3 involvement in protein N-glycosylation and demonstrate the effects of TUSC3 loss on ER stress response in prostate carcinogenesis.

Results

TUSC3 interacts with the STT3B subunit of the oligosaccharyltransferase complex and affects N-glycosylation. TUSC3 homologue Ost3p has been described as a subunit of the yeast OST complex responsible for OST substrate specificity and efficiency^{14,29}. We could confirm the physical interaction between

endogenous and exogenous human TUSC3, respectively, and the STT3B (Figures 1a and b), the core catalytic protein of the complex, by co-immunoprecipitation in HEK293T cells. In contrast, STT3A did not co-immunoprecipitate with TUSC3 in these cells (data not shown). To answer the question if and how TUSC3 regulates N-glycosylation within the OST complex, we employed a luciferase based assay described by Contessa et al³⁰. In this assay, wild type firefly luciferase containing three N-glycosylation consensus sites is fused with the EGFR derived endoplasmic reticulum targeting sequence. N-glycosylation of the wild type firefly luciferase in HEK293T cells leads to a change in molecular weight in SDS-PAGE (Supplementary Figure S1a) and decreased enzymatic activity (Figure 1c). We used an overexpression approach to study the effects of TUSC3 on N-glycosylation of ER-luciferase (ER-Luc). Silencing would possibly lead to further inhibition of already decreased activity of the ER-Luciferase, making an evaluation difficult (Figure 1c). We overexpressed ER-Luc and wild-type TUSC3 in HEK293T cells and assessed the enzymatic activity of the ER-luciferase after 48 hours. We treated transfected HEK293T cells with 0.5 μM tunicamycin for 24 hours to show that deglycosylation results in a decrease in molecular weight of the ER-Luc (Supplementary Figure S1a). We observed an increase in luciferase

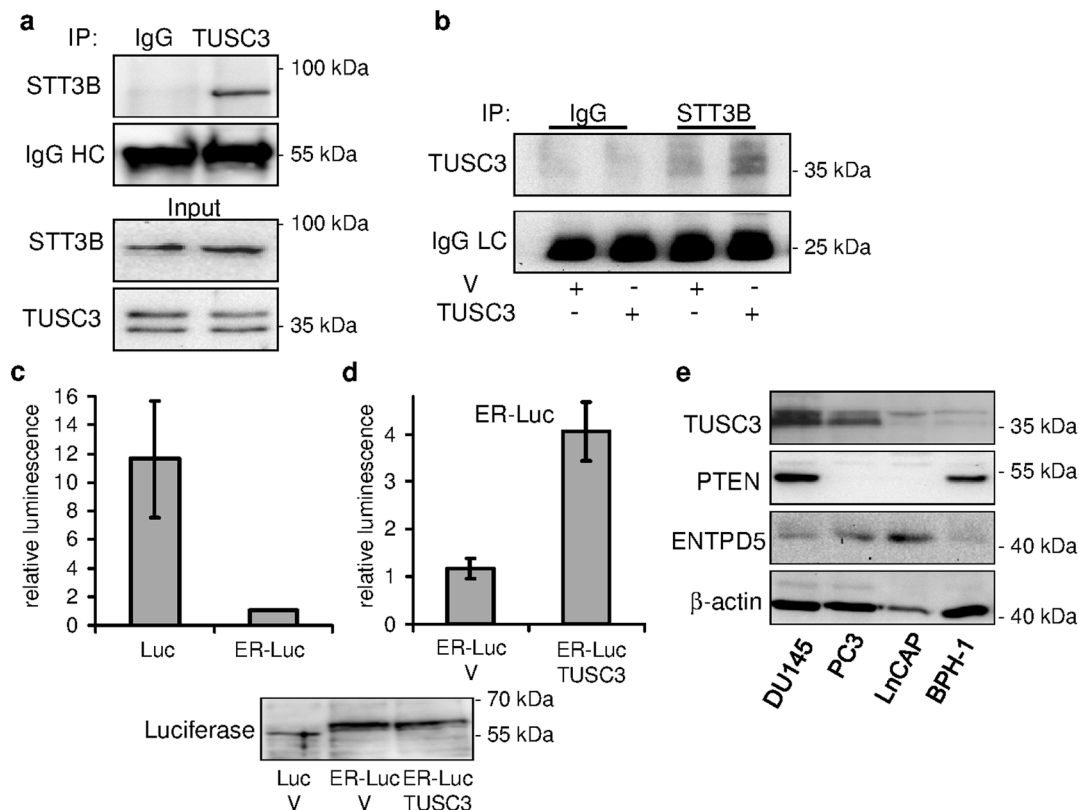


Figure 1 | TUSC3 associates with oligosaccharyltransferase subunit STT3B. (a) TUSC3 co-immunoprecipitates with STT3B in HEK293T cells. Lysates from HEK293T cells were immunoprecipitated with TUSC3 antibody or control IgG and detected with STT3B antibody on a western blot. IgG heavy chain (IgG HC) represents the loading control. Endogenous input STT3B and TUSC3 levels are shown. (b) HEK293T cells were transfected with TUSC3 or an empty control pcDNA 3.1 vector (V). Lysates from transfected cells were immunoprecipitated using STT3B antibody or control IgG and TUSC3 was detected using western blot. IgG light chain (IgG LC) serves as loading control. **TUSC3 overexpression affects ER-Luciferase N-glycosylation in HEK293T cells.** (c) HEK293T cells were transfected with wild type firefly luciferase (Luc) or luciferase fused to an endoplasmic reticulum targeting sequence (ER-Luc) and seeded in 96-well plates. Luminescence was measured 32–48 hours after transfection and normalized to the cell count. (d) HEK293T cells were co-transfected with ER-Luc and empty pcDNA 3.1 vector (V) or full length TUSC3. Luminescence was measured and normalized to the cell count. The luciferase experiments are representative of several biological replicates and were performed in triplicates (depicted as means and standard deviations). Electrophoretic gel shift of the fusion construct (ER-Luc) in contrast to wild type luciferase (Luc) is shown. TUSC3 overexpression does not have an effect on the molecular weight of the ER-Luciferase. (e) A panel of cell lines derived from human prostate cancers (DU145, PC3, LNCaP) and benign prostatic hyperplasia (BPH-1) were assessed for expression of TUSC3, PTEN and ENTPD5. Cropped blots are depicted for clarity reasons and full-length blots will be provided upon request.

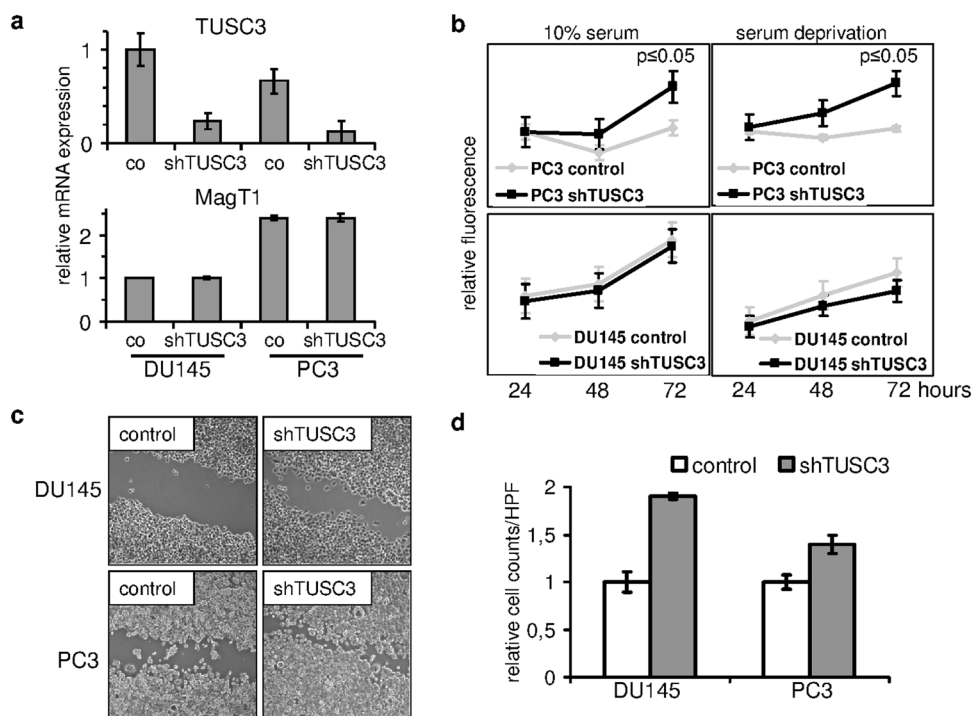


Figure 2 | TUSC3 loss promotes carcinogenesis. (a) Prostate cancer cell lines DU145 and PC3 demonstrated shRNA mediated downregulation of *TUSC3* mRNA (shTUSC3) versus scrambled shRNA (co) and unchanged expression of its closest homologue *MagT1*. (b) TUSC3 silenced cells proliferate in serum and under serum deprivation *in vitro*. Cells were plated in 96-well plates and allowed to adhere overnight, followed by addition of serum free or serum complemented medium. Cell viability for up to 72 hours was assessed in triplicates. (c) Cell motility was compared 18 hours after wounding of a DU145 and PC3 monolayer under conditions of serum deprivation. Representative images are shown in 200 \times magnification. (d) Invasion of prostate cancer cell lines through Matrigel was assessed in a transwell migration assay towards cell culture medium with 20% FCS as chemoattractant. Crystal violet stained cells from triplicate experiments were counted in 3 high power fields (HPF, 400 \times magnification) per well and normalized to migration without Matrigel. Results are depicted as means and standard deviations.

activity in TUSC3 overexpressing cells compared to controls (Figure 1d), suggesting reduced N-glycosylation efficiency caused by TUSC3 overexpression, although not attaining the wild-type luciferase activity. TUSC3 overexpression in HEK293T cells also does not lead to a large band shift due to decreased glycosylation (Figure 1d), suggesting a small effect of TUSC3 on ER-luciferase N-glycosylation. This result might support the notion of a TUSC3 role in the regulation of N-glycosylation substrate specificity²⁹.

We also analyzed the expression of TUSC3 in three cell lines derived from human prostate cancer (DU145, PC3, LNCaP) and one cell line from benign prostatic hyperplasia (BPH-1). We can demonstrate varied levels of TUSC3 expression in these cell lines, with LNCaP and BPH-1 cells having lowest levels of TUSC3 expression. The ER UDPase ENTPD5 has been recently implicated in the pathogenesis of PTEN negative prostate cancer through ER stress modulation²⁵, and for this reason we also assessed its expression. In contrast to the PTEN negative LNCaP cells, DU145 and PC3 cells display higher TUSC3 expression levels while their basal expression of ENTPD5 is relatively low (Figure 1e).

Knockdown of TUSC3 leads to increased proliferation and invasion of prostate cancer cells *in vitro*. We were curious about the phenotypic effects of TUSC3 loss in a prostate cancer cell line model. We knocked down TUSC3 expression in two well characterized androgen resistant prostate cancer cell lines, PC3 and DU145, and analyzed them *in vitro*. Silencing efficiency of 5 short hairpin RNAs against TUSC3 was first tested in the HEK293T cell line (Supplementary Figure S1c). PC3 and DU145 cell lines were lentivirally transduced to achieve a considerable reduction of TUSC3 expression (Figure 2a). mRNA levels of the closest TUSC3 homologue, *MagT1* remained unchanged, thus validating knockdown

specificity (Figure 2a). Cell lines with silenced TUSC3 expression (shTUSC3) and cell lines transduced with scrambled shRNA (control) were assessed for proliferation using a resazurin based cell viability assay. TUSC3 silenced PC3 prostate cancer cell lines demonstrate a significant growth advantage over control cells, which is retained under conditions of cellular stress, such as serum deprivation. Interestingly, knockdown of TUSC3 in DU145 cells did not demonstrate similar effects (Figure 2b). Next, we tested if shTUSC3 cells were displaying increased migratory and invasive properties consistent with increased tumorigenicity. In a wound healing assay, 18 hours after wounding, both silenced cell lines show accelerated wound closure (Figure 2c). To assess invasion through extracellular matrix, we used a Matrigel transwell invasion assay using medium with 20% FCS as chemoattractant. In comparison to control cells, and corrected for migration through the 8 μ m pore membrane, shTUSC3 cells demonstrate increased invasion through extracellular matrix (Figure 2d). These results suggest that TUSC3 loss might accelerate tumorigenesis in prostate cancer cells under specific circumstances.

TUSC3 loss under serum deprivation promotes Akt activity. Growing cancer cells often encounter lack of nutrients leading to cellular stress response and adaptation, including induction of ER stress and autophagy. Interestingly, both cell lines continue to proliferate without serum for up to 72 hours (Figure 2b) and the difference between TUSC3 silenced cells and controls remains unaffected. Next, we looked at the downstream activation of MAPK and PI3K/Akt pathways as major drivers of cellular proliferation and survival in the two prostate cancer cell lines. For this purpose, we serum starved the prostate cells for 36 hours and stimulated growth factor activation with FCS for 30 minutes before lysis. We observe

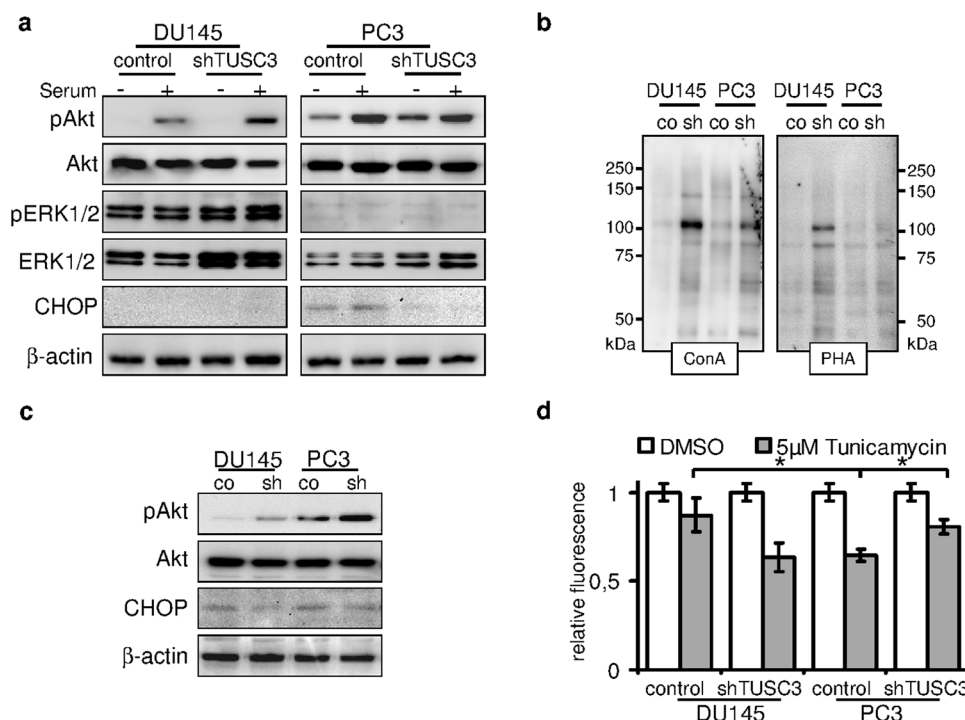


Figure 3 | TUSC3 loss leads to increased viability, N-glycosylation and Akt signaling. (a) shTUSC3 and control cells were serum starved for 36 hours (–) and serum was added for 30 minutes before lysis (+). PI3K/Akt and MAPK signaling pathway were evaluated by immunoblotting. Increased downstream activation of Akt can be observed in serum starved TUSC3 silenced PC3 cells as well as in DU145 cells after stimulation with serum. ER stress and CHOP are induced by prolonged serum starvation (lane 5 and 6) in PC3 cells. Loss of TUSC3 decreases CHOP levels in PC3 cells (lane 7 and 8). (b) Increased N-glycosylation in shTUSC3 cells. Lectin blotting using Concanavalin A and Phytohaemagglutinin-L lectins on isolated cell surface proteins was performed in cell membrane fractions of PC3 and DU145 cells following 72 h serum starvation. Control for protein loading was performed by amido black staining (Supplementary Figure S2C). (c) DU145 and PC3 prostate cancer cell lines were serum starved for 72 hours before lysis. Silencing of TUSC3 (sh) leads to sustained phosphorylation of Akt and decreased expression of CHOP in both cell lines. (d) Viability of TUSC3 silenced (shTUSC3) and control (scrambled shRNA) prostate cancer cells was assessed with the CellTiter-Blue® Assay after treatment with 5 μM tunicamycin or DMSO for 72 hours in full medium. Experiments were performed in triplicates and results are representative of several independent experiments. * $p = 0.01$.

differential phosphorylation of ERK1/2 and Akt (Ser473) between the PC3 and DU145 cell lines as a result of their PTEN mutational status (Figure 3a). PTEN levels remain unaffected by TUSC3 status (Supplementary Figure S1d). MAPK pathway seems to be the predominant signaling pathway in the DU145 cell line as evidenced by ERK1/2 phosphorylation. In PTEN negative PC3 cells however, loss of TUSC3 further induces basal Akt activity in serum starved cells (Figure 3c).

TUSC3 function within the OST complex may define distinct OST isoforms and confer target specificity^{16,29}. In order to assess the level of global protein glycosylation in shTUSC3 cells, we employed lectin based assays using Concanavalin A and Phytohaemagglutinin-L. There was no difference in binding of these two lectins to glycosylated residues of isolated whole cell protein lysates or whole cells (Supplementary Figures S2a and b). To specifically analyze the N-glycosylation of cell surface proteins, we used cell surface biotinylation and purification. Surprisingly, within the isolated cell membrane fraction we could detect increased N-glycosylation of unspecified cell surface proteins in both cell lines (Figure 3b).

Given the possible alterations in N-glycosylation and ER stress induction through loss of TUSC3, we looked at a downstream target of UPR, the pro-apoptotic transcription factor CHOP (GADD 153). When we evaluated induction of CHOP in serum starved PC3 and DU145 cells at 36 h, we can see an increase of CHOP primarily in PC3 cells while we simultaneously observe a reduction of CHOP levels in PC3 shTUSC3 cells (Figure 3a). To induce physiological and long term ER stress induction in prostate cancer cells, we deprived them of serum for up to 72 hours. Under these conditions, sustained Akt phosphorylation in both shTUSC3 cell lines is present,

although a stronger signal is observable in PC3 cells (Figure 3b). At this time point, we also observe CHOP induction in both cell lines. Repeatedly, this pro-apoptotic response is partly abolished in shTUSC3 cells. We were curious how loss of TUSC3 in prostate cancer cells may affect the ER stress induced cell death in general. We treated shTUSC3 and control cell lines with tunicamycin at concentrations ranging from 0.5 μM to 10 μM and evaluated their viability for up to 72 hours after induction of ER stress. We observed that at 5 μM tunicamycin, PC3 cell were generally more sensitive to ER stress than DU145 cells (Figure 3d) and that knockdown of TUSC3 significantly increased their resistance to tunicamycin (Figure 3d), while no difference was observed in DU145 cells. Taken together, we speculate that TUSC3 loss may control and increase Akt activity in serum deprived tumor cells especially under ER stress conditions.

TUSC3 loss alleviates endoplasmic reticulum stress in prostate cancer cells. Disruption of the OST complex and N-glycosylation leads to accumulation of misfolded proteins in the ER lumen, which triggers the unfolded protein response and activation of pro-apoptotic PERK/CHOP as well the adaptive IRE-1/XBP-1 pathways. In resting cells, the ER stress receptors are inactivated through their association with the ER chaperone BiP (GRP78). We wondered, if TUSC3 loss may lessen the pro-apoptotic ER stress caused by tunicamycin treatment. Induction of CHOP following tunicamycin is markedly reduced in shTUSC3 PC3 cells (Figure 4a). Previously, induction of N-glycosylation by ENTPD5 expression was shown to alleviate ER stress in prostate cancer cells³¹. ENTPD5 expression is slightly increased in TUSC3 knockdown cells,



consistent with adaptation to increased glycosylation. However, its expression is abolished upon tunicamycin treatment in PC3 cells, thus it is not sufficient to explain ER stress reduction in these cells.

To further examine the role of TUSC3 in ER stress response, we looked at the transcriptional regulation of TUSC3 expression under ER stress. Following a 24 h treatment with 5 μ M tunicamycin, we measured a twofold induction of TUSC3 mRNA in PC3 cells (Figure 4b).

Next, in order to dissect the responsible ER stress pathways and addressing adaptive as well as pro-apoptotic branches, we analyzed BiP, IRE-1 and XBP-1 expression in TUSC3 silenced cell lines after 72 h of serum starvation. Interestingly, BiP (GRP78) was recently identified as an essential factor for Akt activation in PTEN negative prostate cancer³². Interestingly, levels of BiP were elevated in shTUSC3 PC3 cells (Figure 4c) whereas the induction of IRE-1 and spliced XBP-1 was repressed. The effect was more pronounced in PC3 cells, although the general expression of IRE-1 was higher in DU145. This effect was confirmed using different methods. We performed a semi-quantitative and quantitative PCR of the XBP-1 splice variants as well as BiP. We find that serum starvation induces BiP mRNA expression predominantly in the PC3 shTUSC3 cell line (Figure 4d). In addition, a shift from spliced to unspliced, inactive isoform of XBP-1 can be detected upon downregulation of TUSC3, which is more pronounced in PC3 cells, indicating less ER stress induction (Figure 4c and d).

These observations prompted us to examine the ultrastructural changes of endoplasmic reticulum in TUSC3 silenced prostate cancer cell lines. Both, PC3 and DU145 cells deficient for TUSC3 displayed ER rearrangement consistent with cross-linked and slightly dilated ER cisternae when compared to controls. These effects on the endoplasmic reticulum may represent morphological correlates of disturbed ER function under ER stress conditions. In our analyses,

only cells with clearly visible nucleus, nucleolus, mitochondria, Golgi apparatus and rough endoplasmic reticulum were evaluated and representative images are shown (Figure 5a).

TUSC3 loss leads to increased tumor formation *in vivo*. To assess the influence of TUSC3 on *in vivo* tumorigenesis, we used a nude mouse xenograft model. Relatively small differences in proliferation, migration and invasion, which we observed *in vitro*, might have a summative effect in an *in vivo* model. We injected the modified shTUSC3 cell lines into the dorsal flanks of male nude athymic (Foxn1nu/nu) mice. The contralateral flanks were inoculated with control (scrambled shRNA) cells of the respective cell line. *In vivo* growth of TUSC3 silenced DU145 and PC3 cell lines did rather resemble the *in vitro* proliferation pattern, disregarding the TUSC3 mediated differences in extracellular matrix invasion and migration of the DU145 cell line. Tumor formation of shTUSC3 DU145 cells did not differ from their control counterparts while shTUSC3 PC3 xenografts developed a growth advantage over control cells after 6–7 weeks *in vivo* (Figure 5b). TUSC3 silencing was maintained in isolated mouse tumors, as evidenced by mRNA levels and histochemistry (Figure 5c). Not unexpectedly, pronounced changes in protein glycosylation were not apparent by ConA lectin histochemistry of mouse tumors as suggested by the *in vitro* data (Figure 5c).

TUSC3 is downregulated in prostate cancer patients. We set out to identify and characterize a putative tumor suppressor gene in prostate cancer. Although we identified loss of TUSC3 expression through promoter hypermethylation in ovarian cancer^{11,12}, TUSC3 has never been evaluated in a large prostate cancer patient cohort. In order to assess TUSC3 protein expression in clinical samples, we analyzed 143 prostate cancer patients using a tissue microarray. We observed strong cytoplasmic staining of TUSC3 in prostate

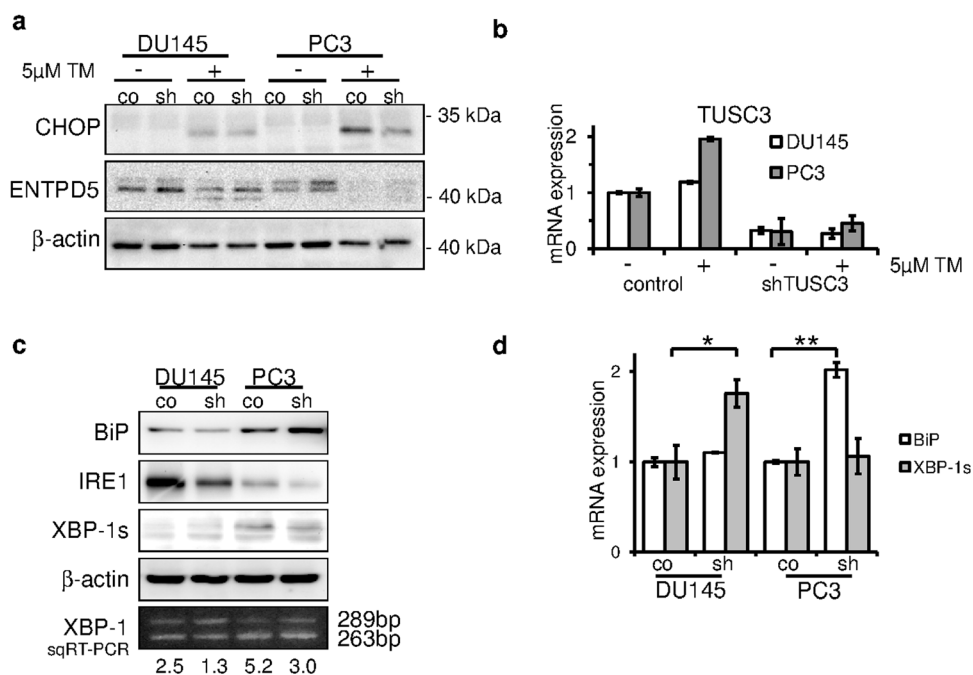


Figure 4 | TUSC3 alleviates ER stress in prostate cancer cell lines. (a) CHOP and ENTPD5 expression was measured after 24 hours of 5 μ M tunicamycin (TM) or DMSO treatment. Decreased CHOP induction in shTUSC3 PC3 cells indicates reduced ER stress response (lane 7 vs. 8). (b) Cells were treated with 5 μ M tunicamycin (TM) or DMSO for 24 hours. TUSC3 mRNA expression was assessed using qRT-PCR. (c) UPR was assessed by expression levels of BiP, IRE-1 and XBP-1s in serum starved (72 h) prostate cancer cells. XBP-1 mRNA splicing was also measured by semiquantitative RT-PCR. Intensity of the bands was quantified and ratio of spliced to unspliced isoform was calculated. Increased ratio indicates elevated levels of ER stress. Cropped blots are depicted for clarity reasons and full-length blots will be provided upon request. (d) qRT-PCR was used to evaluate the mRNA expression of BiP and spliced XBP-1 isoform. Silencing of TUSC3 leads to an increase in BiP expression in PC3 cells and conversely to an increase in spliced XBP-1 in DU145 cells, suggesting opposing effects on UPR signaling. * $p = 0.03$ and ** $p = 0.04$.

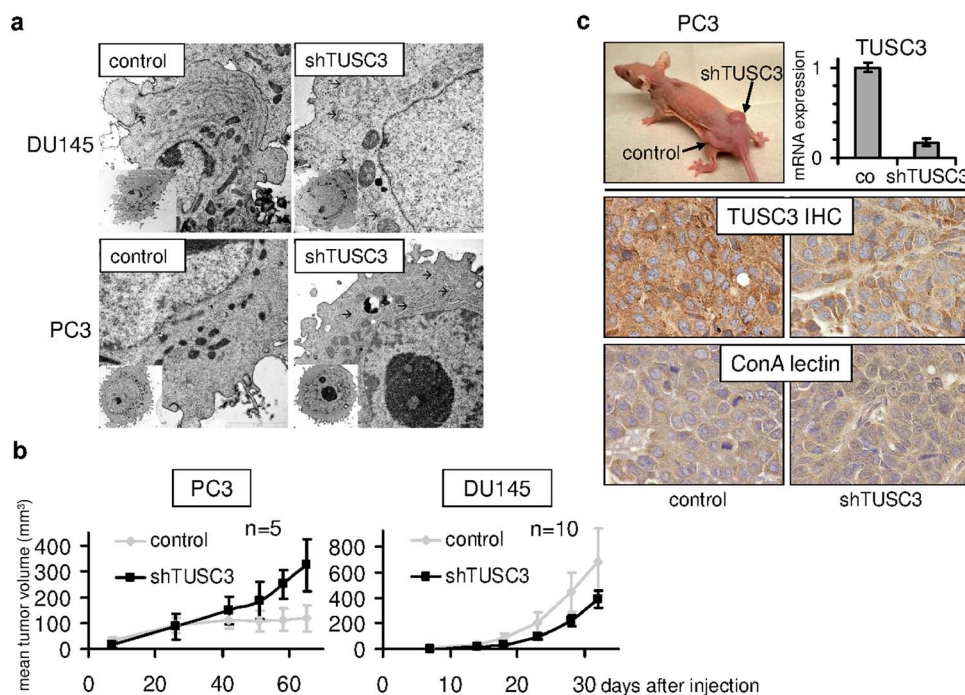


Figure 5 | TUSC3 silencing is associated with ultrastructural changes in endoplasmic reticulum. (a) shTUSC3 and control (scrambled shRNA) PC3 and DU145 cells, respectively, were evaluated using transmission electron microscopy in ultrathin sections. Only cells with intact plasma membrane, nucleus, nucleolus, mitochondria, ER and Golgi apparatus were included into the analysis. We examined 20 cells of each cell type. Arrows indicate branching or dilatation of ER cisternae. Scale bars correspond to 2 μ m. **TUSC3 silencing promotes prostate cancer xenograft growth.** (b) shTUSC3 and control (scrambled shRNA) PC3 and DU145 cells, respectively, were injected into the flanks of 6–8-week old male nude mice. Tumor growth was monitored and is shown as mean tumor size (\pm SEM). (c) Representative tumor formed by the TUSC3 silenced PC3 xenograft in the right flank of a Foxn1^{nu/nu} mouse (top left). Sustained downregulation of TUSC3 in mouse tumors was analyzed by qRT-PCR (top right) and immunohistochemistry (TUSC3 IHC, middle graphs). Major differences in N-glycosylation in mouse tumors were not identified by Concanavalin A lectin histochemistry (ConA lectin, bottom graphs).

cancer as well as normal tissues, consistent with its subcellular localization in the endoplasmic reticulum (representative stainings are shown in Supplementary Figure S3a). We found that 13.3% of tissue samples demonstrated starkly reduced protein expression of TUSC3 (assessed as absent and weak staining in more than 30% of cells, Supplementary Figure S3b). We could not detect significant differences in TUSC3 expression between the clinicopathological subgroups (Supplementary Table 1). The follow-up of this cohort was not sufficient to assess the influence of TUSC3 on progression-free or overall survival (Supplementary Table 1). Additionally, we performed a comprehensive *in silico* evaluation of TUSC3 gene expression, promoter methylation and gene copy number using publicly available datasets of The Cancer Genome Atlas (TCGA). We could define a large number of homozygous (11.8%) and heterozygous (42.9%) deletions of TUSC3, confirming a high percentage of 8p deletions in prostate cancer³ (Supplementary Figure S3b). Consistent with the data in ovarian cancer^{11,12}, TUSC3 expression was significantly correlated with promoter hypermethylation as well as downregulated in higher stage tumors (Supplementary Figure S3c). This data further supports the notion of TUSC3 acting as a tumor suppressor in prostate cancer.

Discussion

Functional knowledge about the origins of altered glycosylation of tumor cell surface proteins is limited^{33,34}. Deregulated enzymatic activities of proteins directly involved in N-glycosylation or the availability of potential glycosylation sites determined by the branching of N-glycans are considered to be crucial for these effects^{25,35}. TUSC3 is the human homologue to *S. cerevisiae* Ost3p, a non-catalytic subunit of the OST complex^{15,29}. Analyses of the Ost3p and its yeast paralogue Ost6p (human MagT1/IAP) demonstrated their function in

regulating glycosylation substrate specificity²⁹, glycosylation efficiency³⁶ as well as their recently uncovered role in magnesium transport³⁷. We find that mammalian TUSC3 binds the STT3B isoform of the catalytic subunit of the OST complex, but not STT3A. It is conceivable that TUSC3 modulates the function of STT3B, which has been described to have a salvage role in N-glycosylation, while the STT3A based complex is primarily responsible for the bulk of co-translational N-glycosylation^{15,38,39}. This distinct role of STT3B complex might explain the relatively modest effect of TUSC3 overexpression on ER-Luc glycosylation and no global changes in lectin binding upon TUSC3 knockdown. In contrast to ENTDP5, which has been described as an oncogenic factor in PTEN negative prostate cancer²⁵, TUSC3 might have a selective role in regulating N-glycosylation, affecting target specificity and OST efficiency. Moreover, ENTDP5 acts downstream of the OST complex, hydrolyzing UDP in the endoplasmic reticulum to promote further glycosylation and protein folding following OST mediated transfer of the core glycan on the nascent protein. Therefore it is conceivable that TUSC3 downregulation and ENTDP5 overexpression in prostate cancer may confer an additive effect on tumor growth.

Our finding of increased N-glycosylation of cell surface proteins being mediated by TUSC3 loss is somehow unexpected, as we previously described an opposite role for TUSC3 in ovarian cancer¹³. These differences might be attributable to a number of factors, such as different cancer model (prostate vs. ovarian), different expression system (knockdown vs. overexpression) as well as different lectins used (ConA and PHA vs. SNA). We believe that TUSC3 mediated N-glycosylation might exert several different functions in tumorigenesis depending on cancer type and genetic background. Integrins as well as growth factor receptors are likely candidates for N-glycosylated target proteins involved in carcinogenesis^{40–42}, an our further



efforts are aimed at the successful identification of a TUSC3 target protein in prostate and ovarian cancers. In our study, however, we cannot prove a direct effect of increased N-glycosylation caused by TUSC3 loss to prostate carcinogenesis.

We observe that ER structure is altered depending on TUSC3 status in prostate cancer cells and we detect an effect of TUSC3 on the unfolded protein response. UPR is triggered by endoplasmic reticulum stress caused by accumulation of misfolded proteins, which causes simultaneous activation of both adaptive and pro-apoptotic pathways. ER stress receptors are activated by binding of unfolded proteins to the BiP (GRP78) and its dissociation from IRE-1, ATF6 and PERK²⁷. The pro-apoptotic response consists of the PERK mediated activation of the transcription factor CHOP. The adaptive pathway is primarily regulated by IRE-1, a conserved UPR stress sensor, which splices XBP-1 into its active form²⁶. We observe ER stress induction in both prostate cancer cell lines studied, although serum starved PTEN negative cells demonstrate generally higher levels of XBP-1 splicing and CHOP induction. This response is blunted in TUSC3 silenced cell lines and particularly in PTEN negative cells, which may result in a better adaptation to ER stress and growth advantage *in vivo*. We are aware that there might be further differences between the two prostate cancer cell lines than their PTEN status, but we have reason to believe that the PTEN/Akt pathway disruption is the main driver for increased ER stress in prostate cancer³¹. The importance of a crosstalk between ER stress response through BiP/GRP78 and Akt activation in prostate cancer pathogenesis has been demonstrated recently³². We speculate that TUSC3 might be responsible for regulation of N-glycosylation and UPR under ER stress conditions of serum starvation, leading to alteration of Akt signaling. The possibly deleterious effects of increased ER stress are ameliorated in PTEN negative cells, leading to a survival advantage.

In our previous work, we characterized the prognostic relevance of TUSC3 promoter hypermethylation in ovarian cancer^{11,12}. TUSC3 promoter methylation has been described in prostatic intraepithelial neoplasia as well as prostate adenocarcinoma⁴³. Here we offer further evidence for a loss of TUSC3 expression in two large cohorts of prostate cancer patients as well as indications for its epigenetic regulation through promoter hypermethylation.

We hypothesize that loss of TUSC3 in prostate epithelium may facilitate cancer initiation and progression under certain circumstances, such as PTEN loss. In conclusion, we propose that loss of TUSC3 in PTEN negative prostate cancer cells further enhances their carcinogenic potential by increased N-glycosylation of yet unknown target proteins and alleviation of ER stress and unfolded protein response.

Methods

Cell culture conditions and treatments. The cancer cell lines PC3, DU145, BPH-1, LNCaP, HEK293T were obtained from European Collection of Cell Cultures (ECACC) or American Type Culture Collection (ATCC). Cells were cultivated at 37°C in a humidified atmosphere with 5% CO₂ in growth medium (HEK293T: DMEM; DU145, PC3: RPMI; all enriched with 10% FCS (fetal calf serum), 50 units ml⁻¹ penicillin G, and 50 µg ml⁻¹ streptomycin sulfate; LNCaP, BPH-1: RPMI enriched with 20% FCS (fetal calf serum), 50 units ml⁻¹ penicillin G, and 50 µg ml⁻¹ streptomycin sulfate. In addition, BPH-1 cells received 5 mg/ml transferrin, 5 ng/ml sodium selenite, 5 mg/ml insulin (Invitrogen, Carlsbad, CA, USA). Tunicamycin (T7765) was obtained from Sigma Aldrich (St. Louis, MO, USA) and reconstituted in DMSO.

Semiquantitative and quantitative reverse transcription-polymerase chain reaction. Total RNA was isolated from a confluent 6-well plate using RNAzol® RT (Molecular Research Center, Inc.). RNA concentration was measured on a Nanodrop 8000 and cDNAs were generated by reverse transcription of isolated mRNAs using SuperScript II RNase H-Reverse Transcriptase (Invitrogen) according to the manufacturer's instructions. Quantitative real-time PCR was performed using TaqMan® Gene Expression Assays by Applied Biosystems (Carlsbad, CA, USA) for TUSC3 (Hs00185147_m1), MagT1 (Hs00259564_m1), huHPRT (Hs99999909_m1) or SYBR® Green based assays for CHOP, BiP and XBP-1 using published primers and

conditions^{44,45}. For the semiquantitative determination of XBP-1 splicing, primers and conditions as described previously were used⁴⁶.

Proliferation and cytotoxicity assays. Cells were plated at a density of 5 × 10³ in 100 µl of culture medium in a 96-well plate and were left overnight to adhere. On the next day medium was aspirated, cells were washed once with 1 × PBS, and appropriate medium containing 5 µM tunicamycin (Sigma Aldrich) or DMSO was added. Cells were then incubated for 24 to 72 hours. Cell viability was measured by CellTiter-Blue® Assay (Promega, Madison, WI, USA) according to the manufacturer's instructions.

Matrigel assay. 50,000 cells were seeded in triplicates onto a 24-well plate with modified Boyden chambers (BD Biosciences, San Jose, CA, USA). The lower chamber contained 20% FCS/culture medium as a chemoattractant. Cells were incubated for 18 hours, stained with crystal violet and counted under a microscope.

Lentiviral transduction and transfection. Downregulation of TUSC3 in prostate cancer cell lines DU145 and PC3 was performed by lentiviral delivery using pLKO.1 vector containing TUSC3 shRNA (Open Biosystems, Thermo Fisher Scientific, Lafayette, CO, USA) and HEK293T packaging cell line. Transduced cells were selected and maintained in medium containing puromycin (3 µg/ml). ER-Luc, Luc and TUSC3 constructs were cloned into the pcDNA 3.1+ vector according to Contessa et al.³⁰ and transfected into HEK293T cells using the CalPhos™ Mammalian Transfection Kit (Clontech, Saint-Germain-en-Laye, France).

Luciferase assay. Luciferase activity was measured using Promega's Luciferase Assay System according to the manufacturer's protocol. Measurements were performed on a Berthold TriStar LB 941 Multimode Microplate Reader (Berthold Technologies, Bad Wildbad, Germany). In experiments using tunicamycin at cytotoxic concentrations, the final values of bioluminescence were normalized to cell counts of treated wells.

Immunoblotting and co-immunoprecipitation. Cells were lysed with RIPA buffer supplemented with cOmplete Protease Inhibitor Cocktail Tablets (Roche Diagnostics, Mannheim, Germany) and PhosSTOP Phosphatase Inhibitor Cocktail Tablets (Roche Diagnostics). After incubation for 10 minutes on ice, cell lysates were cleared by centrifugation at 15,000 rpm for 10 minutes at 4°C and protein concentration was determined by Bradford absorbance assay (Sigma Aldrich). Equal amounts of protein lysates (40 µg) were separated by SDS-PAGE, blotted on PVDF membranes (GE Healthcare, Chalfont St. Giles, UK), incubated with the appropriate primary antibody and horseradish peroxidase (HRP)-conjugated secondary antibodies and detected with enhanced chemiluminescence detection system (Pierce ECL Western Blotting Substrate, Thermo Scientific, Rockford, IL, USA). Following antibodies and dilutions were used: luciferase (1 : 500, AB3256, Millipore, Billerica, MA, USA), TUSC3 (1 : 500, ab65213, Abcam), actin (1 : 500, sc-1616, Santa Cruz Biotechnology, Santa Cruz, CA), phospho-ERK 1/2 (Thr202/Tyr204, 1 : 1000, #9101, Cell Signaling Technology, Danvers, MA, USA), ERK (1 : 1000, sc-93, Santa Cruz), phospho-Akt (Ser473, 1 : 1000, Cell Signaling #4060), Akt (1 : 1000, Cell Signaling #9272), PTEN (1 : 500, Cell Signaling #9552), ENTPD5 (1 : 500, HPA002927, Sigma Aldrich), CHOP (1 : 500, MA1-250, Thermo Scientific), IRE1α (14C10) (Cell Signaling #3294), BiP (C50B12) (Cell Signaling #3177), STT3B (1 : 500, 15323-1-AP, Proteintech, Chicago, IL, USA) and XBP-1s (D2C1F) (Cell Signaling #12782).

For co-immunoprecipitations, cells were lysed in PBS with 0.75% NP40 and cOmplete Protease Inhibitor as well as PhosSTOP Phosphatase Inhibitor. After incubation for 10 minutes on ice, cell lysates were cleared by centrifugation at 15,000 rpm for 10 minutes at 4°C. 1000 µg of the protein lysate were incubated with Protein A/G Sepharose beads for 1 hour at 4°C. Pre-cleared lysates were then incubated overnight at 4°C with the respective antibody (TUSC3, ab65213, Abcam; STT3B, 15323-1-AP, Proteintech; normal rabbit IgG, sc-2027, Santa Cruz), followed by precipitation with protein A Sepharose (GE Healthcare) at 4°C for 1 hour. Beads were washed three times in lysis buffer, bound proteins separated with SDS/PAGE and visualized by western blotting.

Cell Surface Protein isolation. Selective isolation of the cell membrane proteins was performed using the Pierce Cell Surface Protein Isolation Kit according to the manufacturer's instructions (Thermo Scientific).

Immunohistochemistry. 5 µm thick tissue sections were deparaffinized by heating at 60°C and subsequently rehydrated in xylene and graded alcohols. Antigen retrieval was performed with DEPP-9 epitope retrieval solution (EB-depp9-250, eubio, Vienna, Austria), followed by treatment with 0.3% H₂O₂ in PBS (pH 7.4) to quench endogenous peroxidase activity. After blocking with 10% secondary antibody host serum for 10 minutes, the sections were incubated in primary antibody (rabbit polyclonal to TUSC3, dilution 1 : 300, ab65213, Abcam, Cambridge, UK) for 1 hour at room temperature. Primary antibody dilutions were made in 10% secondary antibody host serum. The sections, after 2xPBS washes, were incubated in respective biotinylated secondary antibodies [biotinylated anti-rabbit IgG (BA-1000), Vector Laboratories, Burlingame, CA, USA], diluted 1 : 200 in 10% serum for 30 minutes at room temperature, followed by 45 minute incubation in StreptABComplex/HRP (K0377 Dako, Glostrup, Denmark). The sections were again washed twice with PBS and incubated in Dako Liquid DAB + Substrate-Chromogen System (K3468) until



the development of brown color. This was followed by counterstaining with Meyer's hematoxylin, dehydration, and mounting using Eukitt medium.

Three tissue microarrays of prostate cancer from 143 patients were used to assess the TUSC3 protein expression. Each tissue microarray consisted of 3 biopsies of tumor material and 2 biopsies of adjacent benign tissue from each patient. Stained cells per 5 high-power fields were counted and grouped according to percentage of positive cells as < 10%, 10%–30%, and > 30%. The intensity of staining was determined on a scale of 0 to 3, with 0 for absent, 1 for weak, 2 for moderate, and 3 for strong. The microscopic assessment and quantification of the staining was performed independently by three investigators (R.H., M.A. and P.H.).

Lectin histochemistry and lectin blotting. 5 μ m thick paraffin embedded tissue sections and cell lines grown on glass chamber slides (Nunc, Langensfeld, Germany) were used. Lectin histochemistry and cytochemistry was performed using Concanavalin A (ConA) HRP conjugate in a concentration of 1:40 in PBS (USBiological, Swampscott, MA, USA) overnight at 4°C, followed by 2xPBS washes and visualized with Dako Liquid DAB + Substrate-Chromogen System (K3468). This was followed by counterstaining with haematoxylin, dehydration and mounting using Eukitt medium (O. Kindler GmbH, Freiburg, Germany).

Lectin blotting was performed after cell lysis in lysis buffer (1% Triton X-100, 20 mM Tris-HCl (pH 7.4), 150 mM NaCl, and 5 mM EDTA) containing protease and phosphatase inhibitors. Protein lysates were separated by SDS-PAGE, blotted on PVDF membranes (GE Healthcare) and blocked with PBST + 2% gelatin for 1 hour. Membranes were incubated 4 hours at 4°C with 2 μ g/ml Concanavalin A (ConA) or Phytohaemagglutinin-L (PHA) HRP lectin conjugates and washed three times in PBST. Bound lectins were visualized with enhanced chemiluminescence detection system (Pierce ECL Western Blotting Substrate).

Transmission electron microscopy. For electron microscopy analysis, cell lines were harvested from cell culture plates using trypsin-EDTA and suspended in RPMI medium. Cells were fixed in 3% glutaraldehyde with 0.2% tannin in 0.1 M cacodylate buffer for 1 hour and post-fixed in 1% OsO₄ in the same buffer for 50 minutes. Cells were then washed three times in cacodylate buffer and then embedded in small blocks of 1% agar of 1 mm³ in size. Those blocks were then dehydrated in ascending series of ethanol (50%, 70%, 96%, and 100%), treated 2 \times 10 minutes with 100% acetone and embedded in Durcupan resin (Sigma Aldrich). Ultrathin sections were prepared on LKB 8802A ultramicrotome, stained with OsO₄ and examined on Morgagni 286(D) (FEI, Hillsboro, OR, USA) transmission electron microscope.

Mouse xenograft experiments. We treated 8-week old male, athymic Foxn1nu/nu mice, which were maintained under specific pathogen-free conditions. shTUSC3 DU145 (10⁷ cells) and shTUSC3 PC3 (5 \times 10⁶ cells) prostate cancer cell lines as well as the same number of scrambled shRNA control cells were subcutaneously injected into the right and left dorsal flanks of nu/nu mice, respectively. Matrigel (BD Biosciences, San Jose, CA, USA) was used for the engraftment of PC3 cells and mixed with shTUSC3 and control cells in a 1:1 volume ratio. Tumor size was measured three times weekly in two perpendicular axes using a caliper. Tumor volume was calculated using the formula: volume = $\frac{1}{2}$ (length \times width²). Animal experiments were carried out in adherence to protocols approved by the Austrian Federal Ministry for Science and Research and the Animal Ethics Committee of the Medical University of Vienna.

Statistical and in silico analysis. All statistical computations were performed using the SPSS software version 20 (SPSS Inc., Chicago, IL, USA). Comparison of means in normally distributed data was performed using Student's t-test, otherwise the nonparametric Mann-Whitney U test was applied. Pearson's correlation coefficient (r) was used to examine significant correlations. P-values of equal or less than 0.05 were considered statistically significant. All bar graphs are depicted using means and standard deviations as error bars, unless stated otherwise. TUSC3 gene expression, promoter methylation and gene copy number were analyzed using the Caleydo visualization software⁴⁷ and publicly available TCGA (<http://cancergenome.nih.gov/>) datasets for prostate adenocarcinoma after obtaining a written permission from the TCGA Research Network.

- Jemal, A. *et al.* Global cancer statistics. *CA Cancer J. Clin.* **61**, 69–90 (2008).
- Berger, M. F. *et al.* The genomic complexity of primary human prostate cancer. *Nature* **470**, 214–220 (2011).
- Taylor, B. S. *et al.* Integrative genomic profiling of human prostate cancer. *Cancer Cell* **18**, 11–22 (2011).
- Bergerheim, U. S., Kunimi, K., Collins, V. P. & Ekman, P. Deletion mapping of chromosomes 8, 10, and 16 in human prostatic carcinoma. *Gene Chromosome. Canc.* **3**, 215–220 (1991).
- Bova, G. S. *et al.* Physical mapping of chromosome 8p22 markers and their homozygous deletion in a metastatic prostate cancer. *Genomics* **35**, 46–54 (1996).
- MacGrogan, D., Levy, A., Bova, G. S., Isaacs, W. B. & Bookstein, R. Structure and methylation-associated silencing of a gene within a homozygously deleted region of human chromosome band 8p22. *Genomics* **35**, 55–65 (1996).
- Levy, A., Dang, U. C. & Bookstein, R. High-density screen of human tumor cell lines for homozygous deletions of loci on chromosome arm 8p. *Gene Chromosome. Canc.* **24**, 42–47 (1999).
- Arbieva, Z. H. *et al.* High-resolution physical map and transcript identification of a prostate cancer deletion interval on 8p22. *Genome Res.* **10**, 244–257 (2000).
- Cooke, S. L. *et al.* High-resolution array CGH clarifies events occurring on 8p in carcinogenesis. *BMC Cancer* **8**, 288 (2008).
- Pribill, I. *et al.* High frequency of allelic imbalance at regions of chromosome arm 8p in ovarian carcinoma. *Cancer Genet. Cytogenet.* **129**, 23–29 (2001).
- Pils, D. *et al.* Five genes from chromosomal band 8p22 are significantly down-regulated in ovarian carcinoma: N33 and EFA6R have a potential impact on overall survival. *Cancer* **104**, 2417–2429 (2005).
- Pils, D. *et al.* Methylation status of TUSC3 is a prognostic factor in ovarian cancer. *Cancer* **119**, 946–954 (2013).
- Vanhara, P. *et al.* Loss of the oligosaccharyl transferase subunit TUSC3 promotes proliferation and migration of ovarian cancer cells. *Int. J. Oncol.* **42**, 1383–1389 (2013).
- Kelleher, D. J. & Gilmore, R. An evolving view of the eukaryotic oligosaccharyltransferase. *Glycobiology* **16**, 47R–62R (2006).
- Kelleher, D. J., Karaoglu, D., Mandon, E. C. & Gilmore, R. Oligosaccharyltransferase isoforms that contain different catalytic STT3 subunits have distinct enzymatic properties. *Mol. Cell* **12**, 101–111 (2003).
- Mohorko, E., Glockshuber, R. & Aeby, M. Oligosaccharyltransferase: the central enzyme of N-linked protein glycosylation. *J. Inherit. Metab. Dis.* **34**, 869–878 (2011).
- Garshasbi, M. *et al.* A defect in the TUSC3 gene is associated with autosomal recessive mental retardation. *Am. J. Hum. Genet.* **82**, 1158–1164 (2008).
- Khan, M. A. *et al.* A novel deletion mutation in the TUSC3 gene in a consanguineous Pakistani family with autosomal recessive nonsyndromic intellectual disability. *BMC Med. Genet.* **12**, 56 (2011).
- Molinari, F. *et al.* Oligosaccharyltransferase-subunit mutations in nonsyndromic mental retardation. *Am. J. Hum. Genet.* **82**, 1150–1157 (2008).
- Garshasbi, M. *et al.* A novel nonsense mutation in TUSC3 is responsible for nonsyndromic autosomal recessive mental retardation in a consanguineous Iranian family. *Am. J. Med. Genet. A* **155A**, 1976–1980 (2011).
- Ohtsubo, K. & Marth, J. D. Glycosylation in cellular mechanisms of health and disease. *Cell* **126**, 855–867 (2006).
- Helenius, A. & Aeby, M. Intracellular functions of N-linked glycans. *Science* **291**, 2364–2369 (2001).
- Freeze, H. H. Genetic defects in the human glycome. *Nat. Rev. Genet.* **7**, 537–551 (2006).
- Hakomori, S. Glycosylation defining cancer malignancy: new wine in an old bottle. *Proc. Natl. Acad. Sci. U S A* **99**, 10231–10233 (2002).
- Fang, M. *et al.* The ER UDPase ENTPD5 promotes protein N-glycosylation, the Warburg effect, and proliferation in the PTEN pathway. *Cell* **143**, 711–724 (2011).
- Hetz, C., Martinon, F., Rodriguez, D. & Glimcher, L. H. The unfolded protein response: integrating stress signals through the stress sensor IRE1 α . *Physiol. Rev.* **91**, 1219–1243 (2011).
- Ozcan, L. & Tabas, I. Role of endoplasmic reticulum stress in metabolic disease and other disorders. *Annu. Rev. Med.* **63**, 317–328 (2012).
- Harding, H. P., Calton, M., Urano, F., Novoa, I. & Ron, D. Transcriptional and translational control in the mammalian unfolded protein response. *Annu. Rev. Cell. Dev. Biol.* **18**, 575–599 (2002).
- Schulz, B. L. *et al.* Oxidoreductase activity of oligosaccharyltransferase subunits Ost3p and Ost6p defines site-specific glycosylation efficiency. *Proc. Natl. Acad. Sci. U S A* **106**, 11061–11066 (2009).
- Contessa, J. N. *et al.* Molecular imaging of N-linked glycosylation suggests glycan biosynthesis is a novel target for cancer therapy. *Clin. Cancer Res.* **16**, 3205–3214 (2010).
- Shen, Z., Huang, S., Fang, M. & Wang, X. ENTPD5, an endoplasmic reticulum UDPase, alleviates ER stress induced by protein overloading in AKT-activated cancer cells. *Cold Spring Harb. Symp. Quant. Biol.* **76**, 217–223 (2011).
- Fu, Y. *et al.* Pten null prostate tumorigenesis and AKT activation are blocked by targeted knockout of ER chaperone GRP78/BiP in prostate epithelium. *Proc. Natl. Acad. Sci. U S A* **105**, 19444–19449 (2008).
- Dennis, J. W., Granovsky, M. & Warren, C. E. Glycoprotein glycosylation and cancer progression. *Biochim. Biophys. Acta* **1473**, 21–34 (1999).
- Fukuda, M. Possible roles of tumor-associated carbohydrate antigens. *Cancer Res.* **56**, 2237–2244 (1996).
- Lau, K. S. *et al.* Complex N-glycan number and degree of branching cooperate to regulate cell proliferation and differentiation. *Cell* **129**, 123–134 (2007).
- Karaoglu, D., Kelleher, D. J. & Gilmore, R. Functional characterization of Ost3p. Loss of the 34-kD subunit of the *Saccharomyces cerevisiae* oligosaccharyltransferase results in biased underglycosylation of acceptor substrates. *J. Cell Biol.* **130**, 567–577 (1995).
- Zhou, H. & Clapham, D. E. Mammalian MagT1 and TUSC3 are required for cellular magnesium uptake and vertebrate embryonic development. *Proc. Natl. Acad. Sci. U S A* **106**, 15750–15755 (2009).
- Ruiz-Canada, C., Kelleher, D. J. & Gilmore, R. Cotranslational and posttranslational N-glycosylation of polypeptides by distinct mammalian OST isoforms. *Cell* **136**, 272–283 (2009).
- Sato, T. *et al.* STT3B-dependent posttranslational N-glycosylation as a surveillance system for secretory protein. *Mol. Cell* **47**, 99–110 (2012).
- Goel, H. L., Li, J., Kogan, S. & Languino, L. R. Integrins in prostate cancer progression. *Endocr. Relat. Cancer* **15**, 657–664 (2008).



41. Kariya, Y. & Gu, J. N-glycosylation of ss4 integrin controls the adhesion and motility of keratinocytes. *PLoS One* **6**, e27084 (2011).
42. Gabius, H. J., M, V. D. W., Andre, S. & Villalobo, A. Down-regulation of the Epidermal Growth Factor Receptor by Altering N-Glycosylation: Emerging Role of beta1,4-Galactosyltransferases. *Anticancer Res.* **32**, 1565–1572 (2012).
43. Kekeeva, T. V. *et al.* [Abberant methylation of p16, HIC1, N33 and GSTP1 genes in tumor epithelium and tumor-associated stromal cells of prostate cancer]. *Mol. Biol. (Mosk)* **41**, 79–85 (2007).
44. Hirota, M., Kitagaki, M., Itagaki, H. & Aiba, S. Quantitative measurement of spliced XBP1 mRNA as an indicator of endoplasmic reticulum stress. *J. Toxicol. Sci.* **31**, 149–156 (2006).
45. van Schadewijk, A., van't Wout, E. F., Stolk, J. & Hiemstra, P. S. A quantitative method for detection of spliced X-box binding protein-1 (XBP1) mRNA as a measure of endoplasmic reticulum (ER) stress. *Cell Stress Chaperones* **17**, 275–279 (2012).
46. Samali, A., Fitzgerald, U., Deegan, S. & Gupta, S. Methods for monitoring endoplasmic reticulum stress and the unfolded protein response. *Int. J. Cell Biol.* **2010**, 830307 (2010).
47. Streit, M., Lex, A., Kalkusch, M., Zatloukal, K. & Schmalstieg, D. Caleydo: connecting pathways and gene expression. *Bioinformatics* **25**, 2760–2761 (2009).

Acknowledgments

This work was supported by the Austrian Science Fund (FWF) [grant number P17891]; Funds of the Oesterreichische Nationalbank [project number 14109]; Initiative Krebsforschung; Centre for International Cooperation & Mobility of the Austrian Agency for International Cooperation in Education and Research [project number CZ 04/2012];

Ministry of Education, Youth and Sports of Czech Republic [project number 7AMB12AT019]. We thank Miroslava Sedláčková for cytological assessment and ER analysis, Dobromila Klemová, Andrea Schanzer, Maria König and Martina Hammer for expert technical support. We are grateful to Christopher J. Sweeney, William K. Oh, Massimo Loda and Rosina Lis for providing the prostate cancer tissue microarray.

Author contributions

P.H., P.V. and M.K. designed the study and the experiments; P.H., E.T., P.V., K.K., M.A., M.M., C.E.L., M.G. and D.P. collected and assembled data in figures 1–4 as well as supplementary figures; P.H., K.K. and M.A. collected and assembled data in figure 5; P.H., E.T., P.V., K.K., M.A., M.M. and C.E.L. analyzed and interpreted the data; P.H. and E.T. wrote the manuscript; R.H. provided pathological support and review; M.S. supervised the animal experiments; M.K. provided financial support; all authors reviewed the manuscript.

Additional information

Supplementary information accompanies this paper at <http://www.nature.com/scientificreports>

Competing financial interests: The authors declare no competing financial interests.

How to cite this article: Horak, P. *et al.* TUSC3 Loss Alters the ER Stress Response and Accelerates Prostate Cancer Growth *in vivo*. *Sci. Rep.* **4**, 3739; DOI:10.1038/srep03739 (2014).



This work is licensed under a Creative Commons Attribution-NonCommercial-NoDerivs 3.0 Unported license. To view a copy of this license, visit <http://creativecommons.org/licenses/by-nc-nd/3.0>

4. Kratochvílová K, Horak P, Ešner M, Souček K, Pils D, Anees M, Tomasich E, Dráfi F, Jurtíková V, Hampl A, Krainer M, **Vaňhara P. Tumor suppressor candidate 3 (TUSC3) prevents the epithelial-to-mesenchymal transition and inhibits tumor growth by modulating the endoplasmic reticulum stress response in ovarian cancer cells.** *International Journal of Cancer* 2015; **137**(6):1330-40.

Commentary:

In this publication, detailed molecular mechanism TUSC3-driven UPR was revealed. TUSC3 was definitely established as a novel ovarian cancer tumor suppressor using an immunodeficient xenograft mouse model. Also we demonstrated that loss of TUSC3 altered the molecular response to ER stress and induced hallmarks of the EMT in ovarian cancer cells towards highly invasive malignant phenotype.

DOI: 10.1002/ijc.29502
Journal: International Journal of Cancer
Impact factor (WOS, 2015): 5.531
Number of citations (WOS, 2018): 23
Cited in: Nature Communications, Cancer Biomarkers, Cancer research, European Journal of Cell Biology, Tumor biology, Oncotarget, Journal of Pathology, etc.

Most important citation:

Jeon Y-J, Kim T, Park D, Nuovo G, Rhee S, Joshi P et al. **miRNA-mediated TUSC3 deficiency enhances UPR and ERAD to promote metastatic potential of NSCLC.** *Nature Communications* 2018; **9**:5110. doi: 10.1038/s41467-018-07561-8. (IF2018 12.353)

Contribution of the author: Corresponding author. Collection and/or assembly of data, data analysis and interpretation, manuscript writing.

Awarded in 2016 by the Czech Society for Analytical Cytometry for the best publication in basic research.

Tumor suppressor candidate 3 (TUSC3) prevents the epithelial-to-mesenchymal transition and inhibits tumor growth by modulating the endoplasmic reticulum stress response in ovarian cancer cells

Kateřina Kratochvílová^{1,2}, Peter Horak³, Milan Ešner¹, Karel Souček^{2,4,5}, Dietmar Pils⁶, Mariam Anees^{3,7}, Erwin Tomasich³, František Dráfi¹, Veronika Jurtíková¹, Aleš Hampl¹, Michael Krainer³ and Petr Vaňhara¹

¹ Department of Histology and Embryology, Faculty of Medicine, Masaryk University, Brno, Czech Republic

² Center of Biomolecular and Cellular Engineering, International Clinical Research Center, St. Anne's University Hospital, Brno, Czech Republic

³ Department of Internal Medicine I and Comprehensive Cancer Center, Medical University of Vienna, Vienna, Austria

⁴ Department of Cytokinetics, Institute of Biophysics, Academy of Sciences of the Czech Republic, v.v.i., Brno, Czech Republic

⁵ Department of Experimental Biology, Faculty of Science, Masaryk University, Brno, Czech Republic

⁶ Department of Obstetrics and Gynecology, Molecular Oncology Group, Medical University of Vienna, Vienna, Austria

⁷ Department of Biochemistry, Quaid-i-Azam University, Islamabad, Pakistan

Ovarian cancer is one of the most common malignancies in women and contributes greatly to cancer-related deaths. Tumor suppressor candidate 3 (*TUSC3*) is a putative tumor suppressor gene located at chromosomal region 8p22, which is often lost in epithelial cancers. Epigenetic silencing of *TUSC3* has been associated with poor prognosis, and hypermethylation of its promoter provides an independent biomarker of overall and disease-free survival in ovarian cancer patients. *TUSC3* is localized to the endoplasmic reticulum in an oligosaccharyl transferase complex responsible for the N-glycosylation of proteins. However, the precise molecular role of *TUSC3* in ovarian cancer remains unclear. In this study, we establish *TUSC3* as a novel ovarian cancer tumor suppressor using a xenograft mouse model and demonstrate that loss of *TUSC3* alters the molecular response to endoplasmic reticulum stress and induces hallmarks of the epithelial-to-mesenchymal transition in ovarian cancer cells. In summary, we have confirmed the tumor-suppressive function of *TUSC3* and identified the possible mechanism driving *TUSC3*-deficient ovarian cancer cells toward a malignant phenotype.

Ovarian cancer (OC) is one of the most common malignancies and the fifth leading cause of cancer-related death in women.¹ Despite the recent progress in OC diagnosis and

Key words: TUSC3, N33, endoplasmic reticulum stress, epithelial-to-mesenchymal transition, ovarian cancer, tumor suppressor
Additional Supporting Information may be found in the online version of this article.

Grant sponsor: Grant Agency of Masaryk University; **Grant numbers:** MUNI/M/1050/2013, MUNI/A/1558/2014; **Grant sponsor:** Grant Agency of the Ministry of Health of the Czech Republic; **Grant number:** IGA MZD NT13573-4/2012; **Grant sponsor:** Czech Academy of Sciences; **Grant number:** AV PIPPMS ĀR M 200041203; **Grant sponsor:** European Regional Fund; **Grant numbers:** FNUSA-ICRC CZ.1.05/1.1.00/02.0123 and HistoPARK CZ.1.07/2.3.00/20.0185

DOI: 10.1002/ijc.29502

History: Received 13 Sep 2014; Accepted 18 Feb 2015; Online 3 Mar 2015

Correspondence to: Petr Vaňhara, PhD, Department of Histology and Embryology, Faculty of Medicine, Masaryk University, Kamenice 3, CZ-62500, Brno, Czech Republic, Tel.: 420-54949-7780, Fax: 420-54949-1320, E-mail: pvanhara@med.muni.cz

therapy, its overall prognosis remains unfavorable. The heterogeneity of its clinical display reflects the diverse molecular mechanisms contributing to malignant transformation and dissemination of the primary cancer. The tumor suppressor candidate 3 (*TUSC3* or *N33*) gene has been located to chromosomal region 8p22, which is often lost in common epithelial cancers, such as breast, prostate, oral squamous or ovarian cancer.^{2–6} According to the Oncomine database, expression of *TUSC3* gene is significantly downregulated in OC cases, suggesting the potential clinical relevance of *TUSC3* in OC pathogenesis (www.oncomine.org, Supporting Information Fig. 1). Moreover, epigenetic silencing of *TUSC3* has been associated with poor prognosis of OC, and hypermethylation of its promoter provides an independent biomarker of overall and disease-free survival in OC patients.⁷ Until recently, the molecular function of *TUSC3* was inferred from its sequence homology to the yeast protein Ost3p, which forms a subunit of the oligosaccharyltransferase (OST) complex that is responsible for post- and co-translational N-glycosylation of proteins in the endoplasmic reticulum (ER).⁸

We demonstrated recently that in embryonic kidney (HEK293) and ovarian cancer cells, *TUSC3* localizes to the

What's new?

While epigenetic silencing of the tumor suppressor candidate 3 (*TUSC3*) gene is associated with poor outcome in ovarian cancer, the molecular role of *TUSC3* in ovarian malignancies is unknown. In this study, loss of *TUSC3* expression in ovarian cancer cells was associated with alterations in endoplasmic reticulum (ER) ultrastructure, as well as with alterations in ER stress signaling. *TUSC3* silencing was further associated with the loss of epithelial phenotype and epithelial-to-mesenchymal transition. In mice, loss of *TUSC3* promoted massive tumor growth of ovarian cancer cells. The results establish *TUSC3* as a novel tumor suppressor in ovarian cancer.

rough ER and binds to the core OST proteins STT3A/B.^{9,10} Moreover, downregulation of *TUSC3* protein is associated with changes in the expression of markers of the ER stress response in DU-145 and PC3 prostate cancer cell lines, while its overexpression in HEK293 cells attenuates N-glycosylation.⁹ In ovarian cancer, hypermethylation of the *TUSC3* promoter is clearly correlated with clinical outcome,⁷ and small hairpin RNA (shRNA)-mediated silencing of *TUSC3* in ovarian cancer cells promotes proliferation and migration under serum free conditions *in vitro*.¹⁰ Despite its potential clinical significance, the detailed molecular mechanism linking *TUSC3* to cancer remains unclear.

In this work we establish *TUSC3* as a novel ER-associated tumor suppressor involved in ovarian cancer pathobiology. On both the morphological and molecular levels, we document that *TUSC3* is involved in rough ER homeostasis and that its loss induces markers of the epithelial-to-mesenchymal transition (EMT) and enhances tumor growth *in vivo*.

Material and Methods**Cell culture conditions and treatments**

Ovarian cancer cell line SKOV-3 was obtained from the American Type Culture Collection (ATCC), and ovarian cancer cell lines H134 and TR170 were a kind gift from Prof. Thomas Grunt, Medical University of Vienna, Vienna, Austria. Prior to use, all cell lines were authenticated *via* short tandem repeat (STR) profiling carried out by a commercial service (Generi Biotech, Czech Republic), which confirmed the identity (SKOV-3) or purity (TR170, H134) of the cell populations and established reference STR profiles for the TR170 and H134 cell lines (Supporting Information Table 1). Mycoplasma contamination was investigated on a routine basis using PCR.^{11,12} TR170 and H134 cells were cultured in high glucose (4.5 g l⁻¹) Dulbecco's Modified Eagle Medium (DMEM), SKOV-3 cells in McCoy's 5A Modified Medium enriched with 10% fetal calf serum (FCS) (Invitrogen, Life Technologies, Czech Republic), 50 U ml⁻¹ penicillin G, and 50 µg ml⁻¹ streptomycin sulfate (PAA, GE Healthcare, Austria) at 37 °C in a humidified atmosphere with 5% CO₂. In cell lines SKOV-3 and TR170, expression of *TUSC3* was silenced as described previously^{9,10} using lentiviral-mediated delivery of a pLKO.1 puro vector containing *TUSC3* shRNA (Open Biosystems, Thermo Fisher Scientific, Czech Republic). Scrambled shRNA sequence was used as a control (Open Biosystems, Thermo Fisher Scientific, Czech Republic). Cell

line H134 with rescued expression of *TUSC3* was derived previously using the cytomegalovirus (CMV)-driven *TUSC3* cDNA cloned into the pLP-IRESneo plasmid (pLP-IRES-*TUSC3*). An empty pLP-IRESneo vector (pLP-IRES) was used as a control.⁷ To specifically induce ER stress *via* disruption of N-glycosylation, tunicamycin solution in dimethyl sulfoxide (DMSO; Sigma Aldrich, Czech Republic) was used at concentrations 0.2, 0.5 or 1 µg ml⁻¹ for 12, 24 or 48 hr.

MTT assay and annexin V/propidium iodide fluorescence-activated cell sorting (FACS) analysis

First, 1 × 10⁴ cells were seeded in triplicate on 96-well plates (Corning, USA) and cultured for the indicated time in complete medium containing either DMSO or tunicamycin at concentrations 0.2, 0.5 or 1 µg ml⁻¹. Then, thiazolyl blue tetrazolium bromide (Sigma-Aldrich, Czech Republic) solution in water (5 mg ml⁻¹) was added at one-tenth of culture volume and incubated for 4 hr. Absorbance was measured at 570 nm. The plots derived represent mean normalized, background subtracted absorbance ± the standard deviation (SD) from three independent experiments. To analyze cell death, cell suspensions were washed with 1× phosphate buffered saline (PBS), stained with annexin V-fluorescein isothiocyanate (FITC) conjugate (Apronex, Czech Republic) and propidium iodide (Sigma-Aldrich, Czech Republic), and incubated for 15 min in the dark at room temperature. Then, cells were washed using HEPES buffered solution (10 mM HEPES, 140 mM NaCl, and 10 mM CaCl₂ pH 7.4) and the fluorescence was quantified using an Attune® Acoustic Focusing Cytometer (Life Technologies, Czech Republic).

Real-time, impedance-based cell analysis (RTCA, xCELLigence)

To assess adhesion and proliferation of ovarian cancer cells, the commercially available, impedance-based, label-free xCELLigence RTCA SP system (Acea Biosciences, USA) was employed as described previously.^{13,14} Briefly, an Acea E-plate 96 was coated with fibronectin dissolved in 1× PBS to a final concentration of 5 µg cm⁻² and incubated for 1 hr at room temperature. Coated wells were washed with deionized water and filled with 100 µl complete medium containing either tunicamycin (0.2 µg ml⁻¹) or DMSO, according to the experimental design. Prior to analysis, standard background measurements were performed. Then, tunicamycin (0.2 µg ml⁻¹) or DMSO pretreated cells were trypsinized, quantified using a Casy® Cell Counter (Roche Applied Science,

Czech Republic), seeded in 100 μ l their respective medium at a final concentration of 5×10^4 cells per well, and monitored every minute for the first 6 hr post-seeding, then every 5 min for 18 hr, and finally every 15 min, for a total of 120 hr. To monitor cell migration, 3×10^4 serum-starved cells were resuspended in serum-free medium and seeded in an uncoated Acea cell invasion and migration (CIM)-plate 16 with the appropriate cell culture media containing 10% serum as an attractant. The cell index was recorded every 15 min for 56 hr. Resulting plots represent the mean cell index \pm SD.

Spheroid culture and analysis

Formation of 3D spheroids was induced by culturing cells under low-adhesion conditions in low melting point agarose-coated (Sigma-Aldrich, Czech Republic) 96-well plates (Greiner Bio-ONE, Germany). Briefly, 5×10^2 cells were seeded in a hexaplicate layout, centrifuged at 2,000 rpm for 1 min, and cultured in presence of tunicamycin at concentrations 0.2, 0.5 or 1 μ g ml⁻¹ or DMSO. To monitor spheroid formation, we performed time-lapse microscopy, imaging the plate immediately after centrifugation; one image was taken every 30 min for 24 hr. We acquired bright field images using a 10 \times objective with an automated microscope equipped with an environmental chamber (Image Xpress MicroXL, Molecular Devices, USA). For the end-point assay, spheroids were stained with Hoechst stain and propidium iodide (5 μ g ml⁻¹; Sigma-Aldrich, Czech Republic) and imaged with the same microscope. Images were analyzed using Cell Profiler 2.0 software (Broad Institute, USA) to determine spheroid size (in pixels) and shape (as a form factor from 0–1, with 1 representing an ideal sphere).

Transmission electron microscopy (TEM)

Ovarian cancer cell lines with altered expression of *TUSC3* were treated for 24 hr with either 0.2 μ g ml⁻¹ tunicamycin or DMSO, harvested using trypsin-EDTA, washed in 1 \times PBS, fixed in 3% glutaraldehyde with 0.2% tannin in 0.1 M cacodylate buffer for 1 hr, and postfixed in 1% OsO₄ in the same buffer for 50 min. After post-fixation, cells were washed three times in cacodylate buffer and embedded in small blocks of 1% agar 1 mm³ in size. Agar blocks were dehydrated in increasing concentrations of ethanol (50%, 70%, 96% and 100%), treated 2 \times 10 min with 100% acetone, and embedded in Durcupan resin. Ultrathin sections were prepared on an LKB 8802A ultramicrotome, stained with OsO₄, and examined with an FEI Morgagni 286(D) TEM. One hundred cells from each experimental group in two independent experiments were examined. Images were analyzed using ImageJ software.¹⁵ Cytological analysis of TEM images was validated by two independent reviewers.

RNA isolation, cDNA synthesis and quantitative reverse transcription PCR (qRT-PCR)

Total RNA from cancer cell lines was extracted using an RNeasy Mini Kit (Qiagen) and quantified using a NanoDrop

(Thermo Scientific, USA). cDNA was synthesized from 1 μ g DNase I-treated total RNA using a First Strand Reverse Transcription Kit (Roche). Relative expression was quantified using exon-spanning TaqMan probes specific for *TUSC3* (N33, Hs00185147_m1), binding immunoglobulin protein (*BiP*; GRP78, HSPA5, Hs00607129_gH), DNA-damage-inducible transcript 3 (*CHOP*; DDIT3, Hs00358796_g1), growth differentiation factor 15 (*GDF-15*; Hs00171132_m1), transforming growth factor β 1 (*TGF- β 1*; Hs99999918_m1) and glyceraldehyde 3-phosphate dehydrogenase (*GAPDH*; Hs99999905_m1) (Applied Biosystems, Life Technologies, Czech Republic), as described elsewhere,¹⁶ and expressed as relative ratio units. All PCR reactions were performed in triplicate from three independent experiments, and reverse transcriptase-negative and template-negative controls were included.

SDS-PAGE and western blotting

Trypsinized cells were washed two times with ice-cold 1 \times PBS and resuspended in NP-40 lysis buffer containing 50 mM Tris-Cl (pH 7.4), 150 mM NaCl, 2 mM EDTA, 1% NP-40, 50 mM NaF supplemented with phosphatase inhibitor cocktail (PhosStop, Roche Applied Science, Czech Republic) and protease inhibitor cocktail (Complete, Roche Applied Science, Czech Republic). Next, 15 μ g protein extract, quantified using the Bradford-based BioRad protein Assay Kit (BioRad), was mixed with 2 \times Laemmli sample buffer (100 mM Tris pH 6.8, 4% SDS, 200 mM DTT, 20% glycerol, and 0.1% Bromophenol Blue),¹⁷ boiled for 3 min, and resolved using 10% sodium dodecylsulfate-polyacrylamide gel electrophoresis (SDS-PAGE). Resolved proteins were then electroblotted to a 0.45 μ m polyvinylidene difluoride (PVDF) membrane (Millipore, Czech Republic) and incubated with the indicated primary antibodies diluted 1:500–1:1,000 at 4 $^{\circ}$ C overnight (ZO-1 cat. no: #8193; Slug #9585; TCF8/ZEB1 #3396; E-Cadherin #3195; BiP #3177; Calnexin #2679; Ero1 α #3264; Ire1 α #3294; CHOP #2895; PERK #5683, all from Cell Signaling, USA; TUSC3 (Ab65213), Vimentin (Ab92547) and Actin (Ab1801) from Abcam, UK). Blots were developed using horseradish peroxidase (HRP)-conjugated secondary antibodies, including anti-rabbit HRP #7074 (Cell Signaling, USA) or anti-mouse HRP Ab50043 (Abcam, UK), both diluted 1:5,000, and Immobilon Western HRP Substrate (Millipore, Czech Republic), according to the manufacturer's protocols. Quantitative densitometry was performed using ImageJ software.¹⁵ Values above the band represent the integrated density for the particular band normalized to the control of equal loading.

Mouse xenograft experiments

A colony of NOD scid gamma mice (NSG, NOD.Cg-Prkdcscid Il2rgtm1Wjl/Szj) was obtained from the Jackson laboratory, maintained under specific-pathogen-free conditions with 12/12 light cycles, and fed *ad libitum*. For xenograft experiments, thirty 8- to 10-week-old mice were subcutaneously injected with 5×10^6 control and TUSC3-altered cells in sterile 1 \times PBS in the left and right ventral flanks, respectively. Animals were

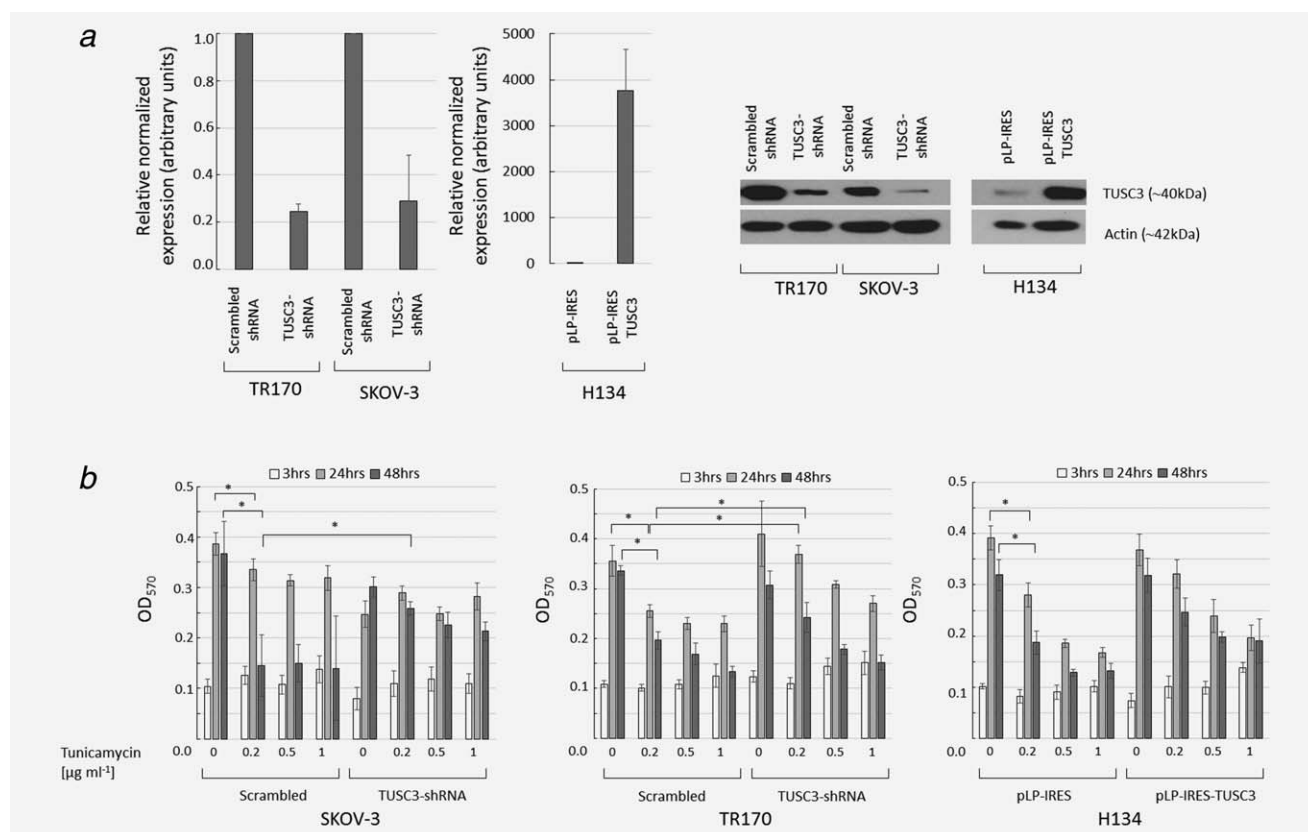


Figure 1. Expression of *TUSC3* in ovarian cancer cell lines. (a) Cells were cultured under optimal conditions and harvested, then, the total RNA was extracted, reverse transcribed, and analyzed *via* qRT-PCR. Plots represent mean relative *GAPDH*-normalized expression \pm SD, determined from three independent experiments. In parallel, *TUSC3* protein was documented by SDS-PAGE and immunoblotting. (b) Metabolic activity of tunicamycin-treated cells as determined by the MTT conversion assay. First, 1×10^4 cells were seeded in triplicate on 96-well plates and cultured for the indicated time in complete medium containing either DMSO or tunicamycin at concentrations 0.2, 0.5 or $1 \mu\text{g ml}^{-1}$. Then, thiazolyl-blue-tetrazolium bromide was added and incubated for 4 hrs. Absorbance was measured at 570 nm. Plots represent mean normalized (*i.e.*, background subtracted) absorbance \pm SD from three independent experiments. Asterisks indicate statistical significance at $p < 0.05$ as determined by Student's *t* test.

checked daily and tumor size was measured three times a week along perpendicular axes using an external caliper. Tumor volume was calculated using the equation $\text{volume} = \frac{1}{2}(\text{length} \times \text{width}^2)$. To minimize suffering, animals were sacrificed when tumor size exceeded 1 cm^3 or after 8 weeks, whichever occurred first. Prior to sacrifice, animals were anesthetized with isoflurane and tumor mass was visualized and independently measured using a high-frequency ultrasound Vevo 2100 System (Fujifilm Visual Sonic, Canada) at 30 MHz. Isolated tumors were snap-frozen or fixed in formalin for subsequent analyses. For analysis of tumor growth in the peritoneal cavity, 3×10^6 control and *TUSC3*-altered cells in sterile DMEM were injected intraperitoneally into eighteen 8- to 10-week-old mice. Tumors were measured in regular intervals using a high-frequency ultrasound Vevo 2100 System in isoflurane anesthesia. Animals were sacrificed 4 weeks after tumor induction, dissected and analyzed semiquantitatively (number of “+” corresponds with tumor size or extent of metastasizing, n/a – animal excluded from the set).

Animal experiments were approved by the Ministry of Education, Youth, and Sport of the Czech Republic under project number MSMT-15876/2013-310; supervised by the local ethi-

cal committee of the Faculty of Medicine, Masaryk University; and performed by certified individuals (KK, FD, PV).

Immunohistochemistry

First, 5- μm -thick tissue sections were deparaffinized by heating at 60°C ; subsequently, they were rehydrated in xylene and decreasing concentrations of ethanol. Antigen retrieval was performed with Target Retrieval Solution, pH 9 (Dako, Germany) for 40 min at 98°C , followed by treatment with 0.3% H_2O_2 in $1 \times$ PBS (pH 7.4) to quench endogenous peroxidase activity. After blocking with 1% bovine serum albumin (BSA) for 10 min, sections were incubated in primary antibody (rabbit polyclonal to *TUSC3*, dilution 1:100, ab65213, Abcam, UK) for 1 hr at room temperature. Primary antibody dilutions were made in Antibody Diluent (Dako, Germany). The sections were washed three times in $1 \times$ PBS and incubated in biotinylated detection agent (LSAB + System HRP, Dako, Germany) for 30 min at room temperature, followed by 45-min incubation in StreptAB-Complex/HRP (K0377 Dako, Denmark). Sections were washed three times with $1 \times$ PBS and incubated in

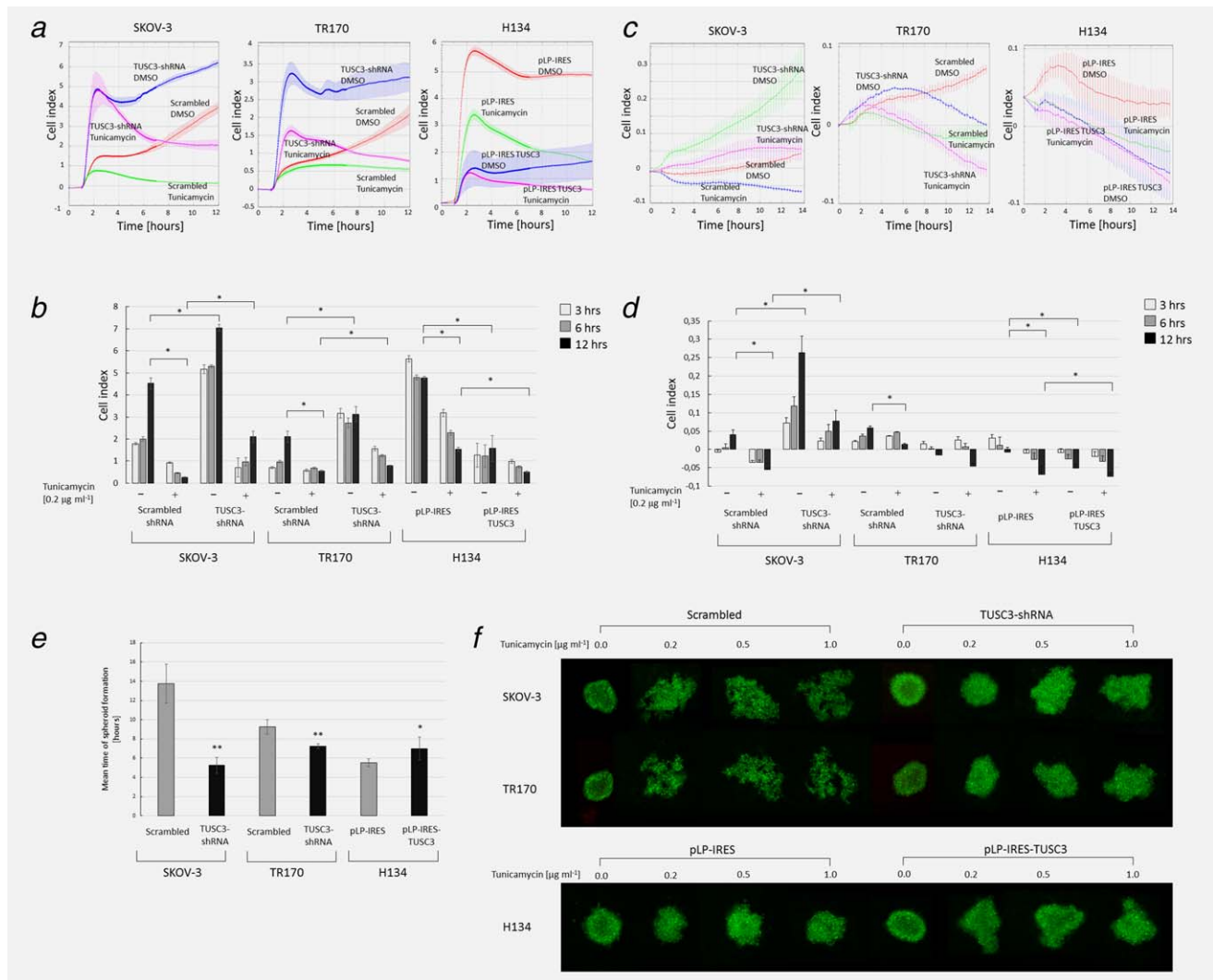


Figure 2. (a) Adhesion of ovarian cancer cells as a function of cell index over time as determined by the xCELLigence RTCA SP system. Cells were seeded on a fibronectin-coated Acea E-plate®96 and monitored every 1 min. for the first 6 hr post-seeding, then every 5 min for 18 hr, and finally every 15 min for a total of 120 hr. Plots represent the mean cell index \pm SD over the first 12 hr. (b) Plots of mean cell index \pm SD at 3, 6 and 12 hr. Asterisks indicate statistical significance at $p < 0.05$ as determined by Student's *t* test. (c) Migration of ovarian cancer cells as a function of cell index over time as determined by the xCELLigence RTCA SP system. The upper chamber of an uncoated Acea CIM-plate®16 was seeded with serum-starved cells containing 10% serum as an attractant. The cell index was recorded every 15 min for 56 hr. Plots represent mean cell index \pm SD over the first 12 hr. (d) Plots demonstrating mean cell index \pm SD at 3, 6 and 12 hr. Asterisks indicate statistical significance at $p < 0.05$ as determined by Student's *t* test. (e) Mean time \pm SD required for assembly of 3D spheroids from ovarian cancer cells expressing or not expressing *TUSC3* in low-adhesion conditions. Asterisks indicate statistical significance at $p < 0.05$ (*) or $p < 0.005$ (**) as determined by Student's *t* test. (f) Structure of 3D spheroids revealed by Hoechst staining and fluorescent microscopy.

Streptavidin-HRP (LSAB + System HRP, Dako, Germany) until a brown color developed. Sections were then counterstained with Gill's hematoxylin, dehydrated, and mounted using Pertex medium.

Immunofluorescent microscopy

Nearly 5×10^3 of cells were seeded into 24-well plate either in presence of tunicamycin ($0.2 \mu\text{g ml}^{-1}$) or DMSO and cultured for 24 hr. Then, cells were washed in $1 \times$ PBS, fixed in 4% formaldehyde for 15 min, washed three times in $1 \times$ PBS, permeabilized in 0.1% Triton-X100 in PBS for 10 min/RT,

blocked in 3% BSA in PBS for 1 hr. Then, cells were incubated with anti-vimentin primary antibody (Abcam, UK, Ab92547; 1:2000 in 3% BSA/PBS) for 2 hr at room temperature. The cells were then washed three times in $1 \times$ PBS and incubated for 1 hr with secondary antibody conjugated with AlexaFluor 455 (Life Technologies, Czech Republic, A21429, 1:2000 in 3% BSA/PBS) followed by additional wash in $1 \times$ PBS. Hoechst stain was added to the final concentration $5 \mu\text{g ml}^{-1}$. Images were acquired using an automated microscope equipped with an environmental chamber and $10 \times$ objective with (Image Xpress MicroXL, Molecular Devices, USA).

Results

Modeling TUSC3 loss *in vitro*

We investigated the role of *TUSC3* in ovarian cancer development using a panel of three established and previously characterized serous ovarian adenocarcinoma cell lines H134, SKOV-3 and TR170, selected to reflect the substantial intrinsic heterogeneity of high-grade serous ovarian cancer. These lines are tumorigenic in nude mice and differ in several aspects, including p53 status, karyotype, and resistance to chemotherapeutic agents.^{18–22} In SKOV-3 and TR170, *TUSC3* expression was dampened to roughly 30% that of the scrambled-shRNA control. The H134 cell line has virtually no basal *TUSC3* expression due to the hypermethylation of the entire 8p22 region,⁷ mimicking *in vitro* to some extent the epigenetic loss of *TUSC3* *in vivo* without the use of shRNA. To rescue *TUSC3* expression, H134 cells were stably transfected with *TUSC3* cDNA (Fig. 1a).

TUSC3-silenced cells are resistant to tunicamycin

TUSC3 is an ER integral protein involved in *N*-glycosylation by the OST complex. This fact prompted us to investigate whether the potential tumor-suppressive role of *TUSC3* is linked to its function in the ER. We exposed control and *TUSC3*-silenced cells to the *N*-glycosylation inhibitor tunicamycin and induced ER stress conditions *in vitro*. Cells were treated with three different concentrations of tunicamycin (0.2, 0.5 and 1 $\mu\text{g ml}^{-1}$) for 3, 24 or 48 hr, and overall metabolic activity was determined using the colorimetric MTT assay. In control cells, we observed both a dose- and time-dependent decrease in total cellular reductase activity. Interestingly, *TUSC3*-silenced SKOV-3 and TR170 cells did not respond to non-toxic doses tunicamycin with a drop in metabolic activity when compared to control cells (Fig. 1b). Differences diminished when the cells were exposed to high concentrations of tunicamycin or were treated for prolonged time, probably due to the cytotoxic effects of tunicamycin. Therefore, the determined minimal effective concentration of tunicamycin was used in following experiments. To determine if the difference in MTT conversion rate was caused by cell death, we treated cells with the minimal effective concentration of tunicamycin (0.2 $\mu\text{g ml}^{-1}$) for 24 hr, stained them with annexin V/PI, and performed the FACS analysis. However, we did not identify any significant changes in apoptotic or necrotic cell death rate (Supporting Information Fig. 2), confirming that effects induced by 0.2 $\mu\text{g ml}^{-1}$ tunicamycin are not associated with cytotoxicity.

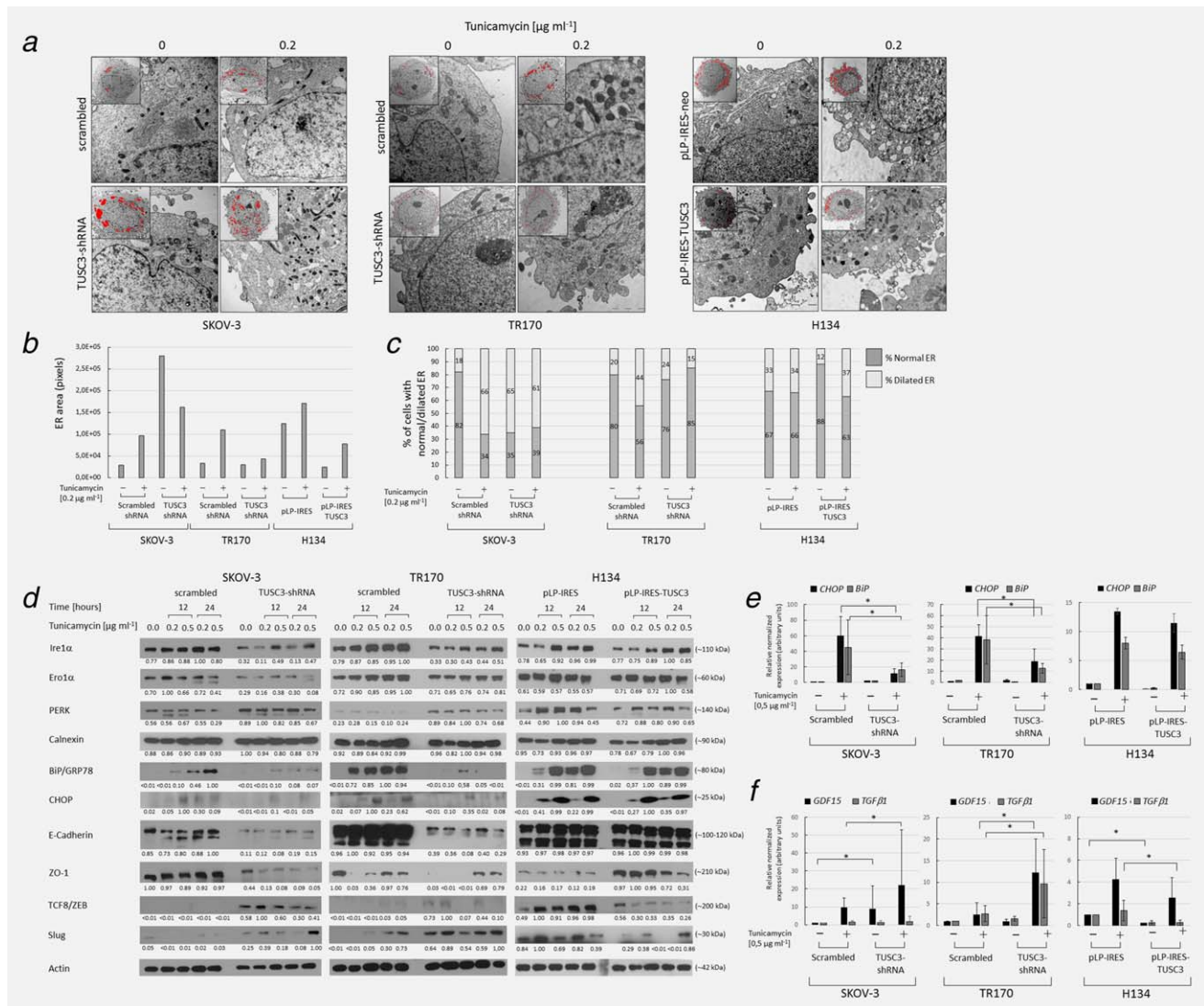
Silencing TUSC3 enhances cell adhesion and migration

Next, we quantified the effects of *TUSC3* loss on cell proliferation, adhesion, and migration. To measure cellular processes in real-time, we employed the impedance-based, label-free xCELLigence (RTCA) system. First, we monitored simple adhesion to a fibronectin-coated E-plate of either tunicamycin (0.2 $\mu\text{g ml}^{-1}$) or DMSO-pretreated cells in medium containing

either tunicamycin (0.2 $\mu\text{g ml}^{-1}$) or DMSO, recording the cell index for 12 hr. Tunicamycin clearly interfered with the adhesion capability of control cells, substantially reducing the cell index. By contrast, *TUSC3*-silenced cells showed an increase in cell index over the same interval when compared to control cells. Therefore, even in the presence of tunicamycin, cells lacking *TUSC3* were capable of adhering efficiently (Figs. 2ab). During further cultivation (up to 120 hr), tunicamycin-treated samples reduced the cell index irrespective of *TUSC3* expression, and we also did not identify any significant growth advantage of *TUSC3*-silenced cells over controls (Supporting Information Fig. 3a). To analyze the migration rate, we seeded the upper chamber of an uncoated 16-well CIM plate with pre-treated cells in serum-free medium and recorded the cell index of penetrating cells for 12 hr. SKOV-3 and H134 cells with attenuated *TUSC3* expression, but not TR170 cells, migrated at a significantly higher rate than *TUSC3*-expressing variants (Figs. 2cd). Tunicamycin clearly interfered with the migration capacity of all cells; however, *TUSC3*-silenced cells migrated more efficiently than the respective controls. During prolonged culture (up to 56 hr), differences between controls and *TUSC3*-manipulated cells diminished (Supporting Information Fig. 3b).

TUSC3 loss augments formation of 3D spheroids

Ovarian cancer cells typically delaminate from the primary tumor site and spread throughout the peritoneal cavity in the form of multicellular aggregates, adhering to the mesothelium and extracellular matrix (ECM).²³ To gain further insight into the role of *TUSC3* in the dissemination of ovarian cancer, we generated three-dimensional (3D) spheroids from control and *TUSC3*-manipulated ovarian cancer cells. All three ovarian cell lines were capable of spheroid formation within 24 hr under low-adhesion conditions. Using time-lapse microscopy, we monitored the first 24 hr of culture in 30-min intervals. *TUSC3*-expressing cells assembled into compact clusters within 8–10 hr. Interestingly, *TUSC3*-silenced cells assembled into 3D aggregates in a significantly shorter time than controls (Fig. 2e); however, no significant difference in spheroid size was observed (Supporting Information Fig. 4a). Next, we were curious if induction of ER stress would affect formation of 3D spheroids. Ovarian cancer cells were treated with three different concentrations of tunicamycin (0.2, 0.5 and 1.0 $\mu\text{g ml}^{-1}$) and monitored using time-lapse microscopy. Surprisingly, tunicamycin treatment resulted in massive disintegration of spheroids derived from cells that physiologically or ectopically expressed *TUSC3* protein; this was not observed in spheroids generated from cells lacking *TUSC3* (Fig. 1f). Data obtained from visual analysis were confirmed by automated image analysis that determined spheroid shape (Supporting Information Fig. 4b). To determine whether *TUSC3*-expressing spheroids were more sensitive to cell death, we counterstained cell nuclei with propidium iodide. All spheroids displayed a percentage of propidium iodide-positive nuclei that increased with tunicamycin treatment, but we did not observe any significant



difference in cell death rate between *TUSC3*-silenced cells and their controls (Supporting Information Figs. 4c and 4d). In summary, downregulation of *TUSC3* enhanced the formation of 3D spheroids and also attenuated the effect of tunicamycin treatment without directly effecting cell viability.

Loss of *TUSC3* induces morphological alterations in the ER and alters expression of ER stress markers

N-glycosylation of proteins in the ER is a complex process tightly linked to the proper folding of nascent peptides and

quality control and shuttling.²⁴ Improper function of the ER glycosylation machinery or extrinsic environmental cues may induce alterations in ER structure and function, termed ER stress. Response to ER stress involves a number of complex signaling pathways that alter cell phenotype.²⁵

We asked whether *TUSC3* loss is linked to alterations in ER architecture that can be visualized using TEM. Processing cultured cells for TEM requires detaching them from plastic and embedding a cell suspension in solid resin; direct analysis of adherent cells typically does not provide a sufficient number in

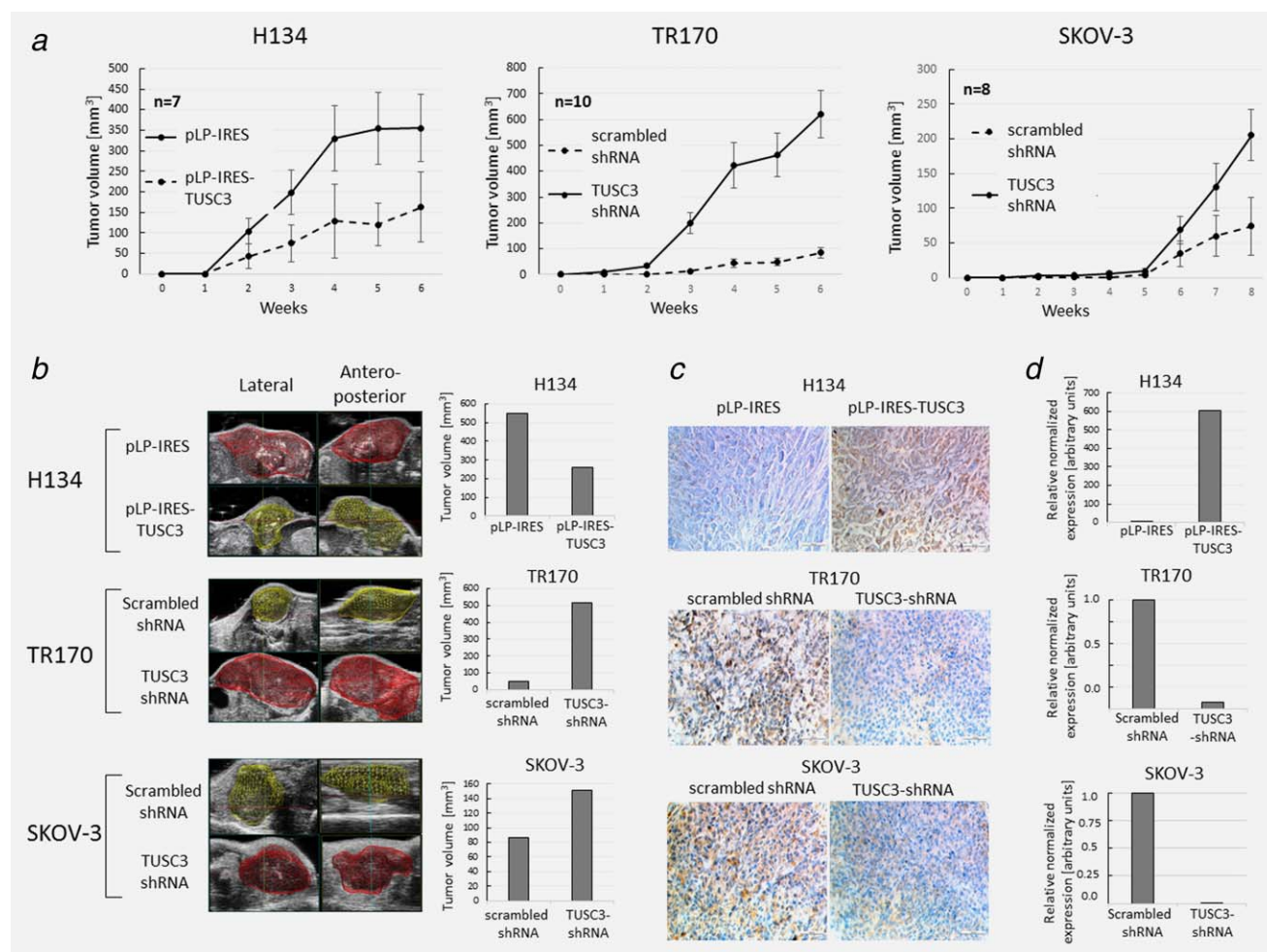


Figure 4. (a) First, thirty 8- to 10-week-old mice were subcutaneously injected with 5×10^6 control or *TUSC3*-altered cells in sterile $1 \times$ PBS in the left and right ventral flanks, respectively. Animals were checked daily, and tumor size was measured three times a week along two perpendicular axes using an external caliper. Tumor volume was calculated using the formula $\text{volume} = \frac{1}{2}(\text{length} \times \text{width}^2)$. Plots represent mean tumor volume \pm SEM. (b) Representative images of tumor masses visualized and independently measured using the high-frequency ultrasound Vevo 2100 System (Fujifilm Visual Sonic) at 30 MHz. The tumor volume (μm^3) of representative images is provided. (c) Immunohistochemical analysis of dissected tumors visualized in (b) documenting expression of *TUSC3* in formalin-fixed, paraffin-embedded tissue sections. (d) Expression of *TUSC3* transcript in dissected tumor samples visualized in (b). Tumors were snap frozen, then total RNA was extracted, reverse transcribed, and analyzed using qRT-PCR.

any one plane of the section. To check whether undesirable changes in cell cytoarchitecture were induced by the enzymatic detachment of cells, we first prepared TEM samples from both trypsinized cells and cells adherent to culture plastic. We did not identify any pathological changes in the nuclei, mitochondria or membrane compartments of detached cells compared to cells adherent to the culture substrate (data not shown). Next, we treated SKOV-3, TR170 and H134 cells with $0.2 \mu\text{g ml}^{-1}$ tunicamycin for 24 hr and analyzed cell ultrastructure. In scrambled-control/DMSO-treated SKOV-3 and TR170 cells, the rough ER formed thin, regularly arranged cisternae with attached ribosomes. Treatment with tunicamycin induced vast dilation of the rough ER and detachment of ribosomes, though other organelles, *e.g.*, mitochondria, were unaffected. Interestingly, in *TUSC3*-silenced SKOV-3 and H134 cells, similar ER abnormalities were observed even without tunicamycin treat-

ment (Fig. 3a), suggesting loss of *TUSC3* can destabilize the rough ER system and induce inflation of the cisternae system. Importantly, overexpression of *TUSC3* in H134 cells restored ER morphology and partially prevented the disruptive effects of tunicamycin (Figs. 3bc).

Next we investigated whether altered ER ultrastructure was associated with activation of the ER stress response. We treated monolayers of SKOV-3, TR170 and H134 cells with 0.2 and $0.5 \mu\text{g ml}^{-1}$ tunicamycin for 12 and 24 hr, and then determined expression of ER stress markers *via* immunoblotting. Under optimal conditions, all cell lines expressed virtually no levels of the major effectors of the adaptive or apoptotic pathways, BiP and CHOP. Upon tunicamycin treatment, however, expression of BiP and CHOP was upregulated in all control cells. Surprisingly, *TUSC3*-silenced SKOV-3 and TR170 cells failed to respond with CHOP and BiP upregulation to

the same extent as control cells (Figs. 3*df*). In H134 cells, induction of BiP and CHOP expression followed tunicamycin treatment irrespective of *TUSC3* expression. Three upstream sensors of ER homeostasis, Ire1 α , Ero1 α and PERK, but not calnexin, were upregulated in response to tunicamycin treatment. In *TUSC3*-silenced TR170 and SKOV-3 cells, the levels of Ire1 α and Ero1 α were markedly reduced, while PERK levels were increased (Fig. 3*d*). Taken together, the data indicate that loss of *TUSC3* alters ER stress response signaling, affecting BiP and CHOP-mediated pathways.

Silencing of TUSC3 decreases expression of E-cadherin and ZO-1

Alterations in cell phenotype induced by loss of *TUSC3* prompted us to investigate expression of markers associated with the EMT. We treated cells with 0.2 or 0.5 $\mu\text{g ml}^{-1}$ tunicamycin for 12 or 24 hr, as described above, and determined induction of markers associated with epithelial and mesenchymal cell types. Downregulation of *TUSC3*, either alone or in combination with tunicamycin, led to a significant decrease in levels of E-Cadherin and tight junction protein 1 (ZO-1). A decrease in cell junction molecules was accompanied by upregulation of the mesenchymal transcription factors Slug and TCF8/ZEB1. Interestingly, the effect of *TUSC3* on the expression of ZO-1 and Slug was enhanced by tunicamycin, suggesting a combined effect of down-regulated *TUSC3* and ER stress induction (Fig. 3*d*).

Next, we determined by immunoblotting and immunofluorescence microscopy the expression of the intermediate filament protein vimentin, associated with the mesenchymal phenotype. However, we did not observe any significant change in vimentin expression or distribution in cytoplasm under these conditions (Supporting Information Fig. 5). In conclusion, our data documents that *TUSC3* silencing is associated with loss of epithelial characteristics of ovarian cancer cells.

Cells lacking TUSC3 enhance expression of GDF15 and TGF β 1

The ER stress response is associated with altered expression of various secreted molecules, including cytokines and immunomodulators.²⁶ We examined expression of the cytokines *TGF β 1* and *GDF15* using qRT-PCR. All tunicamycin-treated cells exhibited enhanced expression of *GDF15*, suggesting activation of a general cellular stress state. Interestingly, we found significantly elevated levels of *GDF15* in *TUSC3*-silenced cells irrespective of tunicamycin treatment. Moreover, the loss of *TUSC3* enhanced expression of *TGF β 1* upon induction of ER stress in *TUSC3*-silenced TR170 cells (Fig. 1*f*). Thus, we documented that loss of *TUSC3* induces complex cellular alterations contributing to the malignant phenotype *in vitro*.

Loss of TUSC3 promotes tumor growth in immunocompromised mice

To confirm whether our *in vitro* data were also relevant *in vivo*, we performed a xenograft growth assay. Ovarian cancer cell lines with altered *TUSC3* expression and their controls

were subcutaneously injected into the contralateral flanks of immunocompromised NSG mice, followed by regular evaluation of the growth of xenografted tumor tissue. The latency period differed between the H134, SKOV-3 and TR170 cell lines, but tumors from cells with attenuated *TUSC3* expression developed earlier and formed significantly larger masses (Fig. 4*a*). Calculation of tumor mass based on external caliper measurements was *ex post* confirmed by ultrasound measurement and *in vivo* 3D visualization of representative animals (Fig. 4*b*). After sacrifice, expression of *TUSC3* was quantified in formalin-fixed and snap frozen mouse tumors *via* immunohistochemistry and qRT-PCR, respectively (Figs. 4*cd*).

Ovarian cancer, however, disseminates preferentially into peritoneal cavity. To assess the tumor growth in clinically relevant locations, we injected ovarian cancer cell lines with altered *TUSC3* expression and their respective controls intraperitoneally and monitored the tumor growth by ultrasound measurements for 4 weeks. Tumor mass and dissemination were then assessed by dissection semiquantitatively. All animals developed tumors rapidly with frequent ascites. In concordance with subcutaneous xenografts, all three cell lines with silenced *TUSC3* induced earlier formation of tumors and larger tumor mass. Interestingly, in case of SKOV-3 and H134 cells with silenced *TUSC3*, the tumor growth was followed by massive invasion to peritoneal cavity when compared to control cells (Supporting Information Fig. 5). In conclusion, we experimentally confirmed the status of *TUSC3* as a tumor suppressor in ovarian cancer *in vivo*.

Discussion

Great effort has been dedicated in recent decades to identifying the most important genetic drivers of high-grade serous epithelial ovarian cancer.²⁷ A majority of the known oncogenes and tumor suppressors are regulators of fundamental biological events, such as the cell cycle and DNA repair (AURKA, TP53, BRCA, cyclin E1), mitogenic outside-in signaling (HER2, FGF1, PTEN, AKT, KRAS), the immune response (IL-10), angiogenesis (VEGF) or mutual interactions within the tumor microenvironment.^{28–30} Systematic screening has also revealed genes linked to malignancy without any clear contribution to the cancer phenotype.

TUSC3 was identified as a putative tumor suppressor by systematic cloning analysis of the 8p22 chromosomal region, which is frequently lost in many epithelial cancers, including ovarian.² Loss of expression by hypermethylation of *TUSC3* promoter is associated with poor clinical outcomes in ovarian cancer patients⁷ and our previous data have demonstrated that loss of *TUSC3* contributes to the development of prostate cancer mouse xenografts.⁹ The sequence of *TUSC3* shows high homology to the yeast Ost3p protein, which constitutes one of the subunits of the OST complex that catalyzes N-glycosylation of newly synthesized proteins in the ER,⁸ and our previous work has localized *TUSC3* to the OST complex in the ER of ovarian cancer cells.¹⁰ A detailed structural analysis of interactions between *TUSC3* and defined peptide

substrates at atomic level by Mohorko *et al.*³¹ that was published recently, suggested a role of TUSC3 in selective glycosylation of target proteins potentially involved in diverse TUSC3-associated phenotypes.^{32,33} It is well established that N-glycosylation of proteins is associated with cancer development and progression,³⁴ but the intrinsic molecular mechanisms that result in altered glycosylation profiles and clinically relevant phenotypes, including the role of TUSC3, remain unclear.

Perturbations in protein folding and biochemical modifications of the ER lead to activation of an adaptive mechanism termed the unfolded protein response (UPR). The accumulation of misfolded proteins changes the activity and localization of molecular chaperones, triggering a signaling network that activates the adaptive or apoptotic signaling pathways. The adaptive response mediated by PERK attenuates the expression of general translation factors (*e.g.*, eIF2 α) and induces expression of molecular chaperones such as BiP (GRP78/HSPA5). The proapoptotic branch is primarily activated *via* IRE1 α /JNK kinases in response to permanent and irreversible ER stress and involves the UPR effector CHOP (DDIT3). The mechanism for ER stress induction and the UPR has been described in detail elsewhere.^{35–38} We found PERK kinase levels were constitutively elevated and IRE1 α was downregulated in TUSC3-silenced cells, even in the absence of tunicamycin treatment, suggesting the permanent state of ER-stress. After tunicamycin treatment, levels of the chaperones CHOP and BiP were massively upregulated in control cells only. We suggest that cells lacking TUSC3 alleviate the massive ER stress response *via* the PERK-mediated adaptive pathway rather than by initiating programmed cell death. Downregulation of BiP and CHOP was observed previously in TUSC3-silenced prostate cancer cell lines with inhibited N-glycosylation.⁹ In these scenarios, cancer cells can probably alleviate ER-stress by alternative pathways, such as translation inhibition or autophagy, generally contributing to malignant phenotype.^{39–41} In a tissue microenvironment, various extrinsic signals, including the level of oxygen saturation and the generation of reactive oxygen species (ROS), inflammatory or mitogenic cues, and lipid metabolism, combine with intrinsic signals from the proteosynthetic and cell cycle machinery on the ER to modulate a cell's response to the microenvironment.⁴² In a tumor microenvironment, which is far from being normal tissue in many respects, including hypoxia signaling, extracellular matrix or intercellular signaling,⁴³ and chemotherapy exposure,^{44,45} the integrated response of ER-distabilized cancer cells can result either in enhanced malignity or represent a target for therapy in resistant tumors.^{46,47}

Activation of the ER stress response effectors BiP and Xbp-1 was recently shown to be associated with a shift of epithelial alveolar cancer cells toward a more invasive mesenchymal phenotype, including deregulation of ZO-1 and E-Cadherins.⁴⁸ Similar observations have been reported by Zhao *et al.* for a model of non-cancerous pulmonary fibrosis, in which bleomycin-induced ER stress evoked hallmarks of the EMT in lung alveolar cells.⁴⁹ In thyroid cell line PCCL3, perturbation of ER homeostasis leads to upregulation of ER stress markers and

substantial changes in cell phenotype, toward dedifferentiation and the EMT.⁵⁰ Interestingly, activation of the PERK-eIF2 α signaling pathway has been reported in cells undergoing the EMT, suggesting the existence of mutual signaling and functional feedbacks between the EMT phenotype and cellular responses to ER stress.⁵¹ In our model, TUSC3-silenced cells showed decreased expression of E-Cadherin and ZO-1 and upregulation of the EMT-associated transcription factors Slug and TCF8/ZEB. When we overexpressed TUSC3 in H134 cells, levels of ZO-1 and E-Cadherin increased markedly and Slug and TCF8/ZEB protein levels were attenuated. Of particular importance, these effects were augmented by the ER stress inductor tunicamycin. Our previous *in vitro* studies have also documented that prostate and ovarian cancer cells lacking TUSC3 and stressed by serum starvation are capable of effective migration in wound-healing assays driven by the Akt signaling pathway.^{9,10}

The EMT phenotype is also associated with the formation of multicellular spheroids. Recently, Pease *et al.*⁵² reported spontaneous formation of 3D aggregates budding from monolayers of ovarian cancer cells. Interestingly, these buds lacked cortical E-Cadherin, could effectively detach from the monolayer, and survived even in the presence of commonly used cytotoxic drugs. To form secondary tumors, cancer cells must retain the capability to adhere to the ECM in the peritoneal cavity, usually *via* the integrin family of proteins.⁵³ In our model, TUSC3 loss enhanced formation of 3D spheroids in low-adhesion conditions and provided resistance to tunicamycin treatment, while cells retained the ability to bind to fibronectin-coated surfaces. In addition, downregulation of TUSC3 induced expression of the mRNA of *GDF15* and *TGF β 1* cytokines, suggesting possible paracrine modulation of complex interactions within the tumor microenvironment.

In light of these findings, we conclude that the cumulative effect of (i) TUSC3 silencing and (ii) extrinsic microenvironment cues that trigger the ER stress response significantly contributes to the phenotypic changes involved in the EMT and tumor dissemination observed in ovarian cancer cells. Consistent with our *in vitro* results, xenograft experiments confirmed the tumor-suppressive character of TUSC3 *in vivo*. Despite the intrinsic heterogeneity of cell lines used, the loss of TUSC3 resulted in earlier tumor development and larger tumor masses. In summary, we experimentally proved the tumor-suppressive function of TUSC3 in ovarian cancer and demonstrated for the first time that TUSC3 might link distinct biological mechanisms regulating the ER stress response and the EMT *in vitro*, and promoting tumor growth *in vivo*.

Acknowledgments

The authors thank prof. Thomas Grunt for the kind provision of the TR170 and H134 cell lines, Ms. Dobromila Klemová and Mr. Ladislav Ilkovic for their excellent preparation of TEM samples and TEM technical support, Ms. Dana Strítecká for preparation of FFPE samples, Pavel Matula Ph.D. for image analysis of the TEM samples, Miroslava Sedláčková, M.D. and Lenka Krejčířová, M.D. for independently evaluating the TEM samples, Eva Slabáková, Ph.D. for help with the RTCA setup and Sabina Ševčířková, Ph.D. for critical reading of the manuscript.

References

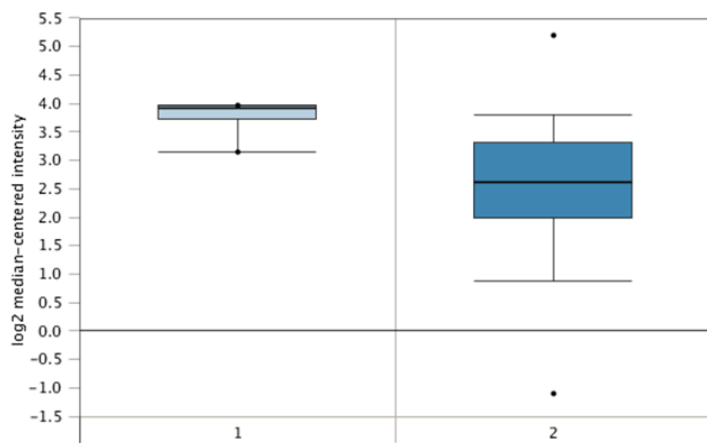
1. Siegel R, Naishadham D, Jemal A. Cancer statistics, 2013. *CA Cancer J Clin* 2013;63:11–30.
2. Pils D, Horak P, Gleiss A, et al. Five genes from chromosomal band 8p22 are significantly down-regulated in ovarian carcinoma—N33 and EFA6R have a potential impact on overall survival. *Cancer* 2005;104:2417–29.
3. Pribill I, Speiser P, Leary J, et al. High frequency of allelic imbalance at regions of chromosome arm 8p in ovarian carcinoma. *Cancer Genet Cytogen* 2001;129:23–9.
4. Ribeiro I, Marques F, Caramelo F, et al. Genetic gains and losses in oral squamous cell carcinoma: impact on clinical management. *Cell Oncol* 2014; 37:29–39.
5. Voegtly LM, Mamula K, Campbell JL, et al. Molecular alterations associated with breast cancer mortality. *PLoS One* 2012;10:e46814.
6. Wiklund F, Jonsson BA, Goransson I, et al. Linkage analysis of prostate cancer susceptibility: confirmation of linkage at 8p22-23. *Hum Genet* 2003;112:414–8.
7. Pils D, Horak P, Vanhara P, et al. Methylation status of TUSC3 is a prognostic factor in ovarian cancer. *Cancer* 2013;119:946–54.
8. Mohorko E, Glockshuber R, Aebi M. Oligosaccharyltransferase: the central enzyme of N-linked protein glycosylation. *J Inher Metab Dis* 2011; 34:869–78.
9. Horak P, Tomasich E, Vanhara P, et al. TUSC3 loss alters the ER stress response and accelerates prostate cancer growth in vivo. *Sci Rep* 2014;4:3739.
10. Vanhara P, Horak P, Pils D, et al. Loss of the oligosaccharyl transferase subunit TUSC3 promotes proliferation and migration of ovarian cancer cells. *Int J Oncol* 2013;42:1383–9.
11. Uphoff CC, Drexler HG. Detection of mycoplasma in leukemia-lymphoma cell lines using polymerase chain reaction. *Leukemia* 2002;16: 289–93.
12. Uphoff CC, Drexler HG. Comparative antibiotic eradication of mycoplasma infections from continuous cell lines. *In Vitro Cell Dev-An* 2002;38:86–9.
13. Starsichova A, Kubala L, Lincova E, et al. Dynamic monitoring of cellular remodeling induced by the transforming growth Factor-beta 1. *Biol Proced Online* 2009;11:316–24.
14. Vistejnova L, Dvorakova J, Hasova M, et al. The comparison of impedance-based method of cell proliferation monitoring with commonly used metabolic-based techniques. *Neuroendocrinol Lett* 2009;30:121–7.
15. Schneider CA, Rasband WS, Eliceiri KW. NIH image to ImageJ: 25 years of image analysis. *Nat Methods* 2012;9:671–5.
16. Pfaffl MW. A new mathematical model for relative quantification in real-time RT-PCR. *Nucleic Acids Res* 2001;29:e45.
17. Laemmli UK. Cleavage of structural proteins during the assembly of the head of bacteriophage T4. *Nature* 1970;227:680–5.
18. De Feudis P, Debernardis D, Beccaglia P, et al. DDP-induced cytotoxicity is not influenced by p53 in nine human ovarian cancer cell lines with different p53 status. *Br J Cancer* 1997;76:474–9.
19. Debernardis D, Sire EG, De Feudis P, et al. p53 status does not affect sensitivity of human ovarian cancer cell lines to paclitaxel. *Cancer Res* 1997;57:870–4.
20. Hill BT, Shellard SA, Hosking LK, et al. Characterization of a Cisplatin-resistant human Ovarian-carcinoma Cell-line expressing Cross-resistance to 5-fluorouracil but collateral sensitivity to methotrexate. *Cancer Res* 1992;52:3110–8.
21. Hill BT, Whelan RD, Gibby EM, et al. Establishment and characterization of three new human ovarian carcinoma cell lines and initial evaluation of their potential in experimental chemotherapy studies. *Int J Cancer J Int Cancer* 1987;39:219–25.
22. Vakifahmetoglu H, Olsson M, Tamm C, et al. DNA damage induces two distinct modes of cell death in ovarian carcinomas. *Cell Death Differ* 2008;15:555–66.
23. Burleson KM, Casey RC, Skubitz KM, et al. Ovarian carcinoma ascites spheroids adhere to extracellular matrix components and mesothelial cell monolayers. *Gynecol Oncol* 2004;93:170–81.
24. Aebi M. Nlinked protein glycosylation in the ER. *Bba-Mol Cell Res* 2013;1833:2430–7.
25. Gardner BM, Pincus D, Gotthardt K, et al. Endoplasmic reticulum stress sensing in the unfolded protein response. *Cold Spring Harb Perspect Biol* 2013;3:a013169.
26. Claudio N, Dalet A, Gatti E, et al. Mapping the crossroads of immune activation and cellular stress response pathways. *EMBO J* 2013;32:1214–24.
27. TCGA Research Network. Integrated genomic analyses of ovarian carcinoma. *Nature* 2011;474:609–15.
28. Gevaert O, Villalobos V, Sikic BI, et al. Identification of ovarian cancer driver genes by using module network integration of multi-omics data. *Interface Focus* 2013;4:20130013.
29. Kalamathan S, Bates V, Lord R, et al. The mutational profile of sporadic epithelial ovarian carcinoma. *Anticancer Res* 2011;31:2661–8.
30. Lavoue V, Theirez A, Leveque J, et al. Immunity of human epithelial ovarian carcinoma: the paradigm of immune suppression in cancer. *J Transl Med* 2013;11:147–58.
31. Mohorko E, Owen RL, Malojcic G, et al. Structural basis of substrate specificity of human oligosaccharyl transferase subunit N33/Tusc3 and its role in regulating protein N-glycosylation. *Structure* 2014;22:590–601.
32. Garshabi M, Hadavi V, Habibi H, et al. A defect in the TUSC3 gene is associated with autosomal recessive mental retardation. *Am J Hum Genet* 2008;82:1158–64.
33. Zhou H, Clapham DE. Mammalian MagT1 and TUSC3 are required for cellular magnesium uptake and vertebrate embryonic development. *Proc Natl Acad Sci USA* 2009;106:15750–5.
34. Hauselmann I, Borsig L. Altered tumor-cell glycosylation promotes metastasis. *Front Oncol* 2014;4:28.
35. Hetz C. The unfolded protein response: controlling cell fate decisions under ER stress and beyond. *Nat Rev Mol Cell Biol* 2012;13:89–102.
36. Hetz C, Chevet E, Harding HP. Targeting the unfolded protein response in disease. *Nat Rev Drug Discov* 2013;12:703–19.
37. Chen Y, Brandizzi F. IRE1: ER stress sensor and cell fate executor. *Trends Cell Biol* 2013;23:547–55.
38. Ozcan L, Tabas I. Role of endoplasmic reticulum stress in metabolic disease and other disorders. *Annu Rev Med* 2012;63:317–28.
39. Moon SY, Kim HS, Nho KW, et al. Endoplasmic reticulum stress induces epithelial-mesenchymal transition through autophagy via activation of c-src kinase. *Nephron Exp Nephrol* 2014;126:127–40.
40. Penas C, Font-Nieves M, Fores J, et al. Autophagy, and BiP level decrease are early key events in retrograde degeneration of motoneurons. *Cell Death Differ* 2011;18:1617–27.
41. Yang ZNJ, Chee CE, Huang SB, et al. The role of autophagy in cancer: therapeutic implications. *Mol Cancer Ther* 2011;10:1533–41.
42. Ackerman D, Simon MC. Hypoxia, lipids, and cancer: surviving the harsh tumor microenvironment. *Trends Cell Biol* 2014;24:472–8.
43. Davidson B, Trope C, Reich R. The role of the tumor stroma in ovarian cancer. *Front Oncol* 2014;4:1–11.
44. Li W, Wang W, Dong H, et al. Cisplatin-induced senescence in ovarian cancer cells is mediated by GRP78. *Oncol Rep* 2014;31:2525–34.
45. Zhang LC, Wang JR, Zhao L, et al. GRP78 upregulation-induced increase in cisplatin sensitivity of SPCA1 lung cancer cells. *Chin Med J Peking* 2011;124:3341–6.
46. Cha W, Park SW, Kwon TK, et al. Endoplasmic reticulum stress response as a possible mechanism of Cyclooxygenase-2-independent anticancer effect of celecoxib. *Anticancer Res* 2014;34:1731–5.
47. Wang J, Yin YC, Hua H, et al. Blockade of GRP78 sensitizes breast cancer cells to microtubules-interfering agents that induce the unfolded protein response. *J Cell Mol Med* 2009; 13:3888–97.
48. Zhong Q, Zhou BY, Ann DK, et al. Role of endoplasmic reticulum stress in epithelial-mesenchymal transition of alveolar epithelial cells. *Am J Resp Cell Mol* 2011;45:498–509.
49. Zhao H, Wu QQ, Cao LF, et al. Melatonin inhibits endoplasmic reticulum stress and epithelial-mesenchymal transition during Bleomycin-induced pulmonary fibrosis in mice. *PLoS One* 2014;5:e97266.
50. Ulianich L, Garbi C, Treglia AS, et al. ER stress is associated with dedifferentiation and an epithelial-to-mesenchymal transition-like phenotype in PCCl3 thyroid cells. *J Cell Sci* 2008;121: 477–86.
51. Feng YX, Sokol ES, Del Vecchio CA, et al. Epithelial-to-mesenchymal transition activates PERK-eIF2alpha and sensitizes cells to endoplasmic reticulum stress. *Cancer Discov* 2014;4:702–15.
52. Pease JC, Brewer M, Tirnauer JS. Spontaneous spheroid budding from monolayers: a potential contribution to ovarian cancer dissemination. *Biol Open* 2012;1:622–8.
53. Mikula-Pietrasik J, Sosinska P, Ksiązek K. Resveratrol inhibits ovarian cancer cell adhesion to peritoneal mesothelium in vitro by modulating the production of alpha5beta1 integrins and hyaluronic acid. *Gynecol Oncol* 2014;134:624–30.



TUSC3 Expression in TCGA Ovarian
Ovarian Serous Cystadenocarcinoma vs. Normal

TCGA Ovarian Statistics

Under-expression Gene Rank: 143 (in top 2%)
Reporter: 209228_x_at
P-value: 1.72E-7
t-Test: -11.331
Fold Change: -2.446

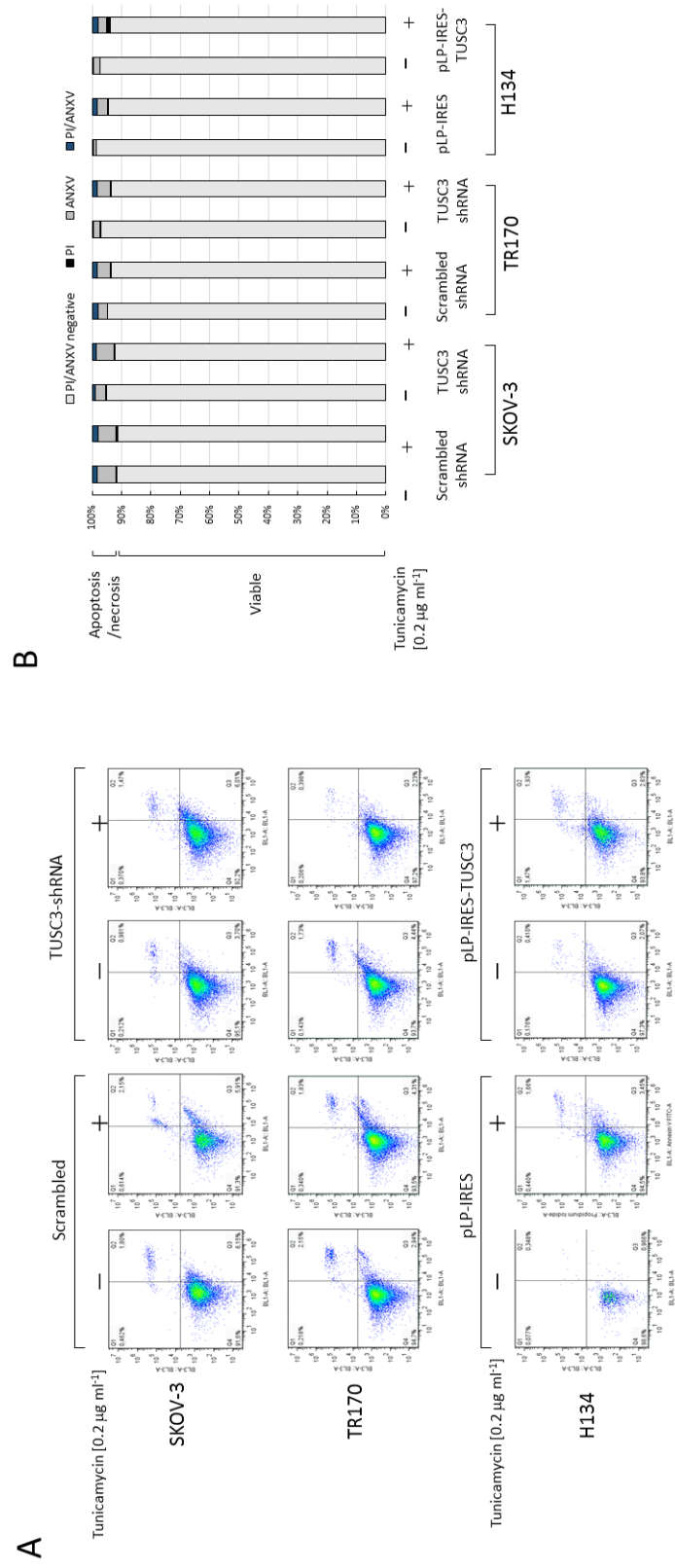


Legend

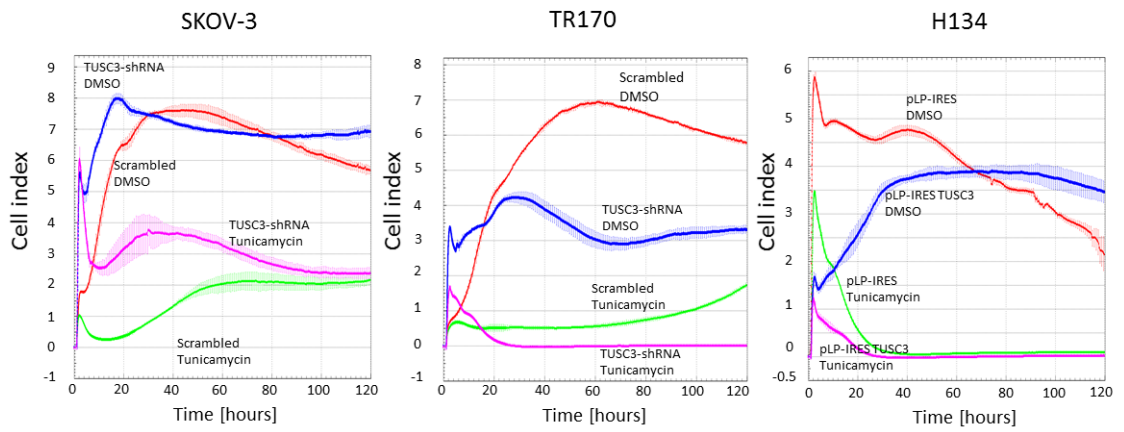
- 1. Ovary (8)
- 2. Ovarian Serous Cystadenocarcinoma (586)

TCGA Ovarian

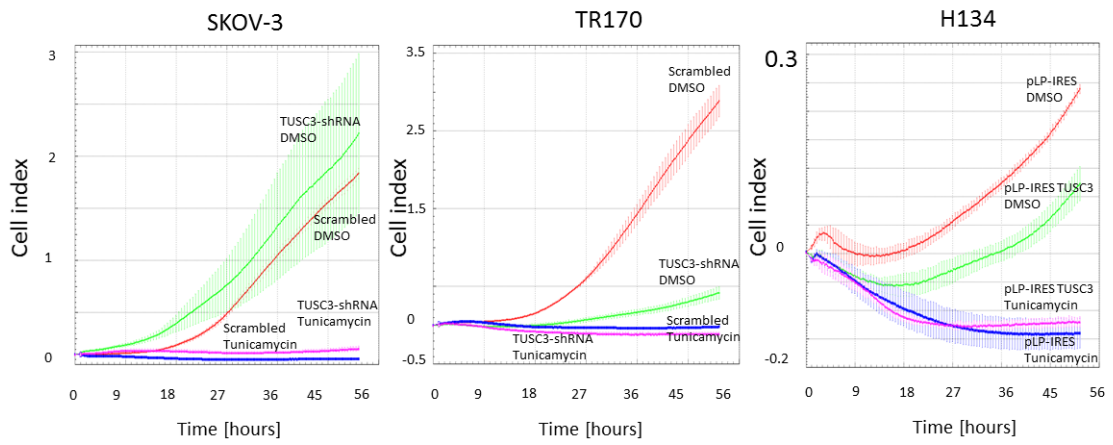
No Associated Paper 2013/06/03 594 samples [TUSC3 Information](#)
mRNA 12,624 measured genes [Reporter Information](#)
Human Genome U133A Array

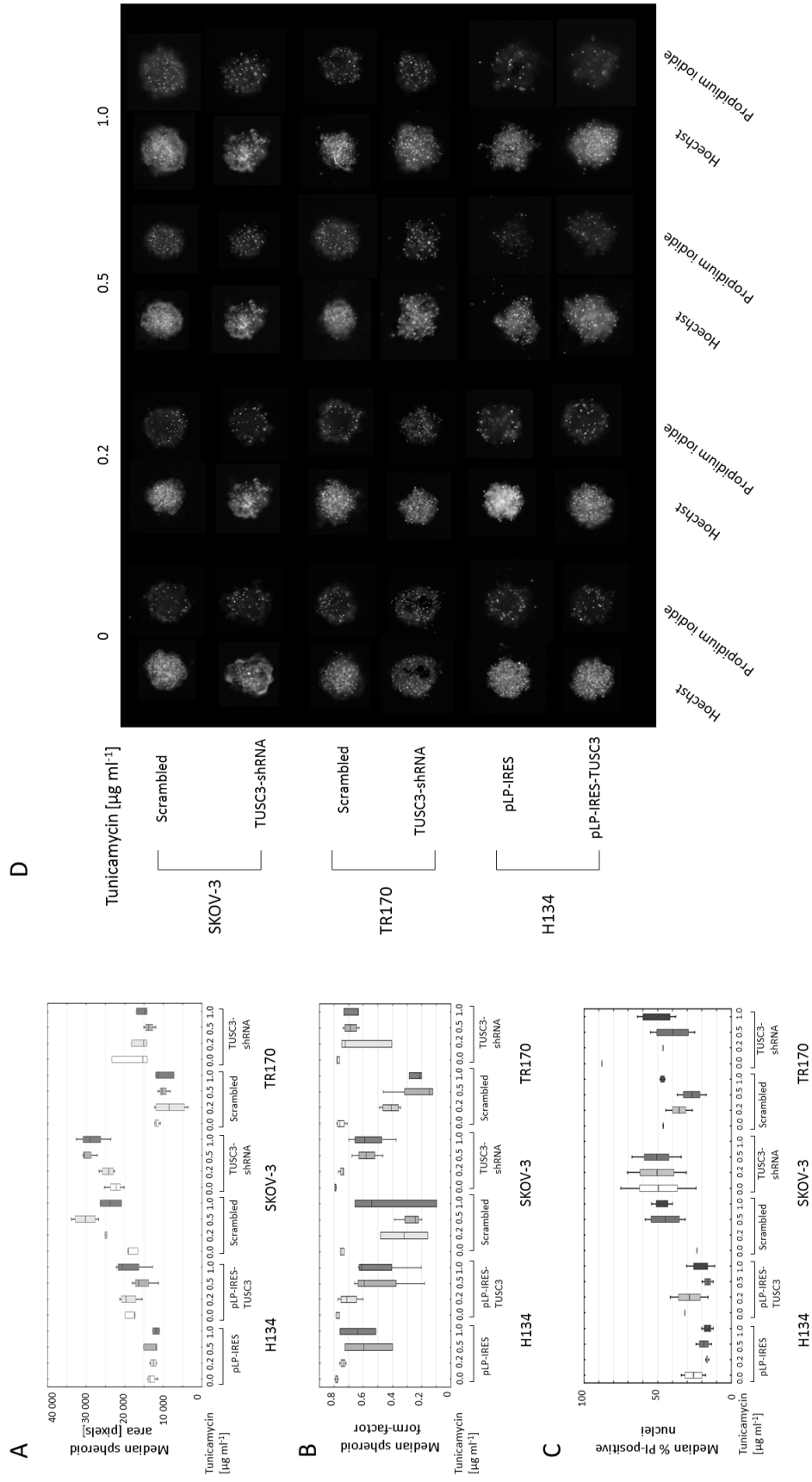


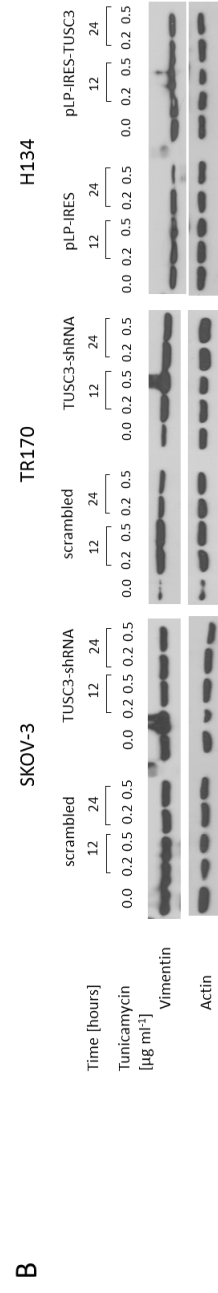
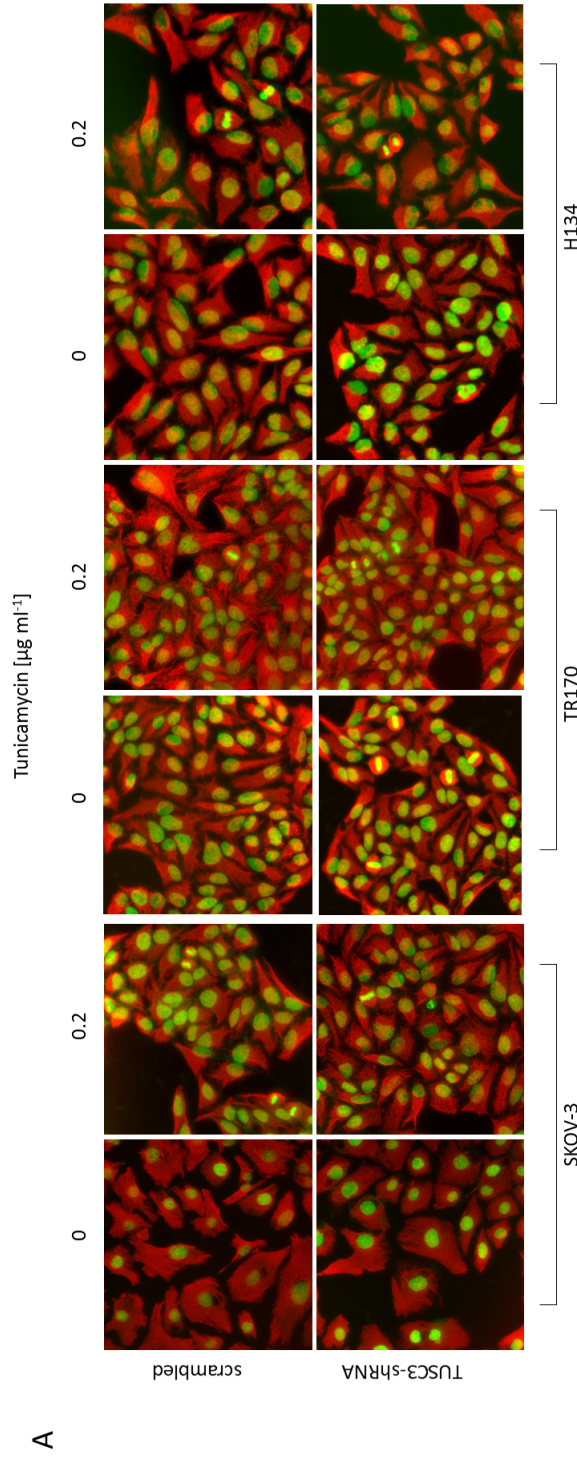
A



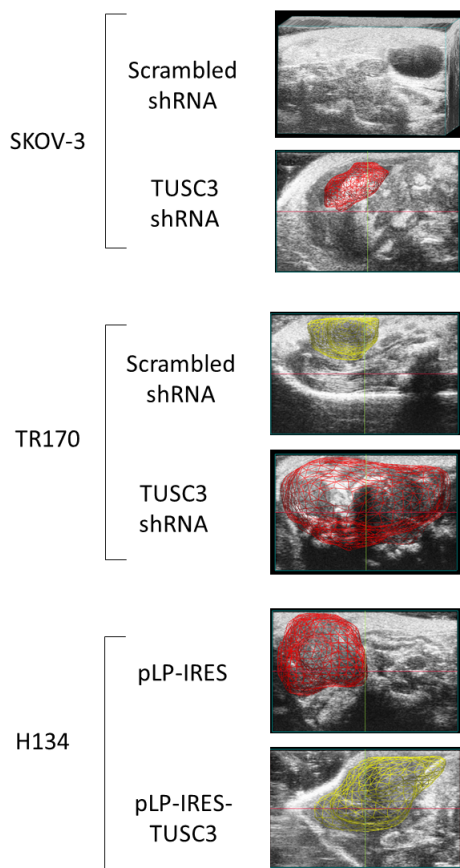
B







A



B

Cell line		Mouse #	Tumor size	Metastases	Ascites
SKOV3	Scrambled shRNA	1	+	+	NO
		2	+	+	NO
		3	+	-	NO
	TUSC3 shRNA	1	++	+++	YES
		2	++	+++	NO
		3	++	+++	YES
TR-170	Scrambled shRNA	1	++	++	YES
		2	+	++	YES
		3	+	++	YES
	TUSC3 shRNA	1	+++	-	YES
		2	++	-	YES
		3	n/a	n/a	n/a
H134	pLP-IRES	1	++	-	NO
		2	+++	+++	YES
		3	+	++	NO
	pLP-IRES-TUSC3	1	++	+++	YES
		2	+	-	NO
		3	+	+	NO

5. Kratochvílová K, Moráň L, Paďourová S, Stejskal S, Tesařová L, Šimara P, Hampl A, Koutná I, **Vaňhara P**. **The role of the endoplasmic reticulum stress in stemness, pluripotency and development.** *European Journal of Cell Biology* 2016; **95**(3-5):115-23.

Commentary:

In this review publication we complemented the current ER literature with developmental aspects of ER-associated machinery, and provided a summary of the important findings on the role of the ER stress and UPR in embryonic development and pluripotent stem cells.

DOI: 10.1016/j.ejcb.2016.02.002

Journal: European Journal of Cell Biology

Impact factor (WOS, 2016): 4.082

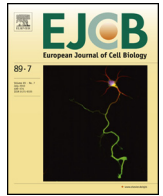
Number of citations (WOS, 2018): 5

Cited in: Journal of Molecular Biology.

Most important citation:

Noormohammadi A, Calculli G, Gutierrez-Garcia R, Khodakarami A, Koyuncu S, Vilchez D. **Mechanisms of protein homeostasis (proteostasis) maintain stem cell identity in mammalian pluripotent stem cells.** *Cellular and Molecular Life Sciences* 2018; **75**(2):275-290.
doi: 10.1007/s00018-017-2602-1. (IF 2016: 5.788)

Contribution of the author: Corresponding author. Design and writing of manuscript.



Review

The role of the endoplasmic reticulum stress in stemness, pluripotency and development



Kateřina Kratochvílová^{a,b}, Lukáš Moráň^a, Stanislava Paďourová^{b,c}, Stanislav Stejskal^{b,c}, Lenka Tesařová^{b,c}, Pavel Šimara^{a,b,c}, Aleš Hampl^{a,b}, Irena Koutná^{b,c}, Petr Vaňhara^{a,b,*}

^a Masaryk University, Faculty of Medicine, Department of Histology and Embryology, Brno, Czech Republic

^b International Clinical Research Center, St. Anne's University Hospital, Brno, Czech Republic

^c Centre for Biomedical Image Analysis, Faculty of Informatics, Masaryk University, Brno, Czech Republic

ARTICLE INFO

Article history:

Received 10 December 2015

Received in revised form 1 February 2016

Accepted 5 February 2016

Keywords:

Endoplasmic reticulum stress

Unfolded protein response

Embryonic stem cells

Pluripotency

Development

ABSTRACT

The molecular machinery of endoplasmic reticulum (ER) integrates various intracellular and extracellular cues to maintain homeostasis in diverse physiological or pathological scenarios. ER stress and the unfolded protein response (UPR) have been found to mediate molecular and biochemical mechanisms that affect cell proliferation, differentiation, and apoptosis. Although a number of reviews on the ER stress response have been published, comprehensive reviews that broadly summarize ER physiology in the context of pluripotency, embryonic development, and tissue homeostasis are lacking. This review complements the current ER literature and provides a summary of the important findings on the role of the ER stress and UPR in embryonic development and pluripotent stem cells.

© 2016 Elsevier GmbH. All rights reserved.

Contents

1. Introduction	115
2. ER homeostasis and the molecular response to ER stress	116
3. The ER stress response in embryonic development	118
4. The ER stress response in pluripotency and differentiation	119
5. Conclusion	121
Conflict of interest statement	121
Acknowledgements	121
References	121

1. Introduction

The endoplasmic reticulum (ER) is the principal organelle involved in the synthesis, maturation, and post- or co-translational modification of secreted and membrane proteins, as well as in various metabolic processes including dynamic ion storage and biogenesis of membrane structures (Kleizen and Braakman, 2004). The rough ER (rER) is an extensive membranous network of cisterns, branched tubules, and flattened sacs that form a unique

microenvironment consisting of oxidizing conditions and a high calcium concentration, which are necessary for the formation of disulfide bonds and supramolecular conformations of proteins (Ulianich et al., 2007). During proteosynthesis, nascent proteins are translated into the ER lumen where they are co-translationally and/or post-translationally modified with oligosaccharyl residues. These glycosylated motifs are targets for intra-ER chaperones, such as Calnexin and Calreticulin. Properly folded proteins are then addressed to the Golgi apparatus and to the extracellular surface by the secretory pathway or to other intracellular organelles (Ogata et al., 2006). Since the discovery of the ER by Albert Claude in the early 1940s (Claude, 1943) and a series of pioneering publications that identified the fundamental structure of the ER and suggested the proteosynthetic function of the ER (Porter et al., 1945) and liver and pancreatic microsomal structures (Palade, 1956; Palade and

* Corresponding author at: Masaryk University, Faculty of Medicine, Department of Histology and Embryology, Kamenice 3, Brno 62500, Czech Republic. Tel.: +00 420 54949 7780; fax: +00 420 54949 1320.

E-mail address: pvanhara@med.muni.cz (P. Vaňhara).

Siekevitz, 1956a,b; Zamecnik and Keller, 1954), the ER has been shown to be a complex hub that regulates numerous aspects of cellular life.

The ER machinery integrates various intracellular and extracellular signals including growth, differentiation, and inflammatory signals, and executes a unique set of molecular responses, which are conserved among various eukaryotes, including yeasts, plants, nematodes, insects, and mammals (for a detailed review see Ruberti and Brandizzi, 2014). The ability of the ER to sense properly folded and post-translationally modified proteins is at the core of a complex signaling network that evaluates the ER work load and initiates molecular responses to imbalanced homeostasis and ER stress.

2. ER homeostasis and the molecular response to ER stress

Disruption of ER homeostasis, the ER stress, may occur during cell differentiation, tissue development, and senescence or as a result of increased protein synthesis, perturbation of calcium homeostasis, DNA damage, altered redox status or the expression of mutant proteins (Zhong et al., 2011). In addition, exogenous chemical and physical inducers, such as hypoxia, glucose deprivation, and mechanical forces may cause ER stress. ER stress typically triggers a complex signaling process called the unfolded protein response (UPR) (Uliianich et al., 2007; Ozcan and Tabas, 2012). The common hallmarks of ER stress are proteosynthesis overload and attenuation of the secretory pathway by metabolic inhibition. Dilatations of ER cisterns, ribosome detachment, and abnormal cistern crosslinking (Fig. 1) have been described in many cell types, including somatic, cancer or stem cells, in the presence of various ER stress inducers (Duan et al., 2014; Horak et al., 2014; Kratochvílová et al., 2015). These molecular responses include upregulation of molecular chaperones, downregulation of mRNA translation, and degradation of misfolded proteins in a sequence of biochemical events termed UPR and ER associated degradation (ERAD). In cases of long-lasting ER stress, proapoptotic signaling pathways, which involve downregulation of Bcl-2 and induction of Bim or Puma, may be initiated (Kim et al., 2008).

UPR is initiated by three stress-sensing transmembrane proteins in the ER: 1) leucine zipper activating transcription factor 6 (ATF6), 2) inositol-requiring kinase/endoribonuclease 1 (IRE1), and 3) protein kinase RNA-like ER kinase (PERK) (Nishitoh, 2012). In unstressed cells, these sensors are maintained in an inactive state by the ATP-dependent ER chaperone GRP78 (BiP), which binds to their luminal domains. GRP78 belongs to the HSP70 family of heat shock proteins and is the most abundant protein in the ER lumen (Lane et al., 2014; Csala et al., 2012). Under physiological conditions, GRP78 binds to nascent or unfolded proteins through its peptide-binding domain and uses the energy from hydrolyzing ATP to promote proper folding and to prevent protein aggregation (Luo et al., 2006). When there are excessive amounts of misfolded proteins in the ER lumen, unbound GRP78 is depleted and bound GRP78 dissociates from PERK, ATF6, and IRE1. The release of GRP78 allows these transmembrane receptors to oligomerize, autophosphorylate, and activate their respective downstream pathways.

Upon release from GRP78, the 90 kDa ATF6 protein is dispatched to the Golgi apparatus where it is processed by Site-1 and Site-2 proteases (Yoshida et al., 2006). The 50 kDa active soluble form of ATF6 is then transported into the nucleus and binds directly to the mammalian consensus sequence of the cis-acting ER stress response element (ERSE) and to conserved GRP promoters to activate ER chaperones, such as GRP78, GRP94, C/EBP homologous protein (CHOP), Calnexin, Calreticulin, and X-box binding protein 1 (XBP-1) (Kober et al., 2012). ER chaperones and their functions in protein folding are described in detail elsewhere (Ni and Lee, 2007; Halperin et al., 2014).

Activated PERK phosphorylates the α subunit of eukaryotic initiating factor 2 (eIF2 α) leading to inhibition of general mRNA translation activity and protein synthesis, as well as to the subsequent diminution of nascent peptides entering the ER lumen (Lane et al., 2014). On the other hand, transcription of some genes, such as activating transcription factor 4 (ATF4), is triggered by phosphorylated eIF2 α . ATF4 then activates transcription of the proapoptotic transcription factor CHOP (DDIT3, GADD153) which transitions the balance between anti- and pro-apoptotic members of the BCL2 family towards programmed cell death. CHOP can also induce apoptosis through death receptor 5 (DR5). In addition, CHOP activates transcription of ER oxidase 1 α (ERO1 α) and downregulates intracellular glutathione, thereby elevating levels of reactive oxygen species (Nishitoh, 2012; Kim et al., 2008). Activated ERO1 α also ensures oxidative protein folding and enables the release of Ca²⁺ ions from the ER through the IP3 receptor, which can also initiate apoptosis. Another function of CHOP is to activate growth arrest DNA damage-inducible gene 34 (GADD34), which is responsible for dephosphorylating eIF2 α and restoring protein translation (Marciniak et al., 2004).

When the PERK pathway is knocked-out, cells are exposed to more intracellular stress and are more sensitive to its lethal effects (Harding et al., 2000). In Wolcott–Rallinson syndrome, PERK is mutated and the eIF2 α -ATF6-ATF4 axis is deregulated leading to uncompensated ER stress predominantly in the endocrine compartment of the pancreas and other tissues engaged in high-rate synthesis of proteins. Clinically, the absence of functional PERK causes neonatal or early-onset diabetes, bone dysplasia, and hepatic failure (Zhang et al., 2002; Julier and Nicolino, 2010). Moreover, PERK deficient cells show a rapid increase of IRE1-mediated UPR pathway (Harding et al., 2000).

The ER transmembrane protein IRE1 has endoribonuclease and protein kinase activity and its pathway is conserved among all eukaryotic models studied (Calfon et al., 2002; Yoshida et al., 2006). IRE1 activity is regulated by oligomerization, and the oligomerization state of IRE1 determines the molecular outcomes of IRE1 binding to cytoplasmic targets. Dimerization of IRE1 catalyzes alternative splicing of XBP-1 mRNA by the IRE1 endonuclease domain (Yoshida et al., 2001; Chen and Brandizzi, 2013). IRE1 removes a 26-nucleotide sequence from XBP-1 mRNA, which induces a shift in the reading frame leading to translation of the highly active basic leucine zipper transcription factor form of XBP-1. This spliced form of XBP-1 interacts with other bZIP transcription factors, such as c-Fos (Ono et al., 1991) and ATF6. The target genes induced by XBP-1 include ER enzymes, such as ER mannosidase alpha-like 1 (EDE1), ER chaperones, as well as a variety of other genes, which are regulated in a tissue-dependent context (He et al., 2010). Upregulation of major transcription factors, such as AP-1, that enhances proliferation or immune responses, can then modulate directly the tissue microenvironment. Unspliced XBP-1 negatively regulates the spliced form of XBP-1 and the PERK pathway (Yoshida et al., 2006). IRE1 multimers catalyze the degradation of various RNAs, including microRNAs, mRNAs, and rRNAs, in cell- or tissue-specific manners by regulated IRE1-dependent decay (RIDD) mechanisms (Maurel et al., 2014). The kinase activity of IRE1 was identified under chronic ER stress conditions, triggering the proapoptotic pathway by assembling a signaling complex consisting of autophosphorylated IRE1, TRA2, and apoptosis signal-regulated kinase (ASK1). This signaling complex activates c-Jun NH2-terminal kinase (JNK) and its downstream targets (Urano et al., 2000).

UPR mediates an adaptive process that directly reduces the amount of misfolded proteins in the ER lumen. Substantial proportions of the proteins that enter the lumen of the ER are excluded by rigorous quality control mechanisms and are eliminated as defective ribosomal products (DRiPs) (Schubert et al., 2000). ERAD is

hESCs CCTL 14

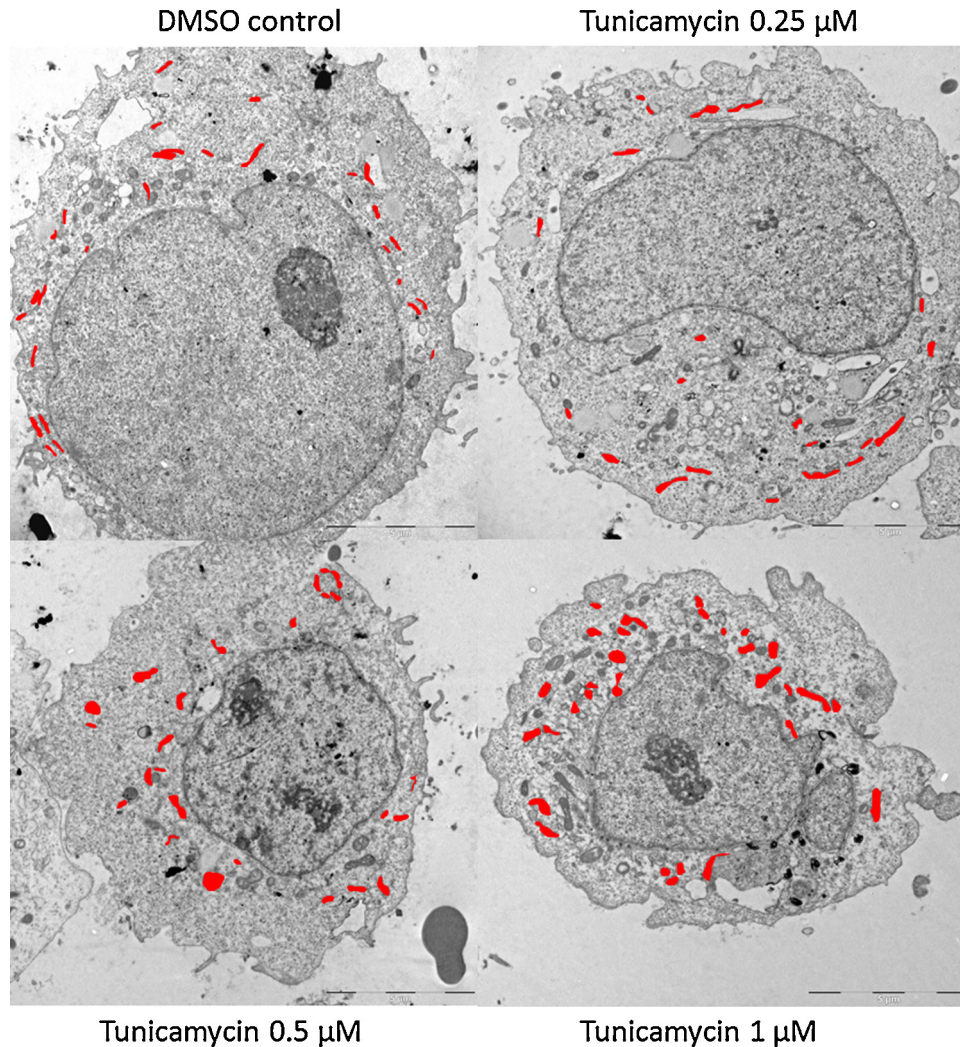


Fig. 1. Transmission electron microscope (TEM) images of ER structures in the human embryonic stem cell line CCTL14 (scale bars: 5 μm) exposed to ER stress induced by tunicamycin. Red areas point to ER structures. Upon the tunicamycin treatment, the ER dilates, expands and loses its regular architecture in dose-dependent manner.

a multistep enzymatic process that is conserved among eukaryotes, and it begins by recognizing DRiPs and selecting misfolded and unfolded proteins (Ni and Lee, 2007). These proteins are first processed by ER α 1,2-mannosidase I (ERman I), which sequentially trims three to four mannose residues from the *N*-glycans attached to these polypeptides (Benyair et al., 2015). Then, three mannosidase-like proteins termed EDEM1, EDEM2, and EDEM3 recognize the mannose-trimmed moieties and target them for degradation. Additionally, GRP78 and its co-chaperones may select ERAD substrates by binding to the exposed hydrophobic regions commonly found in misfolded proteins. Next, selected proteins are retro-translocated to the cytosol where they are finally ubiquitinated and degraded by the proteasome (Lemus and Goder, 2014).

The ER stress response can be artificially induced by chemically inhibiting critical metabolic processes in the ER by exposure to pathogens, environmental pollutants, and cytostatic chemotherapy. The most common inhibitors, thapsigargin, tunicamycin, and dithiothreitol, target Ca^{2+} ATPase enzymes in the sarco/endoplasmic reticulum leading to depletion of luminal calcium stores, inhibit protein glycosylation or prevent disulfide bond formation during protein folding (Urano et al., 2000). Time-dependent proteomic analyses of endosomal fractions of

tunicamycin and thapsigargin treated fibroblasts revealed a gradual accumulation of ER chaperones and ER-residing enzymes, whereas production of secreted proteins, such as collagen alpha chains, was attenuated (Mintz et al., 2008). Recently, engineered silica nanoparticles (SiO_2 -NPs) and silica nanoparticles doped with silver (SiO_2 -Ag-NPs) were found to cause perturbations in ER morphology, to increase ER stress, and to interact with metabolic enzymes and efflux transporters. In addition, nanoparticle agglomerates were found free in the cytosol, as well as in vesicular structures, such as endosomes (Christen and Fent, 2012). Thus, the rapid and prominent ER stress response may be used as an early and sensitive biomarker of nanotoxins (Chen et al., 2014b). Recently, a direct link between ER stress and ATF-6 mediated formation of the inflammasome and induction of pyroptosis was demonstrated in the human monocyte cell line THP-1 upon exposure to 15 nm silver nanoparticles (Simard et al., 2015). The link between the ER stress response and proapoptotic and proinflammatory paracrine signaling extends the ER stress response from a single cell to the tissue microenvironment, thus the ER stress response may affect tissue regeneration and carcinogenesis. In addition to chemical compounds, biological inducers may initiate ER stress. *In vitro* experiments demonstrated that cyanobacterial hepatotoxins, microcystins, affect ER

homeostasis and induce UPR by inhibition of type-1 and type-2A protein phosphatase catalytic subunits (PP-1c and PP-2Ac) (Christen et al., 2013). Additionally, viruses, such as West Nile virus, can induce ER stress by overriding control of cell proteosynthesis and causing an abnormal workload for the ER (Medigeschi et al., 2007). Recently, Li et al., reported ER stress-dependent changes in mechanically compressed mandibular cartilage, which led to pathological tissue remodeling and cartilage thinning. In isolated chondrocytes, mechanotransduction was found to expand the ER and induce expression of ER stress markers. Upon prolonged exposure to stress, chondrocytes were arrested in the cell cycle, ceased to proliferate, and induced apoptosis. Alleviation of ER stress restored the altered architecture of the ER, increased cell numbers, and reduced cartilage thinning (Li et al., 2013). In a mouse model of myocardial infarction, *in vivo* inhibition of ER stress improved heart tissue regeneration by downregulating apoptosis and preventing fibrosis (Luo et al., 2015).

To pharmacologically modulate ER stress response, chemical chaperones 4-phenylbutyric acid (4-PBA) and tauroursodeoxycholic acid (TUDCA) which are both capable to alleviate ER stress *in vivo* and *in vitro* were introduced (Michalak and Gye, 2015; Ozcan et al., 2006). TUDCA is a natural endogenous bile acid composed of taurine and UDCA. 4-PBA is a low-molecular-weight synthetic-fatty acid derivative known to stabilize protein conformation, improve ER folding capacity and additionally inhibit histone deacetylase (HDAC) (Luo et al., 2015; Ozcan et al., 2006). Both TUDCA and 4-PBA have been shown to alleviate expression of molecules from all three branches of UPR and also to inhibit ER-stress-induced apoptosis. Another ER stress inhibitor is a small heterocyclic molecule salubrinal, originally identified by Boyce et al. (2005), which selectively inhibits dephosphorylation of eIF2 α and reduces globally the proteosynthesis rate. Salubrinal has been shown to protect cells from ER-stress-induced apoptosis and damage caused by a wide range of xenotoxins (Matsuoka and Komoike, 2015). In addition to chemical inhibition, the selective disruption of UPR signaling can be achieved by deletion of some important regulators of UPR such as XBP-1, IRE1 α (Kim et al., 2015) or ATF4 (Armstrong et al., 2010).

3. The ER stress response in embryonic development

Mammalian zygotes and early embryos are exposed to various intrinsic or extrinsic stressors in their surrounding microenvironments, e.g., mechanical, oxidative, osmotic, and pH stress, as well as immunological and direct embryo-endometrium interactions. All these signals, together with a high rate of embryonic proteosynthesis, integrate at the ER and induce UPR in exposed cells (Michalak and Gye, 2015). Recently, the role of ER stress in mammalian embryonic development has been investigated and it has been found that alleviation of ER stress by UPR inhibitors, such as TUDCA, enhanced and improved the maturation and development of *in vitro* produced bovine and mice embryos (Yoon et al., 2014; Zhang et al., 2012). Similarly, direct induction of ER stress by tunicamycin in pregnant mice resulted in preterm birth and consequent low fetal weight and elevated fetal death rate (Kawakami et al., 2014).

To compensate for ER stress embryonic cells recruit a wide range of ER chaperones and elements of the UPR network. In fact, homozygous deletions of ER stress and UPR effectors, such as GRP78, GRP94, GRP58/ERp57, Ire1 α , XBP-1, Calreticulin, and double deletion of both ATF6 α and ATF6 β , result in embryonic lethality in mice (Fig. 2) (Ni and Lee, 2007; Reimold et al., 2001; Yamamoto et al., 2007; Wanderling et al., 2008; Garbi et al., 2006; Lee et al., 2005).

It has been demonstrated that *GRP78* gene is transcriptionally activated in the trophectoderm and inner cell mass of E3.5 mice

embryos and this induction largely depends on the genomic ERSEs that are available for ATF-6 and TFII-I transcription factors (Parker et al., 2001). Loss of one copy of *GRP78* is compensated for by overexpression of chaperones *GRP94* and *PDI* suggesting complex regulatory circuits stabilizing the ER; however, the complete loss of *GRP78* cannot be substituted and results in embryonic lethality at the peri-implantation stage because the embryos cannot hatch from the *zona pellucida in vitro*, fail to grow in culture, exhibit proliferation defects and a massive increase in apoptosis of the inner cell mass of the preimplantation blastocyst. Similarly, a complete depletion of the ER chaperone *GRP94* also results in embryonic lethality around E7 and knockout embryos fail to develop mesoderm, primitive streak, or proamniotic cavity (Wanderling et al., 2008). Interestingly, heterozygous *GRP94* deletions showed no compensating overexpression of other UPR elements and no obvious abnormal phenotypes under physiological conditions (Mao et al., 2010). The robustness of ER signaling is well documented on ATF6-mediated UPR pathway. ATF6 has two related isoforms, ATF6 α and ATF6 β that can compensate for each other in single ATF6 α or β knock-outs. The double ATF6 α and ATF6 β knock-out then results in embryonic death by the E8.5 documenting the overlapping function for ATF6 isoforms (Yamamoto et al., 2007). It was also demonstrated that single knock-out of ATF6 α decreases cellular tolerance to ER stress by affecting the proteins involved in quality control of protein folding and degradation pathways, such as EDEM 1 (Wu et al., 2007).

Expansion of pool of tissue stem cells and proper organ development are dependent on availability of downstream UPR targets. Mice embryos lacking XBP-1 develop hypoplasia of the fetal liver and die of anemia *in utero* (Reimold et al., 2001). Although the embryonic development of XBP1-null mice can be rescued by inducing the XBP1 transgene to the liver, these mice nevertheless die soon after the birth due to the pancreatic dysfunction (Lee et al., 2005). The upstream inducer of Xbp-1, IRE1 α is necessary for liver development and its deficiency in mice results in embryonic death between 9.5 and 13 days of gestation (Zhang et al., 2005). The affected embryos are pale, small in size and with hypoplastic liver. Heterozygous mutants of IRE1 α are viable and show no visible abnormalities in phenotype. While the precise molecular cause of IRE1 α embryonic lethality is still uncertain, the loss of IRE1 α in extraembryonic tissues causes downregulation of vascular endothelial growth factor- A (VEGF-A) followed by severe dysfunction of the vascular labyrinth region in the placenta (Iwawaki et al., 2009). In addition, IRE1 α -/- embryos can be born alive when supplied with functionally normal IRE1 α -positive placentas and these embryos show no placental abnormalities or liver hypoplasia. These results indicate a vital function of IRE1 α in extraembryonic tissues. Altogether, it is apparent that all of the listed UPR regulators are essential for embryonic cell growth and pluripotent cell survival, and their loss cannot be compensated by other UPR effectors or ER chaperones. PERK-knockout mice are viable, however, they show a severe degeneration of endocrine and exocrine pancreatic cells and subsequent development of diabetes mellitus after birth, which strikingly resembles the Wolcott-Rallison syndrome in humans (Harding et al., 2001). The loss of the proapoptotic-mediator CHOP in mice has no effect on viability, but female CHOP-/- mice had significantly greater body weight and adiposity than wild type littermates on the equivalent diet (Ariyama et al., 2007). However, there was no weight difference in male mice. Another study discovered that CHOP deletion improves the capacity of pancreatic β -cell function by reducing protein oxidation and lipid peroxidation (Song et al., 2008). GRP58 (ERp57, PDIA3), is a member of the PDI family of oxidoreductases, that in complex with Calreticulin or Calnexin contributes to protein folding. Specifically, it constitutes the peptide loading complex of the major histocompatibility complex I (MHC I), extending the ER

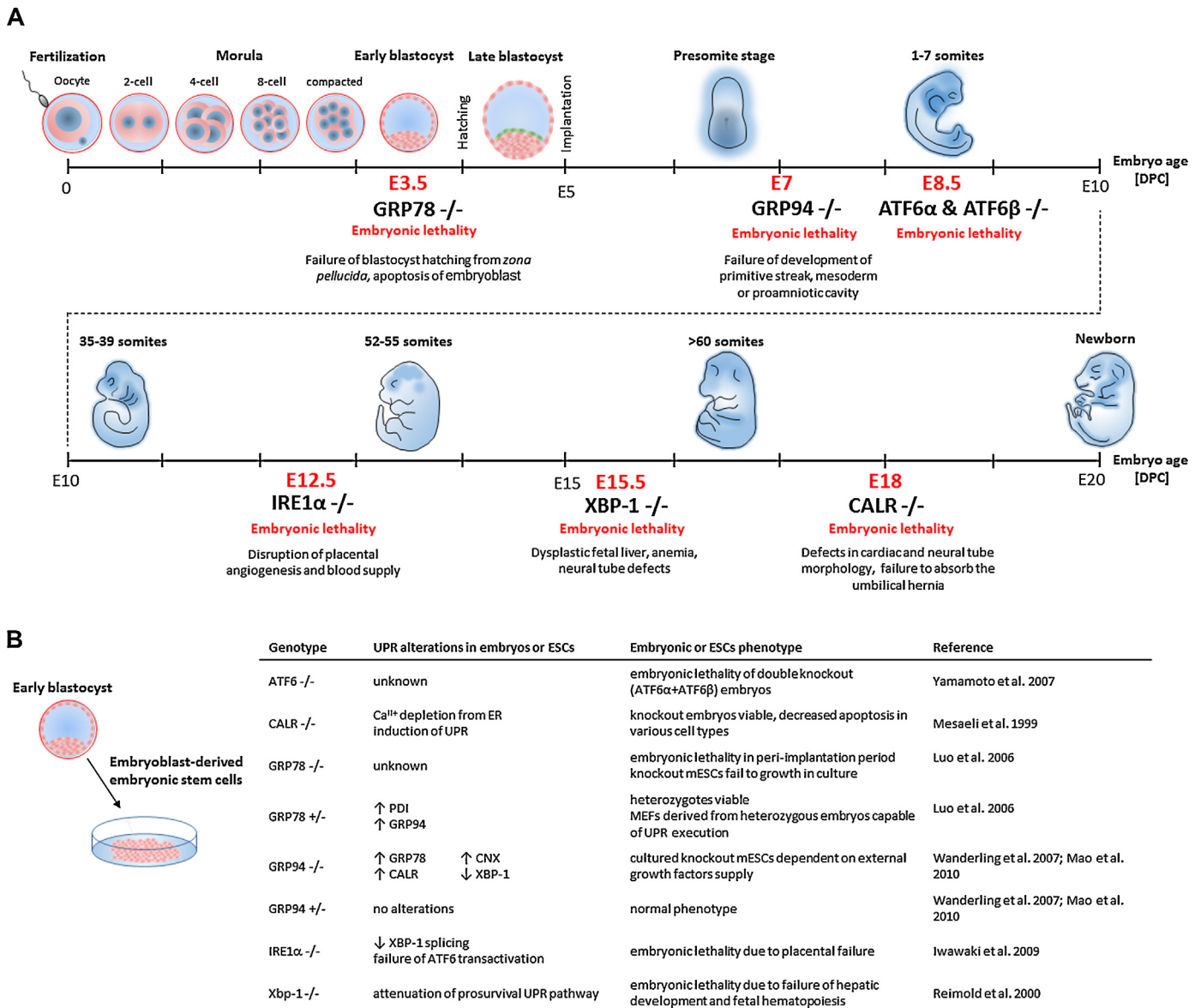


Fig. 2. (A) Experimentally induced loss of fundamental components of UPR during mouse development results in embryonic lethality due to failure of implantation, germ layer definition or organogenesis. (B) Alterations of UPR in mouse embryos or embryonic stem cells (ESCs) induce similar phenotypes affecting proliferation, differentiation capacity or sensitivity to apoptosis.

molecular interactions indirectly to the immune system. Ubiquitous knockout of *GRP58* is embryonically lethal (Garbi et al., 2006). Deletion of Calreticulin leads to embryonic lethality in mice around day E18 (Mesaeli et al., 1999). It has been demonstrated that the Calreticulin gene (*CALR*) is activated to high levels in the cardiovascular system during early stages of embryonic development and its loss causes defects in heart development and function. In later stages of embryogenesis, activation of *CALR* was also seen in the brain, midgut, intersomitic vessels, and liver. Calnexin is a part of the Calnexin/Calreticulin chaperone pair, yet surprisingly, unlike Calreticulin, Calnexin knockout mice embryos are viable, although they display a phenotype. Approximately 50% of Calnexin knockout mice die in two days after birth, and the surviving mice were about one-third smaller than their wild-type littermates and exhibited obvious motor disorders (Denzel et al., 2002). Deletion of one *calnexin* allele showed no detectable phenotype.

4. The ER stress response in pluripotency and differentiation

Pluripotent stem cells (PSCs) are characterized by their ability to self-renew indefinitely and to differentiate into all of the three germ layers. In mammals, the PSC population typically includes embryonic stem cells (ESCs) derived from the inner cell mass of a preimplantation blastocyst (Thomson et al. in 1998). It has been demonstrated that human and murine ESCs have a higher tolerance for various cellular stressors than differentiated cells (Saretzki et al., 2004, 2008). During spontaneous differentiation of hESCs and mESCs, ROS level was increased while several major genes involved in different types of DNA damage repair (e.g., BRCA1, MSH3, DMC1 TLK1) were downregulated, suggesting presence of distinct stem- and somatic-molecular regimens responding to general stress. Liu et al. (2012) studied hESC cell line H9 after retinoic acid (RA) induced differentiation and showed that hESCs express high

levels of UPR markers such as XBP1 and p-eIF2 α that are substantially downregulated in differentiated cells.

Pluripotent-specific inhibitors or PluriSIns were developed to specifically eliminate PSCs, without affecting the viability of more differentiated cells, including stem or progenitor cells in clinically-oriented scenarios (Ben-David et al., 2013). After the exposure of PSCs to PluriSIns, the UPR was induced, including upregulation of CHOP expression, XBP1 splicing and eIF2 α phosphorylation, while no such response was found in differentiated cells. PluriSIn treatment also inhibited the normal development of mice blastocyst. The high sensitivity of PSCs to PluriSIns thus involves induction of pro-apoptotic branch of UPR and allows PSCs elimination due to specific ER-stress associated molecular context. On the other hand, PSCs aimed to be used in regenerative medicine are challenged by low rates of cell survival after transplantation due to unfavourable microenvironments *in situ*, such as hypoxia, nutrient deprivation, growth factor gradients and reactive oxygen species that can induce apoptosis, alter differentiated phenotype or promote carcinogenesis. Recently, a method called hypoxic preconditioning (HPC) has been shown to improve survival and engraftment of stem cells in the host environment. HPC involves exposure of stem cells to non-damaging hypoxia or ischemia, which induces a more stress-resistant phenotype and enables cells to avoid apoptosis. Although the mechanism of HPC is not yet well understood, Mao and Crowder (2010) have shown in nematodes that HPC induces the UPR response through IRE1 activation and that induction of UPR by misfolded proteins is sufficient to stimulate an ongoing protective response. The involvement of UPR in HPC was recently confirmed in human hippocampal neurons (Bickler et al., 2015). Furthermore, it has been shown that signaling by the upstream PERK pathway and inhibition of protein synthesis are important for HPC-induced protection. Additionally, inhibition of ATF6 and IRE1 abolished HPC-induced phenotype.

The method of long-term culturing PSCs, including ESC or induced PSCs (iPSCs) (Takahashi and Yamanaka, 2006), aims to preserve pluripotency and self-renewal. Usually, the leukemia inhibitory factor (LIF) alone or in combination with bone morphogenetic protein (BMP4) are used to maintain mouse ESCs (mESCs), and fibroblast growth factor (FGF2) and TGF β /activin/Nodal are

used to maintain human ESCs (hESCs) (Chen et al., 2014a). Nevertheless, even with the LIF treatment, mESCs in prolonged culture spontaneously differentiate into meso-endodermal lineages and secrete vascular endothelial growth factors (VEGFs). Chen et al. found that hypoxia-inducible factor α (HIF α) and ER stress are involved in the production of VEGFs, and, interestingly, inhibition of ER stress reduced VEGF expression and supported self-renewal of mESCs. Additionally, blocking VEGF expression with a small molecule inhibitor of receptor tyrosine kinases, sunitinib, also resulted in enhanced self-renewal of mESCs. Blanco-Gelaz et al. (2010) provided a detailed report on culture-dependent UPR activation in the human hESC lines HS181 and SHEF-1 cultured on a feeder layer composed of human embryonic fibroblasts (HEFs) and in a feeder-free system composed of a mixture of extracellular matrix proteins (Matrigel). When HS181 was grown on Matrigel in conditioned media derived from HEFs, GRP78 was substantially upregulated compared to the same cells growing on HEFs. In addition, XBP-1 was ectopically expressed in HS181 cells cultured on adipose derived stem cells (ASCs) feeder. In SHEF1 cells grown on Matrigel with HEF-CM, expression of ATF6 and GRP78 was not affected, but XBP-1 expression was elevated. In summary, the expression of UPR markers, including GRP78, XBP-1, and CHOP, varied in different culture conditions and was generally higher in cells growing on Matrigel than in cells growing on feeder cells. These results highlight the importance of controlling culture conditions and also demonstrate the importance of balancing ER stress in order to enhance survival and maintain pluripotency of PSCs *in vitro* (Fig. 3). In the committed progeny derived from mesenchymal tissues, the UPR may play a role in defining specific stem cell populations responding to different forms of cell-stress. Heneidi et al. described populations of stem cells isolated from lipo-aspirated adipose tissue that showed a high degree of resistance to ER stress when compared to general mesenchymal- or adipose-stem cells. In addition, these lipo-aspirated stem cells expressed high levels of the stem markers Oct-4, Sox-2, Klf4, and c-Myc and were capable of differentiating into endodermal, mesodermal, and ectodermal lineages (Heneidi et al., 2013). MUSE (Multilineage differentiating Stress-Enduring) cells are graftable, *in vitro*-manipulated, and have potential for use in tissue engineering and regenerative medicine.

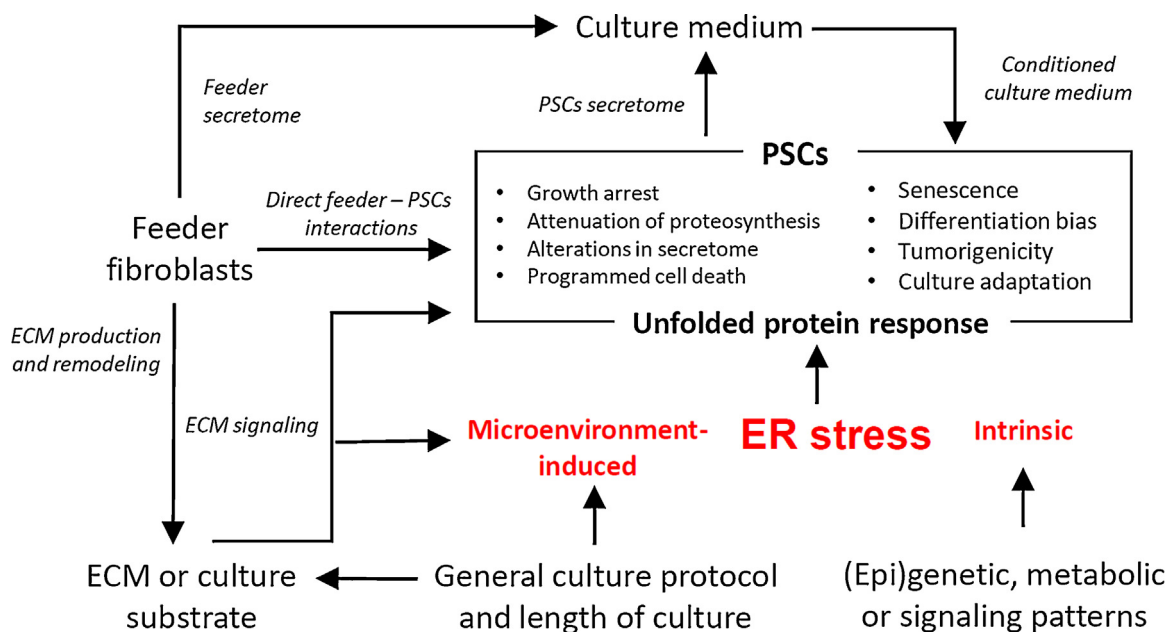


Fig. 3. ER stress and UPR are evoked in pluripotent stem cells (PSCs) cultures *in vitro*. The global effects of the culture microenvironment and particular genetic, epigenetic, metabolic or signaling cues integrates on ER, modulate UPR, and promote phenotypic changes.

Induction of the ER stress response and UPR was observed during differentiation into various proteosynthetically active cell types.

During chondrocyte differentiation, bone morphogenetic protein 2 (BMP2) induces mild ER stress and activates the UPR-associated molecules XBP-1, GRP78, and IRE1 α (Han et al., 2013). Then, XBP-1s enhances chondrocyte hypertrophy and positively regulates endochondral bone formation (Guo et al., 2014). Overexpression of ATF6 also enhances chondrocyte differentiation and endochondral bone growth, whereas knockdown of ATF6 abolishes chondrocyte differentiation and endochondral bone growth (Xiong et al., 2015). Activation of the UPR effectors GRP78, CHOP, XBP-1, and ATF4 was also observed during neuronal differentiation, and induction of ER stress by tunicamycin or thapsigargin resulted in increased expression of the neuronal marker NF-L (Cho et al., 2009). This suggests that UPR plays an active role in neuronal differentiation. Recently, it has been shown that ER stress accelerates neuronal differentiation and suppresses differentiation into glial cells (Kawada et al., 2014). The effect of UPR induction on endodermal differentiation has been studied in mouse embryonic stem cells (ESCs) (Xu et al., 2014). ESCs were differentiated to the endodermal lineage by treatment with Activin A, ER stress was then induced with tunicamycin or thapsigargin supplementation, and genes involved in the formation of the primitive and definitive endoderm (*Sox17*, *FoxA2*, *Sox7*, *Gata4*, and *Gata6*) were found upregulated in the ER stress-induced ESCs. Concordant with these findings, alleviation of ER stress by TUDCA resulted in abrogation of endodermal differentiation even when Activin A was added. These results suggest that UPR is also needed for definitive endodermal cell commitment during gastrulation.

In hematopoietic differentiation, GRP78 contributes to the survival and proliferation of hematopoietic stem cells (HSCs) in endosteal hypoxic niches (Miharada et al., 2011; Wey et al., 2012). Activation of UPR components was found higher in HSCs than in downstream progenitor cells isolated from cord blood and adult bone marrow. Induction of ER stress by tunicamycin led to increased upregulation of CHOP and ATF4 in HSCs than in progenitor cells and induced selective apoptosis in HSCs (Galen et al., 2014). Interestingly, alleviation of ER stress in HSCs resulted in a robust increase in reconstitution capacity and reduced apoptosis of HSCs after bone marrow transplantation, suggesting that ER homeostasis is critical for proper HSC function *in vivo* (Miharada et al., 2014). These findings emphasize the need to consider UPR signaling in HSCs and the benefit of alleviating ER stress *in vitro* during development and long-term propagation of HSCs and PSCs in general.

5. Conclusion

The endoplasmic reticulum represents a complex signaling hub where both intracellular and extracellular cues integrate and

initiate orchestrated molecular mechanisms that lead to adaptation to ER stress and restoration of homeostasis or to programmed cell death to protect tissue integrity. Components of molecular response to ER stress are indispensable during embryonic development and their roles can be recapitulated in ES cells *in vitro* (Table 1). Understanding the UPR as a defined machinery of balanced molecular events induced in cultured stem cells or embryos has therefore a great importance for deciphering the molecular complexity of embryonic development as well as for clinical or translational medicine.

Conflict of interest statement

The authors declare that they have no conflict of interest.

Acknowledgements

This study was supported by funds from (a) the Ministry of Education, Youth and Sports of the Czech Republic (CZ.1.07/2.3.00/30.0030), (b) the Grant Agency of the Czech Republic (302/12/G157, GA15-11707S), (c) Masaryk University (MUNI/M/1050/2013, MUNI/A/1352/2015), (d) from the National Program of Sustainability II (project no. LQ1605). We thank Dr. Sabina Ševčíková from the Faculty of Medicine, Masaryk University, for her critical reading of the manuscript.

References

- Ariyama, Y., Shimizu, H., Satoh, T., Tsuchiya, T., Okada, S., Oyadomari, S., Mori, M., Mori, M., 2007. *Chop*-deficient mice showed increased adiposity but no glucose intolerance. *Obesity* 15 (7), 1647–1656.
- Armstrong, J.L., Veal, G.J., Lovat, P.E., Redfern, C.P.F., 2010. Regulation of endoplasmic reticulum stress-induced cell death by ATF4 in neuroectodermal tumor cells. *J. Biol. Chem.* 285, 6091–6100.
- Benyair, R., Ogen-Shtern, N., Lederkremer, G.Z., 2015. Glycan regulation of ER-associated degradation through compartmentalization. *Semin. Cell Dev. Biol.* 41, 99–109.
- Ben-David, U., Gan, Q.-F., Arora, P., Yanuka, O., Oren, Y.S., Leikun-Frenkel, A., Graf, M., Garippa, R., Boehringer, M., Gromo, G., Benvenisty, N., 2013. Selective elimination of human pluripotent stem cells by an oleate synthesis inhibitor discovered in a high-throughput screen. *Cell Stem Cell* 12 (2), 167–179.
- Bickler, P.E., Clark, J.P., Gabatto, P., Brosnan, H., 2015. Hypoxic preconditioning and cell death from oxygen/glucose deprivation co-opt a subset of the unfolded protein response in hippocampal neurons. *Neuroscience* 310, 306–321.
- Blanco-Gelaz, M.A., Suarez-Alvarez, B., Ligerio, G., Sanchez, L., Vidal-Castiñeira, J.R., Coto, E., Moore, H., Menendez, P., Lopez-Larrea, C., 2010. Endoplasmic reticulum stress signals in defined human embryonic stem cell lines and culture conditions. *Stem Cell Rev.* 6, 462–472.
- Boyce, M., Bryant, K.F., Jousse, C., Long, K., Harding, H.P., Scheuner, D., Kaufman, R.J., Ma, D., Coen, D.M., Ron, D., Yuan, J., 2005. A selective inhibitor of eIF2 α dephosphorylation protects cells from ER stress. *Science* 307 (5711), 935–939.
- Calton, M., Zeng, H., Urano, F., Till, J.H., Hubbard, S.R., Harding, H.P., Clark, S.G., Don, R., 2002. IRE1 couples endoplasmic reticulum load to secretory capacity by processing the XBP-1 mRNA. *Nature* 415, 92–96.
- Chen, G., Xu, X., Zhang, L., Fu, Y., Wang, M., Gu, H., Xie, X., 2014a. Blocking autocrine VEGF signaling by sunitinib, an anti-cancer drug, promotes embryonic stem cell self-renewal and somatic cell reprogramming. *Cell Res.* 24, 1121–1136.
- Chen, R., Huo, L., Shi, X., Bai, R., Zhang, Z., Zhao, Y., Chang, Y., Chen, C., 2014b. Endoplasmic reticulum stress induced by zinc oxide nanoparticles is an earlier biomarker for nanotoxicological evaluation. *ACS Nano* 8, 2562–2574.
- Chen, Y., Brandizzi, F., 2013. IRE1: ER stress sensor and cell fate executor. *Trends Cell Biol.* 23, 547–555.
- Cho, Y.M., Jang, Y.S., Jang, Y.M., Chung, S.M., Kim, H.S., Lee, J.H., Jeong, S.W., Kim, I.K., Kim, J.J., Kim, K.S., Kwon, O.J., 2009. Induction of unfolded protein response during neuronal induction of rat bone marrow stromal cells and mouse embryonic stem cells. *Exp. Mol. Med.* 41, 440–452.
- Christen, V., Fent, K., 2012. Silica nanoparticles and silver-doped silica nanoparticles induce endoplasmic reticulum stress response and alter cytochrome P450A1 activity. *Chemosphere* 87, 423–434.
- Christen, V., Meili, N., Fent, K., 2013. Microcystin-LR induces endoplasmic reticulum stress and leads to induction of NF κ B, interferon-alpha, and tumor necrosis factor-alpha. *Environ. Sci. Technol.* 47, 3378–3385.
- Claude, A., 1943. The constitution of protoplasm. *Science* 97, 451–456 (1943).
- Csala, M., Kereszturi, E., Mandl, J., Banhegyi, G., 2012. The endoplasmic reticulum as the extracellular space inside the cell: role in protein folding and glycosylation. *Antioxid. Redox Signal.* 16, 1100–1108.

Table 1

Hallmarks of UPR in cultured pluripotent stem cells (PSCs) *in vitro* and embryonic development *in vivo*.

Cultured PSCs <i>in vitro</i>	Embryonic development <i>in vivo</i>
PSCs are capable of UPR execution upon induction of ER stress	UPR effectors are critical in different stages of embryonic development
ER stress and UPR follows <i>in vitro</i> differentiation of PSCs to terminal stages	ER stress and UPR follows <i>in vivo</i> differentiation and development
ER stress induced by different culture scenarios affects differentiation capacity of PSCs	Embryos affected by uncompensated ER stress are less viable or cease development
Adaptation to ER stress by preferential activation of pro-survival UPR pathways improves self-renewal, differentiation capacity or grafting capability of PSCs	Alleviation of ER stress improves viability of <i>in vitro</i> manipulated embryos

- Denzel, A., Molinari, M., Trigueros, C., Martin, J.E., Velmurgan, S., Brown, S., Stamp, G., Owen, M.J., 2002. Early postnatal death and motor disorders in mice congenitally deficient in calnexin expression. *Mol. Cell. Biol.* 22, 7398–7404.
- Duan, Z., Zhao, J., Fan, X., Tang, C., Liang, L., Ni, X., Liu, J., Wu, Q., Xu, G., 2014. The PERK-eIF2 α signaling pathway is involved in TCDD-induced ER stress in PC12 cells. *Neurotoxicology* 44, 1–11.
- Galen, P., Kreso, A., Mbon, N., Kent, D.G., Fitzmaurice, T., Chambers, J.E., Xie, S., Laurenti, E., Hermans, K., Eppert, K., Marciniak, S.J., Goodall, J.C., Green, A.R., Wouters, B.G., Wienholds, E., Dick, J.E., 2014. The unfolded protein response governs integrity of the haematopoietic stem-cell pool during stress. *Nature* 510, 268–272.
- Garbi, N., Tanaka, S., Momburg, F., Hämmerling, G.J., 2006. Impaired assembly of the major histocompatibility complex class I peptide-loading complex in mice deficient in the oxidoreductase ERp57. *Nat. Immunol.* 7, 93–102.
- Guo, F.J., Jiang, R., Xiong, Z., Xia, F., Li, M., Chen, L., Liu, C.J., 2014. IRE1 α constitutes a negative feedback loop with BMP2 and acts as a novel mediator in modulating osteogenic differentiation. *Cell Death Dis.* 5, e1239.
- Halperin, L., Jung, J., Michalak, M., 2014. The many functions of the endoplasmic reticulum chaperones and folding enzymes. *IUBMB Life* 66, 318–326.
- Han, X., Zhou, J., Zhang, P., Song, F., Jiang, R., Li, M., Xia, F., Guo, F.J., 2013. IRE1 α dissociates with BiP and inhibits ER stress-mediated apoptosis in cartilage development. *Cell Signal.* 25, 2136–2146.
- Harding, H.P., Zhang, Y., Bertolotti, A., Zeng, H., Ron, D., 2000. Perk is essential for translational regulation and cell survival during the unfolded protein response. *Mol. Cell* 5, 897–904.
- Harding, H.P., Huiqing, Z., Zhang, Y., Jungries, R., Chung, P., Plesken, H., Sabatini, D.D., Ron, D., 2001. Diabetes mellitus and exocrine pancreatic dysfunction in Perk $^{-/-}$ mice reveals a role for translational control in secretory cell survival. *Mol. Cell* 5 (5), 897–904.
- He, Y., Sun, S., Sha, H., Liu, Z., Yang, L., Xue, Z., Chen, H., Qi, L., 2010. Emerging roles for XBP1, a sUPeR transcription factor. *Gene Expr.* 15, 13–25.
- Heneidi, S., Simerman, A.A., Keller, E., Singh, P., Li, X., Dumesic, D.A., Chazenbalk, G., 2013. Awakened by cellular stress: isolation and characterization of a novel population of pluripotent stem cells derived from human adipose tissue. *PLoS ONE* 8, e64752.
- Horak, P., Tomasich, E., Vaňhara, P., Kratochvílová, K., Anees, M., Marhold, M., Lemberger, C.E., Gerschpacher, M., Horvat, R., Sibilia, M., Pils, D., Krainer, M., 2014. TUSC3 loss alters the ER stress response and accelerates prostate cancer growth in vivo. *Sci. Rep.* 4, 3739–3747.
- Iwawaki, T., Akai, R., Yamanaka, S., Kohno, K., 2009. Function of IRE1 α in the placenta is essential for placental development and embryonic viability. *Proc. Natl. Acad. Sci. U.S.A.* 106 (39), 16657–16662.
- Julier, C., Nicolino, M., 2010. Wolcott–Rallison syndrome. *Orphanet J. Rare Dis.* 5 (1), 1–13.
- Kawada, K., Iekumo, T., Saito, R., Kaneko, M., Mimori, S., Nomura, Y., Okuma, Y., 2014. Aberrant neuronal differentiation and inhibition of dendrite outgrowth resulting from endoplasmic reticulum stress. *J. Neurosci. Res.* 92, 1122–1133.
- Kawakami, T., Yoshimi, M., Kadota, Y., Inoue, M., Sato, M., Suzuki, S., 2014. Prolonged endoplasmic reticulum stress-induced placental morphology and causes low birth weight. *Toxicol. Appl. Pharmacol.* 275 (2), 134–144.
- Kim, I., Xu, V., Reed, J.C., 2008. Cell death and endoplasmic reticulum stress: disease relevance and therapeutic opportunities. *Nat. Rev. Drug Discovery* 7, 1013–1030.
- Kim, S., Joe, Y., Kim, Y.S., Jeong, S.O., Pae, H.O., Ryter, S.W., Surh, Y.J., Chung, H.T., 2015. Endoplasmic reticulum stress-induced IRE1 α activation mediates cross-talk of GSK-3 β and XBP-1 to regulate inflammatory cytokine production. *J. Immunol.* 194, 4498–4506.
- Kleizen, B., Braakman, I., 2004. Protein folding and quality control in the endoplasmic reticulum. *Curr. Opin. Cell Biol.* 16, 343–349.
- Kober, L., Zehe, C., Bode, J., 2012. Development of a novel ER stress based selection system for the isolation of highly productive clones. *Biotechnol. Bioeng.* 109, 2599–2611.
- Kratochvílová, K., Horak, P., Ešner, M., Souček, K., Pils, D., Anees, M., Tomasich, E., Dráfi, F., Jurtíková, V., Hampl, A., Krainer, M., Vaňhara, P., 2015. Tumor Suppressor Candidate 3 (TUSC3) prevents the epithelial-to-mesenchymal transition and inhibits tumor growth by modulating the endoplasmic reticulum stress response in ovarian cancer cells. *Int. J. Cancer* 137, 1330–1340.
- Lane, D.J.R., Mills, T.M., Shafie, N.H., Merlot, A.M., Moussa, R.S., Kalinowski, D.S., Kovacevic, Z., Richardson, D.R., 2014. Expanding horizons in iron chelation and the treatment of cancer: role of iron in the regulation of ER stress and the epithelial–mesenchymal transition. *Biochim. Biophys. Acta* 1845, 166–181.
- Lee, A.-H., Chu, G.C., Iwakoshi, N.N., Glimcher, L.H., 2005. XBP-1 is required for biogenesis of cellular secretory machinery of exocrine glands. *EMBO J.* 24, 4368–4380.
- Lemus, L., Goder, V., 2014. Regulation of endoplasmic reticulum-associated protein degradation (ERAD) by ubiquitin. *Cells* 3, 824–847.
- Li, H., Zhang, X.Y., Wu, T.J., Cheng, W., Liu, X., Jiang, T.T., Wen, J., Li, J., Ma, Q.L., Hua, Z.C., 2013. Endoplasmic reticulum stress regulates rat mandibular cartilage thinning under compressive mechanical stress. *J. Biol. Chem.* 288, 18172–18183.
- Liu, L., Liu, C., Zhong, Y., Apostolou, A., Shengyun, F., 2012. ER stress response during the differentiation of H9 cells induced by retinoic acid. *Biochem. Biophys. Res. Commun.* 417 (2), 738–743.
- Luo, S., Mao, C., Lee, B., Lee, A.S., 2006. GRP78/BiP is required for cell proliferation and protecting the inner cell mass from apoptosis during early mouse embryonic development. *Mol. Cell. Biol.* 25, 5688–5697.
- Luo, T., Kim, J.K., Chen, B., Abdel-Latif, A., Kitakaze, M., Yan, L., 2015. Attenuation of ER stress prevents post-infarction-induced cardiac rupture and remodeling by modulating both cardiac apoptosis and fibrosis. *Chem. Biol. Interact.* 225, 90–98.
- Mao, X.R., Crowder, C.M., 2010. Protein misfolding induces hypoxic preconditioning via a subset of the unfolded protein response machinery. *Mol. Cell. Biol.* 30, 5033–5042.
- Mao, C., Wang, M., Luo, B., Wey, S., Dong, D., Wesselschmidt, R., Rawlings, S., Lee, A.S., 2010. Targeted mutation of the mouse Grp94 gene disrupts development and perturbs endoplasmic reticulum stress signaling. *PLoS ONE* 5, e10852.
- Marciniak, S.J., Yun, C.Y., Oyadomari, S., Novoa, I., Zhang, Y., Jungreis, R., Nagata, K., Harding, H.P., Ron, D., 2004. CHOP induces death by promoting protein synthesis and oxidation in the stressed endoplasmic reticulum. *Genes Dev.* 18, 3066–3077.
- Matsuoka, M., Komoike, Y., 2015. Experimental evidence shows salubrinal, an eIF2 α dephosphorylation inhibitor, reduces xenotoxicant-induced cellular damage. *Int. J. Mol. Sci.* 16 (7), 16275–16287.
- Maurel, M., Chevet, E., Tavernier, J., Gerlo, S., 2014. Getting RIDD of RNA: IRE1 in cell fate regulation. *Trends Biochem. Sci.* 5, 245–254.
- Medigeshi, G.R., Lancaster, A.M., Hirsch, A.J., Briese, T., Lipkin, W.I., DeFilippis, V., Früh, K., Mason, P.W., Nikolich-Zugich, J., Nelson, J.A., 2007. West Nile virus infection activates the unfolded protein response, leading to CHOP induction and apoptosis. *J. Virol.* 81, 10849–10860.
- Mesaeli, N., Nakamura, K., Zvaritch, E., Dickie, P., Dziak, E., Krause, K.H., Opas, M., MacLennan, D.H., Michalak, M., 1999. Calreticulin is essential for cardiac development. *J. Cell Biol.* 144, 857–868.
- Michalak, M., Gye, M.C., 2015. Endoplasmic reticulum stress in periimplantation embryos. *Clin. Exp. Reprod. Med.* 42, 1–7.
- Miharada, K., Karlsson, G., Rehn, M., Rörby, E., Siva, K., Jörg, C., Karlsson, S., 2011. Cripto regulates hematopoietic stem cells as a hypoxic-niche-related factor through Cell Surface Receptor GRP78. *Cell Stem Cell* 9, 330–344.
- Miharada, K., Sigurdsson, V., Karlsson, S., 2014. Dppa5 improves hematopoietic stem cell activity by reducing endoplasmic reticulum stress. *Cell Rep.* 7, 1381–1392.
- Mintz, M., Vanderver, A., Brown, K.J., Lin, J., Wang, Z., Kaneski, C., Schiffmann, R., Nagaraju, K., Hoffman, E.P., Hathout, Y., 2008. Time series proteome profiling to study endoplasmic reticulum stress response. *J. Proteome Res.* 6, 2435–2444.
- Ni, M., Lee, A.S., 2007. ER chaperones in mammalian development and human diseases. *FEBS Lett.* 581, 3641–3651.
- Nishitoh, H., 2012. CHOP is a multifunctional transcription factor in the ER stress response. *J. Biochem.* 151, 217–219.
- Ogata, M., Hino, S., Saito, A., Morikawa, K., Kondo, S., Kanemoto, S., Murakami, T., Taniguchi, M., Tani, I., Yoshinaga, K., Shiosaka, S., Hammarback, J.A., Urano, F., Imaizumi, K., 2006. Autophagy is activated for cell survival after endoplasmic reticulum stress. *Mol. Cell. Biol.* 26, 9220–9231.
- Ono, S.J., Liou, H.C., Davidon, R., Strominger, J.L., Glimcher, L.H., 1991. Human X-box-binding protein 1 is required for the transcription of a subset of human class II major histocompatibility genes and forms a heterodimer with c-fos. *Proc. Natl. Acad. Sci. U.S.A.* 88, 4309–4312.
- Ozcan, L., Tabas, I., 2012. Role of endoplasmic reticulum stress in metabolic disease and other disorders. *Annu. Rev. Med.* 63, 317–328.
- Ozcan, U., Yilmaz, E., Ozcan, L., Furuhashi, M., Vaillancourt, E., Smith, R.O., Görgün, C.Z., Hotamisligil, G.S., 2006. Chemical chaperones reduce ER stress and restore glucose homeostasis in a mouse model of type 2 diabetes. *Science* 313, 1137–1140.
- Palade, G.E., 1956. The endoplasmic reticulum. *J. Biophys. Biochem. Cytol.* 2, 85–98.
- Palade, G.E., Siekevitz, P., 1956a. Liver microsomes; an integrated morphological and biochemical study. *J. Biophys. Biochem. Cytol.* 2, 171–200.
- Palade, G.E., Siekevitz, P., 1956b. Pancreatic microsomes; an integrated morphological and biochemical study. *J. Biophys. Biochem. Cytol.* 2, 671–690.
- Parker, R., Phan, T., Baumeister, P., Roy, B., Cheryath, V., Roy, A.L., Lee, A.S., 2001. Identification of TFII-I as the endoplasmic reticulum stress response element binding factor ERSF: its autoregulation by stress and interaction with ATF6. *Mol. Cell. Biol.* 21, 3220–3233.
- Porter, K.R., Claude, A., Fullam, E.F., 1945. A study of tissue culture cells by electron microscopy: methods and preliminary observations. *J. Exp. Med.* 81, 233–246.
- Reimold, A.M., Iwakoshi, N.N., Manisk, J., Vallabhajosyula, P., Szomolanyi-Tsuda, E., Gravalles, E.M., Friend, D., Grusby, M.J., Altk, F., Glimcher, L.H., 2001. Plasma cell differentiation requires the transcription factor XBP-1. *Nature* 412, 300–307.
- Ruberti, C., Brandizzi, F., 2014. Conserved and plant-unique strategies for overcoming endoplasmic reticulum stress. *Front. Plant Sci.* 5, 1–8.
- Saretzki, G., Armstrong, L., Leake, A., Lako, M., von Zglinicki, T., 2004. Stress defense in murine embryonic stem cells is superior to that of various differentiated murine cells. *Stem Cells* 22, 962–971.
- Saretzki, G., Walter, T., Atkinson, S., Passos, J.F., Bareth, B., Keith, W.N., Stewart, R., Hoare, S., Stojkovic, M., Armstrong, L., von Zglinicki, T., Lako, M., 2008. Downregulation of multiple stress defense mechanisms during differentiation of human embryonic stem cells. *Stem Cells* 26, 455–464.
- Simard, J.C., Vallieres, F., de Liz, R., Lavastre, V., Girard, D., 2015. Silver nanoparticles induce degradation of the endoplasmic reticulum stress sensor activating transcription factor-6 leading to activation of the NLRP-3 inflammasome. *J. Biol. Chem.* 290, 5926–5939.
- Schubert, U., Antón, L.C., Gibbs, J., Norbury, C.C., Yewdell, J.W., Bannink, J.R., 2000. Rapid degradation of a large fraction of newly synthesized proteins by proteasomes. *Nature* 404, 770–774.

- Song, B., Scheuner, D., Ron, D., Pennathur, S., Kaufman, R.J., 2008. **Chop deletion reduces oxidative stress, improves β cell function, and promotes cell survival in multiple mouse models of diabetes.** *J. Clin. Invest.* 118, 3378–3389.
- Takahashi, K., Yamanaka, S., 2006. **Induction of pluripotent stem cells from mouse embryonic and adult fibroblast cultures by defined factors.** *Cell* 126, 663–676.
- Thomson, J., Itskovitz-eldor, J., Shapiro, S.S., Waknitz, M., Swiergiel, J.J., Marshall, V.S., Jones, J.M., 1998. **Embryonic stem cell lines derived from human blastocysts.** *Science* 282, 1145–1148.
- Ulianich, L., Garbi, C., Treglia, A.S., Punzi, D., Miele, C., Raciti, G.A., Beguinot, F., Consiglio, E., Di Jeso, B., 2007. **ER stress is associated with dedifferentiation and an epithelial-to-mesenchymal transition-like phenotype in PC C13 thyroid cells.** *J. Cell Sci.* 121, 477–486.
- Urano, F., Wang, X.Z., Bertolotti, A., Zhang, Y., Chung, P., Harding, H.P., Ron, D., 2000. **Coupling of stress in the ER to activation of JNK protein kinases by transmembrane protein kinase IRE1.** *Science* 287, 664–666.
- Wanderling, S., Simen, B.B., Ostrovsky, O., Ahmed, N.T., Vogen, S.M., Gidalevitz, T., Argon, Y., 2008. **GRP94 is essential for mesoderm induction and muscle development because it regulates insulin-like growth factor secretion.** *Mol. Biol. Cell.* 18, 3764–3775.
- Wey, S., Luo, B., Lee, A.S., 2012. **Acute inducible ablation of GRP78 reveals its role in hematopoietic stem cell survival, lymphogenesis and regulation of stress signaling.** *PLoS ONE* 7, e39047 (2012).
- Wu, J., Rutkowski, D.T., Dubois, M., Saunders, T., Wang, J., Yau, G.D., Kaufman, R.J., 2007. **ATF6alpha optimizes long-term endoplasmic reticulum function to protect cells from chronic stress.** *Dev. Cell* 13 (3), 351–364.
- Xiong, Z., Jiang, R., Zhang, P., Han, X., Guo, F.J., 2015. **Transmission of ER stress response by ATF6 promotes endochondral bone growth.** *J. Orthop. Surg. Res.* 10, 141–152.
- Xu, H., Tsang, K.S., Wang, Y., Chan, J.C.N., Xu, G., Gao, W.Q., 2014. **Unfolded protein response is required for the definitive endodermal specification of mouse embryonic stem cells via Smad2 and β -catenin signaling.** *J. Biol. Chem.* 289, 26290–26301.
- Yamamoto, K., Sato, T., Matsui, T., Sato, M., Okada, T., Yoshida, H., Harada, A., Mori, K., 2007. **Transcriptional induction of mammalian ER quality control proteins is mediated by single or combined action of ATF6 α and XBP1.** *Dev. Cell* 13 (3), 365–376.
- Yoon, S.B., Choi, S.A., Sim, B.W., Mun, K.J.S., Jeong, S.E., Yang, P.S., Lee, H.J., Park, Y., Song, Y.H., Kim, B.S., Jeong, Y.H., Huh, K.J., Lee, J.W., Kim, S.R., Chang, S.U.K.T., 2014. **Developmental competence of bovine early embryos depends on the coupled response between oxidative and endoplasmic reticulum stress.** *Biol. Reprod.* 90, 1–10.
- Yoshida, H., Matsui, T., Yamamoto, A., Okada, T., Mori, K., 2001. **XBP1 mRNA is induced by ATF6 and spliced by IRE1 in response to ER stress to produce a highly active transcription factor.** *Cell* 107, 881–891.
- Yoshida, H., Nadanaka, S., Sato, R., Mori, K., 2006. **XBP-1 is critical to protect cells from endoplasmic reticulum stress: evidence from Site-2 protease-deficient Chinese hamster ovary cells.** *Cell Struct. Func.* 31, 117–125.
- Zamecnik, P.C., Keller, E.B., 1954. **Relation between phosphate energy donors and incorporation of labeled amino acids into proteins.** *J. Biol. Chem.* 209, 337–354.
- Zhang, J.Y., Diao, Y.F., Oqani, R.K., Han, R.X., Jin, D.I., 2012. **Effect of endoplasmic reticulum stress on porcine oocyte maturation and parthenogenetic embryonic development in vitro.** *Biol. Reprod.* 86, 128–128.
- Zhang, K., Wong, H.N., Song, B., Miller, C.N., Scheuner, D., Kaufman, R.J., 2005. **The unfolded protein response sensor IRE1 α is required at 2 distinct steps in B cell lymphopoiesis.** *J. Clin. Invest.* 115 (2), 268–281.
- Zhang, P., McGrath, B., Li, S., Frank, A., Zambito, F., Reinert, J., Gannon, M., Ma, K., McNaughton, K., Cavener, D.R., 2002. **The PERK eukaryotic initiation factor 2. Kinase is required for the development of the skeletal system, postnatal growth, and the function and viability of the pancreas.** *Mol. Cell. Biol.* 22, 3864–3874.
- Zhong, Q., Zhou, B., Ann, D.K., Mino, P., Liu, Y., Banfalvi, A., Krishnaveni, M.S., Dubourd, M., Demaio, L., Willis, B.C., Kim, K.J., duBois, R.M., 2011. **Role of endoplasmic reticulum stress in epithelial-mesenchymal transition of alveolar epithelial cells.** *Am. J. Respir. Cell Mol. Biol.* 45, 498–509.

6. Vašíčková K, Horak P, **Vaňhara P. TUSC3: functional duality of a cancer gene.**

Cellular and Molecular Life Sciences 2017; **75**(5):849-857.

Commentary:

TUSC3 emerged as a clinically relevant gene in cancer, involved in regulation of N-glycosylation and ER-stress, and influencing patients' outcome. In this review, we discuss its function in normal and cancerous tissues and describe the molecular mechanisms involved and envisage a possible role of TUSC3 beyond endoplasmic reticulum. We envisage that TUSC3 affects the N-glycosylation of protein substrates, hence alter the spectrum of surface molecules accessible to immune system and determine cell response to immunosurveillance and immunoediting within tissues.

DOI: 10.1007/s00018-017-2660-4

Journal: Nature Communications, Cellular and Molecular Life Sciences

Impact factor (WOS, 2017): 6.721

Number of citations (WOS, 2018): 2

Most important citation:

Jeon Y-J, Kim T, Park D, Nuovo G, Rhee S, Joshi P et al. **miRNA-mediated TUSC3 deficiency enhances UPR and ERAD to promote metastatic potential of NSCLC.** *Nature Communications* 2018; **9**:5110. doi: 10.1038/s41467-018-07561-8. (IF2018 12.353)

Contribution of the author: Corresponding author. Design and writing of manuscript.



TUSC3: functional duality of a cancer gene

Kateřina Vařickov^{1,2} · Peter Horak^{3,4} · Petr Vaňhara^{1,2} 

Received: 3 August 2017 / Accepted: 13 September 2017
© Springer International Publishing AG 2017

Abstract Two decades ago, following a systematic screening of LOH regions on chromosome 8p22, TUSC3 has been identified as a candidate tumor suppressor gene in ovarian, prostate and pancreatic cancers. Since then, a growing body of evidence documented its clinical importance in various other types of cancers, and first initial insights into its molecular function and phenotypic effects have been gained, though the precise role of TUSC3 in different cancers remains unclear. As a part of the oligosaccharyltransferase complex, TUSC3 localizes to the endoplasmic reticulum and functions in final steps of N-glycosylation of proteins, while its loss evokes the unfolded protein response. We are still trying to figure out how this mechanistic function is reconcilable with its varied effects on cancer promotion. In this review, we focus on cancer-related effects of TUSC3 and envisage a possible role of TUSC3 beyond endoplasmic reticulum.

Keywords TUSC3 · Cancer · Tumor suppressor · Oncogene · Endoplasmic reticulum · N-Glycosylation · Immunoediting

Introduction

Development of cancer is a complex process involving stepwise series of molecular events that finally culminate in alterations of normal cellular phenotype towards malignancy. Genes that enhance or inhibit tumor growth—oncogenes and tumor suppressors—are usually assigned various aspects of cellular function, such as mitogenic and differentiation signaling, DNA damage repair, or apoptosis. The classical concept of carcinogenesis is based on impairment or activation of major oncogenes and tumor suppressors, making the development of malignant phenotype a cell-intrinsic and unambiguous process. Today we know, however, that tumor cell independent effects within the tumor microenvironment as well as immunoediting have significant impact on tumor development [1]. Screening of tumors and cancer cells by high-throughput omics technologies that allow global assessment of expression or mutational profiles revealed a high number of unapparent genes that possess a dual character in different cancers and lack a clear link to the classical molecular machineries driving cancer development. These minor drivers involved in general cell and tissue metabolism and homeostasis can switch from oncogene to tumor suppressor function depending on the cell and tissue context as well as the composition of the microenvironmental niche [2]. In this review, we discuss such dual role for Tumor Suppressor Candidate 3 (TUSC3) and envision its function in normal or cancerous tissues within specific contexts.

Tusc3 gene (N33) is localized on the short arm of chromosome 8 in a chromosomal band 8p22. It is encoded by 224 kbp genomic DNA and encompasses 11 exons, constituting three prototypical different transcripts [3]. The product of transcript 1 contains 11 exons encoding 348 amino acids with molecular weight of 39 kDa. Prototypically, it

✉ Petr Vaňhara
PVanhara@med.muni.cz

¹ Department of Histology and Embryology, Faculty of Medicine, Masaryk University, Kamenice 126/3, 625 00 Brno, Czech Republic

² International Clinical Research Center, St. Anne's University Hospital Brno, Pekařská 53, 65691 Brno, Czech Republic

³ Department of Translational Oncology, National Center for Tumor Diseases (NCT), Im Neuenheimer Feld 460, 69120 Heidelberg, Germany

⁴ German Cancer Research Center (DKFZ), Heidelberg, Germany

contains a thioredoxin domain with peptide-binding site and five predicted transmembrane domains, one of which is deleted in the final TUSC3 product. The transcript 2, lacking exon 10, and transcript 3, lacking three exons, encode 347 and 314 amino acids, respectively. Transcripts 1 and 2 are abundantly expressed in most non-lymphoid tissues [3, 4], while the transcript number 3 is predominantly expressed in placenta [4]. Interestingly, according to Ensembl gene annotation system (release 89—May 2017), 13 different transcripts or splice variants were predicted, but not all being translated [5].

Cellular functions of TUSC3: lessons from glycochemistry

Until recently, function of TUSC3 has only been assumed by its partial sequence homology with the yeast Ost3p subunit of the oligosaccharyltransferase (OST) complex within the endoplasmic reticulum (ER). In yeast, OST complex consists of eight subunits including Ost3p (Ost1p, Ost2p, Ost3p or Ost6p, Ost4p, Ost5p, Wbp1p, Swp1p and Stt3p) [6]. OST complex mediates a key step of protein N-glycosylation, the en bloc transfer of a preassembled oligosaccharide from a lipid-linked donor onto asparagine residues of nascent proteins entering the lumen of rough ER. The asparagine residues constitute the Asn-X-Ser/Thr (N-X-T/S) consensus sequence, where X can be any amino acid residue except proline that are read by OST and covalently modified [7]. Human OST complex contains seven subunits—catalytic core STT3A or STT3B, five non-catalytic subunits (ribophorin I, ribophorin II, OST48, DAD1 and OST4) and one of the isoform specific subunits KCP2 or DC2 for STT3A complex and MagT1 or TUSC3 for STT3B as documented for HeLa and Cho cells or using recombinant OST complex in vitro [7, 8].

In human cancer cells, TUSC3 indeed localizes to the rough ER as an intrinsic part of the OST complex directly binding to the STT3A or STT3B catalytic core [9, 10]. The STT3A OST complex is associated with the protein translocation channel and glycosylates the majority of acceptor sites of human glycoproteins as they enter the lumen of the ER, while the STT3B complex binds to and glycosylates acceptor sites that have been skipped by the STT3A complex [11, 12]. Thus, both complexes are essential for achievement of full N-glycoproteome [12].

Both the TUSC3 (yeast Ost3p) and MagT1 (yeast Ost6p) proteins bind to the STT3B complex in vitro and share 73% sequence identity. Both proteins are linked to the ER membrane by four transmembrane spanning segments and their N-terminal luminal domain consists of a thioredoxin fold with a peptide-binding site (CXXC motif) [11]. In yeast, neither Ost3p nor Ost6p are necessary for functional OST,

as the single disruption causes only a moderate hypoglycosylation. However, the double knockdown of Ost3p and Ost6p resulted in a severe defect of N-glycosylation [13]. Such functional redundancy was also observed for MagT1 and TUSC3 in the human OST complex [12]. Similarly, the absence of both MagT1 and TUSC3 subunits or loss of STT3B causes a dramatic reduction of N-glycosylation [14].

TUSC3 seems to increase glycosylation efficiency for specific human glycoproteins by delaying oxidative substrate folding and increasing the probability of recognition of N-glycosylation sequon, envisaging the role for TUSC3 in substrate selection [7]. The direct targets of TUSC3 in OST remain unknown, except for integrin β 1 [10]. Consequently, deregulation of TUSC3 probably does not impair the overall systemic rate of glycosylation, as documented by the absence of hypoglycosylation of total serum transferrin or alteration of the serum N-glycome analyzed by mass spectrometry [12, 15]. In prostate cancer cells, slightly reduced N-glycosylation efficiency was observed in TUSC3-silenced cells using the ER-localized luciferase reporter construct [16].

Apart from N-glycosylation, TUSC3 and MagT1 were proposed to be plasma membrane-associated magnesium transporters [17]. Expression of MagT1, but not TUSC3, was upregulated in yeast cultured in medium depleted of magnesium while overexpression of both MagT1 and TUSC3 resulted in modestly higher cellular Mg^{II+} uptake [18]. However, unequivocal evidence for direct ion transporting has not been provided. Rather, TUSC3 and MagT1 influence the Mg^{II+} homeostasis indirectly by N-glycosylation of a specific protein required for Mg^{II+} transport.

TUSC3 in embryonic development

Expression of TUSC3 differs in individual tissues and stages of embryonic development [3, 15, 18] (Table 1) and what is of particular importance, its normal expression levels can be related with oncogenic or tumor-suppressive function in particular cancers. In contrast, the expression of human TUSC3 paralog, MagT1, is ubiquitous [3].

The roles of TUSC3 and its paralog, MagT1, in general vertebrate development were investigated in zebrafish recently [18]. Zebrafish MagT1 and TUSC3 genes share 80 and 93% homology with their human counterparts, respectively. TUSC3 and MagT1 double knockdown severely reduced hatching of the embryos to only 5%, while a single knockdown only impaired the hatching rate if the expression was reduced at both maternal and zygotic levels. This confirms the requirement of TUSC3 and MagT1 for embryonic development of vertebrates and also their partial functional redundancy.

Table 1 TUSC3 expression in human tissues

High TUSC3	Low or absent TUSC3
Heart	Kidney
Cerebellum	Spinal cord
Fetal brain	Adult brain
Ovary	Trachea
Cervix	Lung
Placenta	Colon
Prostate	Small intestine
Testis	Spleen
Adipose tissue	Bone marrow
	Thyroid gland
	Liver
	Thymus
	Peripheral lymphocytes
	Uterus

While the role of TUSC3 in histogenesis of most tissues is unknown, a pilot study has already been performed for rat testicular development, documenting its elevated expression in seminiferous tubules, including interstitial Leydig cells, and also in prostate epithelial cells [4]. In human trophoblast, TUSC3 is normally highly expressed, but downregulated in response to hypoxia exposure [19] which correlated with human placental pathologies including preeclampsia [20]. Indeed, TUSC3 promoter hypermethylation in trophoblasts was more frequent in patients with preeclampsia than without any metabolic pregnancy complications. TUSC3 hypermethylation was not observed in maternal blood or fetal tissues other than placenta [21].

TUSC3 is abundantly expressed in developing fetal brain, and truncating mutations as well as homozygous germline deletions were associated with autosomal recessive (AR) non-syndromic intellectual disability (NSID) [15, 22, 23]. Typically, AR-NSID affects about 1% of general population with substantial heterogeneity [24]. So far, approximately 40 genes correlating with AR-NSID were identified, including TUSC3 [25]. Molinari et al. performed autozygosity mapping in two siblings affected by intellectual disability born to first-cousin parents and identified a culprit region on 8p22–p23.1. Subsequent sequencing uncovered a 1 bp insertion in TUSC3 gene resulting in a premature stop codon and reduced amount of transcript mRNA [15]. Garshasbi et al. [22] identified a homozygous deletion including the first exon of TUSC3 in a large consanguineous Iranian family with AR-NSID. Third novel deletion mutation involving almost full TUSC3 gene was reported in a large consanguineous Pakistani family [28] and other reports of families with NSID additionally supported TUSC3 role in the development of cognitive functions [23, 26–31]. All affected patients exhibited mild to severe intellectual disability, while

their parents were all heterogeneous for TUSC3 gene and exhibited intelligence in the normal range. Additionally, despite the fact that the TUSC3-induced intellectual disability is mostly referred as non-syndromic, some TUSC3-affected patients across the different studies exhibited similar minor anomalies including short stature, microcephaly, hypoplastic philtrum, hypertelorism and other moderate dysmorphic facial features. Interestingly, three patients studied by Molinari et al. [15] died due to cancer. A population study using common SNPs from 40 genes known to be associated with AR-NSID, including TUSC3, found no association between SNP distribution in these genes and normal range of intelligence, suggesting that intellectual disability is probably genetically divergent from the normal variation of intelligence differences [25]. Except for the localization of TUSC3 expression to the fetal brain and the genetic link to NSID there are currently no functional studies concerning TUSC3 role in developing neural tissue or cognitive functions either in impairing of intracellular signaling or altering N-glycosylation patterns.

Epigenetic regulation of TUSC3 expression

Sequence of TUSC3 gene contains multiple CpG islands spanning its promoter and first exon; hence in several cancer types its expression is frequently silenced by promoter hypermethylation. In particular, hypermethylation of TUSC3 promoter was observed in colorectal cancer (CRC) [32–34], glioblastoma multiforme (GBM) [35], non-small-cell lung cancer (NSCLC) [36], lung cancer [37] and ovarian cancer [38] (Table 2).

In CRC, methylation of TUSC3 was elevated in tumor tissue compared to surrounding normal colon tissue or colonic mucosa of healthy donors [32, 39]. TUSC3 hypermethylation was also confirmed in adenomatous colorectal polyps and in colorectal mucosa of patients with ulcerative colitis which is among the common risk factors for developing CRC, suggesting that TUSC3 hypermethylation might be an early event in CRC [31, 40]. Nevertheless, in an independent cohort, TUSC3 methylation did not significantly differ between the normal mucosa of the non-cancerous patients and adenomatous polyps or tumor samples [34]. Furthermore, TUSC3 showed partial methylation in normal colorectal mucosa which was progressively increasing with age with frequency of around 15% in patients less than 20 years old and up to 58% in patients over 60 years of age [31, 33, 39]. Age-related TUSC3 hypermethylation was also observed in GBM [35], peripheral blood leukocyte DNA [31, 41], and in cases of NSCLC [42].

TUSC3 hypermethylation was found in 59% cases of GBM, and corresponding with methylation of the estrogen receptor (ESR) [35]. Methylation of TUSC3, estrogen

Table 2 Molecular phenotypes associated with TUSC3 in different types of cancer

Cancer	Expression change OF TUSC3	TUSC3-associated molecular phenotype	Integrated role	References
Ovary	Downregulation by promoter hypermethylation	UPR EMT	TSG	[10, 38, 61]
PROSTATE	Downregulation	UPR N-Glycosylation Akt	TSG	[9]
Glioblastoma multiforme	Downregulation by promoter hypermethylation	Akt	TSG	[35, 63]
Breast cancer	Downregulation by miRNA	(1) SOX2 (2) miR-181a-5p (2) miR-30e-5p	TSG	[72, 73]
Pancreatic cancer	Homozygous deletion	NF- κ B	TSG	[48, 62]
Oral squamous cell carcinoma	Homozygous deletion	N/A	TSG	[74]
Hepatocellular carcinoma	Loss of heterozygosity	N/A	N/A	[46]
Small cell lung cancer	Downregulation	N/A	TSG	[75]
Larynx and pharynx carcinoma	Loss	N/A	TSG	[76]
Esophageal squamous cell carcinoma	Downregulation	N/A	TSG	[77]
Non-small-cell lung cancer	Downregulation by promoter hypermethylation	Wnt/ β -catenin	TSG	[78]
Colorectal cancer	Upregulation	Hedgehog	Oncogene	[64]
	Upregulation	MAPK PI3K/Akt Wnt/ β -catenin	Oncogene	[60]
Head and neck squamous carcinoma	Upregulation by amplification	N/A	Oncogene	[59]
Thyroid cancer	Upregulation (gain)	N/A	Oncogene	[57, 59]

N/A not applicable (data unavailable)

receptor and MYOD1 were also found in colonic tissue of healthy individuals and in patients with ulcerative colitis [33, 40]. However, epigenetic patterns seem to be tissue specific, as the TUSC3 methylation is more frequent in the colon than in the liver, while methylation of ESR is higher in the liver [32]. Additionally, TUSC3 is methylated in both colonic epithelial and subepithelial connective tissues, whereas ESR shows higher methylation in the epithelium.

In DNA of peripheral white blood cells in a Chinese population with high risk of gastric cancer, TUSC3 methylation preceded approximately 5 years the clinical manifestation, suggesting that downregulation of TUSC3 can be a part of complex alterations as a biomarker for early diagnosis of gastric cancer [31]. Apart from that, TUSC3 methylation seems to be an effective prognostic marker in lung and ovarian cancers [37, 38]. The promoter of TUSC3 was frequently methylated in tumors, benign bronchi and alveolar lung tissues from lung cancer patients, but not in healthy individuals. No significant association was found between TUSC3 promoter methylation and age, grading, tumor histology, or lymph node or distant metastasis, but TUSC3 methylation correlated with smaller tumor size and longer overall survival of lung cancer patients [37]. In contrast, TUSC3 methylation and consequent low mRNA expression in ovarian cancer were associated with shorter progression-free and overall survival [38]. This correlation was independent of other risk factors including age,

FIGO stage, histologic grade, or response to chemotherapy, making TUSC3 an independent candidate biomarker for ovarian cancer. In acute lymphoblastic leukemia (ALL), TUSC3 is hypermethylated in significantly higher frequency than in AML [43]. Microarray-based DNA methylation analysis covering 249 CpG islands of 57 genes was performed on mononuclear cells from patients with ALL and AML and TUSC3 methylation showed the highest divergence between AML and ALL.

Additionally, there is a potential shift towards increased methylation of TUSC3 promoter in men vs. women, and smokers vs. non-smokers [32, 41]. However, other studies found no correlation between TUSC3 methylation and gender, smoking or alcohol abuse [31, 33, 40, 44], suggesting the presence of complex epigenetic patterns of TUSC3 depending on investigated population, ethnical origin or clinical background. Rigorous population analyses of TUSC3 expression or epigenetic patterns are thus necessary to reveal the role of TUSC3 as a cancer-associated predictor.

TUSC3 in cancer

TUSC3 as tumor suppressor

First evidence for tumor-suppressive functions of TUSC3 came from systematic screenings of the chromosomal band 8p22 that is often lost in wide variety of epithelial cancers, including prostate [45], ovarian [46], breast [47], pancreatic [48], bladder [49], colorectal [46, 50], hepatocellular, NSCLC, or choriocarcinoma [51]. Particularly in prostate cancer, loss of the short arm of chromosome 8 is the most frequent genetic alteration occurring in over 60% of cases [52].

Substantial advance in searching for potential tumor suppressors in 8p22 was achieved by Bova [45], who constructed a deletion map of the 8p22 in prostate cancer and confined the common deletion interval to a 14 cM area. Next, a physical map of a 1–1.5 Mb deletion interval revealed six novel transcription units representing candidate tumor suppressor genes [53]. Pils et al. [54] then reported that five genes from the total of 22 genes located on the 8p22 band showed significantly reduced expression in ovarian tumors and two genes—TUSC3 and EFA6R—correlated with patient survival and offered prognostic information. Additionally, TUSC3 expression was lower in advanced ovarian cancer compared to low-grade tumors. At the same time, Bashyam et al. [48] described a TUSC3 homozygous deletion in pancreatic cancer by comparative genomic hybridization (CGH). Cooke et al. [55] used high-resolution array CGH in breast cancer cell lines and identified two putative tumor suppressors—TUSC3 and ARHGEF10—in the same chromosomal region.

Shortly after TUSC3 was identified as a possible tumor suppressor candidate at 8p22, the evidence for its involvement in pathogenesis of various cancer entities widened. The most common genetic aberration of TUSC3 gene in tumors is homozygous deletion, which was revealed in various human cancers (Table 2). Loss of TUSC3 was also found in cases of canine osteosarcoma [56]. In lung, esophageal, pancreatic, larynx and pharynx cancers, association between low TUSC3 expression and lymph node or distant metastasis formation was described. DNA amplification or elevated expressions of TUSC3 were found in papillary thyroid cancer [57, 58], head and neck squamous carcinoma [59], and CRC [60].

In vitro studies revealed that downregulation of TUSC3 in ovarian cancer cells resulted in increased proliferation, migration and adhesion to extracellular matrix [10, 38]. Similar results were found in prostate cancer [9]. Moreover, knockdown of TUSC3 was accompanied with ER rearrangements and alterations in unfolded protein response (UPR). Additionally, in PTEN negative PC3 cell line, loss of TUSC3 promoted Akt activity in serum starved cells. In ovarian

cancer, cells lacking TUSC3 displayed dilated ER cisternae and activation of PERK-mediated UPR pathway [61]. Loss of TUSC3 was accompanied by decreased expression of epithelial markers together with upregulation of mesenchymal markers and epithelial-to-mesenchymal transition (EMT) transcription factors resulting in enhanced cell migration. Moreover, these effects were enhanced under ER-stress conditions. Interestingly, silencing of TUSC3 augmented formation of 3D cell clusters under low-adhesion conditions, mimicking spreading of ovarian cancer through peritoneum.

The in vivo data based on subcutaneous xenografts were provided for ovarian [61], prostate [9] and pancreatic cancers [62] where cancer cells lacking TUSC3 generally developed larger tumors and in case of ovarian cancer also massively disseminated through peritoneum [61]. In GBM, decreased expression of TUSC3 due to promoter hypermethylation protected GBM cells from apoptosis, while TUSC3 overexpression induced caspase-3 activity. GBM cells lacking TUSC3 had also a high rate of proliferation dependent on Akt signaling [63], similar to the Akt-dependent phenotype observed in prostate cancer [9]. In pancreatic cancer, TUSC3 downregulation corresponded with higher tumor stage and worse patient survival, while in vitro, TUSC3 knockdown in three different cell lines negatively influenced NF- κ B activity [62]. Pancreatic cancer cell lines with decreased TUSC3 also exhibited enhanced proliferation, migration and invasion capability and resulted in more aggressive phenotype with more frequent liver metastases in mouse models [62].

TUSC3 as oncogene

In colorectal carcinoma, TUSC3 levels were found upregulated in tumor tissue when compared to surrounding non-malignant stroma [60]. Interestingly, when the CRC cell lines LS174T and HCT116 were transduced with lentiviral vectors coding for TUSC3, the non-invasive epithelial phenotype was converted to invasive mesenchymal phenotype, followed by downregulation of E-cadherin and upregulation of vimentin. Downregulation of TUSC3 in HT29 and SW480 CRC cell lines repressed the proliferation and migration in vitro and led to a decreased growth of xenografts in vivo. On the molecular level, WNT/ β -catenin and MAPK signaling were activated in TUSC3-overexpressing CRC lines, while Akt and ERK1 phosphorylation was attenuated. Interestingly, physical interaction between TUSC3 and β -catenin was revealed by co-immunoprecipitation by Gu et al. [60]. Similarly, in NSCLC, overexpression of TUSC3 increased proliferation and suppressed apoptosis of NSCLC H322 model cell line. In tumor tissues, staining for TUSC3 positively correlated with the TNM stage and presence of distant metastases, while in normal lung tissue the TUSC3 expression was maintained low or below detection limits [64]. Further screening for molecular pathways affected by

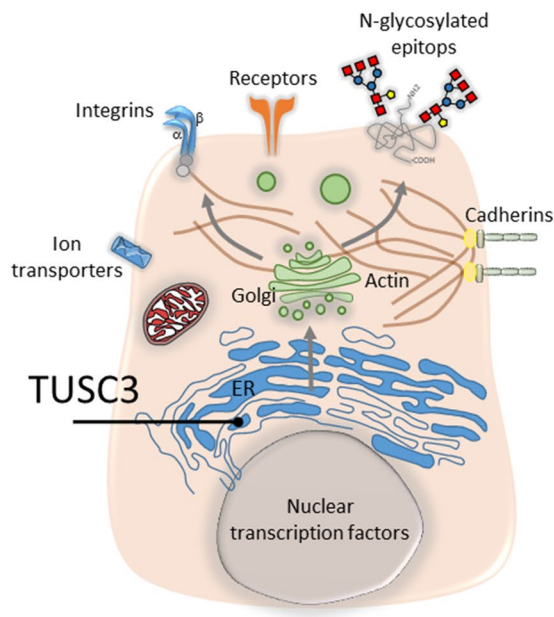


Fig. 1 Immunoediting mechanisms associated with TUSC3. TUSC3 residing in the ER enzymatic machinery determines substrates for N-glycosylation by oligosaccharyl transferase (OST) complex. Depending on the availability of proteins entering the ER and given the gatekeeper function of the OST complex, cancer cells can exhibit

Elimination phase: Cancer cells with immunosuppressive phenotype and low immunogenicity escape eradication

- Modulation of ER-stress response (PERK, IRE1 α)
- Apoptosis
- N-glycosylation (Itg β 1)



Equilibrium phase: Clonal expansion of immuno-evasive cancer cells

- Proliferation (Akt, Hedgehog)
- Direct immunosuppression (TGF β 1 and GDF-15)



Escape phase: Development of invasive cancer

- Adhesion (E-cadherin, ZO-1)
- EMT control (Slug, Snail, TCF8/Zeb)
- Migration and invasion



various patterns of glycosylated surface or secreted proteins with altered functional domains. Regulation of the OST complex through TUSC3 can potentially impact all major classes of signaling molecules involved in immunoediting

TUSC3 in lung cancer identified Hedgehog (HH) signaling axis to be involved in TUSC3-dependent manner. Using A549 cells, levels of proteins downstream to HH signaling, such as GLI1, SMO, PTCH1, and PTCH2 were increased in TUSC3 expressing cells. Physical interaction between TUSC3 and GLI1 was also detected, suggesting so far unknown roles of TUSC3 beyond ER. Missense mutations in TUSC3 have been reported in cases of relapsing ALL [65], further suggesting its role in ER-stress or N glycosylation besides solid cancers. Interestingly, activation of UPR upon induction of ER-stress led to enhanced activity of major leukemic drivers, such as PML-RAR α [66] or inactivation of differentiation factors, such as C/EBP α [67] in AML or BCR-Abl [68] in B cell ALL.

TUSC3 as a cancer-related gene

Experiments performed indicate a convergence on several signaling pathways altered in distinct manner in TUSC3-deregulated cancer cells, such as Akt, suggesting that TUSC3 is involved in selection of particular substrates that directly or indirectly affect the molecular signaling pathways (Table 2). Addressing potential physical interactions of TUSC3 with major components of oncogenic signaling

pathways, such as MTOR/Akt, Wnt/ β -catenin or Hedgehog will raise a question of non-canonical roles of TUSC3 next to ER-localized N-glycosylation. However, TUSC3-driven substrate specificity of OST can alter expression of surface receptors or molecules mediating cell–cell or cell–matrix interactions, as documented for E-cadherin or Integrin β 1 [10, 61]. Portfolio of potential targets is probably extremely broad considering that approximately up to one-fifth of the proteome can be glycosylated in the ER [69]. Due to TUSC3 association with high-grade cancer, it is likely to be involved in the immunoediting of cancer cells by immune system (Fig. 1) [70], providing the hypothetical platform for explaining the molecular or cellular context where TUSC3 acts either as a tumor suppressor or an oncogene. Thus, in addition to cell-intrinsic phenotypic conversions, such as EMT, or reduced sensitivity to apoptosis, subtle alterations of N-glycosylation patterns in TUSC3-deregulated cancer cells enable survival during the elimination phase and immune escape and drive the expansion of non-immunogenic cancer clones [71]. Indeed, we documented that immunosuppressive cytokines TGF β 1 and GDF-15 are upregulated in TUSC3-silenced cells [61], raising the possibility of backwards autocrine signaling or paracrine modulation of tumor cells, tumor-associated cells or immune cells.

Conclusions

Since its initial discovery, many reports emerged documenting TUSC3 as a genuine tumor suppressor in various cancers. However, the variety of molecular machineries affected by TUSC3 deregulation, due to its principal localization within final steps of N-glycosylation machinery in ER, is remarkably diverse. Global signaling alterations due to differential TUSC3 activity integrate on common phenotypic changes and determine whether TUSC3 acts as an oncogene or a tumor suppressor gene. In summary, there is more than one dedicated role for TUSC3 in the life of a cell, but its pathogenic effects are rather mediated through indirect modulation of N-glycosylation of available downstream proteins than through a direct override of cellular homeostasis.

Author contributions KV drafted the manuscript, PH and PV conceptualized, wrote and revised the manuscript.

Compliance with ethical standards

Funding Grant Agency of Masaryk University (MUNI/A/1369/2016), European Regional Development Fund (Center for Analysis and Modeling of Tissues and Organs, CZ.1.07/2.3.00/20.0185), the National Program of Sustainability II (Project no. LQ1605, MEYS CR).

Conflict of interest Authors declare no conflict of interest.

References

- Hanahan D, Weinberg RA (2011) Hallmarks of cancer: the next generation. *Cell* 144(5):646–674
- He Q, He Q, Liu X et al (2014) Genome-wide prediction of cancer driver genes based on SNP and cancer SNV data. *Am J Cancer Res*. 4(4):394–410
- MacGrogan D, Levy A, Bova GS, Isaacs WB, Bookstein R (1996) Structure and methylation-associated silencing of a gene within a homozygously deleted region of human chromosome band 8p22. *Genomics* 35:55–65
- Khalid AM, Asano A, Hosaka YZ, Takeuchi T, Yamano Y (2013) Tumor suppressor candidate TUSC3 expression during rat testis maturation. *Biosci Biotechnol Biochem* 77:2019–2024
- Aken BL, Ayling S, Barrell D et al (2016) The Ensembl gene annotation system. *Database (Oxford)* 2016:baw093. doi:10.1093/database/baw093
- Kelleher DJ, Gilmore R (2006) An evolving view of the eukaryotic oligosaccharyltransferase. *Glycobiology* 16:47–62
- Mohorko E, Owen RL, Malojčić G, Brozzo MS, Aebi M, Glockshuber R (2014) Structural basis of substrate specificity of human oligosaccharyl transferase subunit N33/Tusc3 and its role in regulating protein N-glycosylation. *Structure* 22:590–601
- Shrimal S, Cherepanova NA, Gilmore R (2015) Cotranslational and posttranslational N-glycosylation of proteins in the endoplasmic reticulum. *Semin Cell Dev Biol* 41:71–78
- Horak P, Tomasich E, Vaňhara P et al (2014) TUSC3 loss alters the ER stress response and accelerates prostate cancer growth in vivo. *Sci Rep* 4:3739
- Vaňhara P, Horak P, Pils D et al (2013) Loss of the oligosaccharyl transferase subunit TUSC3 promotes proliferation and migration of ovarian cancer cells. *Int J Oncol* 42:1383–1389
- Cherepanova N, Shrimal S, Gilmore R (2016) N-Linked glycosylation and homeostasis of the endoplasmic reticulum. *Curr Opin Cell Biol* 41:57–65
- Cherepanova NA, Shrimal S, Gilmore R (2014) Oxidoreductase activity is necessary for N-glycosylation of cysteine-proximal acceptor sites in glycoproteins. *J Cell Biol* 206:525–539
- Schwarz M, Knauer R, Lehle L (2005) Yeast oligosaccharyltransferase consists of two functionally distinct sub-complexes, specified by either the Ost3p or Ost6p subunit. *FEBS Lett* 579:6564–6568
- Cherepanova NA, Gilmore R (2016) Mammalian cells lacking either the cotranslational or posttranslational oligosaccharyltransferase complex display substrate-dependent defects in asparagine linked glycosylation. *Sci Rep* 6:20946
- Molinari F, Foulquier F, Tarpey PS, et al (2015) Oligosaccharyltransferase-subunit mutations in nonsyndromic mental retardation. *Am J Hum Gen*. 82:1150–1157
- Contessa JN, Bhojani MS, Freeze HH, Ross BD, Rehemtulla A, Lawrence TS (2010) Molecular imaging of N-linked glycosylation suggests glycan biosynthesis is a novel target for cancer therapy. *Clin Cancer Res* 16(12):3205–3214
- Goytain A, Quamme GA (2005) Identification and characterization of a novel mammalian Mg²⁺ transporter with channel-like properties. *BMC Genomics* 1:48
- Zhou H, Clapham DE (2009) Mammalian MagT1 and TUSC3 are required for cellular magnesium uptake and vertebrate embryonic development. *Proc Natl Acad Sci USA* 106:15750–15755
- Pak BJ, Park H, Chang ER, Pang SC, Graham CH (1998) Differential expression display in first analysis trimester of oxygen-mediated human trophoblast changes cells in gene. *Placenta* 19:483–488
- Soleymanlou N, Jurisica I, Nevo O et al (2005) Molecular evidence of placental hypoxia in preeclampsia. *J Clin Endocrinol Metab* 90(7):4299–4308
- Yuen RKC, Avila L, Peñaherrera MS et al (2009) Human placental-specific epipolymorphism and its association with adverse pregnancy outcomes. *PLoS ONE* 4:1–11
- Garshasbi M, Hadavi V, Habibi H et al (2008) Report a defect in the TUSC3 gene is associated with autosomal recessive mental retardation. *Am J Hum Genet* 2008:1158–1164
- Garshasbi M, Kahrizi K, Hosseini M et al (2011) Clinical report a novel nonsense mutation in TUSC3 is responsible for non-syndromic autosomal recessive mental retardation in a consanguineous Iranian family. *Am J Med Genet* 2011:1976–1980
- Maulik PK, Mascarenhas MN, Mathers CD, Dua T, Saxena S (2011) Prevalence of intellectual disability: a meta-analysis of population-based studies: Research in developmental disabilities. *Res Dev Dis* 32(2):419–436
- Hill WD, Davies G, Liewald DC et al (2016) Examining non-syndromic autosomal recessive intellectual disability (NS-ARID) genes for an enriched association with intelligence differences. *Intelligence* 54:80–89
- Khan MA, Rafiq MA, Noor A et al (2011) A novel deletion mutation in the TUSC3 gene in a consanguineous Pakistani family with autosomal recessive nonsyndromic intellectual disability. *BMC Med Genet* 12:56
- Al-Amri A, Saegh AA, Al-Mamari W et al (2016) Homozygous single base deletion in TUSC3 causes intellectual disability with developmental delay in an Omani family. *Am J Med Genet* 170:1826–1831
- Loddo S, Parisi V, Doccini V et al (2013) Homozygous deletion in TUSC3 causing syndromic intellectual disability: a new patient. *Am J Med Genet* 161:2084–2087

29. Mosrati MA, Schrauwen I, Kamoun H et al (2012) Genome wide analysis in a family with sensorineural hearing loss, autism and mental retardation. *Gene* 510(2):102–106
30. Piovani G, Savio G, Traversa M et al (2014) De novo 1 Mb interstitial deletion of 8p22 in a patient with slight mental retardation and speech delay. *Mol Cytogenet* 7:25
31. Zhang Y, Su HJ, Pan KF et al (2014) Methylation status of blood leukocyte DNA and risk of gastric cancer in a high-risk Chinese population. *Cancer Epidemiol Biomark Prev* 23:2019–2026
32. Ahuja N, Li Q, Mohan AL, Baylin SB (1998) Issa J-PJ. Aging and DNA methylation in colorectal mucosa and cancer. *Cancer Res* 58:5489–5494
33. Hanks J, Ayed I, Kukreja N et al (2013) The association between mthfr 677C>T genotype and folate status and genomic and gene-specific dna methylation in the colon of individuals without colorectal neoplasia. *Am J Clin Nutr* 98:1564–1574
34. Xu XL, Yu J, Zhang HY et al (2004) Methylation profile of the promoter CpG islands of 31 genes that may contribute to colorectal carcinogenesis. *World J Gastroenterol* 10:3441–3454
35. Li Q, Jedlicka A, Ahuja N et al (1998) Concordant methylation of the ER and N33 genes in glioblastoma multiforme. *Oncogene* 16:3197–3202
36. Zemlyakova VV, Zhevlova AI, Zborovskaya IB et al (2003) Methylation profile of several tumor suppressor genes in non-small-cell lung cancer. *Mol Biol* 37:836–840
37. Duppel U, Woenckhaus M, Schulz C, Merk J, Dietmaier W (2016) Quantitative detection of TUSC3 promoter methylation—a potential biomarker for prognosis in lung cancer. *Oncol Lett* 2016:3004–3012
38. Pils D, Horak P, Vanhara P et al (2013) Methylation status of TUSC3 is a prognostic factor in ovarian cancer. *Cancer* 119(5):946–954
39. Belshaw NJ, Elliott GO, Foxall RJ et al (2008) Profiling CpG island field methylation in both morphologically normal and neoplastic human colonic mucosa. *Br J Cancer* 99:136–142
40. Arasaradnam RP, Khoo K, Bradburn M, Mathers J, Kelly S (2010) DNA methylation of ESR-1 and N-33 in colorectal mucosa of patients with ulcerative colitis (UC). *Epigenetics* 5:422–426
41. Yuasa Y, Nagasaki H, Oze I et al (2012) Insulin-like growth factor 2 hypomethylation of blood leukocyte DNA is associated with gastric cancer risk. *Int J Cancer* 131:2596–2603
42. Zhang Y, He RQ, Dang YW et al (2016) Comprehensive analysis of the long noncoding RNA HOXA11-AS gene interaction regulatory network in NSCLC cells. *Cancer Cell Int* 16:89
43. Scholz C, Nimmrich I, Burger M et al (2005) Distinction of acute lymphoblastic leukemia from acute myeloid leukemia through microarray-based DNA methylation analysis. *Ann Hematol* 84:236–244
44. Conway K, Edmiston SN, Tse C-K et al (2015) Racial variation in breast tumor promoter methylation in the Carolina Breast Cancer Study. *Cancer Epidemiol Biomark Prev* 24:921–930
45. Bova GS, Carter BS, Bussemakers MJG et al (1993) Homozygous deletion and frequent allelic loss of chromosome 8p22 loci in human prostate cancer. *Cancer Res* 1993:3869–3873
46. Emi M, Fujiwara Y, Nakajima T, Cancer C, Cancer L (1992) Frequent loss of heterozygosity for loci on chromosome 8p in hepatocellular carcinoma, colorectal cancer, and lung cancer. *Cancer Res* 2:5368–5372
47. Tirkkonen M, Tanner M, Karhu R, Kallioniemi A, Isola J, Kallioniemi OP (1998) Molecular cytogenetics of primary breast cancer by CGH. *Genes Chromosome Cancer* 21(3):177–184
48. Bashyam MD, Bair R, Kim YH et al (2005) Array-based comparative genomic hybridization identifies localized DNA amplifications and homozygous deletions in pancreatic cancer. *Neoplasia* 7:556–562
49. Takle LA, Knowles MA (1996) Deletion mapping implicates two tumor suppressor genes on chromosome 8p in the development of bladder cancer. *Oncogene* 12(5):1083–1087
50. Fujiwara Y, Emi M, Ohata H et al (1993) Evidence for the presence of two tumor suppressor genes on chromosome 8p for colorectal carcinoma. *Cancer Res* 53(5):1172–1174
51. Ahmed MN, Kim K, Haddad B, Berchuck A, Qumsiyeh MB (2000) Comparative genomic hybridization studies in hydatidiform moles and choriocarcinoma: amplification of 7q21–q31 and loss of 8p12–p21 in choriocarcinoma. *Cancer Genet Cytogenet* 116:10–15
52. Cunningham JM, Shan A, Wick MJ et al (1996) Allelic imbalance and microsatellite instability in prostatic adenocarcinoma. *Cancer Res* 56(19):4475–4482
53. Arbieva ZH, Banerjee K, Kim SY et al (2000) High-resolution physical map and transcript identification of a prostate cancer deletion interval on 8p22. *Genome Res* 10:244–257
54. Pils D, Horak P, Gleiss A et al (2005) Five genes from chromosomal band 8p22 are significantly down-regulated in ovarian carcinoma: N33 and EFA6R have a potential impact on overall survival. *Cancer* 104(11):2417–2429
55. Cooke SL, Pole JCM, Chin S-F, Ellis IO, Caldas C, Edwards PAW (2008) High-resolution array CGH clarifies events occurring on 8p in carcinogenesis. *BMC Cancer* 8:288
56. Angstadt AY, Motsinger-Reif A, Thomas R et al (2011) Characterization of canine osteosarcoma by array comparative genomic hybridization and RT-qPCR: signatures of genomic imbalance in canine osteosarcoma parallel the human counterpart. *Genes Chromosome Cancer* 50:859–874
57. Griffith OL, Melck A, Jones SJ, Wiseman SM (2006) Meta-analysis and meta-review of thyroid cancer gene expression profiling studies identifies important diagnostic biomarkers. *J Clin Oncol* 24(31):5043–5051
58. Chung K-W, Kim SW, Kim SW (2012) Gene expression profiling of papillary thyroid carcinomas in Korean patients by oligonucleotide microarrays. *J Korean Surg Soc* 82:271–280
59. Gutierrez VF, Marcos CA, Llorente JL et al (2012) Genetic profile of second primary tumors and recurrences in head and neck squamous cell carcinomas. *Head Neck* 34(6):830–839
60. Gu Y, Wang Q, Guo K et al (2016) TUSC3 promotes colorectal cancer progression and epithelial-mesenchymal transition (EMT) through WNT/beta-catenin and MAPK signalling. *J Pathol* 239:60–71
61. Kratochvílová K, Horak P, Ešner M et al (2015) Tumor suppressor candidate 3 (TUSC3) prevents the epithelial-to-mesenchymal transition and inhibits tumor growth by modulating the endoplasmic reticulum stress response in ovarian cancer cells. *Int J Cancer* 137(6):1330–1340
62. Fan X, Zhang X, Shen J et al (2016) Decreased TUSC3 promotes pancreatic cancer proliferation, invasion and metastasis. *PLoS ONE* 11(2):e0149028
63. Jiang Z, Guo M, Zhang X et al (2016) TUSC3 suppresses glioblastoma development by inhibiting Akt signaling. *Tumor Biol* 37:12039–12047
64. Gu Y, Pei X, Ren Y et al (2017) Oncogenic function of TUSC3 in non-small cell lung cancer is associated with Hedgehog signalling pathway. *Biochim Biophys Acta* 1863(7):1749–1760
65. Mullighan CG, Zhang J, Kasper LH et al (2011) CREBBP mutations in relapsed acute lymphoblastic leukaemia. *Nature* 471(7337):235–239
66. Khan MM, Nomura T, Chiba T et al (2004) The fusion oncoprotein PML-RARalpha induces endoplasmic reticulum (ER)-associated degradation of N-CoR and ER stress. *J Biol Chem* 279(12):11814–11824
67. Schardt JA, Eyholzer M, Timchenko NA, Mueller BU, Pabst T (2010) Unfolded protein response suppresses CEBPA by induction

- of calreticulin in acute myeloid leukaemia. *J Cell Mol Med* 14(6B):1509–1519
68. Kharabi Masouleh B, Geng H, Hurtz C et al (2014) Mechanistic rationale for targeting the unfolded protein response in pre-B acute lymphoblastic leukemia. *Proc Nat Acad Sci USA* 111(21):E2219–E2228
 69. Khoury GA, Baliban RC, Floudas CA (2011) Proteome-wide post-translational modification statistics: frequency analysis and curation of the swiss-prot database. *Sci Rep* 1:90
 70. Li CW, Lim SO, Xia W et al (2016) Glycosylation and stabilization of programmed death ligand-1 suppresses T-cell activity. *Nat Commun* 7:12632
 71. Lauc G, Huffman JE, Pucic M et al (2013) Loci associated with N-glycosylation of human immunoglobulin G show pleiotropy with autoimmune diseases and haematological cancers. *PLoS Genet* 9(1):e1003225
 72. Liu K, Xie F, Gao A et al (2017) SOX2 regulates multiple malignant processes of breast cancer development through the SOX2/miR-181a-5p, miR-30e-5p/TUSC3 axis. *Mol Cancer* 16(1):62
 73. Pole JCM, Courtay-Cahen C, Garcia MJ et al (2006) High-resolution analysis of chromosome rearrangements on 8p in breast, colon and pancreatic cancer reveals a complex pattern of loss, gain and translocation. *Oncogene* 25:5693–5706
 74. Ribeiro IP, Marques F, Caramelo F et al (2014) Genetic gains and losses in oral squamous cell carcinoma: impact on clinical management. *Cell Oncol* 37:29–39
 75. Yu X, Zhang K, Liu F et al (2016) Tumor suppressor candidate 3 as a novel predictor for lymph node metastasis in lung cancer patients. *Oncol Lett* 2016:5099–5105
 76. Guervos MA, Marcos CA, Hermsen M, Nuno AS, Suarez C, Llorente JL (2007) Deletions of N33, STK11 and TP53 are involved in the development of lymph node metastasis in larynx and pharynx carcinomas. *Cell Oncol* 29(4):327–334
 77. Yu X, Zhang J, Zhong H et al (2016) Decreased tumor suppressor candidate 3 predicts poor prognosis of patients with esophageal squamous cell carcinoma. *Int J Med Sci* 13:963–969
 78. Peng Y, Cao J, Yao XY, Wang JX, Zhong MZ, Gan PP, Li JH (2017) TUSC3 induces autophagy in human non-small cell lung cancer cells through Wnt/ β -catenin signaling. *Oncotarget* 8:52960–52974

7. Pernicová Z, Vaňhara P, Souček K. **Formation of secretory senescent cells in prostate tumors: the role of androgen receptor activity and cell cycle regulation.** In: Hayat MA (ed). *Tumor Dormancy, Quiescence, and Senescence, Volume 1: Aging, Cancer, and Noncancer Pathologies.* Springer Netherlands, 2013; pp 303-316.

Commentary:

In this monograph chapter, induction of senescence and senescence-associated phenotypes in prostate cancer are discussed. As the senescent cells remain metabolically active and secrete a variety of molecular factors, they modulate the tissue microenvironment. Moreover, they can potentially promote tumorigenicity and therapy resistance in neighboring malignant cells. We brought examples of such effects and envisage molecular mechanisms associated with androgen depletion in prostate tissue microenvironment.

DOI: 10.1007/978-94-007-5958-9_26

Chapter in monograph

Number of citations (WOS, 2018): Not indexed in WOS

Contribution of the author: Co-authorship. Design and writing of manuscript.

Tumor Dormancy, Quiescence, and Senescence

Volume 1

Tumor Dormancy, Quiescence, and Senescence

Aging, Cancer, and Noncancer
Pathologies

Edited by

M.A. Hayat

Distinguished Professor

Department of Biological Sciences

Kean University, Union, NJ, USA

 Springer

Editor

M.A. Hayat
Department of Biological Sciences
Kean University
Room 213, Library building
Morris Avenue 1000
Union, NJ 07083, USA

ISBN 978-94-007-5957-2 ISBN 978-94-007-5958-9 (eBook)
DOI 10.1007/978-94-007-5958-9
Springer Dordrecht Heidelberg New York London

Library of Congress Control Number: 2013931982

© Springer Science+Business Media Dordrecht 2013

This work is subject to copyright. All rights are reserved by the Publisher, whether the whole or part of the material is concerned, specifically the rights of translation, reprinting, reuse of illustrations, recitation, broadcasting, reproduction on microfilms or in any other physical way, and transmission or information storage and retrieval, electronic adaptation, computer software, or by similar or dissimilar methodology now known or hereafter developed. Exempted from this legal reservation are brief excerpts in connection with reviews or scholarly analysis or material supplied specifically for the purpose of being entered and executed on a computer system, for exclusive use by the purchaser of the work. Duplication of this publication or parts thereof is permitted only under the provisions of the Copyright Law of the Publisher's location, in its current version, and permission for use must always be obtained from Springer. Permissions for use may be obtained through RightsLink at the Copyright Clearance Center. Violations are liable to prosecution under the respective Copyright Law.

The use of general descriptive names, registered names, trademarks, service marks, etc. in this publication does not imply, even in the absence of a specific statement, that such names are exempt from the relevant protective laws and regulations and therefore free for general use.

While the advice and information in this book are believed to be true and accurate at the date of publication, neither the authors nor the editors nor the publisher can accept any legal responsibility for any errors or omissions that may be made. The publisher makes no warranty, express or implied, with respect to the material contained herein.

Printed on acid-free paper

Springer is part of Springer Science+Business Media (www.springer.com)

Formation of Secretory Senescent Cells in Prostate Tumors: The Role of Androgen Receptor Activity and Cell Cycle Regulation

Zuzana Pernicová, Petr Vaňhara, and Karel Souček

Contents

Introduction	304	Summary	313
Prostate Histology and Development	304	References	314
Secretory Phenotypes in the Prostate	306		
Senescence-Associated Secretory Phenotype (SASP)	306		
Senescence, SASP, and Prostate Cancer	307		
Aging and Senescence in Prostate Stroma.....	307		
Senescence in Nonmalignant Prostate Epithelium	307		
Senescence in Prostate Cancer Progression.....	308		
Neuroendocrine Phenotype (NEP)	308		
NE Cells.....	308		
Neuroendocrine Differentiation (NED) of Prostate Cancer Cells	308		
Secretory Phenotype Connected with the NED of Prostate Cancer Cells.....	309		
Changes of Secretory Phenotypes During Cancer Progression and Cancer Therapy	310		
Role of Androgen Receptor in the NEP and SASP of Prostate Cancer Cells	310		
Role of Androgen Receptor in NEP.....	310		
Role of Androgen Receptor in SASP.....	311		
Role of the PTEN—Skp2 Pathway in the Induction of SASP by Inhibition of AR Activity.....	311		

Abstract

The induction of senescence in cancer cells is believed to be a potent mechanism of tumor suppression; however, senescent cells remain metabolically active and secrete a broad spectrum of factors, modulate the tissue microenvironment, and potentially promote tumorigenicity in neighboring malignant cells. Another important subpopulation of secretory cells modulating the prostate tissue microenvironment is represented by neuroendocrine cells. Interestingly, androgen deprivation therapy, a widely used treatment for advanced prostate cancer, induces both the emergence of neuroendocrine-like prostate cancer cells and the senescence-associated secretory phenotype in prostate cancer epithelial cells.

Z. Pernicová
Department of Cytokinetics, Institute of Biophysics,
Academy of Sciences of the Czech Republic,
Kralovopolska 135, CZ-615 65 Brno, Czech Republic

Center of Biomolecular and Cellular Engineering,
International Clinical Research Center, St. Anne's
University Hospital Brno, Brno, Czech Republic

Department of Experimental Biology, Faculty
of Sciences, Masaryk University, Brno, Czech Republic

P. Vaňhara
Department of Histology and Embryology, Faculty
of Medicine, Masaryk University, Kamenice 3,
CZ-62500, Brno, Czech Republic

K. Souček (✉)
Department of Cytokinetics, Institute of Biophysics,
Academy of Sciences of the Czech Republic,
Kralovopolska 135, CZ-615 65 Brno, Czech Republic

Center of Biomolecular and Cellular Engineering,
International Clinical Research Center, St. Anne's
University Hospital Brno, Brno, Czech Republic
e-mail: ksoucek@ibp.cz

The induction of the senescence-associated secretory phenotype by androgen depletion is tightly connected with the regulation of the cell cycle machinery through the downregulation of S-phase kinase-associated protein 2, whereas the emergence of neuroendocrine-like cancer cells (through the process of neuroendocrine differentiation) is under separate control. In this chapter, we summarize possible mechanisms and consequences of the formation of the aforementioned secretory phenotypes in prostate tumors and the role of the androgen receptor and cell cycle regulation in these processes.

Keywords

Prostate cancer • Senescence • Neuroendocrine differentiation • Senescence-associated secretory phenotype • Androgen receptor • Skp2

Introduction

The prostate gland changes substantively in aging men, resulting in the disruption of tissue homeostasis and various clinical symptoms, such as lower urinary tract syndrome, urethral constriction, or the potential development of malignant phenotypes. The anatomical and histological descriptions of the aging prostate were reported decades ago, and they reflected morphological changes at the organ and tissue level rather than deciphered biological processes linked to senescence. Cellular senescence is considered a protective trait that is effective against immortal phenotypes, and many cancers override the induction of senescence by deregulating principal cell regulators such as p53, retinoblastoma (Rb), or cell cycle inhibitors. Despite their permanent growth arrest, senescent cells retain biological activity and can substantially modify the local tissue microenvironment. Various cells that undergo senescence also acquire similar a senescence-associated secretory phenotype (SASP) and secrete a complex set of cytokines and other biomolecules. Soluble growth factors and signaling molecules produced by senescent prostate fibroblasts and epithelial cells contribute to the enhanced proliferation of neigh-

boring preneoplastic cells and induction of the epithelial-to-mesenchymal transition (EMT) and tumor spreading. In addition, SASP is involved in proinflammatory signaling and immune response modulation. A better understanding of normal prostate development and aging will therefore open new possibilities to therapeutically target various pathologies including prostate cancer.

Prostate Histology and Development

The prostate is an exocrine tubuloalveolar gland surrounding the urethra that develops from the pelvic portion of the urogenital sinus (UGS). Development of the prostate is driven by embryonic androgens that stimulate the mesenchyme of the UGS surrounding the presumptive prostatic urethra. Then, the androgen receptors (AR) located in the UGS mesenchyme induce by so far undefined factors the epithelial outgrowth, acinar development and prostate duct canalization (Chung and Cunha 1983). Before the appearance of prostatic buds, the UGS cells of the developing embryonic prostate contain cytokeratin markers of both basal and luminal cell lineages. Differentiation to distinct epithelial cell types occurs concurrently with the development and branching of canalized ducts during prostate morphogenesis, and the pattern of molecular markers of individual cell types defining the secretory phenotype becomes prominent during definitive androgen-dependent maturation of the prostate in puberty.

Histologically, the prostate is composed of two distinct compartments — the fibromuscular stroma and the glandular epithelium — organized into secretory acini and ducts. The stroma consists of fibroblasts/myofibroblasts and smooth muscle cells, with the participation of endothelial cells, nerve cells, and infiltrating inflammatory cells constituting the supportive and regulative architecture for the glandular epithelium. The prostatic epithelium is heterogeneous, largely pseudostratified, tall, and columnar with patches of cuboidal or squamous cells. It consists of two histologically different layers, the morphology of which is essential for clinicopathologic assessment in routine diagnostics. The basal epithelial

Table 26.1 Molecular phenotype of prostate epithelial cells

Cell type in the adult prostate epithelium	Molecular pattern
Prostate-regenerating (stem) cells	Sca-1, Bcl-2, integrin $\alpha 6$, $\alpha 2\beta 1$, CD133 (prominin-1), CD44, CK5, CK14, low AR, GST π , pp32
Basal cells	CK5/6, CK14, p63, calcyclin, Bcl-2, GST π , pp32 Low AR
Amplifying (intermediate) cells	Basal and luminal cytokeratins, absent p27, $\alpha 2\beta 1$, GST π , pp32, CD44
Luminal secretory cells	CK8, CK18, CK19, Nkx3.1, p27, Bcl-2 absent, low epidermal growth factor receptor High AR, prostate-specific antigen (PSA), prostate-specific acid phosphatase (PSAP)
NE cells	Survivin, synaptophysin, CgA, NSE, tubulin β -III, neuropeptides, CK18

layer separates the luminal layer of glandular cells from the stroma and serves as a source of newly differentiating functional cells. The morphology of the basal cells ranges from flattened to cuboidal according to the level of chromatin condensation and amount of cytoplasm. Basal cells express specific high-molecular-weight cytokeratins such as cytokeratins 5/14, p63, and generally low levels of AR (see Table 26.1). The basal layer contains a subpopulation of stem cell-like cells contributing to epithelium renewal. The basal layer exhibits low sensitivity to apoptosis due to Bcl-2 expression and high proliferative capacity and is generally considered androgen-independent (for review see Schalken and van Leenders 2003). The luminal glandular layer is rather heterogeneous and contains several cell types, including secretory cells, intermediate progenitors differentiating from basal cells, and neuroendocrine (NE) cells. The secretory columnar cells arise from cells of the basal layer. These cells are oriented into the lumen of the secretory acinus and are characterized by the prevailing expression of low-molecular-weight cytokeratins (such as 8 and 18) and transcription regulators (such as Nkx3.1). Secretory acinar cells also abundantly produce AR and prostate-specific antigen (PSA). The cells of the luminal epithelium are functionally differentiated and androgen-dependent, having a low proliferative capacity and high apoptotic index. The NE cells are rarely interspersed between secretory cells. They are androgen-independent and produce a

variety of biologically active substances including synaptophysin, chromogranin A (CgA), neuron-specific enolase (NSE), and tubulin β -III, as well as neuropeptides including calcitonin, somatostatin, bombesin, and serotonin (for review see Kasper 2008). The cells constituting the prostatic epithelium possess a different proliferation capacity and sensitivity to androgens or proapoptotic stimuli. Pioneering experiments performed in the 1980s indicated the presence of cells capable of repopulating the glandular epithelium even after androgen removal or castration and re-administration (English et al. 1987). These experiments suggested the localization of these repopulating cells in the basal layer, as this cell population remained intact after castration, whereas the luminal cells underwent programmed cell death. However, fluorescent-based sorting for surface stem cells markers such as CD133, integrin $\alpha 2\beta 1$, and CD44 distinguished several populations with different stem cells characteristics, including the capability of asymmetric division, proliferation, and tumorigenicity in immunodeficient mice (for review see Kasper 2008).

Intermediate, transiently amplifying cells are located within the multilayered epithelium and are possible common precursors for differentiated cell types constituting the functional epithelium (for review see Goldstein et al. 2010). The cell types of the definitive prostate epithelium are defined by particular sets of molecular markers (Table. 26.1).

Secretory Phenotypes in the Prostate

Senescence-Associated Secretory Phenotype (SASP)

The concept of SASP was firstly reported in the work of Krtolica and colleagues in 2001 (Krtolica et al. 2001), in which they described that senescent fibroblasts can support the proliferation and tumorigenesis of preneoplastic and neoplastic cells, but not normal cells. Soluble factors secreted by senescent fibroblast were proposed to be responsible for this protumorigenic effect. This was confirmed also in xenograft models, in which the secretion of matrix metalloproteinases (MMPs) was identified as a factor involved in the promotion of tumor growth and microenvironment changes (Liu and Hornsby 2007). Importantly, the protumorigenic effect of senescent fibroblasts was confirmed by experiments in which senescent fibroblasts supported the invasion and EMT of relatively low-aggressive cancer cells. All of these effects were associated with the secretory function of senescent cells; this secretory function of senescent cells is denoted SASP. SASP development is characteristic of both senescent fibroblasts and senescent epithelial cells (Coppe et al. 2010). A striking similarity in the SASP patterns between senescent cells from different donors, tissues, and different cell types was described. Over 40 factors have been identified to participate in SASP. Factors secreted by senescent cells include inflammatory cytokines and chemokines (interleukin [IL]-6, IL-8, interferon- γ , granulocyte-macrophage colony-stimulating factor, C-X-C chemokine receptor type 2 [CXCR2]), growth factors and regulators (transforming growth factor [TGF]- β , epidermal growth factor [EGF], vascular endothelial growth factor [VEGF], and insulin-like growth factor binding proteins [IGFBPs]), proteases and regulators (tissue inhibitor of metalloproteinases, MMPs, and plasminogen activator inhibitor-I), shed cell surface molecules (tumor necrosis factor-related apoptosis-inducing ligand receptor 3 and Fas), and other factors including collagen, fibronectin and nitric oxide (for review see Coppe et al. 2010).

Because senescence cells secrete a broad spectrum of factors with different functions, SASP influences many biological processes in surrounding cells.

The SASP factors can affect tumor cells and stimulate tumor progression. Senescent fibroblasts were demonstrated to promote the proliferation and tumor formation of premalignant and malignant breast cancer cells, and this growth stimulation was independent of the inducer of senescence (Krtolica et al. 2001). The proliferation-stimulating effect of senescent fibroblasts was confirmed also in prostate and ovarian cancers (Coppe et al. 2010).

The most important proinflammatory cytokine connected with SASP is IL-6, the secretion of which was detected upon oncogene- or DNA damage-induced senescence (Coppe et al. 2010). In addition to senescent fibroblasts, tumor cells also undergo senescence in response to drug treatment and DNA damage due to the secretion of a broad spectrum of inflammatory cytokines (IL-6, IL-8, IL-24, and TGF- α) (Novakova et al. 2010). Further, SASP factors can influence the motility and invasiveness of cancer cells. Namely, it was found that senescent fibroblasts stimulate the EMT of cancer cells. Further, senescent fibroblasts can affect epithelial differentiation via secreted SASP factors (Coppe et al. 2010).

Taken together, the aforementioned pro- and antitumorigenic effects of senescence induction lead to the hypothesis of so-called antagonistic pleiotropy. Briefly, although senescence can have cancer-preventive effects early in life, it may promote aging later in life because the regenerative capacity of cells and tissues is reduced when increased numbers of senescent cells are present in the body (for review see Giaimo and d'Adda di Fagagna 2012). Conversely, the authors of that review note that using senescence as an example of antagonistic pleiotropy is not unequivocal. Factors secreted by senescent cells support tumor cell proliferation, but on the contrary, these factors can trigger innate immune responses, support wound healing, and prevent organ degradation, thus acting in a positive manner. Secondly, there is no evidence that the beneficial effects of senescence prevail in young age and the detrimental effects prevail in older age, which is one of the characteristics of antagonistic pleiotropy.

Therefore, more studies of this phenomenon are needed, especially in humans.

Senescence, SASP, and Prostate Cancer

Senescence (aging) plays an important role in the development of both benign prostate hyperplasia (BPH) and prostate cancer. Both prostate epithelial cells and prostate stroma can undergo senescence. The histological changes in the senescent prostate include focal atrophy of a small number of secretory acini, the development of epithelial atypia, increased stromal disorganization, disordered orientation of smooth muscle cells, and increased numbers of foci of inflammatory infiltrate (Bianchi-Frias et al. 2010). Array-based transcriptional profiling of fibromuscular stroma adjacent to the glandular epithelium revealed the enhanced expression of genes associated with inflammation or genotoxic and oxidative stress (Bianchi-Frias et al. 2010).

Aging and Senescence in Prostate Stroma

It was confirmed that senescent fibroblasts can change the structure and function of normal epithelium and support the proliferation of premalignant and malignant, but not normal, epithelial cells (Krtolica et al. 2001). Three main groups of genes deregulated in senescent fibroblasts were identified: (a) secreted autocrine- and paracrine-acting growth factors (VEGF, GDF-15, BMP-1, IGFBPs, and others), (b) chemokines and cytokines (CXCL12, CCL11, IL-6, IL-8, and others), and (c) extracellular matrix proteins, proteases, and protease inhibitors (several types of collagen, integrin α V, β 1, β 4, fibronectin, laminin β 2, and others) (for review see Dean and Nelson 2008).

The molecular profile of the prostate microenvironment significantly changes with aging, and several genes with altered expression during aging were also upregulated in the SASP of fibroblasts induced to senesce by different approaches (Bianchi-Frias et al. 2010). Further, components of the extracellular matrix were downregulated and inflammation-associated genes were upregulated

in aged stroma. In another study, the transcription profile of senescent prostate fibroblasts was evaluated. Among others, genes encoding the senescent factors fibroblasts growth factor 7 (FGF-7), MMP2, and IGFBP-2, -3, and -5, all associated with SASP, were upregulated in senescent fibroblasts (Bavik et al. 2006). Another factor, CCL5, was identified as the factor that stimulated the proliferation of BPH-1 immortalized primary human prostate cells grown in conditioned medium from fibroblasts derived from elderly donors (Eyman et al. 2009). Furthermore, CCL5 was found to enhance the expression of genes involved in angiogenesis.

Therefore, based on these facts, senescent fibroblasts must be considered potential targets for cancer prevention and therapy.

Senescence in Nonmalignant Prostate Epithelium

There is an evident connection between senescence and BPH development because senescent cells accumulate in tissues with aging and the incidence of BPH also increases with increasing age. Generally, the presence of senescent cells in premalignant state is considered a cancer-preventive mechanism that blocks neoplastic transformation. When this senescent state is broken or bypassed, premalignant lesions can become malignant. Using SA- β -gal staining, it was revealed that there were significantly more senescent prostate epithelial cells in tissue from patients with enlarged prostates than from patients without this enlargement. Importantly, senescence was evident only in epithelial cells, not in prostate stroma (Choi et al. 2000). Moreover, it was confirmed that the presence of senescent cells drives BPH in older men. These senescent prostate epithelial cells express IL-1 α , which activates FGF-7 secretion, leading to the proliferation of nonsenescent epithelial cells (Castro et al. 2003). Taken together, BPH is associated with increased numbers of senescent cells, and beneficial effects of senescence induction are desired in this case because senescence halts the progression of BPH to prostate cancer.

A similar effect of senescence was observed in connection with prostatic intraepithelial neoplasia (PIN), a precursor of invasive prostate cancer. Using transgenic mice, in which Akt expression led to PIN development, the relationship between PIN and senescence was investigated. In this model, high levels of the cyclin-dependent kinase (CDK) inhibitor p27^{Kip1} were reported (Majumder et al. 2008). This overexpression was associated with the induction of a senescence checkpoint, whereas p27^{Kip1} inhibition rescued the senescent phenotype, concomitantly increasing the proliferation of epithelial cells and promoting the development of invasive prostate cancer.

Senescence in Prostate Cancer Progression

As mentioned previously, senescence is primarily considered a tumor-suppressing mechanism that is present in pretumorigenic states and halts malignant transformation. Therefore, the induction of senescence in malignant cells is one possible mechanism of treating different cancers. Although senescent cells do not undergo apoptosis, they do not proliferate, which halts tumor growth. Therefore, treatment with senescence inducers together with other therapeutics may be beneficial for patients. However, because we know that senescent cells acquire SASP and we know the factors involved in SASP, we must account for the negative effects of senescence induction, which can support tumor promotion.

The detailed role of senescence in prostate cancer progression in relationship to AR status and the role of selected signaling pathways will be discussed later in this chapter.

Neuroendocrine Phenotype (NEP)

NE Cells

NE cells, the minor cell type scattered throughout the prostate epithelium, were identified originally by Prettl in 1944 as cells with the dual properties

of endocrine cells and neurons, acting in both secretory and autocrine/paracrine manner (for review see Komiya et al. 2009). There are two types of NE cells: open and closed. The open NE cells have an apical cytoplasmic process through which they extend to the glandular lumen, and the closed NE cells do not express this process; both types have thin branching dendritic-like processes, which they extend between adjacent epithelial cells. NE cells are postmitotic and terminally differentiated and lack evidence of the presence of AR in the nucleus. Moreover, NE cells are characterized by the presence of many dense core granules, which correlates with their important secretory function (Komiya et al. 2009). NE cells secrete a broad spectrum of substances and biological active factors, such as calcitonin gene products, CgA, gastrin-releasing peptide (GRP), histamine, NSE, serotonin, and VEGF. Via these factors, NE cells regulate prostatic growth, differentiation, and secretion.

Neuroendocrine Differentiation (NED) of Prostate Cancer Cells

As mentioned previously, NE cells are postmitotic. However, it is known that the number of cells with NE properties increases in prostate cancer. We can find pure NE prostate tumors only rarely, but we can find foci of cells with NE characteristics in almost every prostate tumor.

The increasing number of cells with NE characteristics is thought to arise via the NED (trans-differentiation) of prostate cancer cells (Yuan et al. 2007). NED in tumors is often described as scattered clusters of cells with NE properties among a predominant population of non-NE malignant cells (for review see Komiya et al. 2009). Cancer cells undergoing NED acquire properties similar to NE cells, and thus they have been termed NE-like prostate cancer cells. They are characterized by the expression of markers distinct from those of basal or luminal cells (Huang et al. 2006). Importantly, NE-like cancer cells are negative for AR staining and therefore are androgen-independent and resistant to hormonal

(androgen ablation) therapy. Moreover, they overexpress the antiapoptotic protein survivin, making them resistant to apoptosis (Gong et al. 2007).

Many mechanisms of NED induction in prostate cancer cells have been identified, in particular via *in vitro* models of NED. NED was induced in prostate cancer cells by androgen depletion, increased levels of IL-6, ionizing radiation, and activation of several signaling pathways, such as the Wnt and cyclic adenosine 3', 5'-monophosphate (cAMP) signaling pathways (for review see Komiya et al. 2009).

Recently, Germann et al. investigated the role of NE cells in tumor recurrence in an androgen-dependent BM18 xenograft model after castration (Germann et al. 2012). They revealed that only two populations of cells, stem cell-like cells and NE cells survive the castration process. However, they simultaneously demonstrated that NE cells are nonproliferative both before and after castration and therefore are not responsible for initiating the recurrence of tumor growth after castration. Whether this holds true for other models remains for further investigation.

Secretory Phenotype Connected with the NED of Prostate Cancer Cells

One of the important characteristics connected with NED in prostate cancer cells is their secretory function. The transdifferentiation of cancer cells into NE-like prostate cancer cells is associated with the acquisition of the ability to express and secrete a broad spectrum of NED markers and biologically active factors, similar to normal NE cells. It is hypothesized that through these factors, NE-like cancer cells can influence surrounding non-NE-like cancer cells, support their survival during androgen deprivation therapy (ADT), and thus contribute to disease progression.

Some of these NED markers have been used to detect NED, and their levels are correlated with the disease stage and cancer progression. Immunohistochemical detection of CgA is correlated with the clinical stage of the disease, whereas NSE and synaptophysin are correlated

with the grade (Ather et al. 2008). Circulating CgA appears to be a useful marker for obtaining detailed information about the disease stage and progression (Berruti et al. 2001). In addition to potentially being a useful marker, the biological properties of CgA were also elucidated. CgA can induce the phosphorylation of Akt, and this activation of Akt leads to the increased expression of survivin and protection from apoptosis (Gong et al. 2007).

Another factor secreted by NE cells is serotonin, which activates mitogen-activated protein kinase and the phosphoinositide 3-kinase (PI3K)/Akt pathway in prostate cancer cells and supports their migration (Dizeyi et al. 2011). Together with bombesin and GRP, serotonin influences angiogenesis in patients with prostate cancer (Heinrich et al. 2011). Additionally, bombesin was found to stimulate the expression of the proangiogenic factors VEGF and IL-8 through nuclear factor- κ B activation (Levine et al. 2003). This correlates with the fact that the increased presence of NED correlates with higher neovascularization in prostate cancer (Grobholz et al. 2000).

Chemokines also play an important role in prostate cancer progression. Both benign NE cells and NE-like cancer cells produce IL-8 (Huang et al. 2005). There are two receptors for IL-8: CXCR1 and CXCR2. CXCR1 is overexpressed by malignant prostate cells, whereas CXCR2 is overexpressed by NE-like cancer cells. This suggests that NED induced in response to androgen withdrawal leads to the induction of IL-8, and IL-8 can influence the androgen-independent growth of prostate cancer cells through a paracrine mechanism; simultaneously, IL-8 can regulate NED and the function of NE-like cancer cells in an autocrine manner.

In summary, the induction of NED by different stimuli leads to the transdifferentiation of cancer cells into NE-like cancer cells. These cells acquire the ability to secrete many factors, several of which are useful markers of NED, whereas other factors have important biological functions. NE-like cancer cells can influence surrounding non-NE cells in a paracrine manner, whereas simultaneously they are regulated by other factors in an autocrine manner.

Changes of Secretory Phenotypes During Cancer Progression and Cancer Therapy

Role of Androgen Receptor in the NEP and SASP of Prostate Cancer Cells

Androgens (male steroid sex hormones) are important for the terminal differentiation of luminal epithelial cells in the prostate gland. Androgens act through their binding to AR. AR is a ligand-dependent transcription factor and a member of the nuclear receptor superfamily. After ligand binding, AR sheds inhibitory chaperons, undergoes homodimerization, and translocates to the nucleus, where it binds to DNA at specific sequences (androgen-responsive elements). By regulating the transcription of many different genes, AR signaling affects secretory function, cell survival, and cell cycle initiation in prostate cells (for review see Knudsen and Scher 2009).

Generally, AR and AR signaling are critical regulators of the G1 to S phase transition in prostate cancer; AR regulates the translation of the family of cyclin D proteins through the mTOR pathway and therefore enables cyclin D/CDK4 complex assembly; further, AR downregulates the CDK inhibitor p27^{Kip1}, which enables the activation of CDK2 (for review see Balk and Knudsen 2008). This activation of cyclin/CDK complexes leads to the phosphorylation and inactivation of Rb, which enables the G1 to S transition.

ADT is a standard treatment for advanced stages of prostate cancer and is usually achieved by medical or surgical castration. This leads to the depletion of gonadal testosterone, which is the main source of circulating androgens. Despite the primary response of prostate tumors to ADT, metastatic disease almost always progresses to currently incurable castration-resistant prostate cancer (CRPC) connected with re-activated AR. This re-activation may occur via direct AR modulation (deregulation, mutation, or alternative splicing; posttranslational modifications of AR), alterations in AR cofactors (coactivator enhancement, loss of function of corepressors), and intratumoral androgen

synthesis mediated by autocrine or paracrine mechanisms (for review see Knudsen and Scher 2009). Therefore, in the following section, we will focus on the role of androgen withdrawal and AR signaling in the induction of both secretory phenotypes of prostate cancer cells (NEP and SASP).

Role of Androgen Receptor in NEP

NED is hypothesized as one of the mechanisms responsible for the progression of CRPC. The presence of NED is significantly more common in patients with hormone-refractory prostate cancer following long-term treatment with different hormone-deprivation therapies and chemotherapy (Hirano et al. 2004). In accordance with these results, AR silencing using RNA interference *in vitro* led to induction of NED in both androgen-dependent and androgen-independent prostate cancer cell lines, which implies that AR may actively repress NED in prostate cancer cells (Wright et al. 2003). Importantly, NE-like cancer cells in both primary and recurrent disease lack AR expression (Bonkhoff 2001). Thus, NE-like cancer cells are insensitive to ADT, and possibly through factors that they secrete, they can influence surrounding non-NE-like cancer cells in a paracrine manner and stimulate the proliferation of these non-NE-like cancer cells during ADT.

With regard to the activation of AR by ligands other than androgens, IL-6 can stimulate both AR expression and activity in the absence of androgens in LNCaP prostate cancer cells (Lin et al. 2001). Further, treatment of prostate cancer cells with IL-8 resulted in increased proliferation of these cells in androgen-depleted conditions accompanied by increased AR expression and activation (Seaton et al. 2008). Both IL-6 and IL-8 are associated with prostate cancer progression; IL-8 is secreted by NE cells and NE-like cancer cells (Huang et al. 2005), and importantly, both IL-6 and IL-8 are associated with the SASP. The ability to stimulate the growth of cancer cells in the absence of androgens was also confirmed for other neuropeptides secreted by NE-like cells, namely GRP and parathyroid hormone-related protein.

The important role of NE cells in supporting the growth of cancer cells through AR activation was confirmed in the work of Jin and colleagues, in which they implanted LNCaP cells into one flank and NE-prostate tumors into the opposite flank of castrated immunodeficient mice (Jin et al. 2004). Interestingly, NE tumors supported the proliferation of LNCaP prostate cancer cells; this was mediated by the increased sensitivity of LNCaP cells to androgens, increased AR expression, and NE tumor-secreted factors. Overall, NE tumor cells increased the activity of functional AR in LNCaP prostate cancer cells. Therefore, targeting the signaling of factors secreted by NE cells may be beneficial for prostate cancer treatment.

Role of Androgen Receptor in SASP

One of the hallmarks of senescence is cell cycle arrest. It is known that in the prostate epithelium, AR drives cell cycle progression, and therefore, primarily the protumorigenic role of AR is well documented. Contradictory to this, a recent publication by Mirochnik and colleagues indicated that persistent AR activity drives senescence in both normal and cancer prostate epithelial cells; this AR-driven senescence was associated with decreased tumorigenicity (Mirochnik et al. 2012). They demonstrated that via increased ROS production, AR decreases Rb phosphorylation, which leads to cell cycle arrest. Subsequently, AR causes the accumulation of p21^{Cip1/Waf}, leading to the attenuation of p63 expression.

As previously mentioned, the senescent phenotype is accompanied by the secretion of a broad spectrum of biological factors. Some of these factors can interact with AR and affect its activity. Both IL-6 and IL-8, factors associated with both the NEP and SASP of prostate cancer cells, can activate AR signaling. Moreover, keratinocyte growth factor and EGF treatment of prostate cancer cells induced AR transactivation (Culig et al. 1994). Thus, SASP factors can transactivate AR in androgen-depleted conditions in the same manner as NED factors.

Role of the PTEN—Skp2 Pathway in the Induction of SASP by Inhibition of AR Activity

Skp2 is an important component of the SCF multisubunit complex (Skp1, Cullins, F-box proteins), which acts as an important E3-ubiquitin ligase. Skp2 recognizes and subsequently degrades many substrates, such as p21^{Cip1/Waf}, p27^{Kip1}, p57, cyclin E, cyclin D1, cyclin A, E2F-1, Orc-1, TOB1, FOXO1, c-Myc, B-MYB, Cdt1, CDK9, and Smad-4 (for review see Frescas and Pagano 2008). Many of these substrates are known tumor suppressors, and thus, Skp2 is classified as an oncogene that is crucial for the regulation of cell cycle progression, proliferation, differentiation, apoptosis, and cell survival. Skp2 overexpression was documented in several types of cancer, including colorectal, prostate, breast, gastric, and lung cancers (for review see Hershko 2008). This overexpression usually correlates with poor overall survival.

One of the important targets of Skp2 is the CDK inhibitor p27^{Kip1}. Skp2 physically interacts with phosphorylated p27^{Kip1}, and this interaction targets p27^{Kip1} for ubiquitin-mediated degradation (Carrano et al. 1999). In prostate cancer samples, Skp2 expression was increased in PIN lesions and prostate cancer, compared to its very low expression in normal epithelium (Yang et al. 2002). Moreover, Skp2 overexpression is inversely correlated with the expression of its downstream target p27^{Kip1} and its regulator PTEN (Phosphatase and tensin homolog). It was confirmed that PTEN regulates p27^{Kip1} levels through Skp2 (Mamillapalli et al. 2001).

PTEN is an important tumor suppressor gene that is commonly mutated in cancer, and its expression is decreased to various degrees in several cancers including prostate cancer. In the prostate, PTEN drives cancer progression; deletion of one PTEN allele causes hyperplasia, dysplasia, and low-grade PIN, and further downregulation of PTEN using a hypomorphic allele leads to the development of high-grade PIN that developed into carcinoma in 25% of mice (Trotman et al. 2003). Moreover, homozygous loss of PTEN induces cellular senescence mediated

by the p53 signaling pathway and suppresses tumorigenesis, whereas the loss of both PTEN and p53 accelerates prostate cancer (Chen et al. 2005). A novel type of cellular senescence, PTEN-loss-induced cellular senescence, was recently described (Alimonti et al. 2010). In that study, PTEN-loss-induced cellular senescence occurred in the absence of massive proliferation and the DNA damage response.

Interestingly, the reciprocal feedback regulation between AR and the PTEN-PI3K/Akt pathway was elucidated. The loss of PTEN causes activation of the PI3K pathway, which is connected with decreased AR expression. Inhibition of the PI3K pathway led to the partial rescue of AR protein expression and activity (Carver et al. 2011). Further, this crosstalk was confirmed in the work of Mulholland and colleagues, in which PTEN-null prostate cancer cells were less dependent on AR signaling; prostate cancer cells with AR loss were more dependent on the PI3K/Akt/mTOR pathway (Mulholland et al. 2011). Therefore, the combined inhibition of AR/androgen signaling and the PI3K/Akt/mTOR pathway may be more effective for treating CRPC with PTEN loss.

The role of Skp2 in cellular senescence was elucidated in experiments in which the loss of Skp2 alone did not induce senescence, but concomitant Skp2 loss together with PTEN inactivation or Arf deficiency led to the acquisition of a senescence phenotype in mouse embryonic fibroblasts (Lin et al. 2010). This Skp2 loss-mediated induction of senescence impaired tumorigenesis independent of the p19^{Arf}-p53 pathway. Currently, it is therefore desirable to target Skp2 or some other components of the SCF E3 ubiquitin ligase complex because targeting these components by different approaches leads to senescence, apoptosis, and autophagy, processes that impair cancer cell growth (for review see Jia and Sun 2011). As mentioned previously, Skp2 is a part of the SCF complex involved in ubiquitin-proteasome-mediated degradation. One of the components of this complex is cullin-1, which must be posttranslationally modified by neddylation to support Skp2-SCF complex formation (for review see Chan et al. 2010). Although there are no direct inhibitors of Skp2, one potential

mechanism of Skp2 inhibition is to inhibit the entire complex by inhibiting neddylation. NEDD-8 is carried to cullin-1 by a specific E1 ligase called the NEDD-8 activating enzyme. Recently, MLN4924, a small molecule inhibitor of NEDD-8 activating enzyme, was identified (Soucy et al. 2009). This inhibitor inhibited neddylation in cancer cells, resulting in defects in S phase of the cell cycle, induction of apoptosis, and importantly inhibition of tumor xenograft growth. Interestingly, MLN4924 treatment induced both partial apoptosis and irreversible senescence that was mediated by the p21^{Cip1/Kip} pathway, leading to tumor growth suppression (Jia et al. 2011).

In our recent publication, we revealed that long-term androgen depletion leads to cell cycle arrest associated with the irreversible induction of senescence (Pernicova et al. 2011). This was mediated by the downregulation of Skp2 and upregulation of its downstream target p27^{Kip1}. In our model, this effect was independent of PTEN because we observed similar effects in cell lines expressing (LAPC-4) and lacking PTEN (LNCaP). Moreover, the induction of senescence by androgen depletion was paralleled by the acquisition of both aforementioned secretory phenotypes: SASP and NED. However, only the induction of senescence was dependent on the PTEN/Skp2/p27^{Kip1} pathway, whereas modulating the levels of Skp2 did not lead to the modulation of NED. Additionally, we determined that both androgen depletion and a high cellular density in the presence of androgens can induce NED, but not senescence, in prostate cancer cells (Pernicova et al., manuscript in preparation). A high cellular density increased AR activity and induced NED only transiently; this NED induction was not paralleled with the induction of senescence. Both a high cellular density and androgen depletion caused cell cycle arrest, but the induction of cell cycle arrest was not crucial for the induction of NED. Additional investigation revealed the involvement of cAMP signaling in high density-induced NED.

We suggest that androgen depletion leads to the formation of highly secretory senescent NE-like cancer cells possessing the characteristics of both NE-like cancer cells and senescent

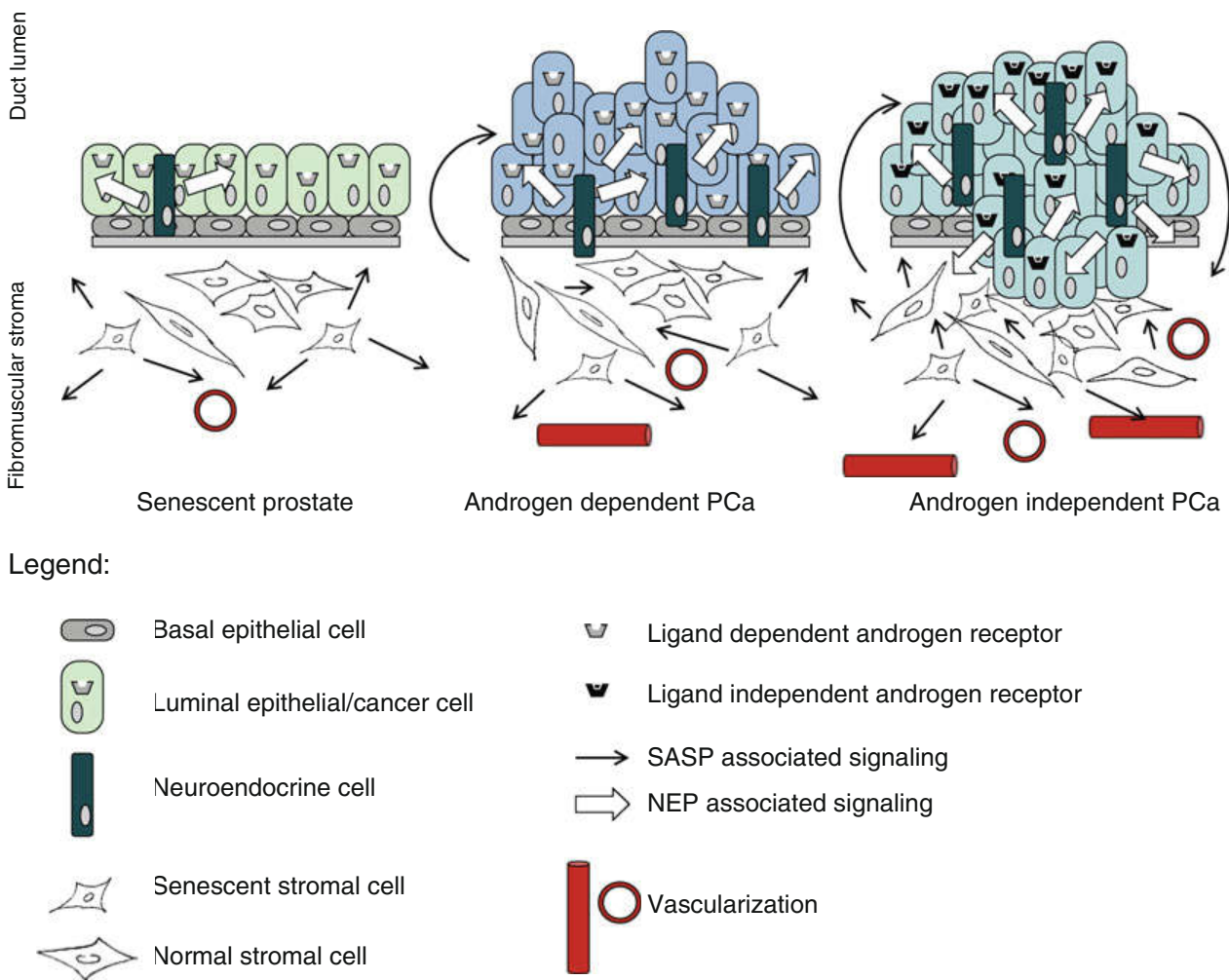


Fig. 26.1 Senescent stromal as well as neuroendocrine cells modify prostate microenvironment by autocrine and/or paracrine soluble molecules (see the text for details). In

PCa, cancer cells acquire both SASP and NEP that promote formation of epithelial neoplasia as well development of the androgen independent phenotype

cells. As mentioned previously, some of the secreted factors may transactivate AR in the absence of androgens, and consequently, acquisition of this highly secretory phenotype may contribute to the acquisition of androgen independence and development of CRPC. These results are in accordance with published observations, which revealed that androgens regulate Skp2 expression; in particular, AR was found to stabilize Skp2 (Wang et al. 2008). Moreover, the depletion of AR or Skp2 alone lead to cell cycle arrest, but only AR depletion to the induction of NED. Using an AR-positive castration resistant subline of LNCaP cells, the connection between AR and Skp2 was confirmed; treatment of this subline with androgens led to the suppression of proliferation through AR, Skp2, and c-Myc

(Chuu et al. 2011). Skp2 is regulated by androgens in a biphasic manner, primarily at the mRNA level. Subphysiological concentrations of androgens slightly increase Skp2 levels, and physiological levels decrease Skp2 levels in LNCaP cells. Moreover, the pocket protein p107 was identified as an important molecule that mediates the androgenic repression of Skp2 in LNCaP cells, but not the only such molecule (Jiang et al. 2012).

Summary

In summary, based on the literature and our own work, we assume that there is a clear connection among androgen depletion, senescence, and NED

in prostate cancer cells. Androgen depletion induces complete changes in the phenotype of cancer cells; these cells display the characteristics of both NE and senescent cells. Importantly, both of these phenotypes are accompanied by massive secretory function; many of these secreted factors associated with NEP, SASP, or both were confirmed to support proliferation, differentiation, and other biological processes in neighboring cancer cells (Fig. 26.1). These factors may contribute at least in part to the survival of cancer cells during ADT because several of these secreted factors can transactivate AR. Interestingly, it was demonstrated that antagonists of bombesin/GRP inhibited the growth of androgen-independent tumors in mouse xenograft models (Stangelberger et al. 2005). Moreover, the neuropeptides endothelin-1 and bombesin stimulated the proliferation of prostate cancer cells and expression of IL-8 and VEGF, and this effect was abrogated by neuropeptide inhibition using bortezomib (Tsapakidis et al. 2012). Therefore, these promising results indicate that targeting these secretory factors could improve the efficiency of anticancer therapy.

Acknowledgements This work was supported by grant IGA MZD NT13573-4/2012 and by the project FNUSA-ICRC (no. CZ.1.05/1.1.00/02.0123) from the European Regional Development Fund and by the project HistoPARK (CZ.1.07/2.3.00/20.0185). Institutional support was provided by the Academy of Sciences of the Czech Republic.

References

- Alimonti A, Nardella C, Chen Z, Clohessy JG, Carracedo A, Trotman LC, Cheng K et al (2010) A novel type of cellular senescence that can be enhanced in mouse models and human tumor xenografts to suppress prostate tumorigenesis. *J Clin Invest* 120(3):681–693
- Ather MH, Abbas F, Faruqui N, Israr M, Pervez S (2008) Correlation of three immunohistochemically detected markers of neuroendocrine differentiation with clinical predictors of disease progression in prostate cancer. *BMC Urol* 8:21
- Balk SP, Knudsen KE (2008) AR, the cell cycle, and prostate cancer. *Nucl Recept Signal* 6:e001
- Bavik C, Coleman I, Dean JP, Knudsen B, Plymate S, Nelson PS (2006) The gene expression program of prostate fibroblast senescence modulates neoplastic epithelial cell proliferation through paracrine mechanisms. *Cancer Res* 66(2):794–802
- Berruti A, Dogliotti L, Mosca A, Gorzegno G, Bollito E, Mari M, Tarabuzzi R et al (2001) Potential clinical value of circulating chromogranin a in patients with prostate carcinoma. *Ann Oncol* 12(Suppl 2):S153–S157
- Bianchi-Frias D, Vakar-Lopez F, Coleman IM, Plymate SR, Reed MJ, Nelson PS (2010) The effects of aging on the molecular and cellular composition of the prostate microenvironment. *PLoS One* 5(9):e12501
- Bonkhoff H (2001) Neuroendocrine differentiation in human prostate cancer. Morphogenesis, proliferation and androgen receptor status. *Ann Oncol* 12(Suppl 2):S141–S144
- Carrano AC, Eytan E, Hershko A, Pagano M (1999) SKP2 is required for ubiquitin-mediated degradation of the CDK inhibitor p27. *Nat Cell Biol* 1(4):193–199
- Carver BS, Chapinski C, Wongvipat J, Hieronymus H, Chen Y, Chandralapaty S, Arora VK et al (2011) Reciprocal feedback regulation of PI3K and androgen receptor signaling in PTEN-deficient prostate cancer. *Cancer Cell* 19(5):575–586
- Castro P, Giri D, Lamb D, Ittmann M (2003) Cellular senescence in the pathogenesis of benign prostatic hyperplasia. *Prostate* 55(1):30–38
- Chan CH, Lee SW, Wang J, Lin HK (2010) Regulation of Skp2 expression and activity and its role in cancer progression. *Scientific World J* 10:1001–1015
- Chen Z, Trotman LC, Shaffer D, Lin HK, Dotan ZA, Niki M, Koutcher JA et al (2005) Crucial role of p53-dependent cellular senescence in suppression of Pten-deficient tumorigenesis. *Nature* 436(7051):725–730
- Choi J, Shendrik I, Peacocke M, Peehl D, Buttyan R, Ikeguchi EF, Katz AE, Benson MC (2000) Expression of senescence-associated beta-galactosidase in enlarged prostates from men with benign prostatic hyperplasia. *Urology* 56(1):160–166
- Chung LW, Cunha GR (1983) Stromal-epithelial interactions: II. Regulation of prostatic growth by embryonic urogenital sinus mesenchyme. *Prostate* 4(5):503–511
- Chuu CP, Kokontis JM, Hiipakka RA, Fukuchi J, Lin HP, Lin CY, Huo C, Su LC, Liao S (2011) Androgen suppresses proliferation of castration-resistant LNCaP 104-R2 prostate cancer cells through androgen receptor, Skp2, and c-Myc. *Cancer Sci* 102(11):2022–2028
- Coppe JP, Desprez PY, Krtolica A, Campisi J (2010) The senescence-associated secretory phenotype: the dark side of tumor suppression. *Annu Rev Pathol* 5:99–118
- Culig Z, Hobisch A, Cronauer MV, Radmayr C, Trapman J, Hittmair A, Bartsch G, Klocker H (1994) Androgen receptor activation in prostatic tumor cell lines by insulin-like growth factor-I, keratinocyte growth factor, and epidermal growth factor. *Cancer Res* 54(20):5474–5478
- Dean JP, Nelson PS (2008) Profiling influences of senescent and aged fibroblasts on prostate carcinogenesis. *Br J Cancer* 98(2):245–249
- Dizeyi N, Hedlund P, Bjartell A, Tinzl M, Austild-Tasken K, Abrahamsson PA (2011) Serotonin activates MAP

- kinase and PI3K/Akt signaling pathways in prostate cancer cell lines. *Urol Oncol* 29(4):436–445
- English HF, Santen RJ, Isaacs JT (1987) Response of glandular versus basal rat ventral prostatic epithelial cells to androgen withdrawal and replacement. *Prostate* 11(3):229–242
- Eyman D, Damodarasamy M, Plymate SR, Reed MJ (2009) CCL5 secreted by senescent aged fibroblasts induces proliferation of prostate epithelial cells and expression of genes that modulate angiogenesis. *J Cell Physiol* 220(2):376–381
- Frescas D, Pagano M (2008) Deregulated proteolysis by the F-box proteins SKP2 and beta-TrCP: tipping the scales of cancer. *Nat Rev Cancer* 8(6):438–449
- Germann M, Wetterwald A, Guzman-Ramirez N, van der Pluijm G, Culig Z, Cecchini MG, Williams ED, Thalmann GN (2012) Stem-like cells with luminal progenitor phenotype survive castration in human prostate cancer. *Stem Cells* 30(6):1076–1086
- Giaimo S, d'Adda di Fagnana F (2012) Is cellular senescence an example of antagonistic pleiotropy? *Aging Cell* 11(3):378–383
- Goldstein AS, Stoyanova T, Witte ON (2010) Primitive origins of prostate cancer: in vivo evidence for prostate-regenerating cells and prostate cancer-initiating cells. *Mol Oncol* 4(5):385–396
- Gong J, Lee J, Akio H, Schlegel PN, Shen R (2007) Attenuation of apoptosis by chromogranin a-induced Akt and survivin pathways in prostate cancer cells. *Endocrinology* 148(9):4489–4499
- Grobholz R, Bohrer MH, Siegsmond M, Junemann KP, Bleyl U, Woenckhaus M (2000) Correlation between neovascularisation and neuroendocrine differentiation in prostatic carcinoma. *Pathol Res Pract* 196(5):277–284
- Heinrich E, Trojan L, Friedrich D, Voss M, Weiss C, Michel MS, Grobholz R (2011) Neuroendocrine tumor cells in prostate cancer: evaluation of the neurosecretory products serotonin, bombesin, and gastrin—impact on angiogenesis and clinical follow-up. *Prostate* 71(16):1752–1758
- Hershko DD (2008) Oncogenic properties and prognostic implications of the ubiquitin ligase Skp2 in cancer. *Cancer* 112(7):1415–1424
- Hirano D, Okada Y, Minei S, Takimoto Y, Nemoto N (2004) Neuroendocrine differentiation in hormone refractory prostate cancer following androgen deprivation therapy. *Eur Urol* 45(5):586–592, discussion 592
- Huang J, Yao JL, Zhang L, Bourne PA, Quinn AM, di Sant' Agnese PA, Reeder JE (2005) Differential expression of interleukin-8 and its receptors in the neuroendocrine and non-neuroendocrine compartments of prostate cancer. *Am J Pathol* 166(6):1807–1815
- Huang J, Yao JL, di Sant' Agnese PA, Yang Q, Bourne PA, Na Y (2006) Immunohistochemical characterization of neuroendocrine cells in prostate cancer. *Prostate* 66(13):1399–1406
- Jia L, Sun Y (2011) SCF E3 ubiquitin ligases as anticancer targets. *Curr Cancer Drug Targets* 11(3):347–356
- Jia L, Li H, Sun Y (2011) Induction of p21-dependent senescence by an NAE inhibitor, MLN4924, as a mechanism of growth suppression. *Neoplasia* 13(6):561–569
- Jiang J, Pan Y, Regan KM, Wu C, Zhang X, Tindall DJ, Huang H (2012) Androgens repress expression of the F-box protein Skp2 via p107 dependent and independent mechanisms in LNCaP prostate cancer cells. *Prostate* 72(2):225–232
- Jin RJ, Wang Y, Masumori N, Ishii K, Tsukamoto T, Shappell SB, Hayward SW, Kasper S, Matusik RJ (2004) NE-10 neuroendocrine cancer promotes the LNCaP xenograft growth in castrated mice. *Cancer Res* 64(15):5489–5495
- Kasper S (2008) Exploring the origins of the normal prostate and prostate cancer stem cell. *Stem Cell Rev* 4(3):193–201
- Knudsen KE, Scher HI (2009) Starving the addiction: new opportunities for durable suppression of AR signaling in prostate cancer. *Clin Cancer Res* 15(15):4792–4798
- Komiya A, Suzuki H, Imamoto T, Kamiya N, Nihei N, Naya Y, Ichikawa T, Fuse H (2009) Neuroendocrine differentiation in the progression of prostate cancer. *Int J Urol* 16(1):37–44
- Krtolica A, Parrinello S, Lockett S, Desprez PY, Campisi J (2001) Senescent fibroblasts promote epithelial cell growth and tumorigenesis: a link between cancer and aging. *Proc Natl Acad Sci USA* 98(21):12072–12077, U S A
- Levine L, Lucci JA 3rd, Pazdrak B, Cheng JZ, Guo YS, Townsend CM Jr, Hellmich MR (2003) Bombesin stimulates nuclear factor kappa B activation and expression of proangiogenic factors in prostate cancer cells. *Cancer Res* 63(13):3495–3502
- Lin DL, Whitney MC, Yao Z, Keller ET (2001) Interleukin-6 induces androgen responsiveness in prostate cancer cells through up-regulation of androgen receptor expression. *Clin Cancer Res* 7(6):1773–1781
- Lin HK, Chen Z, Wang G, Nardella C, Lee SW, Chan CH, Yang WL et al (2010) Skp2 targeting suppresses tumorigenesis by Arf-p53-independent cellular senescence. *Nature* 464(7287):374–379
- Liu D, Hornsby PJ (2007) Senescent human fibroblasts increase the early growth of xenograft tumors via matrix metalloproteinase secretion. *Cancer Res* 67(7):3117–3126
- Majumder PK, Grisanzio C, O'Connell F, Barry M, Brito JM, Xu Q, Guney I et al (2008) A prostatic intraepithelial neoplasia-dependent p27 Kip1 checkpoint induces senescence and inhibits cell proliferation and cancer progression. *Cancer Cell* 14(2):146–155
- Mamillapalli R, Gavrilova N, Mihaylova VT, Tsvetkov LM, Wu H, Zhang H, Sun H (2001) PTEN regulates the ubiquitin-dependent degradation of the CDK inhibitor p27(KIP1) through the ubiquitin E3 ligase SCF(SKP2). *Curr Biol* 11(4):263–267
- Mirochnik Y, Veliceasa D, Williams L, Maxwell K, Yemelyanov A, Budunova I, Volpert OV (2012) Androgen receptor drives cellular senescence. *PLoS One* 7(3):e31052
- Mulholland DJ, Tran LM, Li Y, Cai H, Morim A, Wang S, Plaisier S et al (2011) Cell autonomous role of PTEN in regulating castration-resistant prostate cancer growth. *Cancer Cell* 19(6):792–804

- Novakova Z, Hubackova S, Kosar M, Janderova-Rossmeislova L, Dobrovolna J, Vasicova P, Vancurova M et al (2010) Cytokine expression and signaling in drug-induced cellular senescence. *Oncogene* 29(2): 273–284
- Pernicova Z, Slabakova E, Kharraishvili G, Bouchal J, Kral M, Kunicka Z, Machala M, Kozubik A, Soucek K (2011) Androgen depletion induces senescence in prostate cancer cells through down-regulation of Skp2. *Neoplasia* 13(6):526–536
- Schalken JA, van Leenders G (2003) Cellular and molecular biology of the prostate: stem cell biology. *Urology* 62(5 Suppl 1):11–20
- Seaton A, Scullin P, Maxwell PJ, Wilson C, Pettigrew J, Gallagher R, O'Sullivan JM, Johnston PG, Waugh DJ (2008) Interleukin-8 signaling promotes androgen-independent proliferation of prostate cancer cells via induction of androgen receptor expression and activation. *Carcinogenesis* 29(6):1148–1156
- Soucy TA, Smith PG, Milhollen MA, Berger AJ, Gavin JM, Adhikari S, Brownell JE et al (2009) An inhibitor of NEDD8-activating enzyme as a new approach to treat cancer. *Nature* 458(7239):732–736
- Stangelberger A, Schally AV, Varga JL, Hammann BD, Groot K, Halmos G, Cai RZ, Zarandi M (2005) Antagonists of growth hormone releasing hormone (GHRH) and of bombesin/gastrin releasing peptide (BN/GRP) suppress the expression of VEGF, bFGF, and receptors of the EGF/HER family in PC-3 and DU-145 human androgen-independent prostate cancers. *Prostate* 64(3):303–315
- Trotman LC, Niki M, Dotan ZA, Koutcher JA, Di Cristofano A, Xiao A, Khoo AS et al (2003) Pten dose dictates cancer progression in the prostate. *PLoS Biol* 1(3):E59
- Tsapakidis K, Vlachostergios PJ, Voutsadakis IA, Befani CD, Patrikidou A, Hatzidaki E, Daliani DD, Moutzouris G, Liakos P, Papandreou CN (2012) Bortezomib reverses the proliferative and antiapoptotic effect of neuropeptides on prostate cancer cells. *Int J Urol* 19(6):565–574
- Wang H, Sun D, Ji P, Mohler J, Zhu L (2008) An AR-Skp2 pathway for proliferation of androgen-dependent prostate-cancer cells. *J Cell Sci* 121(Pt 15):2578–2587
- Wright ME, Tsai MJ, Aebersold R (2003) Androgen receptor represses the neuroendocrine transdifferentiation process in prostate cancer cells. *Mol Endocrinol* 17(9):1726–1737
- Yang G, Ayala G, De Marzo A, Tian W, Frolov A, Wheeler TM, Thompson TC, Harper JW (2002) Elevated Skp2 protein expression in human prostate cancer: association with loss of the cyclin-dependent kinase inhibitor p27 and PTEN and with reduced recurrence-free survival. *Clin Cancer Res* 8(11):3419–3426
- Yuan TC, Veeramani S, Lin MF (2007) Neuroendocrine-like prostate cancer cells: neuroendocrine transdifferentiation of prostate adenocarcinoma cells. *Endocr Relat Cancer* 14(3):531–547

8. Vanhara P, Hampl A, Kozubik A, Soucek K. **Growth/Differentiation Factor-15: Prostate Cancer Suppressor or Promoter?** *Prostate Cancer and Prostatic Diseases* 2012; **15**(4):320-8.

Commentary:

In this review, we envisaged the new roles of Growth/Differentiation Factor-15 (GDF-15) cytokine in prostate development and histophysiology. GDF-15 is a cytokine upregulated in many cancers associated with poor prognosis. Molecularly, GDF-15 was shown to possess immunosuppressive activities evoked upon generalized cell stress, senescence or tissue disturbance.

DOI: 10.1038/pcan.2012.6
Journal: Prostate Cancer and Prostatic Diseases
Impact factor (WOS, 2012): 2.811
Number of citations (WOS, 2018): 24
Cited in: Journal of Cell Biology, International Journal of Oncology, Oncotarget, Cell Cycle, Journal of Biological Chemistry, etc.

Most important citation:

Chung HK, Ryu D, Kim KS, Chang JY, Kim YK, Yi HS, Kang SG, Choi MJ, Lee SE, Jung SB, Ryu MJ, Kim SJ, Kweon GR, Kim H, Hwang JH, Lee CH, Lee SJ, Wall CE, Downes M, Evans RM, Auwerx J, Shong M. **Growth differentiation factor 15 is a myomitokine governing systemic energy homeostasis.** *Journal of Cell Biology* 2017; **216**(1):149-165.
doi: 10.1083/jcb.201607110. (IF 2016: 7.955)

Contribution of the author: 1st author. Design and writing of manuscript.

REVIEW

Growth/differentiation factor-15: prostate cancer suppressor or promoter?

P Vaňhara¹, A Hampl^{1,2}, A Kozubík^{3,4} and K Souček^{2,3}

Deregulation of expression and function of cytokines belonging to the transforming growth factor- β (TGF- β) family is often associated with various pathologies. For example, this cytokine family has been considered a promising target for cancer therapy. However, the detailed functions of several cytokines from the TGF- β family that could have a role in cancer progression and therapy remain unclear. One of these molecules is growth/differentiation factor-15 (GDF-15), a divergent member of the TGF- β family. This stress-induced cytokine has been proposed to possess immunomodulatory functions and its high expression is often associated with cancer progression, including prostate cancer (PCa). However, studies clearly demonstrating the mechanisms for signal transduction and functions in cell interaction, cancer progression and therapy are still lacking. New GDF-15 roles have recently been identified for modulating osteoclast differentiation and for therapy for PCa bone metastases. Moreover, GDF-15 is as an abundant cytokine in seminal plasma with immunosuppressive properties. We discuss studies that focus on the regulation of GDF-15 expression and its role in tissue homeostasis, repair and the immune response with an emphasis on the role in PCa development.

Prostate Cancer and Prostatic Diseases advance online publication, 28 February 2012; doi:10.1038/pcan.2012.6

Keywords: growth/differentiation factor-15; macrophage inhibitory cytokine 1; transforming growth factor- β

INTRODUCTION

Cancer does not merely affect a single cell or an enclosed population of homogenous tumor cells. Thus, studying processes that modulate the tumor microenvironment, particularly the relationship between cancer or stromal cells and the immune system, has immense clinical potential. New findings that describe potential methods to modulate particular cell populations can offer novel strategies for cancer prevention and therapy. Cytokines represent important signaling molecules that regulate the fate of both cancer cells and other cell types within the tumor microenvironment. Several examples exist in clinical practice, where revelation regarding the role of a particular cytokine in cancer progression led to a novel anti-cancer therapy design and significantly improved its efficiency.¹

Deregulation of expression and function of cytokines belonging to transforming growth factor- β (TGF- β) family is often associated with cancer.² Thus, cytokines in this family represent potential candidates for drug targeting. However, the detailed cancer-related functions of several TGF- β family members are still not clear. One of these, growth/differentiation factor-15 (GDF-15), is a divergent member of TGF- β family.³ This cytokine has been proposed to possess immunomodulatory functions and its high expression is often associated with cancer progression (for review see⁴). However, studies clearly demonstrating its function in tissue development and hematopoiesis and cancer progression have not been conducted. More detailed elucidation of the physiological function of GDF-15 may lead to innovative new cancer treatment strategies to benefit future patients.

GDF-15 SEQUENCE AND STRUCTURE

GDF-15 (synonyms: macrophage inhibitory cytokine 1, non-steroidal anti-inflammatory drug (NSAID) activated gene-1, prostate differentiation factor, placental bone morphogenetic protein; placental TGF- β) was discovered simultaneously by several groups^{3,5–8} at the end of 1990s and is localized to chromosome 19 in the region p13.11. Its DNA sequence is 2746 bp long and consists of two exons separated by a single intron.⁹ There are at least two GDF-15 alleles, which were identified and characterized in detail by Breit's group.¹⁰ The polymorphism, labeled H6D, consists of a single C-G transversion in exon II at 2423 bp, resulting in a switch from histidine to aspartic acid at codon 202 of the mature protein. This substitution changes the biochemical properties of the mature protein and may alter GDF-15 interactions. The H6D form of GDF-15 has potential clinical relevance, as several studies indicated better prognosis in prostate cancer (PCa) patients carrying the G allele (H6D protein) than those with wild-type GDF-15.^{11,12} According to the Hardy–Weinberg equilibrium, the genotype frequencies in the healthy population were estimated to be 54% for homozygotes containing only histidine (alleles CC), 7% for aspartic acid homozygotes (GG) and 39% for heterozygotes (CG).¹⁰

The unprocessed translated form of GDF-15 (pre-pro-GDF-15) is 308 amino-acids (aa) long, including the signal sequence (29 aa), the propeptide (167 aa) and a mature protein (112 aa), which contains a cysteine knot typical for the TGF- β family. The N-terminal region (28 aa) of the proprotein was shown to be involved in the endoplasmic reticulum quality control and

¹Department of Histology and Embryology, Faculty of Medicine, Masaryk University, Brno, Czech Republic; ²Centre of Biomolecular and Cellular Engineering, International Clinical Research Center, St Anne's University Hospital Brno, Brno, Czech Republic; ³Department of Cytokinetics, Institute of Biophysics, Academy of Sciences of the Czech Republic, Brno, Czech Republic and ⁴Department of Experimental Biology, Faculty of Science, Masaryk University, Brno, Czech Republic. Correspondence: Dr K Souček, Department of Cytokinetics, Institute of Biophysics, Academy of Sciences of the Czech Republic, Královopolská 135, Brno, CZ-612 65, Czech Republic.
E-mail: ksoucek@ibp.cz

Received 16 November 2011; revised 10 January 2012; accepted 13 January 2012

subsequent proteasomal degradation of the incorrectly folded GDF-15 precursor.¹³ The generation of the biologically active form requires removal of the hydrophobic signal sequence followed by disulfide-linked dimerization of GDF-15 monomers and a final cleavage by furin-like protease at the canonic RXXR site (RRAR, position 196). This process generates the C-terminal form of GDF-15 with a molecular weight of ~20 kDa that subsequently enters secretion pathway.³ Further posttranslational modifications utilize a potential N-glycosylation consensus site at 70 aa (NQS); however, the phosphorylation of mannose residues targeting TGF- β proteins to lysosomes has not been found,¹³ suggesting the N-glycosylation of GDF-15 is probably not critical to enter the secretory pathway as in case of TGF- β .¹⁴ The secreted mature protein is a 25-kDa dimer cleaved from the 62-kDa intracellular precursor.⁶

The production of biologically active GDF-15 is remarkably complex, and variability in the pool of available GDF-15 forms was suggested to be involved in modulating the tumor microenvironment when differences in GDF-15 expression between malignant and normal tissues were described. The premature proprotein is produced preferentially by cancer cells over normal tissues, and the preprocessed or mature GDF-15 forms have been suggested to be differentially deposited in extracellular matrix (ECM).¹⁵ Current data supports the assertion, that it is the propeptide that mediates interactions of pro-GDF-15 with ECM.¹⁵ Therefore, the tissue availability of GDF-15 depends on ECM degradation, histological composition and architecture or presence of enzymes capable of conversion of pro-GDF-15 to GDF-15, implying a regulation similar to TGF- β .^{15,16} However, direct binding of GDF-15 to latent TGF- β -binding protein-1, which normally sequesters TGF- β and induces binding to the ECM, has not yet been described. Interestingly, GDF-15 stimulates the expression and surface stabilization of matrix metalloproteinases (MT1-MMP) in different cell types, including breast cancer (MCF-7) or human embryonic kidney cells (HEK293) that are sensitive to GDF-15-induced growth arrest. Because GDF-15 is simultaneously a substrate for MT1-MMP, the inhibitory effects on cancer cells are abrogated after MT1-MMP stimulation by GDF-15. This feedback circuit may have particular significance for ECM remodeling in the tumor environment, tissue permeability in metastatic spreading and for tumor growth.¹⁶ The availability of mature GDF-15 or activation of the proprotein by ECM-deposited and microenvironment-regulated proteinases increases the complexity of the GDF-15 regulatory network in a manner tightly linked to the cell and tissue microenvironment, especially under pathological conditions.

GDF-15 IN TISSUE HOMEOSTASIS AND REPAIR

Expression of GDF-15 is tightly associated with conditions of stress or damage in tissues, indicating its role in tissue regeneration or healing, as documented in numerous cases, such as for myocardium.¹⁷⁻²³ Because GDF-15 is not normally expressed in the healthy heart, it is rapidly upregulated upon stress or with markers of heart damage, such as pressure overload, inflammation, oxidative stress or ischemia, suggesting an anti-apoptotic or protective function during heart failure, arterial hypertension or other cardiovascular insufficiencies. GDF-15 can also offer clinical prognostic information. For example, high-GDF-15 levels in plasma indicate worsened outcomes for particular cardiac malfunctions.^{19,20,22-25} Biological functions of GDF-15 for tissue regeneration in myocardium have not been satisfactorily clarified so far; however, the polymorphonuclear leukocytes²⁶ or macrophages²⁷ infiltrating the effected site have been proposed as target populations for GDF-15. The pathological accumulation of polymorphonuclear leukocytes in infarcted myocardium may be prevented by GDF-15 secretion, as it reduces polymorphonuclear leukocyte adhesion by the inhibition of integrin β 2 and

small GTPase signaling *in vitro*.²⁶ Along with outside-in signaling, GDF-15-mediated signal transduction in cardiomyocytes involves the canonical SMAD pathway (SMAD2/3). Both actions not only prevent pathological changes in tissue architecture, such as cardiac hypertrophy and ventricular dilation, but can also inhibit an inappropriate immune response. Under hypoxic conditions in human umbilical vein endothelial cells *in vitro*, treatment with GDF-15 significantly enhances HIF1 α -mediated expression of VEGF and also stabilizes the p53-MDM2 complex leading to ubiquitination and subsequent degradation of p53.²⁸ Besides cardiovascular tissue, elevated GDF-15 expression has been found in patients with rheumatoid arthritis,²⁹ congenital anemia^{30,31} and metabolic disorders, such as obesity, diabetes mellitus or preeclampsia.^{32,33} In cases of ineffective hematopoiesis, GDF-15 is likely involved in iron metabolism and erythrocyte differentiation.³⁴ GDF-15 overexpression was measured after mechanical liver or kidney injury³⁵ and was capable of inducing the renewal of specific cell populations, including renal acid-secreting collecting duct cells.³⁶ In mice, GDF-15 may function as a neurotrophic and neuroprotective cytokine, as GDF-15 knock-out mice show postnatal loss of motoneurons in spinal cord and brainstem motor nuclei and dorsal root ganglionic sensory neurons in superior cervical ganglion.³⁷ In this study, Strelau *et al.*³⁷ also demonstrated that GDF-15 produced by Schwann cells promotes the survival of axotomized dopaminergic neurons both *in vivo* and *in vitro*. Further investigation in ischemia-induced brain lesions showed strong and rapid induction of GDF-15 mRNA in neurons and partially in microglial cells; however, a comparison of identically lesioned GDF-15-knock-out and wild-type mice did not reveal a significant difference in infarct area, suggesting a role for GDF-15 in post-lesion adaptation and regeneration rather than general protection or neuronal tissue nutrition.³⁸

In addition to tissue regeneration and repair, GDF-15 is involved in human embryonic development, as it is highly expressed in the placenta during pregnancy, and low levels of GDF-15 in the first weeks of gestation correlate with a higher risk of miscarriage.³⁹⁻⁴¹ However, GDF-15 deficient mice do not show abnormalities in the embryonic development and are fully viable and fertile.³⁷ Soucek *et al.*⁴² measured high levels of GDF-15 in seminal plasma from male donors irrespective of fertility status. Seminal GDF-15 does not appear to influence sperm cell viability or interact with vaginal or cervical cells, but it is capable of inhibiting the proliferation of peripheral blood mononuclear cells in a manner similar to TGF- β -1, but at higher effective concentrations. Moreover, GDF-15-induced the expression of FOXP3 in the CD4 + CD25 + peripheral blood mononuclear cells population from healthy donors.⁴² Thus, the role of GDF-15 in human reproduction might comprise the meticulous regulation of the immune response during conception, implantation and early embryonic development.

Research showing that GDF-15 is linked to low body weight, nutritional disorders, cancer-associated cachexia and the metabolic response in cancer patients may be critical for clinical practice.^{32,43-45} Similar effects were also observed in experimental animals.⁴⁶ Therefore, if GDF-15 contributes to complex stimulatory or inhibitory circuits for the regulation of adipose tissue homeostasis, novel therapeutic approaches for the management of unfavorable disease outcomes or therapeutic side effects may be offered. Johnen *et al.*⁴⁷ showed that GDF-15 can modulate both orexigenic and anorexigenic hypothalamic mediators and therefore indirectly suppress food intake. However, recent results show a direct role for GDF-15, as it was found to be expressed in different adipose tissue depots, and being regulated by, for example, leptin and IL1- β .⁴⁸ Expression of GDF-15 is elevated in patients with obesity comorbidities, suggesting a response to cellular stress or tissue damage.⁴⁵ Interestingly, Kim *et al.*⁴⁹ demonstrated that breast cancer cell line MDA-MB-231 responses to adipocyte-conditioned medium by dramatic increase of GDF-15 expression, resulting in enhanced invasivity of cancer cells.

The physiological role for GDF-15 in adipose tissue remains largely unknown, and further research in this field is needed.

In summary, these findings suggest a role for GDF-15 in the regulation of immune activity, particularly for regulating the inflammatory response and mediating tissue protection or regeneration.

REGULATION OF GDF-15 EXPRESSION

Transcriptional regulation of GDF-15 expression is complex and consists of several independent pathways that depend on tissue, cellular and signaling contexts. GDF-15 is differentially expressed in a variety of adult tissues, especially in reproductive or neural tissue. Moreover, GDF-15 is expressed in extraembryonic tissues, indicating some involvement in embryonic development.^{39–41,50} This complexity in tissue distribution is reflected on the molecular level, implying the utilization of particular transcription machinery or tissue-specific upstream signaling. The GDF-15 promoter sequence is conserved in murine, rat and human tissues and consists of a TATA-like sequence as well as SP1 and AP1/2 consensus sites.⁹ The promoter of GDF-15 contains two distinct p53-binding sites with different binding affinity to p53 *in vitro*. Interestingly, Wong *et al.*⁵¹ identified a novel p53 transcriptional repressor element in close proximity of the p53-binding sites, suggesting a complex regulation of activation of GDF-15 in a manner dependent on cell or signaling context. GDF-15 represents a typical gene of the adaptive response to cellular stress, as its expression is generally low in quiescent cells, but is rapidly enhanced by different stress stimuli that employ different signaling pathways. Upon stimulation, GDF-15 is strongly expressed in response to NSAIDs and generally results in an antiproliferative phenotype. NSAIDs, used commonly to treat pain and inflammation, inhibit cyclooxygenase-1 and -2 and subsequently activate Egr-1 and p53 transcription factors to induce cell-cycle arrest.⁵² GDF-15 was shown to be activated by NSAIDs through the p53 pathway⁵³ and is presumed to be one of the core mediators of NSAID-mediated cell-cycle arrest. However, the effects of NSAIDs on GDF-15 expression are not necessarily mediated by cyclooxygenase inhibition,⁵⁴ and other mechanisms have been proposed. GDF-15 expression-mediated cell growth arrest or apoptosis has been induced by various chemicals, particularly NSAIDs, and has often required p53/p21^{Cip1/Waf1} activation.⁵³ More recent studies also demonstrated p53-independent activation of GDF-15, including GSK3 β , C/EBP, ATF3⁵⁵ or Sp-1/Egr-1.⁵⁶ Lincova *et al.*⁵⁷ separated the mechanisms for GDF-15 induction by NSAIDs and cell growth arrest induced by cyclooxygenase-2 inhibition, suggesting GDF-15 transcriptional regulation independent of cell cycle or lipid signaling. The engagement of GDF-15 in antitumor activities appears to be highly complex, depending on the structure and pharmacokinetic properties of particular NSAID or its metabolites. In APC/Min mice fed the NSAID sulindac either as a prodrug (DM-sulindac) or a pharmacologically active chemical with antitumor effects (sulindac sulfide), GDF-15 was induced in the liver parenchyma only with sulindac sulfide and not the prodrug.⁵⁸ Similarly, GDF-15 expression follows NSAID-induced apoptosis in oral cavity SCC1483 cancer cells, and conditioned medium containing GDF-15 potently inhibits proliferation of these cells.⁵⁹ The direct effects of GDF-15-mediated inhibition of cancer cell growth were also described in ovarian cancer cell lines SKOV3 and OVCAR3 that were treated with different NSAIDs.⁶⁰

A number of plant-derived organic compounds promising novel anti-tumor effects were shown to induce GDF-15 expression that was preceded by p53 activation (e.g., organosulfuryl structures).⁶¹ Heavy metals, DNA damaging agents, hypoxia or high cell density also stimulate GDF-15 expression in a p53-dependent manner.⁶² In addition, particular saponins induce GDF-15 in a PI3K-dependent manner.⁶³ Further evidence that GDF-15 has a role

in cellular stress responses was presented in the work of Schlittenhardt *et al.*, which showed enhanced expression of GDF-15 induced by oxidized low-density lipoproteins, TNF α , certain ceramides or hydrogen peroxide. This group also demonstrated the immunohistochemical colocalization of GDF-15 with PARP, caspase-3, manganese, super-oxide dismutase, c-Jun and p53 in native atherosclerotic tissue.⁶⁴ Taken together, these findings suggest that GDF-15 can be induced by a broad spectrum of cellular or tissue events leading to activation of different intracellular pathways that result in complex phenotypes.

GDF-15 IN CANCER PROGRESSION, SYSTEMIC AND IMMUNE RESPONSE

GDF-15 is generally considered to be part of the cell's antitumor actions, largely because its expression is crucial for the chemopreventive effects of various compounds.^{57,58} However, elevated GDF-15 expression has often been reported during cancer progression, including gastric, ovarian, prostate or breast cancers (see Table 1) with various impact on tumors.^{4,65,66} Despite that the GDF-15 expression profile has been well described in various cancers, its specific role in tumor development remains unclear (Figure 1). For example, in breast or gastric cancer, GDF-15 has been shown to be upregulated upon the activation of the MAPK-ERK1/2 or PKB/Akt pathways recruiting the SP-1 family of transcription factors.⁶⁷ GDF-15 also induces the phosphorylation and activation of ErbB receptors, mTOR/Akt and ERK1/2 pathways. A potential result of these signal integrations is HIF-1 and VEGF activation. Moreover, inhibition or specific downregulation of ErbB2 also inhibited GDF-15-mediated downstream signaling.⁶⁸ These findings indicate the importance of GDF-15 clinically, especially in ErbB2 (HER2)-positive cancers that are sensitive to small molecular inhibitors, such as lapatinib.⁶⁹ GDF-15 is strongly upregulated in hepatocellular carcinoma and other liver diseases, such as fibrosis or cirrhosis induced by hepatitis C virus.⁷⁰ GDF-15 autocrine signaling of transformed or infected hepatocytes then induces Akt, GSK-3 β catenin, Raf phosphorylation and other downstream targets, such as cell-cycle regulators (cyclins A2, E1 and D2) or adhesion molecules (E-cadherin). Interestingly, impairing GDF-15 can inhibit viral replication.⁷⁰ In malignant melanomas, GDF-15 is highly overexpressed,⁷¹ and it is able to mimic VEGF in the neovascularization in the tumor site.⁷² Similarly, in malignant glioblastomas, GDF-15 is upregulated as a reaction to anoxia, suggesting more general involvement in vascularization development.⁷³ Moreover, experimental decrease in GDF-15 expression clearly enhanced natural killer T-cell-mediated cytotoxicity, which increased the immunogenicity of glioma cells⁷⁴ similar to the effects of TGF- β downregulation.⁷⁵ Furthermore, GDF-15 depletion delays the growth of gliomas in mice *in vivo*. It is likely that GDF-15 acts as a potent suppressor of immune cells while simultaneously enhancing cancer cell growth through autocrine signaling. These observations emphasize the importance of assessing the role of the interactions within the tumor microenvironment for a context-dependent role of GDF-15. Interestingly, two antagonistic *in vivo* studies were published recently. Senapati *et al.*⁷⁶ demonstrated that ectopic overexpression of GDF-15 led to increased dissemination capacity of PCa cells. However, Zimmers *et al.*⁵⁸ showed that loss of GDF-15 expression abolished the chemopreventive effects of NSAIDs in animal models of hereditary colon cancer.

Thus, the primary effect of GDF-15 on cancer progression can be linked to the regulation of immune responses in the process of tissue regeneration. GDF-15 has been described as a negative regulator of macrophage activation by suppressing the release of TNF- α , IL-1, IL-2 and MCS-F, thus inhibiting the positive feedback of local inflammatory signaling similar to the effects of TGF- β .³ However, the molecular mechanisms behind these immunosuppressive effects remain unclear despite several hypotheses that

Table 1. Clinical and biological aspects of GDF-15 expression in different cancer types

Cancer type	Clinical prognostic information	Expression change and upstream regulation	Downstream signaling induced by GDF-15	Molecular and/or cellular phenotype induced by GDF-15	References
Bladder	Candidate epigenetic biomarker	?	?	?	101
Breast	?	↑ via AKT ERK1/2-mTOR	ErbB2-AKT-ERK1/2- c-Src-p38-JNK	Enhanced invasion via c-Src	67,68,81,102
Colorectal	Association with tumor progression	↑ via p53	?	p53 dependent apoptosis	103,104
Gastric	Candidate biomarker	↑	EGFR(ErbB2)-MAPK1/2- ERK 1/2-Akt/mTOR	HIF-1 α -VEGFA expression	65,68
Glioblastoma	Candidate biomarker	↑	?	Enhanced proliferation immune escape <i>in vivo</i>	74,105
Hepatocellular (HCV associated)	Candidate biomarker	↑	AKT-GSK-3 β -c-Raf	Enhanced proliferation and invasion	70
Head and neck	Associated with radioresistant phenotype	↑	?	?	106
Melanoma	Association with tumor progression, metastases formation and vascular development	↑ via B-Raf	?	B-Raf-GDF-15 dependent vascularization	66,71,72
Oesophagus/ gastric	Elevated; association with inflammation	↑	?	?	107
Ovarian	Prognostic biomarker	↑	?	?	50,108
Pancreas	Candidate biomarker	↑	?	?	109,110
Prostate	Prognostic biomarker	↑	PKB/Akt-FAK/RhoA	Reorganization of actin architecture enhanced motility metastatic development <i>in vivo</i>	57,76,79, 86,89,111

Abbreviations: FAK, focal adhesion kinases; GDF-15, growth/differentiation factor-15; JNK, c-Jun N-terminal kinase; mTOR, mammalian target of rapamycin. ↑ Indicates elevated expression, ? indicates unknown or so far insufficient data.

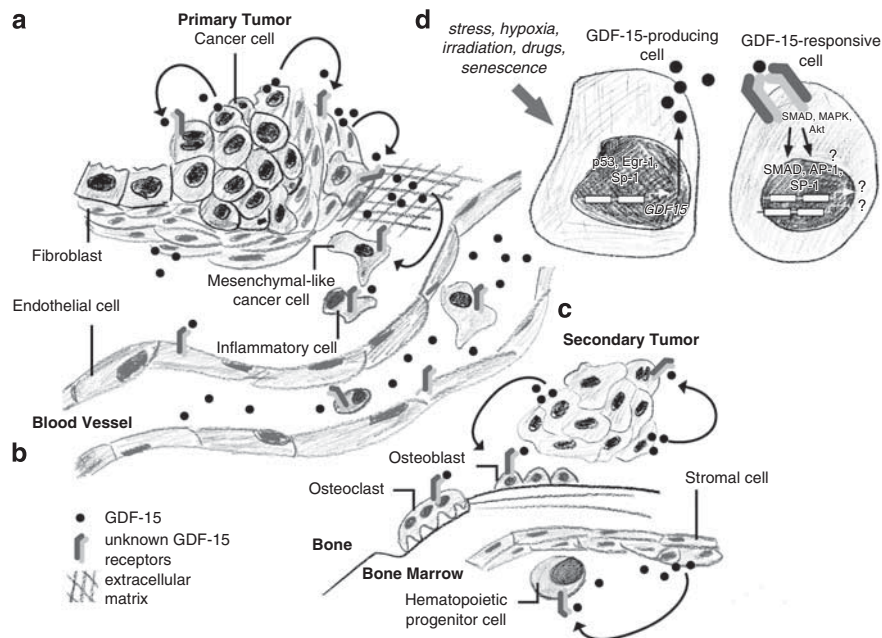


Figure 1. Schematic illustration of growth/differentiation factor-15 (GDF-15) action in tissue microenvironment and cancer progression. **(a)** GDF-15 is secreted by a primary tumor or released from extracellular matrix, affecting both the tumor and adjacent stromal or immune cells responsive to GDF-15. **(b)** GDF-15 is released to blood stream and contributing to tumor spreading, vascularization and immunosuppression. **(c)** GDF-15 is involved in remodeling of bone architecture by action on both osteoblasts and osteoclasts, affecting the bone-marrow microenvironment and stem-cell niche formation. **(d)** GDF-15 expression is induced upon various stimuli, for example, by p53 and/or Sp1-Egr-1 dependent transcription. GDF-15 induces signaling pathway comprising of so far identified SMAD, MAPK and Akt and activating transcription from SMAD, AP-1 and Sp-1 driven promoters.

focus on interactions with regulatory T lymphocytes in a context already defined for TGF- β in various cancers.^{42,77} Taken together, the cancer-associated elevated expression of GDF-15 may have strong predictive potential that could justify the introduction of GDF-15 clinically as a biomarker for particular cancers. Moreover, focusing on its immunosuppressive characteristics, GDF-15 may be specifically targeted to restore the immune-mediated anti-tumor response.

GDF-15 IN PCA

GDF-15 as a biomarker

For PCA, there is a long-term need for both specific and robust markers that would allow precise prediction and estimation of disease outcome. At present, only PSA was introduced to clinical practice. However, total levels of PSA in serum are not cancer specific, as they are found even in benign diseases, leading to potential false-positive diagnosis of PCA. Improvement was achieved by analyzing alternative molecular forms of PSA, which decreased the number of cancer-negative biopsies in indicated cases.⁷⁸ Of particular importance, the measurement of GDF-15 in serum was shown to increase the precision of the information potential of PSA and its forms. The presence of GDF-15 in serum is slightly decreased in BPH or localized PCA compared with normal prostate tissue,⁷⁹ but it is elevated in metastatic disease.^{80,81} Interestingly, the inflammatory events in prostate tissue are considered to trigger the transition from normal to benign hyperplastic state and probably reflect an individual's sensitivity to autoimmune lesions.^{82,83} Inflammatory changes of glandular architecture followed by increase of stromal tissue in BPH negatively correlate with GDF-15 expression.^{84,85}

Despite the presence of several molecular forms of GDF-15, the analysis of total GDF-15 serum levels showed its clear discriminative capacity for PCA mortality and disease outcome, which justifies further prospective studies to potentially introduce GDF-15 as a clinically important biomarker for PCA.⁸⁶ As such, the analysis of overall GDF-15 may offer a robust screening method.

Role of GDF-15 in PCA development

Tumor development can be considered either as uncontrolled regeneration or as cellular reprogramming or reversion to the early developmental stages. Thus, lessons from embryonic development can shed light on the complex signaling in organogenesis and tissue formation. In the early development of the normal mouse prostate, GDF-15 is dynamically expressed in dividing epithelium originating from the urogenital sinus and buds, and its expression falls when the stage of developed prostate lobes has been reached.⁸⁷ GDF-15 is then reactivated during prostate maturation, and its expression correlates with differentiation markers (e.g., K19). Thus, data from embryonic, fetal and early postnatal murine development suggest a clear dual function for GDF-15 in the regulation of epithelial proliferation in the urogenital sinus as well as its differentiation in the later stages of prostate lobular structure formation.⁸⁷ A PCA model based on modified SV-40 region driven by the prostate-specific rat probasin promoter developed by Kasper *et al.*⁸⁸ (*CD-1-Tg(Pbsn-Tag) 12T10Rjm*, according to the Cancer Model Database) allowed for the detailed study of GDF-15 in the development of prostate intraepithelial neoplasias, which is considered comparable to human prostate intraepithelial neoplasias. Using this model, Noorali *et al.*⁸⁷ showed clear differences in GDF-15 expression among normally developing prostate, prostate hyperplasia and prostate intraepithelial neoplasias. Although the GDF-15 pattern of expression in normal tissue shows two clear peaks (epithelial proliferation in buds and lobes, differentiation of mature prostate), its expression is attenuated in the maturing prostate and is accompanied with a loss of differentiation markers in transgenic

tissue showing progression from hyperplasia to prostate intraepithelial neoplasias. Furthermore, GDF-15 expression is strongly upregulated in the tumorigenic state that follows. Moreover, GDF-15 expression is enhanced in developed PCA similar to other cancer types.

Despite that there is low genetic variation in the GDF-15 coding sequence, and existing single nucleotide polymorphisms were not associated with PCA susceptibility,⁸⁹ the function of wild-type GDF-15 and its H6D variant can be discriminated in developed PCA. In athymic nude mice inoculated with DU145 PCA cells transfected with appropriate coding sequences, the H6D variant clearly interfered with tumor development by lowering levels of cyclin D1 and IGF-1 in the serum resulting in smaller tumors than in controls with wild-type GDF-15.⁹⁰ However, the systemic role for body-weight regulation and the induction of tumor associated cachexia is likely not compromised in the H6D variant compared with wild-type GDF-15, as both proteins significantly reduce the amount of abdominal fat in experimental mice and reduce adipose tissue signaling.⁹⁰

A common problem associated with long-term PCA therapy is the development of hormone refractory PCA and resistance to chemotherapy. It is estimated that about 50% of patients treated by first-line castration do not respond to second-line of chemotherapy with Docetaxel.⁹¹ The expression of GDF-15 in PC3 cells with acquired resistance to Docetaxel is increased after chemotherapy exposure compared with parental PC3s. Moreover, a similar trend has been observed in the serum/plasma of patients with Docetaxel-resistant PCA with a clear impact on patients' survival.⁹² This correlates well with previously published data,⁹³ however, *in vitro* data showed a direct link between GDF-15 and Docetaxel resistance. Androgen independent PCA PC3 cells treated with GDF-15 became partially resistant to Docetaxel and Docetaxel-resistant PC3 cells treated with GDF-15 shRNA showed restored susceptibility to Docetaxel.⁹²

In androgen-sensitive LNCaP cells, GDF-15 is expressed and supports proliferation and clonogenic cell growth. GDF-15 silencing in the LN3 subline of LNCaP cells, which are characterized by a high-metastatic potential, decreased proliferation rate and reduced anchor-independent cell growth on soft agar.⁹⁴ In PC3 and DU145 cells, GDF-15 is virtually unexpressed,⁹⁵ however, these cells retain sensitivity to GDF-15 under particular conditions. The p53-negative PC3 cells responded to GDF-15 treatment by reducing mobility through matrigel columns.⁹⁶ Similarly, for DU145, a slight tumor suppressive effect was reported *in vivo*.⁹⁰

To identify a systemic role of GDF-15 in PCA bone metastasis, Wakchoure *et al.*⁴⁶ inoculated athymic nude mice with DU-145 PCA cells overexpressing GDF-15. The histomorphological and X-ray analyses showed enhanced osteoblast differentiation and bone-remodeling activity in sites of bone metastases. This study also showed enhanced osteoclast numbers in metastasis sites; however, using an *in vitro* macrophage model, another study demonstrated clear inhibitory effects of GDF-15 on osteoclast formation. Under experimental *in vitro* conditions, GDF-15 inhibited MCSF-RANKL-induced osteoclast differentiation that were derived either from the macrophage cell line RAW264.7 or mononuclear precursors isolated from murine bone marrow. Impaired differentiation resulted in reduced osteoclast numbers in culture and decreased bone resorption. On the molecular level, GDF-15 induced the retention of I κ B, an inhibitor of the NF κ B transcription factor, in the cytoplasm, thus preventing NF κ B-mediated expression of the key transcription factor *c-fos* and the osteoclast hallmark enzymes cathepsin K and carbonic anhydrase II.⁹⁷ Interestingly, GDF-15 is upregulated by vitamin D3 (1,25(OH)₂D₃) in the androgen-dependent PCA cells LNCaP.⁹⁸ The GDF-15 protein produced by 1,25(OH)₂D₃-stimulated LNCaP cells was the biologically active form that interferes with MCSF-RANKL signaling independently of osteoprotegerin, a physiological

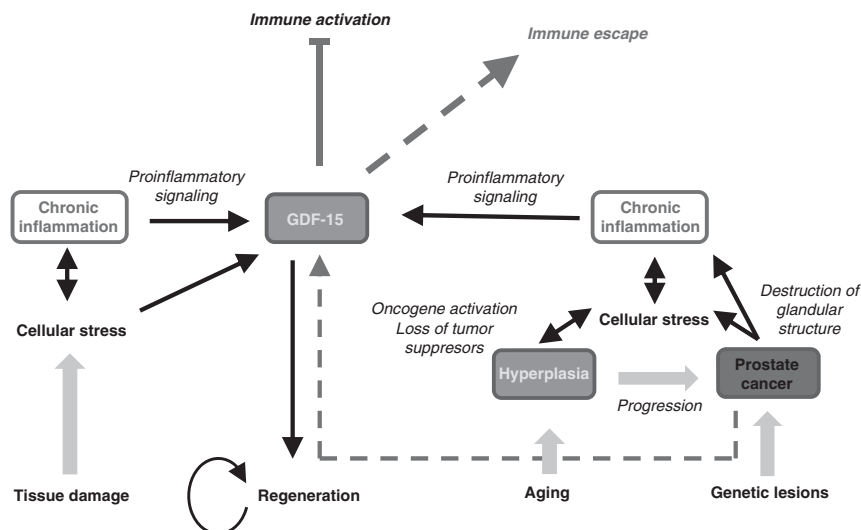


Figure 2. Proposed role of growth/differentiation factor-15 (GDF-15) in prostate cancer (PCa) progression. GDF-15 is induced by cellular stress upon tissue damage or inflammation and physiologically protects the lesion site from the inadequate reaction of immune system. Under pathological conditions, such as developed PCa, GDF-15 is induced as a result of cellular stress caused by changes and/or destruction of prostate tissue architecture, therefore inducing immunoprotective status of cancer-lesioned site.

regulator of osteoclast differentiation and activity.⁹⁷ Further evidences for a role for GDF-15 in cancer spreading and distant metastasis formation were reported by Senapati *et al.*⁷⁶ This *in vitro* study described enhanced motility and invasion capabilities and changes in the actin cytoskeletal architecture of PC3 and LNCaP cells overexpressing GDF-15. The induction of intracellular signaling by GDF-15 led to the activation of focal adhesion kinases and the small GTPase RhoA, suggesting that GDF-15 moderates direct control over architectural rearrangements and subsequent cell motility. However, using ovarian and prostate SKOV-3 and PC3 cells, respectively, Cheng *et al.*⁹⁶ showed that GDF-15 inhibited cellular migration through matrigel columns through a p53-dependent mechanism. Similarly, GDF-15 has been described as a mediator of NSAIDs-induced inhibition of migration of PCa cells.⁹⁹ According to these experimental data, GDF-15 effects may vary depending on signaling status, the genetic background of target cell populations, particularly on the presence of the androgen receptor and/or p53 activity and interaction with immune system (Figure 2). Contextual pleiotropy and dual role in cancer, which is general characteristic of TGF- β family cytokines¹⁰⁰ is most likely characteristic also of GDF-15. However, detail mechanisms of its both tumor suppressor and/or promoter action needs to be revealed.

CONCLUSIONS

GDF-15 is a distant member of the TGF- β family and is strongly expressed in a great variety of human cancers including PCa; however, its role in cancer pathophysiology remains ambiguous. Nevertheless, the link between GDF-15 expression and the tumor stage or disease outcome is informative, suggesting that GDF-15 may be a clinically relevant biomarker for particular cancers. The physiological role of GDF-15 may involve mediating interactions between different cellular populations and the immune system or enabling mutual regulation in certain microenvironments. Thus, the suppression of certain immune cell populations may be the core systemic mechanism for the role of GDF-15 in cancer development and progression. GDF-15 was first recognized as a factor interfering with macrophage activation. Later studies showed its inhibitory role on the effects of NSAIDs and the suppression of macrophage-derived osteoclasts or regulatory T lymphocytes. The role of GDF-15 in embryonic development

remains unresolved. In mice, GDF-15 is not necessary for proper development and knockouts are fully viable and fertile; however, in humans, it likely has a role in fetomaternal interactions and may prevent immune rejection *in utero*. There is increasing evidence for the involvement of GDF-15 in tissue regeneration or the reaction to different stress conditions. GDF-15-mediated suppressive effects often mimic those observed by generic TGF- β s, but there are differences in target population responses. Of particular importance is to clarify the intracellular signals ranging from the receptor formation to the interacting partners that mediate the effects of GDF-15. Increased knowledge of GDF-15-induced signaling pathways in either producing or receptive cells will contribute to the understanding of events that form the complex communication network within the tumor microenvironment. The nature of GDF-15 proteins has two sides, with both tumor-suppressor and oncogenic characteristics. As the cellular, tissue and systemic effects of GDF-15 signaling in well-defined experimental conditions has shown, it is likely that GDF15 is an active and important player in the development of PCa rather than a stress-induced bystander. Therefore, introducing GDF-15 into clinical discussions may offer new possibilities to better understand cancer development and potentially enhance diagnostic or therapeutic strategies.

CONFLICT OF INTEREST

The authors declare no conflict of interest.

ACKNOWLEDGEMENTS

This work was supported by grants IGA MZD 9600-4/2008 and IGA MZD 9956-4/2008, Grant number MSM0021622430 from the Ministry of Education, Youth and Sports of the Czech Republic and by the project FNUSA-ICRC (no. CZ.1.05/1.1.00/02.0123) from the European Regional Development Fund.

REFERENCES

- 1 Dranoff G. Cytokines in cancer pathogenesis and cancer therapy. *Nat Rev Cancer* 2004; **4**: 11–22.
- 2 Yang L, Moses HL. Transforming growth factor beta: tumor suppressor or promoter? Are host immune cells the answer? *Cancer Res* 2008; **68**: 9107–9111.

- 3 Bootcov MR, Bauskin AR, Valenzuela SM, Moore AG, Bansal M, He XY et al. MIC-1, a novel macrophage inhibitory cytokine, is a divergent member of the TGF-beta superfamily. *Proc Natl Acad Sci USA* 1997; **94**: 11514-11519.
- 4 Bauskin AR, Brown DA, Kuffner T, Johnen H, Luo XW, Hunter M et al. Role of macrophage inhibitory cytokine-1 in tumorigenesis and diagnosis of cancer. *Cancer Res* 2006; **66**: 4983-4986.
- 5 Baek SJ, Kim KS, Nixon JB, Wilson LC, Eling TE. Cyclooxygenase inhibitors regulate the expression of a TGF-beta superfamily member that has proapoptotic and antitumorigenic activities. *Mol Pharmacol* 2001; **59**: 901-908.
- 6 Fairlie WD, Moore AG, Bauskin AR, Russell PK, Zhang HP, Breit SN. MIC-1 is a novel TGF-beta superfamily cytokine associated with macrophage activation. *J Leukoc Biol* 1999; **65**: 2-5.
- 7 Hromas R, Hufford M, Sutton J, Xu D, Li Y, Lu L. PLAB, a novel placental bone morphogenetic protein. *Biochim Biophys Acta* 1997; **1354**: 40-44.
- 8 Yokoyama-Kobayashi M, Saeiki M, Sekine S, Kato S. Human cDNA encoding a novel TGF-beta superfamily protein highly expressed in placenta. *J Biochem* 1997; **122**: 622-626.
- 9 Bottner M, Laaff M, Schechinger B, Rappold G, Unsicker K, Suter-Crazzolara C. Characterization of the rat, mouse, and human genes of growth/differentiation factor-15/macrophage inhibiting cytokine-1 (GDF-15/MIC-1). *Gene* 1999; **237**: 105-111.
- 10 Brown DA, Bauskin AR, Fairlie WD, Smith MD, Liu T, Xu N et al. Antibody-based approach to high-volume genotyping for MIC-1 polymorphism. *Biotechniques* 2002; **33**: 118-120, 122, 124 passim.
- 11 Hayes VM, Severi G, Southey MC, Padilla EJ, English DR, Hopper JL et al. Macrophage inhibitory cytokine-1 H6D polymorphism, prostate cancer risk, and survival. *Cancer Epidemiol Biomarkers Prev* 2006; **15**: 1223-1225.
- 12 Lindmark F, Zheng SL, Wiklund F, Bensen J, Balter KA, Chang B et al. H6D polymorphism in macrophage-inhibitory cytokine-1 gene associated with prostate cancer. *J Natl Cancer Inst* 2004; **96**: 1248-1254.
- 13 Bauskin AR, Zhang HP, Fairlie WD, He XY, Russell PK, Moore AG et al. The propeptide of macrophage inhibitory cytokine (MIC-1), a TGF-beta superfamily member, acts as a quality control determinant for correctly folded MIC-1. *EMBO J* 2000; **19**: 2212-2220.
- 14 Brunner AM, Lioubin MN, Marquardt H, Malacko AR, Wang WC, Shapiro RA et al. Site-directed mutagenesis of glycosylation sites in the transforming growth factor-beta 1 (TGF beta 1) and TGF beta 2 (414) precursors and of cysteine residues within mature TGF beta 1: effects on secretion and bioactivity. *Mol Endocrinol* 1992; **6**: 1691-1700.
- 15 Bauskin AR, Brown DA, Junankar S, Rasiah KK, Eggleton S, Hunter M et al. The propeptide mediates formation of stromal stores of PROMIC-1: role in determining prostate cancer outcome. *Cancer Res* 2005; **65**: 2330-2336.
- 16 Abd El-Aziz SH, Endo Y, Miyamaori H, Takino T, Sato H. Cleavage of growth differentiation factor 15 (GDF15) by membrane type 1-matrix metalloproteinase abrogates GDF15-mediated suppression of tumor cell growth. *Cancer Sci* 2007; **98**: 1330-1335.
- 17 Anand IS, Kempf T, Rector TS, Tapken H, Allhoff T, Jantzen F et al. Serial measurement of growth-differentiation factor-15 in heart failure: relation to disease severity and prognosis in the Valsartan Heart Failure Trial. *Circulation* 2010; **122**: 1387-1395.
- 18 Daniels LB, Clopton P, Laughlin GA, Maisel AS, Barrett-Connor E. Growth-differentiation factor-15 is a robust, independent predictor of 11-year mortality risk in community-dwelling older adults: the Rancho Bernardo study. *Circulation* 2011; **123**: 2101-2110.
- 19 Kempf T, Horn-Wichmann R, Brabant G, Peter T, Allhoff T, Klein G et al. Circulating concentrations of growth-differentiation factor 15 in apparently healthy elderly individuals and patients with chronic heart failure as assessed by a new immunoradiometric sandwich assay. *Clin Chem* 2007; **53**: 284-291.
- 20 Kempf T, von Haehling S, Peter T, Allhoff T, Ciccoira M, Doehner W et al. Prognostic utility of growth differentiation factor-15 in patients with chronic heart failure. *J Am Coll Cardiol* 2007; **50**: 1054-1060.
- 21 Kempf T, Wollert KC. Growth-differentiation factor-15 in heart failure. *Heart Fail Clin* 2009; **5**: 537-547.
- 22 Wang F, Guo Y, Yu H, Zheng L, Mi L, Gao W. Growth differentiation factor 15 in different stages of heart failure: potential screening implications. *Biomarkers* 2010; **15**: 671-676.
- 23 Wiklund FE, Bennet AM, Magnusson PK, Eriksson UK, Lindmark F, Wu L et al. Macrophage inhibitory cytokine-1 (MIC-1/GDF15): a new marker of all-cause mortality. *Aging Cell* 2010; **9**: 1057-1064.
- 24 Dinh W, Futh R, Lankisch M, Hess G, Zdunek D, Scheffold T et al. Growth-differentiation factor-15: a novel biomarker in patients with diastolic dysfunction? *Arq Bras Cardiol* 2011; **97**: 65-75.
- 25 Stahrenberg R, Edelmann F, Mende M, Kockskamper A, Dungen HD, Luers C et al. The novel biomarker growth differentiation factor 15 in heart failure with normal ejection fraction. *Eur J Heart Fail* 2010; **12**: 1309-1316.
- 26 Kempf T, Zarbock A, Widera C, Butz S, Stadtmann A, Rossaint J et al. GDF-15 is an inhibitor of leukocyte integrin activation required for survival after myocardial infarction in mice. *Nat Med* 2011; **17**: 581-588.
- 27 de Jager SC, Bermudez B, Bot I, Koenen RR, Bot M, Kavelaars A et al. Growth differentiation factor 15 deficiency protects against atherosclerosis by attenuating CCR2-mediated macrophage chemotaxis. *J Exp Med* 2011; **208**: 217-225.
- 28 Song H, Yin D, Liu Z. GDF-15 promotes angiogenesis through modulating p53/HIF-1 α signaling pathway in hypoxic human umbilical vein endothelial cells. *Mol Biol Rep* 2011; e-pub ahead of print 20 July 2011.
- 29 Brown DA, Moore J, Johnen H, Smeets TJ, Bauskin AR, Kuffner T et al. Serum macrophage inhibitory cytokine 1 in rheumatoid arthritis: a potential marker of erosive joint destruction. *Arthritis Rheum* 2007; **56**: 753-764.
- 30 Tamary H, Shalev H, Perez-Avraham G, Zoldan M, Levi I, Swinkels DW et al. Elevated growth differentiation factor 15 expression in patients with congenital dyserythropoietic anemia type I. *Blood* 2008; **112**: 5241-5244.
- 31 Theurl I, Finkenstedt A, Schroll A, Nairz M, Sonnweber T, Bellmann-Weiler R et al. Growth differentiation factor 15 in anaemia of chronic disease, iron deficiency anaemia and mixed type anaemia. *Br J Haematol* 2009; **148**: 449-455.
- 32 Dostalova I, Roubicek T, Bartlova M, Mraz M, Lacinova Z, Haluzikova D et al. Increased serum concentrations of macrophage inhibitory cytokine-1 in patients with obesity and type 2 diabetes mellitus: the influence of very low calorie diet. *Eur J Endocrinol* 2009; **161**: 397-404.
- 33 Sugulle M, Dechend R, Herse F, Weedon-Fekjaer MS, Johnsen GM, Brosnihan KB et al. Circulating and placental growth-differentiation factor 15 in preeclampsia and in pregnancy complicated by diabetes mellitus. *Hypertension* 2009; **54**: 106-112.
- 34 Tanno T, Noel P, Miller JL. Growth differentiation factor 15 in erythroid health and disease. *Curr Opin Hematol* 2011; **17**: 184-190.
- 35 Zimmers TA, Jin X, Hsiao EC, McGrath SA, Esqueda AF, Koniaris LG. Growth differentiation factor-15/macrophage inhibitory cytokine-1 induction after kidney and lung injury. *Shock* 2005; **23**: 543-548.
- 36 Duong Van Huyen JP, Cheval L, Bloch-Faure M, Belair MF, Heudes D, Bruneval P et al. GDF15 triggers homeostatic proliferation of acid-secreting collecting duct cells. *J Am Soc Nephrol* 2008; **19**: 1965-1974.
- 37 Strelau J, Strzelczyk A, Rusu P, Bendner G, Wiese S, Diella F et al. Progressive postnatal motoneuron loss in mice lacking GDF-15. *J Neurosci* 2009; **29**: 13640-13648.
- 38 Schindowski K, von Bohlen und Halbach O, Strelau J, Ridder DA, Herrmann O, Schober A et al. Regulation of GDF-15, a distant TGF-beta superfamily member, in a mouse model of cerebral ischemia. *Cell Tissue Res* 2011; **343**: 399-409.
- 39 Marjono AB, Brown DA, Horton KE, Wallace EM, Breit SN, Manuelpillai U. Macrophage inhibitory cytokine-1 in gestational tissues and maternal serum in normal and pre-eclamptic pregnancy. *Placenta* 2003; **24**: 100-106.
- 40 Tong S, Marjono B, Brown DA, Mulvey S, Breit SN, Manuelpillai U et al. Serum concentrations of macrophage inhibitory cytokine 1 (MIC 1) as a predictor of miscarriage. *Lancet* 2004; **363**: 129-130.
- 41 Wallace EM, Marjono B, Brown DA, Crossley J, Tong S, Aitken D et al. Maternal serum and amniotic fluid levels of macrophage inhibitory cytokine 1 in Down syndrome and chromosomally normal pregnancies. *Prenat Diagn* 2004; **24**: 224-226.
- 42 Soucek K, Slabakova E, Ovesna P, Malenovska A, Kozubik A, Hampl A. Growth/differentiation factor-15 is an abundant cytokine in human seminal plasma. *Hum Reprod* 2010; **25**: 2962-2971.
- 43 Dostalova I, Kavalkova P, Papezova H, Domluvilova D, Zikan V, Haluzik M. Association of macrophage inhibitory cytokine-1 with nutritional status, body composition and bone mineral density in patients with anorexia nervosa: the influence of partial realimentation. *Nutr Metab (Lond)* 2010; **7**: 34.
- 44 Jatoi A. Weight loss in patients with advanced cancer: effects, causes, and potential management. *Curr Opin Support Palliat Care* 2008; **2**: 45-48.
- 45 Vila G, Riedl M, Anderwald C, Resl M, Handisurya A, Clodi M et al. The relationship between insulin resistance and the cardiovascular biomarker growth differentiation factor-15 in obese patients. *Clin Chem* 2011; **57**: 309-316.
- 46 Wakchoure S, Swain TM, Hentunen TA, Bauskin AR, Brown DA, Breit SN et al. Expression of macrophage inhibitory cytokine-1 in prostate cancer bone metastases induces osteoclast activation and weight loss. *Prostate* 2009; **69**: 652-661.
- 47 Johnen H, Lin S, Kuffner T, Brown DA, Tsai VW, Bauskin AR et al. Tumor-induced anorexia and weight loss are mediated by the TGF-beta superfamily cytokine MIC-1. *Nat Med* 2007; **13**: 1333-1340.
- 48 Ding Q, Mracek T, Gonzalez-Muniesa P, Kos K, Wilding J, Trayhurn P et al. Identification of macrophage inhibitory cytokine-1 in adipose tissue and its secretion as an adipokine by human adipocytes. *Endocrinology* 2009; **150**: 1688-1696.

- 49 Kim JH, Kim KY, Jeon JH, Lee SH, Hwang JE, Lee JH et al. Adipocyte culture medium stimulates production of macrophage inhibitory cytokine 1 in MDA-MB-231 cells. *Cancer Lett* 2008; **261**: 253-262.
- 50 Bock AJ, Stavnes HT, Kempf T, Trope CG, Berner A, Davidson B et al. Expression and clinical role of growth differentiation factor-15 in ovarian carcinoma effusions. *Int J Gynecol Cancer* 2010; **20**: 1448-1455.
- 51 Wong J, Li PX, Klamut HJ. A novel p53 transcriptional repressor element (p53TRE) and the asymmetrical contribution of two p53 binding sites modulate the response of the placental transforming growth factor-beta promoter to p53. *J Biol Chem* 2002; **277**: 26699-26707.
- 52 Baek SJ, Kim JS, Moore SM, Lee SH, Martinez J, Eling TE. Cyclooxygenase inhibitors induce the expression of the tumor suppressor gene EGR-1, which results in the up-regulation of NAG-1, an antitumorigenic protein. *Mol Pharmacol* 2005; **67**: 356-364.
- 53 Yang H, Filipovic Z, Brown D, Breit SN, Vassilev LT. Macrophage inhibitory cytokine-1: a novel biomarker for p53 pathway activation. *Mol Cancer Ther* 2003; **2**: 1023-1029.
- 54 Baek SJ, Wilson LC, Lee CH, Eling TE. Dual function of nonsteroidal anti-inflammatory drugs (NSAIDs): inhibition of cyclooxygenase and induction of NSAID-activated gene. *J Pharmacol Exp Ther* 2002; **301**: 1126-1131.
- 55 Lee SH, Krisanapun C, Baek SJ. NSAID-activated gene-1 as a molecular target for capsaicin-induced apoptosis through a novel molecular mechanism involving GSK3beta, C/EBPbeta and ATF3. *Carcinogenesis* 2010; **31**: 719-728.
- 56 Yoshioka H, Kamitani H, Watanabe T, Eling TE. Nonsteroidal anti-inflammatory drug-activated gene (NAG-1/GDF15) expression is increased by the histone deacetylase inhibitor trichostatin A. *J Biol Chem* 2008; **283**: 33129-33137.
- 57 Lincova E, Hampl A, Pernicova Z, Starsichova A, Krcmar P, Machala M et al. Multiple defects in negative regulation of the PKB/Akt pathway sensitise human cancer cells to the antiproliferative effect of non-steroidal anti-inflammatory drugs. *Biochem Pharmacol* 2009; **78**: 561-572.
- 58 Zimmers TA, Gutierrez JC, Koniaris LG. Loss of GDF-15 abolishes sulindac chemoprevention in the ApcMin/+ mouse model of intestinal cancer. *J Cancer Res Clin Oncol* 2010; **136**: 571-576.
- 59 Kim KS, Rhee KH, Yoon JH, Lee JG, Lee JH, Yoo JB. Ginkgo biloba extract (EGb 761) induces apoptosis by the activation of caspase-3 in oral cavity cancer cells. *Oral Oncol* 2005; **41**: 383-389.
- 60 Kim JS, Baek SJ, Sali T, Eling TE. The conventional nonsteroidal anti-inflammatory drug sulindac sulfide arrests ovarian cancer cell growth via the expression of NAG-1/MIC-1/GDF-15. *Mol Cancer Ther* 2005; **4**: 487-493.
- 61 Bottone Jr FG, Baek SJ, Nixon JB, Eling TE. Diallyl disulfide (DADS) induces the antitumorigenic NSAID-activated gene (NAG-1) by a p53-dependent mechanism in human colorectal HCT 116 cells. *J Nutr* 2002; **132**: 773-778.
- 62 Kelly JA, Lucia MS, Lambert JR. p53 controls prostate-derived factor/macrophage inhibitory cytokine/NSAID-activated gene expression in response to cell density, DNA damage and hypoxia through diverse mechanisms. *Cancer Lett* 2009; **277**: 38-47.
- 63 Auyeung KK, Cho CH, Ko JK. A novel anticancer effect of astragalus saponins: Transcriptional activation of NSAID-activated gene. *Int J Cancer* 2009; **125**: 1082-1091.
- 64 Schlittenhardt D, Schober A, Strelau J, Bonaterra GA, Schmiedt W, Unsicker K et al. Involvement of growth differentiation factor-15/macrophage inhibitory cytokine-1 (GDF-15/MIC-1) in oxLDL-induced apoptosis of human macrophages *in vitro* and in arteriosclerotic lesions. *Cell Tissue Res* 2004; **318**: 325-333.
- 65 Baek KE, Yoon SR, Kim JT, Kim KS, Kang SH, Yang Y et al. Upregulation and secretion of macrophage inhibitory cytokine-1 (MIC-1) in gastric cancers. *Clin Chim Acta* 2009; **401**: 128-133.
- 66 Riker AI, Enkemann SA, Fodstad O, Liu S, Ren S, Morris C et al. The gene expression profiles of primary and metastatic melanoma yields a transition point of tumor progression and metastasis. *BMC Med Genomics* 2008; **1**: 13.
- 67 Wollmann W, Goodman ML, Bhat-Nakshatri P, Kishimoto H, Goulet Jr RJ, Mehrotra S et al. The macrophage inhibitory cytokine integrates AKT/PKB and MAP kinase signaling pathways in breast cancer cells. *Carcinogenesis* 2005; **26**: 900-907.
- 68 Kim KK, Lee JJ, Yang Y, You KH, Lee JH. Macrophage inhibitory cytokine-1 activates AKT and ERK-1/2 via the transactivation of ErbB2 in human breast and gastric cancer cells. *Carcinogenesis* 2008; **29**: 704-712.
- 69 Burris 3rd HA. Dual kinase inhibition in the treatment of breast cancer: initial experience with the EGFR/ErbB-2 inhibitor lapatinib. *Oncologist* 2004; **9** (Suppl 3): 10-15.
- 70 Si Y, Liu X, Cheng M, Wang M, Gong Q, Yang Y et al. Growth differentiation factor 15 is induced by hepatitis C virus infection and regulates hepatocellular carcinoma-related genes. *PLoS One* 2011; **6**: e19967.
- 71 Boyle GM, Pedley J, Martyn AC, Banducci KJ, Strutton GM, Brown DA et al. Macrophage inhibitory cytokine-1 is overexpressed in malignant melanoma and is associated with tumorigenicity. *J Invest Dermatol* 2009; **129**: 383-391.
- 72 Huh SJ, Chung CY, Sharma A, Robertson GP. Macrophage inhibitory cytokine-1 regulates melanoma vascular development. *Am J Pathol* 2010; **176**: 2948-2957.
- 73 Albertoni M, Shaw PH, Nozaki M, Godard S, Tenan M, Hamou MF et al. Anoxia induces macrophage inhibitory cytokine-1 (MIC-1) in glioblastoma cells independently of p53 and HIF-1. *Oncogene* 2002; **21**: 4212-4219.
- 74 Roth P, Junker M, Tritschler I, Mittelbronn M, Dombrowski Y, Breit SN et al. GDF-15 contributes to proliferation and immune escape of malignant gliomas. *Clin Cancer Res* 2010; **16**: 3851-3859.
- 75 Friese MA, Wischhusen J, Wick W, Weiler M, Eisele G, Steinle A et al. RNA interference targeting transforming growth factor-beta enhances NKG2D-mediated antiglioma immune response, inhibits glioma cell migration and invasiveness, and abrogates tumorigenicity *in vivo*. *Cancer Res* 2004; **64**: 7596-7603.
- 76 Senapati S, Rachagani S, Chaudhary K, Johansson SL, Singh RK, Batra SK. Overexpression of macrophage inhibitory cytokine-1 induces metastasis of human prostate cancer cells through the FAK-RhoA signaling pathway. *Oncogene* 2010; **29**: 1293-1302.
- 77 Ostroukhova M, Qi Z, Oriss TB, Dixon-McCarthy B, Ray P, Ray A. Treg-mediated immunosuppression involves activation of the Notch-HES1 axis by membrane-bound TGF-beta. *J Clin Invest* 2006; **116**: 996-1004.
- 78 Catalona WJ, Partin AW, Slawin KM, Brawer MK, Flanigan RC, Patel A et al. Use of the percentage of free prostate-specific antigen to enhance differentiation of prostate cancer from benign prostatic disease: a prospective multicenter clinical trial. *JAMA* 1998; **279**: 1542-1547.
- 79 Brown DA, Stephan C, Ward RL, Law M, Hunter M, Bauskin AR et al. Measurement of serum levels of macrophage inhibitory cytokine 1 combined with prostate-specific antigen improves prostate cancer diagnosis. *Clin Cancer Res* 2006; **12**: 89-96.
- 80 Nakamura T, Scorilas A, Stephan C, Yousef GM, Kristiansen G, Jung K et al. Quantitative analysis of macrophage inhibitory cytokine-1 (MIC-1) gene expression in human prostatic tissues. *Br J Cancer* 2003; **88**: 1101-1104.
- 81 Welsh JB, Sapinoso LM, Kern SG, Brown DA, Liu T, Bauskin AR et al. Large-scale delineation of secreted protein biomarkers overexpressed in cancer tissue and serum. *Proc Natl Acad Sci USA* 2003; **100**: 3410-3415.
- 82 Kramer G, Marberger M. Could inflammation be a key component in the progression of benign prostatic hyperplasia? *Curr Opin Urol* 2006; **16**: 25-29.
- 83 Kramer G, Mitteregger D, Marberger M. Is benign prostatic hyperplasia (BPH) an immune inflammatory disease? *Eur Urol* 2007; **51**: 1202-1216.
- 84 Taniguchi S, Taoka R, Inui M, Sugimoto M, Kakehi Y. Influence of inflammation and aging on macrophage inhibitory cytokine-1 gene expression in rat ventral prostate. *Urology* 2009; **73**: 410-414.
- 85 Taoka R, Tsukuda F, Ishikawa M, Haba R, Kakehi Y. Association of prostatic inflammation with down-regulation of macrophage inhibitory cytokine-1 gene in symptomatic benign prostatic hyperplasia. *J Urol* 2004; **171** (6 Pt 1): 2330-2335.
- 86 Brown DA, Lindmark F, Stattin P, Balter K, Adami HO, Zheng SL et al. Macrophage inhibitory cytokine 1: a new prognostic marker in prostate cancer. *Clin Cancer Res* 2009; **15**: 6658-6664.
- 87 Noorali S, Kurita T, Woolcock B, de Alarga TR, Lo M, Paralkar V et al. Dynamics of expression of growth differentiation factor 15 in normal and PIN development in the mouse. *Differentiation* 2007; **75**: 325-336.
- 88 Kasper S, Sheppard PC, Yan Y, Pettigrew N, Borowsky AD, Prins GS et al. Development, progression, and androgen-dependence of prostate tumors in probasin-large T antigen transgenic mice: a model for prostate cancer. *Lab Invest* 1998; **78**: i-xv.
- 89 Cheng I, Krumroy LM, Plummer SJ, Casey G, Witte JS. MIC1 and IL1RN genetic variation and advanced prostate cancer risk. *Cancer Epidemiol Biomarkers Prev* 2007; **16**: 1309-1311.
- 90 Wang X, Chrysovergis K, Bienstock RJ, Shim M, Eling TE. The H6D variant of NAG-1/GDF15 inhibits prostate xenograft growth *in vivo*. *Prostate* 2011; e-pub ahead of print 1 August 2011.
- 91 Galsky MD, Vogelzang NJ. Docetaxel-based combination therapy for castration-resistant prostate cancer. *Annals Oncol* 2010; **21**: 2135-2144.
- 92 Zhao L, Lee BY, Brown DA, Molloy MP, Marx GM, Pavlakis N et al. Identification of candidate biomarkers of therapeutic response to docetaxel by proteomic profiling. *Cancer Res* 2009; **69**: 7696-7703.
- 93 Huang CY, Beer TM, Higano CS, True LD, Vessella R, Lange PH et al. Molecular alterations in prostate carcinomas that associate with *in vivo* exposure to chemotherapy: identification of a cytoprotective mechanism involving growth differentiation factor 15. *Clin Cancer Res* 2007; **13**: 5825-5833.
- 94 Chen S-J, Karan D, Johansson SL, Lin F-F, Zeckser J, Singh AP et al. Prostate-derived factor as a paracrine and autocrine factor for the proliferation

- of androgen receptor-positive human prostate cancer cells. *Prostate* 2007; **67**: 557-571.
- 95 Karan D, Chen S-J, Johansson SL, Singh AP, Paralkar VM, Lin M-F *et al*. Dysregulated expression of MIC-1/PDF in human prostate tumor cells. *Biochem and Biophys Res Commun* 2003; **305**: 598-604.
- 96 Cheng JC, Chang HM, Leung PC. Wild-Type p53 attenuates cancer cell motility by inducing growth differentiation factor-15 expression. *Endocrinology* 2011; **152**: 2987-2995.
- 97 Vanhara P, Lincova E, Kozubik A, Jurdic P, Soucek K, Smarda J. Growth/differentiation factor-15 inhibits differentiation into osteoclasts—a novel factor involved in control of osteoclast differentiation. *Differentiation* 2009; **78**: 213-222.
- 98 Lambert JR, Kelly JA, Shim M, Huffer WE, Nordeen SK, Baek SJ *et al*. Prostate derived factor in human prostate cancer cells: gene induction by vitamin D via a p53-dependent mechanism and inhibition of prostate cancer cell growth. *J Cell Physiol* 2006; **208**: 566-574.
- 99 Wynne S, Djakiew D. NSAID inhibition of prostate cancer cell migration is mediated by Nag-1 induction via the p38 MAPK-p75(NTR) pathway. *Mol Cancer Res* 2010; **8**: 1656-1664.
- 100 Massague J. TGFbeta in Cancer. *Cell* 2008; **134**: 215-230.
- 101 Costa VL, Henrique R, Danielsen SA, Duarte-Pereira S, Eknaes M, Skotheim RI *et al*. Three epigenetic biomarkers, GDF15, TMEFF2, and VIM, accurately predict bladder cancer from DNA-based analyses of urine samples. *Clin Cancer Res* 2010; **16**: 5842-5851.
- 102 Park YJ, Lee H, Lee JH. Macrophage inhibitory cytokine-1 transactivates ErbB family receptors via the activation of Src in SK-BR-3 human breast cancer cells. *BMB Rep* **43**: 91-96.
- 103 Brown DA, Ward RL, Buckhaults P, Liu T, Romans KE, Hawkins NJ *et al*. MIC-1 serum level and genotype: associations with progress and prognosis of colorectal carcinoma. *Clin Cancer Res* 2003; **9**: 2642-2650.
- 104 Kim IY, Park SY, Kang Y, Thapa D, Choi HG, Kim JA. Role of nonsteroidal anti-inflammatory drug-activated gene-1 in docetaxel-induced cell death of human colorectal cancer cells with different p53 status. *Arch Pharm Res* 2011; **34**: 323-330.
- 105 Shnaper S, Desbaillets I, Brown DA, Murat A, Migliavacca E, Schluep M *et al*. Elevated levels of MIC-1/GDF15 in the cerebrospinal fluid of patients are associated with glioblastoma and worse outcome. *Int J Cancer* 2009; **125**: 2624-2630.
- 106 Lin TY, Chang JT, Wang HM, Chan SH, Chiu CC, Lin CY *et al*. Proteomics of the radioresistant phenotype in head-and-neck cancer: Gp96 as a novel prediction marker and sensitizing target for radiotherapy. *Int J Radiat Oncol Biol Phys* 2010; **78**: 246-256.
- 107 Skipworth RJ, Deans DA, Tan BH, Sangster K, Paterson-Brown S, Brown DA *et al*. Plasma MIC-1 correlates with systemic inflammation but is not an independent determinant of nutritional status or survival in oesophago-gastric cancer. *Br J Cancer* 2010; **102**: 665-672.
- 108 Staff AC, Bock AJ, Becker C, Kempf T, Wollert KC, Davidson B. Growth differentiation factor-15 as a prognostic biomarker in ovarian cancer. *Gynecol Oncol* 2010; **118**: 237-243.
- 109 Koopmann J, Buckhaults P, Brown DA, Zahurak ML, Sato N, Fukushima N *et al*. Serum macrophage inhibitory cytokine 1 as a marker of pancreatic and other periampullary cancers. *Clin Cancer Res* 2004; **10**: 2386-2392.
- 110 Koopmann J, Rosenzweig CN, Zhang Z, Canto MI, Brown DA, Hunter M *et al*. Serum markers in patients with resectable pancreatic adenocarcinoma: macrophage inhibitory cytokine 1 versus CA19-9. *Clin Cancer Res* 2006; **12**: 442-446.
- 111 Selander KS, Brown DA, Sequeiros GB, Hunter M, Desmond R, Parpala T *et al*. Serum macrophage inhibitory cytokine-1 concentrations correlate with the presence of prostate cancer bone metastases. *Cancer Epidemiol Biomarkers Prev* 2007; **16**: 532-537.

9. Trudu F, Amato F, **Vanhara P**, Pivetta T, Pena-Mendez EM, Havel J. **Coordination Compounds In Cancer: Past, Present And Perspectives**. *Journal of Applied Biomedicine* 2015; **13**(2):79-103.

Commentary:

A review publication on major metal cytotoxic compounds, integrating the chemical and biological roles in development of resistance to cancer therapy. Principal coordination compound classes covering platinum and non-platinum (ruthenium, gold, silver, copper, iron, cobalt, gallium, rhodium, etc.) are discussed with the emphasis on molecular response to generalized cell- or endoplasmic reticulum stress.

DOI: 10.1016/j.jab.2015.03.003

Journal: Journal of Applied Biomedicine

Impact factor (WOS, 2015): 1.509

Number of citations (WOS, 2018): 34

Cited in: Journal of Inorganic Biochemistry, Polyhedron, European Journal of Inorganic Chemistry, Inorganic Chemistry, Molecules, Critical Reviews in Therapeutic Drug Carrier Systems, etc.

Most important citation: Ringhieri P, Morelli G, Accardo A. **Supramolecular Delivery Systems for Non-Platinum Metal-Based Anticancer Drugs**. *Critical Reviews™ in Therapeutic Drug Carrier Systems* 2017; **34**(2):149-183. doi: 10.1615/ CritRevTherDrugCarrierSyst.2017016936 (IF 2016: 6.667)

Contribution of the author: Co-authorship. Design and writing of manuscript.

Available online at www.sciencedirect.com

ScienceDirect

journal homepage: <http://www.elsevier.com/locate/jab>

Review Article

Coordination compounds in cancer: Past, present and perspectives



Federica Trudu ^{a,b,1,2}, Filippo Amato ^{a,1}, Petr Vaňhara ^c,
Tiziana Pivetta ^b, E.M. Peña-Méndez ^d, Josef Havel ^{a,*}

^a Department of Chemistry, Faculty of Science, Masaryk University, Brno, Czech Republic

^b Department of Chemical and Geological Sciences, University of Cagliari, Monserrato (CA), Italy

^c Department of Histology and Embryology, Faculty of Medicine, Masaryk University, Brno, Czech Republic

^d Department of Chemistry, Faculty of Science, University of La Laguna, La Laguna, Tenerife, Spain

ARTICLE INFO

Article history:

Received 24 October 2014

Received in revised form

4 March 2015

Accepted 9 March 2015

Available online 27 March 2015

Keywords:

Cancer

Coordination metal complexes

Cisplatin

Omics

Perspectives

ABSTRACT

Metal-based coordination compounds have been used throughout the history of human medicine to treat various diseases, including cancer. Since the discovery of cisplatin in 1965, a great number of metal coordination complexes, such as platinum, ruthenium, gold or copper have been designed, synthesized and tested in order to develop clinically effective and safe drugs. Currently, many reviews cover applications of cytostatic metal complexes pointing out the most promising examples of platinum- and non-platinum-based compounds in preclinical and clinical trials. However, recent comprehensive reviews covering chemical and biological aspects of metal-based coordination compounds in cancer therapy are still rare. In this review we wish to provide an overview of the coordination chemistry of current and novel cytostatic compounds, including an outline of their design and rationale of synthesis, and summarize bio-chemical reactivity and physicochemical properties of candidate metal complexes.

© 2015 Faculty of Health and Social Studies, University of South Bohemia in Ceske Budejovice. Published by Elsevier Sp. z o.o. All rights reserved.

Introduction

Cancer is nowadays one of the leading causes of death in the developed world. Biologically, cancer represents a vastly heterogenic group of diseases sharing several common traits. One of these hallmarks is sustained proliferation, resulting in uncontrolled tumour growth (Hanahan and Weinberg, 2011). An extensive research has been done to characterize

antiproliferative effect of various classes of compounds, ranging from naturally occurring molecules and their derivatives, to organometallic and inorganic compounds and their application in cancer therapy. The fortuitous discovery of the cytotoxic properties of cisplatin (diamminedichloroplatinum (II)) in 1965, opened new avenue for the application of metal complexes in cancer therapy (Arnesano et al., 2011) (Fig. 1). The antiproliferative effect of cisplatin and other compounds, however, induces adverse effects on normal tissues,

* Corresponding author at: Department of Chemistry, Faculty of Science, Masaryk University, Kamenice 5/A14, 625 00 Brno, Czech Republic. Tel.: +420 54949 4114; fax: +420 54949 2494.

E-mail address: havel@chemi.muni.cz (J. Havel).

¹ These authors contributed equally to this paper.

² On leave from affiliation 'b'.

1214-021X/\$ – see front matter © 2015 Faculty of Health and Social Studies, University of South Bohemia in Ceske Budejovice. Published by Elsevier Sp. z o.o. All rights reserved.

<http://dx.doi.org/10.1016/j.jab.2015.03.003>

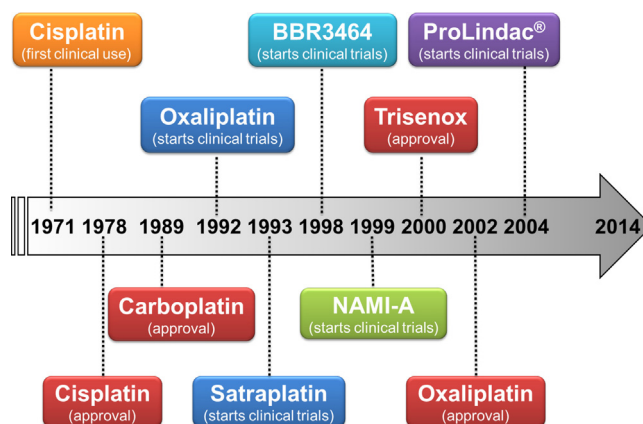


Fig. 1 – Historical overview of the cytotoxic metal and metalloids complexes that have been approved or entered the clinical practice.

decreasing therapeutic effectivity. Moreover, in many cancers, tumour cells may acquire resistance to the metal-based cytotoxic therapy resulting in virtually incurable relapsing disease (Desoize, 2004).

In the last 15 years, a great effort has been dedicated to the development of more effective and less toxic drugs. Various new trans-platinum(II) and platinum(IV) complexes have been synthesized, and some of them have been selected for clinical trials (Kelland et al., 1999), but with varying effectivity and safety. Therefore, less toxic metals, such as ruthenium, gold or copper were introduced as promising candidates for effective and safe therapy (Tiekink, 2002; Clarke, 2002; Marzano et al., 2009; Nobili et al., 2010). Various reviews have been published on the use of metal complexes as anticancer agents, with the intent to give an overview of the proposed approaches concerning the application of these systems in clinical practice (Tiekink, 2002; Boulikas et al., 2007; Milacic et al., 2008; Bruijninx and Sadler, 2008; Todd and Lippard, 2009; Vilmar and Sørensen, 2009; Esteban-Fernández et al., 2010; Tisato et al., 2010; Wang and von Recum, 2011; Beija et al., 2012; Babu et al., 2013; Maldonado et al., 2013; Sukumar et al., 2013; Cao-Milán and Liz-Marzán, 2014; Mjos and Orvig, 2014; Muhammad and Guo, 2014; Petrelli et al., 2014). However, the majority of the available reviews point out the most relevant examples of platinum- or non-platinum-based compounds, eventually focusing on one particular metal ion or making a compendium on two or more metal ions. The aim of this review is to bridge a gap by summarizing on historical background, novel trends in synthesis of new metal complexes with antiproliferative effects and to describe their chemical reactivity, pharmacokinetic properties and interactions in the biological and biomedical context.

Cisplatin has been a first-line therapy in many cancers and nowadays is used either alone or in combination with other compounds in many cancers, e.g. testicular, ovarian or bladder cancers or leukaemias. Due to low chemical stability of cisplatin, the direct intravenous administration is preferred over the other forms. In the blood stream, cisplatin rapidly interacts with plasma proteins such as human serum albumin (HSA), haemoglobin (Hb) or transferrin (Tf) (Rudnev et al., 2005) and 24 h after administration, 95% of cisplatin is bound to plasma proteins (Sooriyaarachchi et al., 2011). Cisplatin is widely distributed into body fluids and tissues, reaching the highest concentrations in kidneys (0.4–2.9 $\mu\text{g/g}$), liver (0.5–3.7 $\mu\text{g/g}$ wet weight), and prostate (1.6–3.6 $\mu\text{g/g}$). Minor concentration levels can be found in muscles, bladder, testes, pancreas, and spleen (Stewart et al., 1982). Penetration of cisplatin into tumour tissue differs in different cancers. However, the concentration of cisplatin and its analogues positively correlates with reduction of tumour mass and clinical parameters, such as recurrence free and overall survival, e.g. in non-small-cell lung cancer (Kim et al., 2012).

Cisplatin enters the cells either passively by a simple diffusion or by active protein-mediated transport systems, e.g. human organic cation transporter (hOCT2) and the copper transport protein (Ctr1) (Ishida et al., 2002; Song et al., 2004; Burger et al., 2010). In cytoplasm, cisplatin is hydrolysed and one of the two chloride ligands is displaced by a water molecule to form the $[\text{PtCl}(\text{H}_2\text{O})(\text{NH}_3)_2]^+$ species, allowing for the binding of the platinum ion to DNA bases, especially in the N7 position of guanine and adenine and the N3 of cytosine, forming the monofunctional adduct $[\text{PtCl}(\text{DNA})(\text{NH}_3)_2]^+$. The second chloride ligand can be displaced by a water molecule to

Platinum-based complexes

Platinum(II) complexes

Cisplatin and transplatin

Diamminedichloroplatinum(II) is a complex with square planar geometry and two possible cis and trans geometrical isomers, cisplatin and transplatin (Fig. 2).

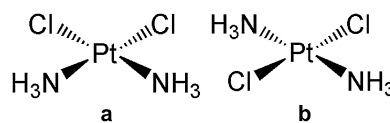


Fig. 2 – Structures of the cis (a) and trans (b) isomers of diamminedichloroplatinum(II), the cisplatin and transplatin, respectively.

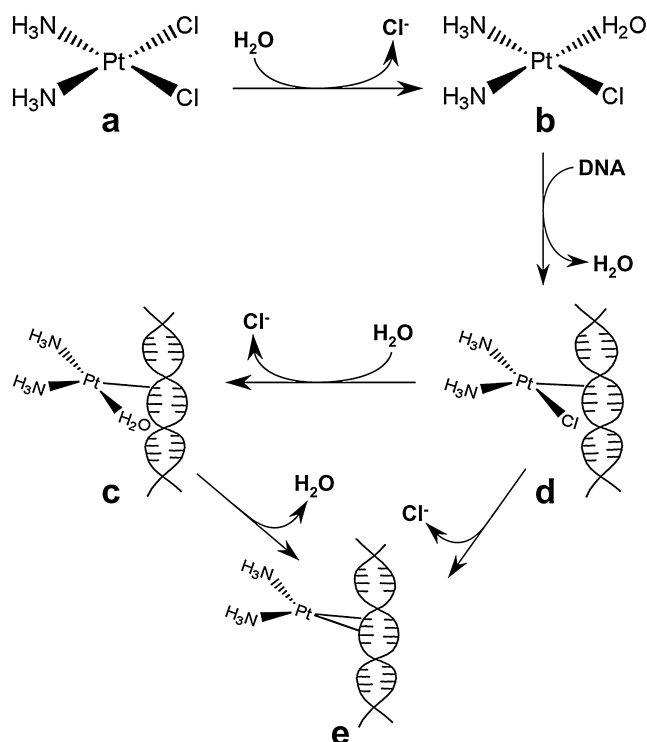


Fig. 3 – Scheme of the reaction pathway leading to the formation of adducts between cisplatin (a) and DNA. One chloride ligand is displaced by water to form the aqua-complex $[\text{PtCl}(\text{H}_2\text{O})(\text{NH}_3)_2]^+$ (b) which interacts with DNA forming the monofunctional adduct $[\text{PtCl}(\text{DNA})(\text{NH}_3)_2]^+$ (c). This last might exchange the chloride ligand with one molecule of water forming the hydrated monofunctional adduct $[\text{Pt}(\text{H}_2\text{O})(\text{DNA})(\text{NH}_3)_2]^{2+}$ (d). Both the monofunctional adduct (c) and its hydrated form (d) lead to the formation of the bifunctional adduct $[\text{Pt}(\text{H}_2\text{O})(\text{DNA})(\text{NH}_3)_2]^{2+}$ (e).

form the adduct $[\text{Pt}(\text{H}_2\text{O})(\text{DNA})(\text{NH}_3)_2]^{2+}$. These species may re-interact with DNA by crosslinking forming a bifunctional adduct (Alderden et al., 2006) (Fig. 3) and trigger programmed cell death.

Several modes of cisplatin crosslinking with DNA have been proposed (Trzaska, 2005). The main adducts with DNA form 1,2-intrastrand cross-links with two adjacent guanines (1,2-d(GpG)) and 1,2-intrastrand cross-links with an adenine and an adjacent guanine (1,2-d(ApG)) (Jamieson and Lippard, 1999). The adducts 1,2-d(GpG) are supposed to be responsible for the cytotoxic activity of the drug (Todd and Lippard, 2009). Minor adducts are 1,3-intrastrand cross-links formed with nonadjacent guanines and interstrand adducts.

In contrast to cisplatin, the *trans* isomer of the diammine-dichloroplatinum(II), transplatin, shows only mild cytotoxic activity. This could be explained by different way of formation of DNA adducts. The interstrand cross-links between guanine and cytosine are formed by both isomers, while the 1,2-intrastrand cross-links are prevented by the geometry in the case of transplatin (Bernal-Méndez et al., 1997). In addition, the conversion of the monofunctional adducts into the bifunctional ones occurs particularly slowly for transplatin. In fact,

after 24 h, the majority of DNA adducts formed by transplatin are still monofunctional (Bernal-Méndez et al., 1997). The difference between cytotoxic effects of cisplatin and transplatin is therefore in the formation of the 1,2-intrastrand bifunctional adduct and in the fast conversion rate of the monofunctional adduct into the bifunctional one.

Other cis-Pt complexes

Because of the cisplatin success in clinical therapy, various new cis-Pt(II) complexes have been synthesized by substitution of either chlorine or ammonia ligands with different structures. Up to now, only carboplatin and oxaliplatin, have shown better performance than cisplatin in some types of cancers, and their use has been approved worldwide.

The promising compound named picoplatin (cis-amine-dichloro-(2-methylpyridine)-Pt(II)) (Fig. 4) has been introduced for the treatment of patients with solid tumours, and its clinical trials started in 1997 (Kelland, 2007a; Wheate et al., 2010). Picoplatin has a marked steric bulk around the platinum ion that reduces its inactivation by thiol-containing species. Its cytotoxic activity is due to the interaction with DNA that leads mainly to the formation of intrastrand adducts. Picoplatin was found to be active against cisplatin- and oxaliplatin-resistant cell lines (Kelland, 2007b). When used as single agent its main dose-limiting side effect is myelosuppression. However, phase III trials did not confirm the previous promising results in the treatment of small-cell lung cancer and new trials are not currently planned (Lopez-Chavez and Sandler, 2012; Hamilton and Olszewski, 2013).

Recently, cis-Pt(II) complexes has been reconsidered and used as a scaffold for biologically active ligands. One example is the complex *cis*- $[\text{Pt}(\text{NH}_3)_2(\text{L})\text{Cl}]$ (L = 3-aza-5H-phenanthridin-6-one) which contains a poly(ADP-ribose) polymerase (PARP-1) inhibitor as (B. Wang et al., 2014a). PARP-1 is a poly (ADP-ribose) polymerase involved in DNA replication, damage repair, and transcriptional regulation. After DNA damage, the activity of PARP-1 increases, stimulating the response of DNA-damage repairing proteins. This platinum complex exhibits increased activity and enhanced solubility with respect to those of the free inhibitor.

Other cis-Pt(II) compounds conjugated with side-directing molecules have been introduced with the aim to increase their selectivity. Analogues of cisplatin, carboplatin and oxaliplatin have been prepared with estrogens-like compounds in order to increase selectivity towards hormone-dependent breast, ovarian and uterine tumours (Descôteaux et al., 2003, 2008; Saha et al., 2012). The estrogens-derived cisplatin and carboplatin ligands possess a high affinity for the oestrogen

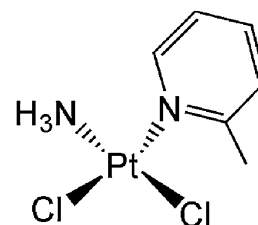


Fig. 4 – Structure of picoplatin (cis-amine-dichloro-(2-methylpyridine)-Pt(II)).

receptor α (ER α) and improved cytotoxic activity. Interestingly, the cisplatin analogues show a better tumour regression than cisplatin alone in human breast cancer estrogens-receptor positive mouse xenograft model (Themsche et al., 2009). However, the substitution of cisplatin ligands has not extended significantly the range of applicability of platinum-based drugs in cisplatin-resistant cancers probably because of the use of only one structural motif (Quiroga, 2012). Therefore, the research focused on platinum complexes with different geometry (e.g., *trans*-Pt(II) complexes) and oxidation state (e.g., Pt(IV) complexes).

Other *trans*-Pt complexes

Beside the low cytotoxic efficacy of transplatin, other *trans*-Pt (II) compounds with substituents different from ammonia have shown cytotoxic activity equal or higher than that of cisplatin. The cytotoxic effect induced by such complexes might be due to the formation of monofunctional adducts and interstrand crosslinking with DNA as well as to the interactions with proteins. The biological activity of these complexes appears related to the steric hindrance of the substituents that slow down the displacement of the chlorides (Marzano et al., 2010). Planar amines such as pyridine, quinoline, isoquinoline and thiazole were firstly used as substituents (Aris and Farrell, 2009). The first *trans*-platinum complex with marked antitumor efficacy *in vivo* was the *trans*-ammine-(cyclohexylamine)-dichloro-dihydroxo-Pt(IV) (known as JM335) (Fig. 5a) which combines the *trans* geometry with the higher oxidation state of the metal ion (Kelland et al., 1994). In *trans* platinum complexes, the substituents are chosen in order to modulate the solubility and stability in aqueous media. For example, the use of ligands containing carboxylic groups leads to *trans*-platinum complexes stable towards hydrolysis but water soluble and able to accumulate in cisplatin-resistant cell lines (Quiroga et al., 2005). Complexes containing iminoethers or aliphatic amines in place of planar ones were found active in cisplatin-resistant cell lines (Aris and Farrell, 2009). Various *trans*-[Pt(amine)₂(amidine)₂]Cl₂ compounds with four N-ligands bound to the platinum core have been synthesized (Fig. 5b) and tested with relevant results against a large panel of human cancer cell lines (Marzano et al., 2010). In addition, it has been observed that the size of the substituents and the cytotoxicity of the resulting molecule are directly correlated. The cyclohexyl derivative appears, in fact, as the most active. *In vivo* tests

against Lewis lung carcinoma show a reduction in tumour size similar to that achieved using cisplatin (68 and 72%, respectively) but without the side effects typical of this last one (Marzano et al., 2010). Recently, the class of *trans*-Pt(II) compounds has been extended to complexes containing iminothioether ligands with general formula *trans*-[Pt(N(H) = C(SEt)R)₂Cl₂] (R = Me, Et, Ph, CH₂Ph) (Fig. 5c). The most active compound of such series is the *trans*-[Pt(N(H) = C(SEt)CH₂Ph)₂Cl₂] that shows higher cytotoxic activity than cisplatin against a broad panel of human solid tumour cell lines (Sgarbossa et al., 2013). The aforementioned complexes are active against cisplatin-resistant and Multi Drug Resistance (MDR) cell lines. The MDR phenomenon occurs when the acquired resistance to a specific drug causes resistance to other drugs, even not chemically related.

Another interesting example is the family of *trans*-Pt(II) complexes with sulphonamide ligands. This class of compounds shows antitumor activity against cisplatin-resistant cell lines of cervix adenocarcinoma, ovarian carcinoma and ductal breast epithelial tumour (Pérez et al., 2014).

Platinum(IV) complexes

Complexes of Pt(IV) are thermodynamically stable, kinetically inert and diamagnetic. The metal ion is hexa-coordinated and its complexes have octahedral geometry. The biological properties of such complexes can be finely tuned thanks to the six coordination sites available.

Despite some contradictory results (Khokhar et al., 1993; Talman et al., 1998), it is now widely accepted that the antitumor activity of Pt(IV) complexes is due to their reduction to Pt(II) analogues. It was experimentally observed that DNA-binding activity of Pt(IV) complexes is increased in presence of some intracellular reductants (Choi et al., 1998), and Pt(IV) complexes are reduced by various biomolecules present in blood and cells. Pt(IV) complexes also show lower chemical reactivity in comparison to their Pt(II) counterparts. These findings suggest that Pt(IV) compounds undergo reduction prior getting a cytotoxic activity. Physiologically, these Pt(IV) complexes are reduced by biomolecules such as glutathione (GSH), methionine, cysteine, metallothioneins, serum albumin, ascorbate, DNA nucleobases, nucleotides and their analogues. Depending on the reduction potential of the Pt(IV) complex, the reduction may occur into the bloodstream instead of within the cells, giving rise to side-reactions that lead to systemic toxicity (Hall and Hambley, 2002). The reduction rate of the Pt(IV) complexes increases by using bulky equatorial and axial electron-withdrawing ligands (Choi et al., 1998). Besides, the reduction rate may be also influenced from the low kinetics of axial ligand dissociation in Pt(IV) complexes (Wong and Giandomenico, 1999).

The cellular uptake of Pt(IV) complexes is higher than that of Pt(II) ones. This has been correlated with their higher lipophilicity which facilitates their passive diffusion into the cells. This could be also an explanation for their efficacy against some cisplatin resistant cancer cell lines (Hall and Hambley, 2002). However, the *in vivo* reduction of the Pt(IV) complex is accompanied by the loss of the axial ligands, and the resulting compound may show a lower activity due to decreased lipophilicity (Hall and Hambley, 2002).

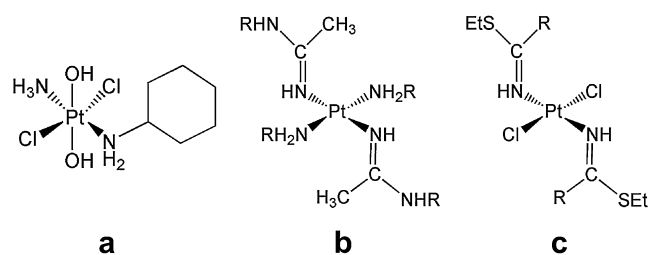


Fig. 5 – Structures of *trans*-ammine-(cyclohexylamine)-dichloro-dihydroxo-Pt(IV) (JM335) (a), *trans*-[Pt(amine)₂(amidine)₂]Cl₂ complex (b) and *trans*-[Pt(N(H) = C(SEt)R)₂Cl₂] (R = Me, Et, Ph, CH₂Ph) complexes (c).

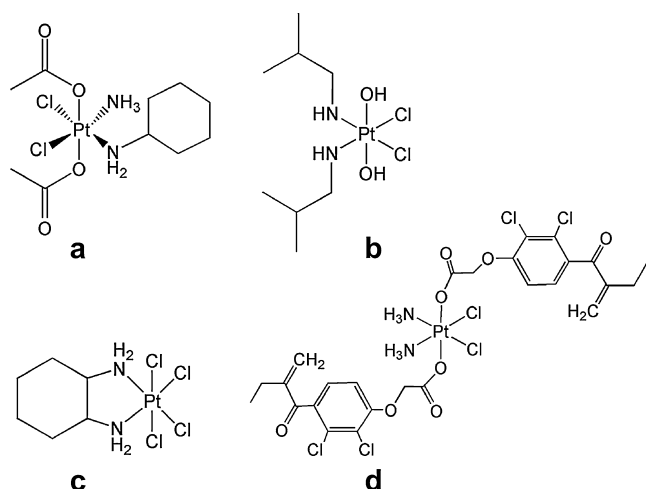


Fig. 6 – Structures of satraplatin (a), tetraplatin (or ormaplatin) (b), iproplatin (c) and Pt(IV) complex containing ethacrynic acid as ligand (d).

Satraplatin

Satraplatin (bis-acetate-amine-dichloro-cyclohexylamine-Pt(IV)) (Fig. 6a), also known as JM216, is a drug for oral administration containing two acetate ligands that increase the lipophilicity of the compound. In the bloodstream it is reduced with consequent loss of the two acetate ligands, forming its main metabolite labelled JM118. This compound unwinds DNA and induces apoptosis. Unlike cisplatin and carboplatin, the DNA adducts formed by satraplatin are not detected by DNA mismatch repair proteins (Fink et al., 1996). Satraplatin is active against some cancers that show acquired resistance to cisplatin, thanks to its higher influx and reduced DNA-repair (Fokkema et al., 2002; Kelland, 2007b). Clinical trials using satraplatin for the treatment of advanced prostate cancer documented, however, only mild recurrence-free survival, but without overall survival benefits (Bhargava and Vaishampayan, 2009). In addition, it has been proposed for the treatment of non-small cell lung, and squamous head and neck cancers (Wong and Ang, 2012).

Besides satraplatin, other two Pt(IV) complexes have been tested in clinical trials: iproplatin and tetraplatin. The iproplatin, $[\text{Pt}(\text{isopropylamine})_2(\text{OH})_2(\text{Cl})_2]$ (Fig. 6b), has been extensively studied in phases I, II, and III trials for the treatment of a wide range of cancers, with lower efficacy than cisplatin and some cases of toxic death were reported (Clavel et al., 1988). The tetraplatin, $[\text{Pt}(\text{trans-1,2-diaminocyclohexane})\text{Cl}_4]$, also known as ormaplatin (Fig. 6c), shows a good cytotoxic activity both *in vitro* and *in vivo*, but severe neurotoxicity observed in phase I trials prevents further clinical applications (Boulikas et al., 2007).

A different approach is to combine a cytotoxic metal compound with biologically active molecules. It is possible to prepare Pt(IV) platinum complex with small molecular inhibitors of enzymes that inactivate platinum complexes in resistant cells. Ethacrynic acid is an inhibitor of glutathione-S-transferase (GST) which catalyses the reaction of cisplatin with glutathione (Ang et al., 2011). Overexpression of GST enzyme

has been reported in cisplatin-resistant cell lines and the GST inhibitors have already been used in combination with other drugs in anticancer therapy. The GST inhibition induced by the Pt(IV) complex containing ethacrynic acid (Fig. 6d) is more effective than that induced by the ethacrynic acid alone. In addition, it shows cytotoxic activity higher than that of cisplatin in the first 24 h and equal to that of cisplatin after 72 h. The high GST inhibition shown by the complex has been attributed to its covalent binding to the enzyme and subsequent binding of ethacrynic acid ligands at the active sites (Parker et al., 2011).

Polynuclear platinum complexes

Polynuclear platinum complexes containing aliphatic amines as bridging linkers have been designed with the intent to overcome drug resistance. They react rapidly with DNA forming long-range interstrand and intrastrand cross-links (Wong and Giandomenico, 1999; Wang and Guo, 2008). Some of them have been found to be active even against cisplatin-resistant cells.

The triplatin tetranitrate or dichloro-hexamine-bis(μ -1,6-hexane-1,6-diamine)-tri-Pt(II), known as BBR3464 (Fig. 7a), is a multiply charged (+4) trinuclear complex that interacts with DNA by forming 1,4-intrastrand and 1,4-interstrand cross-links that cannot be repaired by the excision repair mechanism. The cytotoxic activity of the drug is due to the long life of the intra- and interstrand cross-links (Kasparkova et al., 2002). The BBR3464 shows no cross-resistance in cisplatin-resistant cell lines (Perego et al., 1999), but phase II trials were not convincing (Wheate et al., 2010). Its lack of activity is probably due to the binding with plasma proteins that results in drug deactivation. Among trinuclear Pt(II) complexes, the $[\{\text{trans-Pt}(\text{NH}_3)_2(\text{NH}_2(\text{CH}_2)_6(\text{NH}_3^+))\}_2-\mu-\{\text{trans-Pt}(\text{NH}_3)_2(\text{NH}_2(\text{CH}_2)_6(\text{NH}_2)_2)\}]^8+$ (Fig. 7b) shows a peculiar interaction with DNA. In fact, it binds via hydrogen bond to the oxygen atoms of the phosphate groups on the DNA backbone. This complex has been presented as the first example of a non-covalent platinum compound with cytotoxicity equivalent to that of cisplatin (Komeda et al., 2006). Polynuclear complexes with rigid bridging ligands such as aromatic compounds and with more flexible linkers like 4,4-methylenedianiline have been developed (Mlcouskova et al., 2012; Zerkankova et al., 2010; Olivova et al., 2012). The substitution of chloride ligands with alkylcarboxylates leads to a class of polynuclear complexes with increased stability and reduced ability to bind plasma proteins with respect to BBR3464. Among these compounds, dinuclear platinum complex CT-47463 (Fig. 7c) possesses a cytotoxic activity against cisplatin-resistant ovarian and squamous cell carcinoma, and osteosarcoma human cell lines with IC_{50} (i.e., drug concentration required for 50% inhibition of cell growth) of 0.003, 0.77 and 0.041 μM (Gatti et al., 2009). The CT-47463 inhibits tumour growth in platinum-resistant human ovarian carcinoma xenograft by 80% (Barry and Sadler, 2013).

Platinum drugs approved for clinical practice

Despite the huge number of platinum complexes synthesized up to now, less than 30 have reached the human

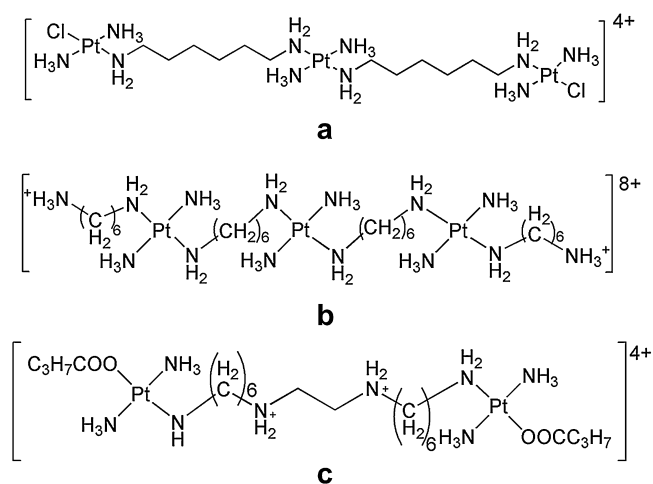


Fig. 7 – Structures of BBR3464 (a), $[[\text{trans-Pt}(\text{NH}_3)_2(\text{NH}_2(\text{CH}_2)_6(\text{NH}_3^+))]_2-\mu-\{\text{trans-Pt}(\text{NH}_3)_2(\text{NH}_2(\text{CH}_2)_6(\text{NH}_2)_2}\}]^{8+}$ (b) and CT-47463 (c).

experimentation. Among them, only cisplatin, carboplatin, and oxaliplatin have been approved worldwide for clinical use. Nedaplatin, heptaplatin, and lobaplatin have been approved only in Japan, China, and South Korea, respectively. Other drugs previously tested have evidenced severe side-effects or lack of activity in phase I or II trials, and their development has been abandoned (Wheate et al., 2010). Recently, satraplatin and picoplatin development has been stopped as well (Hamilton and Olszewski, 2013).

Carboplatin

Carboplatin (cis-diamine(1,1-cyclobutanedicarboxylato)-Pt(II)) (Fig. 8a) is the first cisplatin derivative used in clinical therapy. In this complex, the metal ion is coordinated by a bidentate

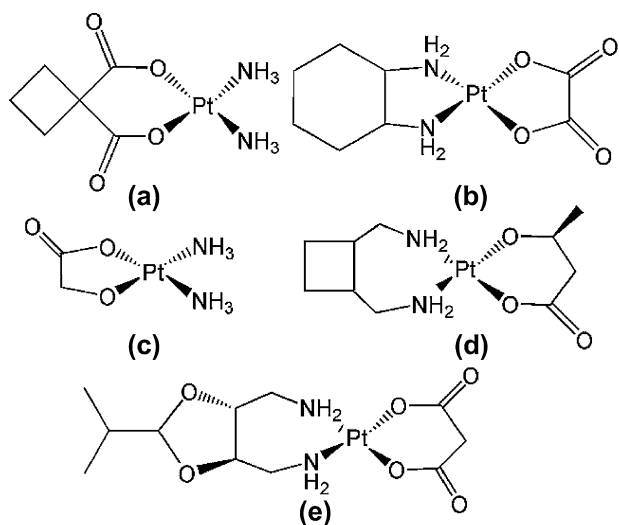


Fig. 8 – Overview of platinum-based drugs used in clinical practice: carboplatin (a), oxaliplatin (b), nedaplatin (c), lobaplatin (d) and heptaplatin (e).

dicarboxylic ligand. Because the carboxylate group is more stable than the chloride, carboplatin exhibits lower reactivity and slower DNA binding kinetics. Within the cellular environment it forms the same DNA adducts formed by cisplatin, but with a product profile noticeably different (Blommaert et al., 1995). The major carboplatin adduct identified is the cis-[Pt(NH₃)₂(dG)₂] (40%). Minor products are 1,2-d(GpG) (30%), 1,2-d(ApG) (16%), and a small number of interstrand cross-links (3–4%), together with monofunctional adducts. The lower reactivity of carboplatin results also in less toxicity for urinary and gastrointestinal tract, when compared to cisplatin (Kelland, 2007a). The dose-limiting toxicity (e.g., adverse side-effects) is myelosuppression (Calvert et al., 1982). Despite many studies have shown that carboplatin and cisplatin present the same cytotoxic activity, carboplatin has successfully replaced cisplatin in the treatment of some kinds of cancers, such as advanced, metastasized or recurrent non-small cell lung, and advanced or recurrent ovarian cancer (see www.cancer.gov). Moreover, the lower toxicity allows the use of higher doses and the prolongation of treatment time (Lebwohl and Canetta, 1998). However, carboplatin does not overcome the problem of drug resistance due to the cross-resistance with cisplatin (Desoize, 2004).

Oxaliplatin

Oxaliplatin (1R,2R-diaminocyclohexane-oxalate Pt(II)) (Fig. 8b) is now used for the treatment of cancers resistant to other platinum drugs, particularly in colorectal cancer. It is typically administered with fluorouracil and leucovorin in a combination known as FOLFOX (Maindrault-Goebel et al., 1999; Desoize, 2004). In oxaliplatin, the metal ion is coordinated by 1,2-diaminocyclohexane and oxalate ligands. The cytotoxic activity of this drug arises from the inhibition of DNA synthesis in cancer cells. In fact, it forms both inter- and intrastrand cross links in DNA, preventing DNA replication and transcription, and triggering cell death (Graham et al., 2004). Oxaliplatin does not show cross-resistance with other platinum drugs because it binds DNA differently than cisplatin, and the resulting adducts are not recognized by the DNA mismatch repair proteins (Fink et al., 1996). Also, it seems that no interaction with the copper transporter CTR1 occurs, and this prevents its efflux outside the cell in some kinds of cisplatin-resistant cancers (Holzer et al., 2006). Oxaliplatin is less toxic than cisplatin but its dose-limiting toxicity is associated with a not predictable occurrence of sensory neuropathy.

Nedaplatin

Nedaplatin (diamine(1,2-(O,O')-2-hydroxyacetato)-Pt(II)) (Fig. 8c) is a second-generation cisplatin analogue. This drug was developed with the aim to avoid the nephrotoxicity and gastrotoxicity of cisplatin while maintaining the same efficacy (Mabuchi and Kimura, 2010). It presents two ammonia and a glycolate ligand which forms a five-membered ring with the platinum ion. The water solubility of nedaplatin is ten times higher than that of cisplatin. It is actually less nephrotoxic than cisplatin and carboplatin (Alberto et al., 2009; Kuwahara, 2009), presenting anticancer activity comparable to that of cisplatin (Kawai et al., 2005; Alberto et al., 2009). Nedaplatin interacts with DNA forming mainly interstrand cross-links. It reacts with GSH and metallothioneins in

minor extent because of the presence of the five-membered ring which prevents the binding to the platinum core. Nedaplatin can cause thrombocytopenia and also nephrotoxicity in absence of a pre- and post-treatment hydration. Its efficacy is not higher than that of cisplatin, but it has been proved to be less toxic for kidneys, gastrointestinal tract, and nervous system. It is currently registered in Japan for the treatment of head and neck, testicular, lung, ovarian, cervical, and non-small-cell lung cancer (Wheate et al., 2010). Clinical trials are ongoing for the use of nedaplatin in different schedules, in particular in combination with other drugs (Oshita et al., 2004; Gong et al., 2009; Kurita et al., 2010), against non-small-cell lung, cervical, oesophageal, testicular, and head and neck cancers.

Lobaplatin

In lobaplatin (1,2-diaminomethyl-cyclobutane-lactate-Pt(II)) (Fig. 8d), the Pt(II) ion is coordinated by the nitrogen atoms of a 1,2-diaminomethyl-cyclobutane and by one molecule of lactic acid. Lobaplatin binds DNA preferentially at guanine residues, forming mainly intrastrand cross-links, and in parallel probably inhibits the DNA and RNA polymerases. Lobaplatin shows *in vitro* cytotoxic activity against a wide range of cancer cell lines, including some cisplatin and carboplatin resistant ones (McKeage, 2001). In clinical trials the dose-limiting side-effect was found to be thrombocytopenia (Gietema et al., 1993). Lobaplatin has been approved in China for the treatment of chronic myeloid leukaemia, and inoperable metastatic small-cell lung and breast cancers. Phase II clinical trials have been also completed in other countries such as USA, Australia, Europe, Brazil, and South Africa for the treatment of breast, oesophageal, lung, and ovarian cancers, and chronic myelogenous leukaemia (Boulikas et al., 2007). Despite the lack of cross-resistance established *in vitro*, in a clinical trial lobaplatin has shown no activity against a cisplatin-resistant form of ovarian cancer (Kavanagh et al., 1995).

Heptaplatin

Heptaplatin (2-(1-methylethyl)-1,3-dioxolane-4,5-dimethanamine-[N,N']-[propanedioato-O,O']-Pt(II)) (Fig. 8e) has been proposed for the treatment of gastric cancers and was approved for clinical therapy in South Korea. It is a Pt(II) square planar complex with a malonato ligand as leaving group and a dimethanamine-1,3-dioxolane derivative. It has been designed to have higher antitumor activity and lower toxicity with respect to cisplatin. It shows activity *in vitro* and in human tumour xenografts against different types of cisplatin-resistant tumours (Kim et al., 1995). The activity of heptaplatin on cisplatin-resistant cell lines is partially due to a major resistance to deactivation by metallothioneins (Choi et al., 2004). Nephrotoxicity, hepatotoxicity, and myelosuppression are its dose-limiting side-effects. The toxicity of heptaplatin has been confirmed to be lower than that of cisplatin as supposed by its developers but it does not present a higher cytotoxic activity, at least in advanced gastric adenocarcinoma and small-cell lung cancer (Kim et al., 1999; Zang et al., 1999). Currently, heptaplatin is used for the treatment of advanced gastric and lung cancers (Graf et al., 2012).

Overcoming of platinum resistance – lessons from the “omics”

Any cytostatic treatment reducing a tumour mass induces a selection pressure on proliferating cancer cells. Cells that survive are either slow-cycling, quiescent or those that acquired resistance to the cytostatic drug. Generally, metal-based compounds, such as cisplatin, induce programmed cell death by DNA damage or interactions with other cytoplasmic targets. However, the cell response triggered by cytotoxic compounds is highly dependent on cancer type and its particular genetic and epigenetic context. Genes affecting the therapeutic effectivity are remarkably diverse, coding for membrane transporters, DNA damage response machinery, detoxification enzymes or programmed cell death effectors, affecting greatly the results of the therapy (Scanlon et al., 1989; Andrews and Howell, 1990) (Fig. 9). However, plethora of other genes, involved in many aspects of cell life, increase the enormous complexity of mechanism of action of individual coordination compounds in cancer cells.

Progress in development of global gene expression techniques enabled deeper and complex understanding of development of resistance or even cross-resistance. The classical proteomic approaches identified tens or hundreds of proteins differentially expressed in cisplatin-resistant and sensitive cancers. Interestingly, these proteins fall into virtually all functional families in human proteome, ranging from transcription factors, splicing and translation machinery, cytoskeleton, junction proteins to signalling pathways to microsomal metabolic and detoxication enzymes, mitochondrial respiration proteins or cell cycle (Stewart et al., 2006). Next generation sequencing (NGS) is sufficiently robust to address the expression complexity in various cancer types and models. NGS-based whole exon sequencing, mRNA sequencing, miRNA quantification or global analysis of single nucleotide polymorphisms (SNPs) can provide a multidimensional alteration landscape that can determine the effect of cytotoxic drugs (Roukos et al., 2012). NGS was used to identify and quantify individual mRNAs in cell line models of ovarian cancer chemoresistance, indicating that expression of more 2500 genes is altered in cisplatin-sensitive and resistant cancer cells (Li et al., 2013). Further integration of global gene expression data, miRNA and SNPs into quantitative trait loci (QTLs) allowed for identification of functional links, e.g. between particular SNPs (rs11138019), expression of miRNA (miR30a), activity of membrane efflux transporters (ABCD2) and cisplatin sensitivity in ovarian cancer (LaCroix et al., 2014). Recent global studies focused on other metal-based cytotoxic drugs, e.g. copper and gold that specifically targets proteasome and metabolism of reactive oxygen species (ROS) (Guidi et al., 2012; Ng et al., 2014) or ruthenium, altering the general cell thioredoxin system (Guidi et al., 2013). Particularly relevant are the recent metallomic studies that documented a critical impact of distribution of metal-based drugs in tissues *in vivo* and three dimensional (3D) tissue-like structures *in vitro*. Encapsulation of cisplatin in nanocarriers (Oberoi et al., 2013) or modification of tumour-specific antigens (Dhar et al., 2008) improves homing to the tumour lesion and stabilizes concentration of the cisplatin in the vicinity of the tumour.

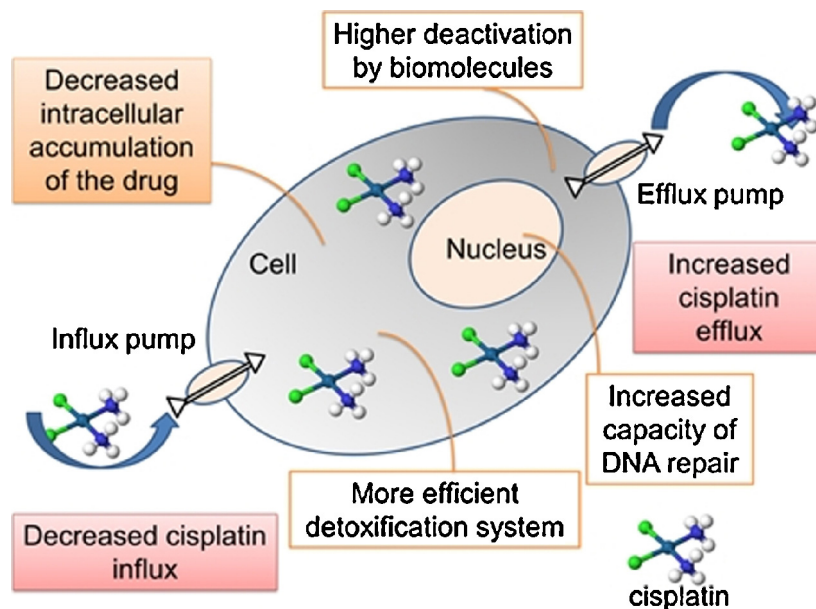


Fig. 9 – Mechanism of cisplatin resistance in cancer cells involves the reduced cisplatin influx and therefore a decreased intracellular accumulation of the drug, a higher enzymatic deactivation, an increased capacity of DNA repair, and an increased cisplatin efflux.

Zhang et al. analysed distribution of platinum in cisplatin- and platinum-anthraquinone conjugate-treated colon cancer 3D spheroids, revealing hotspots of platinum accumulation in necrotic foci, often responsible for tumour relapse. Exposition of such foci to cytotoxic concentrations of cytostatics can eliminate quiescent or stem cell populations (Zhang et al., 2012). Moreover, information provided by integrative global approaches, including NGS, pharmacokinetic analysis and metallomics, can even serve as a biomarker tool predicting a cancer relapse (Araujo et al., 2014). In summary, the integrative approach is important for understanding the cell responses to metal-based compounds and overriding the cancer chemoresistance.

Non-platinum complexes

Despite the extensive research done in last decades, only platinum-based drugs has been approved for clinical practice. Therefore, the possibility to replace platinum with other metal ions has been studied in order to obtain new complexes with low systemic toxicity and active against cancers unresponsive to cisplatin. The rationale behind this approach is that complexes based on other metal ions may act on different targets in cells, including DNA, enzymatic pathways, ROS or mitochondria. Moreover, therapeutic metal-based complexes may mimic endogenous compounds and specifically use physiological endocytic pathways to increase cytotoxic effect and possibly reduce the systemic adverse effects.

Ruthenium

Ruthenium(II) forms either penta- or hexa-coordinated complexes, while ruthenium(III) only hexa-coordinated ones. Both

of them show antitumor activity, but Ru(III) is probably *in vivo* first reduced to Ru(II) acting rather as a prodrug. This reduction process seems to be more effective in hypoxic tumour tissues, lacking normal oxygen partial pressure (Clarke et al., 1999; Clarke, 2002; Spreckelmeyer et al., 2014). The reduction process, $\text{Ru(III)} \rightarrow \text{Ru(II)}$, can be reverted in presence of molecular oxygen. Generally, Ru(II) compounds show lower systemic toxicity than that of platinum ones. Interestingly, Ru(II) is bound by iron-binding proteins such as transferrin and albumin, leading to accumulation of Ru(II) in cancer cells by highly selective iron transport mechanisms and reducing the concentration of the free complex in the bloodstream (Allardyce et al., 2005).

Complexes of Ru(II) with arene ligands represent the most studied anticancer ruthenium compounds because of their amphiphilicity and a relatively easy tunability of their properties. In these complexes the metal ion represents the hydrophilic part while the arene ligand the hydrophobic one. Cationic arene-ruthenium compounds can act as cage for molecules containing other drugs representing an interesting strategy for the development of synergic anticancer drugs (Süss-Fink, 2010). Cytotoxic activity of ruthenium complexes is due to their interaction with DNA and with other biological targets influencing different cellular mechanisms (Fig. 10). The DNA is the target of a family of ruthenium compounds with general formula $[\text{Ru}(\eta^6\text{-arene})(\text{N},\text{N}')\text{X}]^+$ ($\text{X} = \text{Cl}^-$ or I^- , $\text{N}, \text{N}' = \text{ethylenediamine}$ or $\text{N-ethylethylenediamine}$). Monofunctional and bifunctional adducts with DNA are formed by reaction with guanine nucleobases. These Ru(II) compounds show cytotoxic activity similar to that of carboplatin, but lower than that exhibited by cisplatin against human ovarian cancer cell line A2780 (Morris et al., 2001). In addition, these Ru(II)-arene compounds do not present cross-resistance with cisplatin neither *in vitro* nor *in vivo* (Aird et al., 2002). Among

Metal ion	Leader compound	Action mechanism
Ru(II)	RM175	DNA binding
	RAPTA-C	Catepsine B inhibition
	RDC-11	CHOP activation
Ru(III)	KP1019	DNA binding
	NAMI-A	VEGF inhibition

Fig. 10 – Overview of Ru(II) and Ru(III) leading compounds and their main action mechanisms. The acronyms CHOP and VEGF refer to CCAAT/enhancer-binding protein homologous protein and vascular endothelial growth factor, respectively.

Ru(II)-arene complex family, the most interesting compound is [Ru(biphenyl)(en)Cl]PF₆, named as RM175 (Fig. 11a). RM175 binds DNA either by intercalation through the aromatic ligand or by covalent binding with the metal ion (Hayward et al., 2005). Anionic acetylacetonate (acac) derivatives of Ru(II)-arene may be used instead of ethylenediamine with enhanced DNA binding capability and increased extent of hydrolysis. The hydrolysis appears to be a fundamental step for the activation of the Ru(II) complex. The [Ru(η⁶-*p*-cym)(acac)Cl] (*p*-cym = *para*-cymene) compound (Fig. 11b) can undergo the rapid hydrolysis leading to the loss of the chloride ligand. The resulting species is then able to bind amino acids, guanine, and adenine (Fernández et al., 2004). In addition to Ru(II), Ru(III) complexes with indazole motifs as ligands also show interesting antitumor properties due to DNA interaction. One of the most studied Ru(III) complexes is the [Ru(HIn)₂Cl₄](H₂In) (HIn = indazole) (KP1019) (Fig. 11c), which

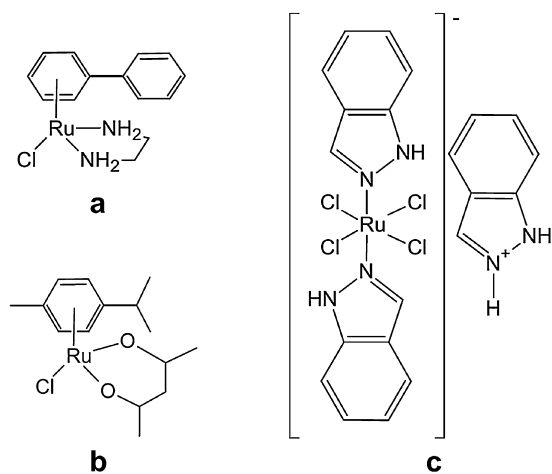


Fig. 11 – Structures of main Ru(II) and Ru(III) complexes: RM175 (a), [Ru(η⁶-*p*-cym)(acac)Cl] (*p*-cym = *para*-cymene) (b) and KP1019 (c).

reacts with DNA and induces apoptosis via the intrinsic mitochondrial pathway, being accumulated mainly in cell nucleus (Pongratz et al., 2004; Hartinger et al., 2006). Although the target of this compound is the same of platinum-based drugs, the induced DNA lesions are different. The complex [Ru(HIn)₂Cl₄](H₂In) shows biological activity against tumour cell lines overexpressing several multidrug-resistance-associated proteins (multidrug resistance protein 1 MRP1, breast cancer resistance protein BCRP, and lung resistance protein LRP) (Hartinger et al., 2006). In phase I trial no dose-limiting toxicity has been observed (Dittrich et al., 2005). The lower occurrence of adverse side effects is probably due to the ability of [Ru(HIn)₂Cl₄](H₂In) to rapidly bind transferrin in blood, maintaining its cytotoxic activity preferentially against tumour cells (Kratz et al., 1994). Recently, a conjugation of a Ru(III)-indazole complexes with PARP-1 was reported, suggesting its role in disrupting DNA repair machinery (Z. Wang et al., 2014b). Interestingly, some compounds derived from Ru(II) complexed with arene ligands and water-soluble phosphines, in particular 1,3,5-triaza-7-phospha-adamantane (PTA), show promising activity against dispersed cancer. [Ru(η⁶-*p*-cym)(PTA)Cl₂] complex (RAPTA-C) (Fig. 12a) is capable of interaction with proteins (Dorcier et al., 2005; Ang et al., 2011) e.g. cathepsin B, a cysteine peptidase responsible for degradation of extracellular matrix (ECM) and promoting metastasis (Casini et al., 2008). RAPTA-C complex also shows a pH-dependent selectivity between cancer and normal cells (Vock et al., 2008). The use of N-methyl-PTA (mPTA) as ligand in water-soluble ruthenium complexes containing chloride and cyclopentadiene (Cp) motifs was found to improve the interaction with supercoiled DNA (Romerosa et al., 2006). The [RuCpCl(mPTA)₂](OSO₂CF₃)₂ (Fig. 12b), shows interesting behaviour during hydrolysis as documented by mass spectrometry (MS) and UV-Vis spectrophotometry (Peña-Méndez et al., 2009). It was found that this complex forms hydrated species and exchanges chloride ions or mPTA and Cp ligands with water, hydroxyl or counter ions following the hydrolysis scheme (Fig. 13), increasing the number of potential targetable molecules. To prevent uncontrolled hydrolysis of [RuCpCl(mPTA)₂]²⁺, it has been suggested either to dissolve the complex in isotonic 0.15 M NaCl solution or to replace the OSO₂CF₃ ligand. Following this strategy, [RuCpCl(mPTA)₂](BF₄) compound has been synthesized but its biological activity has not been evaluated (González et al., 2009). The [Ru(2-phenylpyridine)(NCMe)₂phen]PF₆ (phen is 1,10-phenanthroline) (RDC-11) (Fig. 14a) belongs to RDC family of organometallic Ru(II) compounds, and presents an atypical mechanism of cytotoxic

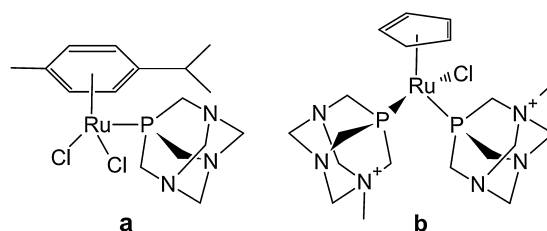


Fig. 12 – Structures of the Ru(II) complexes active against tumour RAPTA-C (a) and [RuCpCl(mPTA)₂](OSO₂CF₃)₂ (b).

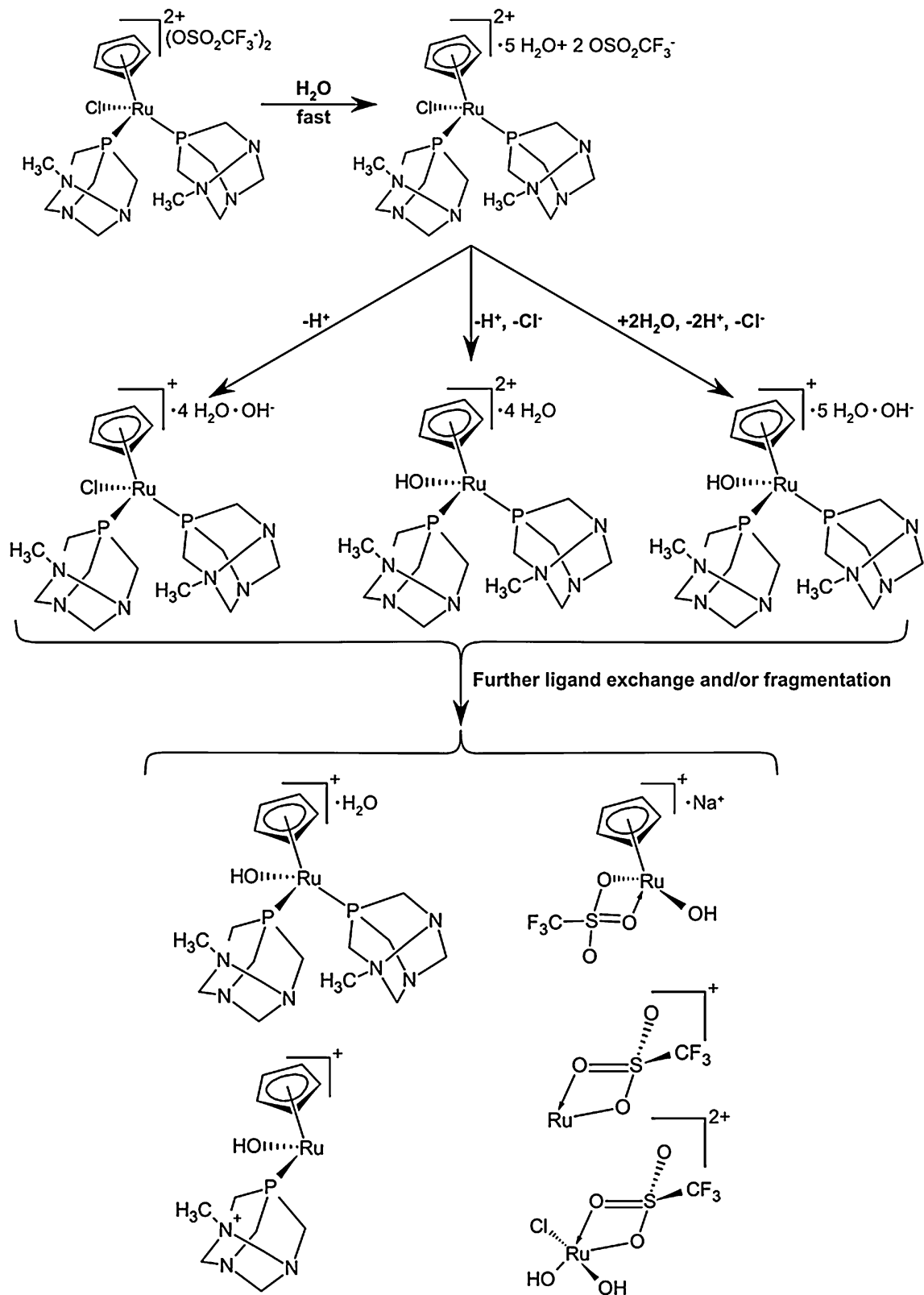


Fig. 13 – Scheme of $[\text{RuCpCl}(\text{mPTA})_2](\text{OSO}_2\text{CF}_3)_2$ hydrolysis as determined by mass spectrometric and spectrophotometric investigation.

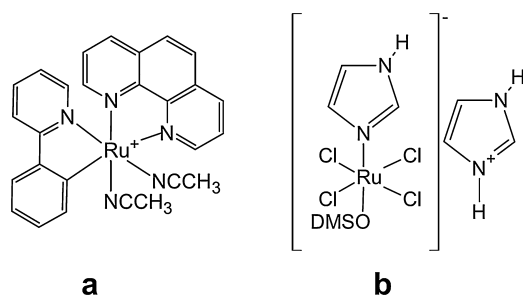


Fig. 14 – Structures of the Ru(II) complexes RDC-11 (a) and NAMI-A (b).

activity (Fernandez et al., 1999). In fact, RDC-11 induces the apoptosis of tumour cells by activating the pro-apoptotic protein CHOP (CCAAT/Enhancer-Binding Protein Homologous Protein), which is a transcription factor involved in unfolded protein response, induced upon endoplasmic reticulum stress (Meng et al., 2009). Moreover, RDC-11 is able to arrest lymphoblastoma (RDM4, TK6) and glioblastoma (A172) cells in G1 phase of cell cycle. RDC-11 also induces the tumour suppressor p53 and p53-regulated effectors, the inhibitor of cell cycle p21 and pro-apoptotic Bax (Gaididon et al., 2005).

An interesting example of ruthenium complex that shows cytotoxic activity due to interaction with non-classical targets is *trans*-[Ru(HIm)(DMSO)Cl₄](H₂Im) (Him = imidazole; DMSO = -dimethylsulfoxide) labelled as NAMI-A (Fig. 14b). Surprisingly, despite the poor activity *in vitro* and no effect on tumour growth *in vivo*, it displays a significant anti-metastasis activity, e.g. in lung cancer. NAMI-A accumulates in kidneys, liver, and collagen-rich tissues (Sava et al., 2003). It interferes with the cell cycle by decreasing the percentage of cells in synthesis phase (S phase) (Gava et al., 2006). NAMI-A also decreases frequency of cells overexpressing receptors for ECM, such as CD44, CD54 and integrin beta 3. Moreover, it presents anti-angiogenic activity due to the inhibition of angiogenesis induced by the vascular endothelial growth factor (VEGF) (Ott and Gust, 2007). The mechanism of action of NAMI-A is therefore supposed to be based on the inhibition of some tumour invasion by the reduction of ECM degradation and prevention of migratory phenotype (Gava et al., 2006).

Promising pilot data therefore led to the introduction of both KP1019 and NAMI-A in clinical evaluation (Rademaker-Lakhai et al., 2004; Hartinger et al., 2006).

In summary, ruthenium compounds act in different way compared to cisplatin. In the majority of ruthenium complexes, ligand affinities, electron transfer, substitution rates, and reduction potentials may be easily tuned. Currently, novel ruthenium compounds are also designed and characterized, as ruthenium half-sandwich complexes comprising combined metal centrochirality and planar chirality and having promising anticancer activity (Meggers et al., 2009; Streu et al., 2011; Martin et al., 2014).

Gold

The attention to gold complexes as antitumor drugs has been attracted when patients treated with auranofin (Fig. 15a) for

rheumatoid arthritis showed unexpectedly lower malignancy rates (Fries et al., 1985). Auranofin is a complex of Au(I) with a phosphine ligand that acts as thioredoxin reductase (TR) inhibitor. The TR is a class of seleno-cysteine enzymes catalyzing the reduction of thioredoxins, which are ubiquitous redox proteins containing a redox-active disulphide bond in the active site (Holmgren, 1989). Thioredoxins are involved in several biological processes, including ROS reduction (Nordberg and Arnér, 2001). Elevated concentrations of TR have been found in human tumour cells and they have been associated with tumour proliferation (Bruijninx and Sadler, 2008). The inhibition of TR induces mitochondria-dependent apoptosis (Gromer et al., 1998). In addition, TR inhibition is also probably responsible for the side-effects observed during the treatment with auranofin (Ott and Gust, 2007).

Complexes of Au(III) have also been extensively studied because its chemistry is similar to that of Pt(II). In fact, Au(III) is isoelectronic with Pt(II) and forms complexes with square planar geometry. However, under physiological conditions Au(III) is rapidly hydrolysed and reduced to Au(I) (Wang and Guo, 2008). Therefore, the stabilization of Au(III) complexes by using suitable ligands is needed. Chelating nitrogen donors such as phen, 2,2'-bipyridine (bipy), 2,6-bis(2-pyridyl)-pyridine (terpy) and ethylenediamine (en) have been proposed for this purpose (Marcon et al., 2002). The Au(III) complexes with phen and bipy derivatives show cytotoxic activity comparable to that of their ligands. On the contrary, the cytotoxicity of [Au(en)₂]Cl₃ (Fig. 15b) was found to be due to the presence of the gold centre (Tiekink, 2002). The cytotoxicity of Au(III) complexes containing terpyridine derivatives as ligands (Fig. 15c) is mainly due to DNA intercalation. Such complexes are also stable towards reduction by GSH and represent the first example of Au(III) complexes interacting with DNA (Wang and Guo, 2008).

The cytotoxic activity of Au(III) complexes with porphyrin ligands might be due to their action on mitochondria. As a consequence, apoptosis is induced by caspase-dependent and caspase-independent pathways (Wang et al., 2005). The leader compound [Au(TPP)]Cl (H₂TPP = tetraphenyl-porphyrin) (Fig. 15d) shows IC₅₀ values on the μM order towards several cell lines, including human cervix epitheloid (HeLa) and hepatocellular (HepG2) carcinoma. It presents a similar activity also against cisplatin-resistant and MDR cell lines (Che et al., 2003). This compound shows tumour inhibition of about 80% (Sun et al., 2007) in cisplatin-resistant nasopharyngeal carcinomas (NPC) cells implanted into mice.

Several Au(III)-thiocarbamates complexes with general formula [Au(dtc)X₂] (X = Cl, Br; dtc = N,N-dimethyl-dithiocarbamate, ethyl-sarcosine-dithiocarbamate) (Fig. 15e) inhibit the proteasome-dependent protein degradation both *in vitro* and *in vivo* (Milacic et al., 2006). Proteasome inhibitors are effective against tumour cells because they induce apoptosis by perturbing the regulated degradation of pro-growth cell cycle proteins (Orlowski, 1999). The Au(III)-thiocarbamate compounds are equally or more active than cisplatin against various human tumour cell lines and show low cross-resistance with cisplatin. These complexes show 50% reduction of tumour growth in human breast cancer MDA-MB-231 and no toxic side-effects *in vivo* (Milacic et al., 2006).

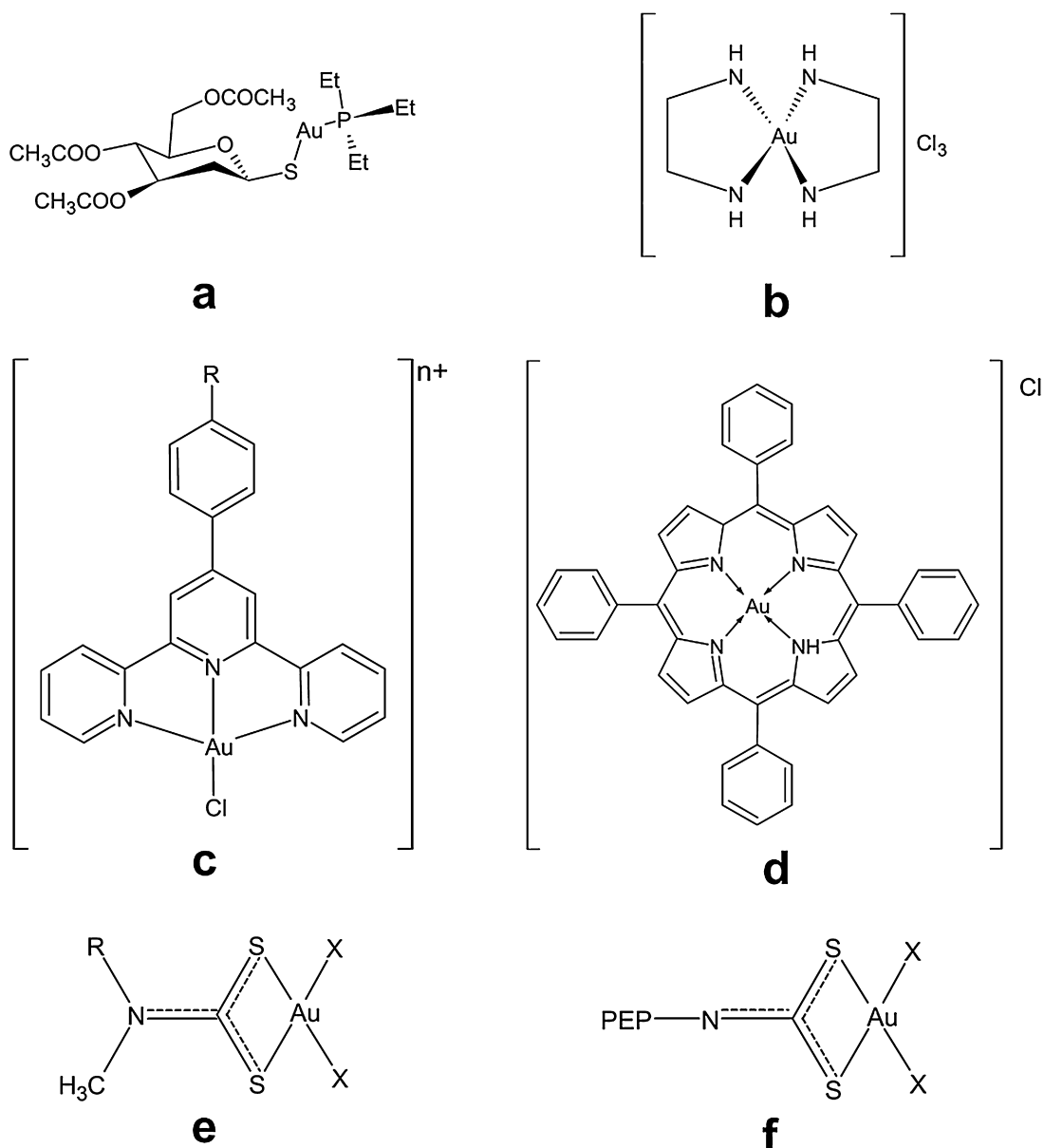


Fig. 15 – Structures of selected antitumor gold complexes: auranofin (a), $[\text{Au}(\text{en})_2]\text{Cl}_3$ (b), Au(III) complex with substituted terpyridine ligand (c), $[\text{Au}(\text{TPP})\text{Cl}]$ (H_2TPP = tetraphenyl-porphyrin) (d), $[\text{Au}(\text{dte})\text{X}_2]$ ($\text{X} = \text{Cl}, \text{Br}$; dte = N,N-dimethyl-dithiocarbamate, ethyl-sarcosine-dithiocarbamate) (e) and $[\text{AuX}_2(\text{pdtc})]$ ($\text{X} = \text{Cl}, \text{Br}$; pdtc = oligopeptide-dithiocarbamate, PEP-N is a di-, tri-, tetra- or penta-peptide) (f).

Recently, Au(III)-peptide-dithiocarbamate complexes with general formula $[\text{AuX}_2(\text{pdtc})]$ ($\text{X} = \text{Cl}, \text{Br}$; pdtc = oligopeptide-dithiocarbamate) (Fig. 15f) have been synthesized using di-, tri-, tetra- and pentapeptides (Kouodom et al., 2012). The incorporation of peptides makes the complex recognizable by intracellular peptide transporters (PEPTs). Therefore, cellular uptake is enhanced, and side-effects reduced. The most promising results have been obtained with the tripeptide derivatives, such as H-Sar-Aib₂-O(t-Bu) and H-D,L-Pro-Aib₂-O(t-Bu) (Sar = sarcosine (N-methylglycine)); Aib = α -aminoisobutyric acid (2-methylalanine), which show IC_{50} values lower

than that of cisplatin *in vitro*. They also show no cross-resistance with cisplatin, confirming a different cytotoxic mechanism. The study of *in vivo* activity and mechanism started recently (Kouodom et al., 2012).

The variety of cytotoxic mechanisms reported for gold complexes (Fig. 16) expands the possibility to find out new compounds able to overcome platinum-drug resistance. Nevertheless, the application of gold complexes in clinical practice still requires an extensive evaluation of their chemical and pharmaceutical properties such as hydrolysis equilibria, cellular uptake, biodistribution, and pharmacokinetics.

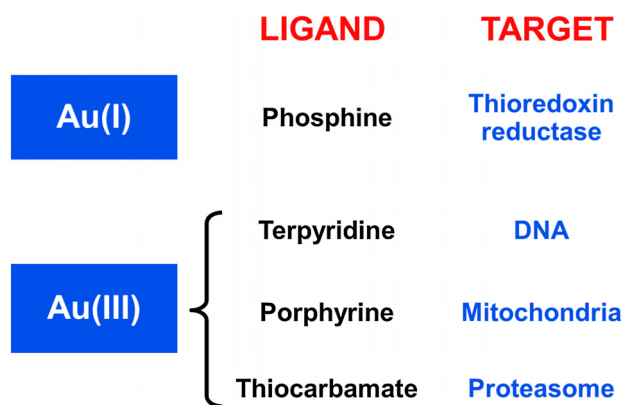


Fig. 16 – Overview of main ligand families used in Au(I) and Au(III) antitumor complexes and principal biological targets.

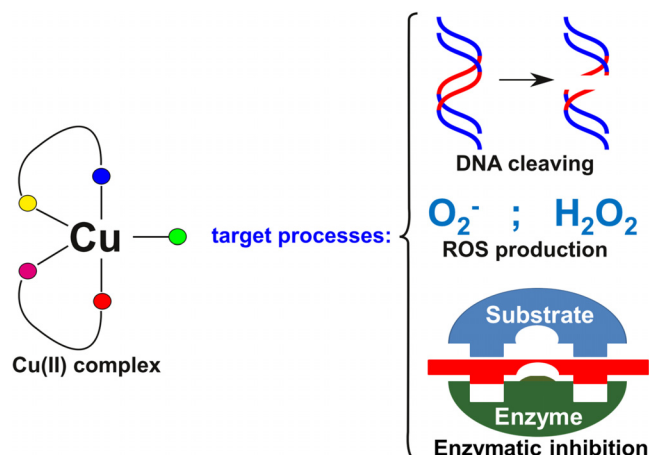


Fig. 17 – Biological target processes of Cu(II) complexes with antitumor activity.

Silver

Silver complexes show therapeutic potential in treating bacterial infections but detailed reports on the antitumor activity of silver (I) are scarce. Recently, the anti-proliferative activity of silver (I) complexes containing various type of ligands such as carboxylic acids, amino acids, nitrogen, phosphorus or sulphur donor ligands, was reviewed (Banti and Hadjikakou, 2013). In this review comparison with the corresponding activity of cisplatin is given, and it was found that under specific conditions silver(I) complexes are more active than cisplatin *in vitro*.

Interestingly, it was reported that complexes of copper, silver, and gold show enhanced selectivity for breast cancer while causing fewer and weaker adverse side-effects (Biersack et al., 2012) when compared to platinum based drugs, being promising new candidates (Tan et al., 2010, 2014; Kyros et al., 2014).

Copper

Copper is an essential metal ion present as cofactor in many enzymes. It is involved in haemoglobin formation, xenobiotics and carbohydrates metabolism, catecholamine biosynthesis, cross-linking of collagen, elastin, and hair keratin. Copper ion is also engaged in antioxidant defence mechanism. In fact, copper-dependent enzymes, such as cytochrome C oxidase, superoxide dismutase, ferroxidases, monoamine oxidase, and dopamine β -monooxygenase, are involved in neutralizing ROS or molecular oxygen. Importantly, efflux of cisplatin outside the cells employs specific copper-efflux transporters ATP7A and ATP7B, next to the multidrug efflux pumps belonging to the ABC superfamily (P-glycoprotein (Pgp, ABCB1) and multidrug resistance protein 2 (MRP2, ABCC2)) (Samimi et al., 2004; Leslie et al., 2005).

Copper has been selected for the synthesis of antitumor drugs under the hypothesis that complexes with endogenous metal ions might give lower systemic toxicity. Several Cu(II) complexes with a variety of N-, S-, or O-containing ligands have been designed, synthesized and tested as antitumor drugs. The different biological actions of these complexes, in

comparison to that of cisplatin, suggest that different mechanisms for their antitumor activity are involved (Fig. 17). However, such mechanisms are not completely clarified to date (Santini et al., 2013).

Copper(II) is also an angiogenesis promoter because it enhances the formation of new blood vessels from pre-existing ones. In cancer cells, this physiological process may eventually trigger the transition from a benign to malignant state of tumours. Further studies are required to completely clarify the role of copper in angiogenesis processes.

Copper(II) complexes are supposed to act by triggering cell apoptosis or inhibiting enzymes (Tripathi et al., 2007). In fact, the expression of tyrosine-protein kinase CSK is inhibited by complexes of Cu(II) with pyridine-2-carbohydrazide derivatives. Copper(II) chelate of salicylaldehyde induces cell cycle arrest and apoptosis, perhaps involving the inhibition of the topoisomerase II enzyme (Jayaraju and Kondapi, 2001). Topoisomerases (Topo) are ubiquitous enzymes able to break and reseal the DNA polyphosphate backbone, preventing the overwinding or underwinding of the double helix. The disruption of Topo activity leads to single and double stranded breaks in DNA, inducing apoptosis. Among Topo-I inhibitors, the [Cu(phen)L](NO₃)₂ (L = 2,4,6 tri-(1H-pyrazol-1-yl)-pyrimidine) is a Cu(II) complex containing a ligand derived from barbituric acid and pyrazole (Tabassum et al., 2014). This complex inhibits Topo-I at 10 μ M concentration. Another family of Topo-I inhibitors with general formula [Cu(N)L]Cl (N = phen, bipy or 5,5'-dimethyl-2,2'-bipyridine; L = doubly deprotonated 5-(triphenyl-phosphonium-methyl)-salicylaldehyde-benzoyl-hydrazone) show a good cytotoxic activity against human lung carcinoma (A549) and prostate adenocarcinoma (PC-3) cell lines (Chew et al., 2014). The most active compound of this family is the one containing phen motif. It shows an IC₅₀ value of 3.2 μ M against PC-3 cell line and starts to inhibit Topo I at 40 μ M. A metalloprotease activity (Shrivastava et al., 2002) is evidenced by the complex 2,6-bis-(benzimidazo-2-yl)-pyridine copper(II) chloride. Proteasome inhibition resulting in apoptosis was reported when Cu(II) binary complexes containing neutral or anionic molecules such as phen, 8-hydroxyquinolate, pyrrolidine dithiocarbamate,

or (pyridine-2-ylmethylamino)-methyl phenolate are used. Evaluation of proteasome inhibition shows that both the complexes and the copper ion inhibit the enzyme in the same extent while the free ligands have no activity. Then, the complex behaves as carrier of the metal ion through the cell membrane. This is achieved by tuning the lipophilicity of the complexes by suitable ligands (Hindo et al., 2009).

Copper complexes with thiosemicarbazone ligands, which possess antitumor activity and are used in clinical practice, inhibit enzymatic activity and induce cell apoptosis (Tisato et al., 2010). The cytotoxic properties of copper complexes with phen ligand have been firstly reported by Sigman (Sigman et al., 1979). The complex with two phen ligands is able to cleave DNA by binding to the deoxyribose units and thus acting as a chemical nuclease. It has been tested against a great number of cancer cell lines, both solid and hematologic (Cai et al., 2007; Pivetta et al., 2012). Consequently, many other copper complexes with phen, phen-derivatives or structurally related compounds such as bipy have been studied. Modulation of the cytotoxic activity of $[\text{Cu}(\text{phen})_2]^{2+}$ species with insertion of substituted imidazolidine-2-thione ligands (Fig. 18a) has been evaluated against acute T-lymphoblastic leukaemia (CCRF-CEM), acute B-lymphoblastic leukaemia (CCRF-SB), lung squamous carcinoma (K-MES-1), and prostate carcinoma (DU-145). Correlation between the dipole moment of the complexes and the cytotoxic activity has been found (Pivetta et al., 2011). Complexes with high dipole moment result more active against haematological tumour cell lines, while less polar complexes show higher activity against solid tumour ones. The use of serinol bridge (called Clip) in position 2 or 3 to link two phenanthroline (phen) units has led to the preparation of a new class of compounds (Pitie et al., 1998). The copper(II) complexes obtained by reaction with 2- and 3-Clip-phen show a 2- to 60-fold increased ability to cleave DNA in comparison to phen complexes (Pitie et al., 1998). Further studies have shown that the optimal length of the bridge to achieve optimal DNA cleavage activity corresponds to three methylene units (Pitié et al., 2003). Compounds with a functionalized serinol bridge have also been prepared by using a conjugate of 3-Clip-phen (Fig. 18b) with a cisplatin derivative (De Hoog et al., 2007). A class of Cu(II) complexes with general formula $[\text{Cu}(\text{N-N})(\text{A-A})\text{NO}_3]$, where N-N is phen or bipy and A-A is either a nitrogen-oxygen or oxygen-oxygen

donor ligand is capable of inducing autophagy and programmed cell death of glioma cells by ROS and JNK activation (Trejo-Solis et al., 2012) or caspase activity in colon cancer cells. They also exhibit high DNA binding and nuclease activity towards plasmid, genomic, and internucleosomal DNA (Marín-Hernández et al., 2003). Other complexes of Cu(II) with Schiff bases and 2-amino-2-thiazoline show interesting anti-inflammatory, antibacterial, and anticancer activity against various cell lines (Chaviara et al., 2005). The development and use of Cu(I) complexes as antitumor agents is limited by their low stability and their tendency to be easily oxidized. Some complexes, such as $[\text{Cu}(\text{N,N}'\text{-disubstituted thioureas})\text{Cl}]$ and $[\text{Cu}(1,3,5\text{-triazol-7-phosphaadamantane})_4]^+$, exhibit moderate cytotoxicity against various human cell lines (Porchia et al., 2009). In analogy with gold, Cu(I)-phosphine complexes have been synthesized and evaluated as antitumor compounds (Marzano et al., 2006; Plotek et al., 2013; Porchia et al., 2013; Santini et al., 2013). Some mixed Cu(I) complexes of triazolylborate and alkyl- or aryl-phosphines have been found to be effective against A549 adenocarcinoma cisplatin resistant cells (Marzano et al., 2006).

Iron

Iron is involved especially in oxygen transport, DNA synthesis, oxidative phosphorylation, and cell cycle progression, and all of them have a role in carcinogenesis (Boult et al., 2008; Brookes et al., 2008; Coombs et al., 2012). The potential cytotoxic activity of iron complexes appears to be related to the redox reactions occurring between Fe(II) and Fe(III) in physiological conditions (Jungwirth et al., 2011). A promising compound is a complex between iron and bleomycin, a molecule already used for the treatment of testicular carcinoma. The biological activity of this complex arises from the ROS production that leads to the apoptosis of the cancer cells (Chen and Stubbe, 2005). Also complexes with ferrocene (ferrocifenes) show anticancer activity, with a selectivity that depends on the present substituents. Several hydroxy-substituted ferrocifens present high affinity with oestrogen receptor and are used for the treatment of breast cancer (Lange et al., 2008; Rafique et al., 2010). Interestingly, the ferrocene alone does not show anticancer activity.

Iron deprivation by selective chelators is a promising strategy in reduction of tumour growth. Treatment with iron chelator has been then proposed in cancer therapy by using iron selective chelators such as triapine and desferrioxamine (DFO) (Kalinowski and Richardson, 2005). It has been suggested that the antitumor activity exhibited by these molecules may be due to the inhibition of ribonucleotide reductase by bonding the iron(II,III) ion. In fact, the enzyme requires iron and oxygen for its biological activity that is elevated in tumour tissues (Richardson, 2002). The thiosemicarbazone triapine (3-aminopyridine-2-carboxaldehyde thiosemicarbazone) is able to overpass the blood-brain barrier showing a potent activity against leukaemia brain metastasis. It is also able to inhibit the growth of mouse M109 lung and human A2780 ovarian cancer cells *in vivo* (Finch et al., 2000). Desferrioxamine (DFO) is a hexadentate siderophore currently in use for β -thalassaemia treatment because of its great affinity for iron (Richardson, 2002).

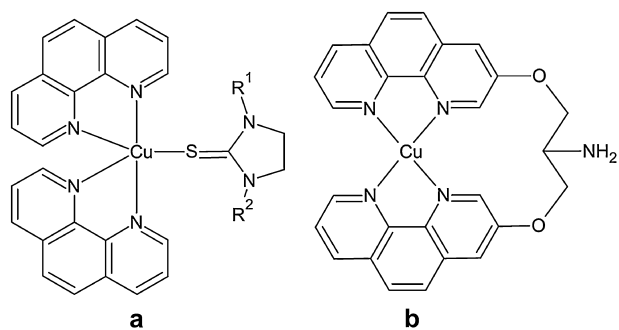


Fig. 18 – Structures of some Cu(II)-phen complexes: $[\text{Cu}(\text{phen})_2(\text{imidazolidine-2-thione})]^{2+}$ ($\text{R}^1, \text{R}^2 = \text{H}, \text{Me}$ or Et) (a) and $[\text{Cu}(\text{phen})_2]^{2+}$ with serinol bridge. Charges are omitted.

Clinical trials have confirmed that some cancers, as neuroblastoma and leukaemia, are sensitive to DFO therapy while normal tissues are affected only in little extent (Desoize, 2004). Nowadays, iron depletion has been proposed for the treatments of several kinds of cancers and metastatic progression (Kovacevic, 2012; Keeler and Brookes, 2013; Richardson et al., 2013; Torti and Torti, 2013). A triapine derivative, di-2-pyridylketone-4-cyclohexyl-4-methyl-3-thiosemicarbazone (DpC) is currently under preclinical evaluation (Lane et al., 2014). From several clinical evidences, it seems that iron deprivation could be an effective therapeutic approach. However, adverse effects, such as anaemia, induced by the iron-chelating agents, can develop (Beguin et al., 2014). However, more studies *in vitro* and *in vivo* should be done, to clarify the action mechanisms and in particular their extra- and intracellular effects. This kind of studies will help in the design and synthesis of more potent iron chelators.

Cobalt

The Co-ASS (Fig. 19) is a cobalt(II) complex containing an acetylsalicylic acid (ASA) derivative which inhibits the cyclooxygenase enzymes COX-1 and COX-2. Recently, it was found that the regular use of aspirin reduces cancer incidence (Algra and Rothwell, 2012). The COX inhibition induced by Co-ASS complex is more efficient than that induced by ASA alone and this probably determines the resulting higher cytotoxic properties, in particular against breast cancer cell lines (Ott et al., 2004; Bruijninx and Sadler, 2008). The use of COX inhibitors is suggested in combinational therapies with other antitumor drugs (Ott and Gust, 2007). Cobalt(III) complexes have been developed as prodrugs which exploit the hypoxic environment in tumours to release highly cytotoxic ligands. In fact, in hypoxic environment Co(III) complexes can be reduced to Co(II) with subsequent release of one neutral ligand. This strategy has been widely exploited for the release of compounds such as DNA alkylators and a matrix metalloproteinase inhibitor (Ahn et al., 2006; Failes et al., 2007; Lu et al., 2011).

Gallium

Gallium is a metalloid that has been used in different medical applications, such as the treatment of accelerated bone resorption, autoimmune and infective diseases (Gârban et al., 2014). Using the isotope ^{67}Ga for imaging in rodents, it has been reported that gallium accumulates in tumour tissues.

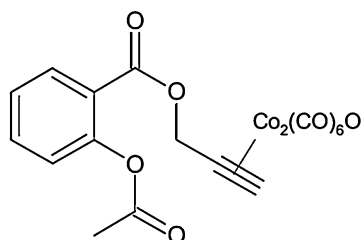


Fig. 19 – The Co-ASS cobalt(II) complex containing an acetylsalicylic acid (ASA) derivative.

This observation led to the introduction of gallium compounds in anticancer therapy. The biological activity of gallium derives from its chemical similarity with iron. In fact, Ga(III) and Fe(III) have similar ionic radius, ionization potential, and electron affinities (Chitambar, 2012). These characteristics allow gallium to bind transferrin. Because some cancers, as lymphoma (Gatter et al., 1983), bladder (Smith et al., 1990) and breast (Ding Cheng Yang et al., 2001) cancers, overexpress transferrin receptors, gallium is selectively delivered to tumour cells *via* iron transporters similarly to ruthenium complexes (Chitambar and Antholine, 2013). The gallium uptake perturbs iron homeostasis, reducing the intracellular iron concentration. In addition, the activity of the enzyme ribonucleotide reductase is blocked by iron-substitution in the active site by gallium and by gallium-induced iron deprivation. This results in the inhibition of DNA synthesis and cell proliferation. An interaction with mitochondria has been also recently proposed as a possible cytotoxic mechanism (Chitambar et al., 2007).

The first gallium compound that has been investigated in phases I and II trials as anticancer agent was the gallium nitrate. Some antitumor activity in advanced bladder cancer and non-Hodgkin's lymphoma was demonstrated (Chitambar, 2012). Since it does not show myelosuppressive activity, it can be safely administered in patient with pancytopenia. Despite the good activity shown by gallium nitrate, its administration is dependent on long intravenous infusions and pre- and post-hydration required to prevent nephrotoxicity (Chitambar, 2012).

Gallium chloride has been also tested, showing an *in vitro* cytotoxicity similar to that of gallium nitrate. A modified formulation of gallium nitrate suitable for oral administration, G4544, is currently in phase I clinical trial. G4544 ensures an increased level of gallium in blood *in vivo* and a longer circulation time, when compared with gallium nitrate. In humans, the gallium levels in blood are similar to those obtained with the continuous intravenous infusion of gallium nitrate and no adverse side-effects are observed (Novick et al., 2008). Also gallium maltolate (tris(3-hydroxy-2-methyl-4H-pyran-4-onato)gallium(III)) (Fig. 20a) has been studied as anticancer agent. This complex is degraded after the administration and the free gallium can bind transferrin in blood (Bernstein et al., 2011). Gallium maltolate has been tested on

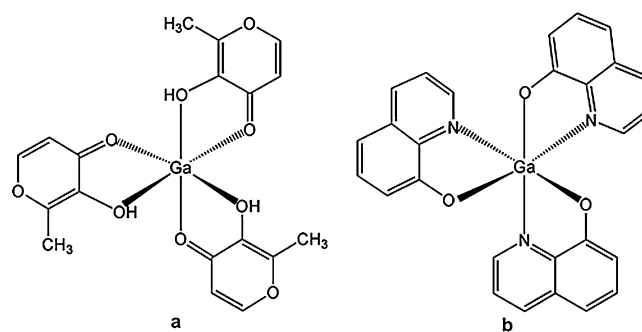


Fig. 20 – Structure of gallium maltolate (tris(3-hydroxy-2-methyl-4H-pyran-4-onato)gallium(III)) (a) and KP46 (tris(8-quinolonato)gallium(III)) (b).

phase I trials, and it is effective in advanced hepatocellular carcinoma (Bernstein et al., 2011). Gallium maltolate shows activity also in gallium nitrate-resistant lymphoma cell lines (Chitambar and Purpi, 2010). This lack of cross-resistance allows to expand the action spectrum range of gallium compounds. To enhance their antitumor activity and bio-availability, complexes of gallium(III) stable in physiological conditions were investigated (Tan et al., 2014). An interesting example of a gallium compound developed for oral administration is the tris(8-quinolinolato)gallium(III), also known as KP46 (Fig. 20b). Interestingly, this complex is not destroyed in the blood (Enyedy et al., 2012, 2015; Hummer et al., 2012). It shows *in vitro* a cytotoxic activity higher than that of gallium nitrate (Lessa et al., 2012). The cytotoxicity mechanism involves p53 activation mediated by Ca^{2+} -signalling and ROS production (Gogna et al., 2012; Madan et al., 2013). Recently, new insights onto the mechanism of action have been highlighted (Jungwirth et al., 2014). KP46 has been tested in various phase II clinical trials and no dose-limiting toxicity was found. In particular, the results in renal cancer treatment are promising, improving the remission rate (Timerbaev, 2009). Gallium complexes with thiosemicarbazone ligands are widely studied (Ismail et al., 2013; Lessa et al., 2013). In these compounds, the cytotoxic activity of the thiosemicarbazone ligands is enhanced of several folds by the formation of the metal complex (Mendes et al., 2009). A family of gallium complexes with pyridine and derivatives of phenolate as ligands shows cytotoxic activity greater than that of cisplatin (Shakya et al., 2006). The biological action of these complexes is due to the inhibition of proteasome with activation of apoptosis (Chen et al., 2007). Recently, the antitumor activity of phosphinoarylthiolato gallium(III) complexes was reported (Fischer-Fodor et al., 2014). They bind DNA in 7-methylguanine and 8-oxoguanine positions, oxidizing the pyrimidine bases and inducing apoptosis. These complexes show *in vitro* antitumor activity against the cisplatin-resistant ovarian tumour cell line A2780cis (Fischer-Fodor et al., 2014). Complexes with N,N,O donors have been also tested against ovarian, breast, and prostate adenocarcinoma cell lines. Against these tumour cell lines, the complex bis(2-(benzothiazol-2-yl-hydrazone)methyl)-6-methoxyphenolate) gallium(III) nitrate shows a good cytotoxic activity, with CC_{50} on the micromolar range (Machado et al., 2014). In order to combine chemotherapy with photodynamic therapy, a gallium(III) complex with the photosensitizer hypocrellin A has been recently proposed (Xie et al., 2014). This complex induces *in vitro* nuclear morphological changes in tumour cells after light irradiation. Up-to-now, the research of gallium complexes for anticancer treatment has led to the clinical evaluation of the two candidate compounds KP46 and gallium maltolate. They both seem to possess interesting activity in renal malignancies. The search for new compounds extending the activity of gallium complexes to other types of cancer is ongoing, especially in context of chemoresistance developed in some cancers. For example, lung cancers seem to be resistant to gallium compounds because of over-expression of tyrosine-protein kinase receptors (Oyewumi et al., 2014). Starting from the promising results of gallium compounds undergoing clinical trials, the development of new gallium compounds, as well as the study of their mechanism of activity, seems to be

one of the key topics of anticancer research in the next years (Mikuš et al., 2014).

Rhodium

Many complexes of rhodium have been synthesized but most of them show severe nephrotoxicity and thus no further studies were done (Katsaros and Anagnostopoulou, 2002). Recently, it has been suggested that rhodium(III) complexes that are inert towards substitution may show low systemic toxicity (Geldmacher et al., 2012). Some interesting rhodium complexes are $[Rh(2-(2'-hydroxy-5'-methylphenyl)-benzotriazole)_2(H_2O)_2]Cl$ that shows promising activity against human breast cancer (MDA-MB231) and human ovarian cancer (OVCAR-8) cell lines (El-Asmy et al., 2014) and also a series of rhodium(I)-N-heterocyclic carbene complexes with CO as secondary ligand, which shows marked antiproliferative effects together with moderate inhibitory activity of thiorodoxin reductase and efficient binding to biomolecules (e.g., DNA, albumin). With the use of these complexes, modifications in the mitochondrial membrane potential and DNA fragmentation were observed in wild-type and daunorubicin- or vincristine-resistant Nalm-6 leukaemia cell lines (Oehninger et al., 2013).

Despite the encouraging results, in order to define their activity spectrum, selectivity and systemic toxicity, *in vivo* studies need to be performed (Zhong et al., 2014).

Titanium

The *cis*- $[Ti(CH_3CH_2O)_2(bzac)_2]$ (*bzac* = 1-phenylbutane-1,3-dionato) complex was the first non-platinum compound tested in clinical trials but surprisingly, it has no antitumor activity. Afterwards, complexes with arene ligands have been tested. The titanocene dichloride (Fig. 21) binds DNA *via* the phosphate backbone, inducing apoptosis (Meléndez, 2002). It shows *in vitro* cytotoxic activity against a broad spectrum of cancers, in particular human stomach and colon adenocarcinomas, and has been tested in phases I and II trials. Its development has been abandoned because it shows, as the others Ti(IV) complexes, nephrotoxicity as dose-limiting toxicity and poor antitumor activity, probably due to low water solubility and high deactivation by plasma proteins (Ott and Gust, 2007).

Recently, coordination compounds of Ti(IV) with isopropoxide supported by pyrrolyl Schiff base ligands were synthesized and tested against human colon (HCT-116), prostate (PC3) and breast (MCF-7) cancer cell lines showing cytotoxic activity either lower or higher than cisplatin (Lin et al., 2014).

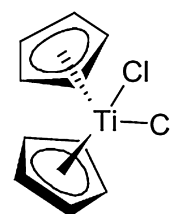


Fig. 21 – Structure of the titanocene dichloride.

The reasons for the different behaviour observed are still not clear. Perhaps high hydrolytic resistant ligands strongly bound to the metal centre and are probably responsible for the high cytotoxicity observed for some complexes.

Titanium(IV) complexes with ortho-bromo-para-methyl-substituted diaminobis(phenolato) ligands were prepared with NH-, NMe-, and bipyridine-based diamino bridges. The hydrolytic stability of such compounds as well as their cytotoxic activity in human colon cancer cells (HT-29) was investigated (Miller and Tshuva, 2014). The NMe-based complexes, although highly hydrolytically stable, were found inactive while, the NH- and bipyridine-based compounds were found active. Interestingly, the highest cytotoxic activity of such compounds was observed when pure enantiomers were used in place of racemic mixtures (Miller and Tshuva, 2014).

Arsenic

Arsenic trioxide (As_2O_3) represents an important metalloid compound for cancer treatment. It has been used in leukaemia treatment with increased rate of survival (Wang and von Recum, 2011). It has been approved by FDA under the name of trisenox and it is the most active single agent for acute promyelocytic leukaemia treatment (Barry and Sadler, 2013). However, the antitumor mechanism is still unclear and cardiotoxicity has been reported as side-effect (Desoize, 2004). The compound darinaparsin (S-dimethylarsino-glutathione) (Fig. 22) has been approved for clinical therapy in the treatment of peripheral T-cell lymphoma and other arsenic compounds are currently under clinical trials (Barry and Sadler, 2013).

Antimony

Antimony in form of potassium antimonyl tartrate (PAT) shows antibacterial activity and antiangiogenic effect in non-small cell lung cancer *in vitro*, in an extent comparable to doxorubicin or cisplatin (Duffin and Campling, 2002). Sodium stibogluconate (SSG) is used as drug to treat leishmaniasis but recently, its synergistic effect with IFN- α to overcome IFN- α resistance in various human cancer cell lines was demonstrated (Yi et al., 2002). Complexes of antimony(V) shows 10-fold lower toxicity than the corresponding antimony(III) ones (Asghar et al., 2012). Furthermore, ferrocenyl benzoate-antimony complexes have been shown to be promising

chemotherapeutic compounds (Liu et al., 2003; Li et al., 2004; Yu et al., 2004) but their mechanism of action is not yet known. Studies attempting to investigate interaction of ferrocenyl benzoate-antimony complexes with DNA and other biomolecules are currently under investigation.

Final remarks

From all the results presented in literature in the field of various anticancer metal complexes so far, it appears necessary to choose a more constructive and rational approach. The continued study to optimize the design and potency of a particular metal complex used as anticancer agent, sometimes has led to undesirable results. Therefore, to overcome these obstacles, the effective design of metal complexes with potential antitumor properties should now focus not separately on achieving the high cytotoxic activity or interactions with the biomolecules, but rather on the simultaneous evaluation of all the involved parameters. In particular, it must be clearly understood that the proper strategy for the possible use of the metal complex, the selection of the target and interactions of the drug with biomolecules should involve highly interdisciplinary approach.

The proper strategy

Two different strategies can be exploited for the use of a metal complex, and it is fundamental to choose in advance the strategy most suitable to the needs. A metal complex, in fact, might be used as active agent if it presents cytotoxic activity, or as a carrier of organic ligands that present independent biological activity, or as a carrier for metal ions that present some other biological activity.

The selection of the target

The optimal design of a metal complex and its potential target should be considered and estimated before its synthesis. In this way, a molecule with features suitable to specifically interact with the chosen target may be prepared, and the antitumor activity might be exerted according to the expected mechanism. The traditional approaches in this field are still founded mainly on the interaction of the metal complex with DNA. Unfortunately, the continuous research for compounds able to form more stable DNA-adducts, by intercalation, groove binding or electrostatic interactions, does not always lead to a better drug. Instead, other types of targets may play a key role and should be seriously considered. In fact, the antitumor activity can be obtained also through reactions with proteome, disruption of mitochondrial processes or through inhibition of angiogenesis or metastatic routes.

Drug and biomolecules

In parallel with the choice of the proper strategy and the required target, the interaction of the drug with the biomolecules naturally present in the body should be estimated or at least hypothesized. In fact, the resulting biochemical reactions may eventually trigger the onset of side effects. Moreover, the

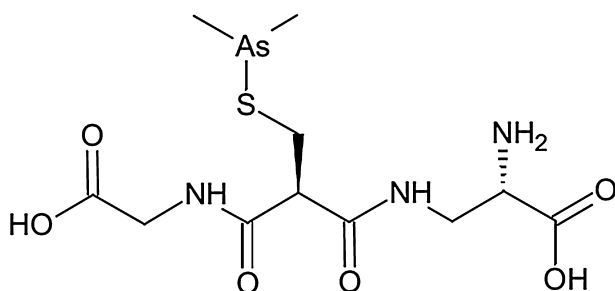


Fig. 22 – Structure of darinaparsin (S-dimethylarsino-glutathione).

metal complex, due to its structural characteristics, might be susceptible to mechanisms that can cause the drug resistance, deactivation for transformation or loss of the functional groups, for hydrolysis or redox reactions.

In the last three years (2012–2014) the drugs that have obtained FDA approval for oncology are primarily monoclonal antibody and kinase inhibitors. This fact shows that the development of new metal complexes has come to a break since the approval of oxaliplatin in 2002. However, rational development of coordination compounds acting in specific cellular and tissue contexts in patient-tailored therapy has an immense potential in oncology.

Acknowledgements

This study was supported by Grant Agency of Masaryk University (MUNI/A/1558/2014) and HistoPARK – Centre for Analysis and Modeling of Tissues and Organs (no. CZ.1.07/2.3.00/20.0185) from the European Regional Development Fund.

Federica Trudu gratefully acknowledges the Masaryk University and its Department of Chemistry, for the kind hospitality and for funding her stay in Brno, and the Sardinia Regional Government, for the financial support of her PhD scholarship (P.O.R. Sardegna F.S.E. Operational Programme of the Autonomous Region of Sardinia, European Social Fund 2007-2013 – Axis IV Human Resources, Objective 1.3, Line of Activity 1.3.1.). Peña-Méndez E.M. acknowledges La Laguna University for support.

REFERENCES

- Ahn, G.-O., Botting, K.J., Patterson, A.V., Ware, D.C., Tercel, M., Wilson, W.R., 2006. Radiolytic and cellular reduction of a novel hypoxia-activated cobalt(III) prodrug of a chloromethylbenzindoline DNA minor groove alkylator. *Biochem. Pharmacol.* 71, 1683–1694.
- Aird, R.E., Cummings, J., Ritchie, A.A., Muir, M., Morris, R.E., Chen, H., Sadler, P.J., Jodrell, D.I., 2002. *In vitro* and *in vivo* activity and cross resistance profiles of novel ruthenium (II) organometallic arene complexes in human ovarian cancer. *Br. J. Cancer* 86, 1652–1657.
- Alberto, M.E., Lucas, M.F.A., Pavelka, M., Russo, N., 2009. The second-generation anticancer drug nedaplatin: a theoretical investigation on the hydrolysis mechanism. *J. Phys. Chem. B* 113, 14473–14479.
- Alderden, R.A., Hall, M.D., Hambley, T.W., 2006. The discovery and development of cisplatin. *J. Chem. Educ.* 83, 728.
- Algra, A.M., Rothwell, P.M., 2012. Effects of regular aspirin on long-term cancer incidence and metastasis: a systematic comparison of evidence from observational studies versus randomised trials. *Lancet Oncol.* 13, 518–527.
- Allardyce, C.S., Dorcier, A., Scolaro, C., Dyson, P.J., 2005. Development of organometallic (organo-transition metal) pharmaceuticals. *Adv. Organomet. Chem.* 19, 1–10.
- Andrews, P.A., Howell, S.B., 1990. Cellular pharmacology of cisplatin: perspectives on mechanisms of acquired resistance. *Cancer Cells* 2, 35–43.
- Ang, W.H., Casini, A., Sava, G., Dyson, P.J., 2011. Organometallic ruthenium-based antitumor compounds with novel modes of action. *J. Organomet. Chem.* 696, 989–998.
- Araujo T. de, O., Costa, L.T., Fernandes, J., Aucelio, R.Q., de Campos, R.C., 2014. Biomarkers to assess the efficiency of treatment with platinum-based drugs: what can metallomics add? *Met. Integr. Biometal Sci.* 6, 2176–2188.
- Aris, S.M., Farrell, N.P., 2009. Towards antitumor active trans-platinum compounds. *Eur. J. Inorg. Chem.* 2009, 1293–1302.
- Amesano, F., Banci, L., Bertini, I., Felli, I.C., Losacco, M., Natile, G., 2011. Probing the interaction of cisplatin with the human copper chaperone Atox1 by solution and in-cell NMR spectroscopy. *J. Am. Chem. Soc.* 133, 18361–18369.
- Asghar, F., Badshah, A., Shah, A., Rauf, M.K., Ali, M.I., Tahir, M. N., Nosheen, E., Zia-Ur-Rehman Qureshi, R., 2012. Synthesis, characterization and DNA binding studies of organoantimony(V) ferrocenyl benzoates. *J. Organomet. Chem.* 717, 1–8.
- Babu, A., Templeton, A.K., Munshi, A., Ramesh, R., 2013. Nanoparticle-based drug delivery for therapy of lung cancer: progress and challenges. *J. Nanomater.* 2013, e863951.
- Banti, C.N., Hadjikakou, S.K., 2013. Anti-proliferative and anti-tumor activity of silver(I) compounds. *Metallomics* 5, 569–596.
- Barry, N.P.E., Sadler, P.J., 2013. Exploration of the medical periodic table: towards new targets. *Chem. Commun.* 49, 5106–5131.
- Beguin, Y., Aapro, M., Ludwig, H., Mizzen, L., Österborg, A., 2014. Epidemiological and nonclinical studies investigating effects of iron in carcinogenesis – a critical review. *Crit. Rev. Oncol. Hematol.* 89, 1–15.
- Beija, M., Salvayre, R., Lauth-de Viguier, N., Marty, J.-D., 2012. Colloidal systems for drug delivery: from design to therapy. *Trends Biotechnol.* 30, 485–496.
- Bernal-Méndez, E., Boudvillain, M., González-Vílchez, F., Leng, M., 1997. Chemical versatility of transplatin monofunctional adducts within multiple site-specifically platinated DNA. *Biochemistry (Mosc.)* 36, 7281–7287.
- Bernstein, L.R., van der Hoeven, J.J.M., Boer, R.O., 2011. Hepatocellular carcinoma detection by gallium scan and subsequent treatment by gallium maltolate: rationale and case study. *Anticancer Agents Med. Chem.* 11, 585–590.
- Bhargava, A., Vaishampayan, U.N., 2009. Satraplatin: leading the new generation of oral platinum agents. *Expert Opin. Investig. Drugs* 18, 1787–1797.
- Biersack, B., Ahmad, A., Sarkar, F.H., Schobert, R., 2012. Coinage metal complexes against breast cancer. *Curr. Med. Chem.* 19, 3949–3956.
- Blommaert, F.A., van Dijk-Knijnenburg, H.C.M., Dijt, F.J., den Engelse, L., Baan, R.A., Berends, F., Fichtinger-Schepman, A. M.J., 1995. Formation of DNA adducts by the anticancer drug carboplatin: different nucleotide sequence preferences *in vitro* and in cells. *Biochemistry (Mosc.)* 34, 8474–8480.
- Boulikas, T., Pantos, A., Bellis, E., Christofis, P., 2007. Designing platinum compounds in cancer: structures and mechanisms. *Cancer Ther.* 5, 537–584.
- Boult, J., Roberts, K., Brookes, M.J., Hughes, S., Bury, J.P., Cross, S. S., Anderson, G.J., Spychal, R., Iqbal, T., Tselepis, C., 2008. Overexpression of cellular iron import proteins is associated with malignant progression of esophageal adenocarcinoma. *Clin. Cancer Res.* 14, 379–387.
- Brookes, M.J., Boult, J., Roberts, K., Cooper, B.T., Hotchin, N.A., Matthews, G., Iqbal, T., Tselepis, C., 2008. A role for iron in Wnt signalling. *Oncogene* 27, 966–975.
- Bruijninx, P.C., Sadler, P.J., 2008. New trends for metal complexes with anticancer activity. *Curr. Opin. Chem. Biol.: Biocatal. Biotransform./Bioinorg. Chem.* 12, 197–206.
- Burger, H., Zoumaro-Djajoon, A., Boersma, A., Helleman, J., Berns, E., Mathijssen, R., Loos, W., Wiemer, E., 2010. Differential transport of platinum compounds by the human organic cation transporter hOCT2 (hSLC22A2). *Br. J. Pharmacol.* 159, 898–908.

- Cai, X., Pan, N., Zou, G., 2007. Copper-1,10-phenanthroline-induced apoptosis in liver carcinoma Bel-7402 cells associates with copper overload, reactive oxygen species production, glutathione depletion and oxidative DNA damage. *Biometals* 20, 1–11.
- Calvert, A.H., Harland, S.J., Newell, D.R., Siddik, Z.H., Jones, A.C., McElwain, T.J., Raju, S., Wiltshaw, E., Smith, I.E., Baker, J.M., Peckham, M.J., Harrap, K.R., 1982. Early clinical studies with cis-diammine-1,1-cyclobutane dicarboxylate platinum II. *Cancer Chemother. Pharmacol.* 9, 140–147.
- Cao-Milán, R., Liz-Marzán, L.M., 2014. Gold nanoparticle conjugates: recent advances toward clinical applications. *Expert Opin. Drug Deliv.* 11, 741–752.
- Casini, A., Gabbiani, C., Sorrentino, F., Rigobello, M.P., Bindoli, A., Geldbach, T.J., Marrone, A., Re, N., Hartinger, C.G., Dyson, P.J., Messori, L., 2008. Emerging protein targets for anticancer metallodrugs: inhibition of thioredoxin reductase and cathepsin B by antitumor ruthenium(II)-arene compounds. *J. Med. Chem.* 51, 6773–6781.
- Chaviara, A.T., Christidis, P.C., Papageorgiou, A., Chrysogelou, E., Hadjipavlou-Litina, D.J., Bolos, C.A., 2005. *In vivo* anticancer, anti-inflammatory, and toxicity studies of mixed-ligand Cu (II) complexes of dien and its Schiff dibases with heterocyclic aldehydes and 2-amino-2-thiazoline. Crystal structure of [Cu(dien)(Br)(2a-2tzn)](Br)(H₂O). *J. Inorg. Biochem.* 99, 2102–2109.
- Che, C.-M., Sun, R.W.-Y., Yu, W.-Y., Ko, C.-B., Zhu, N., Sun, H., 2003. Gold(III) porphyrins as a new class of anticancer drugs: cytotoxicity, DNA binding and induction of apoptosis in human cervix epitheloid cancer cells. *Chem. Commun.* 1718–1719.
- Chen, D., Frezza, M., Shakya, R., Cui, Q.C., Milacic, V., Verani, C. N., Dou, Q.P., 2007. Inhibition of the proteasome activity by gallium(III) complexes contributes to their anti-prostate tumor effects. *Cancer Res.* 67, 9258–9265.
- Chen, J., Stubbe, J., 2005. Bleomycins: towards better therapeutics. *Nat. Rev. Cancer* 5, 102–112.
- Chew, S.T., Lo, K.M., Lee, S.K., Heng, M.P., Teoh, W.Y., Sim, K.S., Tan, K.W., 2014. Copper complexes with phosphonium containing hydrazone ligand: topoisomerase inhibition and cytotoxicity study. *Eur. J. Med. Chem.* 76, 397–407.
- Chitambar, C.R., 2012. Gallium-containing anticancer compounds. *Future Med. Chem.* 4, 1257–1272.
- Chitambar, C.R., Purpi, D.P., 2010. A novel gallium compound synergistically enhances bortezomib-induced apoptosis in mantle cell lymphoma cells. *Leuk. Res.* 34, 950–953.
- Chitambar, C.R., Antholine, W.E., 2013. Iron-targeting antitumor activity of gallium compounds and novel insights into triapine[®]-metal complexes. *Antioxid. Redox Signal.* 18, 956–972.
- Chitambar, C.R., Purpi, D.P., Woodliff, J., Yang, M., Wereley, J.P., 2007. Development of gallium compounds for treatment of lymphoma: gallium maltolate, a novel hydroxypyrrone gallium compound, induces apoptosis and circumvents lymphoma cell resistance to gallium nitrate. *J. Pharmacol. Exp. Ther.* 322, 1228–1236.
- Choi, C.-H., Cha, Y.-J., An, C.-S., Kim, K.-J., Kim, K.-C., Moon, S.-P., Lee, Z.H., Min, Y.-D., 2004. Molecular mechanisms of heptaplatin effective against cisplatin-resistant cancer cell lines: less involvement of metallothionein. *Cancer Cell Int.* 4, 6.
- Choi, S., Filotto, C., Bisanzo, M., Delaney, S., Lagasee, D., Whitworth, J.L., Jusko, A., Li, C., Wood, N.A., Willingham, J., Schwenker, A., Spaulding, K., 1998. Reduction and anticancer activity of platinum(IV) complexes. *Inorg. Chem.* 37, 2500–2504.
- Clarke, M.J., 2002. Ruthenium metallopharmaceuticals. *Coord. Chem. Rev.* 232, 69–93.
- Clarke, M.J., Zhu, F., Frasca, D.R., 1999. Non-platinum chemotherapeutic metallopharmaceuticals. *Chem. Rev.* 99, 2511–2533.
- Clavel, M., Monfardini, S., Gundersen, S., Kaye, S., Siegenthaler, P., Renard, J., van Glabbeke, M., Pinedo, H.M., 1988. Phase II study of iproplatin (CHIP, JM-9) in advanced testicular cancers progressing after prior chemotherapy. *Eur. J. Cancer Clin. Oncol.* 24, 1345–1348.
- Coombs, G.S., Schmitt, A.A., Canning, C.A., Alok, A., Low, I.C.C., Banerjee, N., Kaur, S., Utomo, V., Jones, C.M., Pervaiz, S., Toone, E.J., Virshup, D.M., 2012. Modulation of Wnt/ β -catenin signaling and proliferation by a ferrous iron chelator with therapeutic efficacy in genetically engineered mouse models of cancer. *Oncogene* 31, 213–225.
- De Hoog, P., Boldron, C., Gamez, P., Sliedregt-Bol, K., Roland, I., Pitié, M., Kiss, R., Meunier, B., Reedijk, J., 2007. New approach for the preparation of efficient DNA cleaving agents: ditopic copper-platinum complexes based on 3-clip-phen and cisplatin. *J. Med. Chem.* 50, 3148–3152.
- Descôteaux, C., Provencher-Mandeville, J., Mathieu, I., Perron, V., Mandal, S.K., Asselin, É., Bérubé, G., 2003. Synthesis of 17 β -estradiol platinum(II) complexes: biological evaluation on breast cancer cell lines. *Bioorg. Med. Chem. Lett.* 13, 3927–3931.
- Descôteaux, C., Leblanc, V., Bélanger, G., Parent, S., Asselin, É., Bérubé, G., 2008. Improved synthesis of unique estradiol-linked platinum(II) complexes showing potent cytotoxic activity and affinity for the estrogen receptor alpha and beta. *Steroids* 73, 1077–1089.
- Desoize, B., 2004. Metals and metal compounds in cancer treatment. *Anticancer Res.* 24, 1529–1544.
- Dhar, S., Gu, F.X., Langer, R., Farokhzad, O.C., Lippard, S.J., 2008. Targeted delivery of cisplatin to prostate cancer cells by aptamer functionalized Pt(IV) prodrug-PLGA-PEG nanoparticles. *Proc. Natl. Acad. Sci. U. S. A.* 105, 17356–17361.
- Ding Cheng Yang, Wang F., Elliott, R.L., Head, J.F., 2001. Expression of transferrin receptor and ferritin H-chain mRNA are associated with clinical and histopathological prognostic indicators in breast cancer. *Anticancer Res.* 21, 541–549.
- Dittrich, C., Scheulen, M.E., Jaehde, U., Kynast, B., Gneist, M., Richly, H., Schaad, S., Arion, V.B., Keppler, B.K., 2005. Phase I and pharmacokinetic study of sodium trans-[tetrachlorobis(1H-indazole)ruthenate(III)]/indazole hydrochloride (1:1.1) (FFC14A, KP1019) in patients with solid tumors. In: *Proc. Am. Assoc. Cancer Res.* p. P472.
- Dorcier, A., Dyson, P.J., Gossens, C., Rothlisberger, U., Scopelliti, R., Tavernelli, I., 2005. Binding of organometallic ruthenium (II) and osmium(II) complexes to an oligonucleotide: a combined mass spectrometric and theoretical study. *Organometallics* 24, 2114–2123.
- Duffin, J., Campling, B.G., 2002. Therapy and disease concepts: the history (and future?) of antimony in cancer. *J. Hist. Med. Allied Sci.* 57, 61–78.
- El-Asmy, H.A., Butler, I.S., Mouhri, Z.S., Jean-Claude, B.J., Emmam, M.S., Mostafa, S.I., 2014. Zinc(II), ruthenium(II), rhodium(III), palladium(II), silver(I), platinum(II) and complexes of 2-(2'-hydroxy-5'-methylphenyl)-benzotriazole as simple or primary ligand and 2,2'-bipyridyl, 9,10-phenanthroline or triphenylphosphine as secondary ligands: structure and anticancer activity. *J. Mol. Struct.* 1059, 193–201.
- Enyedy, É.A., Dömötör, O., Varga, E., Kiss, T., Trondl, R., Hartinger, C.G., Keppler, B.K., 2012. Comparative solution equilibrium studies of anticancer gallium(III) complexes of 8-hydroxyquinoline and hydroxy(thio)pyrrone ligands. *J. Inorg. Biochem.* 117, 189–197.
- Enyedy, É.A., Dömötör, O., Bali, K., Hetényi, A., Tuccinardi, T., Keppler, B.K., 2015. Interaction of the anticancer gallium(III) complexes of 8-hydroxyquinoline and maltol with human serum proteins. *J. Biol. Inorg. Chem.* 20, 77–88.

- Esteban-Fernández, D., Moreno-Gordaliza, E., Cañas, B., Palacios, M.A., Gómez-Gómez, M.M., 2010. Analytical methodologies for metallomics studies of antitumor Pt-containing drugs. *Metallomics* 2, 19–38.
- Failes, T.W., Cullinane, C., Diakos, C.I., Yamamoto, N., Lyons, J. G., Hambley, T.W., 2007. Studies of a cobalt(III) complex of the MMP inhibitor marimastat: a potential hypoxia-activated prodrug. *Chem. Eur. J.* 13, 2974–2982.
- Fernández, R., Melchart, M., Habtemariam, A., Parsons, S., Sadler, P.J., 2004. Use of chelating ligands to tune the reactive site of half-sandwich ruthenium(II)-arene anticancer complexes. *Chem. Eur. J.* 10, 5173–5179.
- Fernandez, S., Pfeffer, M., Ritleng, V., Sirlin, C., 1999. An effective route to cycloruthenated N-ligands under mild conditions. *Organometallics* 18, 2390–2394.
- Finch, R.A., Liu, M.-C., Grill, S.P., Rose, W.C., Loomis, R., Vasquez, K.M., Cheng, Y.-C., Sartorelli, A.C., 2000. Triapine (3-aminopyridine-2-carboxaldehyde-thiosemicarbazone): a potent inhibitor of ribonucleotide reductase activity with broad spectrum antitumor activity. *Biochem. Pharmacol.* 59, 983–991.
- Fink, D., Nebel, S., Aebi, S., Zheng, H., Cenni, B., Nehmé, A., Christen, R.D., Howell, S.B., 1996. The role of DNA mismatch repair in platinum drug resistance. *Cancer Res.* 56, 4881–4886.
- Fischer-Fodor, E., Vălean, A.-M., Virag, P., Ilea, P., Tatomir, C., Imre-Lucaci, F., Schrepler, M.P., Krausz, L.T., Tudoran, L.B., Precup, C.G., Lupan, I., Hey-Hawkins, E., Silaghi-Dumitrescu, L., 2014. Gallium phosphinoarylbisthiolato complexes counteract drug resistance of cancer cells. *Metallomics* 6, 833–844.
- Fokkema, E., Groen, H.J.M., Helder, M.N., de Vries, E.G.E., Meijer, C., 2002. JM216-, JM118-, and cisplatin-induced cytotoxicity in relation to platinum-DNA adduct formation, glutathione levels and p53 status in human tumour cell lines with different sensitivities to cisplatin. *Biochem. Pharmacol.* 63, 1989–1996.
- Fries, J.F., Bloch, D., Spitz, P., Mitchell, D.M., 1985. Cancer in rheumatoid arthritis: a prospective long-term study of mortality. *Am. J. Med. Neoplasms Rheumatoid Arthrit.: Update Clin. Epidemiol. Data* 78, 56–59.
- Gaiddon, C., Jeannequin, P., Bischoff, P., Pfeffer, M., Sirlin, C., Loeffler, J.P., 2005. Ruthenium (II)-derived organometallic compounds induce cytostatic and cytotoxic effects on mammalian cancer cell lines through p53-dependent and p53-independent mechanisms. *J. Pharmacol. Exp. Ther.* 315, 1403–1411.
- Gârban, Z., Silaghi-Dumitrescu, R., Gârban, G., Avacovici, A., Hădărugă, N., Baltă, C., Ghibu, G.-D., Bischin, C., Rada, O.-A., 2014. Metallomics related to gallium compounds, biochemical and xenobiochemical aspects. *Maced. J. Chem. Chem. Eng.* 33, 39–52.
- Gatter, K.C., Brown, G., Strowbridge, I., Woolston, R.E., Mason, D. Y., 1983. Transferrin receptors in human tissues: their distribution and possible clinical relevance. *J. Clin. Pathol.* 36, 539–545.
- Gatti, L., Perego, P., Leone, R., Apostoli, P., Carenini, N., Corna, E., Allievi, C., Bastrup, U., De Munari, S., Di Giovine, S., Nicoli, P., Grugni, M., Natangelo, M., Pardi, G., Pezzoni, G., Singer, J.W., Zunino, F., 2009. Novel bis-platinum complexes endowed with an improved pharmacological profile. *Mol. Pharmacol.* 7, 207–216.
- Gava, B., Zorzet, S., Spessotto, P., Cocchietto, M., Sava, G., 2006. Inhibition of B16 melanoma metastases with the ruthenium complex imidazolium trans-imidazole-dimethylsulfonate-tetrachlororuthenate and down-regulation of tumor cell invasion. *J. Pharmacol. Exp. Ther.* 317, 284–291.
- Geldmacher, Y., Oleszak, M., Sheldrick, W.S., 2012. Rhodium(III) and iridium(III) complexes as anticancer agents. *Inorg. Chim. Acta* 393 (Special Issue: Metals in Medicine), 84–102.
- Gietema, J.A., Guchelaar, H.J., de Vries, E.G., Aulenbacher, P., Sleijfer, D.T., Mulder, N.H., 1993. A phase I study of lobaplatin (D-19466) administered by 72 h continuous infusion. *Anticancer. Drugs* 4, 51–55.
- Gogna, R., Madan, E., Keppler, B., Pati, U., 2012. Gallium compound GaQ 3-induced Ca²⁺ signalling triggers p53-dependent and -independent apoptosis in cancer cells. *Br. J. Pharmacol.* 166, 617–636.
- Gong, Y., Ren, L., Zhou, L., Zhu, J., Huang, M., Zhou, X., Wang, J., Lu, Y., Hou, M., Wei, Y., 2009. Phase II evaluation of nedaplatin and paclitaxel in patients with metastatic esophageal carcinoma. *Cancer Chemother. Pharmacol.* 64, 327–333.
- González, B., Lorenzo-Luis, P., Gili, P., Romerosa, A., Serrano-Ruiz, M., 2009. Behaviour of [RuClCp(mPTA)₂](OSO₂CF₃)₂ in water vs. the pH: synthesis and characterisation of [RuCpX(mPTA)₂](OSO₂CF₃)_n, X = (H₂O-(O, DMSO-(S, n = 3); OH⁻(O, n = 2))) (mPTA = N-methyl-1,3,5-triaza-7-phosphaadamantane). *J. Organomet. Chem.* 694, 2029–2036.
- Graf, N., Mokhtari, T.E., Papayannopoulos, I.A., Lippard, S.J., 2012. Platinum(IV)-chlorotoxin (CTX) conjugates for targeting cancer cells. *J. Inorg. Biochem.* 110, 58–63.
- Graham, J., Muhsin, M., Kirkpatrick, P., 2004. Oxaliplatin. *Nat. Rev. Drug Discov.* 3, 11–12.
- Gromer, S., Arscott, L.D., Williams, C.H., Schirmer, R.H., Becker, K., 1998. Human placenta thioredoxin reductase isolation of the selenoenzyme, steady state kinetics, and inhibition by therapeutic gold compounds. *J. Biol. Chem.* 273, 20096–20101.
- Guidi, F., Landini, I., Puglia, M., Magherini, F., Gabbiani, C., Cinellu, M.A., Nobili, S., Fiaschi, T., Bini, L., Mini, E., Messori, L., Modesti, A., 2012. Proteomic analysis of ovarian cancer cell responses to cytotoxic gold compounds. *Metallomics* 4, 307–314.
- Guidi, F., Modesti, A., Landini, I., Nobili, S., Mini, E., Bini, L., Puglia, M., Casini, A., Dyson, P.J., Gabbiani, C., Messori, L., 2013. The molecular mechanisms of antimetastatic ruthenium compounds explored through DIGE proteomics. *J. Inorg. Biochem.* 118, 94–99.
- Hall, M.D., Hambley, T.W., 2002. Platinum(IV) antitumour compounds: their bioinorganic chemistry. *Coord. Chem. Rev.* 232, 49–67.
- Hamilton, G., Olszewski, U., 2013. Picoplatin pharmacokinetics and chemotherapy of non-small cell lung cancer. *Expert Opin. Drug Metab. Toxicol.* 9, 1381–1390.
- Hanahan, D., Weinberg, R.A., 2011. Hallmarks of cancer: the next generation. *Cell* 144, 646–674.
- Hartinger, C.G., Zorbas-Seifried, S., Jakupec, M.A., Kynast, B., Zorbas, H., Keppler, B.K., 2006. From bench to bedside—preclinical and early clinical development of the anticancer agent indazolium trans-[tetrachlorobis(1H-indazole) ruthenate(III)] (KP1019 or FFC14A). *J. Inorg. Biochem.* 100, 891–904 Special Issue Containing Contributions from the 12th International Conference on Biological Inorganic Chemistry.
- Hayward, R.L., Schornagel, Q.C., Tente, R., Macpherson, J.S., Aird, R.E., Guichard, S., Habtemariam, A., Sadler, P., Jodrell, D.I., 2005. Investigation of the role of Bax, p21/Waf1 and p53 as determinants of cellular responses in HCT116 colorectal cancer cells exposed to the novel cytotoxic ruthenium(II) organometallic agent, RM175. *Cancer Chemother. Pharmacol.* 55, 577–583.
- Hindo, S.S., Frezza, M., Tomco, D., Heeg, M.J., Hryhorczuk, L., McGarvey, B.R., Dou, Q.P., Verani, C.N., 2009. Metals in anticancer therapy: copper(II) complexes as inhibitors of the 20S proteasome. *Eur. J. Med. Chem.* 44, 4353–4361.
- Holmgren, A., 1989. Thioredoxin and glutaredoxin systems. *J. Biol. Chem.* 264, 13963–13966.
- Holzer, A.K., Manorek, G.H., Howell, S.B., 2006. Contribution of the major copper influx transporter CTR1 to the cellular

- accumulation of cisplatin, carboplatin, and oxaliplatin. *Mol. Pharmacol.* 70, 1390–1394.
- Hummer, A.A., Bartel, C., Arion, V.B., Jakupec, M.A., Meyer-Klaucke, W., Geraki, T., Quinn, P.D., Mijovilovich, A., Keppler, B.K., Rempel, A., 2012. X-ray absorption spectroscopy of an investigational anticancer gallium(III) drug: interaction with serum proteins, elemental distribution pattern, and coordination of the compound in tissue. *J. Med. Chem.* 55, 5601–5613.
- Ishida, S., Lee, J., Thiele, D.J., Herskowitz, I., 2002. Uptake of the anticancer drug cisplatin mediated by the copper transporter Ctr1 in yeast and mammals. *Proc. Natl. Acad. Sci. U. S. A.* 99, 14298–14302.
- Ismail, T., Rossouw, D.D., Beukes, P., Slabbert, J.P., Smith, G.S., 2013. Synthesis, characterization and preliminary *in vitro* cellular uptake studies of ⁶⁷Ga(III) thiosemicarbazones. *Inorg. Chem. Commun.* 33, 154–157.
- Jamieson, E.R., Lippard, S.J., 1999. Structure, recognition, and processing of cisplatin–DNA adducts. *Chem. Rev.* 99, 2467–2498.
- Jayaraju, D., Kondapi, A.K., 2001. Anti-cancer copper salicylaldehyde complex inhibits topoisomerase II catalytic activity. *Curr. Sci.* 81.
- Jungwirth, U., Kowol, C.R., Keppler, B.K., Hartinger, C.G., Berger, W., Heffeter, P., 2011. Anticancer activity of metal complexes: involvement of redox processes. *Antioxid. Redox Signal.* 15, 1085–1127.
- Jungwirth, U., Gojo, J., Tuder, T., Walko, G., Holcman, M., Schöfl, T., Nowikovsky, K., Wilfinger, N., Schoonhoven, S., Kowol, C.R., Lemmens-Gruber, R., Heffeter, P., Keppler, B.K., Berger, W., 2014. Calpain-mediated integrin deregulation as a novel mode of action for the anticancer gallium compound KP46. *Mol. Cancer Ther.* 13, 2436–2449.
- Kalinowski, D.S., Richardson, D.R., 2005. The evolution of iron chelators for the treatment of iron overload disease and cancer. *Pharmacol. Rev.* 57, 547–583.
- Kasparkova, J., Zehnulova, J., Farrell, N., Brabec, V., 2002. DNA interstrand cross-links of the novel antitumor trinuclear platinum complex BBR3464. Conformation, recognition by high mobility group domain proteins, and nucleotide excision repair. *J. Biol. Chem.* 277, 48076–48086.
- Katsaros, N., Anagnostopoulou, A., 2002. Rhodium and its compounds as potential agents in cancer treatment. *Crit. Rev. Oncol. Hematol.* 42, 297–308.
- Kavanagh, J.J., Edwards, C.L., Freedman, R.S., Finnegan, M.B., Balat, O., Tresukosol, D., Bunk, K., Loechner, S., Hord, M., Franklin, J.L., Kudelka, A.P., 1995. A trial of lobaplatin (D-19466) in platinum-resistant ovarian cancer. *Gynecol. Oncol.* 58, 106–109.
- Kawai, Y., Taniuchi, S., Okahara, S., Nakamura, M., Gemba, M., 2005. Relationship between cisplatin or nedaplatin-induced nephrotoxicity and renal accumulation. *Biol. Pharm. Bull.* 28, 1385–1388.
- Keeler, B.D., Brookes, M.J., 2013. Iron chelation: a potential therapeutic strategy in oesophageal cancer. *Br. J. Pharmacol.* 168, 1313–1315.
- Kelland, L., 2007a. The resurgence of platinum-based cancer chemotherapy. *Nat. Rev. Cancer* 7, 573–584.
- Kelland, L., 2007b. Broadening the clinical use of platinum drug-based chemotherapy with new analogues. Satraplatin and picoplatin. *Expert Opin. Investig. Drugs* 16, 1009–1021.
- Kelland, L.R., Barnard, C.F., Mellish, K.J., Jones, M., Goddard, P.M., Valenti, M., Bryant, A., Murrer, B.A., Harrap, K.R., 1994. A novel trans-platinum coordination complex possessing *in vitro* and *in vivo* antitumor activity. *Cancer Res.* 54, 5618–5622.
- Kelland, L.R., Sharp, S.Y., O'Neill, C.F., Raynaud, F.I., Beale, P.J., Judson, I.R., 1999. Mini-review: discovery and development of platinum complexes designed to circumvent cisplatin resistance. *J. Inorg. Biochem.* 77, 111–115.
- Khokhar, A.R., Deng, Y., Kido, Y., Siddik, Z.H., 1993. Preparation, characterization, and antitumor activity of new ethylenediamine platinum(IV) complexes containing mixed carboxylate ligands. *J. Inorg. Biochem.* 50, 79–87.
- Kim, D.-K., Kim, H.-T., Cho, Y.-B., Tai, J.H., Ahn, J.S., Kim, T.-S., Kim, K.H., Hong, W.-S., 1995. Antitumor activity of cis-malonato[(4R,5R)-4,5-bis(aminomethyl)-2-isopropyl-1,3-dioxolane]platinum(II), a new platinum analogue, as an anticancer agent. *Cancer Chemother. Pharmacol.* 35, 441–445.
- Kim, E.S., Lee, J.J., He, G., Chow, C.W., Fujimoto, J., Kalhor, N., Swisher, S.G., Wistuba, I.I., Stewart, D.J., Siddik, Z.H., 2012. Tissue platinum concentration and tumor response in non-small-cell lung cancer. *J. Clin. Oncol.* 30, 3345–3352.
- Kim, N.K., Im, S.-A., Kim, D.-W., Lee, M.H., Jung, C.W., Cho, E.K., Lee, J.T., Ahn, J.S., Heo, D.S., Bang, Y.-J., 1999. Phase II clinical trial of SKI-2053R, a new platinum analog, in the treatment of patients with advanced gastric adenocarcinoma. *Cancer* 86, 1109–1115.
- Komeda, S., Moulaei, T., Woods, K.K., Chikuma, M., Farrell, N.P., Williams, L.D., 2006. A third mode of DNA binding: phosphate clamps by a polynuclear platinum complex. *J. Am. Chem. Soc.* 128, 16092–16103.
- Kouodom, M.N., Boscutti, G., Celegato, M., Crisma, M., Sitran, S., Aldinucci, D., Formaggio, F., Ronconi, L., Fregona, D., 2012. Rational design of gold(III)-dithiocarbamate peptidomimetics for the targeted anticancer chemotherapy. *J. Inorg. Biochem.* 117, 248–260 Special Issue from the Eleventh International Symposium on Applied Bioinorganic Chemistry.
- Kovacevic, Z., 2012. Targeting Iron in Cancer Cells: A New Strategy to Inhibit Metastatic Progression. *Vitam. Trace Elem.* 01.
- Kratz, F., Hartmann, M., Keppler, B., Messori, L., 1994. The binding properties of two antitumor ruthenium(III) complexes to apotransferrin. *J. Biol. Chem.* 269, 2581–2588.
- Kurita, H., Yamamoto, E., Nozaki, S., Wada, S., Furuta, I., Miyata, M., Kurashina, K., 2010. Multicenter phase 2 study of induction chemotherapy with docetaxel and nedaplatin for oral squamous cell carcinoma. *Cancer Chemother. Pharmacol.* 65, 503–508.
- Kuwahara, A., 2009. Replacement of cisplatin with nedaplatin in a definitive 5-fluorouracil/cisplatin-based chemoradiotherapy in Japanese patients with esophageal squamous cell carcinoma. *Int. J. Med. Sci.* 305.
- Kyros, L., Banti, C.N., Kourkoumelis, N., Kubicki, M., Sainis, I., Hadjikakou, S.K., 2014. Synthesis, characterization, and binding properties towards CT-DNA and lipoxygenase of mixed-ligand silver(I) complexes with 2-mercaptothiazole and its derivatives and triphenylphosphine. *J. Biol. Inorg. Chem.* 19, 449–464.
- LaCroix, B., Gamazon, E.R., Lenkala, D., Im, H.K., Gleeleher, P., Ziliak, D., Cox, N.J., Huang, R.S., 2014. Integrative analyses of genetic variation, epigenetic regulation, and the transcriptome to elucidate the biology of platinum sensitivity. *BMC Genomics* 15, 292.
- Lane, D.J.R., Mills, T.M., Shafie, N.H., Merlot, A.M., Saleh Moussa, R., Kalinowski, D.S., Kovacevic, Z., Richardson, D.R., 2014. Expanding horizons in iron chelation and the treatment of cancer: role of iron in the regulation of ER stress and the epithelial-mesenchymal transition. *Biochim. Biophys. Acta – Rev. Cancer* 1845, 166–181.
- Lange, T.S., Kim, K.K., Singh, R.K., Strongin, R.M., McCourt, C.K., Brard, L., 2008. Iron(III)-salophene: an organometallic compound with selective cytotoxic and anti-proliferative properties in platinum-resistant ovarian cancer cells. *PLoS ONE* 3.
- Lebwohl, D., Canetta, R., 1998. Clinical development of platinum complexes in cancer therapy: an historical perspective and an update. *Eur. J. Cancer Oxf. Engl.* 1990 (34), 1522–1534.

- Leslie, E.M., Deeley, R.G., Cole, S.P.C., 2005. Multidrug resistance proteins: role of P-glycoprotein, MRP1, MRP2, and BCRP (ABCG2) in tissue defense. *Toxicol. Appl. Pharmacol.: Membr. Transport. Toxicol.* 204, 216–237.
- Lessa, J.A., Parrilha, G.L., Beraldo, H., 2012. Gallium complexes as new promising metallodrug candidates. *Inorg. Chim. Acta* 393, 53–63.
- Lessa, J.A., Soares, M.A., Dos Santos, R.G., Mendes, I.C., Salum, L. B., Daghestani, H.N., Andricopulo, A.D., Day, B.W., Vogt, A., Beraldo, H., 2013. Gallium(III) complexes with 2-acetylpyridine-derived thiosemicarbazones: antimicrobial and cytotoxic effects and investigation on the interactions with tubulin. *Biometals* 26, 151–165.
- Li, J.-S., Liu, R.-C., Chi, X.-B., Wang, G.-C., Guo, Q.-S., 2004. Synthesis, characterization and structure of some arylantimony ferrocenylacrylates. *Inorg. Chim. Acta* 357, 2176–2180.
- Li, L., Liu, J., Yu, W., Lou, X., Huang, B., Lin, B., 2013. Deep transcriptome profiling of ovarian cancer cells using next-generation sequencing approach. *Methods Mol. Biol.* 1049, 139–169.
- Lin, M., Cao, Y., Pei, H., Chen, Y., Wu, J., Li, Y., Liu, W., 2014. Titanium isopropoxide complexes supported by pyrrolyl Schiff base ligands, syntheses, structures, and antitumor activity. *RSC Adv.* 4, 9255–9260.
- Liu, R.-C., Ma, Y.-Q., Yu, L., Li, J.-S., Cui, J.-R., Wang, R.-Q., 2003. Synthesis, characterization and *in vitro* antitumor activity of some arylantimony ferrocenecarboxylates and crystal structures of $C_5H_5FeC_5H_4CO_2SbPh_4$ and $(C_5H_5FeC_5H_4CO_2)_2Sb(4-CH_3C_6H_4)_3$. *Appl. Organomet. Chem.* 17, 662–668.
- Lopez-Chavez, A., Sandler, A., 2012. Systemic issues in small cell lung cancer. *Curr. Probl. Cancer: Small Cell Lung Carcinoma* 36, 131–155.
- Lu, G.-L., Stevenson, R.J., Chang, J.Y.-C., Brothers, P.J., Ware, D.C., Wilson, W.R., Denny, W.A., Tercel, M., 2011. N-alkylated cyclen cobalt(III) complexes of 1-(chloromethyl)-3-(5,6,7-trimethoxyindol-2-ylcarbonyl)-2,3-dihydro-1H-pyrrolo[3,2-f]quinolin-5-ol DNA alkylating agent as hypoxia-activated prodrugs. *Bioorg. Med. Chem.* 19, 4861–4867.
- Mabuchi, S., Kimura, T., 2010. Nedaplatin: a radiosensitizing agent for patients with cervical cancer. *Chemother. Res. Pract.* 2011, e963159.
- Machado, I., Fernández, M., Becco, L., Garat, B., Brissos, R.F., Zabarska, N., Gamez, P., Marques, F., Correia, I., Costa Pessoa, J., Gambino, D., 2014. New metal complexes of NNO tridentate ligands: effect of metal center and co-ligand on biological activity. *Recent Adv. Vanadium Chem.: Inorg. Chim. Acta* 420, 39–46.
- Madan, E., Gogna, R., Keppler, B., Pati, U., 2013. p53 increases intra-cellular calcium release by transcriptional regulation of calcium channel TRPC6 in GaQ3-treated cancer cells. *PLoS ONE* 8.
- Maindrault-Goebel, F., Louvet, C., André, T., Carola, E., Lotz, J.P., Molitor, J.L., Garcia, M.L., Gilles-Amar, V., Izrael, V., Krulik, M., de Gramont, A., 1999. Oxaliplatin added to the simplified bimonthly leucovorin and 5-fluorouracil regimen as second-line therapy for metastatic colorectal cancer (FOLFOX6). *Eur. J. Cancer* 35, 1338–1342.
- Maldonado, C.R., Salassa, L., Gomez-Blanco, N., Mareque-Rivas, J.C., 2013. Nano-functionalization of metal complexes for molecular imaging and anticancer therapy. 11th European Biological Inorganic Chemistry Conference. 12–16 September 2012, Granada, Spain, *Coord. Chem. Rev.* 257, 2668–2688.
- Marcon, G., Carotti, S., Coronello, M., Messori, L., Mini, E., Orioli, P., Mazzei, T., Cinellu, M.A., Minghetti, G., 2002. Gold(III) complexes with bipyridyl ligands: solution chemistry, cytotoxicity, and DNA binding properties. *J. Med. Chem.* 45, 1672–1677.
- Marín-Hernández, A., Gracia-Mora, I., Ruiz-Ramírez, L., Moreno-Sánchez, R., 2003. Toxic effects of copper-based antineoplastic drugs (Casiopéinas[®]) on mitochondrial functions. *Biochem. Pharmacol.* 65, 1979–1989.
- Martin, E.K., Pagano, N., Sherlock, M.E., Harms, K., Meggers, E., 2014. Synthesis and anticancer activity of ruthenium half-sandwich complexes comprising combined metal centrochirality and planar chirality. *Inorg. Chim. Acta* 423, 530–539.
- Marzano, C., Pellei, M., Alidori, S., Brossa, A., Lobbia, G.G., Tisato, F., Santini, C., 2006. New copper(I) phosphane complexes of dihydridobis(3-nitro-1,2,4-triazolyl)borate ligand showing cytotoxic activity. *J. Inorg. Biochem.* 100, 299–304.
- Marzano, C., Pellei, M., Tisato, F., Santini, C., 2009. Copper complexes as anticancer agents. *Anticancer Agents Med. Chem.* 9, 185–211.
- Marzano, C., Mazzega Sbovata, S., Gandin, V., Colavito, D., Del Giudice, E., Michelin, R.A., Venzo, A., Seraglia, R., Benetollo, F., Schiavon, M., Bertani, R., 2010. A new class of antitumor trans-amine-amidine-Pt(II) cationic complexes: influence of chemical structure and solvent on *in vitro* and *in vivo* tumor cell proliferation. *J. Med. Chem.* 53, 6210–6227.
- McKeage, M.J., 2001. Lobaplatin: a new antitumour platinum drug. *Expert Opin. Investig. Drugs* 10, 119–128.
- Meggers, E., Atilla-Gokcumen, G.E., Gründler, K., Frias, C., Prokop, A., 2009. Inert ruthenium half-sandwich complexes with anticancer activity. *Dalton Trans. Camb. Engl.* 2003, 10882–10888.
- Meléndez, E., 2002. Titanium complexes in cancer treatment. *Crit. Rev. Oncol. Hematol.* 42, 309–315.
- Mendes, I.C., Soares, M.A., dos Santos, R.G., Pinheiro, C., Beraldo, H., 2009. Gallium(III) complexes of 2-pyridineformamide thiosemicarbazones: cytotoxic activity against malignant glioblastoma. *Eur. J. Med. Chem.* 44, 1870–1877.
- Meng, X., Leyva, M.L., Jenny, M., Gross, I., Benosman, S., Fricker, B., Harlepp, S., Hébraud, P., Boos, A., Wlosik, P., Bischoff, P., Sirlin, C., Pfeffer, M., Loeffler, J.-P., Gaiddon, C., 2009. A ruthenium-containing organometallic compound reduces tumor growth through induction of the endoplasmic reticulum stress gene CHOP. *Cancer Res.* 69, 5458–5466.
- Mikuš, P., Melník, M., Forgáčsová, A., Krajčiová, D., Havránek, E., 2014. Gallium compounds in nuclear medicine and oncology. *Main Group Met. Chem.* 37, 53–65.
- Milacic, V., Chen, D., Ronconi, L., Landis-Piwowar, K.R., Fregona, D., Dou, Q.P., 2006. A novel anticancer gold(III) dithiocarbamate compound inhibits the activity of a purified 20S proteasome and 26S proteasome in human breast cancer cell cultures and xenografts. *Cancer Res.* 66, 10478–10486.
- Milacic, V., Fregona, D., Dou, Q.P., 2008. Gold complexes as prospective metal-based anticancer drugs. *Histol. Histopathol.* 23, 101–108.
- Miller, M., Tshuva, E.Y., 2014. Cytotoxic titanium(IV) complexes of chiral diaminobis(phenolato) ligands: better combination of activity and stability by the bipyroldine moiety. *Eur. J. Inorg. Chem.* 1485–1491.
- Mjos, K.D., Orvig, C., 2014. Metallodrugs in medicinal inorganic chemistry. *Chem. Rev.* 114, 4540–4563.
- Mlcuskova, J., Malina, J., Novohradsky, V., Kasparkova, J., Komeda, S., Brabec, V., 2012. Energetics, conformation, and recognition of DNA duplexes containing a major adduct of an anticancer azolato-bridged dinuclear Pt(II) complex. *Biochim. Biophys. Acta BBA – Gen. Subj.* 1820, 1502–1511.
- Morris, R.E., Aird, R.E., del Socorro Murdoch, P., Chen, H., Cummings, J., Hughes, N.D., Parsons, S., Parkin, A., Boyd, G., Jodrell, D.I., Sadler, P.J., 2001. Inhibition of cancer cell growth by ruthenium(II) arene complexes. *J. Med. Chem.* 44, 3616–3621.
- Muhammad, N., Guo, Z., 2014. Metal-based anticancer chemotherapeutic agents. *Curr. Opin. Chem. Biol.: Biocatal. Biotransform. Bioinorg. Chem.* 19, 144–153.

- Ng, C.H., Kong, S.M., Tiong, Y.L., Maah, M.J., Sukram, N., Ahmad, M., Khoo, A.S., 2014. Selective anticancer copper(II)-mixed ligand complexes: targeting of ROS and proteasomes. *Metallomics* 6, 892–906.
- Nobili, S., Mini, E., Landini, I., Gabbiani, C., Casini, A., Messori, L., 2010. Gold compounds as anticancer agents: chemistry, cellular pharmacology, and preclinical studies. *Med. Res. Rev.* 30, 550–580.
- Nordberg, J., Arnér, E.S.J., 2001. Reactive oxygen species, antioxidants, and the mammalian thioredoxin system. *Free Radic. Biol. Med.* 31, 1287–1312.
- Novick, S.C., Julian, T.N., Majuru, S., Mangelus, M., Brown, B.D., Mehta, B., Warrell, R.P., 2008. Initial phase I clinical and pharmacokinetic assessment of G4544, an oral gallium-containing compound. *ASCO Meet. Abstr.* 26, 8592.
- Oberoi, H.S., Nukolova, N.V., Kabanov, A.V., Bronich, T.K., 2013. Nanocarriers for delivery of platinum anticancer drugs. *Adv. Drug Deliv. Rev.* 65, 1667–1685.
- Oehninger, L., Küster, L.N., Schmidt, C., Muñoz-Castro, A., Prokop, A., Ott, I., 2013. A chemical-biological evaluation of rhodium(I) N-heterocyclic carbene complexes as prospective anticancer drugs. *Chem. Eur. J.* 19, 17871–17880.
- Olivova, R., Stepankova, J., Kuchova, T., Novohradsky, V., Novakova, O., Vrana, O., Kasparkova, J., Brabec, V., 2012. Mechanistic insights into toxic effects of a benzotriazole-bridged dinuclear platinum(II) compound in tumor cells. *Inorg. Chim. Acta* 393, 204–211 Special Issue: Metals in Medicine.
- Orlowski, R.Z., 1999. The role of the ubiquitin-proteasome pathway in apoptosis. *Cell Death Differ.* 6, 303–313.
- Oshita, F., Yamada, K., Saito, H., Noda, K., Hamanaka, N., Ikehara, M., 2004. Phase II study of nedaplatin and irinotecan for elderly patients with advanced non-small cell lung cancer. *J. Exp. Ther. Oncol.* 4, 343–348.
- Ott, I., Gust, R., 2007. Non platinum metal complexes as anticancer drugs. *Arch. Pharm. (Weinheim)* 340, 117–126.
- Ott, I., Schmidt, K., Kircher, B., Schumacher, P., Wiglenda, T., Gust, R., 2004. Antitumor-active cobalt-alkyne complexes derived from acetylsalicylic acid: studies on the mode of drug action. *J. Med. Chem.* 48, 622–629.
- Oyewumi, M.O., Alazizi, A., Liva, S., Lin, L., Geldenhuys, W.J., 2014. Screening and identification of novel compounds with potential anti-proliferative effects on gallium-resistant lung cancer through an AXL kinase pathway. *Bioorg. Med. Chem. Lett.* 24, 4553–4556.
- Parker, L.J., Italiano, L.C., Morton, C.J., Hancock, N.C., Ascher, D. B., Aitken, J.B., Harris, H.H., Campomanes, P., Rothlisberger, U., De Luca, A., Lo Bello, M., Ang, W.H., Dyson, P.J., Parker, M. W., 2011. Studies of glutathione transferase P 1-1 bound to a platinum(IV)-based anticancer compound reveal the molecular basis of its activation. *Chem. Eur. J.* 17, 7806–7816.
- Peña-Méndez, E.M., González, B., Lorenzo, P., Romerosa, A., Havel, J., 2009. Mass spectrometry and UV-vis spectrophotometry of ruthenium(II) [RuClCp(mPTA)₂](OSO₂CF₃)₂ complex in solution. *Rapid Commun. Mass Spectrom.* 23, 3831–3836.
- Perego, P., Caserini, C., Gatti, L., Carenini, N., Romanelli, S., Supino, R., Colangelo, D., Viano, I., Leone, R., Spinelli, S., Pezzoni, G., Manzotti, C., Farrell, N., Zunino, F., 1999. A novel trinuclear platinum complex overcomes cisplatin resistance in an osteosarcoma cell system. *Mol. Pharmacol.* 55, 528–534.
- Pérez, C., Díaz-García, C.V., Agudo-López, A., del Solar, V., Cabrera, S., Agulló-Ortuño, M.T., Navarro-Ranninger, C., Alemán, J., López-Martín, J.A., 2014. Evaluation of novel trans-sulfonamide platinum complexes against tumor cell lines. *Eur. J. Med. Chem.* 76, 360–368.
- Petrelli, F., Coinu, A., Borgonovo, K., Cabiddu, M., Ghilardi, M., Lonati, V., Barni, S., 2014. The value of platinum agents as neoadjuvant chemotherapy in triple-negative breast cancers: a systematic review and meta-analysis. *Breast Cancer Res. Treat.* 144, 223–232.
- Pitie, M., Sudres, B., Meunier, B., 1998. Dramatic increase of the DNA cleavage activity of Cu(clip-phen) by fixing the bridging linker on the C3 position of the phenanthroline units. *Chem. Commun.* 2597–2598.
- Pitié, M., Boldron, C., Gornitzka, H., Hemmert, C., Donnadieu, B., Meunier, B., 2003. DNA cleavage by copper complexes of 2- and 3-clip-phen derivatives. *Eur. J. Inorg. Chem.* 2003, 528–540.
- Pivetta, T., Cannas, M.D., Demartin, F., Castellano, C., Vascellari, S., Verani, G., Isaia, F., 2011. Synthesis, structural characterization, formation constants and in vitro cytotoxicity of phenanthroline and imidazolidine-2-thione copper(II) complexes. *J. Inorg. Biochem.* 105, 329–338.
- Pivetta, T., Isaia, F., Verani, G., Cannas, C., Serra, L., Castellano, C., Demartin, F., Pilla, F., Manca, M., Pani, A., 2012. Mixed-1,10-phenanthroline-Cu(II) complexes: synthesis, cytotoxic activity versus hematological and solid tumor cells and complex formation equilibria with glutathione. *J. Inorg. Biochem.* 114, 28–37.
- Plotek, M., Dudek, K., Kyzioł, A., 2013. Selected copper(I) complexes as potential anticancer agent. *Chem. Int.* 67, 1181–1190.
- Pongratz, M., Schluga, P., Jakupec, M.A., Arion, V.B., Hartinger, C. G., Allmaier, G., Keppler, B.K., 2004. Transferrin binding and transferrin-mediated cellular uptake of the ruthenium coordination compound KP1019, studied by means of AAS, ESI-MS and CD spectroscopy. *J. Anal. At. Spectrom.* 19, 46–51.
- Porchia, M., Benetollo, F., Refosco, F., Tisato, F., Marzano, C., Gandin, V., 2009. Synthesis and structural characterization of copper(I) complexes bearing N-methyl-1,3,5-triaza-7-phosphaadamantane (mPTA): cytotoxic activity evaluation of a series of water soluble Cu(I) derivatives containing PTA, PTAH and mPTA ligands. *J. Inorg. Biochem.* 103, 1644–1651.
- Porchia, M., Dolmella, A., Gandin, V., Marzano, C., Pellei, M., Peruzzo, V., Refosco, F., Santini, C., Tisato, F., 2013. Neutral and charged phosphine/scorpionate copper(I) complexes: effects of ligand assembly on their antiproliferative activity. *Eur. J. Med. Chem.* 59, 218–226.
- Quiroga, A.G., 2012. Understanding trans platinum complexes as potential antitumor drugs beyond targeting DNA. *J. Inorg. Biochem.* 114, 106–112.
- Quiroga, A.G., Pérez, J.M., Alonso, C., Navarro-Ranninger, C., Farrell, N., 2005. Novel transplatinum(II) complexes with [N₂O₂] donor sets. Cellular pharmacology and apoptosis induction in Pam 212-ras cells. *J. Med. Chem.* 49, 224–231.
- Rademaker-Lakhai, J.M., van den Bongard, D., Pluim, D., Beijnen, J. H., Schellens, J.H.M., 2004. A Phase I and pharmacological study with imidazolium-trans-DMSO-imidazole-tetrachlororuthenate. A novel ruthenium anticancer agent. *Clin. Cancer Res.: Off. J. Am. Assoc. Cancer Res.* 10, 3717–3727.
- Rafique, S., Idrees, M., Nasim, A., Akbar, H., Athar, A., 2010. Transition metal complexes as potential therapeutic agents. *Biotechnol. Mol. Biol. Rev.* 5, 38–45.
- Richardson, A., Kovacevic, Z., Richardson, D.R., 2013. Iron chelation, inhibition of key signaling pathways in the induction of the epithelial mesenchymal transition in pancreatic cancer and other tumors. *Crit. Rev. Oncog.* 18, 409–434.
- Richardson, D.R., 2002. Iron chelators as therapeutic agents for the treatment of cancer. *Crit. Rev. Oncol. Hematol.* 42, 267–281.
- Romerosa, A., Campos-Malpartida, T., Lidrissi, C., Saoud, M., Serrano-Ruiz, M., Peruzzini, M., Garrido-Cárdenas, J.A., García-Maroto, F., 2006. Synthesis, characterization, and DNA binding of new water-soluble cyclopentadienyl ruthenium(II) complexes incorporating phosphines. *Inorg. Chem.* 45, 1289–1298.

- Roukos, D., Batsis, C., Baltogiannis, G., 2012. Assessing tumor heterogeneity and emergence mutations using next-generation sequencing for overcoming cancer drugs resistance. *Expert Rev. Anticancer Ther.* 12, 1245–1248.
- Rudnev, A.V., Aleksenko, S.S., Semenova, O., Hartinger, C.G., Timerbaev, A.R., Keppler, B.K., 2005. Determination of binding constants and stoichiometries for platinum anticancer drugs and serum transport proteins by capillary electrophoresis using the Hummel–Dreyer method. *J. Sep. Sci.* 28, 121–127.
- Saha, P., Descôteaux, C., Brasseur, K., Fortin, S., Leblanc, V., Parent, S., Asselin, É., Bérubé, G., 2012. Synthesis, antiproliferative activity and estrogen receptor α affinity of novel estradiol-linked platinum(II) complex analogs to carboplatin and oxaliplatin: potential vector complexes to target estrogen-dependent tissues. *Eur. J. Med. Chem.* 48, 385–390.
- Samimi, G., Katano, K., Holzer, A.K., Safaei, R., Howell, S.B., 2004. Modulation of the cellular pharmacology of cisplatin and its analogs by the copper exporters ATP7A and ATP7B. *Mol. Pharmacol.* 66, 25–32.
- Santini, C., Pellei, M., Gandin, V., Porchia, M., Tisato, F., Marzano, C., 2013. Advances in copper complexes as anticancer agents. *Chem. Rev.* 114, 815–862.
- Sava, G., Zorzet, S., Turrin, C., Vita, F., Soranzo, M., Zabucchi, G., Cocchiello, M., Bergamo, A., DiGiovine, S., Pezzoni, G., Sartor, L., Garbisa, S., 2003. Dual action of NAMI-A in inhibition of solid tumor metastasis: selective targeting of metastatic cells and binding to collagen. *Clin. Cancer Res.: Off. J. Am. Assoc. Cancer Res.* 9, 1898–1905.
- Scanlon, K.J., Kashani-Sabet, M., Miyachi, H., Sowers, L.C., Rossi, J., 1989. Molecular basis of cisplatin resistance in human carcinomas: model systems and patients. *Anticancer Res.* 9, 1301–1312.
- Sgarbossa, P., Sbovata, S.M., Bertani, R., Mozzon, M., Benetollo, F., Marzano, C., Gandin, V., Michelin, R.A., 2013. Novel imino thioether complexes of platinum(II): synthesis, structural investigation, and biological activity. *Inorg. Chem.* 52, 5729–5741.
- Shakya, R., Peng, F., Liu, J., Heeg, M.J., Verani, C.N., 2006. Synthesis, structure, and anticancer activity of gallium(III) complexes with asymmetric tridentate ligands: growth inhibition and apoptosis induction of cisplatin-resistant neuroblastoma cells. *Inorg. Chem.* 45, 6263–6268.
- Shrivastava, H.Y., Kanthimathi, M., Nair, B.U., 2002. Copper(II) complex of a tridentate ligand: an artificial metalloprotease for bovine serum albumin. *Biochim. Biophys. Acta BBA – Gen. Subj.* 1573, 149–155.
- Sigman, D.S., Graham, D.R., D'Aurora, V., Stern, A.M., 1979. Oxygen-dependent cleavage of DNA by the 1,10-phenanthroline cuprous complex. Inhibition of *Escherichia coli* DNA polymerase I. *J. Biol. Chem.* 254, 12269–12272.
- Smith, N.W., Strutton, G.M., Walsh, M.D., Wright, G.R., Seymour, G.J., Lavin, M.F., Gardiner, R.A., 1990. Transferrin receptor expression in primary superficial human bladder tumours identifies patients who develop recurrences. *Br. J. Urol.* 65, 339–344.
- Song, I.-S., Savaraj, N., Siddik, Z.H., Liu, P., Wei, Y., Wu, C.J., Kuo, M.T., 2004. Role of human copper transporter Ctr1 in the transport of platinum-based antitumor agents in cisplatin-sensitive and cisplatin-resistant cells. *Mol. Cancer Ther.* 3, 1543–1549.
- Sooriyaarachchi, M., Narendran, A., Gailer, J., 2011. Comparative hydrolysis and plasma protein binding of cis-platin and carboplatin in human plasma *in vitro*. *Metallomics* 3, 49–55.
- Spreckelmeyer, S., Orvig, C., Casini, A., 2014. Cellular transport mechanisms of cytotoxic metallodrugs: an overview beyond cisplatin. *Molecules* 19, 15584–15610.
- Stewart, D.J., Benjamin, R.S., Luna, M., Feun, L., Caprioli, R., Seifert, W., Loo, T.L., 1982. Human tissue distribution of platinum after cis-diamminedichloroplatinum. *Cancer Chemother. Pharmacol.* 10, 51–54.
- Stewart, J.J., White, J.T., Yan, X., Collins, S., Drescher, C.W., Urban, N.D., Hood, L., Lin, B., 2006. Proteins associated with cisplatin resistance in ovarian cancer cells identified by quantitative proteomic technology and integrated with mRNA expression levels. *Mol. Cell. Proteomics* 5, 433–443.
- Streu, C., Feng, L., Carroll, P.J., Maksimoska, J., Marmorstein, R., Meggers, E., 2011. P-donor ligand containing ruthenium half-sandwich complexes as protein kinase inhibitors. *Inorg. Chim. Acta* 377, 34–41.
- Sukumar, U.K., Bhushan, B., Dubey, P., Matai, I., Sachdev, A., Packirisamy, G., 2013. Emerging applications of nanoparticles for lung cancer diagnosis and therapy. *Int. Nano Lett.* 3, 1–17.
- Sun, R.W.-Y., Ma, D.-L., Wong, E.L.-M., Che, C.-M., 2007. Some uses of transition metal complexes as anti-cancer and anti-HIV agents. *Dalton Trans.* 4884–4892.
- Süss-Fink, G., 2010. Arene ruthenium complexes as anticancer agents. *Dalton Trans.* 39, 1673–1688.
- Tabassum, S., Zaki, M., Afzal, M., Arjmand, F., 2014. Synthesis and characterization of Cu(II)-based anticancer chemotherapeutic agent targeting topoisomerase I α : *in vitro* DNA binding, pBR322 cleavage, molecular docking studies and cytotoxicity against human cancer cell lines. *Eur. J. Med. Chem.* 74, 509–523.
- Talman, E.G., Kidani, Y., Mohrmann, L., Reedijk, J., 1998. Can Pt(IV) – amine complexes act as prodrugs? *Inorg. Chim. Acta* 283, 251–255.
- Tan, C.-P., Lu, Y.-Y., Ji, L.-N., Mao, Z.-W., 2014. Metallomics insights into the programmed cell death induced by metal-based anticancer compounds. *Metallomics* 6, 978–995.
- Tan, S.J., Yan, Y.K., Lee, P.P.F., Lim, K.H., 2010. Copper, gold and silver compounds as potential new anti-tumor metallodrugs. *Future Med. Chem.* 2, 1591–1608.
- Themsche, C.V., Parent, S., Leblanc, V., Descôteaux, C., Simard, A.-M., Bérubé, G., Asselin, E., 2009. VP-128, a novel oestradiol-platinum(II) hybrid with selective anti-tumour activity towards hormone-dependent breast cancer cells *in vivo*. *Endocr. Relat. Cancer* 16, 1185–1195.
- Tiekink, E.R.T., 2002. Gold derivatives for the treatment of cancer. *Crit. Rev. Oncol. Hematol.* 42, 225–248.
- Timerbaev, A.R., 2009. Advances in developing tris(8-quinolinolato)gallium(III) as an anticancer drug: critical appraisal and prospects. *Metallomics* 1, 193–198.
- Tisato, F., Marzano, C., Porchia, M., Pellei, M., Santini, C., 2010. Copper in diseases and treatments and copper-based anticancer strategies. *Med. Res. Rev.* 30, 708–749.
- Todd, R.C., Lippard, S.J., 2009. Inhibition of transcription by platinum antitumor compounds. *Met. Integr. Biometal Sci.* 1, 280–291.
- Torti, S.V., Torti, F.M., 2013. Cellular iron metabolism in prognosis and therapy of breast cancer. *Crit. Rev. Oncog.* 18, 435–448.
- Trujo-Solis, C., Jimenez-Farfan, D., Rodriguez-Enriquez, S., Fernandez-Valverde, F., Cruz-Salgado, A., Ruiz-Azuara, L., Sotelo, J., 2012. Copper compound induces autophagy and apoptosis of glioma cells by reactive oxygen species and jnk activation. *BMC Cancer* 12, 156.
- Tripathi, L., Kumar, P., Singhai, A., 2007. Role of chelates in treatment of cancer. *Indian J. Cancer* 44, 62.
- Trzaska, S., 2005. Cisplatin. *Chem. Eng. News Arch.* 83, 52.
- Vilmar, A., Sørensen, J.B., 2009. Excision repair cross-complementation group 1 (ERCC1) in platinum-based treatment of non-small cell lung cancer with special emphasis on carboplatin: a review of current literature. *Lung Cancer* 64, 131–139.

- Vock, C.A., Renfrew, A.K., Scopelliti, R., Juillerat-Jeanneret, L., Dyson, P.J., 2008. Influence of the diketonato ligand on the cytotoxicities of [Ru(6-p-cymene)(R2acac)(PTA)]⁺ complexes (PTA = 1,3,5-triaza-7-phosphaadamantane). *Eur. J. Inorg. Chem.* 2008, 1661-1671.
- Wang, B., Qian, H., Yiu, S.-M., Sun, J., Zhu, G., 2014a. Platinated benzonaphthyrindone is a stronger inhibitor of poly(ADP-ribose) polymerase-1 and a more potent anticancer agent than is the parent inhibitor. *Eur. J. Med. Chem.* 71, 366-373.
- Wang, N.X., von Recum, H.A., 2011. Affinity-based drug delivery. *Macromol. Biosci.* 11, 321-332.
- Wang, X., Guo, Z., 2008. Towards the rational design of platinum (II) and gold(III) complexes as antitumour agents. *Dalton Trans.* 1521-1532.
- Wang, Y., He, Q.-Y., Sun, R.W.-Y., Che, C.-M., Chiu, J.-F., 2005. Gold(III) porphyrin 1a induced apoptosis by mitochondrial death pathways related to reactive oxygen species. *Cancer Res.* 65, 11553-11564.
- Wang, Z., Qian, H., Yiu, S.-M., Sun, J., Zhu, G., 2014b. Multi-targeted organometallic ruthenium(II)-arene anticancer complexes bearing inhibitors of poly(ADP-ribose) polymerase-1: a strategy to improve cytotoxicity. *J. Inorg. Biochem.* 131, 47-55.
- Wheate, N.J., Walker, S., Craig, G.E., Oun, R., 2010. The status of platinum anticancer drugs in the clinic and in clinical trials. *Dalton Trans.* 39, 8113-8127.
- Wong, D.Y.Q., Ang, W.H., 2012. Development of platinum(IV) complexes as anticancer prodrugs: the story so far. *COSMOS* 08, 121-134.
- Wong, E., Giandomenico, C.M., 1999. Current status of platinum-based antitumor drugs. *Chem. Rev.* 99, 2451-2466.
- Xie, W., Wei, S., Liu, J., Ge, X., Zhou, L., Zhou, J., Shen, J., 2014. Combination anticancer therapy activity studies for the complex of hypocrellin A and gallium ion. *Dyes Pigm.* 101, 43-50.
- Yi, T., Pathak, M.K., Lindner, D.J., Ketterer, M.E., Farver, C., Borden, E.C., 2002. Anticancer activity of sodium stibogluconate in synergy with IFNs. *J. Immunol.* 169, 5978-5985.
- Yu, L., Ma, Y.-Q., Liu, R.-C., Wang, G.-C., Li, J.-S., Du, G.-H., Hu, J.-J., 2004. Synthesis, characterization and *in vitro* antitumor activity of some arylantimony ferrocenylcarboxylate derivatives and the crystal structures of [C₅H₅FeC₅H₄C(CH₃)=CHCOO]. *Polyhedron* 23, 823-829 (see abstract).
- Zang, D.Y., Lee, K.H., Lee, J.S., Lee, J.H., Kim, W.K., Kim, S.H., Kim, W.D., Kim, D.S., Kim, J.H., Kim, B.S., Cho, Y.B., Kim, D.K., Kim, K.H., 1999. Phase II trial of a novel platinum analog, SKI 2053R, in patients with previously untreated extensive-stage small-cell lung cancer. *Am. J. Clin. Oncol.* 22, 495-498.
- Zerzankova, L., Kostrhunova, H., Vojtiskova, M., Novakova, O., Suchankova, T., Lin, M., Guo, Z., Kasparkova, J., Brabec, V., 2010. Mechanistic insights into antitumor effects of new dinuclear cis PtII complexes containing aromatic linkers. *Biochem. Pharmacol.* 80, 344-351.
- Zhang, J.Z., Bryce, N.S., Lanzirotti, A., Chen, C.K., Paterson, D., de Jonge, M.D., Howard, D.L., Hambley, T.W., 2012. Getting to the core of platinum drug bio-distributions: the penetration of anti-cancer platinum complexes into spheroid tumour models. *Met. Integr. Biometal Sci.* 4, 1209-1217.
- Zhong, H.-J., Leung, K.-H., Liu, L.-J., Lu, L., Chan, D.S.-H., Leung, C.-H., Ma, D.-L., 2014. Antagonism of mTOR activity by a kinetically inert rhodium(III) complex. *ChemPlusChem* 79, 508-511.

10. Vašíčková K, Moráň L, Gurín D, Vaňhara P. Alleviation of endoplasmic reticulum stress by tauroursodeoxycholic acid delays senescence of mouse ovarian surface epithelium. *Cell and Tissue Research* 2018; **374(3):643-652.**

Commentary:

In this work we documented that mouse ovarian surface epithelium suffers from ER stress during replicative senescence *in vitro*, develop abnormalities in ER and elicit UPR. Attenuation of ER stress in senescent OSE by tauroursodeoxycholic acid (TUDCA) rescues ER architecture and leads to delayed onset of senescence. Moreover, we show for the first time a mutual molecular link between ER stress response and replicative senescence leading to phenotypic changes of non-malignant ovarian surface epithelium.

DOI: 10.1007/s00441-018-2888-9
Journal: Cell and Tissue Research
Impact factor (WOS, 2017): 3.043
Number of citations (WOS, 2018): not cited yet
Contribution of the author: Corresponding author. Collection and/or assembly of data, data analysis and interpretation, manuscript writing.

Pilot data summarized in this manuscript were awarded the Best Poster Prize by International Congress of Cell Biology, Prague 2016, and Journal of Cell Biology (to Kateřina Vašíčková-Kratochvílová).



Alleviation of endoplasmic reticulum stress by tauroursodeoxycholic acid delays senescence of mouse ovarian surface epithelium

Kateřina Vařířková¹ · Lukáš Moráň¹ · Dominik Gurín² · Petr Vaňhara¹

Received: 23 April 2018 / Accepted: 4 July 2018 / Published online: 31 July 2018
© Springer-Verlag GmbH Germany, part of Springer Nature 2018

Abstract

Ovarian surface epithelium (OSE) forms a single layer of mostly cuboidal cells on surface of mammalian ovaries that is inherently exposed to cell stress evoked by tissue damage every ovulation and declines morphologically after menopause. Endoplasmic reticulum (ER) is a principal cell organelle involved in proteosynthesis, but also integrating various stress signals. ER stress evokes a conserved signaling pathway, the unfolded protein response (UPR), leading to cell death or adaptation to stress conditions. In this work, we document that mouse OSE suffers from ER stress during replicative senescence *in vitro*, develops abnormalities in ER and initiates UPR. Attenuation of ER stress in senescent OSE by tauroursodeoxycholic acid (TUDCA) reconditions ER architecture and leads to delayed onset of senescence. In summary, we show for the first time a mutual molecular link between ER stress response and replicative senescence leading to phenotypic changes of non-malignant ovarian surface epithelium.

Keywords Ovarian surface epithelium · Endoplasmic reticulum stress · Unfolded protein response · Senescence · Tauroursodeoxycholic acid

Introduction

Ovarian surface epithelium (OSE) is a remarkably dynamic structure, developmentally enabling formation of ovarian follicles, during fertile period undergoing regular cyclic repairs of ovulatory ruptures to eventually decline both functionally and structurally after the menopause. Depending on the cell position and phase of the ovarian cycle, OSE forms a simple layer of squamous-to-cubic cells that express markers of both epithelial and mesenchymal phenotypes (Auersperg et al. 2001). In addition, ovarian hilum contains a slow cycling cell population expressing markers of tissue stem cells that is capable of

regeneration of postovulatory cortex (Flesken-Nikitin et al. 2013). Ovulation disturbs integrity of surface epithelial lining and induces cell stress in OSE by mechanical shear forces as well as by alteration of paracrine signaling in the tissue microenvironment and induces morphological and functional responses (Okamura et al. 2006). Despite the recent re-evaluation of ovarian cancer origin (Kurman and Shih Ie 2016) also to extraovarian tissues, repeated ovulations or ovarian stimulation affecting OSE were described to increase the risk of ovarian cancer (Fathalla 2013). In aged, post-menopausal ovaries, the OSE proliferation and regeneration are uncoupled from the endocrine control and decline, epithelial lining flattens, but cancer-prone inclusion cysts and epithelial invaginations often develop in the stroma, representing a potentially hazardous precancerous condition. During menopause, imbalance of the ovarian microenvironment towards increased cells stress is evoked mostly by estrogen loss, increase of reactive oxygen species (ROS) and DNA damage, or by alterations in levels of soluble endocrine, growth, and inflammatory factors and cytokines (King et al. 2013).

Cell stress induced by accumulation of deleterious alterations of biomolecules in cells, resulting in their abnormal functions, leads to tissue decay and ultimately to tissue aging.

Electronic supplementary material The online version of this article (<https://doi.org/10.1007/s00441-018-2888-9>) contains supplementary material, which is available to authorized users.

✉ Petr Vaňhara
pvanhara@med.muni.cz

¹ Department of Histology and Embryology, Faculty of Medicine, Masaryk University, Kamenice 126/3, 625 00 Brno, Czech Republic

² First Department of Pathological Anatomy, St. Anne's University Hospital Brno, Brno, Pekařská 53, 656 91 Brno, Czech Republic

Virtually in all mammalian somatic cells, various stress factors disturbing cell and tissue homeostasis integrate on endoplasmic reticulum (ER) and evoke a general stress response termed unfolded protein response (UPR). UPR then drives a cell towards adaptation to ER stress through pro-survival signaling or induces apoptosis. Crosstalk of three canonical UPR signaling pathways mediated by PERK, IRE1, and ATF6 then elicits the variable transcriptional and translational output that determines the cell fate. Recent findings identified ER stress as a factor that is deeply involved in alterations of normal tissue morphology and propensity towards cancer initiation and progression (Kratochvílová et al. 2016; Wang and Kaufman 2014). In ovaries, UPR is activated in ovarian cycle during follicular growth and maturation (Huang et al. 2017). Moreover, UPR is activated in cancer cells harboring mutations in genes crucially involved in ovarian cancer carcinogenesis, such as BRCA1/2 (Miki et al. 1994; Yeung et al. 2008). Interestingly, increased levels of ER stress effectors and pro-inflammatory cytokines were reported in atrophying uterine lining of menopausal women, and ultrastructural hallmarks of ER stress were experimentally documented in uterine epithelium of ovariectomized animals (Kyathanahalli et al. 2015), suggesting that ER stress is functionally linked to loss of ovarian function by integration of signaling cues coming from the tissue microenvironment beyond ovaries, particularly during aging of female reproductive system. Tauroursodeoxycholic acid (TUDCA) was described to alleviate ER stress by relieving aggregation of potentially misfolded proteins (Uppala et al. 2017), acting as chemical chaperon. Moreover, it is involved in various signaling pathways leading to cell adaptation and survival. It prevents dissociation of GRP78 from PERK, attenuating downstream UPR signaling. Moreover, it upregulates PI3K/Akt signaling enhancing cell viability in various cell models (Xie et al. 2016; Yoon et al. 2016).

While most of the information on ER stress in ovaries comes from tumors or cancer cell lines, the link between ER stress, aging, and alterations of OSE has not been yet sufficiently addressed. In this work, we document that normal OSE is capable of induction of UPR during replicative senescence in vitro and show that alleviation of ER stress by TUDCA decreases frequency of OSE cells entering senescence.

Material and methods

Mouse OSE Isolation, cultivation, and treatment Protocol for isolation and culture of mouse ovarian surface epithelium (mOSE) was adapted from Kido and Shibuya (Kido and Shibuya 1998). mOSE were isolated from 8 to 12-week-old female mice (ICR/CD-1 strain). First, mice were euthanized by cervical dislocation, and ovaries were aseptically

dissected immediately after sacrifice. Animal experiments were supervised by the local ethical committee of the Faculty of Medicine, Masaryk University and performed by certified individuals (KV, PV, and LM). Dissected ovaries were incubated at 37 °C for 40 min in DMEM GlutaMAX (Gibco, ThermoFisher Scientific, Prague, Czech Republic) supplemented with 2.5 mg ml⁻¹ trypsin (Sigma-Aldrich, Prague, Czech Republic), 2.5 mg ml⁻¹ collagenase (Sigma-Aldrich, Prague, Czech Republic), and 5% fetal bovine serum (GE Healthcare, Prague, Czech Republic). Then, the ovaries were removed and the isolated cell suspension was filtered through 100-µm cell strainer. Isolated mOSE cells were maintained in DMEM GlutaMAX (Gibco, ThermoFisher Scientific, Prague, Czech Republic) supplemented with 10% fetal bovine serum (GE Healthcare, Czech Republic), 1% ITS liquid media supplement (Sigma-Aldrich, Prague, Czech Republic), 500 ng ml⁻¹ hydrocortisone (Sigma-Aldrich, Czech Republic), and 10 ng ml⁻¹ EGF (PeproTech Czech, Prague, Czech Republic) at 37 °C with 5% CO₂ in humidified atmosphere. mOSE were passaged at 80% confluence. To modulate ER stress, tunicamycin and tauroursodeoxycholic acid (TUDCA) (both by Sigma-Aldrich, Prague, Czech Republic) were used.

Immunohistochemistry

Immunohistochemistry was performed on formalin-fixed and paraffin-embedded ovaries explanted from healthy 8–10-week-old female mice (ICR/CD 1 strain). First, 5 µm thick tissue sections were deparaffinized by heating at 60 °C, followed by xylene wash, and rehydrated in decreasing concentrations of ethanol. Antigen retrieval was performed using Target Retrieval Solution, pH 6 (Dako, Hamburg, Germany) for 40 min at 98 °C, followed by treatment with 0.3% H₂O₂ in 1× PBS (pH 7.4) to quench endogenous peroxidase activity. After blocking with 1% bovine serum albumin (BSA) for 10 min, sections were incubated in primary antibody (KRT8, ab53708 Abcam; CDH1, #3195 Cell Signaling; CDH2, ab12221 Abcam; VIM, ab92547 Abcam; HSPA5, #3177 Cell Signaling; DDIT3, #2895 Cell Signaling) for 1 h at room temperature in wet chamber. Primary antibody were diluted 1:100–1:500 in Antibody Diluent (Dako, Hamburg, Germany). The sections were washed three times in 1× PBS and incubated with enzyme-conjugated biotinylated detection agent The DAKO EnVision™+ Dual Link (Dako, Hamburg, Germany) for 30 min at room temperature. Sections were washed three times with 1× PBS and incubated in Streptavidin-HRP (LSAB + System HRP, Dako, Hamburg, Germany) until a brown color developed. Sections were then counterstained with Gill's hematoxylin, dehydrated, and mounted using Pertex medium.

SDS-Page and western blotting

Trypsinized cells were washed three times with ice cold $1\times$ PBS and resuspended in RIPA lysis buffer containing 50 mM Tris-Cl (pH 7.4), 150 mM NaCl, 2 mM EDTA, 1% Tween, and 0.1% SDS, supplemented with Phosphatase Inhibitor Cocktail PhosSTOP™ (Roche Applied Science, Prague, Czech Republic) and cOmplete™, Mini, EDTA-free Protease Inhibitor Cocktail (Roche Applied Science, Prague, Czech Republic). Protein concentrations were determined by Bradford Bio-Rad protein assay kit (Bio-Rad, Prague, Czech Republic). Lysates were mixed with $5\times$ Laemmli sample buffer (100 mM Tris pH 6.8, 4% SDS, 200 mM DTT, 20% glycerol, and 0.1% Bromophenol Blue) and boiled for 5 min at 95 °C. Equal amounts of total protein were separated using 10% sodium dodecylsulfate-polyacrylamide gel electrophoresis (SDS-PAGE). Resolved proteins were then electroblotted onto Immobilon-P polyvinylidene difluoride (PVDF) membrane (Millipore, Prague, Czech Republic), blocked 60 min in 5% low-fat milk, and incubated with the indicated primary antibodies (actin, Ab1801 Abcam; calnexin, #2679 Cell Signaling; ERO1a, #3264 Cell Signaling; IRE1 α (ERN1), #3294 Cell Signaling; p21^{WAF1/CIP1}, sc-397 Santa Cruz; PERK, #5683 Cell Signaling; for HSPA5, DDIT3 and CDH1 see Immunohistochemistry) diluted 1:250–1:1000 in 5% bovine serum albumin at 4 °C overnight. Then, membranes were washed in TBS-Tween (50 mM Tris-HCl pH 7.5, 150 mM NaCl, 2.7 mM KCl, 0.05% Tween 20) and incubated with the horseradish peroxidase (HRP)-conjugated secondary antibodies (anti-rabbit HRP, #7074 Cell Signaling or anti-mouse HRP, Ab50043 Abcam), diluted 1:5000 in 5% low-fat milk. Proteins were visualized using ECL prime Western Blotting Detection Reagent (GE Healthcare, Prague, Czech Republic, RPN2236). Quantitative densitometry was performed using ImageJ software. Values represent the integrated density for the respective band normalized to the control of equal loading.

Immunofluorescent microscopy

mOSE cells cultured on 96-well plates were washed three times in $1\times$ PBS (pH 7.4), fixed in 4% paraformaldehyde for 15 min at room temperature, washed again three times in PBS and blocked in 0.1% Triton-100X 1% BSA for 1 h on ice. Next, cells were incubated with specific primary antibodies (CDH2, #13116 Cell Signaling; p16^{INK4}, Ab108349 Abcam; for CDH1, KRT8, VIM, γ H2AX, p21^{WAF1/CIP1}, HSPA5 and DDIT3 see Immunohistochemistry and SDS-PAGE and Western blotting) in 3% BSA at 4 °C overnight. Cells were washed three times in $1\times$ PBS and incubated for 1 h with secondary antibody conjugated with AlexaFluor 455 (Life Technologies, Prague, Czech Republic, A21429, 1:2000 in 3% BSA) followed by additional wash in PBS. Nuclei were counterstained using Hoechst dye. Images were acquired by automated microscope

equipped with the environmental chamber (Image Xpress MicroXL, Molecular Devices, San Jose, CA, USA).

RNA isolation, reverse transcription, and real-time qPCR

Total RNA was extracted using an RNeasy Mini Kit (Qiagen, Hilden, Germany) and quantified using a NanoDrop (Thermo Scientific, Waltham, MA, USA). cDNA was synthesized from 1 μ g of DNase I-treated total RNA using a First Strand Reverse Transcription Kit (Roche, Basel, Switzerland). Real-time qPCR was performed using a Roche LightCycler 480 RT PCR Kit according to the manufacturer's instructions. Relative expression was quantified using a UPL probe (Roche Applied Science, Prague, Czech Republic) and gene-specific primers (HSPA5: AAACCCCGATGAGGCTGT, TGTATCCTGATCACCAGAGAGG, UPL #64; DDIT3: ACCTGCGTCCCTAGCTT, ATGTGCGTGTGACCTCTGTT', UPL #36; HPRT1: TCACATTGTGGCCCTCTG, TCTACAGTCATAGGAATGGATCTATCA, UPL #62; p21^{WAF1/CIP1}: TCCACAGCGATATCCAGACA, GGACATCACCAGGATTGGAC, UPL #21; SNAI1: CTTGTGTCTGCACGACCTGT, CAGGAGAATGGCTTCTCACC, UPL #71; SNAI2: AAAGATGAAGTGAAAAGCACATTG, CTGTTCTTTGGTTGAAATGG, UPL #74), and their expression was evaluated as relative ratio units visualized in log scale. All PCR reactions were performed in triplicates in three independent experiments with reverse transcriptase-negative and template-negative controls included.

Senescence-associated β -galactosidase staining

The 2×10^5 mOSE cells were seeded to 24-well plate and cultured for 24 h. Senescence-associated- β -galactosidase staining was performed using Senescence Cells Histochemical Staining Kit (Sigma-Aldrich, CS0030) according to the manufacturer's instructions. Briefly, cells were washed in $1\times$ PBS, fixed for 7 min at room temperature in 2% formaldehyde, washed in $1\times$ PBS, and incubated at 37 °C with SA β -gal stain solution containing 5-bromo-4-chloro-3-indolyl P3-D-galactoside (X-Gal) 1 mg ml⁻¹, 40 mM citric acid, sodium phosphate pH 6.0, 5 mM potassium ferrocyanide, and 5 mM potassium ferricyanide/150 mM NaCl, 2 mM MgCl₂. Images were acquired by TissueFAXS PLUS (Tissue Gnostic, Austria), and frequency of senescent cells was determined.

Transmission Electron microscopy

mOSE cells were transferred to suspension by trypsinization, washed in 0.1 M cacodylate buffer, fixed in 3% glutaraldehyde with 0.2% tannin for 1 h, and postfixed in 1% OsO₄ for 50 min. Then, cells were washed three times in cacodylate buffer, embedded in 1% agar blocks, dehydrated in increasing series of

ethanol (50, 70, 96, and 100%), treated 2×15 min with 100% acetone, and embedded in Durcupan resin. Ultrathin sections were prepared using LKB 8802A Ultramicrotome, stained with uranyl acetate and Reynold's lead citrate, and examined with FEI Morgagni 286(D) TEM. One hundred cells from each experimental group in two independent experimental sets were examined. Images were analyzed using ImageJ software.

MTT viability assay

The 1×10^4 mOSE cells were seeded onto 96-well plate (Corning, USA) and cultured with respective treatments for 24 h. Then, thiazolyl blue tetrazolium bromide (Sigma-Aldrich, Prague, Czech Republic) solution in water was added to culture medium at one-tenth of total volume and incubated for 4 h. Cells were lysed by isopropanol containing 10% Triton and 0.04 M HCl, and absorbance was measured at 570 nm. Plots represent normalized, background subtracted mean absorbance, and the standard deviations (SD) from three independent experiments.

Real-time PCR telomere length assessment

To determine length of mouse telomeres, protocol of Callicott et Womack (2006) was adapted. Briefly, mOSE genomic DNA was extracted using PureLink Genomic DNA minikit (Thermo Fisher Scientific, Prague, Czech Republic) and amplified using the telomere-specific forward and reverse primers: 5' CGG TTT GTT TGG GTT TGG GTT TGG GTT TGG GTT TGG GTT 3' and 5' GGC TTG CCT TAC CCT TAC CCT TAC CCT TAC CCT 3'. As a reference single copy gene, 36B4 (acidic ribosomal phosphoprotein PO) gene was amplified using forward and reverse primers: 5' CAG CAA GTG GGA AGG TGT AAT CC-3' and 5'CCCATT CTA TCA TCA ACG GGT ACA A3'. For a standard curve calculation, DNA extracted from proliferating mOSE was used at different amounts (1, 5, 10, 20, 30 ng). The quantitative PCR on 20 ng of input genomic DNA was performed using SYBR Green PCR Master Mix (Life Technologies, Prague, Czech Republic) with 300 nM concentration of each primer for telomere PCR and 300 nM forward and 500 nM reverse primer concentration for 36B4 gene on the Roche LightCycler 480 (Roche, Basel, Switzerland). Thermal cycler reaction conditions were set to single step of 95 °C/10 min and 30 cycles of 95 °C/15 s, 56 °C/1 min for telomere PCR, and single step of 95 °C/10 min and 35 cycles of 95 °C/15 s, 52 °C/20 s, and 72 °C/30 s for 36B4 control. All reactions were performed in triplicates and included template negative controls. The LightCycler 480 software 1.5.0 was used to determine the cycle threshold (Ct) of each sample, and the telomere relative input amount was assessed from the standard calibration curve. Average ratios of telomere relative input amount to relative input amount of 36B4 ratios were reported as the average telomere length ratio (ATLR).

Cell cycle analysis

To analyze the progression of cell cycle in mOSE, propidium-iodide staining followed by flow cytometry was performed. The 1×10^6 cells were collected by trypsinization, washed in $1 \times$ PBS, and fixed by ice-cold 70% EtOH for 30 min at 4 °C. Then, cells were washed in FACS buffer (2% FBS, 1% EDTA, in PBS) and incubated with 0.1 mg ml⁻¹ RNase for 30 min at 37 °C. After subsequent wash in FACS buffer, cells were finally stained with 50 µg ml⁻¹ propidium iodide and measured on Cytomics FC500 Flow Cytometer (Beckman Coulter). Cell cycle profile was analyzed using FlowJo software (FlowJo LLC, Ashland, Oregon).

Statistical analysis

Statistical analysis was done using Statistica 12 (StatSoft, TIBCO Software, Palo Alto, USA). Where applicable, statistical significance was determined using *t* test at $p < 0.05$.

Results and discussion

To address UPR during aging of mouse ovarian epithelial cells (mOSE), we first established and validated a culture of primary mOSE cells explanted from dissected ovaries of ICR/CD-1 mice. mOSE express both epithelial markers, such as E-cadherin (CDH1) or cytokeratin 8 (KRT8), and mesenchymal markers, e.g., N-cadherin (CDH2) and vimentin (VIM) that clearly distinguish the mOSE layer from fibrous tunica albuginea and cortical connective tissue stroma, as documented by in situ immunohistochemistry (Fig. 1a–d). We confirmed that explanted primary mOSE transferred to the in vitro culture maintains expression of mOSE markers and prior entry to senescence also the typical, cobblestone-like epithelial morphology (Figs. 1e–l and 2n). mOSE thus can be clearly distinguished from stromal, non-epithelial carryovers (Fig. 1m–p). To address functional links between senescence and ER stress in mOSE, we took the advantage of spontaneous replicative senescence occurring in primary cells cultured in vitro. Explanted primary OSE continued cycling until approximately 30 days of culture that is equivalent to passage 4–5. Then, they quit cell cycle and developed the senescent phenotype, as documented by telomere shortening (Fig. 2a), phosphorylation of histone γ H2A.X and upregulation of cell cycle inhibitors p16^{INK4} and p21^{WAF1/CIP1}, and accumulation of senescence-associated beta-galactosidase (SA- β -gal) (Fig. 2b–m). Cells that gradually entered senescence also altered their morphology towards large, flat, fibroblast-like cells (Fig. 2n–r). This prompted us to investigate expression of major drivers of epithelial-to-mesenchymal transition. Indeed, we demonstrated that mRNAs coding for SNAI1 (Slug) and SNAI2 (Snail) transcription factors were

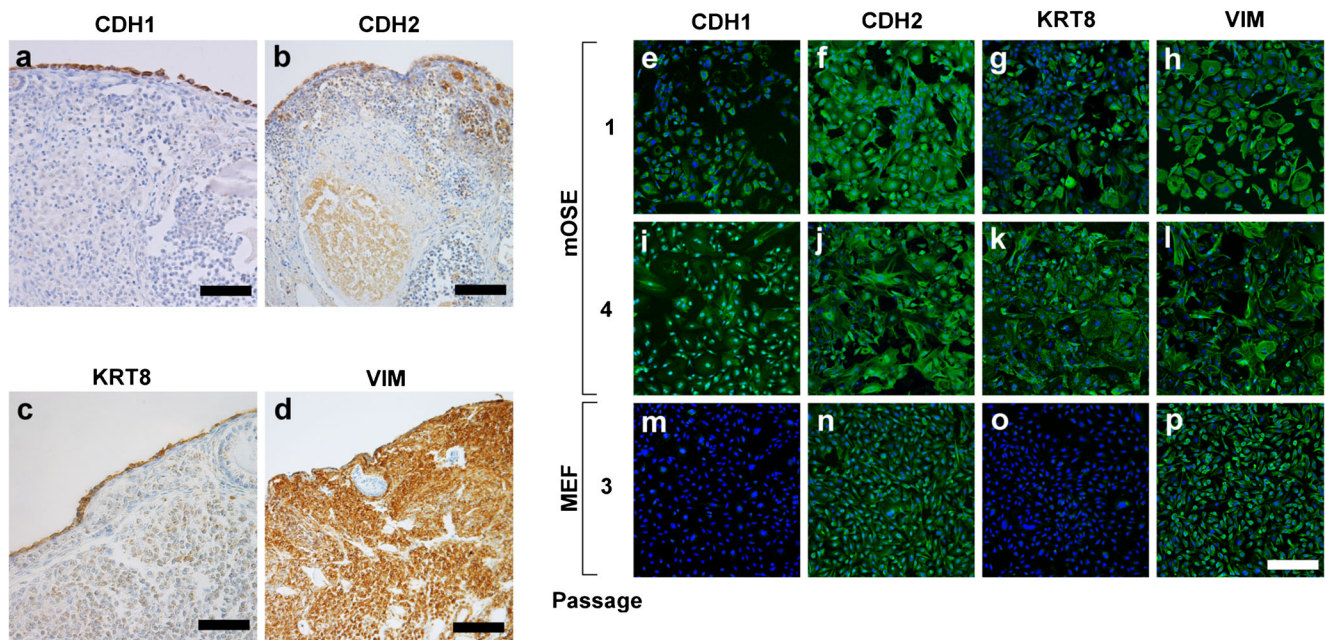


Fig. 1 Mouse ovarian surface epithelium (mOSE) express E-cadherin (CDH1) (a), N-cadherin (CDH2) (b), vimentin (VIM) (c), and cytokeratin 8 (KRT8) (d). Mouse ovaries were dissected, fixed in formalin, embedded in paraffin, and cut to sections covering cortical region of ovaries. CDH1, CDH2, KRT8, and VIM were visualized by immunohistochemistry. Scale bars indicate 200 μm . This expression pattern is maintained after

transferring to in vitro culture. mOSE were enzymatically dissociated from surface of dissected ovaries and cultured in vitro. CDH1, CDH2, KRT8, and VIM were visualized by immunofluorescent microscopy (e–l). Mouse embryonic fibroblasts were obtained from 13.5-d.p.c.-old mouse embryos, expanded in vitro, and used as a control of mesenchymal carryovers (m–p). Scale bar indicates 200 μm

upregulated. In parallel, increased expression of mRNA coding for p21^{WAF1/CIP1}, HSPA5, and DDIT3 was documented (Fig. 2s). On a protein level, upregulation of HSPA5, ERN1a, and ERO1a and increased cleavage of ATF6 resulting in accumulation of active ATF6p⁵⁰ fragment were revealed, while expression of ER-integral chaperon calnexin (CANX) remained unchanged (Fig. 2t). To exclude the possibility, that UPR is upregulated in response to stress induced rather by a desquamation of ovarian surface cells during mOSE isolation than by senescence in culture, we visualized UPR effectors in whole ovarian explants with the mOSE layer undisturbed. The intact ovaries were cultured for 24 h under conditions chemically promoting ER stress by tunicamycin and analyzed by immunohistochemistry (Supplementary Fig. S1). We confirmed that mOSE layer is capable of UPR activation within its tissue spatial context and thus represents a suitable model for revealing molecular mechanisms linking ER stress and tissue aging.

Then, we were curious, if ER stress and senescence are causatively linked. Thus, we used tunicamycin to induce massive ER stress in cultured mOSE by inhibition of N-glycosylation in ER, and chemical chaperon tauroursodeoxycholic acid (TUDCA) that nonspecifically alleviates ER stress. mOSE cells at passages 2 (P2) and 4 (P4) corresponding to proliferating and senescence state, respectively, were treated either with tunicamycin or TUDCA for 24 h and processed for electron microscopy. Tunicamycin-treated cells exhibited massive dilatations and

vacuolization of ER cisterns irrespectively of passage number, thus providing a valid positive control for ER stress induction in mOSE. Interestingly, untreated P4 cells showed significantly higher frequency of abnormally dilated and vacuolized ER cisterns than P2 cells suggesting that deregulation of ER homeostasis was evoked by the time of culture. Treatment of P4 cells by TUDCA reverted dilatations of ER cisterns and restored the normal architecture of ER. In P2 cells, TUDCA increased proportion of dilated ER cisterns and partially cytoplasmic vacuolization (Fig. 3). On molecular level, tunicamycin induced expression of HSPA5 and DDIT3 as well as p21^{WAF1/CIP1}, while TUDCA significantly downregulated these mRNAs in both P2 and P4 cells (Fig. 4a). This prompted us to reveal whether global attenuation of ER stress can substantially alter the phenotype of mOSE and possibly revert the onset of senescence. First, we treated mOSE cells with tunicamycin or TUDCA and determined the metabolic activity and viability by MTT assay. After 24 h exposure to conditions evoking (tunicamycin) or alleviating (TUDCA) ER stress, we documented decreased viability after tunicamycin treatment of both proliferating and senescent cells. Interestingly, TUDCA had no significant effect on viability of P2 cells but enhanced viability of P4 cells (Fig. 4b). In the same experimental setup, tunicamycin induced cell cycle arrest in G0/G1, irrespectively of passage number, while TUDCA reduced the frequency of cells in G0/G1 and increased the number of cells in G2/M phase (Fig. 4c), indicating that alleviation of ER stress mOSE may alter cell cycle machinery towards

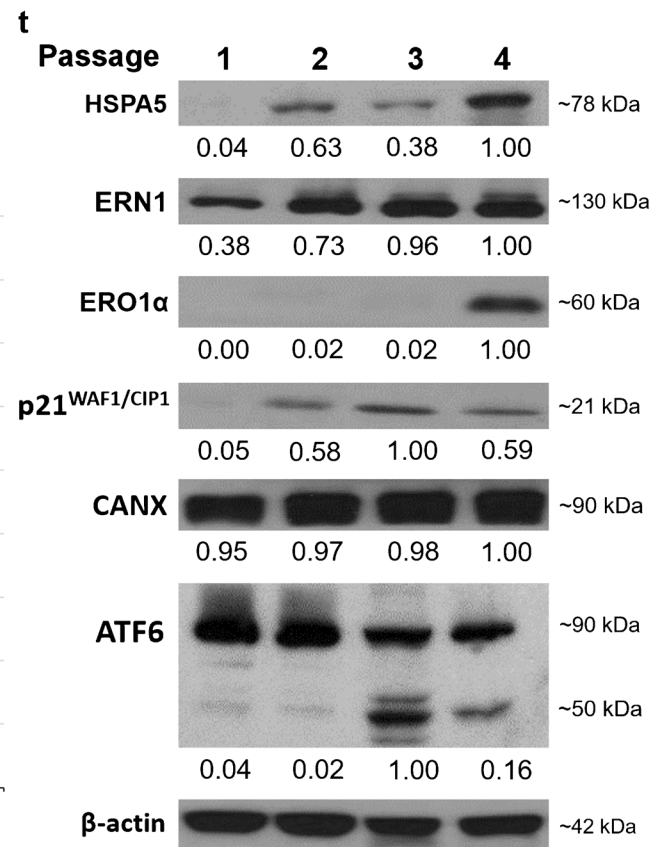
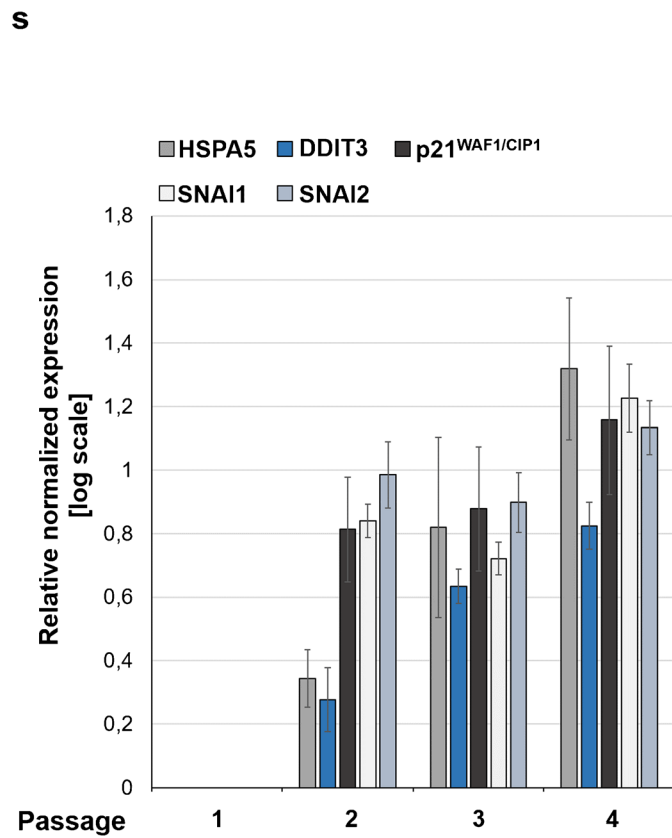
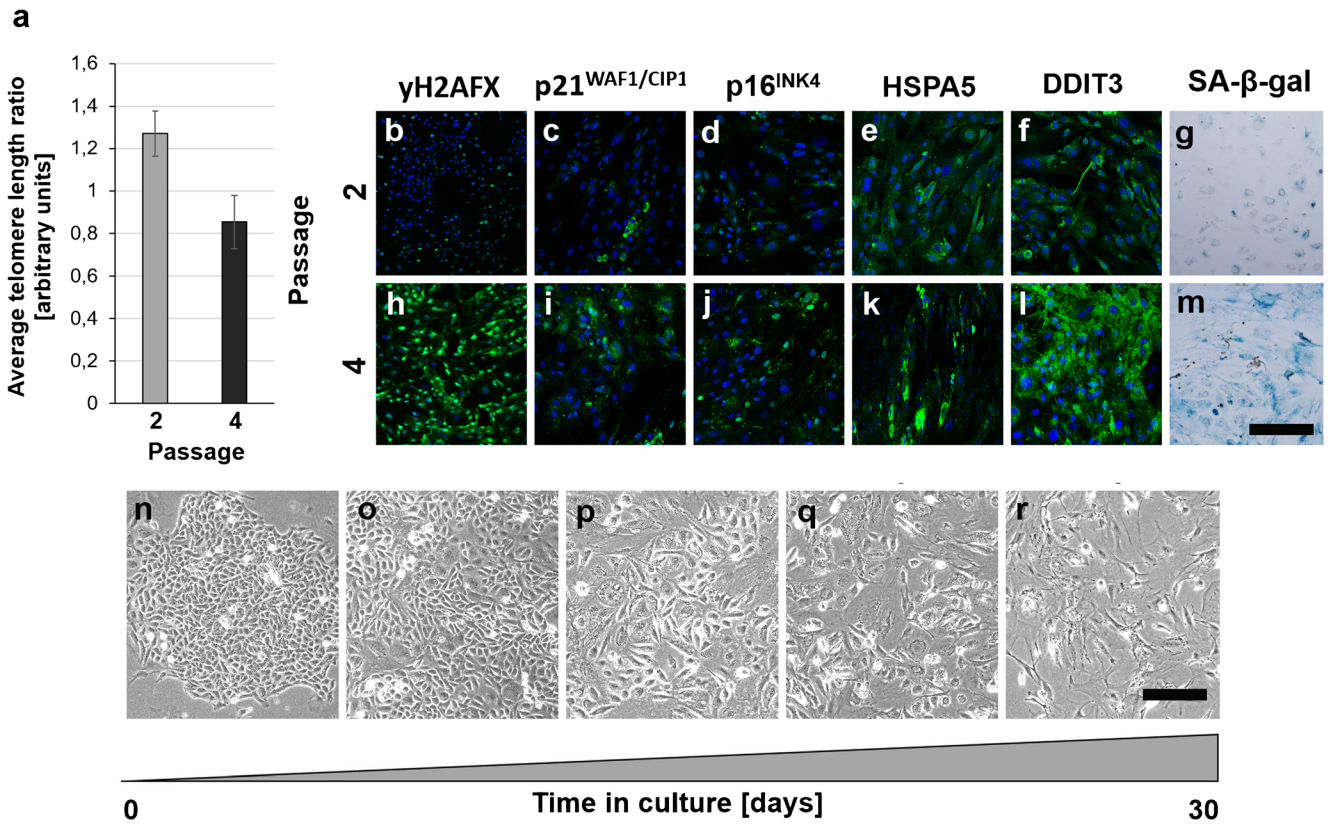


Fig. 2 mOSE cells enter replicative senescence, as documented by telomere shortening. Relative telomere length ratios of cells at passage 2 and 4 were determined using quantitative PCR (a). mOSE cultured in vitro accumulate markers of senescence, such as histone γ H2AFX (b, h), inhibitors of cell cycle p21^{WAF1/CIP1} (c, i) and p16^{INK4} (d, j), and SA- β -gal (g, m) and suffer from ER stress, as documented by immunofluorescence analysis of HSPA5 (e, k) and DDIT3 (f, l). Scale bar indicates 50 μ m. In prolonged culture, mOSE change their morphology from cells with flat, cobblestone-like epithelial appearance to large, flat, fibroblast-like shape cells. Scale bar indicates 50 μ m (n–r). Gene expression levels of HSPA5, DDIT3, p21^{WAF1/CIP1}, SNAI1, and SNAI2 in mOSE over four passages, equivalent to approx. 30 days in vitro, as documented by RT-qPCR (s). Protein levels of HSPA5, ERN1, ERO1A, p21^{WAF1/CIP1}, calnexin (CANX), and ATF6 in mOSE over four passages in culture as documented by immunoblotting (t)

proliferation. Moreover, treatment by TUDCA significantly reduced number of senescent cells in culture (Fig. 4d).

Generally, depletion of follicular pool in ovaries and induction of menopause substantially alter ovarian endocrine activity and morphology. Height of ovarian surface epithelium of postmenopausal ovaries decreases, and the epithelial layer shows tendency to development of invaginations and inclusion cysts, and becomes permissive for development of epithelial ovarian cancer (Laszczynska et al. 2008). In long-term in vitro cultures, mOSE suffer by genomic instability induced by deregulation of mitotic machinery genes and can acquire hazardous pre-malignant phenotype (Urzua et al. 2016). Oxidative stress induced by DNA-damage and ROS can further shift permissive mOSE clones towards malignancy. Interestingly, this process was enhanced by epithelial-stromal interactions (King et al. 2013). Concordantly, Lawrenson and colleagues demonstrated earlier that in vitro-derived senescent fibroblasts promoted neoplastic

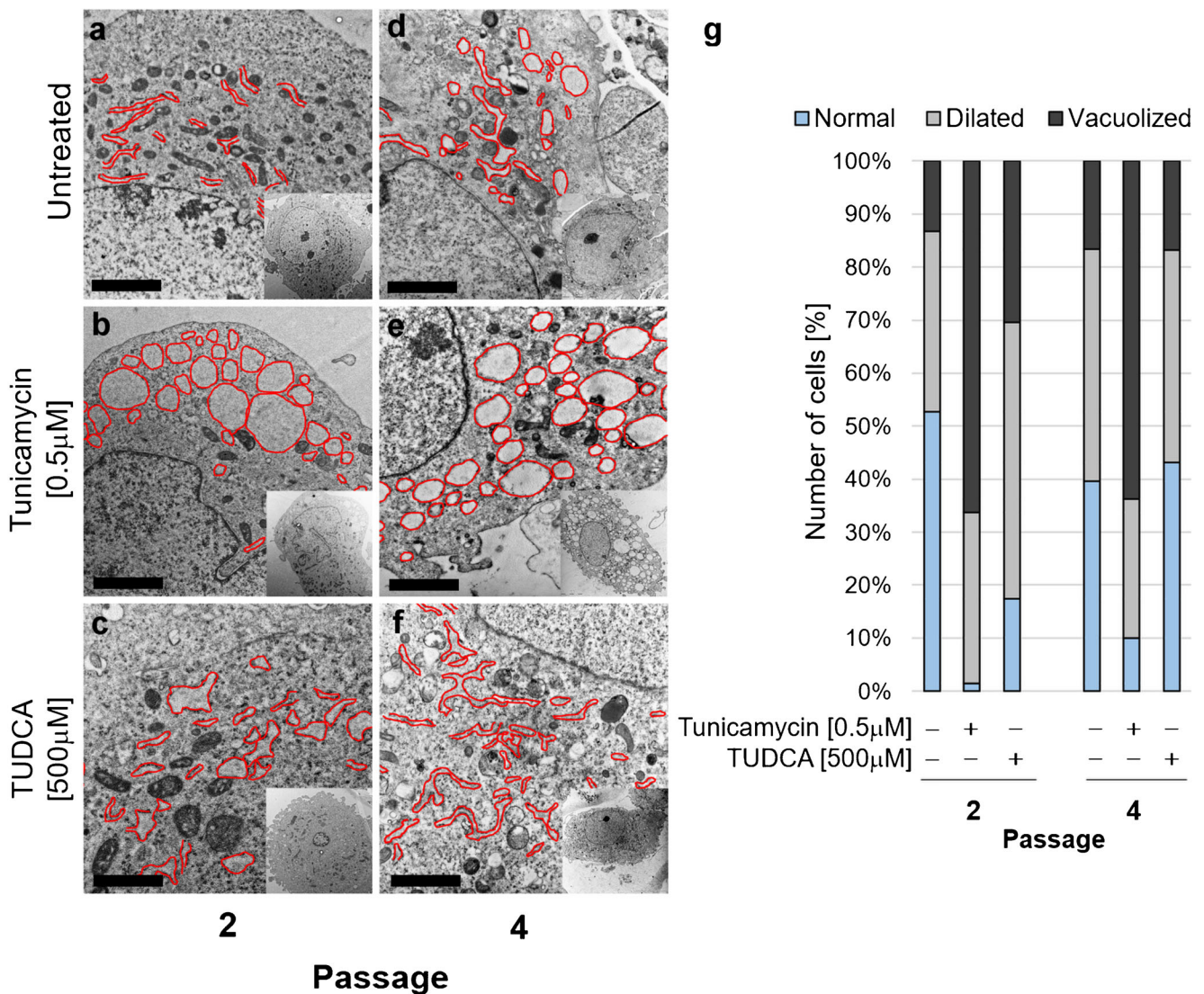
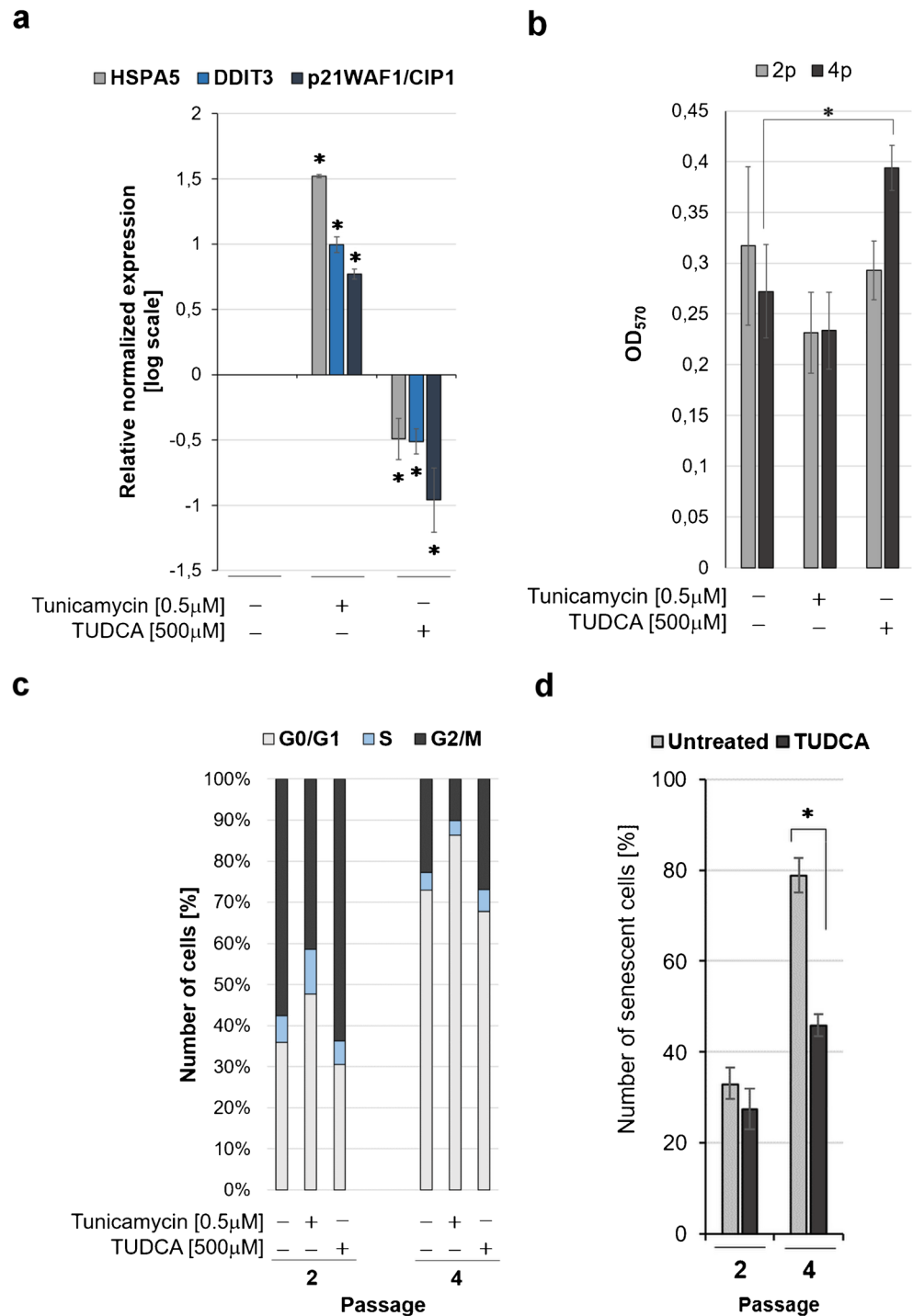


Fig. 3 Transmission electron microscopy (TEM) of passage 2 (a–c) and passage 4 (d–f) mOSE, visualizing cell ultrastructure and quantifying frequency of cell showing ER abnormalities (g). Red contours indicate

ER cisterns. Tunicamycin was used as positive control of ER stress, inducing massive dilatation and vacuolization of ER cisterns. Scale bars indicate 2 μ m

Fig. 4 Tunicamycin upregulates and TUDCA downregulates mRNA expression of principal regulators of ER stress response HSPA5, DDIT3, and cell cycle inhibitor p21^{WAF1/CIP1} in P4 mOSE, as documented by qRT-PCR. Data from three independent experiments. Asterisks indicate statistical significance at $p < 0.05$ (a). Tunicamycin decreases and TUDCA increases viability of mOSE as determined by MTT assay. Data from three independent experiments. Asterisk indicates statistical significance at $p < 0.05$ (b). Untreated mOSE of passage 4 as well as tunicamycin-treated passages 2 and 4 arrest in G1/S phase of cell cycle. TUDCA slightly promotes reentry to cell cycle. Distribution of cell in cell cycle phases was revealed by propidium iodide staining and flow cytometry. Data shows representative of three independent experiments (c). TUDCA decreases number of senescent cells in culture of passage 4 mOSE as documented by SA- β -gal cytochemical staining. Asterisk indicates statistical significance at $p < 0.05$ (d)



phenotype of immortalized OSE and enhanced migration and proliferation of epithelial cells (Lawrenson et al. 2010). Cell senescence is generally considered as a tumor suppressive mechanism. Senescent cells cease dividing but, however, keep a high metabolic activity and alter local microenvironment by acquiring the senescent-associated secretory phenotype leading to potentially deleterious effects on tissue architecture (Coppe et al. 2010).

Induction of senescence integrates various intrinsic and extrinsic stimuli. Typically, replicative senescence is associated with telomere shortening, originally described by Hayflick (Hayflick and Moorhead 1961), but oxidative stress, oncogene activation, or pharmacological treatment induces irreversible cell cycle arrest in p53/p21^{WAF1/CIP1}- or p16^{INK4}-dependent manner in stress-induced senescence. Moreover, protein homeostasis is disturbed in aged cells, and overexpression

of ER chaperons, such as HSPA5, may represent a protective, adaptive mechanism, as documented in cardiomyocytes, neurons, or skeletal muscles (Cummings et al. 2001; Feng et al. 2014; McArdle et al. 2004). ER then represents a signaling hub, where various stress stimuli integrate and evoke HSPA5-dependent response. In aging tissues, development of ER stress follows induction of senescence as documented in various models encompassing both mesenchymal and epithelial phenotypes (Pluquet et al. 2015).

Deregulation of OSE under stress or senescence conditions can represent a potentially hazardous event that either form a permissive microenvironment for direct malignant transformation of OSE or the colonization of ovarian surface by cancer cells from extra-ovarian sources, and development of ovarian cancer. We have shown previously that alleviation of ER stress induced by loss of subunit of ER-integral oligosaccharyltransferase complex, TUSC3, in ovarian or prostate cancer cells enhances their viability, promotes EMT and cell migration in vitro (Horak et al. 2014; Kratochvilova et al. 2015), and decreases overall and disease-free survival of ovarian cancer patients (Pils et al. 2013). Extrinsic alleviation of ER-tress by TUDCA was shown to prevent aggregating of misfolded proteins, alleviate ER stress, and hinder UPR-mediated cell death (Uppala et al. 2017; Yoon et al. 2016). Moreover, TUDCA was demonstrated to recruit endothelial progenitors in neovasculogenesis and tissue repair (Cho et al. 2015). Here, we demonstrate that UPR is evoked in mOSE cells entering senescence and show that alleviation of ER stress by TUDCA delays onset of senescence. In summary, ER stress evoked in ovarian cortex during aging and senescence therefore represents the important cellular mechanism linked to tissue stability and homeostasis

Acknowledgements We acknowledge the core facility CELLIM of CEITEC supported by the Czech-BioImaging large RI project (project no. LM2015062 funded by MEYS CR) for their support with obtaining scientific data presented in this paper.

Funding information This work was supported by the Grant Agency of Masaryk University (project no. MUNI/A/1298/2017) and European Regional Development Fund (Center for Analysis and Modeling of Tissues and Organs, CZ.1.07/2.3.00/20.0185).

Compliance with ethical standards

All procedures performed in studies involving animals were in accordance with the ethical standards of the institution or practice at which the studies were conducted. Animal experiments were supervised by the local ethical committee of the Faculty of Medicine, Masaryk University and performed by certified individuals (KV, PV, and LM). This article does not contain any studies with human participants performed by any of the authors.

Competing interests The authors declare that they have no conflict of interest.

References

- Auersperg N, Wong AS, Choi KC, Kang SK, Leung PC (2001) Ovarian surface epithelium: biology, endocrinology, and pathology. *Endocr Rev* 22:255–288
- Cho JG, Lee JH, Hong SH, Lee HN, Kim CM, Kim SY, Yoon KJ, Oh BJ, Kim JH, Jung SY, Asahara T, Kwon SM, Park SG (2015) Tauroursodeoxycholic acid, a bile acid, promotes blood vessel repair by recruiting vasculogenic progenitor cells. *Stem Cells* 33:792–805
- Coppe JP, Desprez PY, Krtolica A, Campisi J (2010) The senescence-associated secretory phenotype: the dark side of tumor suppression. *Annu Rev Pathol-Mech* 5:99–118
- Cummings CJ, Sun Y, Opal P, Antalffy B, Mestrlil R, Orr HT, Dillmann WH, Zoghbi HY (2001) Over-expression of inducible HSP70 chaperone suppresses neuropathology and improves motor function in SCA1 mice. *Hum Mol Genet* 10:1511–1518
- Fathalla MF (2013) Incessant ovulation and ovarian cancer—a hypothesis re-visited. *Facts Views Vis Obgyn* 5:292–297
- Feng Y, Huang W, Meng W, Jegga AG, Wang Y, Cai W, Kim HW, Pasha Z, Wen Z, Rao F, Modi RM, Yu X, Ashraf M (2014) Heat shock improves Sca-1+ stem cell survival and directs ischemic cardiomyocytes toward a prosurvival phenotype via exosomal transfer: a critical role for HSF1/miR-34a/HSP70 pathway. *Stem Cells* 32:462–472
- Flesken-Nikitin A, Hwang C-I, Cheng C-Y, Michurina TV, Enikolopov G, Nikitin AY (2013) Ovarian surface epithelium at the junction area contains a cancer-prone stem cell niche. *Nature* 495:241
- Hayflick L, Moorhead PS (1961) The serial cultivation of human diploid cell strains. *Exp Cell Res* 25:585–621
- Horak P, Tomasich E, Vanhara P, Kratochvilova K, Anees M, Marhold M, Lemberger CE, Gerschpacher M, Horvat R, Sibilica M, Pils D, Krainer M (2014) TUSC3 loss alters the ER stress response and accelerates prostate Cancer growth in vivo. *Sci Rep* 4:3739
- Huang N, Yu Y, Qiao J (2017) Dual role for the unfolded protein response in the ovary: adaption and apoptosis. *Protein Cell* 8:14–24
- Kido M, Shibuya M (1998) Isolation and characterization of mouse ovarian surface epithelial cell lines. *Pathol Res Pract* 194:725–730
- King SM, Quartuccio SM, Vanderhyden BC, Burdette JE (2013) Early transformative changes in normal ovarian surface epithelium induced by oxidative stress require Akt upregulation, DNA damage and epithelial-stromal interaction. *Carcinogenesis* 34:1125–1133
- Kratochvilova K, Horak P, Esner M, Soucek K, Pils D, Anees M, Tomasich E, Drafi F, Jurtikova V, Hampl A, Krainer M, Vanhara P (2015) Tumor suppressor candidate 3 (TUSC3) prevents the epithelial-to-mesenchymal transition and inhibits tumor growth by modulating the endoplasmic reticulum stress response in ovarian cancer cells. *Int J Cancer* 137:1330–1340
- Kratochvilová K, Morán L, Paďourová S, Stejskal S, Tesařová L, Šimara P, Hampl A, Koutná I, Vaňhara P (2016) The role of the endoplasmic reticulum stress in stemness, pluripotency and development. *Eur J Cell Biol*
- Kurman RJ, Shih Ie M (2016) The dualistic model of ovarian carcinogenesis: revisited, revised, and expanded. *Am J Pathol* 186:733–747
- Kyathanahalli C, Organ K, Moreci RS, Anamthatmakula P, Hassan SS, Caritis SN, Jeyasuria P, Condon JC (2015) Uterine endoplasmic reticulum stress-unfolded protein response regulation of gestational length is caspase-3 and-7-dependent. *Proc Natl Acad Sci U S A* 112:14090–14095
- Laszczynska M, Brodowska A, Starczewski A, Masiuk M, Brodowski J (2008) Human postmenopausal ovary—hormonally inactive fibrous connective tissue or more? *Histol Histopathol* 23:219–226
- Lawrenson K, Grun B, Benjamin E, Jacobs IJ, Dafou D, Gayther SA (2010) Senescent fibroblasts promote neoplastic transformation of partially transformed ovarian epithelial cells in a three-dimensional model of early stage ovarian cancer. *Neoplasia* 12:317–325

- McArdle A, Dillmann WH, Mestrlil R, Faulkner JA, Jackson MJ (2004) Overexpression of HSP70 in mouse skeletal muscle protects against muscle damage and age-related muscle dysfunction. *FASEB journal* : official publication of the Federation of American Societies for Experimental Biology 18:355–357
- Miki Y, Swensen J, Shattuck-Eidens D, Futreal PA, Harshman K, Tavtigian S, Liu Q, Cochran C, Bennett LM, Ding W, Bell R, Rosenthal J, Hussey C, Tran T, McClure M, Frye C, Hattier T, Phelps R, Haugen-Strano A, Katcher H, Yakumo K, Gholami Z, Shaffer D, Stone S, Bayer S, Wray C, Bogden R, Dayananth P, Ward J, Tonin P, Narod S, Bristow PK, Norris FH, Helvering L, Morrison P, Rosteck P, Lai M, Barrett JC, Lewis C, Neuhausen S, Cannon-Albright L, Goldgar D, Wiseman R, Kamb A, Skolnick MH (1994) A strong candidate for the breast and ovarian cancer susceptibility gene BRCA1. *Science* 266:66–71
- Okamura H, Katabuchi H, Nitta M, Ohtake H (2006) Structural changes and cell properties of human ovarian surface epithelium in ovarian pathophysiology. *Microsc Res Tech* 69:469–481
- Pils D, Horak P, Vanhara P, Anees M, Petz M, Alfanzi A, Gugerell A, Wittlinger M, Gleiss A, Auner V, Tong D, Zeillinger R, Braicu EI, Sehouli J, Krainer M (2013) Methylation status of TUSC3 is a prognostic factor in ovarian cancer. *Cancer* 119:946–954
- Pluquet O, Pourtier A, Abbadie C (2015) The unfolded protein response and cellular senescence. A review in the theme: cellular mechanisms of endoplasmic reticulum stress signaling in health and disease. *Am J Physiol Cell Physiol* 308:C415–C425
- Uppala JK, Gani AR, Ramaiah KVA (2017) Chemical chaperone, TUDCA unlike PBA, mitigates protein aggregation efficiently and resists ER and non-ER stress induced HepG2 cell death. *Sci Rep* 7: 3831
- Urzua U, Ampuero S, Roby KF, Owens GA, Munroe DJ (2016) Dysregulation of mitotic machinery genes precedes genome instability during spontaneous pre-malignant transformation of mouse ovarian surface epithelial cells. *BMC Genomics* 17:728
- Wang M, Kaufman RJ (2014) The impact of the endoplasmic reticulum protein-folding environment on cancer development. *Nat Rev Cancer* 14:581–597
- Xie YX, He YG, Cai ZL, Cai JH, Xi MY, Zhang YD, Xi JK (2016) Tauroursodeoxycholic acid inhibits endoplasmic reticulum stress, blocks mitochondrial permeability transition pore opening, and suppresses reperfusion injury through GSK-3 beta in cardiac H9c2 cells. *Am J Transl Res* 8:4586–4597
- Yeung BHY, Kwan BWY, He QY, Lee AS, Liu J, Wong AST (2008) Glucose-regulated protein 78 as a novel effector of BRCA1 for inhibiting stress-induced apoptosis. *Oncogene* 27:6782–6789
- Yoon YM, Lee JH, Yun SP, Han YS, Yun CW, Lee HJ, Noh H, Lee SJ, Han HJ, Lee SH (2016) Tauroursodeoxycholic acid reduces ER stress by regulating of Akt-dependent cellular prion protein. *Sci Rep* 6:39838

11. Kolářová L, Vaňhara P, Pena-Mendez EM, Hampl A, Havel J. Tissue visualization mediated by nanoparticles: from tissue staining to mass spectrometry tissue profiling and imaging. In: Seifalian A (ed). *Nanomedicine*. Manchester, UK: One Central Press 2014; pp. 468-82.

Commentary:

A monograph chapter suggesting applications of MALDI-TOF MS methods in tissue visualizations based on various nanoparticles.

ISBN: 978-1-910086-01-8

Chapter in monograph

Number of citations (WOS, 2017): Not indexed in WOS

Contribution of the author: Shared 1st-authorship. Design and writing of manuscript.

19

Tissue visualization mediated by nanoparticles: from tissue staining to mass spectrometry tissue profiling and imaging

Lenka Kolářová^{1#}, Petr Vaňhara^{2#}, Eladia María Peña-Méndez³, Aleš Hampel^{2,4} and Josef Havel^{1,2,5,6*}

¹Department of Chemistry, Faculty of Science, Masaryk University, Kamenice 5/A14, 625 00 Brno, Czech Republic

²Department of Histology and Embryology, Faculty of Medicine, Masaryk University, Kamenice 3/A1, 625 00 Brno, Czech Republic

³Department of Analytical Chemistry, Nutrition and Food Science, Faculty of Chemistry, University of La Laguna, Campus de Anchieta, 38071 La Laguna, Tenerife, Spain

⁴International Clinical Research Center, St. Anne's University Hospital, Brno, Czech Republic, Pekařská 53, 656 91 Brno, Czech Republic

⁵Department of Physical Electronics, Faculty of Science, Masaryk University, Kotlářská 2, 611 37 Brno, Czech Republic

⁶R&D Centre for Low-Cost Plasma and Nanotechnology Surface Modifications, CEPLANT, Masaryk University, Kotlářská 2, 611 37 Brno, Czech Republic

#These authors contributed equally.

Outline:

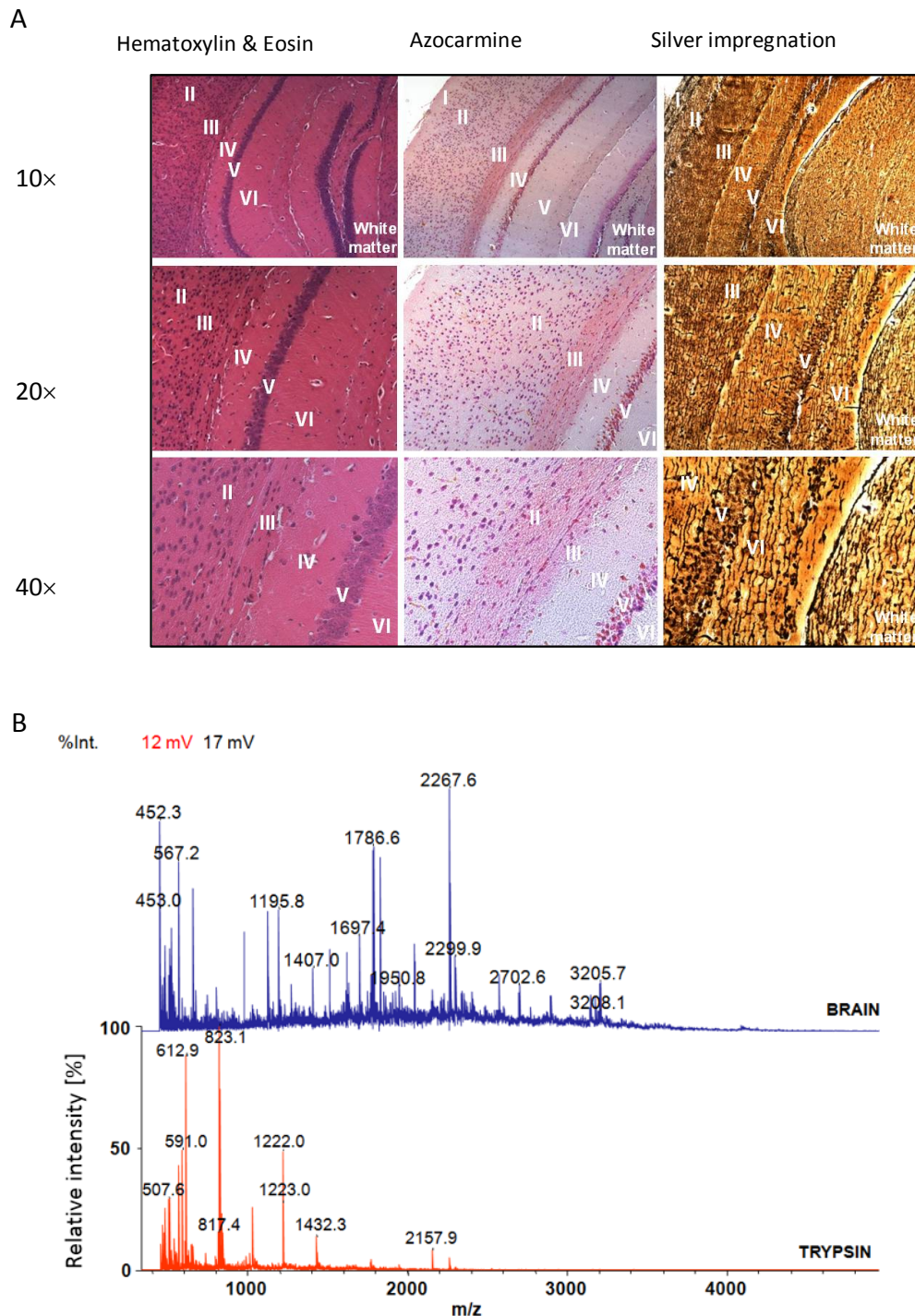
Introduction	469
From tissue staining to tissue imaging	469
Nanoparticles as visualization agents	471
Tissue imaging by MS	475
<i>Ionization methods for IMS</i>	477
<i>MALDI MS</i>	477
<i>SIMS</i>	478
<i>DESI MS</i>	479
<i>Application of MALDI-TOF MS in tissue analysis</i>	479
<i>Histological staining and IMS</i>	480
NP-Mediated IMS	480
Conclusions	482
Acknowledgements	483
References.....	483

Introduction

For decades, visualization of cell and tissue structures by chemical staining developed for optical microscopy was the only option for a clinical histopathological diagnosis or biomedical research in a tissue context. A cardinal breakthrough was later achieved by the introduction of antibody-based techniques that provided spatial resolution and antigen specificity at the cellular and sub-cellular levels. Presently, classical methods of tissue analysis are complemented with various instrumental methods to provide global information on tissue architecture, reflecting the chemical composition of the tissue, including spatial distribution of metabolites, regional structural differences of the extracellular matrix or secreted proteins and other large molecules. These techniques include Raman spectroscopy (RS), magnetic resonance imaging (MRI), ultrasonography (US), computed tomography (CT) or positron emission tomography (PET), single-photon emission CT (SPECT) or mass spectrometry (MS). In this review, we provide a brief overview of the application of nanotechnology in histology methods, particularly in bioanalytical tissue MS imaging.

From tissue staining to tissue imaging

Tissue staining is an established histological technique that reveals structural patterns that are not clear or sufficiently visible to be observed directly. The first dyes used for staining of tissue structures were colored substances isolated from natural resources—e.g., indigo, saffron, hematoxylin, azocarmine, and orcein. These dyes were commonly used for dyeing textile fibers and later found wide application in histology. The onset of synthetic dyes further enhanced histopathological analyses since the invention and application of aniline dyes in 1856 [1]. However, various tissues, including neural or lymphatic tissue, resisted staining using large molecular dyes. When the impregnation by silver salts and other non-classical-dyes was introduced to histological analysis [2], fine molecular structures of complex organs were revealed—e.g., reticulin networks in the spleen or the architecture of the brain isocortex (Fig. 19.1A). Decades later, the application of fluorescent dyes or enzymes linked to specific antibodies, together with confocal microscopy, shifted histological analysis from subjective morphological evaluation to the analysis of particular molecular patterns or epitopes even in an automated manner [3]. Advances in analytical chemistry, particularly in MS, and its orientation in complex biological problems, contributed to the development of techniques for the direct analysis of chemical tissue composition, thereby enhancing the potential of current diagnostics in cancer [4] or pharmaceutical research [5]. Mass spectra with individual peaks corresponding to molecules of a particular molecular weight and charge (i.e., the m/z ratio) provide individual tissues with their unique spectral fingerprint (Fig. 19.1B) and an input for “bottom-up” proteomics. The progress of micromanipulation techniques, such as laser-captured microdissection allowed topologically highly correlated MS-based proteomic analysis on very small but precisely defined cell populations [6].

**FIGURE 19.1**

(A) Architecture of the mouse isocortex and adjacent cerebral white matter, visualized by classical histological techniques. Brain tissue was fixed in formalin and embedded in paraffin (FFPE). Sections of the isocortex were stained with hematoxylin and eosin, azocarmine and silver impregnation according to standard protocols [7]. Roman numerals correspond to individual layers in the isocortex (I: *Lamina zonalis*; II: *L. granularis externa*; III: *L. pyramidalis*; IV: *L. granularis interna*; V: *L. ganglionaris*; VI: *L. multiformis*). Deposition of silver nanocrystals within neural structures and neurons reveals structural patterns that are poorly distinguished by standard staining. (B) A unique molecular fingerprint of mouse brain tissue. The spectral profile of the digested surface proteins was generated by matrix-assisted laser desorption/ionization-time-of-flight (MALDI TOF) MS (blue). Brain tissue in the form of FFPE sections was deparaffinized and trypsinized (red) prior to MS

Presently, the term “tissue imaging” is dedicated to advanced methods of visualizing tissue structures ranging from *in vivo* imaging of whole organs to high-resolution cell tracking or revealing the chemical composition and metabolomic profiles. For decades, classical histological methods have been based on specific chemical staining of tissue sections, selective for proteins, peptides, lipids, metabolites or other biomolecules or drugs. Despite precise positional information within a tissue, standard topological dyes have provided only limited information concerning chemical composition or structural specificity. However, antibody-based techniques developed for visualization of fixed structures are generally not compatible with imaging *in vivo* due to protein degradation or limited penetration into tissues. Nanoparticles containing a metallic core and a functionalized shell that were recently introduced to bioimaging technology showed surprisingly effective capability to migrate to the desired site, interact with the target tissue and deposit in specific sites.

Nanoparticles as visualization agents

A nanoparticle (NP) is defined as a single unit with a size varying between ~1 and 100 nm and showing uniform parameters and properties that are not present on a larger scale [8]. Recent advances in nanotechnology brought NPs to the broad interest of the scientific community due to their unique chemical, optical, electronic, magnetic and structural properties. NPs have found wide applications in biomedicine, ranging from research to diagnostics, prediction or therapeutics [9]. Because the size of NPs reaches cellular or sub-cellular levels while maintaining their capability to directly interact with molecular structures, NPs are greatly attractive in fluorescent microscopy as quantum dots [10, 11] or contrasting agents for tissue *in vivo* imaging (MRI), particularly regarding the labeling and tracking of migrating cancer or stem cells [12] or enhancing other types of analysis—e.g., MS. NPs can be synthesized from various materials ranging from carbon to metals and functionalized according to the desired function or visualization techniques. Functionalization of NPs covers a broad range of modifications of the NP core or engineering of an NP shell. Properties of NPs can be further tuned to a particular task by the composition of different biocompatible compounds that allow use in living cells. This is particularly true for many cancers that preferentially uptake various metabolites or biomolecules compared with normal tissue. Iron oxide NPs coated with the heavy chain of human ferritin (M-HFn) were found to interact with the transferrin receptor that is predominantly expressed on cancer cells. The iron core possesses catalytic activity and allows the oxidation of standard peroxidase substrates—e.g., tetramethylbenzidine or diazoaminobenzene. The deposition of M-HFn NPs in cultured cancer cells or within a fixed tissue allowed for precise identification of malignant cells in histological sections [13]. Recently, fluorescent nanodiamonds were applied to track implanted lung progenitor cells during engraftment from intravenous administration to final homing into terminal bronchioles [14]. Therefore, simple administration of such biospecific NPs provides an analytical output without any further targeting ligand or contrasting substrate. Specific interaction of engineered NPs with cellular or tissue structures opens a possibility to detect bound para- or supermagnetic NPs *in vivo*—e.g., using MRI or other multimodal imaging techniques such as CT, SPECT or fluorescence-based techniques. In a breast cancer cell line study, Tietz and colleagues encapsulated an iron oxide core in an epichlorohydrin cross-linked dextran polymer, conjugated with a cyclopentapeptide with high affinity to a CXCR4 chemokine receptor. Breast cancer MDA-MB-231 cells overexpressing CXCR4 preferentially bound CXCR4-specific NPs and provided a negative contrast MRI image [15]. Iron oxide NPs were used for MRI tracking of implanted mouse embryonic stem cells into the site of the lesion where the labeled cells provide a hypointense MRI signal [16]. The superparamagnetic iron oxide NPs are generally safe and well-tolerated compounds [17] currently approved for administration in patients using various modalities.

Lanthanide core NPs specifically influence the relaxation times of protons in their close proximity and, compared with iron oxide NPs, provide a positive MRI contrast. Contrasting agents based on gadolinium (Gd^{3+}) chelates, however, may induce adverse reaction in some patients—e.g., nephrogenic systemic fibrosis [18]. To overcome this obstacle, modification of the structures coating the Gd core has been described—e.g., polyethyleneglycol/polyethylenimine [19], silica coating [20], various metal-organic frameworks (MOFs) [21] or nanocarbon (nanodiamonds) [22]. Due to their molecular structure, MOFs are highly attractive as drug-delivery vehicles or imaging agents (Fig. 19.2). Targeted complex Gd NPs then show high specificity to the investigated tissue—e.g., cancer-lesioned liver [23] or melanin-containing melanoma cells [24]. Replacement of the coated core metal with an inert element—e.g., gold—and building up a scaffold with similar structural properties to the extracellular matrix or a cell membrane have decreased the toxicity of MRI-contrasting NPs, enhanced the imaging properties [25] and also allowed for multiple analysis using, for example, fluorescence sorting, MS profiling, antibody-based techniques, magnetic labeling or electron microscopy [22, 26, 27]. The mesoporous silica-coated hollow manganese oxide demonstrated low cellular and systemic toxicity when electroporated into the mesenchymal stem cells (MSCs) and tracked by MRI after stereotactic injection into the putamen of the mouse. Moreover, MSCs containing silica-coated manganese NPs retained their viability, and their differentiation potential was uncompromised. Importantly, the architecture of mesoporous silica shell NPs provided access of water molecules to the manganese core and enhanced the positive contrast of the MR image. Deposition of labeled MSCs in hyperintense MRI loci allowed stable tracking with high spatial resolution over prolonged time periods [28].

Recently, nanoscale metal-organic frameworks (NMOFs) emerged as promising biomedical or bioengineering tools for imaging and drug delivery [29-31]. NMOFs are a new class of hybrid materials in nanometer size consisting of metal ions and organic bridging ligands (Fig. 19.2). The chemical properties of these materials, such as their structural and molecular diversity, type of metallic core (e.g., Yb, Gd, Mn, or Fe), high loading capacity, and intrinsic biodegradability make them suitable for direct *in vivo* imaging using near-infrared microscopy [32] or MRI [33].

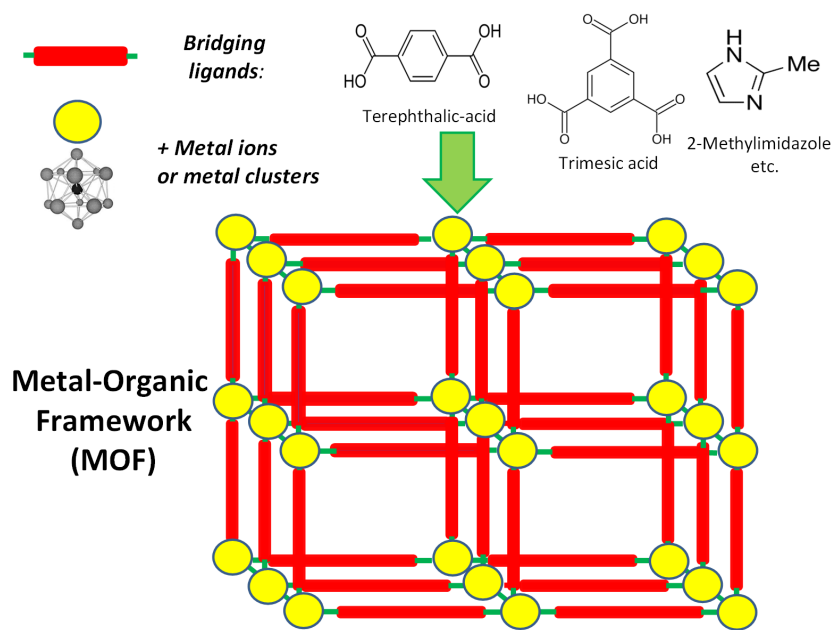


FIGURE 19.2
Molecular structure of an MOF NP

Gold NPs (AuNPs) are a promising class of NPs with a lower frequency of adverse effects of lanthanide NPs *in vivo* and a longer life-time than iron NPs. Individual AuNPs (Fig. 19.3) or their clusters (Fig. 19.4) can be directly modified by various structures that either improve a detection method, enhance specificity or reduce toxicity and improve clearance. For example, nanoflares are highly functionalized NPs that bring extreme detection specificity to the level of single molecules of nucleic acids. Thus, the conjugation of specific oligonucleotides to AuNPs combines very high specificity with a potent fluorescence activity and low toxicity to the cell. Standard techniques for mRNA detection are based on the detection of an interaction event between a fluorophore-labeled oligonucleotide with its target sequence. However, major obstacles lie in the delivery method into cells, a high background compromising the specificity of the assay and enzymatic degradation of the reporters. AuNP-based nanoflares possess the unique capability of detecting individual mRNAs in living cells without enzymatic degradation of the vehicles or the need for transfection reagents for delivery [34, 35].

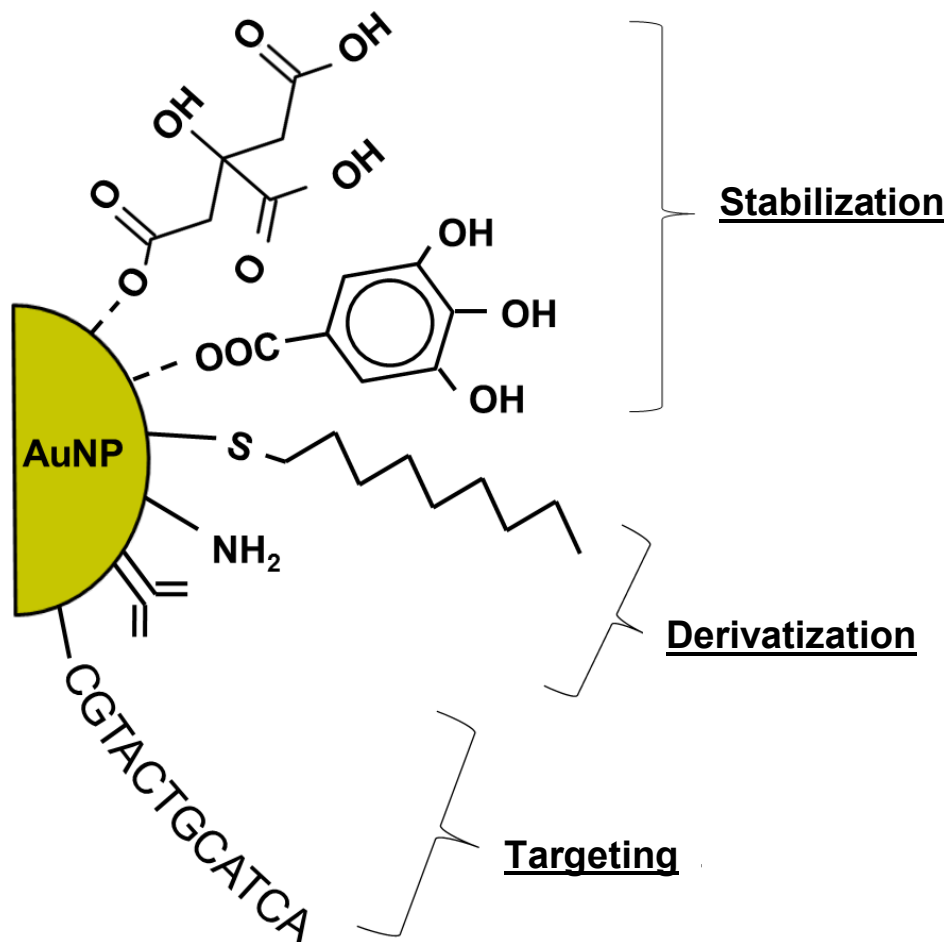
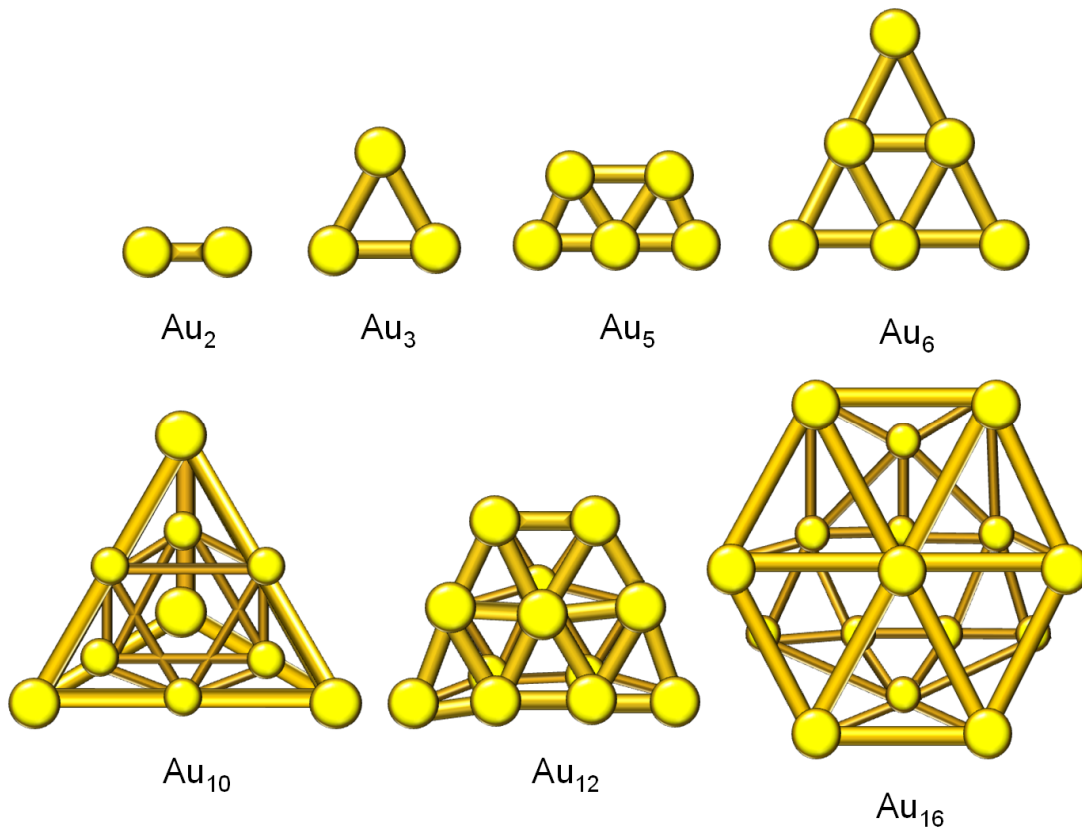


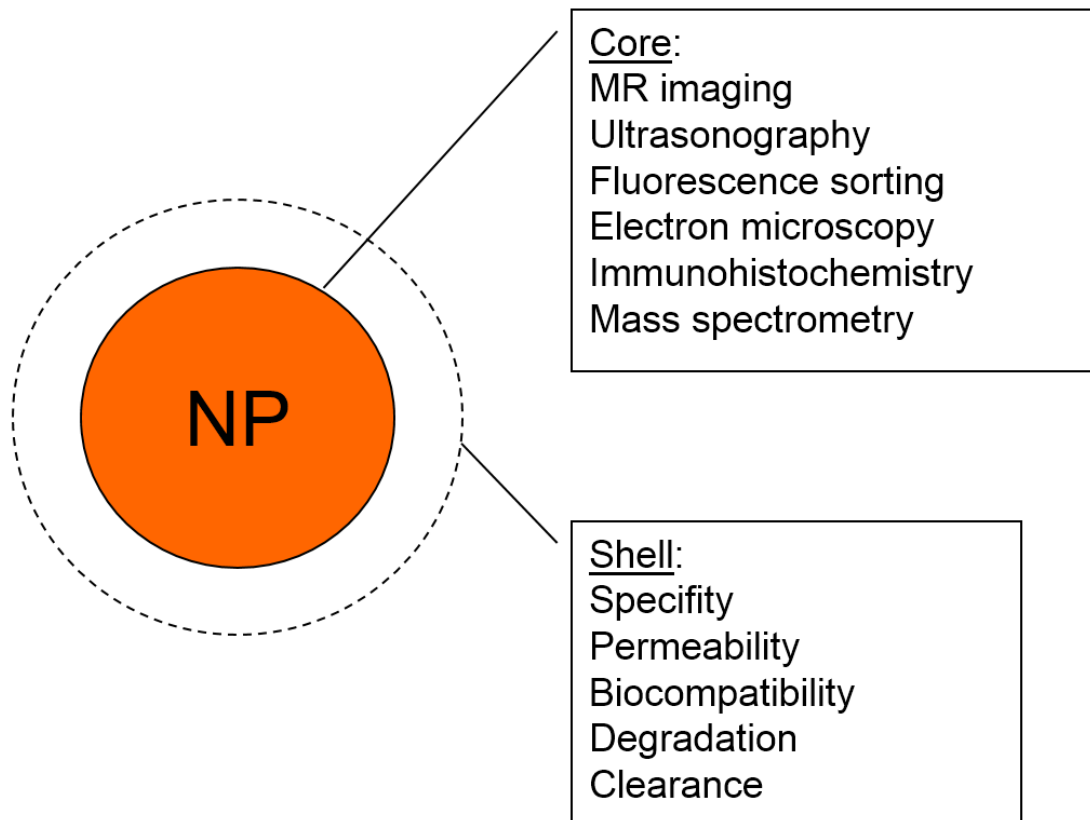
FIGURE 19.3

Example of direct modifications of AuNPs. AuNPs can be stabilized using citric acid or gallic acid. Derivatization by introducing various functional groups or even biomolecules (e.g., thiol, amino, antibody, and oligonucleotides) can enhance the binding specificity to particular tissue structures, antigens or even individual sequences of DNA or RNA. Dashed or full lines indicate non-covalent or covalent bonds, respectively

**FIGURE 19.4**

AuNPs form clusters of various sizes and complexity. Gold clusters up to Au_{10} are known to be planar, higher Au clusters possess three-dimensional structure, and some of them (Au_m , where $m=16,17,18$) might be empty, representing gold fullerenes, which are hollow gold cages that can form endohedral complexes—e.g., $M@Au_{16}$, where M is a foreign metal inside the cage

Therefore, NP engineering defines physical parameters that are critical for the particular imaging method but also determines biological properties, such as target specificity, migration through the tissue environment, retention in the vascular system, renal excretion or the efficacy of the cellular uptake, which can dramatically influence the information value of the diagnostic or analytical output (Fig. 19.5).

**FIGURE 19.5**

Engineering of the core and shell determines performance in various imaging techniques and targeting specificity, and prevents degradation or adverse effects *in vivo*

Tissue imaging by MS

MS allows the rapid detection, localization and identification of many molecules from the very simple to the most complex (e.g., biomolecules). Tissue MS is a label-free technique that can provide detailed understanding of biological processes in a broad cellular context and whole biological systems. A principle of MS techniques is demonstrated in the MALDI-TOF MS example summarized in Fig. 19.6. The development of imaging MS (IMS) provided the unique ability to analyze hundreds of analytes in a one experiment without prior knowledge of the tissue composition or the use of antibodies or staining reagents. Another advantage of this technique is the maintenance of spatial molecular patterns because tissue samples are analyzed without prior homogenization (mechanical disruption of tissue, creating a homogenous mixture) or fractionation (division of homogeneous mixture into individual fractions) [36, 37]. Homogenization and fractionation belong to classical approaches of sample preparation; however, these techniques affect the distribution of particular molecules (spatial information) and destroy morphological structures. Moreover, the IMS approach can visualize the global biochemical heterogeneity of individual cell populations and tissue structures at the single-cell level [38]. IMS can be applied in a wide area of “omics” research such as proteomics, lipidomics,

metabolomics, metallomics, and drug discovery, and is a topic that was reviewed in detail recently [39].

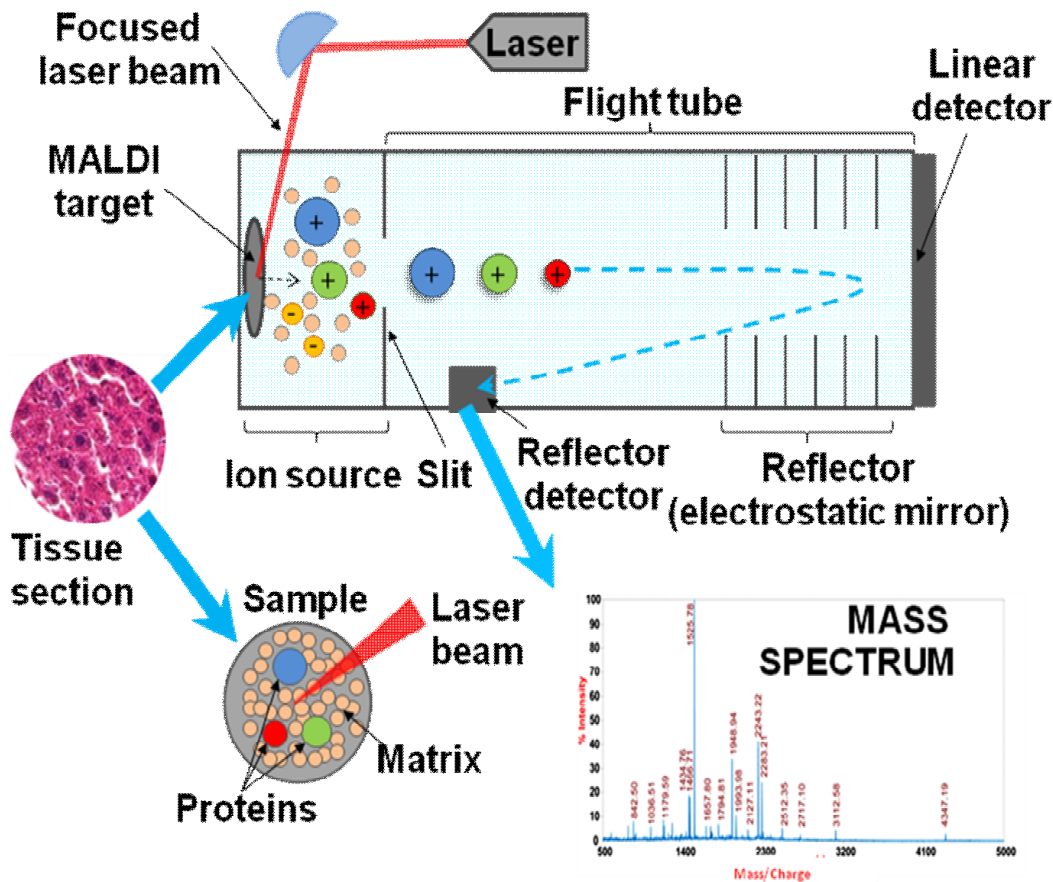


FIGURE 19.6

Principle of MALDI-TOF MS. Tissue molecules co-crystallized with a matrix (defined below) are desorbed by a laser beam from a sample surface. Ions enter into the flight tube towards a detector. The time of flight and intensity of the signal are recorded; next the ratio of the molecular weight (m/z) to charge is determined

Depending on the experimental design, the output is either a single mass profile of a nonspecific tissue region or a homogeneous cell population, or a panel of mass spectra recorded in high resolution from defined coordinates and containing spatial information [40]. The IMS approach efficiently combines the analysis of molecular species and their distribution together with morphological and histopathological information. Moreover, fixed tissues prepared for routine histology are compatible with IMS or other various modifications of MS, enabling analysis of various samples stored at medical facilities [41]. However, IMS requires modifications of virtually all steps of the standard “profiling” MS protocol. To achieve a desired resolution, the sample preparation and application retrieving the surface molecules for ionization, instrumental setup, data acquisition and mass spectra analysis in parallel with histological assessment need to be optimized [42–45]. A scheme depicting the difference between MS profiling and MS imaging is shown in Fig. 19.7.

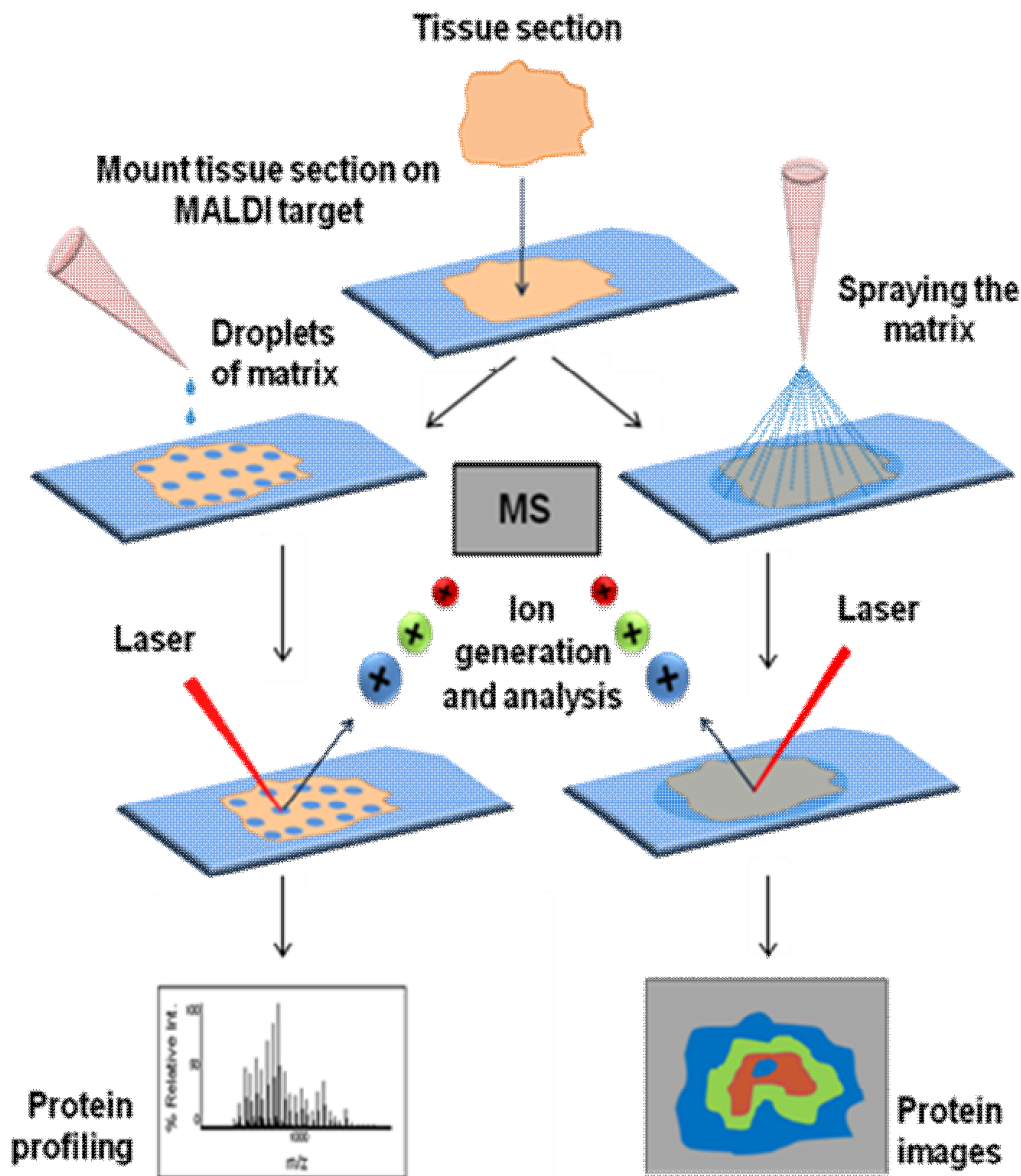


FIGURE 19.6
Principle of mass spectrometry profiling and imaging on intact tissue sections

Ionization methods for IMS

Ionization is a critical step in the entire process of IMS, determining the quality of recorded spectra, spatial resolution and content of biologically relevant information. Presently, there is a broad range of surface ionization methods adopted for IMS from bioanalytical MS; however, MALDI MS, secondary ion MS (SIMS) and desorption electrospray ionization (DESI) are the most common.

MALDI MS

MALDI is a soft ionization technique based on mixing a sample with an excessive amount of a matrix and subsequent desorption and ionization of the sample molecules by a short (~ns) laser pulse usually

in a high vacuum (about 10^{-4} Pa) [46]. The matrix plays a key role in the absorption of laser energy of a certain wavelength, which is then passed to the analyte, causing a transition of the analyte from the solid phase into the gas phase and preventing fragmentation molecules of the sample by using a direct laser beam. The matrix is at the same time a donor or acceptor of protons to the sample molecules in the positive or negative mode. The mechanism of proton transfer from the matrix to the analyte remains unclear. This technique preferentially provides pseudomolecular $[M \pm H]^{\pm}$ ions of the analyte but sometimes can be observed in the spectra of other ions, such as $[M + 2H]^{2+}$, $[M + 3H]^{3+}$ ions or dimers $[2M + H]^+$, and others. MALDI enables the ionization of biomolecules over a wide mass range, including DNA, peptides, proteins, lipids and many other substances. MALDI MS is often the chosen bioanalytical method because of its sensitivity, its tolerance to impurities and simple preparation of the sample [38].

The correct choice of matrix is one of the most important steps in MALDI IMS. As the matrix, organic aromatic acids are usually used. Each matrix is suitable for different analytes. For example, the most commonly used matrix in MALDI-TOF of cellular or tissue samples is sinapinic acid suitable for the detection of higher molecular weight proteins, α -cyano-4-hydroxycinnamic acid for the detection of lipids and lower molecular weight peptides and 2,5-dihydrobenzoic acid or 2,6-dihydroxyacetophenone for the ionization of phospholipids and drugs [47]. Various matrices differently affect desorption and, thus, ionization of the analyte. The interaction of the analyte with the matrix might also improve the ionization efficiency. The application of a MALDI matrix on the sample of tissue section affects substantially the assay output. In MALDI IMS of a tissue section, the matrix solution needs to be homogeneously deposited over the sample—e.g., by spraying the matrix over the entire surface of the tissue. However, the regions desired for single profiling can be defined by simple deposition of matrix droplets to particular regions of the tissue section [48].

Manual methods of matrix deposition such as airbrush spraying or dipping the tissue sections into a matrix-containing solution usually suffer from poor reproducibility [49]. Automated deposition allows the deployment of a very thin layer of matrix with an IMS quality suitable also for high-throughput preparations [50]. The most common mass analyzer in combination with the MALDI technique is the TOF, which provides high mass resolution, excellent mass accuracy, and a rapid acquisition rate over a large mass range [51].

SIMS

SIMS was the first ionization technique in MS used for chemical imaging [52]. The main advantage of SIMS is the spatial resolution level at the submicron level as low as 50 nm, making this approach suitable for investigating the chemical composition of single cells or even subcellular structures [38]. SIMS is based on irradiation of the sample surface by a primary beam of high energy containing metal ions (e.g. Ar^+ , Ge^+ , or In^+). These primary ions generate the emission of secondary ions from the sample surface. The energy of the primary ion is much higher (range 5–25 keV) than the energy of the laser beam in MALDI experiments; thus, SIMS often leads to extensive fragmentation of surface molecules and is classified as a hard ionization technique. SIMS typically desorbs and ionizes elements and small molecules, such as lipids, metabolites, and small drugs, with an upper mass limit about 2 kDa. However, ion beams can be focused with a much higher spatial precision than laser beams. SIMS represents a unique tool for high-resolution IMS of single cells, their organelles and structures or to accurately define tissue regions [53]. This technique does not require any special sample preparation or a matrix. SIMS analyses are carried out in an ultrahigh vacuum ($<10^{-7}$ Pa) to facilitate the transfer of ions after desorption from the sample surface.

SIMS is commonly combined with TOF, magnetic sector or Orbitrap analyzers [54]. According to the experimental design, SIMS works in either the static or dynamic mode. In the static mode, a primary ion beam is used at a dose less than 10^{12} primary ions/cm² for desorption of the molecule from the surface and provides information about the composition of the surface. Static SIMS is mostly used for qualitative imaging. Dynamic SIMS is more destructive because a much larger primary ion dose ($>10^{12}$ primary ions/cm²) is applied on the sample, uncovering deep structures. Dynamic SIMS is mainly used for quantitative elemental imaging [55].

DESI MS

The DESI ionization technique was developed by the Cooks group in 2004 [56] and was first used for MS imaging of biological tissues in 2005 [57]. The DESI principle is based on the concept of the combination of two MS ionization methods—electrospray ionization (ESI) and desorption ionization (DI). DESI occurs by the interaction of charged droplets of solvent (often a mixture of water and methanol at a ratio of 1:1) produced by electrospray with the sample surface. By the collisions of drops with the sample surface, secondary charged droplets containing dissolved surface molecules of sample are generated. These secondary droplets are immediately converted on gaseous ions, which are directed at an appropriate angle into the inlet of the mass analyzer [58]. DESI provides several advantages compared with MALDI and SIMS. DESI is performed at atmospheric pressure and requires no additional sample preparation or addition of the organic matrix. DESI also induces very little fragmentation of the sample, making it suitable for analysis of complex molecules. DESI provides multiply charged ions in the form of $[M + nH]^{n+}$ and $[M - nH]^{n-}$ but at a lower spatial resolution than MALDI or SIMS [53]. The rapid analysis time and its ability to be combined with various MS analyzers make this technique attractive for imaging all types of tissue [51] or particular structures, including polymers, drugs, and lipids [59].

Application of MALDI-TOF MS in tissue analysis

MALDI-TOF MS for tissue analysis has already demonstrated its applicability in clinical and biological problems [60-62]. The generation of tissue-specific molecular weight or m/z maps or images with high resolution and sensitivity provides a tool for pathology, chemotherapeutics, and discovery of disease biomarkers. MALDI-TOF MS allows the rapid detection of more than a thousand peptides and proteins from various tissues covering diverse fields of medicine, ranging from oncology, regenerative medicine, and neurology to pathology, tissue architecture or biomedical research [42, 45, 62-68]. MALDI MS or IMS, with laser capture microdissection, generates expression profiles from individual cells or clinicopathologically relevant regions of tissue. For example, the molecular profiles of tumor tissues can correctly predict tumor behavior, diagnosis, prognosis or response to therapy. Bottom-up proteomics based on complex patterns can lead to the discovery of novel biomarkers [42, 65].

MALDI-TOF MS/IMS has the potential to identify patient subpopulations that are not evident based on the cellular phenotype determined microscopically [58]. In surgical pathology, IMS allows the highly sensitive and rapid evaluation of surgical intraoperative margins [69]. The IMS spectra generated in high resolution from tumor lesions surrounded by healthy tissue requires sophisticated computational analysis to correctly discriminate and classify the samples. For this purpose, a new method was developed involving reconstructing the image from the raw mass-spectral data, preprocessing of IMS data and subsequent classification and identification of IMS data based on artificial neural networks (ANNs) [70]. ANNs are computational simulations of human neural networks for modeling highly nonlinear systems in which the relationship between the variables is unknown or very complex [71].

Histological staining and IMS

Histological staining remains a cornerstone in the routine diagnosis of cellular and tissue pathomorphology. Classical histological techniques require skilled clinical pathologists to diagnose tissue abnormalities. Spectral profiles or images can complement structural information and facilitate or specify a diagnosis [72]. Correct interpretation of MALDI MS/IMS information requires the correlation of specific ion images to histological information. The latter can be accomplished either using the same tissue section for both MALDI MS/IMS and histopathology or by analysis of two consecutive sections. The first approach is complicated by interference of the dye used for tissue staining with ionization during MS. Covalent binding of a dye—e.g., hematoxylin/eosin (H&E)—to the sample surface, reduces the quality of a mass spectrum. However, chemically distinct dyes, such as cresyl violet or methylene blue, are compatible [72]. Nevertheless, the staining pattern provided by these dyes is different than that provided by H&E, and pathological information does not need to be exhaustive. Recently, a staining protocol for tissue sections already analyzed by MS was introduced that allowed a clear correlation to MALDI IMS results [73]. Analysis of consecutive sections requires a precise alignment of neighboring structures. This is often complicated in complex samples, such as neural tissue samples, due to the different microarchitecture and molecular profiles of adjacent tissue sections [74].

The data outlined above apply only to fresh-frozen tissue samples. As the commonly used stains, including H&E, are compatible with formalin-fixed paraffin-embedded tissues [36], the presence of a cross-linked surface due to formalin bridges introduced by fixation of FFPE tissues prevents analysis by MS. The peptide cross-links can be released using enzymatic treatment to make the surface available for MS analysis [75]. The availability of FFPE samples archived throughout the clinical facilities represents an enormously rich material for detailed MS/IMS studies with clear links to clinical practice [76].

NP-Mediated IMS

Nanoscale materials have been widely introduced into bioanalytical MS and IMS research rather recently to overcome obstacles in MS analysis of complex or unstable biological samples. Although it has been demonstrated that classical organic chemical matrices in MALDI-TOF MS enable the detection of peptides, proteins and nucleic acids and other biomolecules [77], there are still unresolved problems in the adaptation of MALDI-TOF MS protocols to IMS:

- 1) The co-crystallization of analytes with matrices does not produce homogeneous mixtures, which cause hot spots, thereby requiring sweet-spot searching [78].
- 2) MALDI-TOF MS can hardly detect small molecules because of the high background signals coming from small organic matrices, which are present in the low-mass region (500 Da) [79].
- 3) The presence of salts in a sample solution increases the intensities of salt-adducted forms [80].
- 4) Neutral molecules such as carbohydrates are poorly ionized by MALDI because of the absence of either a basic or an acidic group in their structures [81].

To resolve these problems, the use of inorganic compounds with NP properties as matrices has been introduced for the determination of analytes ranging from small organic molecules to biopolymers [82-85].

MALDI requires photon-absorbing matrix compounds to enhance desorption [86]. UV-absorbing materials can be used as energy mediators to transfer the photon energy from the laser source to the surrounding analytes for effective desorption and ionization with minimum fragmentation of analyte molecules. Cobalt NPs (30 nm in diameter) as matrices have been used by the pioneers in the MALDI field for the analysis of lysozyme [87]. The cobalt NPs possess a large surface area, show high photoabsorption, and a low heat capacity compared with those of microparticles. Inspired by Tanaka's results, a series of inorganic micro- and nanomaterials have been investigated as potential inorganic matrices—e.g., graphite particles [88], AuNPs [89], silver NPs [90, 91], titanium dioxide NPs [82, 92], silicon NPs and nanorods [93, 94], Au nanorods [95], and carbon nanotubes [96].

Nanomaterial matrices compared with organic matrices offer better sample homogeneity [82, 89, 90, 92-99] and elimination of matrix ion interference. Flocculated and trapped mixtures can be detected using nanomaterials in various matrices [100-102]. AuNPs are suitable matrices for the determination of biomolecules in high-salt solutions, such as biological buffers, by MALDI-TOF MS [102]. AuNP-assisted laser desorption/ionization (LDI) was used for the determination of neutral carbohydrates [81], where the ionization efficiency of neutral carbohydrates can be greatly amplified without derivatization steps. Bare, capped, and functionalized AuNPs are good candidates as new generation matrices for high-resolution imaging and profiling analysis [87]. As described elsewhere, AuNPs are particularly interesting because they do not (or seldom) ionize by laser irradiation; however, a local temperature increase occurs on the particle surface [103]. Heat produced by the laser beam is then rapidly transferred to the analyzed sample. As a result, molecules of the analyte are desorbed/ionized with minimal background signal coming from the matrix. Compared with a commonly used 2,5-dihydrobenzoic acid matrix, the AuNPs showed the successful detection of small carbohydrates up to m/z 500 [101].

AuNPs were demonstrated to mediate the ionization of several peptide systems and small proteins [89, 97, 100-102, 104-108]. Additionally, the complexity and size of AuNPs influence the ionization of biomolecules in MALDI experiments. Russell and co-workers [106] published the detection of peptides with molecular weights of 500–2500 using 2- to 10-nm AuNPs. Moreover, coating AuNPs (functionalization) allows for selective extraction of desired substances from the complex solutions [89, 109]. For example, polyethylene-modified magnetic NPs (Fe_3O_4) to extract phosphoproteins from complex protein digests for MS analysis were used (Chen et al. 2011). Interestingly, the deposition method—e.g., the order of the layout of reagents and sample—influences either the interaction of the AuNP matrix with the sample or exposition of the sample to the laser beam. Samples covered with AuNPs provided better detection sensitivity and sample homogeneity compared with either the deposition of a mixture of matrix and sample onto the target plate or deposition of AuNPs onto the target before the sample [110].

NPs is now widely applied in various fields of tissue visualization—e.g., immunohistochemistry [13], MS profiling and imaging [38, 42, 60], detection of individual biomolecules in living cells, delivery as vectors [34, 35, 111] or systemic tracking of defined cell populations in whole organisms [11, 22]. Modification and functionalization of their surface, selection of their physical properties and biological targeting make NPs highly attractive for diagnosis, targeted therapy and biomedical research. A brief overview of the use of NPs in tissue visualization is provided in Fig. 19.8.

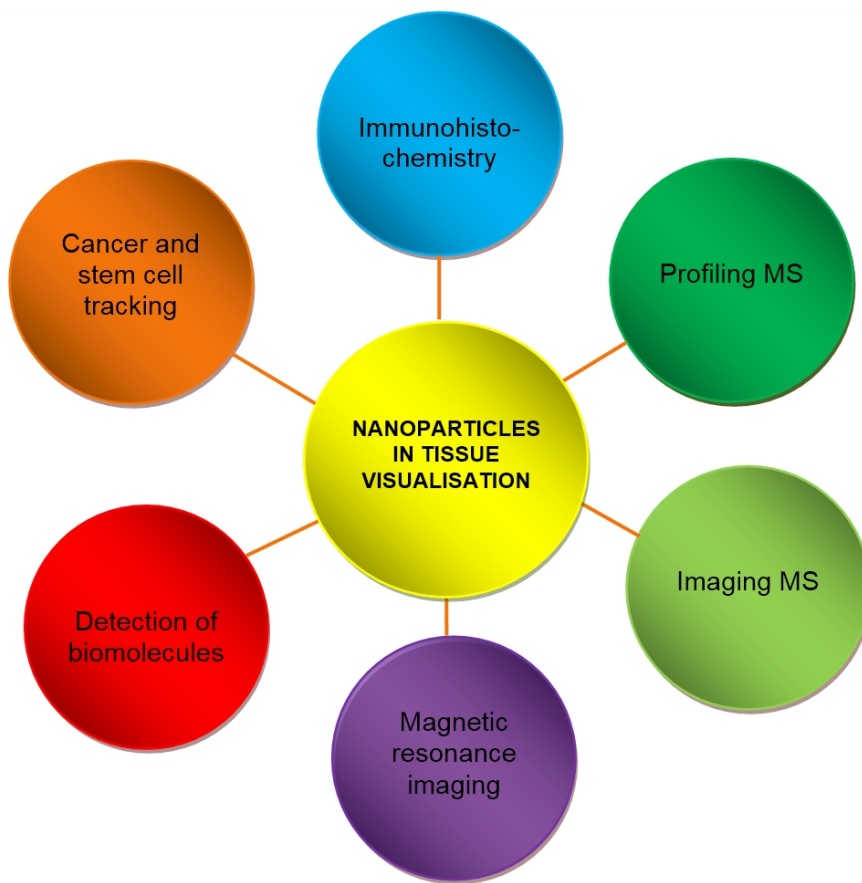


FIGURE 19.8
Brief overview of NP use in tissue visualization

Conclusions

Nanomaterials have wide applications in visualization strategies in cell and tissue biology. In particular, specifically engineered NPs can complement classical techniques of analysis on fixed tissues and enhance the performance of *in vivo* MRI. Biocompatible NPs provide a tool for *in vivo* cell tracking in regenerative medicine or cancer research and provide deep insight into tissue ultrastructure and chemical composition. IMS combines efficient analysis of chemical composition, spatial distribution and structural information, reflecting the complexity of the biological systems. Classical histological staining techniques are still indispensable particularly for daily clinical routine; however, the use of advanced methods such as NP-mediated IMS complement greatly the palette of available diagnostic approaches in the clinic and research.

Bringing the bioanalytical MS analysis to the cellular and subcellular levels allows the identification of molecular composition related to precise spatial localization. The combination of structural visualization and bioanalytical analysis complements greatly and contributes to the entanglement of complex interactions and mechanistic phenomena in tissues. Therefore, nanomaterial-mediated visualization is an important tool in standard clinicopathological techniques and tissue engineering.

Acknowledgements

We thank Mr. Filippo Amato and Ms. Mireia Puig-Romero for their contribution to Fig. 19.1. Work in our laboratories is supported by the Ministry of Education, Youth and Sports of the Czech Republic (Projects MSM0021622411, MSM0021627501, MSM0021622430, the Czech Science Foundation (Projects No. 104/08/0229, 202/07/1669) and the Grant Agency of Masaryk University (MUNI/M/0041/2013). We also thank for the support of CEPLANT, the project R&D Center for Low-Cost Plasma and Nanotechnology Surface Modifications (CZ.1.05/2.1.00/03.0086 funding from the European Regional Development Fund).

References

1. Perkin WH. Producing a new coloring matter for dyeing with a lilac or purple color stuffs of silk, cotton, wool, or other materials. London: British Patent No. 1984. Filed 26th August; 1856.
2. Golgi C. Sulla struttura della sostanza grigiadela cervello. *Gazetta Medica Lombarde*. 1873;33:244-6.
3. Transidico P, Bianchi M, Capra M, Pelicci PG, Faretta M. From cells to tissues: fluorescence confocal microscopy in the study of histological samples. *Microsc Res Tech*. 2004 Jun 1;64(2):89-95.
4. Schone C, Hofler H, Walch A. MALDI imaging mass spectrometry in cancer research: combining proteomic profiling and histological evaluation. *Clin Biochem*. 2013 Apr;46(6):539-45.
5. Yasunaga M, Furuta M, Ogata K, Koga Y, Yamamoto Y, Takigahira M, Matsumura Y. The significance of microscopic mass spectrometry with high resolution in the visualisation of drug distribution. *Sci Rep*. 2013;3:3050.
6. Roulhac PL, Ward JM, Thompson JW, Soderblom EJ, Silva M, Moseley MA, 3rd, Jarvis ED. Microproteomics: quantitative proteomic profiling of small numbers of laser-captured cells. *Cold Spring Harb Protoc*. 2011;2011(2):pdb prot5573.
7. IHC World 2013. Available from: <http://www.ihcworld.com/index.htm>.
8. Auffan M, Rose J, Bottero JY, Lowry GV, Jolivet JP, Wiesner MR. Towards a definition of inorganic nanoparticles from an environmental, health and safety perspective. *Nat Nanotechnol*. 2009 Oct;4(10):634-41.
9. Karathanasis E, Chan L, Balusu SR, D'Orsi CJ, Annapragada AV, Sechopoulos I, Bellamkonda RV. Multifunctional nanocarriers for mammographic quantification of tumor dosing and prognosis of breast cancer therapy. *Biomaterials*. 2008 Dec;29(36):4815-22.
10. Gao X, Yang L, Petros JA, Marshall FF, Simons JW, Nie S. In vivo molecular and cellular imaging with quantum dots. *Current opinion in biotechnology*. 2005;16(1):63-72.
11. Michalet X, Pinaud FF, Bentolila LA, Tsay JM, Doose S, Li JJ, Sundaresan G, Wu AM, Gambhir SS, Weiss S. Quantum dots for live cells, in vivo imaging, and diagnostics. *Science (New York, N.Y.)*. 2005;307(5709):538-44.
12. Hachani R, Lowdell M, Birchall M, Thanh NT. Tracking stem cells in tissue-engineered organs using magnetic nanoparticles. *Nanoscale*. 2013 Oct 9.

13. Fan K, Cao C, Pan Y, Lu D, Yang D, Feng J, Song L, Liang M, Yan X. Magnetoferritin nanoparticles for targeting and visualizing tumour tissues. *Nat Nanotechnol.* 2012 Jul;7(7):459-64.
14. Wu TJ, Tzeng YK, Chang WW, Cheng CA, Kuo Y, Chien CH, Chang HC, Yu J. Tracking the engraftment and regenerative capabilities of transplanted lung stem cells using fluorescent nanodiamonds. *Nat Nanotechnol.* 2013;8(9):682-9.
15. Tietz O, Kamaly N, Smith G, Shamsaei E, Bhakoo KK, Long NJ, Aboagye EO. Design, synthesis and in vitro characterization of fluorescent and paramagnetic CXCR4-targeted imaging agents. *American Journal of Nuclear Medicine and Molecular Imaging.* 2013;3(4):372-83.
16. Sykova E, Jendelova P. Magnetic resonance tracking of implanted adult and embryonic stem cells in injured brain and spinal cord. *Annals of the New York Academy of Sciences.* 2005 May;1049:146-60.
17. Reimer P, Balzer T. Ferucarbotran (Resovist): a new clinically approved RES-specific contrast agent for contrast-enhanced MRI of the liver: properties, clinical development, and applications. *European Radiology.* 2003 Jun;13(6):1266-76.
18. Richmond H, Zwerner J, Kim Y, Fiorentino D. Nephrogenic systemic fibrosis: relationship to gadolinium and response to photopheresis. *Archives of Dermatology.* 2007 Aug;143(8):1025-30.
19. He L, Feng L, Cheng L, Liu Y, Li Z, Peng R, Li Y, Guo L, Liu Z. Multilayer Dual-Polymer-Coated Upconversion Nanoparticles for Multimodal Imaging and Serum-Enhanced Gene Delivery. *ACS Applied Materials & Interfaces.* 2013;5(20):10381-8.
20. Mehravi B, Ahmadi M, Amanlou M, Mostaar A, Ardestani MS, Ghalandarlaki N. Conjugation of glucosamine with Gd(3+)-based nanoporous silica using a heterobifunctional ANB-NOS crosslinker for imaging of cancer cells. *International Journal of Nanomedicine.* 2013;8:3383-94.
21. Rowe MD, Thamm DH, Kraft SL, Boyes SG. Polymer-modified gadolinium metal-organic framework nanoparticles used as multifunctional nanomedicines for the targeted imaging and treatment of cancer. *Biomacromolecules.* 2009 Apr 13;10(4):983-93.
22. Lien Z-Y, Hsu T-C, Liu K-K, Liao W-S, Hwang K-C, Chao J-I. Cancer cell labeling and tracking using fluorescent and magnetic nanodiamond. *Biomaterials.* 2012;33(26):6172-85.
23. Hammerstingl R, Huppertz A, Breuer J, Balzer T, Blakeborough A, Carter R, Fuste LC, Heinz-Peer G, Judmaier W, Laniado M, Manfredi RM, Mathieu DG, Muller D, Mortelet K, Reimer P, Reiser MF, Robinson PJ, Shamsi K, Strotzer M, Taupitz M, Tombach B, Valeri G, van Beers BE, Vogl TJ. Diagnostic efficacy of gadoxetic acid (Primovist)-enhanced MRI and spiral CT for a therapeutic strategy: comparison with intraoperative and histopathologic findings in focal liver lesions. *European Radiology.* 2008 Mar;18(3):457-67.
24. Morlieras J, Chezal JM, Miot-Noirault E, Roux A, Heinrich-Balard L, Cohen R, Tarrit S, Truillet C, Mignot A, Hachani R, Kryza D, Antoine R, Dugourd P, Perriat P, Janier M, Sancey L, Lux F, Tillement O. Development of gadolinium based nanoparticles having an affinity towards melanin. *Nanoscale.* 2013 Feb 21;5(4):1603-15.
25. England CG, Priest T, Zhang G, Sun X, Patel DN, McNally LR, van Berkel V, Gobin AM, Frieboes HB. Enhanced penetration into 3D cell culture using two and three layered gold nanoparticles. *International Journal of Nanomedicine.* 2013;8:3603-17.
26. Deerinck TJ, Giepmans BNG, Smarr BL, Martone ME, Ellisman MH. Light and electron microscopic localization of multiple proteins using quantum dots. *Methods Mol Biol.* 2007;374:43-53.

27. Maltez-da Costa M, de la Escosura-Muñiz A, Nogués C, Barrios L, Ibáñez E, Merkoçi A. Simple monitoring of cancer cells using nanoparticles. *Nano letters*. 2012;12(8):4164-71.
28. Kim T, Momin E, Choi J, Yuan K, Zaidi H, Kim J, Park M, Lee N, McMahon MT, Quinones-Hinojosa A, Bulte JW, Hyeon T, Gilad AA. Mesoporous silica-coated hollow manganese oxide nanoparticles as positive T1 contrast agents for labeling and MRI tracking of adipose-derived mesenchymal stem cells. *Journal of the American Chemical Society*. 2011 Mar 9;133(9):2955-61.
29. Huxford RC, Della Rocca J, Lin W. Metal-organic frameworks as potential drug carriers. *Current opinion in chemical biology*. 2010;14(2):262-8.
30. Rieter WJ, Taylor KML, An H, Lin W, Lin W. Nanoscale metal-organic frameworks as potential multimodal contrast enhancing agents. *Journal of the American Chemical Society*. 2006;128(28):9024-5.
31. Taylor KML, Rieter WJ, Lin W. Manganese-based nanoscale metal-organic frameworks for magnetic resonance imaging. *Journal of the American Chemical Society*. 2008;130(44):14358-9.
32. Foucault-Collet A, Gogick KA, White KA, Villette S, Pallier A, Collet G, Kieda C, Li T, Geib SJ, Rosi NL, Petoud S. Lanthanide near infrared imaging in living cells with Yb³⁺ nano metal organic frameworks. *Proceedings of the National Academy of Sciences of the United States of America*. 2013 Oct 22;110(43):17199-204.
33. Della Rocca J, Liu D, Lin W. Nanoscale metal-organic frameworks for biomedical imaging and drug delivery. *Accounts of chemical research*. 2011;44(10):957-68.
34. Prigodich AE, Seferos DS, Massich MD, Giljohann DA, Lane BC, Mirkin CA. Nano-flares for mRNA regulation and detection. *ACS Nano*. 2009 Aug 25;3(8):2147-52.
35. Seferos DS, Giljohann DA, Hill HD, Prigodich AE, Mirkin CA. Nano-flares: probes for transfection and mRNA detection in living cells. *Journal of the American Chemical Society*. 2007 Dec 19;129(50):15477-9.
36. Seeley EH, Caprioli RM. MALDI imaging mass spectrometry of human tissue: method challenges and clinical perspectives. *Trends in biotechnology*. 2011;29(3):136-43.
37. Seeley EH, Schwamborn K, Caprioli RM. Imaging of intact tissue sections: moving beyond the microscope. *Journal of Biological Chemistry*. 2011;286(29):25459-66.
38. Lanni EJ, Rubakhin SS, Sweedler JV. Mass spectrometry imaging and profiling of single cells. *Journal of proteomics*. 2012;75(16):5036-51.
39. Oppenheimer SR, Drexler DM. Tissue analysis by imaging MS. *Bioanalysis*. 2012;4(1):95-112.
40. Chaurand P, Norris JL, Cornett DS, Mobley JA, Caprioli RM. New developments in profiling and imaging of proteins from tissue sections by MALDI mass spectrometry. *Journal of proteome research*. 2006 Nov;5(11):2889-900.
41. Casadonte R, Caprioli RM. Proteomic analysis of formalin-fixed paraffin-embedded tissue by MALDI imaging mass spectrometry. *Nature Protocols*. 2011 Nov;6(11):1695-709.
42. Caldwell RL, Caprioli RM. Tissue profiling by mass spectrometry: a review of methodology and applications. *Molecular & Cellular Proteomics*. 2005;4(4):394-401.
43. Fuchsberger C, Hübl H, Schäfer G, Pelzer A, Bartsch G, Klocker H, Barbarini N, Bellazzi R, Wieder W, Bonn G. Analysis and Visualization of Spatial Proteomic Data for Tissue Characterization. 2008 21st IEEE International Symposium on Computer-Based Medical Systems. 2008;8(5):185-90.
44. Kaletaş BK, van der Wiel IM, Stauber J, Güzel C, Kros JM, Luiders TM, Heeren RMA. Sample preparation issues for tissue imaging by imaging MS. *Proteomics*. 2009;9(10):2622-33.

45. Reyzer ML, Caprioli RM. MALDI mass spectrometry for direct tissue analysis: a new tool for biomarker discovery. *Journal of proteome research*. 2005;4(4):1138-42.
46. Karas M, Hillenkamp F. Laser desorption ionization of proteins with molecular masses exceeding 10,000 daltons. *Analytical Chemistry*. 1988;60(20):2299-301.
47. Vickerman JC. Molecular imaging and depth profiling by mass spectrometry--SIMS, MALDI or DESI? *The Analyst*. 2011;136(11):2199-217.
48. Liu J, Ouyang Z. Mass spectrometry imaging for biomedical applications. *Analytical and bioanalytical chemistry*. 2013;405(17):5645-53.
49. Schwartz SA, Reyzer ML, Caprioli RM. Direct tissue analysis using matrix-assisted laser desorption/ionization mass spectrometry: practical aspects of sample preparation. *Journal of Mass Spectrometry*. 2003 Jul;38(7):699-708.
50. Mounfield WP, 3rd, Garrett TJ. Automated MALDI matrix coating system for multiple tissue samples for imaging mass spectrometry. *Journal of the American Society for Mass Spectrometry*. 2012 Mar;23(3):563-9.
51. Weaver EM, Hummon AB. Imaging mass spectrometry: from tissue sections to cell cultures. *Advanced Drug Delivery Reviews*. 2013;65(8):1039-55.
52. Castaing R, Slodzian G. Microanalyse par emission ionique secondaire. *Journal of Microscopie*. 1962;1:395-410.
53. Chughtai K, Heeren RMA. Mass spectrometric imaging for biomedical tissue analysis. *Chemical Reviews*. 2010;110(5):3237-77.
54. Boxer SG, Kraft ML, Weber PK. Advances in imaging secondary ion mass spectrometry for biological samples. *Annual review of biophysics*. 2009;38:53-74.
55. Amstalden van Hove ER, Smith DF, Heeren RMA. A concise review of mass spectrometry imaging. *Journal of chromatography. A*. 2010;1217(25):3946-54.
56. Takáts Z, Wiseman JM, Gologan B, Cooks RG. Mass spectrometry sampling under ambient conditions with desorption electrospray ionization. *Science (New York, N.Y.)*. 2004;306(5695):471-3.
57. Wiseman JM, Puolitaival SM, Takáts Z, Cooks RG, Caprioli RM. Mass spectrometric profiling of intact biological tissue by using desorption electrospray ionization. *Angewandte Chemie (International ed. in English)*. 2005;44(43):7094-7.
58. Cooks RG, Ouyang Z, Takats Z, Wiseman JM. *Detection Technologies. Ambient mass spectrometry*. *Science (New York, N.Y.)*. 2006;311(5767):1566-70.
59. Vismeh R, Waldon DJ, Teffera Y, Zhao Z. Localization and quantification of drugs in animal tissues by use of desorption electrospray ionization mass spectrometry imaging. *Analytical Chemistry*. 2012;84(12):5439-45.
60. Agar NYR, Malcolm JG, Mohan V, Yang HW, Johnson MD, Tannenbaum A, Agar JN, Black PM. Imaging of meningioma progression by matrix-assisted laser desorption ionization time-of-flight mass spectrometry. *Analytical Chemistry*. 2010;82(7):2621-5.
61. Agar NYR, Yang HW, Carroll RS, Black PM, Agar JN. Matrix solution fixation: histology-compatible tissue preparation for MALDI mass spectrometry imaging. *Analytical Chemistry*. 2007;79(19):7416-23.
62. Caldwell RL, Opalenik SR, Davidson JM, Caprioli RM, Nanney LB. Tissue profiling MALDI mass spectrometry reveals prominent calcium-binding proteins in the proteome of regenerative MRL mouse wounds. *Wound Repair and Regeneration*. 2008;16(3):442-9.
63. Feng X, Liu X, Luo Q, Liu B-f. Mass spectrometry in systems biology: an overview. *Mass spectrometry reviews*. 2008;27(6):635-60.

64. Liu X, Wen F, Yang J, Chen L, Wei Y-q. A review of current applications of mass spectrometry for neuroproteomics in epilepsy. *Mass spectrometry reviews*. 2010;29(2):197-246.
65. Nanney LB, Caldwell RL, Pollins AC, Cardwell NL, Opalenik SR, Davidson JM. Novel Approaches for Understanding the Mechanisms of Wound Repair. *Journal of Investigative Dermatology Symposium Proceedings*. 2006;11(1):132-9.
66. Narasimhan K, Changqing Z, Choolani M. Ovarian cancer proteomics: Many technologies one goal. *Proteomics. Clinical applications*. 2008;2(2):195-218.
67. Pan S, Aebersold R, Chen R, Rush J, Goodlett DR, McIntosh MW, Zhang J, Brentnall TA. Mass spectrometry based targeted protein quantification: methods and applications. *Journal of proteome research*. 2009;8(2):787-97.
68. Zhang X, Wei D, Yap Y, Li L, Guo S, Chen F. Mass spectrometry-based "omics" technologies in cancer diagnostics. *Mass spectrometry reviews*. 2007;26(3):403-31.
69. Kang S, Kim MJ, An H, Kim BG, Choi YP, Kang KS, Gao MQ, Park H, Na HJ, Kim HK, Yun HR, Kim DS, Cho NH. Proteomic molecular portrait of interface zone in breast cancer. *Journal of proteome research*. 2010 Nov 5;9(11):5638-45.
70. Xiong X-C, Fang X, Ou Y-Z, Jiang Y, Huang Z-J, Zhang Y-K. Artificial Neural Networks for Classification and Identification of Data of Biological Tissue Obtained by Mass-Spectrometry Imaging. *Chinese Journal of Analytical Chemistry*. 2012;40(1):43-9.
71. Amato F, López A, Peña-Méndez EM, Vaňhara P, Hampl A, Havel J. Artificial neural networks in medical diagnosis. *Journal of Applied Biomedicine*. 2013;11(2):47-58.
72. Chaurand P, Schwartz Sa, Billheimer D, Xu BJ, Crecelius A, Caprioli RM. Integrating histology and imaging mass spectrometry. *Analytical Chemistry*. 2004;76(4):1145-55.
73. Schwamborn K, Krieg RC, Reska M, Jakse G, Knuechel R, Wellmann A. Identifying prostate carcinoma by MALDI-Imaging. *International journal of molecular medicine*. 2007;20(2):155-9.
74. Walch A, Rauser S, Deininger S-O, Höfler H. MALDI imaging mass spectrometry for direct tissue analysis: a new frontier for molecular histology. *Histochemistry and cell biology*. 2008;130(3):421-34.
75. Stauber J, MacAleese L, Franck J, Claude E, Snel M, Kaletas BK, Wiel IM, Wisztorski M, Fournier I, Heeren RM. On-tissue protein identification and imaging by MALDI-ion mobility mass spectrometry. *Journal of the American Society for Mass Spectrometry*. 2010 Mar;21(3):338-47.
76. Franck J, Arafah K, Elayed M, Bonnel D, Vergara D, Jacquet A, Vinatier D, Wisztorski M, Day R, Fournier I, Salzet M. MALDI imaging mass spectrometry: state of the art technology in clinical proteomics. *Molecular & Cellular Proteomics*. 2009;8(9):2023-33.
77. Pan C, Xu S, Zhou H, Fu Y, Ye M, Zou H. Recent developments in methods and technology for analysis of biological samples by MALDI-TOF-MS. *Analytical and bioanalytical chemistry*. 2007;387(1):193-204.
78. Tholey A, Heinzle E. Ionic (liquid) matrices for matrix-assisted laser desorption/ionization mass spectrometry-applications and perspectives. *Analytical and bioanalytical chemistry*. 2006;386(1):24-37.
79. Guo Z, Zhang Q, Zou H, Guo B, Ni J. A method for the analysis of low-mass molecules by MALDI-TOF mass spectrometry. *Analytical Chemistry*. 2002;74(7):1637-41.
80. Börnsen KO. Influence of salts, buffers, detergents, solvents, and matrices on MALDI-MS protein analysis in complex mixtures. *Methods Mol Biol*. 2000;146:387-404.
81. Scalf J, West P. Part I : Introduction to Nanoparticle Characterization with AFM. Santa Clara: Pacific Nanotechnology; 2006. 1-8 p.

82. Castro AL, Madeira PJA, Nunes MR, Costa FM, Florêncio MH. Titanium dioxide anatase as matrix for matrix-assisted laser desorption/ionization analysis of small molecules. *Rapid Communications in Mass Spectrometry*. 2008;22(23):3761-6.
83. Shan Z, Han L, Yuan M, Deng C, Zhao D, Tu B, Yang P. Mesoporous tungsten titanate as matrix for matrix-assisted laser desorption/ionization time-of-flight mass spectrometry analysis of biomolecules. *Analytica chimica acta*. 2007;593(1):13-9.
84. Shenar N, Martinez J, Enjalbal C. Laser desorption/ionization mass spectrometry on porous silica and alumina for peptide mass fingerprinting. *Journal of the American Society for Mass Spectrometry*. 2008;19(5):632-44.
85. Zhang H, Hoogenboom R, Meier MaR, Schubert US. Combinatorial and high-throughput approaches in polymer science. *Measurement Science and Technology*. 2005;16(1):203-11.
86. Karas M, Krüger R. Ion formation in MALDI: the cluster ionization mechanism. *Chemical Reviews*. 2003;103(2):427-40.
87. Tanaka K, Ido Y, Akita S, Yoshida Y, Yoshida T, editors. *Detection of high mass molecules by laser desorption time-of-flight mass spectrometry 1987* 1987; Osaka.
88. Zhang H, Cha S, Yeung ES. Colloidal graphite-assisted laser desorption/ionization MS and MS(n) of small molecules. 2. Direct profiling and MS imaging of small metabolites from fruits. *Analytical Chemistry*. 2007;79(17):6575-84.
89. Duan J, Linman MJ, Chen C-Y, Cheng QJ. CHCA-modified Au nanoparticles for laser desorption ionization mass spectrometric analysis of peptides. *Journal of the American Society for Mass Spectrometry*. 2009;20(8):1530-9.
90. Chiu T-C, Chang L-C, Chiang C-K, Chang H-T. Determining estrogens using surface-assisted laser desorption/ionization mass spectrometry with silver nanoparticles as the matrix. *Journal of the American Society for Mass Spectrometry*. 2008;19(9):1343-6.
91. Shrivastava K, Wu H-f. Applications of silver nanoparticles capped with different functional groups as the matrix and affinity probes in surface-assisted laser desorption/ionization time-of-flight and atmospheric pressure matrix-assisted laser desorption/ionization ion trap mass. *Rapid Communications in Mass Spectrometry*. 2008;22(18):2863-72.
92. Chen C-T, Chen Y-C. Fe₃O₄/TiO₂ core/shell nanoparticles as affinity probes for the analysis of phosphopeptides using TiO₂ surface-assisted laser desorption/ionization mass spectrometry. *Analytical Chemistry*. 2005;77(18):5912-9.
93. Piret G, Drobecq H, Coffinier Y, Melnyk O, Boukherroub R. Matrix-free laser desorption/ionization mass spectrometry on silicon nanowire arrays prepared by chemical etching of crystalline silicon. *Langmuir : the ACS journal of surfaces and colloids*. 2010;26(2):1354-61.
94. Wen X, Dagan S, Wysocki VH. Small-molecule analysis with silicon-nanoparticle-assisted laser desorption/ionization mass spectrometry. *Analytical Chemistry*. 2007;79(2):434-44.
95. Chen LC, Yonehama J, Ueda T, Hori H, Hiraoka K. Visible-laser desorption/ionization on gold nanostructures. *Journal of Mass Spectrometry*. 2007;42(3):346-53.
96. Gholipour Y, Nonami H, Erra-Balsells R. In situ analysis of plant tissue underivatized carbohydrates and on-probe enzymatic degraded starch by matrix-assisted laser desorption/ionization time-of-flight mass spectrometry by using carbon nanotubes as matrix. *Analytical biochemistry*. 2008;383(2):159-67.
97. Huang Y-F, Chang H-T. Analysis of adenosine triphosphate and glutathione through gold nanoparticles assisted laser desorption/ionization mass spectrometry. *Analytical Chemistry*. 2007;79(13):4852-9.

98. Peterson DS. Matrix-free methods for laser desorption/ionization mass spectrometry. *Mass spectrometry reviews*. 2007;26(1):19-34.
99. Seino T, Sato H, Yamamoto A, Nemoto A, Torimura M, Tao H. Matrix-free laser desorption/ionization-mass spectrometry using self-assembled germanium nanodots. *Analytical Chemistry*. 2007;79(13):4827-32.
100. Huang Y-f, Chang H-t. Nile Red-adsorbed gold nanoparticle matrixes for determining aminothiols through surface-assisted laser desorption/ionization mass spectrometry. *Analytical Chemistry*. 2006;78(5):1485-93.
101. Su C-l, Tseng W-l. Gold nanoparticles as assisted matrix for determining neutral small carbohydrates through laser desorption/ionization time-of-flight mass spectrometry. *Analytical Chemistry*. 2007;79(4):1626-33.
102. Wu H-P, Yu C-J, Lin C-Y, Lin Y-H, Tseng W-L. Gold nanoparticles as assisted matrices for the detection of biomolecules in a high-salt solution through laser desorption/ionization mass spectrometry. *Journal of the American Society for Mass Spectrometry*. 2009;20(5):875-82.
103. Schürenberg M, Dreisewerd K, Hillenkamp F. Laser desorption/ionization mass spectrometry of peptides and proteins with particle suspension matrixes. *Analytical Chemistry*. 1999;71(1):221-9.
104. Altelaar aFM, Klinkert I, Jalink K, de Lange RPJ, Adan RaH, Heeren RMa, Piersma SR. Gold-enhanced biomolecular surface imaging of cells and tissue by SIMS and MALDI mass spectrometry. *Analytical Chemistry*. 2006;78(3):734-42.
105. Lin P-C, Tseng M-C, Su A-K, Chen Y-J, Lin C-C. Functionalized magnetic nanoparticles for small-molecule isolation, identification, and quantification. *Analytical Chemistry*. 2007;79(9):3401-8.
106. McLean Ja, Stumpo Ka, Russell DH. Size-selected (2-10 nm) gold nanoparticles for matrix assisted laser desorption ionization of peptides. *Journal of the American Chemical Society*. 2005;127(15):5304-5.
107. Pujals S, Bastús NG, Pereiro E, López-Iglesias C, Puentes VF, Kogan MJ, Giralt E. Shuttling gold nanoparticles into tumoral cells with an amphipathic proline-rich peptide. *Chembiochem : a European journal of chemical biology*. 2009;10(6):1025-31.
108. Teng C-H, Ho K-C, Lin Y-S, Chen Y-C. Gold nanoparticles as selective and concentrating probes for samples in MALDI MS analysis. *Analytical Chemistry*. 2004;76(15):4337-42.
109. Vanderpuije BNY, Han G, Rotello VM, Vachet RW. Mixed monolayer-protected gold nanoclusters as selective peptide extraction agents for MALDI-MS analysis. *Analytical Chemistry*. 2006;78(15):5491-6.
110. Wu H-P, Su C-L, Chang H-C, Tseng W-L. Sample-first preparation: a method for surface-assisted laser desorption/ionization time-of-flight mass spectrometry analysis of cyclic oligosaccharides. *Analytical Chemistry*. 2007;79(16):6215-21.
111. Prigodich AE, Randeria PS, Briley WE, Kim NJ, Daniel WL, Giljohann DA, Mirkin CA. Multiplexed nanoflares: mRNA detection in live cells. *Analytical Chemistry*. 2012 Feb 21;84(4):2062-6.

12. Kolářová L, Kučera L, **Vaňhara P**, Hampl A, Havel J. **Use of flower-like gold nanoparticles in time-of-flight mass spectrometry.** *Rapid Communications in Mass Spectrometry* 2015; **29**(17): 1585-95.

Commentary:

This manuscript reports development of novel MALD-TOF MS matrix for enhanced desorption and ionization of biomolecules from complex biological samples, including crude cell extracts.

Commentary:	10.1002/rcm.7265
Impact factor (WOS, 2015):	2.226
Number of citations (WOS, 2018):	5
Cited in:	Carbon, Nanomaterials, Journal of the American Association for Mass Spectrometry
Most important citation:	Li X, Xu GJ, Zhang HY, Liu SJ, Niu H, Peng JX, et al. A homogeneous carbon nanosphere film-spot: For highly efficient laser desorption/ionization of small biomolecules. <i>Carbon</i> 2017. 121 : 343-52. doi: 10.1016/j.carbon.2017.05.099 (IF 2016: 6.337)
Contribution of the author:	Co-authorship. Collection and/or assembly of data, data analysis and interpretation, manuscript writing.

Rapid Commun. Mass Spectrom. 2015, 29, 1585–1595
(wileyonlinelibrary.com) DOI: 10.1002/rcm.7265

Use of flower-like gold nanoparticles in time-of-flight mass spectrometry

Lenka Kolářová^{1†}, Lukáš Kučera^{2†}, Petr Vaňhara², Aleš Hampel² and Josef Havel^{1,2*}

¹Department of Chemistry, Faculty of Science, Masaryk University, Kamenice 5/A14, 62500 Brno, Czech Republic

²Department of Histology and Embryology, Faculty of Medicine, Masaryk University, Kamenice 3/A1, 62500 Brno, Czech Republic

RATIONALE: Many kinds of nanoparticles (NPs) have been used for mass spectrometry (MS) so far. Here we report the first use of flower-like gold nanoparticles (AuNPs) as a mediator to enhance ionization in MS of peptides and proteins. **METHODS:** Flower-like AuNPs were characterized using transmission and scanning electron microscopy, UV-VIS spectrophotometry, and laser desorption/ionization (LDI)-MS and compared with polyhedral AuNPs. Mass spectra were obtained in positive ion mode using a time-of-flight (TOF) analyzer coupled with either matrix-assisted laser desorption/ionization (MALDI) or surface-assisted laser desorption/ionization (SALDI) methods.

RESULTS: The intensities of peptide peaks (m/z 500–3500) were up to 7.5× and up to 7× higher using flower-like AuNPs and flower-like AuNPs-enriched α -cyano-4-hydroxycinnamic acid (CHCA) matrix respectively, than the classical CHCA matrix. The signals of higher mass peptide/protein peaks (m/z 3600–17000) were up to 2× higher with using flower-like AuNPs-enriched CHCA matrix than conventional CHCA matrix. The signal of profile peaks generated by intact cell MALDI-TOFMS of fibroblast suspension (m/z 4000–20000) was 2× higher with using flower-like AuNPs combined with sinapinic acid (SA) compared to SA matrix alone. The use of flower-like AuNPs as internal calibration standard for the calibration of MS spectra of peptides was performed.

CONCLUSIONS: Flower-like AuNPs and flower-like AuNPs combined with CHCA or SA as combined matrices for MS measurement of peptides and proteins were used. Comparison of the conventional MALDI method and our method with flower-like AuNPs was carried out. In addition, gold clusters generated from flower-like AuNPs by SALDI provide a suitable internal calibration standard for MS analysis of peptides. Copyright © 2015 John Wiley & Sons, Ltd.

Gold nanoparticles (AuNPs) possess unique physical and chemical properties that depend on their size, shape or level of clustering.^[1] They were introduced as highly effective tools in a variety of biomedical applications, such as gene and drug delivery, cell tracking or tissue analysis, imaging and diagnosis.^[2–4] AuNPs are also potent catalysts capable of interactions with a broad spectrum of biomolecules that can enhance diagnostic and bioanalytical approaches.^[5] Mass spectrometry (MS) is an established technique for biomarker identification or quantification of small molecules in various biological samples. Surface-assisted and matrix-assisted laser desorption/ionization (SALDI, MALDI) time-of-flight (TOF)MS have become popular and versatile tools for analyses of peptides, proteins and nucleic acids^[6,7] and also various other biomolecules such as lipids, oligonucleotides, carbohydrates, and complex organic natural products and metabolites.^[8] However, classical MALDI-TOFMS has limitations that require consideration and optimization, e.g. heterogeneous co-crystallization of analytes with matrix and existence of

'sweet spots' resulting in a fluctuating signal intensity and a poor reproducibility,^[9] presence of high background signals in low-mass region (~500 Da) corresponding to organic matrices interfering with detection of small molecules,^[10] or presence of salts in the analyte artificially increasing the intensities of salt-adducted forms.^[11] However, biomolecules of interest, e.g. those with biomarker potential, are often rare and difficult to analyze and their proper detection meets limitations of classical SALDI/MALDI-TOFMS. Therefore, a great effort has been dedicated to improve different modes of MS, for sensitive identification and quantification of biomolecules.^[12]

Recent progress in nanotechnology and development of nanomaterials and nanoparticles (NPs) has brought to MS alternative media for efficient analysis of various poorly ionizable and complex biomolecules. Several new techniques, e.g. nanostructured-assisted laser desorption/ionization (NALDI), nanoparticle-assisted laser desorption/ionization (nano-PALDI) or colloidal graphite-assisted laser desorption/ionization (GALDI), have emerged for the brand new methods using nanomaterials in MS, but SALDI is the most common.^[13] Up to now, various NPs (gold, silver, platinum, titanium dioxide, silicon, carbon nanotubes, iron oxides, etc.) were introduced as inorganic matrices for MS analysis.^[14–21] Among them, AuNPs have received the highest attention as potential inorganic matrices in MS analyses of biomolecules^[22] due to their easy preparation and chemical modifications, high absorption

* Correspondence to: J. Havel, Department of Chemistry, Faculty of Science, Masaryk University, Kamenice 5/A14, 62500 Brno, Czech Republic.
E-mail: havel@chemi.muni.cz

† These authors contributed equally to this work.

coefficient, independence from irradiation wavelength and excellent stability and biocompatibility. The AuNPs affect the overall quality of the MS process at the level of sample pretreatment and the desorption/ionization step.^[23] AuNPs dispersed in matrix or representing a surface interacting with sample molecules alter the dissipation of laser energy and may enhance the ionization of poorly ionizable molecules by laser-induced surface plasmon excitation.^[24] We reported recently that polyhedral AuNPs improve the quality and reproducibility of mass spectra generated from frozen tissue samples making them suitable for a MS-based diagnostic process.^[25]

AuNPs form clusters of different size and shape, such as nanorods, nanospheres, polyhedral, flower-like NPs, etc.^[26] The golden nano-flowers are nanometer-scale structures with tree- or bouquet-like morphology with distinct physicochemical properties.^[27] This kind of NPs is widely used in biomedicine for photo-thermal therapy of cancer cells,^[28] imaging of live cells by surface-enhanced Raman scattering,^[29] or drug delivery and tissue engineering.^[30] Platinum (Pt) nanoflowers were also proposed as a matrix^[17] but a very high Pt concentration is needed (15 mg/mL). Another disadvantage is Pt toxicity.^[31] Currently, there is no study using flower-like AuNPs in MS of complex biomolecules. This prompted us to investigate whether distinct forms of AuNPs (polyhedral or flower-like AuNPs) have an impact on MS analysis of complex biomolecules. In this work, we document for the first time the capability of flower-like AuNPs to improve SALDI/MALDI-TOFMS by enhancing the ionization of peptides and providing in parallel an effective internal calibration of mass spectra. Introduction of flower-like AuNPs to MS-based proteomics can offer sensitive analyses of poorly ionizable biomolecules.

EXPERIMENTAL

Chemicals

Auric acid (HAuCl₄), gallic acid, α -cyano-4-hydroxycinnamic acid (CHCA), sinapinic acid (SA), trifluoroacetic acid (TFA), triammonium citrate, 2-mercaptoethanol, ammonium bicarbonate (ABC), and ethanol were purchased from Sigma-Aldrich (Steinheim, Germany). Acetonitrile (purity for isotachopheresis) and triethanolamine were purchased from Merck (Darmstadt, Germany). Ethylene glycol was purchased from Lachema (Neratovice, Czech Republic). Citric acid was purchased from PENTA (Chrudim, Czech Republic). Fetal bovine serum, L-glutamine, minimum essential medium nonessential amino acids, and penicillin-streptomycin were purchased from Invitrogen/Gibco Life Technologies (Prague, Czech Republic). Knockout Dulbecco's modified Eagle's medium (DMEM) was purchased from Gibco Life Technologies (Prague, Czech Republic). Water was double distilled using a quartz apparatus from Heraeus Quarzschmelze (Hanau, Germany). All reagents were of analytical grade purity. IVD bacterial test standard was purchased from Bruker Daltonik GmbH (Bremen, Germany). Bacterial standard contained extract of *Escherichia coli* DH5 alpha that covered mass range from 3.6 to 17 kDa. Peptide calibration Mix 4 (PepMix 4) was purchased from LaserBio Labs (Sophia Antipolis, France). The PepMix 4MS kit contains five individual peptides

(bradykinin fragment 1-5, angiotensin II human, neurotensin, adrenocorticotrophic hormone (ACTH) clip 18-39, and insulin bovine β -chain oxidized) covering the 500–3500 Da mass range. The final concentrations of the peptides were 2 pmol/ μ L bradykinin, 1.2 pmol/ μ L angiotensin II, 0.8 pmol/ μ L neurotensin, 1 pmol/ μ L ACTH, and 5 pmol/ μ L insulin β -chain on one spot for both SALDI-MS and MALDI-MS analysis.

Synthesis of AuNPs

Polyhedral AuNPs were synthesized by reduction of HAuCl₄ (0.3 mM, 3.2 mL) by gallic acid (1 mM, 800 μ L).^[32] The solution of gallic acid was added rapidly to the HAuCl₄ solution and stirred thoroughly at room temperature for 30 min. The color of the solution rapidly changed from colorless to red, indicating the formation of polyhedral AuNPs. The final concentration of Au in the suspension of polyhedral AuNPs was 0.24 mM. Flower-like AuNPs were synthesized by the reduction of HAuCl₄ (25 mM, 200 μ L) by triethanolamine (1 M, 400 μ L) in ethylene glycol as a reaction solvent (pure, 20 mL).^[33] Reaction time for synthesis of flower-like AuNPs was \approx 60 min under mild stirring at 40 °C in a water bath. The color of the solution changed from yellow to colorless and finally to blue. The flower-like AuNPs were collected by centrifugation at 16000 g for 15 min and 21 °C, washed five times with double distilled water and then redispersed in double distilled water (3.2 mL) to a final concentration of Au in the suspension of flower-like AuNPs of 1.6 mM.

Preparation of mouse embryonic fibroblasts

Mouse embryonic fibroblasts (MEF) derived from CF1-mouse were cultured in Knockout DMEM supplemented with 10% fetal bovine serum, 2 mM L-glutamine, 1% minimum essential medium nonessential amino acids, 1% penicillin-streptomycin, and 0.1 mM 2-mercaptoethanol. For analysis, cells were harvested and enzymatically disaggregated using TryPLE™ from Invitrogen Life Technologies (Prague, Czech Republic), resuspended in phosphate-buffered saline solution (PBS) and quantified using a CEDEX XS cell counter operated with CEDEX Control Center software from Roche Life Sciences (Prague, Czech Republic). Aliquots of 1×10^6 cells were washed three times in 150 mM ammonium bicarbonate (ABC) buffer for 3 min., at 2000 g and 4 °C. Then the supernatant was discarded and the resulting cell pellet was resuspended in 10 μ L of ABC buffer solution.

UV-VIS spectrophotometry

Spectrophotometric measurement was performed on a UV mini-1240 spectrophotometer furnished with quartz cells of 1 cm path length (Shimadzu, Kyoto, Japan) in the wavelength range 190 to 1100 nm.

Transmission electron microscopy (TEM)

AuNPs were visualized using a FEI Morgagni 268D transmission electron microscope (FEI, Eindhoven, Netherlands) at an operating voltage of 80 kV. TEM samples were prepared by deposition of a droplet of aqueous suspension

of AuNPs onto a carbon film-coated copper grid. Images were acquired using a Veleta CCD camera (Olympus SIS, Münster, Germany).

Scanning electron microscopy (SEM)

SEM was performed using the MIRA3 scanning electron microscope (TESCAN, Brno, Czech Republic) at the maximal spatial resolution up to 1 nm at 30 kV and the magnification range 2 \times to 1 000 000 \times . The SEM analysis was carried out at a chamber pressure of 0.0014 Pa.

Sample preparation for MS

For LDI-MS of AuNPs, a mixture containing 0.5 mL of AuNPs and 0.5 mL citrate aqueous solution (37.5 mM triammonium citrate/25 mM citric acid) was prepared and deposited in a 1 μ L volume on the sample plate and dried at room temperature in a stream of air. For SALDI-MS analysis of PepMix 4 using polyhedral or flower-like AuNPs, the aqueous solution of PepMix 4 was prepared using citrate buffer as a solvent (7.5 mM triammonium citrate/5 mM citric acid) and deposited on the sample plate by the modified sample-first, matrix-first or three-layer method as published elsewhere.^[34] Briefly: **sample-first method:** 1 μ L of PepMix 4 was deposited on the sample plate and then immediately overlaid by the aqueous suspension of AuNPs (1 μ L); **matrix-first method:** 1 μ L of AuNPs aqueous solution was deposited on the sample plate and then immediately overlaid by 1 μ L of PepMix 4; **three-layer method:** 1 μ L of AuNPs aqueous solution was deposited on the sample plate and allowed to dry. Then, 1 μ L of PepMix 4 was deposited onto the first layer and allowed to dry. Finally 1 μ L of AuNPs aqueous solution was deposited onto the second layer and allowed to dry. For MALDI-MS analysis of PepMix 4 using CHCA or flower-like AuNPs-enriched CHCA, the aqueous solution of PepMix 4 was prepared using ultrapure water with TFA (0.01%) as a solvent. The flower-like AuNPs were enriched with 10 mg/mL α -cyano-4-hydroxycinnamic acid (CHCA) in acetonitrile (ACN) and trifluoroacetic acid (TFA) in 50:50:0.1% volume ratios. Then the peptide mix was mixed with this solution (1:9, v/v), deposited on the sample plate (1 μ L) and allowed to dry in the airstream at the room temperature, according to the PepMix 4 manufacturer's instructions.

For the determination of limits of detection (LODs) of individual peptides ionized by different methods (MALDI, flower-like AuNPs-enriched MALDI and SALDI), diluted solutions of PepMix 4 (8 samples) were processed as described above. The LOD was then calculated as a three times the standard deviation of the noise and average value was used.

Bacterial standard was prepared according to the Bruker Daltonics GmbH protocol. For the conventional MALDI method, 10 mg/mL CHCA in ACN, H₂O and TFA (50:47.5:2.5, v/v/v) was used. For the AuNPs-mediated MALDI method, 10 mg/mL CHCA in ACN, flower-like AuNPs and TFA (50:47.5:2.5, v/v/v) were used.

For analysis of effects of AuNPs on MS of complex biological samples, such as mammalian cells, the suspension of MEF (1 \times 10⁶ cells/10 μ L) in 150 mM ABC was used. For the classical MALDI method of MEF, 30 mg/mL sinapinic

acid (SA) in ACN, H₂O and TFA (70:22.5:7.5, v/v/v) were used. For the MALDI method enriched with flower-like AuNPs, 30 mg/mL SA in ACN, flower-like AuNPs and TFA (70:22.5:7.5, v/v/v) was used. The sample of MEF was mixed with matrix solution (SA or SA enriched with flower-like AuNPs) in a ratio of 2:1 (v/v) and 2 μ L of this mixture were deposited on the sample plate.

Acquisition of mass spectra

Mass spectra were recorded on AXIMA CFR TOF mass spectrometer (Kratos Analytical, Manchester, UK) equipped with a 337 nm nitrogen laser and delayed extraction. The laser energy was expressed in arbitrary units (a.u.) ranging from 0 to 180. The accelerating voltage was set to 20 kV for all of the measurements. The laser fluency was 60 mJ per pulse. All experiments were performed in repetition mode with 5 Hz frequency and pulse time width of 3 ns. The diameter of the irradiated spot size was approximately 150 μ m. Analyses were carried out at 10⁻⁴ Pa pressure in the TOF tube and each mass spectrum was recorded by accumulating spectra from at least 200 laser shots. All measurements were performed in positive linear ion mode. External mass calibration was carried out using gold clusters or the peptide calibration mixture PepMix 4. Internal calibration was carried out using gold clusters and calibration accuracy of \pm 0.01 *m/z* unit was achieved. To avoid carry-over contamination, the target plate was always cleaned carefully with 96% ethanol and double distilled water in an ultrasonic bath and dried before spotting the samples.

Software and computation

Launchpad software (Kompact version 2.3.4, 2003) from Kratos Analytical Ltd (Shimadzu) was used to evaluate the mass spectra in all experiments. NIS Elements HC (v4.30.02, NIS Imaging Ltd, Praha, Czech Republic) was used for particle size analysis. STATISTICA 12 (StatSoft, Inc., Tulsa, OK, USA) was also used.

RESULTS AND DISCUSSION

Characterization of polyhedral and flower-like AuNPs

First, we characterized clustering of polyhedral and flower-like AuNPs by TEM and SEM. Polyhedral AuNPs assembled into various polyhedral particles such as tetra-, hexa- or octahedrons as well as rod-like and spherical (Figs. 1(A) and 1(C)). Flower-like AuNPs assembled into more complex structures with fractal-like geometry (Figs. 1(B) and 1(D)). The sizes of the polyhedral AuNPs (Fig. 1(E)) and flower-like AuNPs (Fig. 1(F)) were defined by a diameter of circles set around each gold particle and statistically evaluated. The mean overall diameters of polyhedral AuNPs and flower-like AuNPs were 57 \pm 8 nm and 88 \pm 16 nm, respectively. The colloidal aqueous solution of polyhedral AuNPs was stable for several months unlike the colloidal aqueous solution of flower-like AuNPs that was stable only for a few minutes before aggregates were formed. The synthesis and purification of flower-like AuNPs is safe, low-cost, easy and fast (\sim 3 h) when compared to platinum nanoflowers^[17] (\sim 24 h).

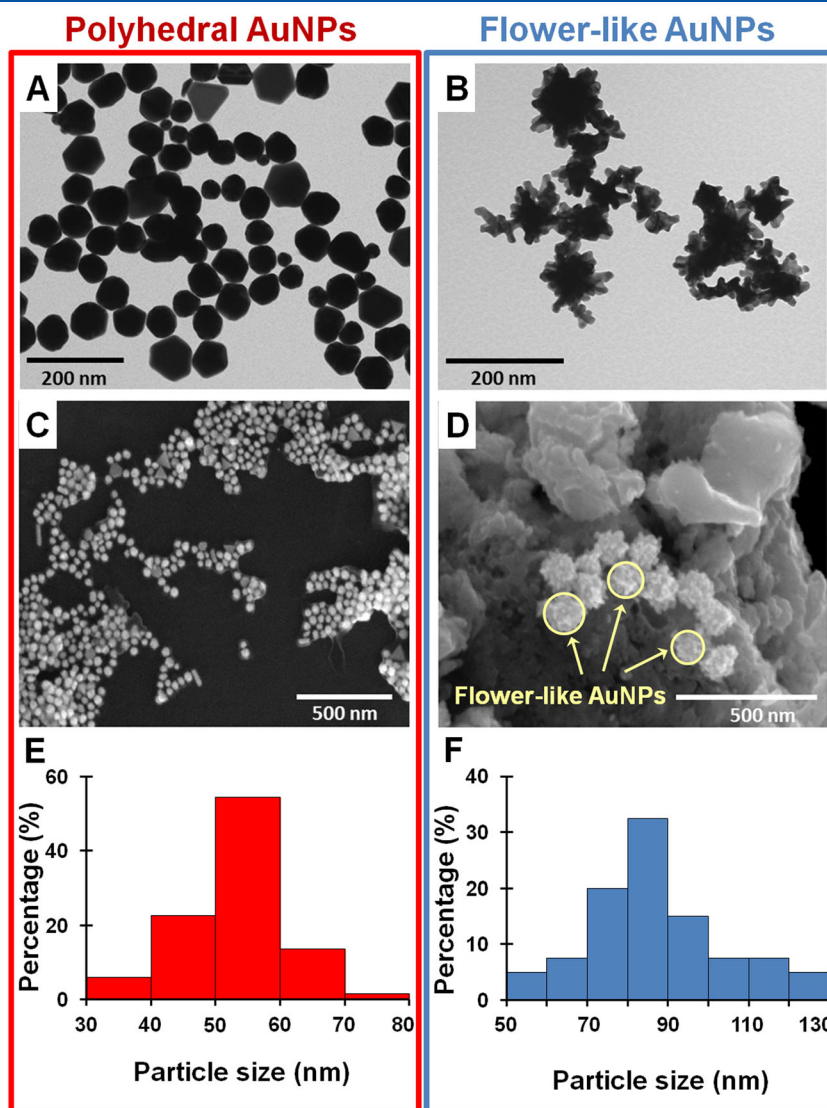


Figure 1. Characterization of polyhedral AuNPs and flower-like AuNPs. TEM of polyhedral AuNPs (A) and flower-like AuNPs (B), SEM images of polyhedral AuNPs (C) and flower-like AuNPs deposited on tellurium crystals (D), and the size distribution of polyhedral AuNPs (E) and flower-like AuNPs (F).

Next we analyzed absorption spectra of the aqueous colloidal suspensions of polyhedral and flower-like AuNPs. By UV-VIS spectroscopy we revealed three absorption maxima at 218, 268 and 555 nm of polyhedral AuNPs. In contrast, the absorption maximum of flower-like AuNPs in colloidal aqueous suspension was shifted to 820 nm, presumably due to the localized surface plasmon resonance, correlating with the shift from the red color of the polyhedral suspension to the light-blue color of the flower-like suspension. This observation is consistent with previously published findings.^[33]

Next we characterized the polyhedral and flower-like AuNPs stabilized in citrate buffer by LDI-TOFMS. The mass spectra were measured in a linear positive ion mode in the range 90–180 a.u. We observed the enhanced ionization of higher gold clusters that was further increased with an increase in the laser energy. LDI-TOFMS of AuNPs led to generation of

Au_m^+ clusters with m up to 74 in the case of polyhedral AuNPs (Fig. 2(A)), and Au_m^+ clusters with m up to 84 in the case of flower-like AuNPs (Fig. 2(B)). However, for both polyhedral and flower-like AuNPs not stabilized in citric buffer, the Au_m^+ clusters were formed only up to m equal to 20 (data not shown). Thus, we suggest that the formation of higher gold clusters of polyhedral and flower-like AuNPs is dependent on the stabilizing effect of citrate buffer.

Flower-like AuNPs enhance SALDI- and MALDI-TOFMS of peptides

Next, we were interested whether flower-like AuNPs affect ionization of peptides either alone (SALDI) or in combination with the commonly used CHCA matrix (MALDI). Possible effects of AuNPs were investigated using a set of well-characterized peptides – bradykinin, angiotensin II, neurotensin,

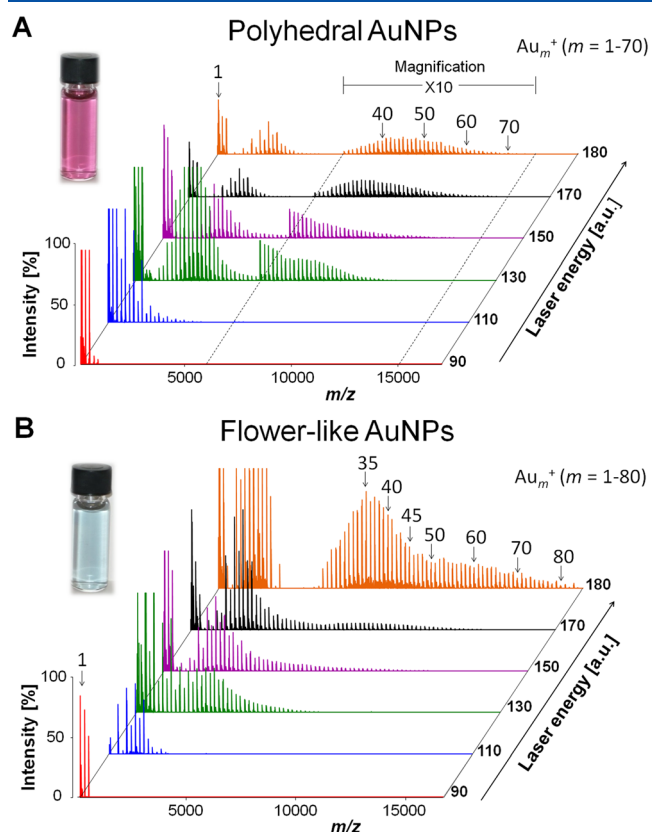


Figure 2. LDI mass spectra of gold clusters generated from polyhedral (A) or flower-like AuNPs (B) with addition of citrate buffer by LDI. Mass range m/z 6000–15000 10 \times magnified (A). All measurements were performed in linear positive ion mode. Mass spectra were normalized to 100 mV (A) and 80 mV (B).

ACTH, and insulin β -chain, commonly used for peptide calibration in various modes of MS. Three sample preparation methods (matrix-first, modified sample-first and three-layer) were used for flower-like AuNPs-assisted SALDI of peptides. The modified sample-first preparation method was the most effective technique for ionization of peptides, generating the highest peak intensities (Fig. 3). Then, we determined the optimal concentrations of polyhedral (1 μ M) and flower-like (800 μ M) AuNPs for efficient and sensitive SALDI of peptides (Supplementary Fig. S1, see Supporting Information). Next we compared mass spectra generated by SALDI and MALDI of peptides using the optimal concentration of polyhedral AuNPs, flower-like AuNPs or CHCA as matrices (Fig. 4). Mass spectra of flower-like AuNPs-mediated MS demonstrated significantly lower background at low masses and enhanced peak intensities of individual peptides. The peak intensities of bradykinin (m/z 573), angiotensin II (m/z 1046), neurotensin (m/z 1672), and ACTH (m/z 2466) were \sim 7.5 \times , 7 \times , 4 \times , and 1.5 \times higher in flower-like AuNPs-mediated SALDI when compared with the classical MALDI method, respectively. Mean values from three independent measurements of peptides measured in combination with CHCA or flower-like AuNPs as matrices are summarized in Table 1. Not only sensitivity was enhanced, but also LODs for peptides were lower than the classical MALDI method using CHCA matrix, where the

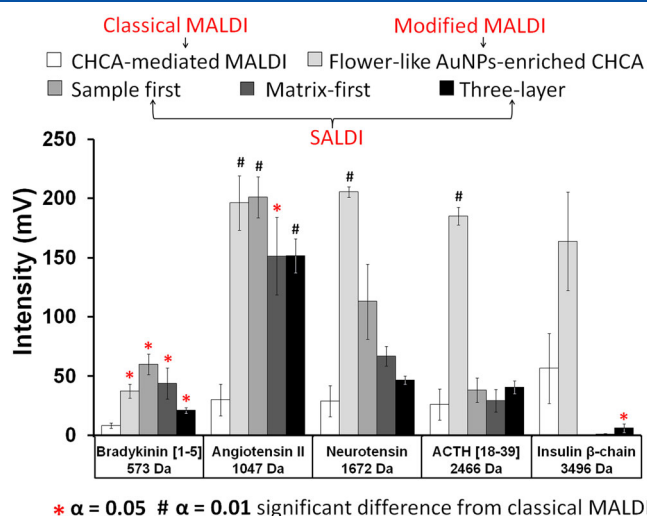


Figure 3. Comparison of peptide intensities and their standard deviations in mass spectra measured either by MALDI-TOFMS (with CHCA and flower-like AuNPs-enriched CHCA as the matrix) or SALDI-TOFMS using different sample deposition techniques. Standard deviations are marked as vertical line segments.

Standard peptides - PepMix 4

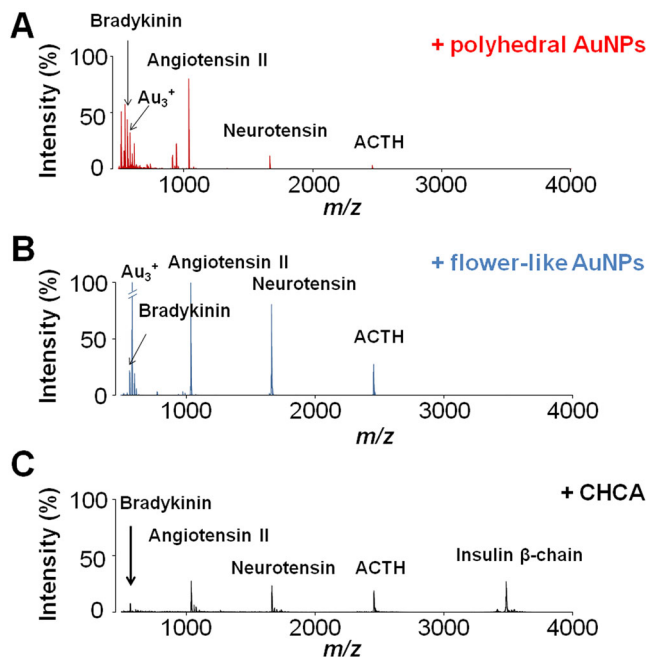


Figure 4. Comparison of AuNPs-mediated SALDI-TOFMS and CHCA-mediated MALDI-TOFMS of peptides. SALDI mass spectrum of PepMix 4 obtained using polyhedral AuNPs as SALDI matrix (A). SALDI-TOF mass spectrum of PepMix 4 obtained using flower-like AuNPs as SALDI matrix (B). MALDI-TOF mass spectrum of PepMix 4 obtained using CHCA as matrix (C). All measurements were performed in linear positive ion mode and laser energy 100 a.u. Mass spectra were normalized to 255 mV.

LOD values were in the range 2–45 fmol. For SALDI the values were significantly lower (1–24 fmol). When compared to the classical MALDI analysis of peptides, the polyhedral

Table 1. Comparison of mass spectra characteristics concerning the use of CHCA or flower-like AuNPs as matrices for PepMix 4 in linear mode (number of measurements were three × 200 shots)

Peptide	m/z [M+H] ⁺	CHCA matrix				flower-like AuNPs			
		R	S/N	I ± SD (mV)	RSD (%)	R	S/N	I ± SD (mV)	RSD (%)
Bradykinin	573.32	397	7	8 ± 2.2	27.5	555	37	60 ± 9	15.0
Angiotensin II	1046.54	398	25	30 ± 13	43.3	534	77	201 ± 17	8.5
Neurotensin	1672.91	424	41	29 ± 13	44.8	539	85	113 ± 32	28.3
ACTH	2466.20	465	40	26 ± 13	50.0	733	432	38 ± 10	26.3
Insulin β-chain	3496.66	443	40	57 ± 30	52.6	848	207	0.5 ± 0.1	20.0

R: resolution, S/N: signal-to-noise ratio, I: peaks intensity, SD: standard deviation, RSD: relative standard deviation.

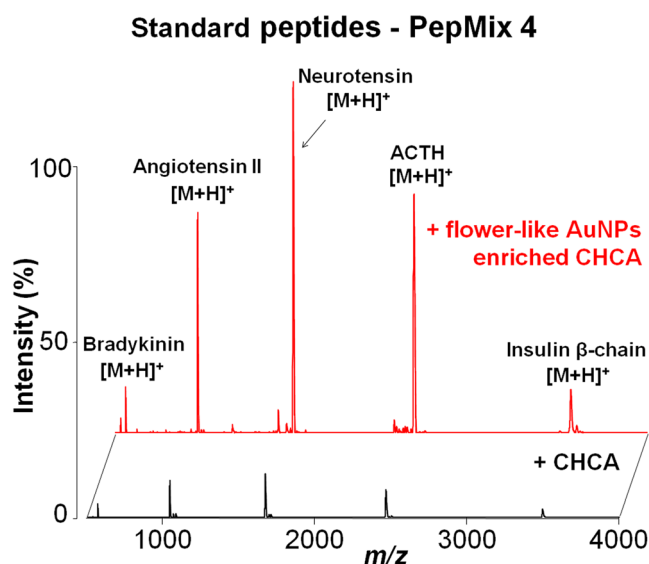
Table 2. Comparison of mass spectra characteristics concerning the use of CHCA or flower-like AuNPs-enriched CHCA as matrices for PepMix 4 in linear mode (number of measurements were three × 200 shots)

Peptide	m/z [M+H] ⁺	CHCA matrix				flower-like AuNPs + CHCA			
		R	S/N	I ± SD (mV)	RSD (%)	R	S/N	I ± SD (mV)	RSD (%)
Bradykinin	573.32	376	104	19 ± 3	15.8	606	279	87 ± 14	16.1
Angiotensin II	1046.54	354	330	63 ± 2	3.2	295	776	412 ± 48	11.6
Neurotensin	1672.91	338	428	83 ± 9	10.8	232	1001	588 ± 13	2.2
ACTH	2466.20	385	269	53 ± 6	11.3	226	673	376 ± 15	4.0
Insulin β-chain	3496.66	415	94	19 ± 4	21.1	326	104	55 ± 14	25.5

R: resolution, S/N: signal-to-noise ratio, I: peaks intensity, SD: standard deviation, RSD: relative standard deviation.

AuNPs-mediated SALDI produced enhanced peak intensities for bradykinin and angiotensin II (~5× and 2×, respectively), but neurotensin, ACTH and insulin β-chain peak intensities showed lower or negligible intensity (Fig. 4(A)). Interestingly, when we used flower-like AuNPs for SALDI analysis of peptides, the peak intensities were significantly higher when compared to polyhedral-AuNPs-mediated SALDI. The precise mechanism of AuNPs-mediated SALDI and MALDI ionization is unclear so far. It is generally accepted that the CHCA matrix provides a proton (H⁺) to the ionization of the analyte molecule to form the [M+H]⁺ ion. The SALDI ionization mediated by polyhedral or flower-like AuNPs utilizes probably the same mechanism as CHCA matrix, but the proton donor here comes from the citrate buffer. Interestingly, no signals of higher peptides/proteins ($m/z > 2500$) by SALDI using only flower-like AuNPs were observed.

Next, we investigated effects of flower-like AuNPs-enriched CHCA matrix on the MALDI analysis of peptides. We tested different concentrations of flower-like AuNPs in the range 0–8 mM in matrix solution and determined the optimal concentration (0.8 mM) for the most efficient ionization of peptides. Mean values from three independent measurements of peptides performed in combination with CHCA or flower-like AuNPs-enriched CHCA as matrices are summarized in Table 2. We demonstrated that a combination of flower-like AuNPs and CHCA improved the intensity of peaks of bradykinin, angiotensin II, neurotensin, ACTH, and insulin β-chain 4.5×, 6.5×, 7×, 7×, and 3× respectively, when compared to

**Figure 5.** Effects of CHCA-mediated MALDI-TOFMS (bottom) and CHCA-mediated MALDI-TOFMS enriched with flower-like AuNPs (upper) on ionization of peptides. All measurements were performed in linear positive ion mode and laser energy 100 a.u. Mass spectra were normalized to 580 mV.

CHCA or flower-like AuNPs only (Fig. 5). This may be due to the fact that the addition of flower-like AuNPs initiates growth of smaller and homogenous co-crystals of the matrix and the analyte, as documented by SEM

and particle size analysis (Fig. 6), and thus leading to equal distribution of laser energy throughout the sample spot and the efficient desorption and ionization of the sample. For flower-like AuNPs-enriched CHCA the LODs were in the range 1 to 15 fmol. Comparison of all of methods used in our analysis of peptides is shown in Fig. 3.

Measurement of peptides with flower-like AuNPs and flower-like AuNPs-enriched CHCA in reflectron mode was performed and data are summarized in Table 3. From Table 3 it is evident that the SALDI method (flower-like AuNPs alone) in reflectron mode is not suitable for measurement of peptides because the metastability of peptides is very high. However, flower-like AuNPs-enriched CHCA provides

higher resolution, signal-to-noise ratio and approximately comparable signals of peptides than the conventional MALDI method.

Flower-like AuNPs as internal calibration standard

Generally, laser radiation induces breakdown of any AuNPs to smaller clusters. Because gold is monoisotopic, such clusters have already been proposed to be used for calibration in MS.^[35–37] The formation of Au_m^+ clusters (m up to 100) by LDI of 2-(4'-hydroxybenzeneazo)benzoic acid/ $HAuCl_4$ mixture and Au_m^+ clusters (m up to 200) by LDI of polyvinylpyrrolidone-stabilized AuNPs has already been demonstrated.^[38,39]

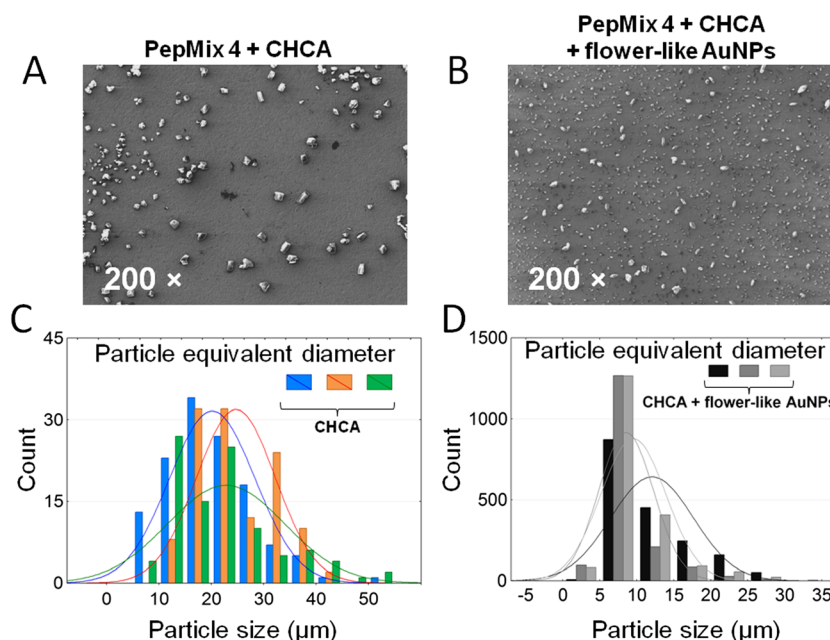


Figure 6. SEM images of sample spots of PepMix 4 co-crystallized with CHCA matrix magnified 200 \times (A) and CHCA matrix enriched with flower-like AuNPs magnified 200 \times (B). Particle size analysis of SEM images in software NIS Elements HC. Particle equivalent diameter of PepMix 4 co-crystals with CHCA (C) or CHCA matrix enriched with flower-like AuNPs (D). Conditions: Central area of images (1300 \times 1300 μ m) was selected for automated measurements.

Table 3. Comparison of mass spectra characteristics concerning the use of CHCA, flower-like AuNPs-enriched CHCA or flower-like AuNPs as matrices for PepMix 4 in reflectron mode (number of measurements were four \times 300 shots)

Peptide	CHCA matrix				flower-like AuNPs + CHCA				flower-like AuNPs			
	R	S/N	I \pm SD (mV)	RSD (%)	R	S/N	I \pm SD (mV)	RSD (%)	R	S/N	I \pm SD (mV)	RSD (%)
Bradykinin	1341	72	58 \pm 8	14	1400	84	66 \pm 1	2	1551	14	2.1 \pm 0.6	28
Angiotensin II	1677	106	52 \pm 4	8	1800	125	70 \pm 3	4	2343	98	8.2 \pm 2.9	36
Neurotensin	679	50	17 \pm 1	6	812	64	22 \pm 4	16	1908	5	0.6 \pm 0.1	43
ACTH	763	70	11 \pm 2	15	817	62	10 \pm 1	6	907	1	0.1 \pm 0.1	82
Insulin β -chain	858	62	8 \pm 1	17	916	65	7 \pm 1	9	-	-	-	-

R: resolution, S/N: signal-to-noise ratio, I: peaks intensity, SD: standard deviation, RSD: relative standard deviation.

In our experiments, we documented that with increasing laser energy the structures of flower-like AuNPs decompose and Au_m^+ clusters of various sizes are generated. This prompted us to investigate a possible use of these gold clusters as internal calibrants in SALDI-MS. We performed a flower-like AuNPs-mediated SALDI analysis of standard peptides at high laser energy (110 a.u.) and recorded a mass spectrum of peptides and gold clusters in the same measurement (Fig. 7(A)). Gold clusters were identified by magnifying individual regions in the spectrum (Fig. 7(B)). We reached a calibration accuracy of $\pm 0.01 m/z$ unit. The accuracy of the mass measurement of peptides reached ~ 130 ppm and is summarized in Table 4. In summary, we demonstrated for the first time an effective improvement of mass spectra of peptides by flower-like AuNPs and a capability to internally calibrate the MS measurement in a single experiment.

Flower-like AuNPs improve MALDI-TOFMS analysis of standard bacterial mixture

Next, we were curious whether the flower-like AuNPs-enriched CHCA matrix enhances ionization of proteins with higher mass. We used a bacterial standard that shows

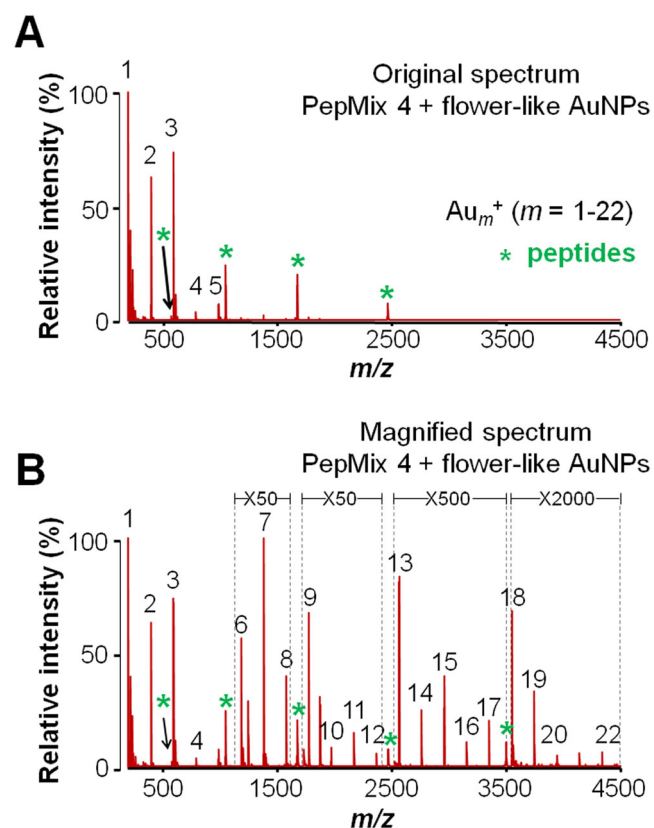


Figure 7. Gold clusters (Au_m^+ , $m=1-22$) were generated during flower-like AuNPs-mediated SALDI-TOF of PepMix 4 internally calibrate the mass spectra. Original (A) and magnified (B) mass spectrum. All measurements were performed in linear positive ion mode and laser energy 110 a.u.; 100% relative intensity corresponds to 1065 mV. The numbers in the graph indicate m values of Au_m^+ clusters.

a characteristic peptide and protein profile in MALDI-TOFMS, covering the mass range from 3600 to 17 000 Da. We tested different concentrations of flower-like AuNPs in

Table 4. Mass accuracy using internal calibration with gold clusters

Peptide	*Theoretical $[M+H]^+$	Measured $[M+H]^+$	Difference [Da]	Error [ppm]
Bradykinin	573.32	573.27	0.05	87
Angiotensin II	1046.54	1046.50	0.04	38
Neurotensin	1672.91	1672.83	0.08	48
ACTH	2466.20	2465.87	0.33	134
Insulin β -chain	3496.66	3496.47	0.19	54

Difference = Theoretical value – Measured value;

Error = (Difference / Theoretical value) $\cdot 10^6$.

For calibration Au_m^+ clusters ($m = 1, 4, 5, 15, 19$) were used. Calibration accuracy was $\pm 0.01 m/z$ units.

*The highest peak from theoretical isotopic envelopes is given.

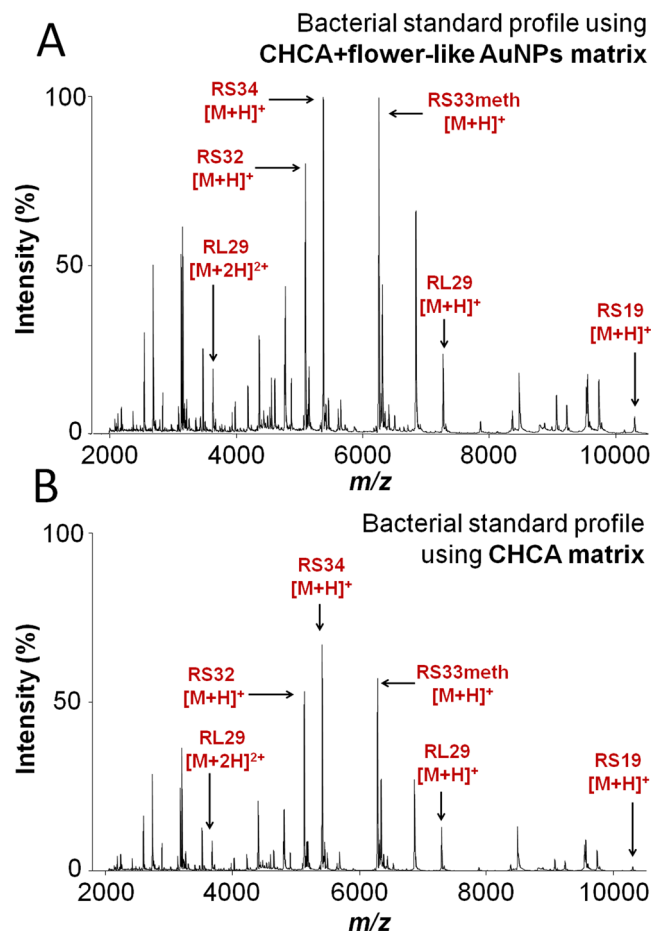
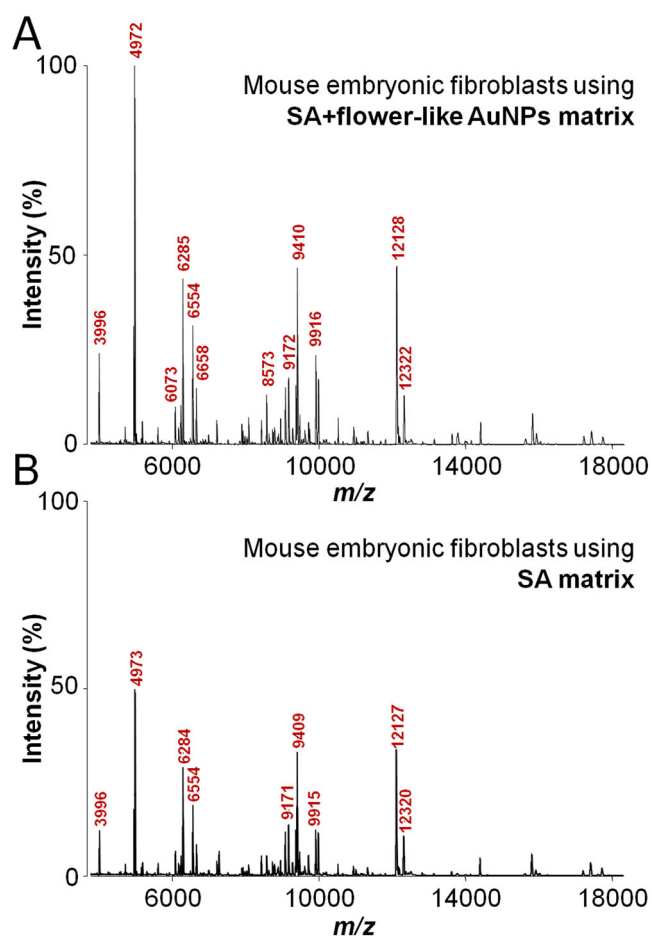


Figure 8. Effects of CHCA-mediated MALDI-TOFMS enriched with flower-like AuNPs (A) and CHCA-mediated MALDI-TOFMS (B) on ionization of bacterial standard. All measurements were performed in linear positive ion mode and laser energy 75 a.u. Mass spectra were normalized to 107 mV.

Table 5. Comparison of mass spectra characteristics concerning the use of CHCA or flower-like AuNPs-enriched CHCA as matrices for bacterial standard (number of measurements were three \times 200 shots)

BTS Peptide/Protein	m/z [M+H] ⁺	CHCA matrix				flower-like AuNPs + CHCA				
		R	S/N	I \pm SD (mV)	RSD (%)	R	S/N	I \pm SD (mV)	RSD (%)	
RL29	[M+2H] ²⁺	3637.8	541	14	9 \pm 0.4	4.4	506	16	14 \pm 5.0	35.7
RS32	[M+H] ⁺	5096.8	684	97	60 \pm 7.6	12.7	680	116	91 \pm 6.2	6.8
RS34	[M+H] ⁺	5381.4	697	120	74 \pm 8.3	11.2	688	144	112 \pm 6.6	5.0
RS33meth	[M+H] ⁺	6255.4	796	104	64 \pm 7.7	12.0	782	135	106 \pm 5.4	5.1
RL29	[M+H] ⁺	7274.5	858	23	15 \pm 0.5	3.3	820	24	20 \pm 3.6	18.0
RS19	[M+H] ⁺	10300.1	838	2	2 \pm 0.3	15.0	782	5	4 \pm 1.0	25.0
RNAse A	[M+H] ⁺	13683.2	638	12	8 \pm 0.8	10.0	560	19	14 \pm 1.2	8.5
Myoglobin	[M+H] ⁺	16952.3	598	1	1 \pm 0.3	30.0	567	1	2 \pm 0.2	20.0

R: resolution, S/N: signal-to-noise ratio, I: peaks intensity, SD: standard deviation, RSD: relative standard deviation.


Figure 9. Effects of SA-mediated MALDI-TOFMS enriched with flower-like AuNPs (A) and SA-mediated MALDI-TOFMS (B) on ionization of mouse embryonic fibroblasts. All measurements were performed in linear positive ion mode and laser energy 97 a.u. Mass spectra were normalized to 41 mV.

the range 0–7.6 mM in matrix solution. We determined the optimal concentration of flower-like AuNPs (7.6 mM) as the most efficient for the ionization of bacterial standard

(Supplementary Fig. S2, see Supporting Information). Next we compared the bacterial standard mass spectra generated in the mass range 2000–10000 m/z under the same conditions, either with the flower-like AuNPs-enriched CHCA matrix or the conventional CHCA matrix (Fig. 8). The presence of flower-like AuNPs in CHCA matrix increased the intensity of individual peptide and protein peaks, e.g. peaks RS34 [M+H]⁺ (5381 Da), RL29 [M+H]²⁺ (3638 Da) and RS19 [M+H]⁺ (10300 Da), up to 2 times when compared to the CHCA matrix alone. Mean values from three independent measurements of bacterial standard in combination with CHCA or flower-like AuNPs-enriched CHCA as matrices are summarized in Table 5.

Flower-like AuNPs improve MALDI-TOFMS analysis of intact mouse embryonic fibroblasts

Mouse embryonic fibroblasts (MEF) were used as a 'real sample' for investigation of effects of flower-like AuNPs-enriched matrix on ionization of complex mixtures of cell peptides and proteins in MALDI-TOFMS. As a standard matrix for MALDI-MS measurement of MEF, sinapinic acid (SA) was used. We determined the optimal concentration of flower-like AuNPs (3.6 mM) dispersed in SA as the most efficient for the ionization of MEF (Supplementary Fig. S3, see Supporting Information) and compared the pure SA matrix with the flower-like AuNPs-enriched SA (Fig. 9). Interestingly, the spectrum of MEF obtained using flower-like AuNPs-enriched SA as the matrix contained more peaks with higher intensities when compared to standard SA matrix. The intensities of the peaks at m/z 3996, 4973, 6554, and 9915 were \sim 2 \times higher using flower-like AuNPs-enriched SA matrix than using SA matrix. Mean values from two independent measurements of MEF measured in combination with SA or flower-like AuNPs-enriched SA as matrices are summarized in Table 6. In summary, despite the relatively low contribution to the overall ionization, the flower-like AuNPs-mediated mass spectrometry of highly complex biological samples, e.g. intact cells, enhances ionization of small peaks corresponding to less abundant biomolecules.

Table 6. Comparison of mass spectra characteristics concerning the use of SA or flower-like AuNPs-enriched SA as matrices for MEF (number of measurements were three × 200 shots)

MEF Peptide/Protein <i>m/z</i>	SA matrix				flower-like AuNPs + SA			
	R	S/N	I ± SD (mV)	RSD (%)	R	S/N	I ± SD (mV)	RSD (%)
3996	369	9	5 ± 1.0	20.0	401	17	10 ± 0.8	8.0
4973	398	33	17 ± 7.1	41.0	427	72	41 ± 6.5	15.7
6554	485	15	8 ± 1.3	16.3	514	26	15 ± 0.0	0.0
9915	600	9	5 ± 1.1	22.0	641	19	11 ± 1.0	9.0

R: resolution, S/N: signal-to-noise ratio, I: peaks intensity, SD: standard deviation, RSD: relative standard deviation.

CONCLUSIONS

We have characterized flower-like AuNPs and demonstrated their capability to enhance MS analysis of complex biomolecules when compared to common polyhedral AuNPs. Flower-like AuNPs modulate crystallization of matrix resulting in homogenous sample-matrix crystals. Flower-like AuNPs-mediated SALDI-MS increased the intensity of specific peptide peaks in the mass range up to 2500 Da. The effect was extended to approx. 3500 Da when flower-like AuNPs were combined with CHCA. Flower-like AuNPs-enriched CHCA or SA matrix increased the intensities of bacterial standard and MEF profile peaks, respectively. What is of particular importance, the gold monoisotopicity and excellent chemical stability of flower-like AuNPs provided an internal calibration standard in LDI. This study extends the spectrum of techniques used for ionization of rare complex biomolecules and may contribute to quantitative and qualitative analysis of putative biomarkers in diagnosis and therapy of various diseases.

ACKNOWLEDGEMENTS

This study was supported by Grant Agency of Masaryk University (Nos. MUNI/M/0041/2013 and MUNI/A/1558/2014, MUNI/A/1014/2013), HistoPARK – Centre for Analysis and Modeling of Tissues and Organs (no. CZ.1.07/2.3.00/20.0185) from the European Regional Development Fund, and by funds from the Faculty of Medicine, Masaryk University, to a junior researcher (Petr Vaňhara).

REFERENCES

- [1] D. Kumar, N. Saini, N. Jain, R. Sareen, V. Pandit. Gold nanoparticles: an era in bionanotechnology. *Expert Opin. Drug Deliv.* **2013**, *10*, 397.
- [2] P. Tiwari, K. Vig, V. Dennis, S. Singh. Functionalized gold nanoparticles and their biomedical applications. *Nanomaterials* **2011**, *1*, 31.
- [3] M. S. Khan, G. D. Vishakante, H. Siddaramaiah. Gold nanoparticles: a paradigm shift in biomedical applications. *Adv. Colloid Interface Sci.* **2013**, *199-200*, 44.
- [4] L. Kolářová, P. Vaňhara, E. M. Peña-Méndez, A. Hampl, J. Havel. Tissue visualization mediated by nanoparticles: from tissue staining to mass spectrometry tissue profiling and imaging, in *Nanomedicine*, (Eds: A. Seifalian, de M. Achala, D.M. Kalaskar). One Central Press, Manchester, **2014**, pp. 467–488.
- [5] M. Chakraborty, S. Jain, V. Rani. Nanotechnology: emerging tool for diagnostics and therapeutics. *Appl. Biochem. Biotechnol.* **2011**, *165*, 1178.
- [6] C. Jurinke, P. Oeth, D. van den Boom. MALDI-TOF mass spectrometry: a versatile tool for high-performance DNA analysis. *Mol. Biotechnol.* **2004**, *26*, 147.
- [7] E. Dudley. MALDI profiling and applications in medicine. *Adv. Exp. Med. Biol.* **2014**, *806*, 33.
- [8] L. Yan, W. Nie, T. Parker, Z. Upton, H. Lu. MS-based metabolomics facilitates the discovery of in vivo functional small molecules with a diversity of biological contexts. *Future Med. Chem.* **2013**, *5*, 1953.
- [9] A. Tholey, E. Heinze. Ionic (liquid) matrices for matrix-assisted laser desorption/ionization mass spectrometry-applications and perspectives. *Anal. Bioanal. Chem.* **2006**, *386*, 24.
- [10] Z. Guo, Q. Zhang, H. Zou, B. Guo, J. Ni. A method for the analysis of low-mass molecules by MALDI-TOF mass spectrometry. *Anal. Chem.* **2002**, *74*, 1637.
- [11] K. O. Börnsen. Influence of salts, buffers, detergents, solvents, and matrices on MALDI-MS protein analysis in complex mixtures. *Methods Mol. Biol.* **2000**, *146*, 387.
- [12] L. F. Marvin, M. A. Roberts, L. B. Fay. Matrix-assisted laser desorption/ionization time-of-flight mass spectrometry in clinical chemistry. *Clin. Chim. Acta* **2003**, *337*, 11.
- [13] W.-T. Chen, I. Tomalová, J. Preisler, H.-T. Chang. Analysis of biomolecules through surface-assisted laser desorption/ionization mass spectrometry employing nanomaterials. *J. Chin. Chem. Soc.* **2011**, *58*, 769.
- [14] J. A. McLean, K. A. Stumpo, D. H. Russell. Size-selected (2–10 nm) gold nanoparticles for matrix assisted laser desorption ionization of peptides. *J. Am. Chem. Soc.* **2005**, *127*, 5304.
- [15] T. Yonezawa, H. Kawasaki, A. Tarui, T. Watanabe, R. Arakawa, T. Shimada, F. Mafuné. Detailed investigation on the possibility of nanoparticles of various metal elements for surface-assisted laser desorption/ionization mass spectrometry. *Anal. Sci.* **2009**, *25*, 339.
- [16] L. Hua, J. Chen, L. Ge, S. N. Tan. Silver nanoparticles as matrix for laser desorption/ionization mass spectrometry of peptides. *J. Nanoparticle Res.* **2007**, *9*, 1133.
- [17] H. Kawasaki, T. Yonezawa, T. Watanabe, R. Arakawa. Platinum nanoflowers for surface-assisted laser desorption/ionization mass spectrometry of biomolecules. *J. Phys. Chem. C* **2007**, *111*, 16278.
- [18] A. L. Castro, P. J. A. Madeira, M. R. Nunes, F. M. Costa, M. H. Florêncio. Titanium dioxide anatase as matrix for matrix-assisted laser desorption/ionization analysis of small molecules. *Rapid Commun. Mass Spectrom.* **2008**, *22*, 3761.

- [19] G. Piret, H. Drobecq, Y. Coffinier, O. Melnyk, R. Boukherroub. Matrix-free laser desorption/ionization mass spectrometry on silicon nanowire arrays prepared by chemical etching of crystalline silicon. *Langmuir* **2010**, *26*, 1354.
- [20] S. Xu, Y. Li, H. Zou, J. Qiu, Z. Guo, B. Guo. Carbon nanotubes as assisted matrix for laser desorption/ionization time-of-flight mass spectrometry. *Anal. Chem.* **2003**, *75*, 6191.
- [21] C.-K. Chiang, N.-C. Chiang, Z.-H. Lin, G.-Y. Lan, Y.-W. Lin, H.-T. Chang. Nanomaterial-based surface-assisted laser desorption/ionization mass spectrometry of peptides and proteins. *J. Am. Soc. Mass Spectrom.* **2010**, *21*, 1204.
- [22] R. Pilolli, F. Palmisano, N. Cioffi. Gold nanomaterials as a new tool for bioanalytical applications of laser desorption ionization mass spectrometry. *Anal. Bioanal. Chem.* **2012**, *402*, 601.
- [23] C. Lei, K. Qian, O. Noonan, A. Nouwens, C. Yu. Applications of nanomaterials in mass spectrometry analysis. *Nanoscale* **2013**, *5*, 12033.
- [24] K. Shibamoto, K. Sakata, K. Nagoshi, T. Korenaga. Laser desorption ionization mass spectrometry by using surface plasmon excitation on gold nanoparticle. *J. Phys. Chem. C* **2009**, *113*, 17774.
- [25] J. Houška, E. M. Peña-Méndez, J. R. Hernandez-Fernaund, E. Salido, A. Hampl, J. Havel, P. Vaňhara. Tissue profiling by nanogold-mediated mass spectrometry and artificial neural networks in the mouse model of human primary hyperoxaluria 1. *J. Appl. Biomed.* **2014**, *12*, 119.
- [26] N. R. Panyala, E. M. Peña-Méndez, J. Havel. Gold and nanogold in medicine: overview, toxicology and perspectives. *J. Appl. Biomed.* **2009**, *7*, 75.
- [27] A. P. Pandey, N. M. Girase, M. D. Patil, P. O. Patil, D. A. Patil, P. K. Deshmukh. Nanoarchitectonics in cancer therapy and imaging diagnosis. *J. Nanosci. Nanotechnol.* **2014**, *14*, 828.
- [28] J. Han, J. Li, W. Jia, L. Yao, X. Li, L. Jiang, Y. Tian. Photothermal therapy of cancer cells using novel hollow gold nanoflowers. *Int. J. Nanomed.* **2014**, *9*, 517.
- [29] Q. Li, Y. Jiang, R. Han, X. Zhong, S. Liu, Z.-Y. Li, Y. Sha, D. Xu. High surface-enhanced Raman scattering performance of individual gold nanoflowers and their application in live cell imaging. *Small* **2013**, *9*, 927.
- [30] S. Kumari, R. P. Singh. Glycolic acid-g-chitosan-gold nanoflower nanocomposite scaffolds for drug delivery and tissue engineering. *Int. J. Biol. Macromol.* **2012**, *50*, 878.
- [31] P. V. Asharani, Y. Lianwu, Z. Gong, S. Valiyaveetil. Comparison of the toxicity of silver, gold and platinum nanoparticles in developing zebrafish embryos. *Nanotoxicology* **2011**, *5*, 43.
- [32] W. Wang, Q. Chen, C. Jiang, D. Yang, X. Liu, S. Xu. One-step synthesis of biocompatible gold nanoparticles using gallic acid in the presence of poly-(N-vinyl-2-pyrrolidone). *Colloids Surfaces A Physicochem. Eng. Asp.* **2007**, *301*, 73.
- [33] Y. Jiang, X.-J. Wu, Q. Li, J. Li, D. Xu. Facile synthesis of gold nanoflowers with high surface-enhanced Raman scattering activity. *Nanotechnology* **2011**, *22*, 385601.
- [34] H.-P. Wu, C.-L. Su, H.-C. Chang, W.-L. Tseng. Sample-first preparation: a method for surface-assisted laser desorption/ionization time-of-flight mass spectrometry analysis of cyclic oligosaccharides. *Anal. Chem.* **2007**, *79*, 6215.
- [35] K. Blaum, A. Herlert, G. Huber, H.-J. Kluge, J. Maul, L. Schweikhard. Cluster calibration in mass spectrometry: laser desorption/ionization studies of atomic clusters and an application in precision mass spectrometry. *Anal. Bioanal. Chem.* **2003**, *377*, 1133.
- [36] K. Blaum, G. Huber, H.-J. Kluge, L. Schweikhard. Laser desorption/ionization cluster studies for calibration in mass spectrometry. *Eur. Phys. J. D – At. Mol. Opt. Phys.* **2003**, *24*, 145.
- [37] N. R. Panyala, E. M. Peña-Méndez, J. Havel. Laser ablation synthesis of new gold phosphides using red phosphorus and nanogold as precursors. Laser desorption ionisation time-of-flight mass spectrometry. *Rapid Commun. Mass Spectrom.* **2012**, *26*, 1100.
- [38] H. Tsunoyama, T. Tsukuda. Magic numbers of gold clusters stabilized by PVP. *J. Am. Chem. Soc.* **2009**, *131*, 18216.
- [39] S. Kéki, L. Nagy, G. Deák, M. Zsuga. Bimetallic silver-gold clusters by matrix-assisted laser desorption/ionization. *J. Am. Soc. Mass Spectrom.* **2004**, *15*, 1455.

SUPPORTING INFORMATION

Additional supporting information may be found in the online version of this article at the publisher's web site.

13. Kolářová L, Prokeš L, Kučera L, Hampl A, Pena-Mendez EM, **Vaňhara P**, Havel J. **Clusters of monoisotopic elements for calibration in (TOF) mass spectrometry.** *Journal of the American Association for Mass Spectrometry* 2017; **28**(3):419-27.

Commentary:

Here we report development of a novel tool for internal calibration in mass spectrometry of complex biological samples, such as cell extracts. This methods overcomes some intrinsic sources or instrumental variability of cell and tissue MALDI-TOF MS.

DOI: 10.1007/s13361-016-1567-x

Impact factor (WOS, 2017): 2.869

Number of citations (WOS, 2018): 4

Most important citation: Rafols P, Castillo ED, Yanes O, Brezmes J, Correig X. **Novel automated workflow for spectral alignment and mass calibration in MS imaging using a sputtered Ag nanolayer.** *Analytica Chimica Acta* 2018; **1022**: 61-69. doi: 10.1016/j.aca.2018.03.031. (IF 2016: 4.950)

Contribution of the author: Co-authorship. Collection and/or assembly of data, data analysis and interpretation, manuscript writing.

RESEARCH ARTICLE

Clusters of Monoisotopic Elements for Calibration in (TOF) Mass Spectrometry

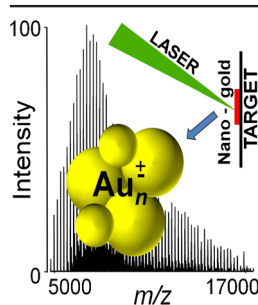
Lenka Kolářová,¹ Lubomír Prokeš,¹ Lukáš Kučera,^{2,3} Aleš Hampl,^{2,3} Eladia Peña-Méndez,⁴ Petr Vaňhara,^{2,3} Josef Havel^{1,3} 

¹Department of Chemistry, Faculty of Science, Masaryk University, Kamenice 5/A14, 625 00, Brno, Czech Republic

²Department of Histology and Embryology, Faculty of Medicine, Masaryk University, Brno, Czech Republic

³International Clinical Research Center, St. Anne's University Hospital, Pekařská 53, 656 91, Brno, Czech Republic

⁴Departamento de Química, Unidad Departamental de Química Analítica, Facultad de Ciencias, Universidad de La Laguna (ULL), Avda. Astrofísico Fco. Sánchez, s/n, 38206, La Laguna, Spain



Abstract. Precise calibration in TOF MS requires suitable and reliable standards, which are not always available for high masses. We evaluated inorganic clusters of the monoisotopic elements gold and phosphorus ($\text{Au}_n^+/\text{Au}_n^-$ and $\text{P}_n^+/\text{P}_n^-$) as an alternative to peptides or proteins for the external and internal calibration of mass spectra in various experimental and instrumental scenarios. Monoisotopic gold or phosphorus clusters can be easily generated in situ from suitable precursors by laser desorption/ionization (LDI) or matrix-assisted laser desorption/ionization mass spectrometry (MALDI-MS). Their use offers numerous advantages, including simplicity of preparation, biological inertness, and exact mass determination even at lower mass resolution. We used citrate-stabilized gold nanoparticles to generate gold calibration

clusters, and red phosphorus powder to generate phosphorus clusters. Both elements can be added to samples to perform internal calibration up to mass-to-charge (m/z) 10–15,000 without significantly interfering with the analyte. We demonstrated the use of the gold and phosphorous clusters in the MS analysis of complex biological samples, including microbial standards and total extracts of mouse embryonic fibroblasts. We believe that clusters of monoisotopic elements could be used as generally applicable calibrants for complex biological samples.

Keywords: Monoisotopic elements, Calibration, Gold clusters, Phosphorus clusters, TOF mass spectrometry

Received: 5 October 2016/Revised: 22 November 2016/Accepted: 25 November 2016/Published Online: 19 December 2016

Introduction

Calibration is a crucial step in almost all instrumental analytical methods. Calibration in time-of-flight mass spectrometry (TOF MS) is mostly based on calibration standards, such as commercially available mixtures of purified peptides and proteins of known masses; polymeric standards, like polyethylene glycol, polypropylene glycol, and polyalanine [1]; or synthetic macromolecules, such as polyester dendrimers (SpheriCal) [2]. These common calibration standards require high instrumental resolution to reveal their accurate masses and

can suffer from low stability and differential ionization due to mutual competition during ionization. Moreover, accurate calibration using peptide standards is complicated by the non-Gaussian distribution of ^{13}C isotopes in proteins over m/z 5 kDa [3]. The price of commercially available standards and the accuracy of in-house preparation protocols are also relevant issues. Therefore, there is a need for alternative calibrants with improved parameters.

Carbon clusters are suitable for the calibration of the tandem Penning-trap mass spectrometric system for the high-precision online detection of short-lived isotopes or heavy radionuclides up to a mass of 240 Da [4, 5]. On the other hand, carbon clusters are not suitable for calibration in higher mass ranges because of their complex isotopic envelope.

Monoisotopic elements, such as phosphorus or cesium, and their clusters have already been proposed for the calibration of mass spectra [6–9]. Clusters composed of isotopically pure

Electronic supplementary material The online version of this article (doi:10.1007/s13361-016-1567-x) contains supplementary material, which is available to authorized users.

Correspondence to: Josef Havel; e-mail: havel@chemi.muni.cz

elements that consist of only one stable isotope offer a great advantage. Clusters of monoisotopic elements provide simple spectra with many monoisotopic peaks covering the mass range of interest with regular mass spacing. In this work, we discuss the calibration of mass spectra by clusters of red phosphorus, which is already established in our laboratory [6, 10–16], and compare it with calibration by gold clusters generated directly on the target by laser desorption ionization (LDI)-MS of various materials, including gold foil [17], various types of gold nanoparticles (AuNPs), chloroauric acid (HAuCl_4), a mixture of 2-(4-hydroxyphenylazo) benzoic acid and HAuCl_4 [18], and polyvinylpyrrolidone-stabilized AuNPs [19]. Gold clusters provide simple and fast determination of accurate mass compared with common calibration standards, such as peptides or proteins. Moreover, AuNPs can enhance ionization in various techniques, such as surface-assisted laser desorption ionization (SALDI), nanoparticle-assisted laser desorption ionization (NALDI), and gold nanoparticle-assisted laser desorption ionization (GALDI) [20–22]. The structure and properties of gold and phosphorus clusters are well known [23–26].

Although the possibility of using gold clusters in negative ion mode (up to m/z 10,000) for the calibration of large biomolecules [17] has already been suggested, the experimental application of gold clusters for the calibration of TOF MS or quadrupole ion trap (QIT)-TOF MS has not yet been published.

Stoermer et al. [27] used a polycrystalline gold target to extensively study the use of gold cluster formation and demonstrated the formation of Au_n^+ (n up to 100). Kéki et al. described the generation of positively charged gold clusters up to m/z 18,000 in positive reflectron ion mode, but they identified only single isotopic peaks for clusters with masses up to 3000 Da and reported the presence of hydride-type ions like Au_nH^+ [18]. Furthermore, they did not provide a detailed evaluation and statistical analysis. Recently, we demonstrated that gold clusters generated from flower-like AuNPs can provide a precise internal calibration standard in SALDI analysis of peptides [22]. That work caused us to ask whether gold clusters are suitable for precise mass determination and the subsequent calibration of TOF analyzers.

In this paper, we provide a comprehensive comparative study of the use of monoisotopic clusters derived from either red phosphorus or gold nanoparticles generated from citrate-stabilized flower-like AuNPs in both positive and negative linear and reflectron ion modes for the external and internal calibration of TOF and QIT-TOF MS.

Experimental

Chemicals

Auric acid (HAuCl_4), α -cyano-4-hydroxycinnamic acid (CHCA), trifluoroacetic acid (TFA), angiotensin I and II, triammonium citrate, and ethanol were purchased from Sigma-Aldrich (Steinheim, Germany). Acetonitrile (ACN; purity for isotachopheresis) and triethanolamine were purchased from Merck (Darmstadt, Germany). Red phosphorus was

purchased from Riedel de Haën (Hannover, Germany). Ethylene glycol was purchased from Lachema (Neratovice, Czech Republic). Citric acid was purchased from PENTA (Chrudim, Czech Republic). Water was double distilled using a quartz apparatus from Heraeus Quarzschmelze (Hanau, Germany). All other reagents were analytical grade. IVD bacterial test standard (BTS) was purchased from Bruker Daltonik GmbH (Bremen, Germany).

Gold Nanoparticles and Sample Preparation for MS

Flower-like and polyhedral AuNPs were synthesized according to procedures described elsewhere [28, 29]. Sample preparation and reaction conditions were described in previous work [22]. Both flower-like and polyhedral AuNPs were collected by centrifugation at 16,000 g for 15 min at 21 °C, washed several times with water, and resuspended at the desired concentration (1.6 mM for flower-like AuNPs and 0.24 mM for polyhedral AuNPs) in double-distilled water. For LDI-MS of the AuNPs, a mixture containing 0.5 mL AuNPs and 0.5 mL citrate aqueous solution (37.5 mM triammonium citrate/25 mM citric acid) was prepared. One microliter of the solution was then deposited on the sample plate and dried at room temperature. For the internal calibration of BTS, 1 μL AuNPs was spotted over the dried drop of BTS prepared according to the Bruker Daltonics GmbH protocol. For the internal calibration of angiotensin I and II, 1 μL peptide mixture was spotted onto the target and allowed to dry; 1 μL 5 mg/mL CHCA matrix (solution for matrix: 50% ACN, 1% TFA) was then spotted onto the target and allowed to dry; and 1 μL red phosphorus (10 mg/mL) was then spotted onto the target. The final concentrations of angiotensin I and II on the target were 4 μM and 6 μM , respectively. The amounts of angiotensin I and II were 4 pmol and 6 pmol per spot, respectively, resulting in 0.7 pmol/ mm^2 and 1 pmol/ mm^2 , respectively.

Cell Culture and Cell Sample Preparation

Mouse embryonic fibroblasts (MEFs) derived from the CF1 mouse strain were cultured at 37 °C in a humidified atmosphere containing 5% CO_2 on tissue culture dishes coated with 0.1% gelatin from Sigma-Aldrich (Prague, Czech Republic) in knockout Dulbecco's modified Eagle's medium (Invitrogen Life Technologies, Prague, Czech Republic) supplemented with 10% fetal bovine serum, 2 mM L-glutamine, 1% minimum essential medium non-essential amino acids, and 1% penicillin-streptomycin, all from Invitrogen/Gibco Life Technologies. The MEFs were harvested by TryPLE Express (1 \times) for 2 min at 37 °C, washed in 1 \times phosphate buffered saline, and counted. To eliminate traces of phosphate buffered saline, the cells were centrifuged (relative centrifugal force 100 g , 2 min) and washed three times in 1 mL 150 mM ammonium bicarbonate buffer. MEF extracts were prepared by osmotic lysis of 1×10^6 cells in 1 mL water. The MEF extracts were then mixed at a 1:1 ratio with matrix containing 10 mg/mL CHCA in 70% ACN, 29% water, and 1% TFA; then 0.5 μL of the mixture was then spotted onto the target plate.

Acquisition of Mass Spectra

Mass spectra were recorded using either an AXIMA CFR TOF mass spectrometer or an AXIMA Resonance QIT-TOF mass spectrometer, both from Kratos Analytical Ltd. (Manchester, UK). Brief schematics of the devices are given in Supplementary Scheme S1 (On-line Resource 3). Both devices were equipped with a microchannel plate detector and used a nitrogen laser (337 nm) and delayed extraction. The laser energy was expressed in arbitrary units (a.u.) ranging from 0 to 180 a.u. The laser power and fluence at 180 a.u. were 6 mW and ≈ 10 mJ/mm²/pulse, respectively. The accelerating voltage was set to 20 kV for all of the measurements. All experiments were performed in repetition mode at a frequency of 5 Hz and with a pulse time width of 3 ns. The diameter of the irradiated spot was approximately 150 μ m. Analyses were carried out at 10^{-4} Pa pressure in the TOF tube, and each mass spectrum was recorded by accumulating the spectra from at least 500 laser shots. All measurements were performed in positive and/or negative linear and/or reflectron ion modes. AXIMA Resonance operates solely in positive/negative reflectron ion mode. Therefore, the AXIMA CFR instrument was used for all linear measurements. The AXIMA Resonance instrument was equipped with a QIT mass analyzer. Mass spectra were recorded in the following ranges: m/z 100–400, 250–1200, 800–3500, 1500–8000, and 3000–15,000. The pressure in the ion source was typically 6×10^{-6} Torr. Spatial focusing was provided by two Einzel lenses separated by a pyramid mirror, and ions were injected axially into the trap. During ion introduction, no rf potential was applied to the ion trap. To trap ions, a retarding potential was applied to the end cap adjacent to the time-of-flight, and an rf with a frequency of 500 kHz was applied to the ring electrode (rapid rf-startup). Amplitudes and corresponding bias voltages were chosen according to the analyte mass under investigation. The rapid rf-startup method provides a trapping efficiency close to 100%. Once trapped, the ions were cooled using argon. The pressure in the trap was held at 6×10^{-3} Torr. QIT has two functions: trapping externally generated MALDI ions and providing a collision cell for MS/MS experiments. All mass spectra were recorded automatically using a regular raster. Mass spectra were plotted as the ion signal relative to the m/z value. The ion signal was defined as the current induced by the impact of the ions on the microchannel plate detector expressed in mV. The spectra were normalized so that the intensity of the maximum peak = 100%. The sample plate was a 2-mm thick stainless steel plate containing 384 wells with a sample spot diameter of 2.8 mm (area = 6 mm²). To avoid carryover contamination, the target plate was regularly cleaned with 96% ethanol and double-distilled water in an ultrasonic bath and dried before the samples were spotted. The Launchpad software (Kompact ver. 2.3.4, 2003) from Kratos Analytical Ltd. was used to evaluate the mass spectra in all experiments.

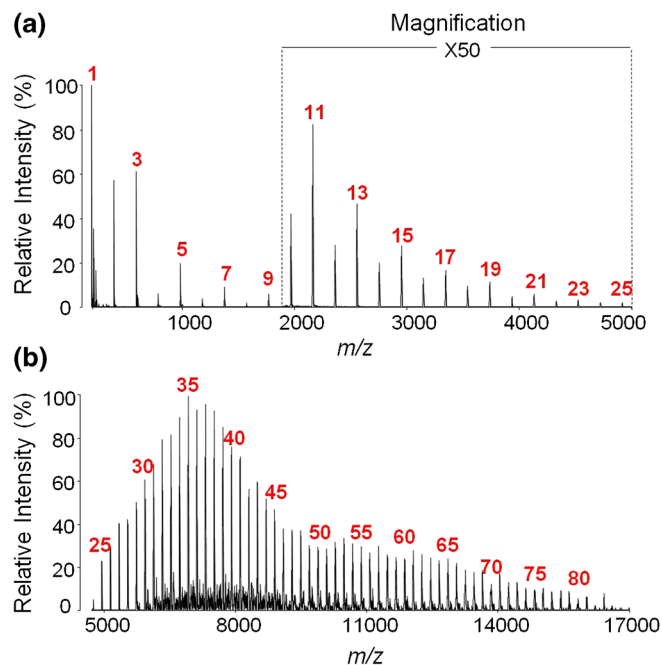


Figure 1. Mass spectra of gold clusters generated by LDI of citrate-stabilized flower-like AuNPs in positive linear ion mode by AXIMA CFR MALDI-TOF MS. **(a)** Spectrum in low mass range m/z 190–5000, and **(b)** higher mass range m/z 5000–17,000. Conditions: average of 500 laser shots, 120 and 170 a.u. laser energy, 100% intensity corresponds to **(a)** 256 mV, and **(b)** 66 mV. Selected n values of Au_n^+ clusters are given in red

Results and Discussion

Precise instrumental calibration is a limiting step in mass spectrometry of biomolecules, especially that of complex biological samples such as peptide and protein mixtures or cell extracts. We performed a comprehensive study of the use of inorganic, monoisotopic gold clusters for the calibration of biomolecules including peptides, bacterial extracts, and total extracts of eukaryotic cells.

Gold Clusters ($Au_n^{+/-}$)

We generated gold clusters ($Au_n^{+/-}$) from citrate-stabilized, flower-like AuNPs in positive and negative linear ion modes. Clusters generated from flower-like AuNPs provide LDI spectra with a slightly wider mass range of Au peaks than those provided by clusters generated from polyhedral AuNPs.

Table 1. Mass Accuracy of $Au_n^{+/-}$ Cluster Peaks Determination

		m/z range		
		100–2000	2000–5000	7000–14,000
Ion modes	Lin +	47 ppm	19 ppm	26 ppm
	Lin -	48 ppm	-	-
	Ref +	4 ppm	4 ppm	-
	Ref -	5 ppm	4 ppm	-

- No peaks or intensities of $Au_n^{+/-}$ clusters too low for detection

Effective ionization of higher gold clusters began at a laser energy of 120 a.u., and gradual increase of the laser energy resulted in the generation of higher gold clusters in both positive and negative linear ion modes (Figure 1). In positive and negative linear ion modes at maximum laser energy, we achieved Au clusters up to m/z 17,000 and m/z 6000, respectively. In positive and negative reflectron ion modes at maximum laser energy, we achieved Au clusters up to m/z 7000 and m/z 6000, respectively. The LDI at higher laser energies of flower-like AuNPs without citrate buffer led to decomposition of the gold clusters (data not shown).

Representative LDI mass spectra of citrate-stabilized flower-like AuNPs in positive ion mode are shown in Figure 1. We observed Au_n^+ clusters ranging in size from $n=1$ up to $n=25$ in the mass range m/z 180–5000 (Figure 1a). We detected additional peaks of clusters of $AuNH_3^+$, $Au(NH_3)_2^+$, and $Au_3NH_3^+$ with very low intensity in the spectrum, probably from the citrate buffer. We observed Au_n^+ clusters ranging in size from $n=25$ up to $n=80$ in the mass range m/z 5000–17,000 (Figure 1b). We observed additional small peaks at cluster sizes of $n=30$ or greater, the nature of which was

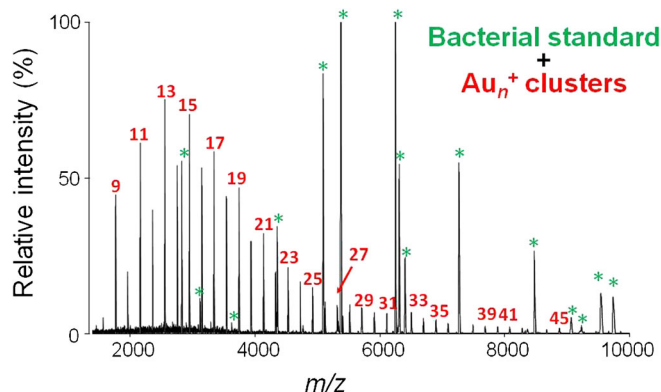


Figure 3. Spectrum of gold clusters (Au_n^+ , red numbers) with peptides/proteins (green stars) from bacterial test standard. Conditions: linear positive mode, 135 a.u. laser energy, mass range m/z 1400–10000, 100% intensity corresponds to 11 mV

unclear. We speculate that NH_4^+ -Au or Au-Fe can form during high laser energy impacts.

We evaluated calibration in three mass ranges: low (m/z 180–2100), medium (m/z 2000–7000), and high (m/z 7000–

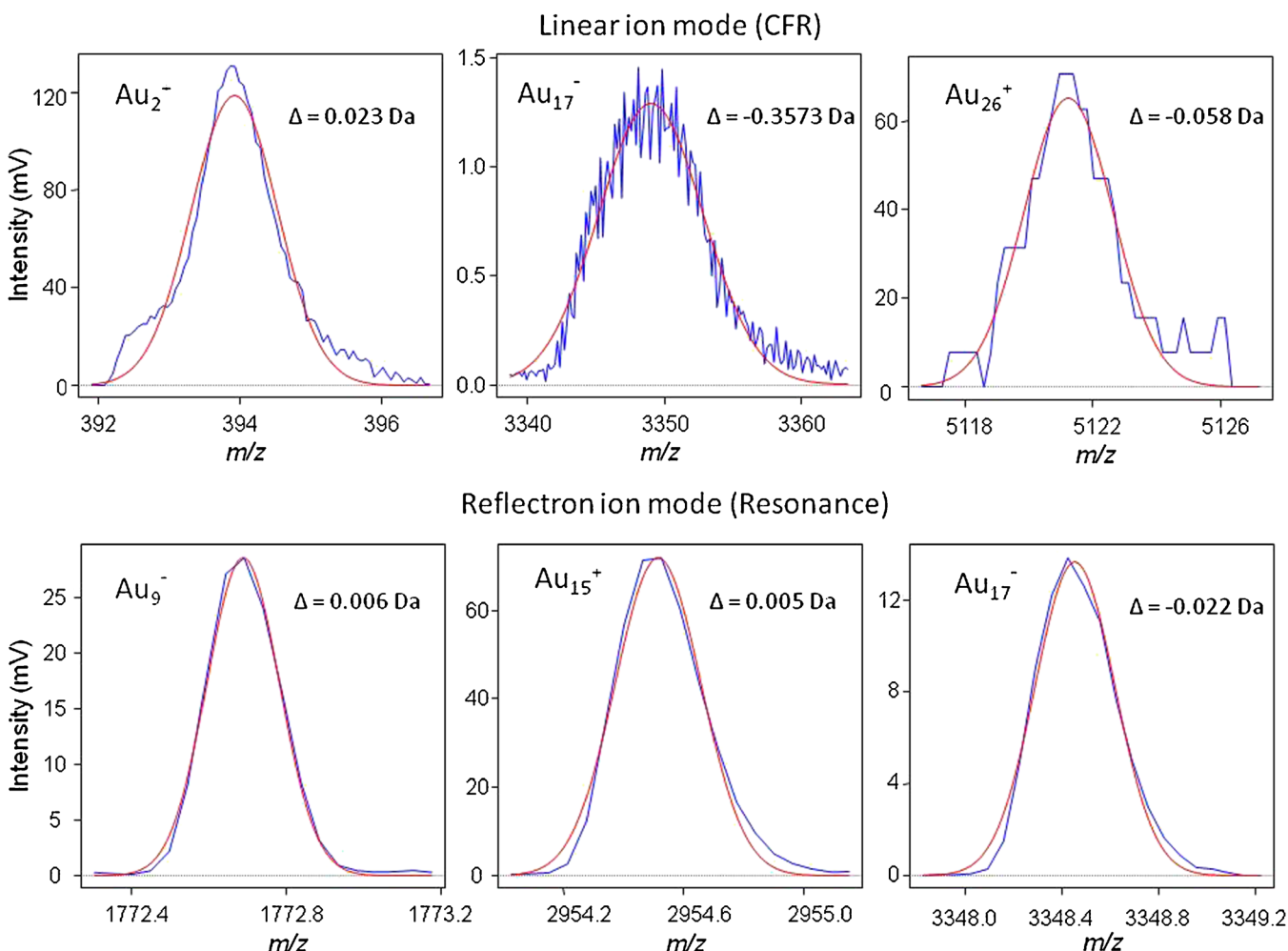


Figure 2. Statistical evaluation of the shape of Au_n cluster peaks fitted to a Gaussian curve (smooth line in red is a Gaussian curve, $\Delta = (m/z)_{\text{theoretical}} - (m/z)_{\text{experimental}}$). Details are given in On-line Resource 1; $(m/z)_{\text{theoretical}}$ is the monoisotopic value according to IUPAC. The experimental value is that found using the Gaussian profile of the peak

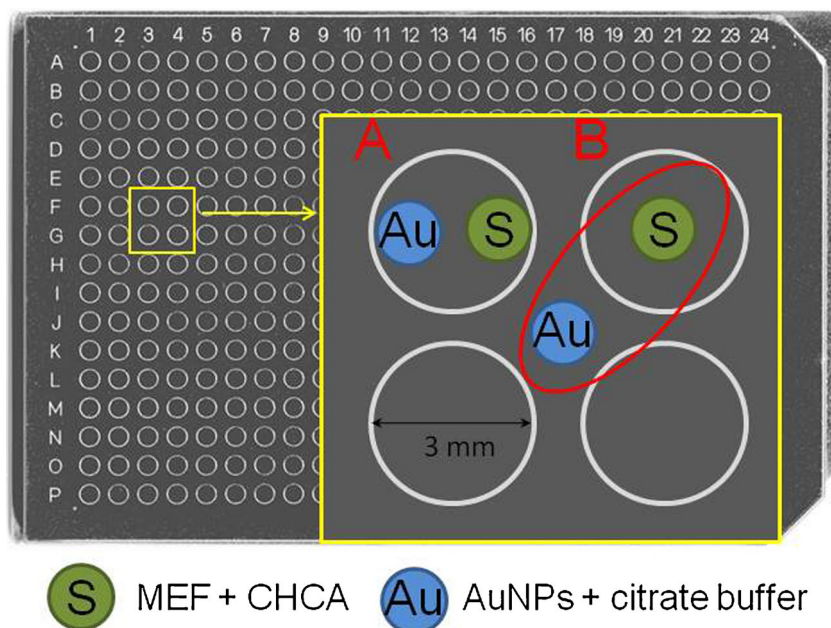


Figure 4. Sample deposition on the steel target plate for semi-internal calibration. Position A: calibrant and sample are spotted to the same well. Position B: calibrant is situated in the center of four neighboring wells. Au = AuNPs; S = sample

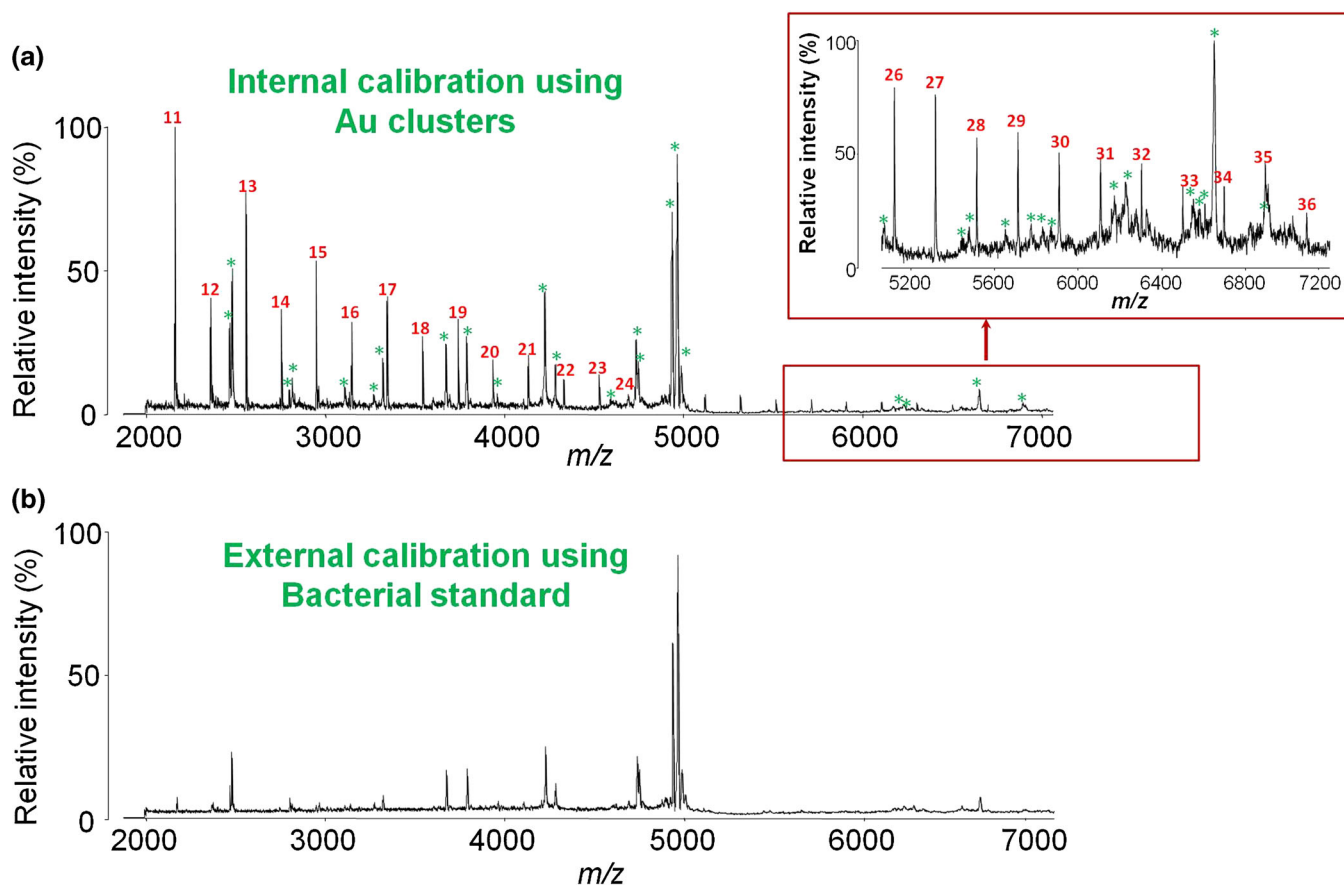


Figure 5. Spectrum of gold clusters (Au_n^+ , red numbers) with peptides/proteins (green stars) from mouse embryonic fibroblasts. Mass spectrum of mouse embryonic fibroblasts with (a) internal calibration using Au_{11-35}^+ clusters with mass accuracy ± 7 ppm, and (b) external calibration using Bacterial Test Standard with mass accuracy ± 33 ppm. Conditions: positive linear ion mode, 95 and 130 a.u. laser energy, mass range m/z 2000–7200, 100% corresponds to (a) 26 mV, and (b) 45 mV

14,000). The intensity of Au clusters from m/z 14,000 up to m/z 17,000 was less than 1 mV and was thus not suitable for calibration. Therefore, we used only the peaks with intensity higher than 1 mV. Peak maxima were determined by Gradient-Centroid peak detection. Table 1 summarizes the accuracy of the mass of the Au clusters in each ion mode, with each value calculated as an average of the absolute errors of mass determination in ppm. The mass list of the gold cluster values (theoretical and experimental), differences between the theoretical and experimental masses, and calculated errors in absolute value of ppm are summarized in Supplementary Tables S1–S8 (On-line Resource 1). The corresponding spectra in the individual modes are shown in Supplementary Figures S1–S8 (On-line Resource 1).

The use of gold clusters for calibration has several advantages. The synthesis of gold nanoflowers or polyhedral AuNPs is facile, fast, and cheap. The determination of the masses of Au clusters is simple and precise because of the mono-isotopicity of gold. Statistical evaluation (Figure 2) of the peak shapes confirmed that the peaks followed an almost perfect Gaussian waveform. Thus, from our results we can conclude that gold clusters are suitable for the calibration of TOF/QIT-TOF analyzers in both low and high mass ranges.

Recently, we showed that flower-like AuNPs deposited on the target plate enhance the ionization of peptides [17]. We were curious whether the gold clusters generated by high-energy LDI could be used for the internal calibration of biomolecules such as small peptides or even proteins. We mixed peptides or BTS with gold flower-like AuNPs and

recorded the mass spectra. The generated gold clusters did not interfere with the peptides or proteins, and the peaks of the clusters were clearly distinguishable among the peaks of the analyte (Figure 3). Based on this promising observation, we investigated whether the same approach could be applied to highly complex mixtures of biomolecules, such as the total extracts of eukaryotic cells. First, we tested the generation of gold clusters from flower-like AuNPs in mixture with total MEF extract. However, the efficacy of fragmentation of the flower-like AuNPs was rather unsatisfactory, and we found virtually no peaks of gold clusters (data not shown). Therefore, we introduced a different calibration approach in which total MEF extract with CHCA matrix and flower-like AuNPs in citrate buffer were spotted separately, either on the sample spot or in close mutual proximity (Figure 4). The samples were close to the calibrant; the distance between them was maximally 1.5 mm. The spotting of the samples is shown in Figure 4. We changed the position of the laser beam and the value of the laser energy manually during the measurement. When the spectra of a sample showed sufficient intensity (from a minimum of 300 laser shots), we moved the position of the laser beam toward that of the calibrant. We increased the laser energy to effectively generate gold clusters and recorded a minimum of 300 profiles of the calibrant. The optimal laser energy for the ionization of the components of the cell extract was 95 a.u., but a minimum laser energy of 130 a.u. was required to effectively generate Au_n^+ clusters. Therefore, we first recorded the signals of the MEF extract at 95 a.u. laser energy. Then, without any interruption of

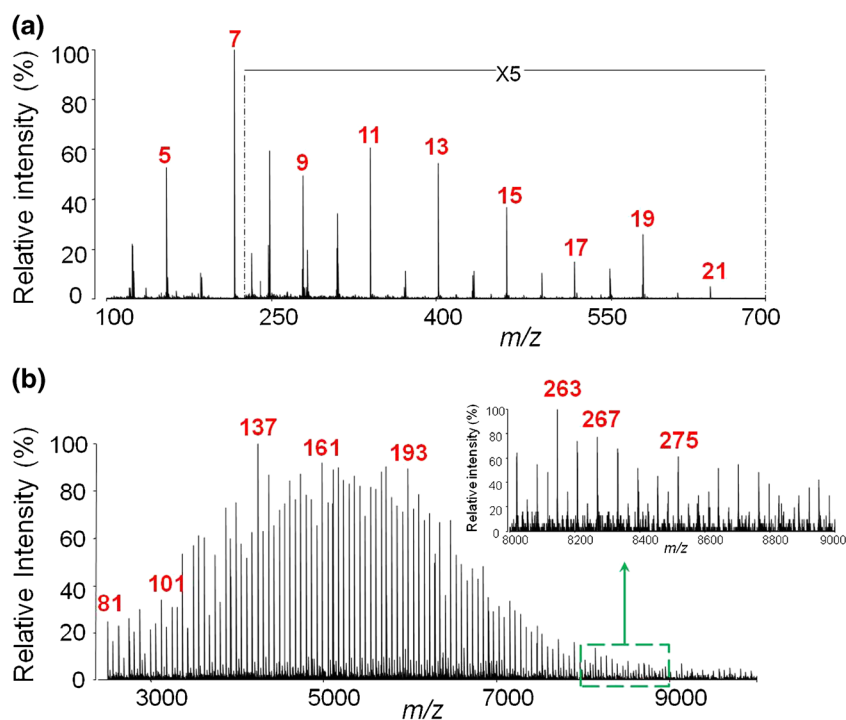


Figure 6. Mass spectrum demonstrating the generation of phosphorus clusters by LDI of red phosphorus in positive reflectron ion mode by AXIMA Resonance MALDI-QIT-TOF MS. **(a)** Spectrum in low mass range m/z 100–700, and **(b)** higher mass range m/z 2500–10,000. Conditions: average of 1000 laser shots, 100 and 120 a.u. laser energy, 100% intensity corresponds to **(a)** 81 mV, and **(b)** 2 mV. Selected n values of P_n^+ clusters are given (in red)

Table 2. Mass Accuracy of $P_n^{+/-}$ Cluster Peaks Determination

		m/z range		
		100–1000	2000–5000	5000–14,000
Ion modes	Lin +	25 ppm	-	-
	Lin -	194 ppm	-	-
	Ref +	5 ppm	7 ppm	-
	Ref -	8 ppm	4 ppm	-

- No peaks or intensities of $P_n^{+/-}$ clusters too low for detection

measurement, we increased the laser energy to 130 a.u. and recorded the signal of the Au_n cluster peaks. Thus, we recorded the final spectrum at two energetic levels, obtaining the

peaks of the gold clusters as well as peaks of the MEF extract. In this way, we eliminated the mutual suppression of signals between the cell extract and gold clusters. The calibration using the Au_n clusters produced significantly better results than external calibration with BTS (Figure 5). The mass precision of MEF spectra generated with internal calibration using Au_{11-35}^+ clusters reached ± 7 ppm (± 0.03 Da), whereas that generated with external calibration using BTS reached ± 33 ppm (± 0.2 Da). The comparison of the two MEF spectra calibrated externally using BTS and internally using Au_n^+ clusters, respectively, led to the conclusion that the differences between the signals of the MEFs are about ± 0.3 Da on average. The data evaluation is summarized in Supplementary Tables S1 and S2 in On-line Resource 2.

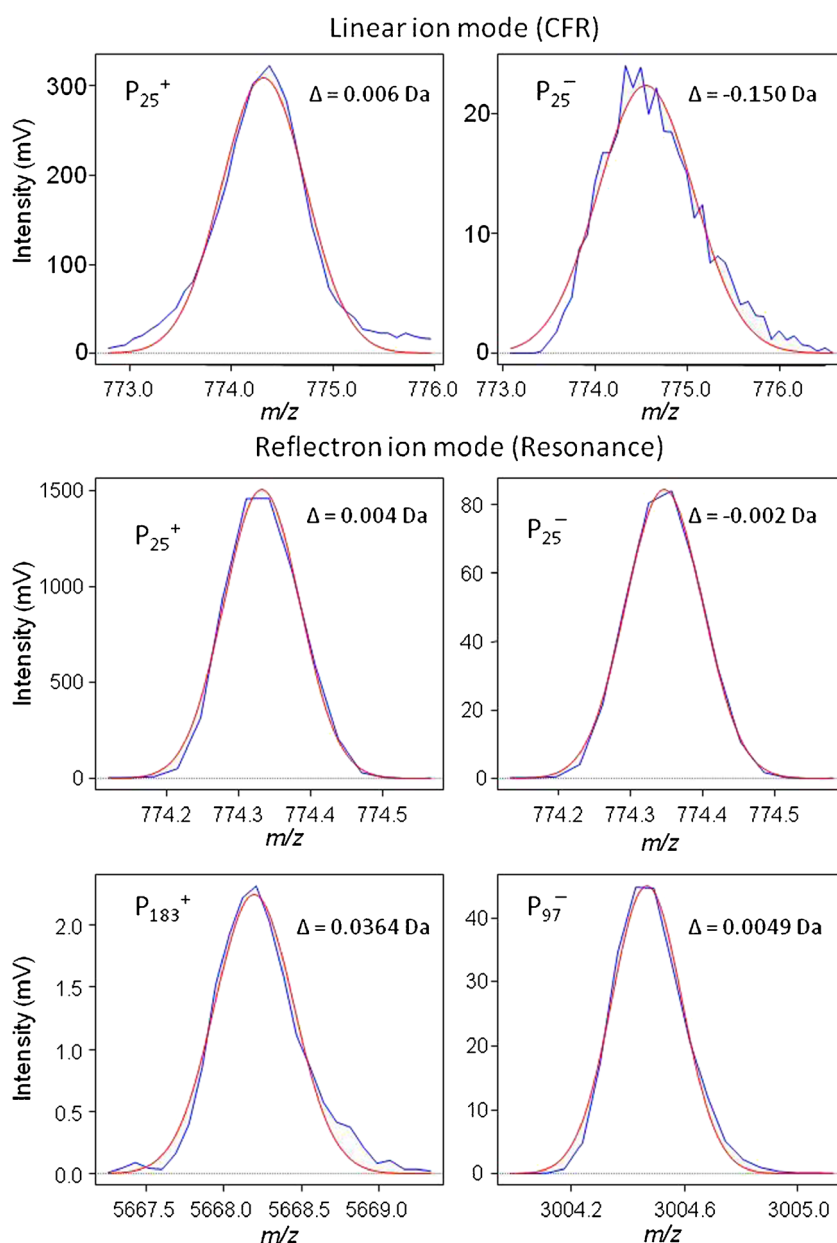


Figure 7. Statistical evaluation of the peak shapes of P_n clusters by the fitting of a Gaussian curve. Smooth line in red is a Gaussian curve, $\Delta = (m/z)_{\text{theoretical}} - (m/z)_{\text{experimental}}$

Overall, our results show that the new calibration approach using gold clusters provides an option for the analysis of highly complex biological samples requiring precise and accurate calibration.

Phosphorus clusters ($P_n^{+/-}$)

Red phosphorus has advantages similar to those of gold. The greatest advantages are its mono-isotopicity and easy formation of peaks of $P_n^{+/-}$ clusters using LDI. In our laboratory, we introduced the calibration of mass spectra using red phosphorus clusters 5 y ago, and we generated excellent results with the technique. The following are new results that extend those of our previous publication [6] regarding of the use of red phosphorus clusters for the calibration of TOF MS in each mode.

We used the AXIMA CFR TOF and AXIMA Resonance QIT-TOF instruments for experiments in linear and reflectron ion modes, respectively. For the generation of $P_n^{+/-}$ cluster peaks, we used a red phosphorus powder. It is recommended that only the peaks of phosphorus clusters with an odd number of phosphorus atoms be used for calibration because peaks with an even number usually have low signal intensity. Moreover, clusters with an even number of peaks may contain hydrogenated forms and therefore entail a high risk of erroneous calibration due to the selection of the wrong peak. At high laser energy in both positive and negative linear ion mode, $P_n^{+/-}$ clusters up to m/z 4000 were achieved. In positive and negative reflectron ion mode at maximum laser energy, we achieved $P_n^{+/-}$ clusters up to m/z 7000 and m/z 10,000, respectively. We achieved higher phosphorus clusters with increased laser energy. We investigated the accuracy of the determination of the phosphorus masses with odd numbers of cluster peaks.

Figure 6 shows selected LDI mass spectra of red phosphorus in positive reflectron ion mode. Figure 6a shows P_n^+ clusters from $n=4$ up to $n=22$ in the mass range m/z 100–700. We detected additional low-intensity peaks of P_4H^+ , P_6H^+ , P_8H^+ , $P_{10}H^+$, $P_{12}H^+$, $P_{14}H^+$, $P_{16}H^+$, and P_7O^+ in the spectrum. Figure 6b shows P_n^+ clusters ($n=81$ up to $n=275$) in the mass range m/z 2500–9000.

We evaluated calibration in three mass ranges: low (m/z 100–1000), medium (m/z 2000–5000), and high (m/z 7000–14,000). The intensity of P_n^+ clusters from m/z 7000–10,000 was less than 1 mV, so those peaks were not suitable for calibration. The mass list of the $P_n^{+/-}$ cluster values (theoretical and experimental), differences between the theoretical and experimental masses, and calculated errors in absolute value of ppm are provided in Supplementary Tables S9–S16 (On-line Resource 1). The corresponding spectra in the individual modes are shown in Supplementary Figures S9–S16 (On-line Resource 1).

For calibration, we used peaks with intensity higher than 1 mV. Table 2 summarizes the accuracy of the mass of the P_n clusters in each ion mode. Peak maxima were determined by gradient-centroid peak detection. Statistical evaluation (Figure 7) of the peak shapes confirmed that the peaks followed an almost perfect Gaussian waveform. From our results, we can conclude that P_n clusters are suitable for the calibration of TOF/QIT-TOF analyzers in both low and high mass ranges.

It is possible to use P_n cluster peaks for the internal calibration of peptides, not only in linear ion mode [6] but also in reflectron ion mode (see Figure 8). One possible disadvantage of internal calibration using P_n cluster peaks is the likelihood of interference with the analyte due to the shorter repetition of the P_n cluster peaks compared with that of Au_n cluster peaks.

In this work, we focused primarily on gold and phosphorus as the prototypical examples of monoisotopic elements. Evidently, clusters of other monoisotopic elements, such as cesium, iodine, or five of lanthanides can be used in similar manner.

Conclusion

We demonstrated that the in situ generation of gold clusters by LDI is suitable for the external and internal calibration of mass spectrometry of biomolecules. The stability, inertness, and monoisotopic nature of gold and phosphorus clusters provide an accurate calibration standard and thus ensure correct mass spectra, even for highly complex biological samples such as peptide mixtures and total cell extracts.

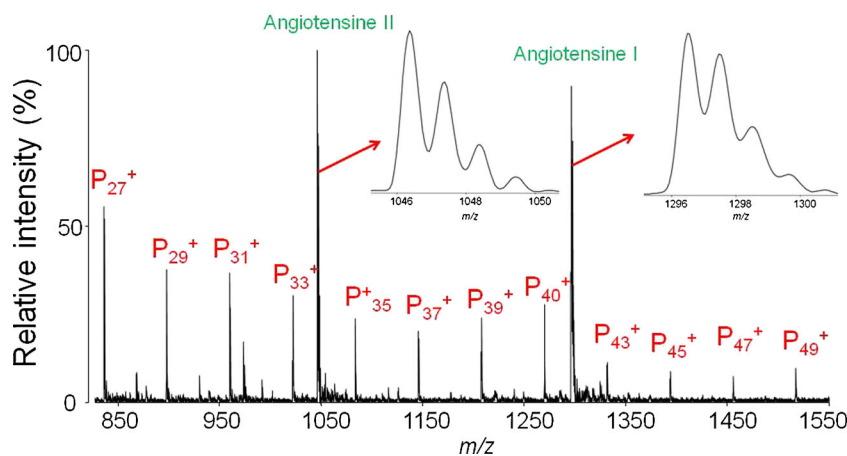


Figure 8. Spectrum of phosphorus clusters (P_n^+ , $n=27-49$) with angiotensin I and II. Conditions: positive reflectron ion mode, 95 a.u. laser energy, mass range m/z 850–1550, 100% intensity corresponds to 495 mV

Acknowledgments

The authors acknowledge support for this work by funds from the National Program of Sustainability II (project no. LQ1605, MEYS CR); Masaryk University, MUNI/A/1352/2015 and Center for Analysis and Modeling of Tissues and Organs (CZ.1.07/2.3.00/20.0185); and the Ministry of Economy and Competitiveness, Spain (MAT2014-57465-R).

References

- Gruending, T., Sauerland, V., Barahona, C., Herz, C., Nitsch, U.: Polyalanine—a practical polypeptide mass calibration standard for matrix-assisted laser desorption/ionization mass spectrometry and tandem mass spectrometry in positive and negative mode. *Rapid Commun. Mass Spectrom.* **30**, 681–683 (2016)
- Grayson, S.M., Myers, B.K., Bengtsson, J., Malkoch, M.: Advantages of monodisperse and chemically robust “SpheriCal” polyester dendrimers as a “universal” MS calibrant. *J. Am. Soc. Mass Spectrom.* **25**, 303–309 (2014)
- Edmondson, R.D., Russell, D.H.: Evaluation of matrix-assisted laser desorption ionization-time-of-flight mass measurement accuracy by using delayed extraction. *J. Am. Soc. Mass Spectrom.* **7**, 995–1001 (1996)
- Kellerbauer, A., Blaum, K., Bollen, G., Herfurth, F., Kluge, H.-J., Kuckein, M., Sauvan, E., Scheidenberger, C., Schweikhard, L.: Carbon cluster ions for a study of the accuracy of ISOLTRAP. In: Knudsen, H., Andersen, J.U., Kluge, H.-J. (eds.) *Atomic physics at accelerators: stored particles and fundamental physics*, pp. 307–312. Springer, Dordrecht (2003)
- Chaudhuri, A., Block, M., Eliseev, S., Ferrer, R., Herfurth, F., Martín, A., Marx, G., Mukherjee, M., Rauth, C., Schweikhard, L., Vorobjev, G.: Carbon-cluster mass calibration at SHIPTRAP. *Eur. Phys. J. D.* **45**, 47–53 (2007)
- Sládková, K., Houška, J., Havel, J.: Laser desorption ionization of red phosphorus clusters and their use for mass calibration in time-of-flight mass spectrometry. *Rapid Commun. Mass Spectrom.* **23**, 3114–3118 (2009)
- Lou, X., van Dongen, J.L.J., Meijer, E.W.: Generation of CsI cluster ions for mass calibration in matrix-assisted laser desorption/ionization mass spectrometry. *J. Am. Soc. Mass Spectrom.* **21**, 1223–1226 (2010)
- Mochizuki, S.: Enhanced measurement of CsI cluster ions for mass calibration in MALDI-MS using sugar alcohols. *Anal. Methods* **7**, 2215–2218 (2015)
- Mochizuki, S.: Effective methods for the measurement of CsI cluster ions using MALDI-MS with suitable solvent combinations and additives. *J. Mass Spectrom.* **49**, 1199–1202 (2014)
- Pangavhane, S.D., Hebedová, L., Alberti, M., Havel, J.: Laser ablation synthesis of new phosphorus nitride clusters from α -P3N5 via laser desorption ionization and matrix assisted laser desorption ionization time-of-flight mass spectrometry. *Rapid Commun. Mass Spectrom.* **25**, 917–924 (2011)
- Panyala, N.R., Peña-Méndez, E.M., Havel, J.: Laser ablation synthesis of new gold phosphides using red phosphorus and nanogold as precursors. *Laser desorption ionisation time-of-flight mass spectrometry. Rapid Commun. Mass Spectrom.* **26**, 1100–1108 (2012)
- Houška, J., Peña-Méndez, E.M., Hernandez-Fernaud, J.R., Salido, E., Hampl, A., Havel, J., Vaňhara, P.: Tissue profiling by nanogold-mediated mass spectrometry and artificial neural networks in the mouse model of human primary hyperoxaluria 1. *J. Appl. Biomed.* **12**, 119–125 (2014)
- Švihlová, K., Prokeš, L., Skácelová, D., Peña-Méndez, E.M., Havel, J.: Laser ablation synthesis of new gold tellurides using tellurium and nano-gold as precursors. *Laser desorption ionisation time-of-flight mass spectrometry. Rapid Commun. Mass Spectrom.* **27**, 1600–1606 (2013)
- Štěpánová, V., Prokeš, L., Slaviček, P., Alberti, M., Havel, J.: Laser ablation generation of clusters from As-Te mixtures, As-Te glass nanolayers, and from Au-As-Te nanocomposites. *Quadrupole ion trap time-of-flight mass spectrometry. Rapid Commun. Mass Spectrom.* **29**, 1000–1008 (2015)
- Mawale, R.M., Amato, F., Alberti, M., Havel, J.: Generation of Au(p)Ag(q)Te(r) clusters via laser ablation synthesis using Au-Ag-Te nano-composite as precursor: quadrupole ion-trap time-of-flight mass spectrometry. *Rapid Commun. Mass Spectrom.* **28**, 1601–1608 (2014)
- Havel, J., Peña-Méndez, E.M., Amato, F., Panyala, N.R., Buršíková, V.: Laser ablation synthesis of new gold carbides. From gold-diamond nanocomposite as a precursor to gold-doped diamonds. *Time-of-flight mass spectrometric study. Rapid Commun. Mass Spectrom.* **28**, 297–304 (2014)
- Blaum, K., Herlert, A., Huber, G., Kluge, H.-J., Maul, J., Schweikhard, L.: Cluster calibration in mass spectrometry: laser desorption/ionization studies of atomic clusters and an application in precision mass spectrometry. *Anal. Bioanal. Chem.* **377**, 1133–1139 (2003)
- Kéki, S., Nagy, L., Deák, G., Zsuga, M.: Bimetallic silver-gold clusters by matrix-assisted laser desorption/ionization. *J. Am. Soc. Mass Spectrom.* **15**, 1455–1461 (2004)
- Tsunoyama, H., Tsukuda, T.: Magic numbers of gold clusters stabilized by PVP. *J. Am. Chem. Soc.* **131**, 18216–18217 (2009)
- Chen, W.-T., Tomalová, I., Preisler, J., Chang, H.-T.: Analysis of biomolecules through surface-assisted laser desorption/ionization mass spectrometry employing nanomaterials. *J. Chinese Chem. Soc.* **58**, 769–778 (2011)
- Pirolli, R., Palmisano, F., Cioffi, N.: Gold nanomaterials as a new tool for bioanalytical applications of laser desorption ionization mass spectrometry. *Anal. Bioanal. Chem.* **402**, 601–623 (2012)
- Kolářová, L., Kučera, L., Vaňhara, P., Hampl, A., Havel, J.: Use of flower-like gold nanoparticles in time-of-flight mass spectrometry. *Rapid Commun. Mass Spectrom.* **29**, 1585–1595 (2015)
- Häkkinen, H.: Atomic and electronic structure of gold clusters: understanding flakes, cages, and superatoms from simple concepts. *Chem. Soc. Rev.* **37**, 1847–1859 (2008)
- Zanti, G., Peeters, D.: Electronic structure analysis of small gold clusters Au_m ($m \leq 16$) by density functional theory. *Theor. Chem. Acc.* **132**, 1300 (2012)
- Pyykkö, P.: Theoretical chemistry of gold. III. *Chem. Soc. Rev.* **37**, 1967 (2008)
- Bulgakov, A.V., Bobrenok, O.F., Kosyakov, V.I.: Laser ablation synthesis of phosphorus clusters. *Chem. Phys. Lett.* **320**, 19–25 (2000)
- Stoermer, C., Friedrich, J., Kappes, M.M.: Observation of multiply charged cluster anions upon pulsed UV laser ablation of metal surfaces under high vacuum. *Int. J. Mass Spectrom.* **206**, 63–78 (2001)
- Jiang, Y., Wu, X.-J., Li, Q., Li, J., Xu, D.: Facile synthesis of gold nanoflowers with high surface-enhanced Raman scattering activity. *Nanotechnology* **22**, 385601–385606 (2011)
- Wang, W., Chen, Q., Jiang, C., Yang, D., Liu, X., Xu, S.: One-step synthesis of biocompatible gold nanoparticles using gallic acid in the presence of poly-(N-vinyl-2-pyrrolidone). *Colloid. Surf. A Physicochem. Eng. Asp.* **301**, 73–79 (2007)

14. Amato F, Lopez A, Pena-Mendez E, **Vanhara P**, Hampf A, Havel J. **Artificial neural networks in medical diagnosis.** *Journal of Applied Biomedicine* 2013; **11**(2):47-58.

Commentary:

A review publication suggesting applications of artificial intelligence (AI) methods in clinical diagnostics including histopathological decisions. This manuscript defines a theoretical background for projects investigating AI-based cell and tissue profiling and analyzes of intrinsic heterogeneity.

DOI:	10.2478/v10136-012-0031-x
Journal:	Journal of Applied Biomedicine
Impact factor (WOS, 2013):	1.775
Number of citations (WOS, 2018):	144
Cited in:	Journal of Medical Systems, Kidney International, Journal of Medical Imaging and Health Informatics, Neural Networks, Journal of Medical and Biological Engineering, Plos One, Gastrointestinal Endoscopy, etc.
Most important citation:	Zhang J, Friberg IM, Kift-Morgan A, Parekh G, Morgan MP, Liuzzi AR, Lin CY, Donovan KL, Colmont CS, Morgan PH, Davis P, Weeks I, Fraser DJ, Topley N, Eberl M. Machine-learning algorithms define pathogen-specific local immune fingerprints in peritoneal dialysis patients with bacterial infections. <i>Kidney International</i> 2017; 92 (1):179-191. doi: 10.1016/j.kint.2017.01.017. (IF 2016: 8.395)
Contribution of the author:	Co-authorship. Design and writing of manuscript.

EDITORIAL

Artificial neural networks in medical diagnosis

Filippo Amato¹, Alberto López^{1*}, Eladia María Peña-Méndez², Petr Vaňhara³, Aleš Hampl^{3,4}, Josef Havel^{1,5,6}

¹Department of Chemistry, Faculty of Science, Masaryk University, Brno, Czech Republic

²Department of Analytical Chemistry, Nutrition and Food Science, Faculty of Chemistry, University of La Laguna, La Laguna, Tenerife, Spain

³Department of Histology and Embryology, Faculty of Medicine, Masaryk University, Brno, Czech Republic

⁴International Clinical Research Center, St. Anne's University Hospital, Brno, Czech Republic

⁵Department of Physical Electronics, Faculty of Science, Masaryk University, Brno, Czech Republic

⁶R&D Centre for low-cost plasma and nanotechnology surface modifications, CEPLANT, Masaryk University, Brno, Czech Republic

* On leave from the University of Salamanca, Spain

Received 17th December 2012.

Published online 7th January 2013.

Summary

An extensive amount of information is currently available to clinical specialists, ranging from details of clinical symptoms to various types of biochemical data and outputs of imaging devices. Each type of data provides information that must be evaluated and assigned to a particular pathology during the diagnostic process. To streamline the diagnostic process in daily routine and avoid misdiagnosis, artificial intelligence methods (especially computer aided diagnosis and artificial neural networks) can be employed. These adaptive learning algorithms can handle diverse types of medical data and integrate them into categorized outputs. In this paper, we briefly review and discuss the philosophy, capabilities, and limitations of artificial neural networks in medical diagnosis through selected examples.

Key words: medical diagnosis; artificial intelligence; artificial neural networks; cancer; cardiovascular diseases; diabetes

INTRODUCTION

Artificial neural networks (ANNs) are widely used in science and technology with applications in various branches of chemistry, physics, and biology.

For example, ANNs are used in chemical kinetics (Amato et al. 2012), prediction of the behavior of industrial reactors (Molga et al. 2000), modeling kinetics of drug release (Li et al. 2005), optimization of electrophoretic methods (Havel et al. 1998), classification of agricultural products such as onion varieties (Rodríguez Galdón et al. 2010), and even species determination (Fedor et al. 2008, Michalkova et al. 2009, Murarikova et al. 2010). In general, very diverse data such as classification of biological objects, chemical kinetic data, or even clinical parameters can be handled in essentially the same way. Advanced computational methods, including ANNs, utilize diverse types of input data that are processed in the context of previous training history

✉ Josef Havel, Department of Chemistry, Faculty of Science, Masaryk University, Kamenice 5/ A14, 625 00 Brno, Czech Republic

✉ havel@chemi.muni.cz

☎ +420 549 494 114

☎ +420 549 492 494

on a defined sample database to produce a clinically relevant output, for example the probability of a certain pathology or classification of biomedical objects. Due to the substantial plasticity of input data, ANNs have proven useful in the analysis of blood and urine samples of diabetic patients (Catalogna et al. 2012, Fernandez de Canete et al. 2012), diagnosis of tuberculosis (Er et al. 2008, Elveren and Yumuşak 2011), leukemia classification (Dey et al. 2012), analysis of complicated effusion samples (Barwad et al. 2012), and image analysis of radiographs or

even living tissue (Barbosa et al. 2012, Saghiri et al. 2012).

The aim of this paper is to present the general philosophy for the use of ANNs in diagnostic approaches through selected examples, documenting the enormous variability of data that can serve as inputs for ANNs. Attention will not only be given to the power of ANNs applications, but also to evaluation of their limits, possible trends, and future developments and connections to other branches of human medicine (Fig. 1).

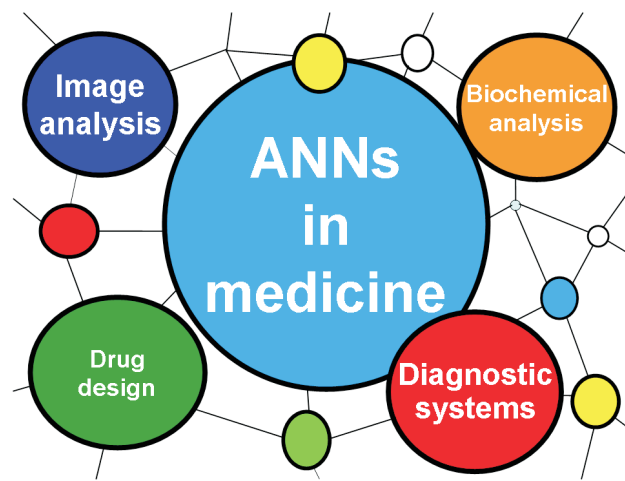


Fig. 1. Overview of the main applications of artificial neural networks in medicine.

ARTIFICIAL NEURAL NETWORKS

An ANN is a mathematical representation of the human neural architecture, reflecting its “learning” and “generalization” abilities. For this reason, ANNs belong to the field of artificial intelligence. ANNs are widely applied in research because they can model highly non-linear systems in which the relationship among the variables is unknown or very complex. A review of various classes of neural networks can be found in (Aleksander and Morton 1995, Zupan and Gasteiger 1999).

Mathematical background

A neural network is formed by a series of “neurons” (or “nodes”) that are organized in layers. Each neuron in a layer is connected with each neuron in the next layer through a weighted connection. The value of the weight w_{ij} indicates the strength of the connection between the i -th neuron in a layer and the j -th neuron in the next one.

The structure of a neural network is formed by an “input” layer, one or more “hidden” layers, and the “output” layer. The number of neurons in a layer and the number of layers depends strongly on the complexity of the system studied. Therefore, the optimal network architecture must be determined. The general scheme of a typical three-layered ANN architecture is given in Fig. 2.

The neurons in the input layer receive the data and transfer them to neurons in the first hidden layer through the weighted links. Here, the data are mathematically processed and the result is transferred to the neurons in the next layer. Ultimately, the neurons in the last layer provide the network’s output. The j -th neuron in a hidden layer processes the incoming data (x_j) by: (i) calculating the weighted sum and adding a “bias” term (θ_j) according to Eq. 1:

$$net_j = \sum_{i=1}^m x_i \times w_{ij} + \theta_j \quad (j = 1, 2, \dots, n) \quad (1)$$

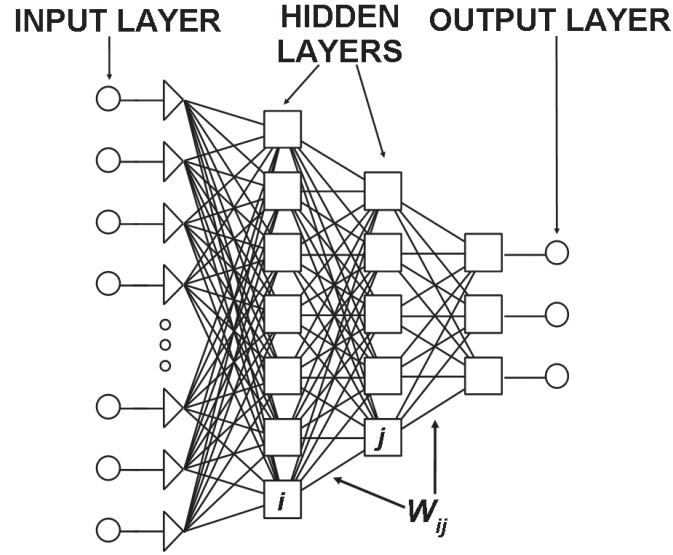


Fig. 2. General structure of a neural network with two hidden layers. The w_{ij} is the weight of the connection between the i -th and the j -th node.

(ii) transforming the net_j through a suitable mathematical “transfer function”, and (iii) transferring the result to neurons in the next layer. Various transfer functions are available (Zupan and Gasteiger 1999); however, the most commonly used is the sigmoid one:

$$f(x) = \frac{1}{1 + e^{-x}} \quad (2)$$

Network learning

The mathematical process through which the network achieves “learning” can be principally ignored by the final user. In this way, the network can be viewed as a “black box” that receives a vector with m inputs and provides a vector with n outputs (Fig. 3). Here we will give only a brief description of the learning process; more details are provided for example in the review by (Basheer and Hajmeer 2000). The network “learns” from a series of “examples” that form the “training database” (Fig. 4). An “example” is formed by a vector $X_{im} = (x_{i1}, x_{i2}, \dots, x_{im})$ of inputs and a vector $Y_{in} = (y_{i1}, y_{i2}, \dots, y_{in})$ of outputs. The objective of the training process is to approximate the function f between the vectors X_{im} and the Y_{in} :

$$Y_{i,n} = f(X_{i,m}) \quad (3)$$

This is achieved by changing iteratively the values of the connection weights (w_{ij}) according to a suitable mathematical rule called the *training algorithm*.

The values of the weights are changed by using the steepest descent method to minimize a suitable function used as the training stopping criteria. One of the functions most commonly used is the sum-of-squared residuals given by Eq. 4:

$$E = \frac{1}{2} \sum_{i=1}^m \sum_{j=1}^n (y_{ij} - y_{ij}^*)^2 \quad (4)$$

where y_{ij} and y_{ij}^* are the actual and network’s j -th output corresponding to the i -th input vector, respectively.

The current weight change on a given layer is given by Eq. (5):

$$\Delta w_{ij} = -\eta \frac{dE}{dw_{ij}} \quad (5)$$

where η is a positive constant called the *learning rate*. To achieve faster learning and avoid local minima, an additional term is used and Eq. 5 becomes:

$$\Delta w_{ij}^k = -\eta \frac{dE}{dw_{ij}} + \mu \Delta w_{ij}^{k-1} \quad (6)$$

where μ is the “momentum” term and Δw_{ij}^{k-1} is the change of the weight w_{ij} from the $(k-1)$ -th learning cycle. The learning rate controls the weight update rate according to the new weight change and the momentum acts as a stabilizer, being aware of the previous weight change.

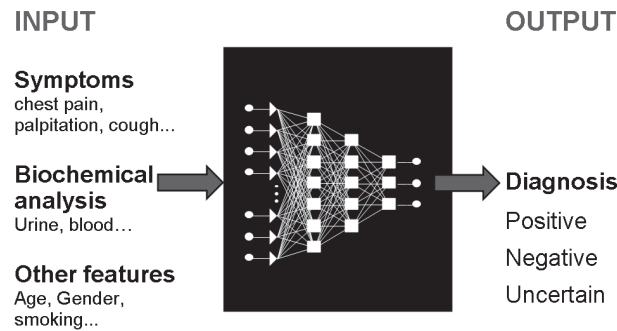


Fig. 3. Details of input and output items concerning ANNs-based diagnosis (ANN architecture is often hidden and it is indicated here as a black box).

Patient code	MEDICAL DATA	DIAGNOSIS
1	data _{1,1} ... data _{1,i} ... data _{1,m}	POSITIVE
2	data _{2,1} ... data _{2,i} ... data _{2,m}	POSITIVE
3	data _{3,1} ... data _{3,i} ... data _{3,m}	POSITIVE
...
k	data _{k,1} ... data _{k,i} ... data _{k,m}	NEGATIVE
k+1	data _{k+1,1} ... data _{k+1,i} ... data _{k+1,m}	NEGATIVE
...
n	data _{n,1} ... data _{n,i} ... data _{n,m}	NEGATIVE

Fig. 4. Example of training database structure. Each row refers to a different patient labeled with a numerical code. The element data_{k,i} refers to the *i*-th medical data (symptom, laboratory data, etc.) of the *k*-th patient.

The function given by Eq. 4 is also used as the criterion to optimize the network architecture because it depends on the number of hidden layers and the number of neurons therein. To find the optimal architecture, the most common approach is to plot the value of *E* (Eq. 4) as a function of the number of nodes in the hidden layer (*q*). An example of such a plot is given in Fig. 5. As *q* increases, *E* decreases. However, after an optimal value of *q* the improvement is rather poor. Usually, the optimal value of *q* is found from the intersection point of the two branches of the plot.

After the optimal neural network architecture is found, the training process is performed until a proper minimum value of *E* is reached. Afterward, the network is checked with examples not previously used in the training step. This process is called verification. Finally, the network can be used to predict outputs for new input vectors.

Structure of the training database

As stated above, the network must be trained using a suitable database. The database is a table (or *matrix*) of data concerning patients for whom the diagnosis (positive or negative) about a certain disease is already known. Each row of the matrix refers to one patient. The first *m* elements of the row are medical data and the last *n* elements represent the output (*diagnosis*). The term “*medical data*” indicates biochemical, nuclear magnetic resonance (NMR), laboratory data, and symptoms and other information provided by the medical specialist (Table 1). An example of such training matrix with one output variable (*n* = 1) that may assume two possible values (*positive* or *negative*) is given in Fig. 4.

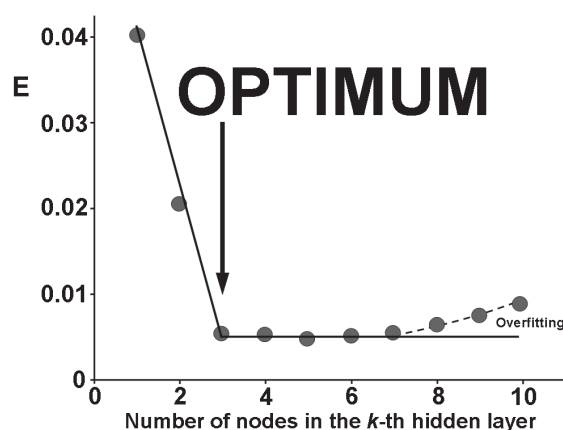


Fig. 5. Example of the plot used to select the optimal number of nodes in a given hidden layer. It is indicated that too high number of nodes might lead to overfitting.

Table 1. Brief overview of data in clinical context used as inputs for ANN.

Input data or method	Clinical context	Output information	Reference
Age, cholesterol concentration, arterial hypertension	Coronary artery disease	Diagnosis	(Atkov et al. 2012)
Heart sound	Valve stenosis	Diagnosis	(Uğuz 2012)
Hematologic profile	Chronic myeloid leukemia	Classification of leukemia	(Dey et al. 2012)
Visual information of wireless capsule endoscopy	Small bowel tumors	Diagnosis, classification of tumor	(Barbosa et al. 2012)
Glucose concentration – Near-infrared spectroscopy	Diabetes	Diagnosis	(Arnold 1996)
Demographic and clinicopathologic data, surgical outcome	Hepatocellular carcinoma	Prediction of disease free survival	(Ho et al. 2012)
Cytology of effusion fluid	Carcinoma	Presence of malignant cells	(Barwad et al. 2012)
Speech record	Oral/Oropharyngeal cancer	Detection of nasalance (hypernasality)	(de Bruijn et al. 2011)
Electroencephalographic (EEG) recordings	Epilepsy	Prediction of seizures	(Fernandez-Blanco et al. 2012)

OVERVIEW OF ANNs IN MEDICAL DIAGNOSIS

There are several reviews concerning the application of ANNs in medical diagnosis. The concept was first outlined in 1988 in the pioneering work of (Szolovits et al. 1988) and since then many papers have been published. The general application of ANNs in medical diagnosis has previously been described

(Alkim et al. 2012). For example, ANNs have been applied in the diagnosis of: (i) colorectal cancer (Spelt et al. 2012), (ii) multiple sclerosis lesions (Mortazavi et al. 2012a, b), (iii) colon cancer (Ahmed 2005), (iv) pancreatic disease (Bartosch-Härlid et al. 2008), (v) gynecological diseases (Siristatidis et al. 2010), and (vi) early diabetes (Shankaracharya et al. 2010). In addition, ANNs have also been applied in the analysis

of data and diagnostic classification of patients with uninvestigated dyspepsia in gastroenterology (Pace and Savarino 2007) and in the search for biomarkers (Bradley 2012). A novel, general, fast, and adaptive disease diagnosis system has been developed based on learning vector quantization ANNs. This algorithm is the first proposed adaptive algorithm and can be applied to completely different diseases, as demonstrated by the 99.5% classification accuracy achieved for both breast and thyroid cancers. Cancer, diabetes, and cardiovascular diseases are among the most serious and diverse diseases. The amount of data coming from instrumental and clinical analysis of these diseases is quite large and therefore the development of tools to facilitate diagnosis is of great relevance. For this reason, we will provide a brief overview of the advances in the application of ANNs to the field of diagnosis for each of these diseases.

Cardiovascular diseases

Cardiovascular diseases (CVDs) are defined as all diseases that affect the heart or blood vessels, both arteries and veins. They are one of the most important causes of death in several countries. According to the National Center of Health Statistics (NCHS, www.cdc.gov/nchs), CVD represents the leading cause of death in the United States. CVD has therefore become an important field of study during the last 20 years.

Based on a bibliography search (ScienceDirect), more than one thousand papers about the use of ANNs in cardiovascular diseases and related topics have been published since 2008. According to the NCHS, coronary artery disease (CAD) is currently the leading cause of death worldwide, therefore early diagnosis is very important. With this aim, Karabulut and Ibrikçi applied ANNs with the Levenberg-Marquardt back propagation algorithm as base classifiers of the rotation forest ensemble method (Karabulut and Ibrikçi 2012). Diagnosis of CAD with 91.2% accuracy was achieved from data collected non-invasively, cheaply, and easily from the patient. Other data such as age, different kinds of cholesterol, or arterial hypertension have been used to diagnose CAD (Atkov et al. 2012). The model that performed with the best accuracy (93%) was the one that included both genetic and non-genetic factors related to the disease. Despite these promising results, it must be noted that for some models the accuracy was lower than 90%. ANNs have also been applied in other heart diseases, such as heart valve defects (Uğuz 2012). Heart sound recordings were obtained from 120 subjects and classified as normal, pulmonary, and mitral stenosis heart valve diseases via stethoscopy. Correct classification was achieved for 95% of the different sounds. An average accuracy

of 99.8% and 99.2% was achieved by two different models developed by (Özbay 2009) for the diagnosis of arrhythmias. Therefore, ANNs can be applied to the medical diagnosis of completely different diseases, for example detection of arrhythmias or coronary artery diseases, which are major causes of death worldwide. Classification accuracies higher than 90% are typically achieved, even exceeding 99% in some cases. As a result, ANNs have substantial potential in CVD diagnosis.

Cancer

According to the American Cancer Society (www.cancer.org), there will be more than 1.6 million newly diagnosed cases of cancer in the US in 2012. A rapid and correct diagnosis is essential for the clinical management of cancer, including selection of the most suitable therapeutic approach. The use of ANNs in distinguishing particular cancer types or the prediction of cancer development emerged in the late 1990s as a promising computational-based diagnostic tool using various inputs. Use of novel molecular approaches, such as micro-RNA screens, broadens the possibilities for the application of ANNs in the search for patterns specific for a certain disease, for example rectal cancer and its response to cytoreductive therapy (Kheirelseid et al. 2012). The application of neural networks trained on defined data sets was evaluated in 1994 for breast and ovarian cancer, opening a discussion on the suitability of particular data as inputs for ANN analysis, for example demographic (age), radiological (NMR), oncologic (tumor markers CA 15-3 or CA 125), and biochemical (albumin, cholesterol, high-density lipoprotein cholesterol, triglyceride, apolipoproteins A1 and B) data (Wilding et al. 1994). Later on, reasonable prediction of the measured *in vitro* chemotherapeutic response based on ¹H NMR of glioma biopsy extracts was achieved using ANNs to obtain automatic differential diagnosis of glioma (El-Dereby et al. 1997).

Moreover, advanced analytical methods, such as mass spectrometry, can offer suitable information for clinically relevant ANN analysis. This technique has recently been applied successfully in the diagnosis of ovarian cancer. Upon identification of the most informative points of the mass spectrum curve, for example by data mining, the integrated feed-forward ANN classifier showed an overall sensitivity of 98% and a specificity of 96%, surpassing standard statistical methods such as Student's t-test (Thakur et al. 2011).

The applications of ANNs in radiology aim to develop automated decision support systems, assisting, for example, in the classification of brain tumors by magnetic resonance (Tate et al. 2006). The

concept and design raised by Tate was also applied by Brougham and colleagues on lung carcinoma (Brougham et al. 2011). In this process, the same experimental protocol was carried out by two different teams of researchers examining two sets of whole-cell ^1H NMR spectra at different times. Whole-cell ^1H NMR spectra were recorded for two groups of human lung carcinoma cell lines, which were grown in culture and included (i) the parent cell line DLKP, a human squamous non-small cell lung carcinoma; (ii) DLKP-A and (iii) DLKP-A5F, two resistant daughter lines; and (iv) A549 a human lung adenocarcinoma cell line. Despite demonstrated operator-induced sources of variation in the network, the ANN was able to classify the cell line correctly in 100% of cases independent of the spectra selected for training and validation. Therefore, the power of ANNs for the classification of different types of lung carcinoma in real clinical or laboratory situations was demonstrated. In summary, ANNs have been shown to use various primary data, ranging from clinical parameters to biochemical values, and provide increased diagnostic accuracy for various kinds of cancers.

Diabetes

Diabetes represents a serious health problem in developed countries, with estimated numbers reaching 366 million diabetes cases globally in 2030 (Leon et al. 2012). The most common type of diabetes is type II, in which the cellular response to insulin is impaired leading to disruption of tissue homeostasis and hyperglycemia. The standard in diabetes diagnosis or monitoring is direct measurement of glucose concentration in blood samples. Non-invasive methods based on near-infrared or Raman spectroscopy to monitor glucose levels were developed in 1992 (Arnold 1996) and nowadays are even available as a smartphone application. The ANNs extrapolate glucose concentrations from spectral curve, thus enabling convenient monitoring of diabetes during daily activities.

Quality of life itself, including satisfaction, social interactions, and depression, has been defined as an integral outcome measure in management of diabetes mellitus. Recently, Narasingarao et al developed a prototype neural network model to measure the quality of life in diabetic patients (Narasingarao et al. 2009). For this particular purpose, biological or biographical variables such as age, gender, weight, or fasting plasma glucose were used as input data. The results were comparable with those from traditional statistical methods. In 1997, simulation studies on neural predictive control of glucose concentration

in subcutaneous tissue were carried out (Trajanoski et al. 1998). As a control strategy, Trajanoski and colleagues combined ANNs and nonlinear model predictive control. This approach allowed for large noise levels and time delays. However, administration of insulin or analogues was found to be unsuitable for rapid control and was adequate only for controlling slow perturbations. Later, a new control system called a *neuro-fuzzy control system*, which uses fuzzy logic principles and neural networks employing a minimal number of input data for correct output, was developed (Dazzi et al. 2001). This system is especially suitable for direct control of critically ill diabetic patients on intravenous nutrition and reduced the need for increased blood glucose testing and even the risk of hypoglycemia. Blood glucose level has also been monitored using inverse optimal neural control as a preliminary study in patients with type I diabetes (Leon et al. 2012). Recurrent neural networks were used to control the level of glucose and insulin following a desired trajectory (normal glucose absorption of a healthy person) to avoid hypoglycemia and hyperglycemia. ANNs have not only been applied in the tracking of glucose, but also in the diagnosis of diabetes. A neural network-based diagnostic system was developed by (Chan et al. 2011) with the aim of predicting fatal hypoglycemia episodes in type I diabetes patients. The data were collected from a cohort of 420 patients and included: (i) physiological parameters, (ii) rate of change of heart rate, (iii) corrected QT interval of electrocardiogram signal, and (iv) rate of change of corrected QT interval. Data from 320 patients were used to train the network and the remainder for its verification. A sensitivity of 79.30% and specificity of 60.53% was achieved, better values than those obtained using other approaches such as statistical or fuzzy regression methods. In conclusion, the use of ANNs in the diagnosis of diabetes provides an improvement in accuracy, sensitivity, and specificity in comparison with other methods, thus contributing to improved clinical management of diabetes mellitus.

FUNDAMENTAL STEPS IN ANNs-BASED MEDICAL DIAGNOSIS

The workflow of ANN analysis arising from the outlined clinical situations is shown in Fig. 6 which provides a brief overview of the fundamental steps that should be followed to apply ANNs for the purposes of medical diagnosis with sufficient confidence.

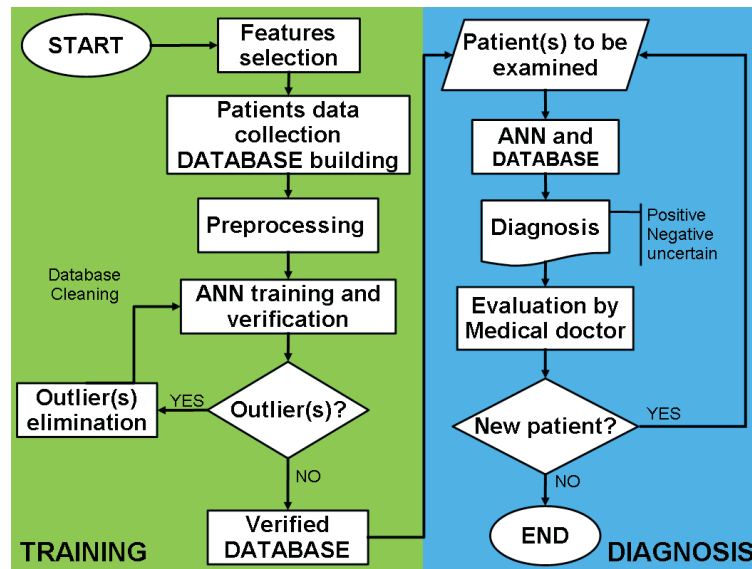


Fig. 6. **Diagram of fundamental steps in ANNs-based medical diagnosis.** Building of the database and “learning” represents the left half (green) and its application for the diagnosis is the right part (blue).

For the reasons discussed above, the network receives patient’s data to predict the diagnosis of a certain disease. After the target disease is established, the next step is to properly select the features (e.g., symptoms, laboratory, and instrumental data) that provide the information needed to discriminate the different health conditions of the patient. This can be done in various ways. Tools used in chemometrics allow the elimination of factors that provide only redundant information or those that contribute only to the noise. Therefore, careful selection of suitable features must be carried out in the first stage. In the next step, the database is built, validated and “cleaned” of outliers. After training and verification, the network can be used in practice to predict the diagnosis. Finally, the predicted diagnosis is evaluated by a clinical specialist. The major steps can be summarized as:

- Features selection
- Building the database
 - Data cleaning and preprocessing
 - Data homoscedasticity
- Training and verification of database using ANN
 - Network type and architecture
 - Training algorithm
 - Verification
 - Robustness of ANN-based approaches
- Testing in medical practice

The individual steps listed above will be shortly commented and some details given.

Features selection

Correct diagnosis of any disease is based on various, and usually incoherent, data (features): for example, clinicopathologic evaluation, laboratory and instrumental data, subjective anamnesis of the patient, and considerations of the clinician. Clinicians are trained to extract the relevant information from each type of data to identify possible diagnoses. In artificial neural network application such data are called “features”. Features can be symptoms, biochemical analysis data and/or whichever other relevant information helping in diagnosis. Therefore, the experience of the professional is closely related to the final diagnosis. The ability of ANNs to learn from examples makes them very flexible and powerful tools to accelerate medical diagnosis. Some types of neural networks are suitable for solving perceptual problems while others are more adapted for data modeling and functional approximation (Dayhoff and Deleo 2001). Regardless of the features selected, those chosen for training the neural network should be “robust” indicators for a given clinical situation or pathology. In general, feature selection relies upon previous clinical experience. Features that bring insufficient, redundant, non-specific, or noisy information about the investigated problem should be avoided. The selection/extraction of suitable features among all

available ones is usually carried out using various approaches. The most important and best-known tools for variable selection are powerful mathematical means of data mining such as principal components analysis, genetic algorithm (Yan et al. 2008), or ANNs (Verikas and Bacauskiene 2002).

Building the database

The neural network is trained using a suitable database of “example” cases. An “example” is provided by one patient whose values for the selected features have been collected and evaluated. The quality of training and the resultant generalization, and therefore the prediction ability of the network, strongly depend on the database used for the training. The database should contain a sufficient number of reliable “examples” (for which the diagnosis is known) to allow the network to learn by extracting the structure hidden in the dataset and then use this “knowledge” to “generalize” the rule to new cases. In addition, clinical laboratory data should be in a form that is readily transferable to programs for computer-aided diagnosis (Strike et al. 1986).

Data cleaning and preprocessing

Data in the training database must be preprocessed before evaluation by the neural network. Several approaches are available for this purpose. Data are normally scaled to lie within the interval [0, 1] because the most commonly used transference function is the so-called logistic one. In addition, it has been demonstrated that cases for which some data are missing should be removed from the database to improve the classification performance of the network (Gannous and Elhaddad 2011). A decrease in the classification performance of the network is observed for imbalanced databases (those with a different number of cases for each class) (Mazurowski et al. 2008).

Data homoscedasticity

Once the suitable features, database, data preprocessing method, training algorithm, and network architecture have been identified, data concerning “new” patients who are not included in the training database can be evaluated by the trained network. The question asked is whether the new data belong to the same population as those in the database (homoscedasticity). Failure at this step might lead the network to misclassify the new data. This problem can be solved by the use of an additional parameter that indicates the population to which a certain sample belongs.

Training and verification of database using ANN

Network type and architecture

Although multilayer feed-forward neural networks are most often used, there are a large variety of other

networks including bayesian, stochastic, recurrent, or fuzzy. The optimal neural network architecture must be selected in the first stage. This is usually done testing networks with different number of hidden layers and nodes therein. The optimal architecture is that for which the minimum value of E (Eq. 4) for both training and verification is obtained.

Training algorithm

Various training algorithms are available. However, the most commonly used is back propagation (Zupan and Gasteiger 1999; Ahmed 2005). As discussed in “*Network learning*” section, backpropagation algorithm requires the use of two training parameters: (i) learning rate and (ii) momentum. Usually, high values of such parameters lead to unstable learning, and therefore poor generalization ability of the network. The optimal values of the training parameters depend upon the complexity of the studied system. In general, the value of momentum is lower than that of learning rate. In addition, the sum of their values should be approximately equal to one.

Verification

ANNs-based medical diagnosis should be verified by means of a dataset different from that one used for training.

Robustness of ANN-based approaches

It is well known that ANNs are able to tolerate a certain level of noise in the data and consequently they typically provide sufficient prediction accuracy. However, this noise might sometimes cause misleading results, especially when modeling very complex systems such as the health condition of a human body. Such noise would not only impact the normal uncertainty of the measured data but might also impact secondary factors, for example the coexistence of more than one disease. Crossed effects cannot be predicted unless they have been considered during building of the training database. Any factor that influences the symptoms of the disease under study must be taken into account by including such cases in the database. Only in this way can the network correctly classify the patient. Of course, one way to avoid this is to combine the experience of the clinical specialist with the discriminative power of ANN-based approaches.

Testing in medical practice

As the final step in ANN-aided diagnosis should be testing in medical practice. For each new patient the network’s outcome is to be carefully examined by a clinician. Medical data of patients for which the predicted diagnosis is correct can be eventually included in the training database.

However, wide and extensive evaluation of ANN-aided diagnosis applications in clinical setting is necessary even throughout different institutions. Verified ANN-aided medical diagnosis support applications in clinical setting are necessary condition for further expansion in medicine.

CONCLUSIONS

ANNs represent a powerful tool to help physicians perform diagnosis and other enforcements. In this regard, ANNs have several advantages including:

- (i) The ability to process large amount of data
- (ii) Reduced likelihood of overlooking relevant information
- (iii) Reduction of diagnosis time

ANNs have proven suitable for satisfactory diagnosis of various diseases. In addition, their use makes the diagnosis more reliable and therefore increases patient satisfaction. However, despite their wide application in modern diagnosis, they must be considered only as a tool to facilitate the final decision of a clinician, who is ultimately responsible for critical evaluation of the ANN output. Methods of summarizing and elaborating on informative and intelligent data are continuously improving and can contribute greatly to effective, precise, and swift medical diagnosis.

ACKNOWLEDGEMENTS

Support from Ministry of Education, Youth and Sports of the Czech Republic (Projects MSM0021622411, MSM0021627501, MSM0021622430, CZ.1.05/1.1.00/02.0123 and HistoPARK CZ.1.07/2.3.00/20.0185), and the Czech Science Foundation (Projects No. 104/08/0229, 202/07/1669) is acknowledged. This research was also supported by CEPLANT, the project R&D center for low-cost plasma and nanotechnology surface modifications (CZ.1.05/2.1.00/03.0086 funding from the European Regional Development Fund). E. M. Peña-Méndez thanks the University of La Laguna for partial support.

REFERENCES

Ahmed F. Artificial neural networks for diagnosis and survival prediction in colon cancer. *Mol Cancer*. 4: 29, 2005.

- Aleksander I, Morton H. An introduction to neural computing. Int Thomson Comput Press, London 1995.
- Alkim E, Gürbüz E, Kiliç E. A fast and adaptive automated disease diagnosis method with an innovative neural network model. *Neur Networks*. 33: 88–96, 2012.
- Amato F, González-Hernández J, Havel J. Artificial neural networks combined with experimental design: a “soft” approach for chemical kinetics. *Talanta*. 93: 72–78, 2012.
- Arnold M. Non-invasive glucose monitoring. *Curr Opin Biotech*. 7: 46–49, 1996.
- Atkov O, Gorokhova S, Sboev A, Generozov E, Muraseyeva E, Moroshkina S and Cherniy N. Coronary heart disease diagnosis by artificial neural networks including genetic polymorphisms and clinical parameters. *J Cardiol*. 59: 190–194, 2012.
- Barbosa D, Roupard D, Ramos J, Tavares A and Lima C. Automatic small bowel tumor diagnosis by using multi-scale wavelet-based analysis in wireless capsule endoscopy images. *Biomed Eng Online*. 11: 3, 2012.
- Bartosch-Härlid A, Andersson B, Aho U, Nilsson J, Andersson R. Artificial neural networks in pancreatic disease. *Br J Surg*. 95: 817–826, 2008.
- Barwad A, Dey P, Susheilia S. Artificial neural network in diagnosis of metastatic carcinoma in effusion cytology. *Cytometry B Clyn Cytom*. 82: 107–111, 2012.
- Basheer I, Hajmeer M. Artificial neural networks: fundamentals, computing, design, and application. *J Microbiol Meth*. 43: 3–31, 2000.
- Bradley B. Finding biomarkers is getting easier. *Ecotoxicology*. 21: 631–636, 2012.
- Brougham D, Ivanova G, Gottschalk M, Collins D, Eustace A, O’Connor R, Havel J. Artificial neural networks for classification in metabolomic studies of whole cells using 1H nuclear magnetic resonance. *J Biomed Biotechnol*. 2011: 158094, 2011.
- Catalogna M, Cohen E, Fishman S, Halpern Z, Nevo U, Ben-Jacob E. Artificial neural networks based controller for glucose monitoring during clamp test. *PLoS One*. 7: e44587, 2012.
- Chan K, Ling S, Dillon T, Nguyen H. Diagnosis of hypoglycemic episodes using a neural network based rule discovery system. *Expert Syst Appl*. 38: 9799–9808, 2011.
- Dayhoff J, Deleo J. Artificial Neur Networks: Opening the Black Box. *Cancer*. 91: 1615–1635, 2001.
- Dazzi D, Taddei F, Gavarini A, Uggeri E, Negro R, Pezzarossa A. The control of blood glucose in the critical diabetic patient: a neuro-fuzzy method. *J Diabet Complicat*. 15: 80–87, 2001.

- de Bruijn M, ten Bosch L, Kuik D, Langendijk J, Leemans C, Verdonck-de Leeuw I. Artificial neural network analysis to assess hypernasality in patients treated for oral or oropharyngeal cancer. *Logoped Phoniatr Vocol.* 36: 168–174, 2011.
- Dey P, Lamba A, Kumari S, Marwaha N. Application of an artificial neural network in the prognosis of chronic myeloid leukemia. *Anal Quant Cytol Histol.* 33: 335–339, 2012.
- El-Deredy W, Ashmore S, Branston N, Darling J, Williams S, Thomas D. Pretreatment prediction of the chemotherapeutic response of human glioma cell cultures using nuclear magnetic resonance spectroscopy and artificial neural networks *Cancer Res.* 57: 4196–4199, 1997.
- Elveren E, Yumuşak N. Tuberculosis disease diagnosis using artificial neural network trained with genetic algorithm. *J Med Syst.* 35: 329–332, 2011.
- Er O, Temurtas F, Tanrikulu A. Tuberculosis Disease Diagnosis Using Artificial Neural Networks. *J Med Syst.* 34: 299–302, 2008.
- Fedor P, Malenovsky I, Vanhara J, Sierka W, Havel J. Thrips (Thysanoptera) identification using artificial neural networks. *Bull Entomol Res.* 98: 437–447, 2008.
- Fernandez de Canete J, Gonzalez-Perez S, Ramos-Diaz JC. Artificial neural networks for closed loop control of *in silico* and ad hoc type 1 diabetes. *Comput Meth Progr Biomed.* 106: 55–66, 2012.
- Fernandez-Blanco E, Rivero D, Rabunal J, Dorado J, Pazos A, Munteanu C. Automatic seizure detection based on star graph topological indices. *J Neurosci Methods.* 209: 410–419, 2012.
- Gannous AS, Elhaddad YR. Improving an Artificial Neural Network Model to Predict Thyroid Bending Protein Diagnosis Using Preprocessing Techniques. *WASET.* 50: 124–128, 2011.
- Havel J, Peña E, Rojas-Hernández A, Doucet J, Panaye A. Neural networks for optimization of high-performance capillary zone electrophoresis methods. *J Chromatogr A.* 793: 317–329, 1998.
- Ho W-H, Lee K-T, Chen H-Y, Ho T-W, Chiu H-C. Disease-free survival after hepatic resection in hepatocellular carcinoma patients: a prediction approach using artificial neural network. *PloS One.* 7: e29179, 2012.
- Karabulut E, Ibrikli T. Effective diagnosis of coronary artery disease using the rotation forest ensemble method. *J Med Syst.* 36: 3011–3018, 2012.
- Kheirelseid E, Miller N, Chang K, Curran C, Hennessey E, Sheehan M, Newell J, Lemetre C, Balls G, Kerin M. miRNA expressions in rectal cancer as predictors of response to neoadjuvant chemoradiation therapy. *Int J Colorectal Dis.* 2012.
- Leon BS, Alanis AY, Sanchez E, Ornelas-Tellez F, Ruiz-Velazquez E. Inverse optimal neural control of blood glucose level for type 1 diabetes mellitus patients. *J Franklin I.* 349: 1851–1870, 2012.
- Li Y, Rauth AM, Wu XY. Prediction of kinetics of doxorubicin release from sulfopropyl dextran ion-exchange microspheres using artificial neural networks. *Eur J Pharm Sci.* 24: 401–410, 2005.
- Mazurowski M, Habas P, Zurada J, Lo J, Baker J, Tourassi G. Training neural network classifiers for medical decision making: the effects of imbalanced datasets on classification performance. *Neural networks.* 21: 427–436, 2008.
- Michalkova V, Valigurova A, Dindo M, Vanhara J. Larval morphology and anatomy of the parasitoid *Exorista larvarum* (Diptera: Tachinidae), with an emphasis on cephalopharyngeal skeleton and digestive tract. *J Parasitol.* 95: 544–554, 2009.
- Molga E, van Woezik B, Westerterp K. Neural networks for modelling of chemical reaction systems with complex kinetics: oxidation of 2-octanol with nitric acid. *Chem Eng Process.* 39: 323–334, 2000.
- Mortazavi D, Kouzani A, Soltanian-Zadeh H. Segmentation of multiple sclerosis lesions in MR images: a review. *Neuroradiology.* 54: 299–320, 2012a.
- Mortazavi D, Kouzani AZ, Soltanian-Zadeh H. Segmentation of multiple sclerosis lesions in MR images: a review. *Neuroradiology.* 54: 299–320, 2012b.
- Murarikova N, Vanhara J, Tothova A, Havel J. Polyphasic approach applying artificial neural networks, molecular analysis and postabdomen morphology to West Palaearctic *Tachina* spp. (Diptera, Tachinidae). *Bull Entomol Res.* 101: 165–175, 2010.
- Narasingarao M, Manda R, Sridhar G, Madhu K, Rao A. A clinical decision support system using multilayer perceptron neural network to assess well being in diabetes. *J Assoc Physicians India.* 57: 127–133, 2009.
- Özbay Y. A new approach to detection of ECG arrhythmias: Complex discrete wavelet transform based complex valued artificial neural network. *J Med Syst.* 33: 435–445, 2009.
- Pace F, Savarino V. The use of artificial neural network in gastroenterology: the experience of the first 10 years. *Eur J Gastroenterol Hepatol.* 19: 1043–1045, 2007.
- Rodríguez Galdón B, Peña-Méndez E, Havel J, Rodríguez Rodríguez E, Díaz Romero C. Cluster Analysis and Artificial Neural Networks Multivariate Classification of Onion Varieties. *J Agric Food Chem:* 11435–11440, 2010.
- Saghiri M, Asgar K, Boukani K, Lotfi M, Aghili H, Delvarani A, Karamifar K, Saghiri A, Mehrvarzfar P,

- Garcia-Godoy F. A new approach for locating the minor apical foramen using an artificial neural network. *Int Endod J.* 45: 257–265, 2012.
- Shankaracharya, Odedra D, Samanta S, Vidyarthi A. Computational intelligence in early diabetes diagnosis: a review. *Rev Diabet Stud.* 7: 252–262, 2010.
- Siristatidis C, Chrelias C, Pouliakis A, Katsimanis E, Kassanos D. Artificial neural networks in gynecological diseases: Current and potential future applications. *Med Sci Monit.* 16: 231–236, 2010.
- Spelt L, Andersson B, Nilsson J, Andersson R. Prognostic models for outcome following liver resection for colorectal cancer metastases: A systematic review. *Eur J Surg Oncol.* 38: 16–24, 2012.
- Strike P, Michaeloudis A, Green AJ. Standardizing clinical laboratory data for the development of transferable computer-based diagnostic programs. *Clin Chem.* 32: 22–29, 1986.
- Szolovits P, Patil RS, Schwartz W. Artificial Intelligence in Medical Diagnosis. *Ann Intern Med.* 108: 80–87, 1988.
- Tate A, Underwood J, Acosta D, Julià-Sapé M, Majós C, Moreno-Torres A, Howe F, van der Graaf M, Lefournier V, Murphy M, Loosemore A, Ladroue C et al. Development of a decision support system for diagnosis and grading of brain tumours using *in vivo* magnetic resonance single voxel spectra. *NMR Biomed.* 19: 411–434, 2006.
- Thakur A, Mishra V, Jain S. Feed forward artificial neural network: tool for early detection of ovarian cancer. *Sci Pharm.* 79: 493–505, 2011.
- Trajanoski Z, Regittnig W, Wach P. Simulation studies on neural predictive control of glucose using the subcutaneous route. *Comput Meth Progr Biomed.* 56: 133–139, 1998.
- Uğuz H. A biomedical system based on artificial neural network and principal component analysis for diagnosis of the heart valve diseases. *J Med Syst.* 36: 61–72, 2012.
- Verikas A, Bacauskiene M. Feature selection with neural networks. *Pattern Recogn Lett.* 23: 1323–1335, 2002.
- Wilding P, Morgan M, Grygotis A, Shoffner M, Rosato E. Application of backpropagation neural networks to diagnosis of breast and ovarian cancer. *Cancer Lett.* 77: 145–153, 1994.
- Yan H, Zheng J, Jiang Y, Peng C, Xiao S. Selecting critical clinical features for heart diseases diagnosis with a real-coded genetic algorithm. *Appl Soft Comput.* 8: 1105–1111, 2008.
- Zupan J, Gasteiger J. Neural networks in chemistry and drug design. Wiley VCH, Weinheim, 380 p. 1999.

15. Houška J, Pena-Mendez EM, Hernandez-Fernaund JR, Salido E, Hampl A, Havel J, **Vaňhara P. Tissue profiling by nanogold-mediated mass spectrometry and artificial neural networks in the mouse model of human primary hyperoxaluria 1.** *Journal of Applied Biomedicine* 2014; **12**(2):119-25.

Commentary:

A pilot publication reporting mass-spectrometry/artificial intelligence based diagnosis of tissue sections derived from mouse model of primary hyperoxaluria I.

DOI: 10.1016/j.jab.2013.12.001
Journal: Journal of Applied Biomedicine
Impact factor (WOS, 2014): 1.302
Number of citations (WOS, 2018): 6
Cited in: Journal of Applied Biomedicine, Plos One, Journal of the American Association for Mass Spectrometry, Rapid Communications in Mass Spectrometry, Stem Cells Translational Medicine

Most important citation:

Sarmanova OE, Burikov SA, Dolenko SA, Isaev IV, Laptinskiy KA, Prabhakar N, Karaman DŞ, Rosenholm JM, Shenderova OA, Dolenko TA. **A method for optical imaging and monitoring of the excretion of fluorescent nanocomposites from the body using artificial neural networks.** *Nanomedicine.* 2018; **14**(4):1371-1380. doi: 10.1016/j.nano.2018.03.009. IF2017: 6.500).

Contribution of the author: Corresponding author. Collection and/or assembly of data, data analysis and interpretation, manuscript writing.

Available online at www.sciencedirect.com

ScienceDirect

journal homepage: <http://www.elsevier.com/locate/jab>

Original Research Article

Tissue profiling by nanogold-mediated mass spectrometry and artificial neural networks in the mouse model of human primary hyperoxaluria 1

Jan Houška^a, Eladia María Peña-Méndez^b, Juan R. Hernandez-Fernaud^c, Eduardo Salido^c, Aleš Hampl^{d,e}, Josef Havel^a, Petr Vaňhara^{d,*}

^aDepartment of Chemistry, Faculty of Science, Masaryk University, Brno, Czech Republic

^bDepartment of Analytical Chemistry, Nutrition and Food Science, Faculty of Chemistry, University of La Laguna, La Laguna, Tenerife, Spain

^cRare Disease Center (CIBERER) and Biomedical Institute (CIBICAN), University La Laguna, Tenerife, Spain

^dDepartment of Histology and Embryology, Faculty of Medicine, Masaryk University, Brno, Czech Republic

^eInternational Clinical Research Center, St. Anne's University Hospital, Brno, Czech Republic

ARTICLE INFO

Article history:

Received 10 October 2013

Received in revised form

2 December 2013

Accepted 12 December 2013

Available online 23 December 2013

Keywords:

MALDI-TOF mass spectrometry

Primary hyperoxaluria I

Artificial neural networks

Diagnostics

Tissue profiling

ABSTRACT

Correct assessment of tissue histopathology is a necessary prerequisite for any clinical diagnosis. Nowadays, classical methods of histochemistry and immunohistochemistry are complemented by various techniques adopted from molecular biology and bioanalytical chemistry. Mass spectrometry profiling or imaging offered a new level of tissue visualization in the last decade, revealing hidden patterns of tissue molecular organization. It can be adapted to diagnostic purposes to improve decisions on complex and morphologically not apparent diagnoses. In this work, we successfully combined tissue profiling by mass spectrometry with analysis by artificial neural networks to classify normal and diseased liver and kidney tissues in a mouse model of primary hyperoxaluria type 1. Lack of the liver L-alanine:glyoxylate aminotransferase catalyzing conversion of L-alanine and glyoxylate to pyruvate and glycine causes accumulation of oxalate salts in various tissues, especially urinary system, resulting in compromised renal function and finally end stage renal disease. As the accumulation of oxalate salts alters chemical composition of affected tissues, it makes it available for examination by bioanalytical methods. We demonstrated that the direct tissue MALDI-TOF MS combined with neural computing offers an efficient tool for diagnosis of primary hyperoxaluria type I and potentially for other metabolic disorders altering chemical composition of tissues.

© 2013 Faculty of Health and Social Studies, University of South Bohemia in Ceske Budejovice. Published by Elsevier Urban & Partner Sp. z o.o. All rights reserved.

Introduction

Primary hyperoxaluria 1 (PH1) is a rare, autosomal-recessive metabolic disorder originating in liver. Due to the deficiency of

a liver-specific enzyme, L-alanine:glyoxylate aminotransferase (AGT, EC 2.6.1.44), PH1 patients suffer from pathological overproduction of oxalate and depositions of oxalate salts, e.g. calcium oxalate, in tissues (Leumann and Hoppe, 2001). Fully active AGT enzyme is a homodimeric transaminase

* Corresponding author. Tel.: +420 549497780; fax: +420 549491320.

E-mail address: PVanhara@med.muni.cz (P. Vaňhara).

1214-021X/\$ – see front matter © 2013 Faculty of Health and Social Studies, University of South Bohemia in Ceske Budejovice. Published by Elsevier Urban & Partner Sp. z o.o. All rights reserved.

<http://dx.doi.org/10.1016/j.jab.2013.12.001>

localized to peroxisomes, where it catalyses conversion of L-alanine and glyoxylate to pyruvate and glycine. About 150 mutations with varying allelic frequency have been identified in the sequence of the gene coding for AGT enzyme (AGXT), causing protein misfolding, impaired dimer assembly, reduced catalytic activity or ectopic localization to mitochondria instead of peroxisomes (Danpure, 2005; Williams et al., 2009). A loss of AGT activity results in decreased glyoxylate detoxification and extensive accumulation of oxalate in renal system and eventually in other organs such as heart, skin, muscles and bones. In kidneys, deposits of poorly soluble oxalate salts and subsequent inflammation often lead to the end-stage renal disease (ESRD) (Hoppe, 2012; Salido et al., 2012). PH1 is a severe pathology in both adult and pediatric medicine, where a correct and rapid diagnosis is necessary to prevent development of ESRD. Diagnosis of PH1 is based on general clinical symptoms, such as nephrolithiasis or nephrocalcinosis, biochemical analysis of urine and ultrasonography of urinary tract. PH1 is then confirmed by AGT immunoreactivity in liver biopsy and genotyping of AGXT gene in case of an established phenotype (Raju et al., 2008). Current specific diagnostic approaches in PH1 are either based on knowledge of particular AGXT mutation or enzyme activity/localization in a tissue or require analysis of rather nonspecific clinical or biochemical symptoms. However, complex phenotype together with wide range of less frequent polymorphisms or mutations can lead to false-negative or positive diagnosis (Rumsby et al., 2004).

Recently, a mouse model of PH1 has been successfully introduced that enabled detailed experimental studies on PH1 pathogenesis and diagnostics. Mice deficient for AGXT demonstrate changes in urine biochemistry or urolithiasis, however, there are no major pathologic changes in normal histology of internal organs, including liver and kidneys, thus resembling early stages of PH1 in human (Salido et al., 2006).

Recent progress in techniques developed for bioanalytical chemistry, e.g. mass spectrometry, enabled analysis of very complex samples, including cells and tissues. Direct-tissue profiling by matrix-assisted laser desorption/ionization – time of flight (MALDI-TOF) mass spectrometry (MS) emerged as an efficient approach for analysis of tissue samples and discriminating even subtle changes in tissue composition that can stay unnoticed by routine histopathological assessments (Caldwell and Caprioli, 2005; Herring et al., 2007). Therefore, we presumed that MS fingerprints of healthy and hyperoxaluric tissues can serve as a robust input for a diagnostics. However, recognition of specific patterns can be difficult due to inherent biological complexity of tissues, technical variability influencing outputs and principles of MALDI analysis. Therefore, the post-measurement analysis has to cover all these issues to provide clear and confident decision (Amato et al., 2013).

Artificial neural networks (ANNs) represent a mathematical algorithm effective for processing of non-linear data. Typical ANN consists of several layers of nodes, or artificial “neurons”, assembled into a defined architecture. Generally, a structure of the ANN consists of an input layer, one or more hidden layers and output layer and its architecture reflects complexity of the analyzed system. Application of ANNs ranges from chemical kinetics (Amato et al., 2012) or biomolecular engineering and structural computing (Armano et al., 2005; Fawcett et al., 2013)

to medical diagnosis e.g. in diabetes, cardiovascular diseases, epilepsy or cancer (Arnold, 1996; Dazzi et al., 2001; Yan et al., 2008; Elveren and Yumuşak, 2011; Chan et al., 2011; Barwad et al., 2012; Bradley, 2012; Spelt et al., 2012). Application of ANNs in medical diagnosis was recently reviewed by Amato et al. (2013).

In this work we raised a question whether a mass spectrum contains sufficient information to discriminate normal and hyperoxaluric tissues and can contribute to diagnosis without previous knowledge of unique markers. We demonstrated that direct tissue MALDI-TOF MS combined with artificial neural networks offer an efficient, biomarker-independent tool for diagnosis of primary hyperoxaluria type I and potentially for classification of other metabolic disorders altering chemical composition of tissues.

Materials and methods

Chemicals and reagents

Gold(III) chloride trihydrate, gallic acid, hydrogen peroxide, trifluoroacetic acid (TFA), Triton® X-100, sinapinic acid (SA) and 2,5-dihydroxybenzoic acid (DHB) all in p.a. or liquid chromatography grade were purchased from Sigma–Aldrich (Steinheim, Germany). Bruker Protein calibration mixture standard I was purchased from Bruker Daltonics (Bremen, Germany). All glass equipment used was washed for 2 h at 70 °C in 10% aqueous nitric acid solution and/or washed in concentrated nitric acid. Gold nanoparticles (AuNPs) were produced from HAuCl₄ using various reducing agents like hydrogen peroxide and gallic acids as described elsewhere (Wang et al., 2007). Formation of AuNPs clusters up to Au₂₅ was confirmed by MALDI-TOF MS.

Sample preparation and matrix deposition

Animal breeding, handling and experimental procedures were approved by the La Laguna University Animal Care. After sacrifice, liver and kidney were extracted and snap frozen in dry ice and kept under –20 °C prior processing. Cryocutting was performed using a Leica cryostat. The 12 µm tissue slices were placed on pre-chilled target plate and fixed with 0.5 µL of SA (20 mg/mL) dissolved in solution of 90% ethanol, 0.5% Triton X-100 and 0.1% TFA. The sample was then washed three times by 3 µL of 50% ethanol and 6 µL of chloroform. Then 2 µL AuNPs solution was applied on sample, dried and subsequently overlaid with three matrix solutions (sinapinic acid in xylene, 90% ethanol and 50% acetonitrile acidified with 0.1% TFA). Dried sample was then processed by MALDI-TOF MS.

MALDI TOF mass spectrometry

Mass spectra were acquired on Bruker Autoflex mass spectrometer (Bruker Daltonics, Bremen, Germany) equipped with a time of flight analyzer (TOF) and 337 nm nitrogen laser. Laser repetition rate was set to 10 Hz, maximal laser energy (100%) was adjusted to 47.0 mJ and the acceleration voltage was set to 20 kV. All measurements were done in linear positive ion mode. Ionic suppression up to 1500 *m/z* was

applied. Bruker Protein calibration mixture standard I was used for external and internal calibration. All mass spectra were obtained from 100 to 3000 shots dispersed randomly through a tissue sample.

Statistical analysis and artificial neural networks

In total ten wild-type and ten *Agxt*^{-/-} mice were included for analysis. The sample set for MALDI-TOF MS consisted of twenty histological sections of kidney and ten of liver tissues. All acquired mass spectra were baseline subtracted. Intensities of twenty peaks at defined *m/z* that reproducibly exceeded the signal to noise ratio of 3 were included for analysis. All statistical analyses including eigenvalue and principal component analyses (PCA) were performed using Statistica 6.0 (StatSoft, Inc., Tulsa, USA). Artificial neural networks were constructed and run in TRAJAN 3 (Trajan Software Ltd., Trajan House, Lincs, UK).

Results and discussion

Discriminative profiling of tissue samples by direct-tissue mass spectroscopy is a novel promising technology, allowing for identification of pathological states without the clear morphological manifestation in the diseased tissue or analysis of a particular biomarker. This is particularly true for inherited metabolic disorders, such as PH1, that can display nonspecifically as nephrolithiasis or nephrocalcinosis, metabolic acidosis or anemia unless confirmed on the genetic or molecular level (Salido et al., 2012).

Processing of mass spectra directly obtained from tissue samples by artificial neural networks can provide additional discriminative capacity to the standard diagnostic process. To test this concept, we employed a recently established model of mouse PH1 (Salido et al., 2006). Mice carrying a homozygous deletions of exons 4–8 of *Agxt* gene as well as wild-type

controls were thoroughly analyzed for histopathological differences previously (Salido et al., 2006), displaying no significant pathological alteration among the genotypes, including brain, stomach, intestine, gonads or cartilage and bone architecture. The renal system of *Agxt* deficient mice showed infrequent dilatations of terminal collecting ducts and occasional deposits in ductal lumen and interstitial parenchyma (Salido et al., 2006).

In this work, cryotome slices of parallel samples of *Agxt*^{-/-} and wild-type tissues were thoroughly washed by ethanol and chloroform, and covered with matrix solutions. Routinely used organic matrices, such as sinapinic acid and dihydroxybenzoic acid provide in complex biological samples noisy and often hardly reproducible spectra. Metal nanoparticles, e.g. cobalt, silver and gold have been shown to enhance discriminative capabilities of mass spectra obtained by MALDI-TOF MS of biomolecules with higher molecular weight, e.g. peptides or proteins that are difficult to ionize properly (Wu et al., 2009). Therefore, we introduced gold-nanoparticles (AuNPs) to the matrix applied on the tissue sample. Comparing to the matrix layout lacking AuNPs, we obtained mass spectra with higher reproducibility and improved peak intensities (Fig. 1). Then we applied AuNPs enriched matrix on sections of cryopreserved kidney and liver tissues of *Agxt*-knockout and wt mice. Mass spectra were recorded for liver and kidney samples obtained from wild-type and PH1 animals. Spectral patterns showed differences in peak distribution and/or peak intensities (Fig. 2A and B) reflecting possible changes in tissue composition between normal and hyperoxaluric samples. Eigenvalue analysis of spectral data of kidney and liver tissues indicated clearly presence of two and three different classes, respectively, contributing to overall variability in the system. Multivariate analysis tools such as principal component analysis (PCA) clearly outlined clusters of the healthy and diseased kidney (Fig. 2C and E) and liver samples (Fig. 2D and F) documenting that spectral profile contains sufficient information for sample discrimination. However, these methods solely discriminate

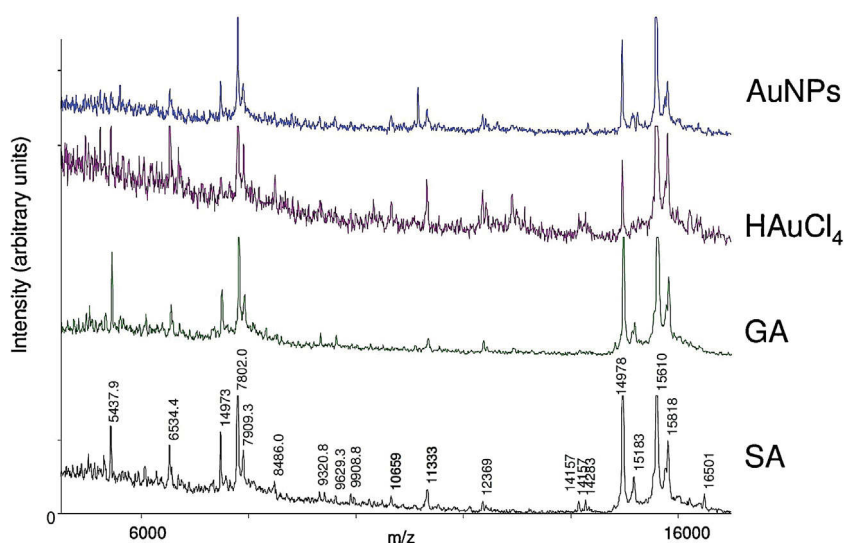


Fig. 1 – Comparison of different matrices used for direct-tissue MALDI-TOF mass spectrometry. Golden nanoparticles enhanced peak intensities and overall reproducibility of mass spectra for subsequent analyses. SA: sinapinic acid; GA: gallic acid; HAuCl₄: hydrogen tetrachloroaurate; AuNPs: golden nanoparticles.

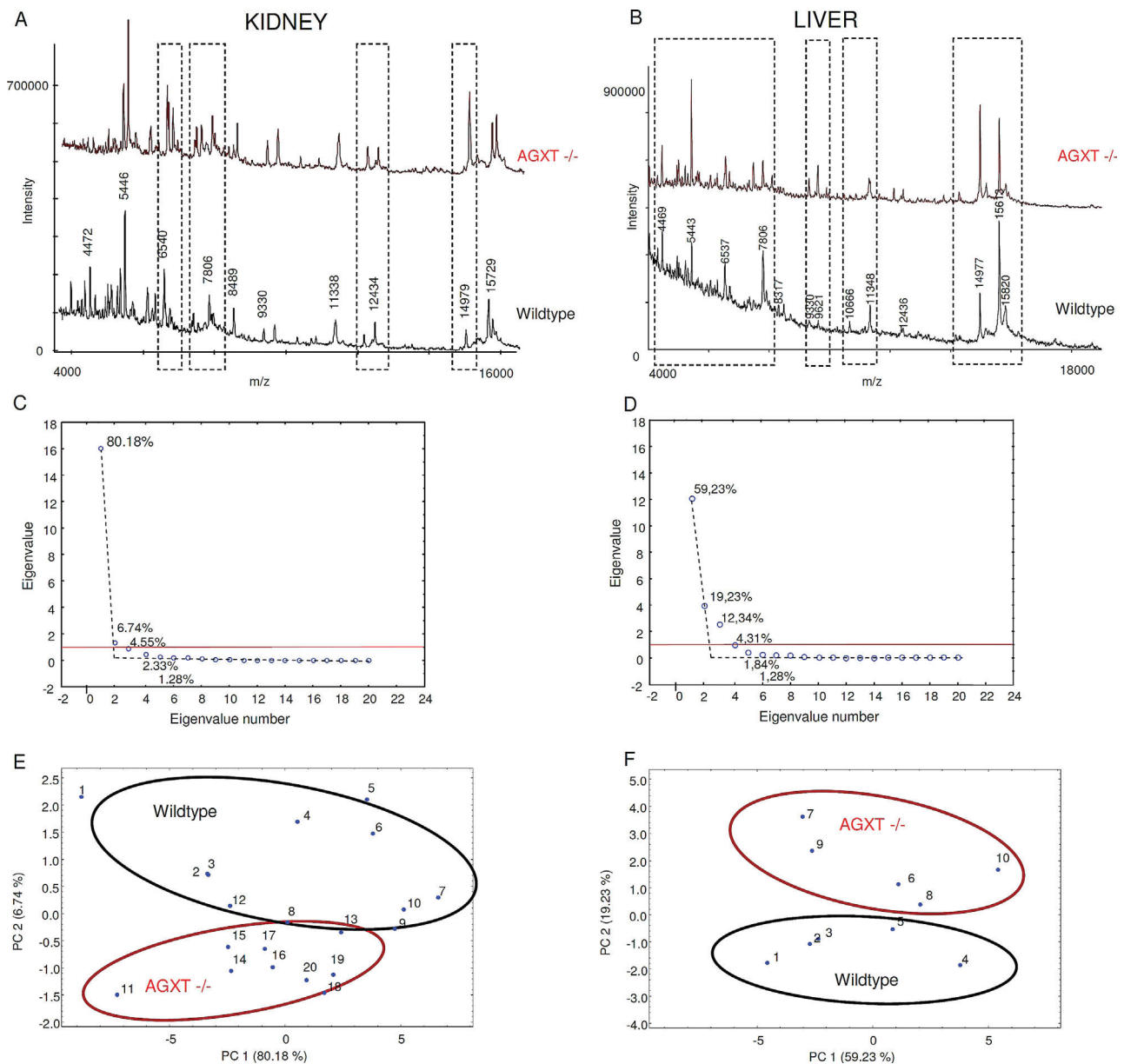


Fig. 2 – Mass spectra of kidney (A) and liver tissues (B) of wild-type and AGXT-deficient mouse were obtained using nano-gold doped matrix. Dotted areas indicate examples of highly reproducible regions of mass spectra with different peak intensities. Eigenvalue analysis performed on peak intensities in individual cases of kidney (C) and liver (D) mass spectra indicated the presence of two or three main classes, respectively, contributing to the overall variability in both data sets. Red line indicates eigenvalue = 1. Projection of the twenty kidney (1–10 wild-type, 11–20 *Agxt*^{-/-}) and ten liver (1–5 wild-type, 6–10 *Agxt*^{-/-}) individual cases on the factor plane by principal component analysis performed on peak intensities revealed presence of two groups corresponding to the wild-type or *Agxt*^{-/-} genotype.

different classes in the data set, but do not contribute to a diagnostic decision on unknown sample. Thus, we wish to develop a system that would identify an individual tissue specimen just by analysis of specific tissue fingerprints.

To test whether our data allow a reliable diagnosis, we constructed an artificial neural network, optimized its architecture using different learning algorithms and applied it on a database spectral fingerprints of liver tissue. As the input variables, intensities of the peaks ranging from *m/z* 4000 to 16000 and exceeding noise-to-signal ratio of 3, were used.

Classification output consisted of two nominal values corresponding to the genotype (wild-type, *Agxt*^{-/-}) (Fig. 3A). Optimal number of nodes (*n*) in the hidden layer was three, as documented by (Fig. 3B). Higher number of nodes had no effect on network accuracy, but no overtraining effects were observed up to *n* = 10. As a result, a training process was fast and the optimum was obtained after few hundreds of iteration cycles (below 1000) (Fig. 3C). After the training, a verification process and cross validation were performed. Finally, the ANN classified 100% of unknown liver samples correctly.

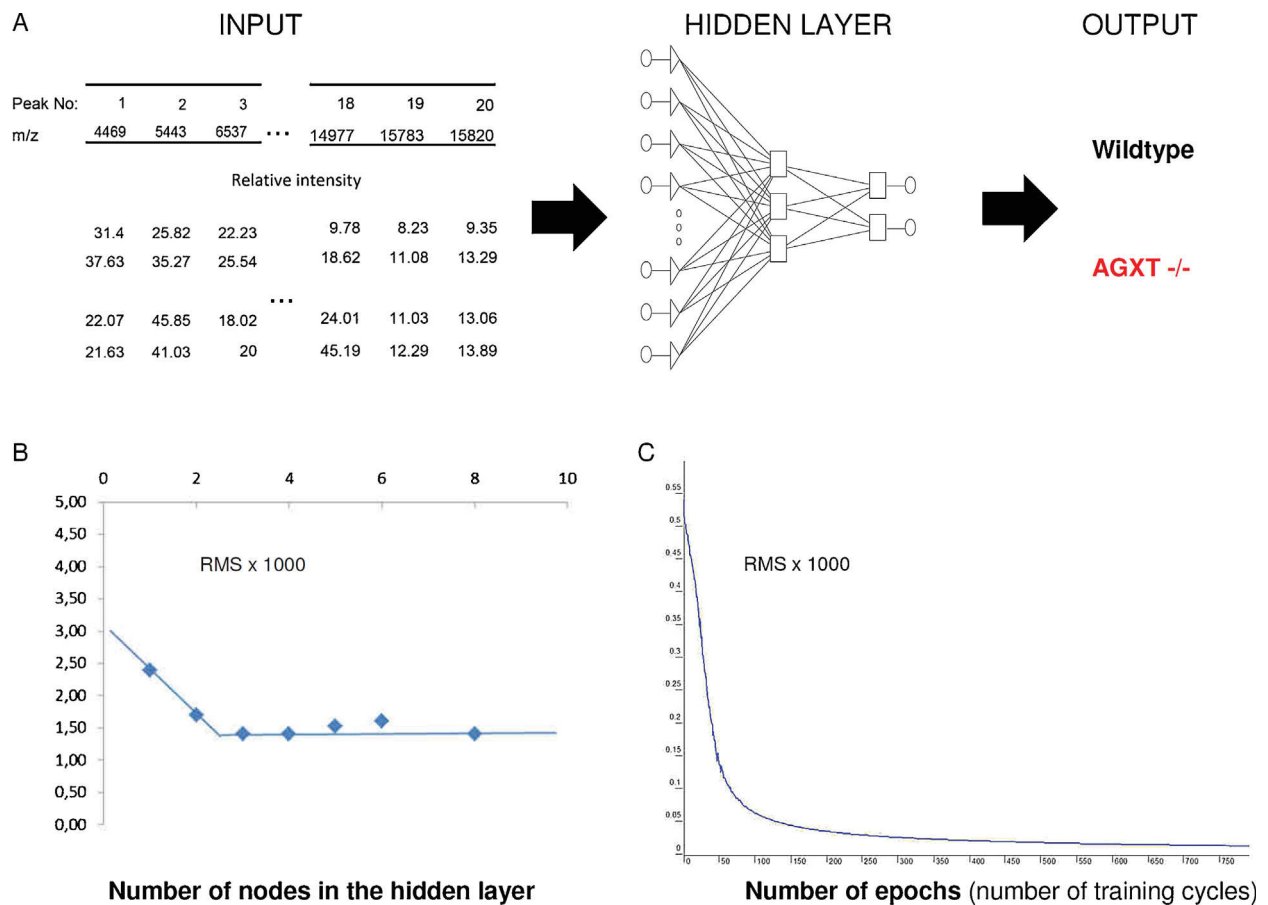


Fig. 3 – (A) Architecture of the artificial neural network used for classifications. The ANN contained one hidden layer with three nodes. As the input variables, intensities of the peaks in mass spectra at particular m/z values were used. The output consisting of two nominal values determines the genotype – wt or AGXT-deficiency. (B) Optimal number of nodes in the hidden layer indicated by root mean square (RMS) as a function of the number of nodes in the hidden layer. (C) Training graph indicating RMS error as function of number of epochs (number of iteration cycles).

Discrimination and classification of biological samples by mass spectrometry was effectively introduced into various fields, ranging from proteome analysis (Ferguson and Smith, 2003), clinical microbiology (Giebel et al., 2010), searching for tumor markers (Chung et al., 2013) or cancer classification (Pietrowska and Widlak, 2012). Recently, tissue mass spectrometry profiling and imaging was introduced to histology visualization, with spatial discrimination ranging from 10 to 50 μm (Chaurand and Caprioli, 2002; Lagarrigue et al., 2011; Seeley and Caprioli, 2011). Classical approach then tries to identify specific information hidden in the spectrum, mechanistically linked to a biomarker – e.g. particular biomolecules, polypeptides or proteins etc., usually obtained after sample fractionation (Cazares et al., 2011). In this work, we rather used the whole spectral fingerprint as a biomarker to perform multifactorial statistics and ANN analysis (Fig. 4).

Such “anonymous” pattern with no distinct marker peaks was previously reported to provide an efficient input for ANN-based classification of complex organic molecules, e.g. humic acids (Pena-Mendez et al., 2007). Combination of MALDI-TOF MS and ANN is particularly suitable also for classification of complex biological samples, mostly cancers (Hu et al., 2012;

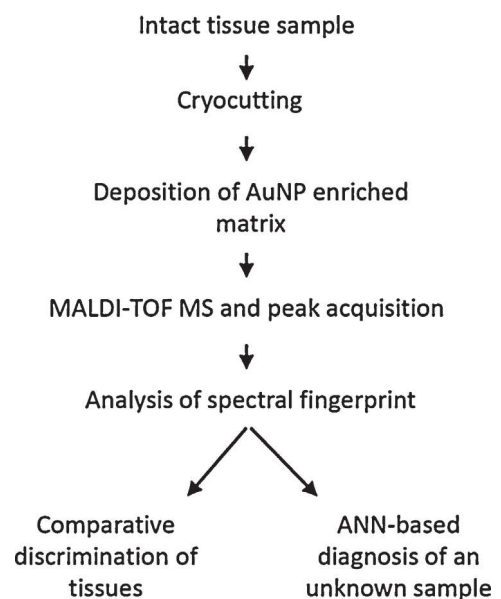


Fig. 4 – Scheme of the experimental workflow underpinning crucial steps in tissue analysis by MALDI-TOF MS and ANNs.

Amato et al., 2013). Moreover, ANNs are capable to process complex data obtained by various methods from biological objects, cell or tissues. ANNs were used for classification in metabolomic studies of whole cells using ^1H nuclear magnetic resonance. Whole-cell ^1H NMR spectra were recorded for cultured human lung carcinoma cell lines differing in their origin or resistance to chemotherapy. Despite the variability within the experimental model or operator-induced sources of variation in the network, the ANN was able to classify the cell line correctly in 100% of cases independent of the spectra selected for training and validation. Application of highly sensitive mass spectrometry combined with artificial intelligence therefore broadens the standard palette of techniques available for histopathological examinations.

In summary, on a mouse model of primary hyperoxaluria type I, we demonstrated the capability of biomarker-independent MALDI-TOF tissue profiling to provide sufficient discriminative information for non-linear analyses by artificial neural networks and contribute to clinical decision and diagnosis.

Acknowledgements

This work was supported by the Ministry of Education, Youth and Sports of the Czech Republic (Projects MSM0021622411, MSM0021627501 and MSM0021622430), the Czech Science Foundation (Project Nos. 104/08/0229 and 202/07/1669), the Grant Agency of Masaryk University (MUNI/M/0041/2013) and the Spanish Ministry of Science (SAF2011-23933). J. Houska and E.M. Peña-Méndez thank Socrates mobility exchange European program.

REFERENCES

- Amato, F., González-Hernández, J., Havel, J., 2012. Artificial neural networks combined with experimental design: a “soft” approach for chemical kinetics. *Talanta* 93, 72–78.
- Amato, F., Lopez, A., Pena-Mendez, E., Vanhara, P., Hampl, A., Havel, J., 2013. Artificial neural networks in medical diagnosis. *J. Appl. Biomed.* 11, 47–58.
- Armano, G., Mancosu, G., Milanese, L., Orro, A., Saba, M., Vargiu, E., 2005. A hybrid genetic-neural system for predicting protein secondary structure. *BMC Bioinf.* 6 (Suppl. 4) S3.
- Arnold, M., 1996. Non-invasive glucose monitoring. *Curr. Opin. Biotechnol.* 7, 46–49.
- Barwad, A., Dey, P., Susheilia, S., 2012. Artificial neural network in diagnosis of metastatic carcinoma in effusion cytology. *Cytometry B* 82, 107–111.
- Bradley, B., 2012. Finding biomarkers is getting easier. *Ecotoxicology* 21, 631–636.
- Caldwell, R.L., Caprioli, R.M., 2005. Tissue profiling by mass spectrometry: a review of methodology and applications. *Mol. Cell. Proteomics* 4, 394–401.
- Cazares, L., Troyer, D., Wang, B., Drake, R., Semmes, O.J., 2011. MALDI tissue imaging: from biomarker discovery to clinical applications. *Anal. Bioanal. Chem.* 401, 17–27.
- Chan, K., Ling, S., Dillon, T., Nguyen, H., 2011. Diagnosis of hypoglycemic episodes using a neural network based rule discovery system. *Expert Syst. Appl.* 38, 9799–9808.
- Chaurand, P., Caprioli, R.M., 2002. Direct profiling and imaging of peptides and proteins from mammalian cells and tissue sections by mass spectrometry. *Electrophoresis* 23, 3125–3135.
- Chung, L., Shibli, S., Moore, K., Elder, E.E., Boyle, F.M., Marsh, D.J., Baxter, R.C., 2013. Tissue biomarkers of breast cancer and their association with conventional pathologic features. *Br. J. Cancer* 108, 351–360.
- Danpure, C.J., 2005. Molecular etiology of primary hyperoxaluria type 1: new directions for treatment. *Am. J. Nephrol.* 25, 303–310.
- Dazzi, D., Taddei, F., Gavarini, A., Uggeri, E., Negro, R., Pezzarossa, A., 2001. The control of blood glucose in the critical diabetic patient: a neuro-fuzzy method. *J. Diabetes Complications* 15, 80–87.
- Elveren, E., Yumuşak, N., 2011. Tuberculosis disease diagnosis using artificial neural network trained with genetic algorithm. *J. Med. Syst.* 35, 329–332.
- Fawcett, T.M., Irausquin, S.J., Simin, M., Valafar, H., 2013. An artificial neural network approach to improving the correlation between protein energetics and the backbone structure. *Proteomics* 13, 230–238.
- Ferguson, P.L., Smith, R.D., 2003. Proteome analysis by mass spectrometry. *Annu. Rev. Biophys. Biomol. Struct.* 32, 399–424.
- Giebel, R., Worden, C., Rust, S.M., Kleinheinz, G.T., Robbins, M., Sandrin, T.R., 2010. Microbial fingerprinting using matrix-assisted laser desorption/ionization time-of-flight mass spectrometry (MALDI-TOF MS) applications and challenges. *Adv. Appl. Microbiol.* 71, 149–184.
- Herring, K.D., Oppenheimer, S.R., Caprioli, R.M., 2007. Direct tissue analysis by matrix-assisted laser desorption/ionization mass spectrometry: application to kidney biology. *Semin. Nephrol.* 27, 597–608.
- Hoppe, B., 2012. An update on primary hyperoxaluria. *Nat. Rev. Nephrol.* 8, 467–475.
- Hu, Q.Y., Huang, Y.S., Wang, Z.A., Tao, H.L., Liu, J.B., Yan, L., Wang, K.Z., 2012. Application of surface-enhanced laser desorption/ionization time-of-flight mass spectrometry coupled with an artificial neural network model for the diagnosis of hepatocellular carcinoma. *Hepatogastroenterology* 59, 1902–1906.
- Lagarigue, M., Becker, M., Lavigne, R., Deininger, S.O., Walch, A., Aubry, F., Suckau, D., Pineau, C., 2011. Revisiting rat spermatogenesis with MALDI imaging at 20-microm resolution. *Mol. Cell. Proteomics* 10 M110.005991.
- Leumann, E., Hoppe, B., 2001. The primary hyperoxalurias. *J. Am. Soc. Nephrol.* 12, 1986–1993.
- Pena-Mendez, E.M., Novotna, K., Gajdosova, D., Gonzalez, V., Havel, J., 2007. Characterization of humic substances of different origin by means of mass spectrometry and neural networks. *Chemosphere* 68, 2047–2053.
- Pietrowska, M., Widlak, P., 2012. MALDI-MS-based profiling of serum proteome: detection of changes related to progression of cancer and response to anticancer treatment. *Int. J. Proteomics* 2012, 926427.
- Raju, D.L., Cantarovich, M., Brisson, M.L., Tchervenkov, J., Lipman, M.L., 2008. Primary hyperoxaluria: clinical course, diagnosis, and treatment after kidney failure. *Am. J. Kidney Dis.* 51, e1–e5.
- Rumsby, G., Williams, E., Coulter-Mackie, M., 2004. Evaluation of mutation screening as a first line test for the diagnosis of the primary hyperoxalurias. *Kidney Int.* 66, 959–963.
- Salido, E.C., Li, X.M., Lu, Y., Wang, X., Santana, A., Roy-Chowdhury, N., Torres, A., Shapiro, L.J., Roy-Chowdhury, J., 2006. Alanine-glyoxylate aminotransferase-deficient mice, a model for primary hyperoxaluria that responds to adenoviral gene transfer. *Proc. Natl. Acad. Sci. U. S. A.* 103, 18249–18254.

- Salido, E., Pey, A.L., Rodriguez, R., Lorenzo, V., 2012. Primary hyperoxalurias: disorders of glyoxylate detoxification. *Biochim. Biophys. Acta* 1822, 1453–1464.
- Seeley, E.H., Caprioli, R.M., 2011. MALDI imaging mass spectrometry of human tissue: method challenges and clinical perspectives. *Trends Biotechnol.* 29, 136–143.
- Spelt, L., Andersson, B., Nilsson, J., Andersson, R., 2012. Prognostic models for outcome following liver resection for colorectal cancer metastases: a systematic review. *Eur. J. Surg. Oncol.* 38, 16–24.
- Wang, W., Chen, Q., Jiang, C., Yang, D., Liu, X., Xu, S., 2007. One-step synthesis of biocompatible gold nanoparticles using gallic acid in the presence of poly-(N-vinyl-2-pyrrolidone). *Colloid Surf. A-Physicochem. Eng. Asp.* 301, 73–79.
- Williams, E.L., Acquaviva, C., Amoroso, A., Chevalier, F., Coulter-Mackie, M., Monico, C.G., Giachino, D., Owen, T., Robbiano, A., Salido, E., Waterham, H., Rumsby, G., 2009. Primary hyperoxaluria type 1: update and additional mutation analysis of the AGXT gene. *Hum. Mutat.* 30, 910–917.
- Wu, H.P., Yu, C.J., Lin, C.Y., Lin, Y.H., Tseng, W.L., 2009. Gold nanoparticles as assisted matrices for the detection of biomolecules in a high-salt solution through laser desorption/ionization mass spectrometry. *J. Am. Soc. Mass Spectrom.* 20, 875–882.
- Yan, H., Zheng, J., Jiang, Y., Peng, C., Xiao, S., 2008. Selecting critical clinical features for heart diseases diagnosis with a real-coded genetic algorithm. *Appl. Soft. Comput.* 8, 1105–1111.

16. Valletta E, Kučera L, Prokeš L, Amato F, Pivetta T, Hampl A, Havel J, Vaňhara P. Multivariate calibration approach for quantitative determination of cell-line cross contamination by intact cell mass spectrometry and artificial neural networks. *PLoS One* 2016; **11(1): E0147414.**

Commentary:

Here we report development of a novel artificial intelligence-based tool for qualitative and quantitative cell authentication. The pioneering proof of concept was documented on binary mixtures of mouse and human embryonic stem cells and/or mouse embryonic fibroblasts.

DOI: 10.1371/journal.pone.0147414
Impact factor (WOS, 2016): 2.806.
Number of citations (WOS, 2017): 4
Cited in: Plos One, Briefings in Bioinformatics

Most important citation: Zhao N, Liu Y, Wei Y, Yan Z, Zhang Q, Wu C, Chang Z, Xu Y. **Optimization of cell lines as tumour models by integrating multi-omics data.** Briefings in Bioinformatics 2017; **18**(3):515-529.
doi: 10.1093/bib/bbw082. (IF 2016: 5.134).

Contribution of the author: Corresponding author. Collection and/or assembly of data, Data analysis and interpretation, manuscript writing.

RESEARCH ARTICLE

Multivariate Calibration Approach for Quantitative Determination of Cell-Line Cross Contamination by Intact Cell Mass Spectrometry and Artificial Neural Networks

Elisa Valletta^{1,2}, Lukáš Kučera³, Lubomír Prokeš¹, Filippo Amato¹, Tiziana Pivetta², Aleš Hampel^{3,4}, Josef Havel¹, Petr Vaňhara^{3*}

1 Department of Chemistry, Faculty of Science, Masaryk University, Brno, Czech Republic, **2** Department of Chemical and Geological Sciences, University of Cagliari, Monserrato (CA), Italy, **3** Department of Histology and Embryology, Faculty of Medicine, Masaryk University, Brno, Czech Republic, **4** International Clinical Research Center, St. Anne's University Hospital Brno, Pekarska 53, 656 91, Brno, Czech Republic

☞ These authors contributed equally to this work.

* pvanhara@med.muni.cz



CrossMark
click for updates

OPEN ACCESS

Citation: Valletta E, Kučera L, Prokeš L, Amato F, Pivetta T, Hampel A, et al. (2016) Multivariate Calibration Approach for Quantitative Determination of Cell-Line Cross Contamination by Intact Cell Mass Spectrometry and Artificial Neural Networks. PLoS ONE 11(1): e0147414. doi:10.1371/journal.pone.0147414

Editor: Patricia Talamas-Rohana, Centro de Investigacion y de Estudios Avanzados del Instituto Politecnico Nacional, MEXICO

Received: September 23, 2015

Accepted: January 4, 2016

Published: January 28, 2016

Copyright: © 2016 Valletta et al. This is an open access article distributed under the terms of the [Creative Commons Attribution License](https://creativecommons.org/licenses/by/4.0/), which permits unrestricted use, distribution, and reproduction in any medium, provided the original author and source are credited.

Data Availability Statement: All relevant data are within the paper and its Supporting Information files.

Funding: This study was supported by Grant Agency of Masaryk University (MUNI/M/0041/2013 and MUNI/A/1558/2014), from the European Regional Development Fund (CZ.1.05/1.1.00/02.0123 and CZ.1.07/2.3.00/20.0185) and by funds from the Faculty of Medicine MU to junior researcher (Petr Vaňhara). Elisa Valletta gratefully acknowledges the Masaryk University and its Department of Chemistry,

Abstract

Cross-contamination of eukaryotic cell lines used in biomedical research represents a highly relevant problem. Analysis of repetitive DNA sequences, such as Short Tandem Repeats (STR), or Simple Sequence Repeats (SSR), is a widely accepted, simple, and commercially available technique to authenticate cell lines. However, it provides only qualitative information that depends on the extent of reference databases for interpretation. In this work, we developed and validated a rapid and routinely applicable method for evaluation of cell culture cross-contamination levels based on mass spectrometric fingerprints of intact mammalian cells coupled with artificial neural networks (ANNs). We used human embryonic stem cells (hESCs) contaminated by either mouse embryonic stem cells (mESCs) or mouse embryonic fibroblasts (MEFs) as a model. We determined the contamination level using a mass spectra database of known calibration mixtures that served as training input for an ANN. The ANN was then capable of correct quantification of the level of contamination of hESCs by mESCs or MEFs. We demonstrate that MS analysis, when linked to proper mathematical instruments, is a tangible tool for unraveling and quantifying heterogeneity in cell cultures. The analysis is applicable in routine scenarios for cell authentication and/or cell phenotyping in general.

Introduction

In current biomedical research, cells cultured *in vitro* are irreplaceable experimental models and biotechnological tools. However, the research performed on immortalized or tumor-derived cell lines is dependent on proper cell identity and faces continuous significant risk of data misinterpretations due to inadvertent cross-contamination by another cell line [1–4].

for the kind hospitality and for funding her stay in Brno. The funders had no role in study design, data collection and analysis, decision to publish, or preparation of the manuscript.

Competing Interests: The authors have declared that no competing interests exist.

Contamination can easily occur by improper passaging, sharing of culture media for multiple cell lines, or inaccurate labeling and storage. Indeed, sophisticated techniques of cell culture and tissue engineering, such as high-throughput reactors, microfluidics, and stem cell or tissue cultures, require stringent monitoring of cell identity and phenotype stability [5–7]. The current gold standard for authentication of individual cell lines is analysis of Short Tandem Repeat sequences (STR) or Simple Sequence Repeats (SSR) widespread throughout the genome, since each cell line theoretically has a unique STR-profile [1,2]. In specific scenarios, such as co-culture setups of two cell lines, use of various cell populations derived from a single individual or from inbred strains, or the occurrence of phenotypic changes within STR- or otherwise stable cell lines, STR analysis cannot provide sufficient discrimination. Furthermore, in cases of intrinsic heterogeneity or impurity of cell cultures, co-culture setups, microsatellite instability, phenotype shifts, or viral or mycoplasma infections, STR analysis can provide ambiguous results, or, in the best case, allow only a qualitative assessment of cell identity without any information on the extent of contamination or heterogeneity in cell populations. Techniques that can complement STR authentication, such as identification of phenotype- or genotype-related markers, e.g. karyotype, isoenzymes, surface markers, or single nucleotide polymorphisms (SNPs) [8,9], are nevertheless dependent on preceding knowledge of the biological background of the model system used. Optimization of high-resolution methods common in physical and analytical chemistry and advanced mathematical modeling can circumvent the need for specific markers by analysis of global cellular or tissue patterns. Spectral techniques, such as Raman near-infrared or mass spectrometry were recently demonstrated to provide global fingerprints with sufficient capacity to distinguish diseased and normal tissues in models of metabolic disorders, or even individual states of cell differentiation or metabolism [10–13].

Matrix-assisted laser desorption/ionization–time of flight mass spectrometry (MALDI-TOF MS) has recently been used in fields beyond analytical and structural chemistry, such as biomedical research or clinical practice, and has been adapted for characterization of complex biological samples by peptide-mass-fingerprinting or peptide sequence tagging. Biotyping of non-fractionated intact microorganisms by MS is now a fast, routine, and cheap technique in clinical microbiology. Similarly, the concept of biotyping eukaryotic cells by intact cell (IC) MALDI-TOF MS has been suggested to allow identification of cell lines [13–18] or to characterize of physiological events occurring in the cells, such as terminal differentiation or programmed cell death [19]. The IC MALDI-TOF MS technique allows for recording the characteristic profiles of eukaryotic cells in quality sufficient for detailed analyses ranging from ultrastructural molecular cytology, to deep cell phenotyping and tissue analyses [13,15,18–22], to species recognition [23] and ecotoxicology [24,25].

However, a simple visual inspection of mass spectra is often not sufficient to establish an unambiguous cell line-specific set of biomarker peaks. Moreover, specific signal intensity and analytic concentration are not linear except in a narrow concentration range due to various stochastic “MALDI effects,” such as variability in matrix/analyte interactions and energy dissipation or quenching or enhancing of ionization [26]. Mathematical methods that are successfully used in chemometrics, such as bivariate regression, polynomial fitting, multiple linear regression, partial least squares, and artificial intelligence, must therefore be applied in MS analysis of complex biological samples [27–29]. Artificial neural networks (ANNs) represent a robust and versatile mathematical tool for many applications in various fields [30]. ANNs mimic the “learning” and “generalization” abilities of human neural structures. ANNs are able to model highly complex non-linear systems and are used for classification, pattern recognition, modeling, and multivariate data analysis [31]. The basic units of ANNs are “nodes” or “neurons.” They are organized in one “input” layer, in one or more “hidden” layers, and in one “output” layer. Each of the i -th neurons in a layer is linked to all the j -th neurons in the next layer. Each

connection is weighted with a weight w_{ij} . The role of the neurons in the input layer is to receive input data and transfer it to the neurons in the hidden layer through the weighted connections. The neurons in the hidden layer(s) perform mathematical operations on the incoming data (summation, addition of a “bias” term, and transformation by a suitable mathematical function). The result is then transferred to the neurons in the output layer where the ANN output is calculated.

Here we study the possibility of using ANNs to determine a quantity of cells of a particular cell line and/or type in two-component mixtures, mimicking a scenario of cell line cross-contamination. To create such situations, we used: a) line CCTL14 of human embryonic stem cells (hESCs), b) mouse embryonic fibroblasts (MEFs), and c) line R1 of mouse embryonic stem cell (mESCs). The cells were arranged into two-component calibration mixtures of hESCs + MEFs and hESCs + mESCs in various ratios. Line CCTL14 of hESCs has previously been thoroughly characterized [32]. MEFs freshly isolated from connective tissue of 11.5 days old mouse embryos are commonly used as a supportive feeder layer for hESCs in a routine co-culture mode. Mouse ESCs [33] represent pluripotent and self-renewing cells that are developmentally and functionally similar to hESCs.

The two-component cell suspensions were analyzed by ANN-coupled IC MALDI-TOF MS in a multivariate calibration approach. We demonstrate that mass spectra contain sufficient information to identify the presence of individual cell types in mixtures, and we report for the first time that ANN analysis of mass spectra from two-component mixtures can correctly predict the level of cell cross-contamination in very complex microenvironment.

Material and Methods

Chemicals

Knockout Dulbecco’s modified Eagle’s medium (DMEM), DMEM/F12, knockout serum replacement, fetal bovine serum, L-glutamine, minimum essential medium non-essential amino acids, penicillin-streptomycin, and TrypLE™ Select were purchased from Gibco, Life Technologies Czech Republic Ltd. (Prague, Czech Republic). Ammonium bicarbonate, sinapinic acid, trifluoroacetic acid, DMEM, 2-mercaptoethanol, phosphate buffered saline (PBS), and gelatin were purchased from Sigma-Aldrich Ltd. (Prague, Czech Republic). Matrigel™ was purchased from BD Bioscience, I.T.A.-Intertact Ltd. (Prague, Czech Republic). Fibroblast growth factor-2 was purchased from PeproTech, Baria Ltd. (Prague, Czech Republic). Leukemia Inhibitory Factor Protein was purchased from Chemicon, Merck Millipore (Prague, Czech Republic). Acetonitrile was purchased from J.T. Baker, VWR International Ltd. (Prague, Czech Republic). PepMix standard was purchased from Laser BioLabs (Sophia-Antipolis, France). Tissue culture dishes were purchased from TPP (Trasadingen, Switzerland).

Cell cultures

Mouse embryonic fibroblasts derived from CF1-mouse embryos were cultured in tissue culture dishes in medium consisting of Knockout DMEM supplemented with 10% fetal bovine serum, 2 mM L-glutamine, 1% minimum essential medium non-essential amino acids, 1% penicillin-streptomycin, and 0.1 mM 2-mercaptoethanol as described previously [34,35]. Human embryonic stem cells [36,37] were cultured in the undifferentiated state in tissue culture dishes coated with Matrigel™ in culture media conditioned by MEFs consisting of DMEM/F12 supplemented with 15% knockout serum replacement, 2 mM L-glutamine, 1% minimum essential medium non-essential amino acids, 0.5% penicillin-streptomycin, 0.1 mM 2-mercaptoethanol, and 4 ng/ml fibroblast growth factor-2. Mouse embryonic stem cells [33] were cultured in tissue culture dishes coated with 0.1% gelatin in medium consisting of DMEM supplemented

with 20% fetal bovine serum, 1% minimum essential medium non-essential amino acids, 1% penicillin-streptomycin, 1 mM 2-mercaptoethanol and 5.5 µg/ml leukemia inhibitory factor (LIF). All cell lines were maintained in an incubator at 37°C with a humidified atmosphere containing 5% CO₂, with daily media exchange.

Sample preparation

Cultured cells were washed with 1×PBS and enzymatically disaggregated to single cell suspension using TrypLE™ Select. After 2 min, the enzymatic activity was stopped by the respective culture medium. Detached cells were pelleted by centrifugation at 200 g for 5 min and washed once again with 1×PBS. Cell number was determined by CEDEX XS cell counter operated with CEDEX Control Center software v. 1.0.3. from Innovatis AG, Roche Life Sciences (Prague, Czech Republic).

Preparation of cell mixtures for MS analysis

hESCs + MEFs mixture. Cell suspensions containing a total of 1×10^6 hESCs and MEFs in 1×PBS in defined ratios were pelleted by centrifugation at 200 g for 5 min at 4°C and washed three times with an aqueous solution of 150 mM ammonium bicarbonate. Then, the cell pellets were resuspended in 10 µl of 150 mM ammonium bicarbonate and mixed with 5 µl of freshly prepared sinapinic acid matrix (30 mg/ml in 70% acetonitrile and 7.5% trifluoroacetic acid). Two microliters of sample/matrix mixture were immediately spotted in pentaplicates onto the MALDI target and dried at room temperature.

hESCs + mESCs mixture. Aliquots of 1×10^6 mESCs or hESCs in 1×PBS were pelleted by centrifugation at 200 g for 5 min at 4°C. Supernatant was discarded and pelleted cells were washed three times with 150 mM ammonium bicarbonate solution. Resulting cell pellets were then snap-frozen and stored until further processing. At the time of analysis, both mESCs and hESCs aliquots were quickly thawed and reconstituted in 20 µl of 150 mM ammonium bicarbonate solution and sonicated briefly in a water ultrasound bath. Then, MEFs and hESCs were mixed in given ratios to a total of 0.5×10^6 cells per sample and total volume was adjusted to 15 µl with 150 mM ammonium bicarbonate. Each cell suspension was mixed with 7.5 µl of freshly prepared sinapinic acid matrix solution. Two microliters of sample/matrix mixture were immediately spotted onto the MALDI target and dried at room temperature. Each sample was spotted in five technical replicates.

Mass spectrometry

Mass spectra were recorded on an AXIMA CFR mass spectrometer from Kratos Analytical (Manchester, UK) in linear positive ion mode. The instrument was equipped with a nitrogen laser (337 nm) and delayed extraction was used. The laser energy was expressed in arbitrary units from 0 to 180 a.u. The power of the laser at 180 a.u. was 6 mW, while the irradiated spot size was approximately 150 µm in diameter. External mass calibration was done using the Pep-Mix4 standard. The laser repetition rate was 5 Hz with a pulse time width of 3 ns. Each mass spectrum was obtained by the accumulation of at least 5000 shots. In order to decrease the contribution of chemical noise and possible errors on the baseline and in calibration, the raw mass spectra were pre-processed, cleaned, transformed, and reduced in dimensionality before the data analysis, as described elsewhere [38].

Mass spectra were analyzed using Launchpad Software (Kompact version 2.9.3, 2011) from Kratos Analytical Ltd. Pre-processing of mass spectra and ANN computation were performed using MATLAB 8.6. 2015 from The MathWorks Inc. (Natick, Massachusetts, USA) and Trajan Neural Network Simulator, Release 3.0 D 1996–1998, from Trajan Software Ltd. (Durham, U.

K.). Partial least squares projection to latent structures regression was performed with “leave-one-out” cross-validated prediction in program R (www.r-project.org) using the external *pls* library [39].

Artificial neural networks

We constructed an artificial neural network containing four neurons in one hidden layer. The intensities of processed mass spectra served as the input, while the number of contaminating cells in the two-component mixtures was the output. The “learning” of the ANN was performed using the back-propagation training algorithm as described elsewhere [40,41]. The back-propagation was achieved by iteratively adjusting the values of connection weights in order to minimize the difference between the ANN calculated output value (o_{pk}^*) and the experimental one (o_{pk}). After each iteration, the root mean square of the sum of $(o_{pk} - o_{pk}^*)^2$ residuals (RMS) was calculated according to Eq 1:

$$\text{RMS} = \sqrt{\frac{\sum_{p=1}^N \sum_{k=1}^M (o_{pk} - o_{pk}^*)^2}{N \times M}} \quad (1)$$

where N is the number of mass spectra, M is the number of outputs, o_{pk}^* is the ANN calculated, and o_{pk} is the experimental output value. The optimal ANN architecture was confirmed by plotting the RMS value against the number of neurons in the hidden layer(s) and number of training cycles (epochs).

Results And Discussion

Preparation of two-component mixtures of different cell types and intact cell MALDI-TOF mass spectrometry

We prepared calibration datasets consisting of twenty-eight defined two-component mixtures of hESCs + MEFs, thirty-four mixtures of hESCs + mESCs (Fig 1A and 1D), and pure cell populations, with total cell numbers of 1×10^6 (Fig 1B and 1E). We then recorded the mass spectra of two-component cell mixtures and pure cell populations in the 2000–20000 m/z range without previous fractionation or extraction. We pre-processed the mass spectra by (i) resampling to 30000 m/z values (homogenizing in a chosen range and reducing the number of m/z values), (ii) aligning (removing the systematic shifts in mass spectra of repeated experiments), (iii) baseline subtraction, (iv) smoothing, and (v) normalization to a vector of unit length ($\sum X_i = 1$), where X_i are the intensities of the peaks of the mass spectrum [42] (Fig 1C and 1F, S1 Fig). Next, we organized the spectral data into a matrix with dimensions $m \times n$, where m represents the number of the mass spectrum of the particular cell mixture and n are the m/z values. The i -th row of the matrix represents the mass spectrometric fingerprint of the i -th mixture. In order to decrease the latent noise in pre-processed mass spectra, we selected only the peaks with intensity higher than an arbitrarily set threshold (1×10^{-3}) for further analysis. Thus, the data matrices of hESCs + MEFs and hESCs + mESCs were reduced from the original $n \times 30000$ to $n \times 84$ and $n \times 122$, respectively. Next, we identified peaks with the highest intrinsic variability in the datasets, as described elsewhere [43–46]. In brief, we selected informative peaks by comparative determination of standard deviations of individual peaks normalized to the total variance of the dataset, Lasso regression, and sparse partial least squares regression. The informative peaks are visualized in S3 Fig. That allowed us to finally reduce the data matrices of hESCs + MEFs and hESCs + mESCs to $n \times 10$ and $n \times 30$, respectively (S1 Table).

Then, we used these datasets to perform principal component analysis aiming to discriminate the pure hESC and MEF cell populations and the cell mixtures containing 50% of each cell

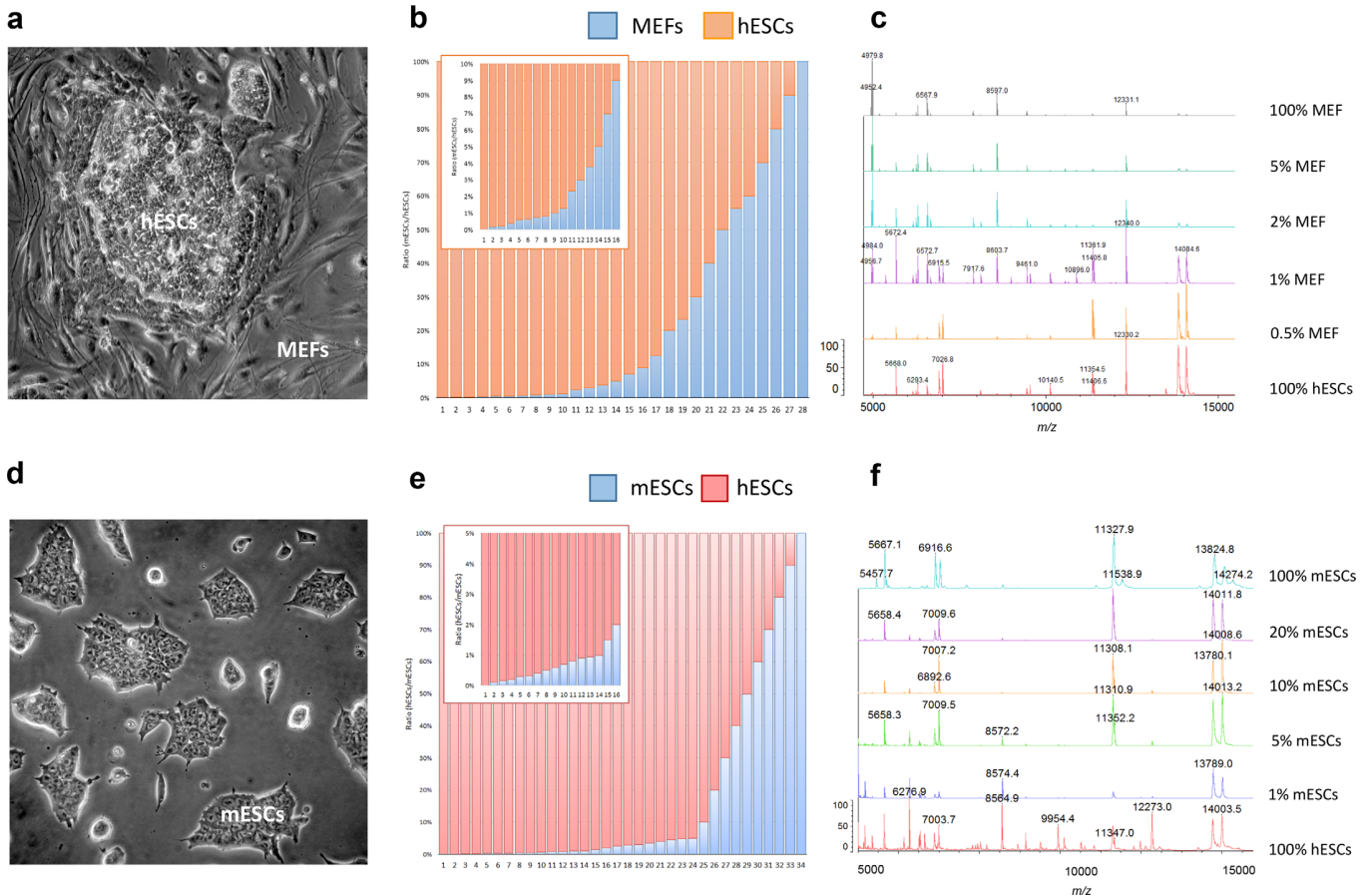


Fig 1. (A) Colony of human embryonic stem cells (hESCs) cultured on a feeder layer of mouse embryonic fibroblasts. (B) Experimental ratios of two-component mixtures of hESCs + MEFs. (C) Representative mass spectra of selected two-component mixtures of hESCs + MEFs. (D) Colony of mouse embryonic stem cells (mESCs) in a feeder-free culture. (E) Experimental ratios of two-component mixtures of hESCs + mESCs. (F) Representative mass spectra of selected two-component mixtures of hESCs + mESCs.

doi:10.1371/journal.pone.0147414.g001

type. Eigenvalue analysis showed the presence of three factors contributing up to 94% of the overall variability. Plotting the principal components revealed three clearly separated clusters and provided proof of principle for the discriminative information of the MEF and hESC mass spectra (Fig 2A and 2B). Similar discrimination was achieved for mESCs and hESCs (data not shown).

Next, we visually compared mass spectra obtained from the pure hESCs and MEFs, and their two-component mixtures. Despite the high similarity of the mass spectra, we identified peaks unique to hESCs and MEFs (m/z 3992 and 9908) (Fig 2C) appearing reproducibly over various mixtures. We presumed that if these two marker peaks are informative for MEFs, their intensities should be proportional to the content of MEFs in the two-component mixtures. However, we did not identify any linear trend between the normalized intensities of these two marker peaks and the percentage of MEFs, especially in two-component mixtures with low concentrations of MEFs (Fig 2D). In the case of highly similar pluripotent cell types, the mass spectra of hESCs + mESCs mixtures lacked any spectral patterns specific for individual pure cell lines (Fig 1F). Therefore, assessment of the individual biomarker peaks was not suitable for precise and unambiguous quantification.

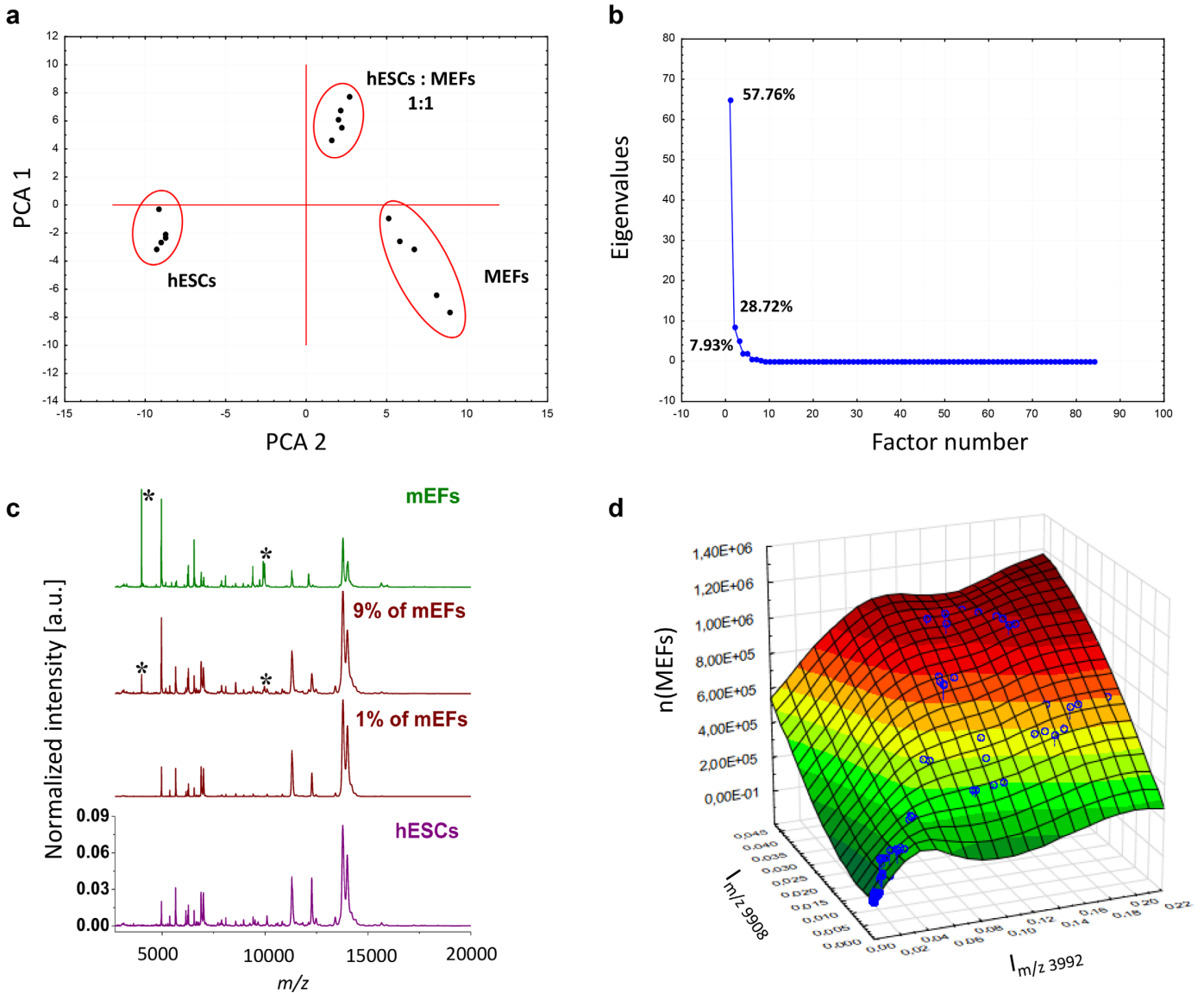


Fig 2. (A) Principal component analysis of mass spectra dataset containing intensities of 84 m/z for pure MEF and hESC populations and their 1:1 mixture. (B) Scree plot documenting the presence of three factors contributing predominantly to the overall variability in the analyzed dataset. (C) Pre-processed MALDI-TOF mass spectra for pure hESCs and MEFs and a hESCs + MEFs two-component mixture containing 99% hESCs and 1% MEFs. The spectra were normalized to vector of unit length (a.u.). Asterisks indicate peaks at m/z 3992 and 9908. (D) Surface plot of intensities of peaks at m/z 3992 and 9908 versus the number of MEFs in hESCs + MEFs two-component mixtures.

doi:10.1371/journal.pone.0147414.g002

Quantitative determination of contamination levels

Because of the data complexity, it was difficult to handle the mass spectral datasets by simple linear analyses. We first examined the data by a method of partial least squares with projection to latent structures regression (PLS) on the full data matrix of the complete mass spectra. PLS has been developed and extended by Herman and Svante Wold, respectively, [47] for quantitative analysis of highly complex multivariate data and is used preferentially in chemometrics. Despite a correlation between predicted and actual cell percentages in the two-component mixtures, the prediction precision by PLS was rather low, with substantial root mean square error

Table 1. Values of RMS calculated as differences between predicted and observed values, k (regression coefficients), and R^2 (determination coefficient).

	hESCs: MEFs		hESCs: mESCs	
	PLS	ANN	PLS	ANN
RMS	51.7×10^3	3.16×10^3	96.6×10^3	7.1×10^3
k	0.976	0.996	0.601	0.975
R²	0.9759	0.9992	0.6010	0.9822

doi:10.1371/journal.pone.0147414.t001

(RMS) showing signs of systematic trends (Table 1, S3 Fig). Therefore, we asked whether non-linear approaches and artificial intelligence methods, such as ANNs, could make predictions with more precision. ANNs were previously reported to provide effective analysis and classification of biological, clinical or bioanalytical, and chemometric non-linear data (for review see [30]), and were found particularly suitable for analysis of MS data [28].

In our analysis the intensities of the selected peaks comprised the ANN-input data and the number of MEFs and/or mESCs cells in the hESC calibration mixtures was the ANN-output data. For the training step of the ANN, we tested several algorithms and found the back-propagation algorithm to be the most suitable (data not shown). We determined the optimal architecture containing four neurons in one hidden layer (Fig 3A) by plotting the RMS against the number of nodes (data not shown) and we validated over 100000 training cycles (epochs), without overfitting the model (Fig 3B). We used the leave-one-out cross-validation method to test the “generalization” ability of the designed network to predict the single cases excluded

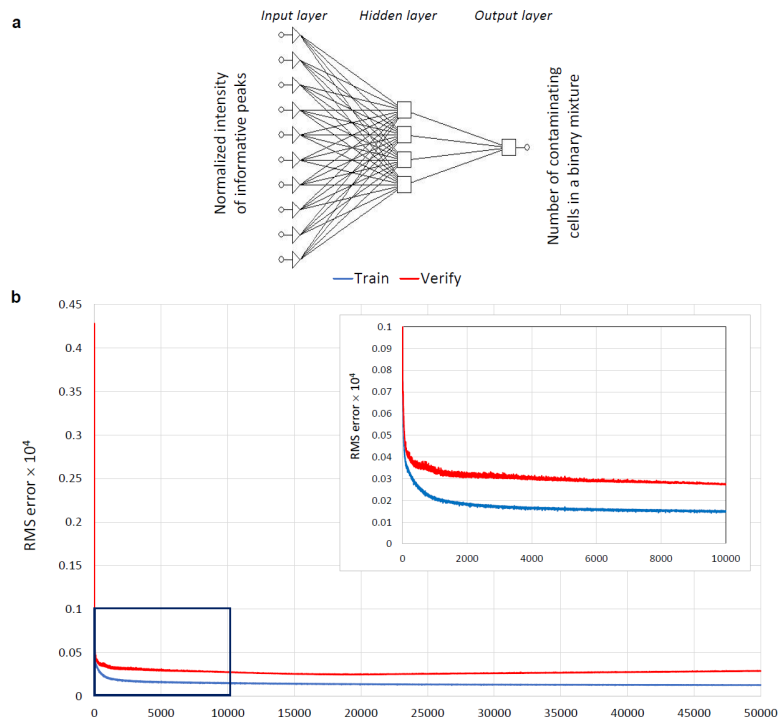


Fig 3. (A) Optimal ANN architecture (one Input layer, one Hidden layer with four neurons, and one Output layer). (B) Training and leave-one-out verification plot of the RMS versus the number of training cycles (epochs). First 50 000 iterations are shown. The inset shows a detailed plot for the first 10 000 training cycles.

doi:10.1371/journal.pone.0147414.g003

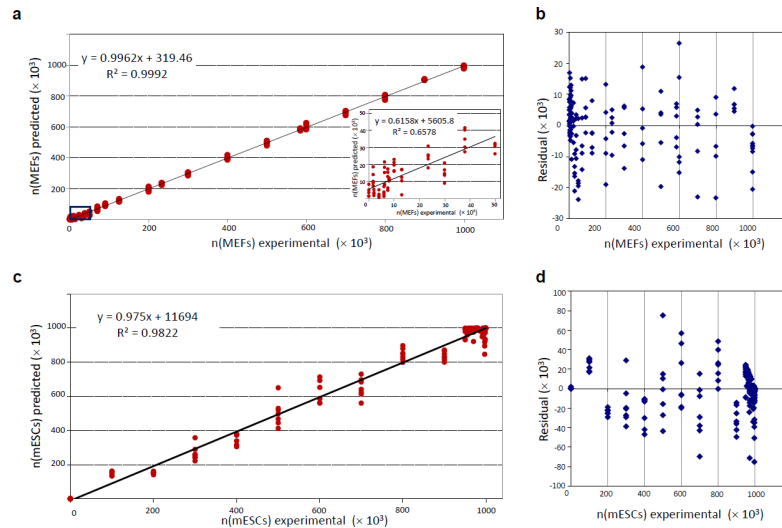


Fig 4. (A) Correlation between ANN-predicted number of cells and the experimental number of MEFs in two-component mixtures of hESCs + MEFs. The inset shows the correlation between experimental and predicted values in low concentration ranges of MEFs up to the 50×10^3 cells in the two-component mixtures. (B) Overview of Residuals (difference between ANN-predicted number of cells and the experimental values) versus the experimental number of MEF cells in two-component mixtures of hESCs + MEFs. (C) Correlation between ANN-predicted number of cells and the experimental number of mESCs in two-component mixtures of hESCs + mESCs. (D) Overview of Residuals (difference between ANN-predicted number of cells and the experimental values) versus the experimental number of mESC cells in the two-component mixtures of hESCs + mESCs.

doi:10.1371/journal.pone.0147414.g004

from the training data set. We used the RMS as a measure of the prediction accuracy. The network was able to evaluate the input data and correctly predict the number of MEFs (Fig 4A) and mESCs (Fig 4C) in the hESC suspensions over the whole range of evaluated ratios. Prediction by ANN was correct even at low percentages of contaminating cells in suspension. To validate the model, the RMS was calculated as the differences between the predicted and experimental values. The residuals reached significantly lower values than in PLS predictions (Table 1). Moreover, the residual values were randomly distributed, and the absence of any systematic error or trend in residuals demonstrated correctness of the model (Fig 4B and 4D). To perform further validation of the method, we analyzed an independent dataset of fifty hESCs + MEFs mixtures. Using a training set described above, the ANN correctly determined the numbers of MEFs in hESCs suspension with high correlation between predicted and experimental values (S4 Fig). In summary, multivariate calibration coupled with a correctly trained ANN was able to determine the ratio of cell numbers in two-component mixtures.

We have identified the conditions and developed a step-by-step protocol for successful quantitation of two distinct cell types in a single two-component mixture by a multivariate calibration approach based on an ANN-coupled IC MALDI-TOF MS analysis. The major steps of the method include:

1. *a priori* knowledge or identification of the contaminating cell line
2. construction of two-component calibration mixtures of the given cell lines
3. mass spectra pre-processing and *m/z* selection
4. parallel recording of mass spectra of pure cell populations and calibration mixtures and building a library of spectral datasets for multivariate calibration

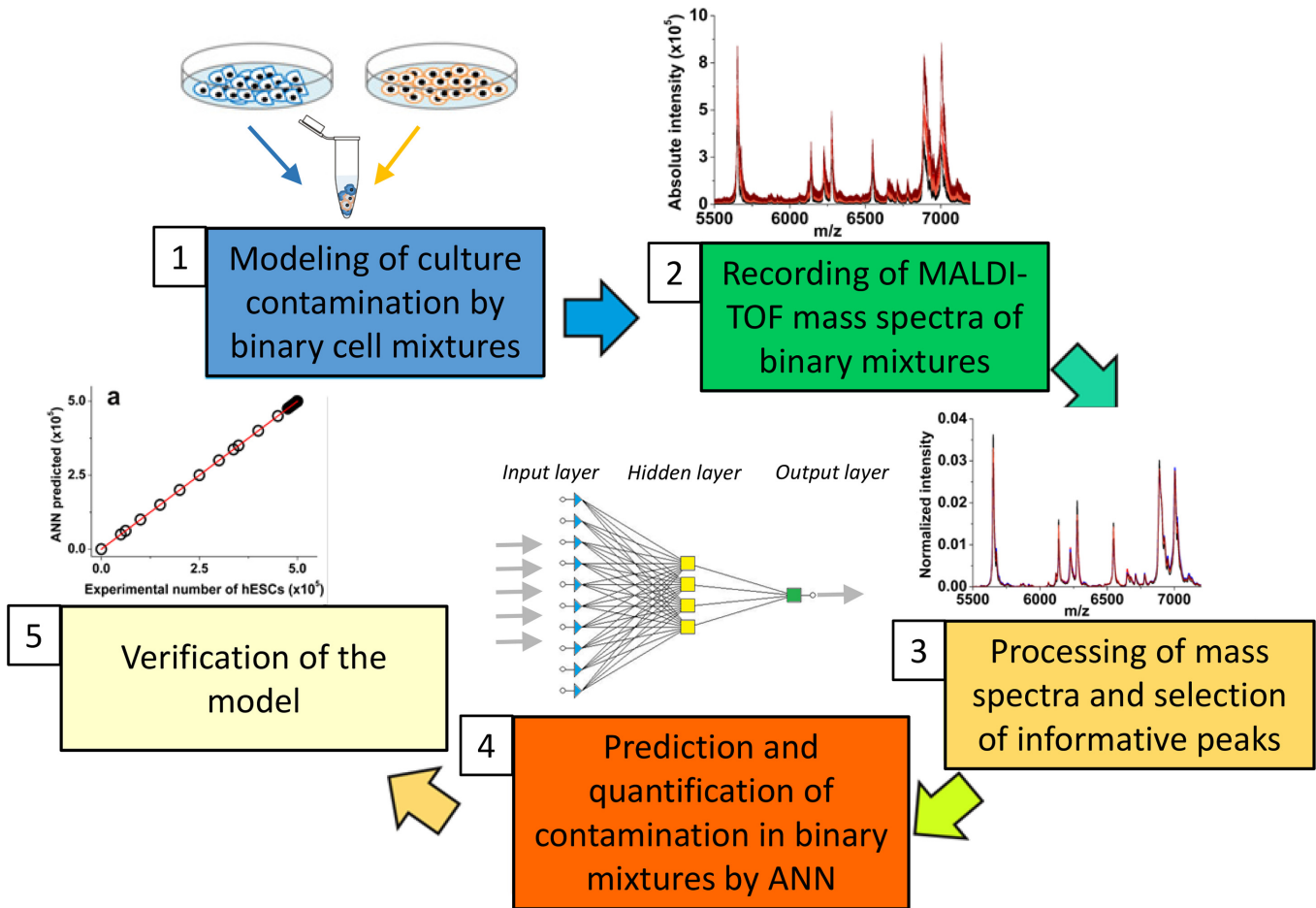


Fig 5. Overview for quantitative ANN-coupled MS-based analysis of cross-contamination.

doi:10.1371/journal.pone.0147414.g005

- estimation of the contamination levels in unknown samples using an ANN model trained on the calibration datasets

The application of ANNs allowed us to overcome the unwanted inconsistency and non-linearity of IC MALDI-TOF MS spectra and reveal hidden patterns in mass spectra to unambiguously identify and quantify MEFs or mESCs in the hESC culture. However, *a priori* knowledge of the contaminating cell line is a prerequisite for correct prediction and selection of the training dataset. The multivariate calibration-based ANN approach can be easily adapted to routine protocols for quantitative determination of cell culture homogeneity and consistency and for thorough MS analyses of cell parameters in various culture platforms, with all steps adaptable for any experimental, routine, or high-throughput culture setup [48,49] (Figs 5 and 6). Currently, methods involving assessment of cell quality in clinical grade cultures, biomedical research or bio-industry involve either genetic authentication confirming the cell identity or functional assays documenting the phenotype. The intact cell mass spectrometry coupled with ANN can reveal inconsistencies occurring in high-throughput or long-term cultures or co-cultures, by monitoring spectral patterns and their alterations.

In conclusion, we demonstrated for the first time that the multivariate calibration approach based on ANN-coupled IC MALDI-TOF MS analysis can provide quantitative information on

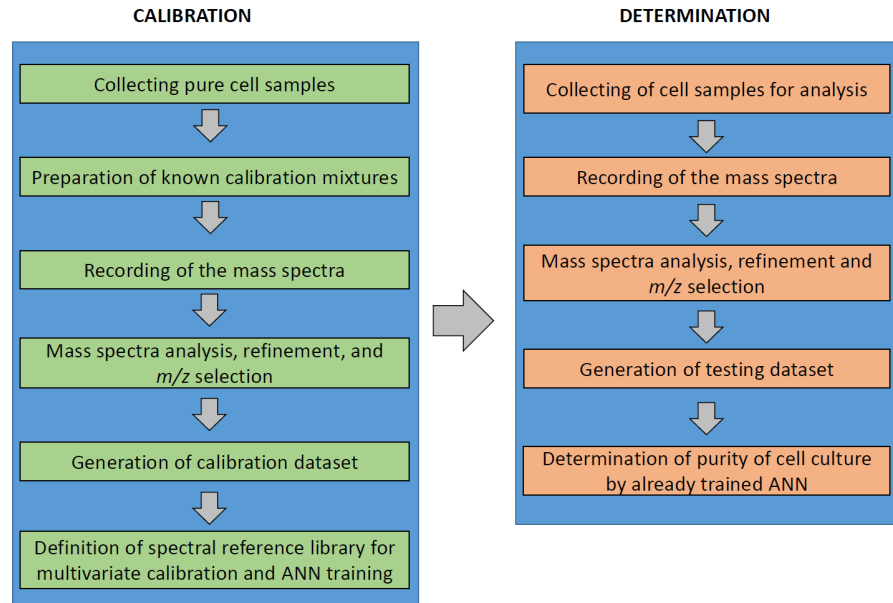


Fig 6. Experimental schematic of the multivariate calibration-based ANN spectral analysis.

doi:10.1371/journal.pone.0147414.g006

cell culture heterogeneity and authenticity and thus complement the portfolio of techniques that are available for characterization of mammalian cell cultures.

Supporting Information

S1 Fig. Comparison of raw (a) and pre-processed (b) mass spectra (five replicates) characterizing human embryonic stem cells (hESCs). The pre-processed mass spectra were normalized to a vector of unit length ($\sum X_i = 1$, where X_i are the intensities of the peaks of the mass spectrum).

(TIF)

S2 Fig. Standard deviations of the mean intensity of peaks of the particular *m/z* in the dataset normalized to the standard deviation of the mean intensity of the hESCs + MEFs (a) and hESCs + mESCs dataset (b). Peaks used in the further analyses are indicated by respective *m/z* values.

(TIF)

S3 Fig. Correlation between PLS-predicted number of cells and the experimental number of MEFs in two-component mixtures of (a) hESCs + MEFs and (b) hESCs + mESCs. Overview of Residuals (difference between PLS-predicted number of cells and the experimental values) versus the experimental number of cells in the two-component mixtures of (c) hESCs + MEFs and (d) hESCs + mESCs.

(TIF)

S4 Fig. Training and verification plot for an independent dataset of 50 cases of hESCs + MEFs mixtures (a). Correlation between experimental and ANN-predicted numbers of MEFs in hESCs suspension.

(TIF)

S1 Table. Overview of normalized mass-to-charge ratios (m/z) of informative peaks used for analysis.

(TIF)

Acknowledgments

We thank Dr. Jiří Pacherník from the Department of Experimental Biology, Faculty of Science, Masaryk University for the kind provision of mouse embryonic stem cell line R1.

Author Contributions

Conceived and designed the experiments: TP JH AH PV. Performed the experiments: EV LK FA. Analyzed the data: LK LP JH PV. Contributed reagents/materials/analysis tools: TP JH AH PV. Wrote the paper: AH JH PV.

References

1. Capes-Davis A, Theodosopoulos G, Atkin I, Drexler HG, Kohara A, MacLeod RAF, et al. (2010) Check your cultures! A list of cross-contaminated or misidentified cell lines. *International Journal of Cancer* 127: 1–8.
2. Marx V (2014) Cell-line authentication demystified. *Nature Methods* 11: 483–.
3. Masters JRW (2010) Cell line misidentification: the beginning of the end. *Nature Reviews Cancer* 10: 441–448. doi: [10.1038/nrc2852](https://doi.org/10.1038/nrc2852) PMID: [20448633](https://pubmed.ncbi.nlm.nih.gov/20448633/)
4. Nardone RM (2007) Eradication of cross-contaminated cell lines: A call for action. *Cell Biology and Toxicology* 23: 367–372. PMID: [17522957](https://pubmed.ncbi.nlm.nih.gov/17522957/)
5. Hynds RE, Giangreco A (2013) Concise Review: The Relevance of Human Stem Cell-Derived Organoid Models for Epithelial Translational Medicine. *Stem Cells* 31: 417–422. doi: [10.1002/stem.1290](https://doi.org/10.1002/stem.1290) PMID: [23203919](https://pubmed.ncbi.nlm.nih.gov/23203919/)
6. Mehling M, Tay S (2014) Microfluidic cell culture. *Current Opinion in Biotechnology* 25: 95–102. doi: [10.1016/j.copbio.2013.10.005](https://doi.org/10.1016/j.copbio.2013.10.005) PMID: [24484886](https://pubmed.ncbi.nlm.nih.gov/24484886/)
7. Nienow AW (2006) Reactor engineering in large scale animal cell culture. *Cytotechnology* 50: 9–33. doi: [10.1007/s10616-006-9005-8](https://doi.org/10.1007/s10616-006-9005-8) PMID: [19003068](https://pubmed.ncbi.nlm.nih.gov/19003068/)
8. Baradez MO, Lekishvili T, Marshall D (2015) Rapid phenotypic fingerprinting of cell products by robust measurement of ubiquitous surface markers. *Cytometry Part A* 87A: 624–635.
9. Didion JP, Buus RJ, Naghashfar Z, Threadgill DW, Morse HC 3rd, de Villena FP (2014) SNP array profiling of mouse cell lines identifies their strains of origin and reveals cross-contamination and wide-spread aneuploidy. *BMC Genomics* 15: 847. doi: [10.1186/1471-2164-15-847](https://doi.org/10.1186/1471-2164-15-847) PMID: [25277546](https://pubmed.ncbi.nlm.nih.gov/25277546/)
10. Brougham DF, Ivanova G, Gottschalk M, Collins DM, Eustace AJ, O'Connor R, et al. (2011) Artificial neural networks for classification in metabolomic studies of whole cells using ¹H nuclear magnetic resonance. *J Biomed Biotechnol* 2011: 158094. doi: [10.1155/2011/158094](https://doi.org/10.1155/2011/158094) PMID: [20886062](https://pubmed.ncbi.nlm.nih.gov/20886062/)
11. Houska J, Pena-Mendez EM, Hernandez-Fernaund JR, Salido E, Hampel A, Havel J, et al. (2014) Tissue profiling by nanogold-mediated mass spectrometry and artificial neural networks in the mouse model of human primary hyperoxaluria 1. *Journal of Applied Biomedicine* 12: 119–125.
12. Lui H, Zhao JH, McLean D, Zeng HS (2012) Real-time Raman Spectroscopy for In Vivo Skin Cancer Diagnosis. *Cancer Research* 72: 2491–2500. doi: [10.1158/0008-5472.CAN-11-4061](https://doi.org/10.1158/0008-5472.CAN-11-4061) PMID: [22434431](https://pubmed.ncbi.nlm.nih.gov/22434431/)
13. Munteanu B, von Reitzenstein C, Hansch GM, Meyer B, Hopf C (2012) Sensitive, robust and automated protein analysis of cell differentiation and of primary human blood cells by intact cell MALDI mass spectrometry biotyping. *Analytical and Bioanalytical Chemistry* 404: 2277–2286. doi: [10.1007/s00216-012-6357-0](https://doi.org/10.1007/s00216-012-6357-0) PMID: [22955673](https://pubmed.ncbi.nlm.nih.gov/22955673/)
14. Buchanan CM, Malik AS, Cooper GJS (2007) Direct visualisation of peptide hormones in cultured pancreatic islet alpha- and beta-cells by intact-cell mass spectrometry. *Rapid Communications in Mass Spectrometry* 21: 3452–3458. PMID: [17918213](https://pubmed.ncbi.nlm.nih.gov/17918213/)
15. Lokhov P, Balashova E, Dashtiev M (2009) Cell proteomic footprint. *Rapid Communications in Mass Spectrometry* 23: 680–682. doi: [10.1002/rcm.3928](https://doi.org/10.1002/rcm.3928) PMID: [19184978](https://pubmed.ncbi.nlm.nih.gov/19184978/)
16. Maurer K, Eschrich K, Schellenberger W, Bertolini J, Rupf S, Remmerbach TW (2013) Oral brush biopsy analysis by MALDI-ToF Mass Spectrometry for early cancer diagnosis. *Oral Oncology* 49: 152–156. doi: [10.1016/j.oraloncology.2012.08.012](https://doi.org/10.1016/j.oraloncology.2012.08.012) PMID: [23000400](https://pubmed.ncbi.nlm.nih.gov/23000400/)

17. Munteanu B, Hopf C (2013) Emergence of whole-cell MALDI-MS biotyping for high-throughput bioanalysis of mammalian cells? *Bioanalysis* 5: 885–893. doi: [10.4155/bio.13.47](https://doi.org/10.4155/bio.13.47) PMID: [23590472](https://pubmed.ncbi.nlm.nih.gov/23590472/)
18. Zhang X, Scalf M, Berggren TW, Westphal MS, Smith LM (2006) Identification of mammalian cell lines using MALDI-TOF and LC-ESI-MS/MS mass spectrometry. *Journal of the American Society for Mass Spectrometry* 17: 490–499. PMID: [16488154](https://pubmed.ncbi.nlm.nih.gov/16488154/)
19. Dong HJ, Shen W, Cheung MTW, Liang YM, Cheung HY, Allmaier G, et al. (2011) Rapid detection of apoptosis in mammalian cells by using intact cell MALDI mass spectrometry. *Analyst* 136: 5181–5189. doi: [10.1039/c1an15750g](https://doi.org/10.1039/c1an15750g) PMID: [22059228](https://pubmed.ncbi.nlm.nih.gov/22059228/)
20. Hanrieder J, Wicher G, Bergquist J, Andersson M, Fex-Svenningsen A (2011) MALDI mass spectrometry based molecular phenotyping of CNS glial cells for prediction in mammalian brain tissue. *Analytical and Bioanalytical Chemistry* 401: 135–147. doi: [10.1007/s00216-011-5043-y](https://doi.org/10.1007/s00216-011-5043-y) PMID: [21553124](https://pubmed.ncbi.nlm.nih.gov/21553124/)
21. Munteanu B, Meyer B, von Reitzenstein C, Burgermeister E, Bog S, Pahl A, et al. (2014) Label-Free in Situ Monitoring of Histone Deacetylase Drug Target Engagement by Matrix-Assisted Laser Desorption Ionization-Mass Spectrometry Biotyping and Imaging. *Analytical Chemistry* 86: 4642–4647. doi: [10.1021/ac500038j](https://doi.org/10.1021/ac500038j) PMID: [24559101](https://pubmed.ncbi.nlm.nih.gov/24559101/)
22. Povey JF, O'Malley CJ, Root T, Martin EB, Montague GA, Feary M, et al. (2014) Rapid high-throughput characterisation, classification and selection of recombinant mammalian cell line phenotypes using intact cell MALDI-ToF mass spectrometry fingerprinting and PLS-DA modelling. *Journal of Biotechnology* 184: 84–93. doi: [10.1016/j.jbiotec.2014.04.028](https://doi.org/10.1016/j.jbiotec.2014.04.028) PMID: [24858576](https://pubmed.ncbi.nlm.nih.gov/24858576/)
23. Volta P, Riccardi N, Lauceri R, Tonolla M (2012) Discrimination of freshwater fish species by Matrix-Assisted Laser Desorption/Ionization-Time Of Flight Mass Spectrometry (MALDI-TOF MS): a pilot study. *Journal of Limnology* 71: 164–169.
24. Chiu NH, Jia Z, Diaz R, Wright P (2015) Rapid differentiation of in vitro cellular responses to toxic chemicals by using matrix-assisted laser desorption/ionization time-of-flight mass spectrometry. *Environ Toxicol Chem* 34: 161–166. doi: [10.1002/etc.2774](https://doi.org/10.1002/etc.2774) PMID: [25319019](https://pubmed.ncbi.nlm.nih.gov/25319019/)
25. Kober SL, Meyer-Alert H, Grienitz D, Hollert H, Frohme M (2015) Intact cell mass spectrometry as a rapid and specific tool for the differentiation of toxic effects in cell-based ecotoxicological test systems. *Anal Bioanal Chem*.
26. Asakawa D, Sakakura M, Takayama M (2012) Matrix effect on in-source decay products of peptides in matrix-assisted laser desorption/ionization. *Mass Spectrom (Tokyo)* 1: A0002.
27. Bas D, Boyaci IH (2007) Modeling and optimization I: Usability of response surface methodology. *Journal of Food Engineering* 78: 836–845.
28. Goodacre R, Neal MJ, Kell DB (1996) Quantitative analysis of multivariate data using artificial neural networks: A tutorial review and applications to the deconvolution of pyrolysis mass spectra. *Zentralblatt Fur Bakteriologie-International Journal of Medical Microbiology Virology Parasitology and Infectious Diseases* 284: 516–539.
29. Li H, Zhang YX, Polaskova P, Havel J (2002) Enhancement of precision in the analysis of medicines by capillary electrophoresis using artificial neural networks. *Acta Chimica Sinica* 60: 1264–1268.
30. Amato F, Lopez A, Pena-Mendez EM, Vanhara P, Hampf A, Havel J (2013) Artificial neural networks in medical diagnosis. *Journal of Applied Biomedicine* 11: 47–58.
31. Basheer IA, Hajmeer M (2000) Artificial neural networks: fundamentals, computing, design, and application. *Journal of Microbiological Methods* 43: 3–31. PMID: [11084225](https://pubmed.ncbi.nlm.nih.gov/11084225/)
32. International Stem Cell Initiative, Adewumi O, Aflatoonian B, Ahrlund-Richter L, Amit M, Andrews PW, et al. (2007) Characterization of human embryonic stem cell lines by the International Stem Cell Initiative. *Nat Biotechnol* 25: 803–816. PMID: [17572666](https://pubmed.ncbi.nlm.nih.gov/17572666/)
33. Kotasova H, Vesela I, Kucera J, Houdek Z, Prochazkova J, Kralickova M, et al. (2012) Phosphoinositide 3-kinase inhibition enables retinoic acid-induced neurogenesis in monolayer culture of embryonic stem cells. *Journal of Cellular Biochemistry* 113: 563–570. doi: [10.1002/jcb.23380](https://doi.org/10.1002/jcb.23380) PMID: [21948563](https://pubmed.ncbi.nlm.nih.gov/21948563/)
34. Barta T, Vinarsky V, Holubcova Z, Dolezalova D, Verner J, Pospisilova S, et al. (2010) Human embryonic stem cells are capable of executing G1/S checkpoint activation. *Stem Cells* 28: 1143–1152. doi: [10.1002/stem.451](https://doi.org/10.1002/stem.451) PMID: [20518019](https://pubmed.ncbi.nlm.nih.gov/20518019/)
35. Holubcova Z, Matula P, Sedlackova M, Vinarsky V, Dolezalova D, Barta T, et al. (2011) Human embryonic stem cells suffer from centrosomal amplification. *Stem Cells* 29: 46–56. doi: [10.1002/stem.549](https://doi.org/10.1002/stem.549) PMID: [20960514](https://pubmed.ncbi.nlm.nih.gov/20960514/)
36. Adewumi O, Aflatoonian B, Ahrlund-Richter L, Amit M, Andrews PW, Beighton G, et al. (2007) Characterization of human embryonic stem cell lines by the International Stem Cell Initiative. *Nature Biotechnology* 25: 803–816. PMID: [17572666](https://pubmed.ncbi.nlm.nih.gov/17572666/)

37. Amps K, Andrews PW, Anyfantis G, Armstrong L, Avery S, Baharvand H, et al. (2011) Screening ethnically diverse human embryonic stem cells identifies a chromosome 20 minimal amplicon conferring growth advantage. *Nature Biotechnology* 29: 1132–U1113. doi: [10.1038/nbt.2051](https://doi.org/10.1038/nbt.2051) PMID: [22119741](https://pubmed.ncbi.nlm.nih.gov/22119741/)
38. Hilario M, Kalousis A, Pellegrini C, Muller M (2006) Processing and classification of protein mass spectra. *Mass Spectrometry Reviews* 25: 409–449. PMID: [16463283](https://pubmed.ncbi.nlm.nih.gov/16463283/)
39. Mevik B-H, Wehrens R (2007) The pls Package: Principal Component and Partial Least Squares Regression in R. *Journal of Statistical Software*, 18: 1–24.
40. Amato F, Gonzalez-Hernandez JL, Havel J (2012) Artificial neural networks combined with experimental design: a "soft" approach for chemical kinetics. *Talanta* 93: 72–78. doi: [10.1016/j.talanta.2012.01.044](https://doi.org/10.1016/j.talanta.2012.01.044) PMID: [22483879](https://pubmed.ncbi.nlm.nih.gov/22483879/)
41. Pivetta T, Isaia F, Trudu F, Pani A, Manca M, Perra D, et al. (2013) Development and validation of a general approach to predict and quantify the synergism of anti-cancer drugs using experimental design and artificial neural networks. *Talanta* 115: 84–93. doi: [10.1016/j.talanta.2013.04.031](https://doi.org/10.1016/j.talanta.2013.04.031) PMID: [24054565](https://pubmed.ncbi.nlm.nih.gov/24054565/)
42. Alfassi ZB (2004) On the normalization of a mass spectrum for comparison of two spectra. *Journal of the American Society for Mass Spectrometry* 15: 385–387. PMID: [14998540](https://pubmed.ncbi.nlm.nih.gov/14998540/)
43. Filzmoser P, Gschwandtner M, Todorov V (2012) Review of sparse methods in regression and classification with application to chemometrics. *Journal of Chemometrics* 26: 42–51.
44. Friedman J, Hastie T, Tibshirani R (2010) Regularization Paths for Generalized Linear Models via Coordinate Descent. *Journal of Statistical Software* 33: 1–22. PMID: [20808728](https://pubmed.ncbi.nlm.nih.gov/20808728/)
45. Chun H, Keles S (2010) Sparse partial least squares regression for simultaneous dimension reduction and variable selection. *Journal of the Royal Statistical Society Series B-Statistical Methodology* 72: 3–25.
46. Rasmussen MA, Bro R (2012) A tutorial on the Lasso approach to sparse modeling. *Chemometrics and Intelligent Laboratory Systems* 119: 21–31.
47. Wold S, Sjöström M, Eriksson L (2001) PLS-regression: a basic tool of chemometrics. *Chemometrics and Intelligent Laboratory Systems* 58: 109–130.
48. Dittrich P, Ibanez AJ (2015) Analysis of metabolites in single cells-what is the best micro-platform? *Electrophoresis*.
49. Xie W, Gao D, Jin F, Jiang Y, Liu H (2015) Study of Phospholipids in Single Cells Using an Integrated Microfluidic Device Combined with Matrix-Assisted Laser Desorption/Ionization Mass Spectrometry. *Anal Chem* 87: 7052–7059. doi: [10.1021/acs.analchem.5b00010](https://doi.org/10.1021/acs.analchem.5b00010) PMID: [26110742](https://pubmed.ncbi.nlm.nih.gov/26110742/)

17. Vaňhara P, Kučera L, Prokeš L, Jurečková L, Peña-Méndez EM, Havel J, Hampl A. **Intact cell mass spectrometry as a quality control tool for revealing minute phenotypic changes of cultured human embryonic stem cells.** *Stem Cells Translational Medicine* 2018; **7**(1): 109-114.

Commentary:

Here we report development of novel tool for precise phenotyping and biotyping of stem cell cultures. At present, the quality control of cell cultures is limited by the lack of reliable (epi)genetic or molecular markers or by the focus on a particular type of instability such as karyotype abnormalities or adverse phenotypic traits. Therefore, new sufficiently sensitive and robust techniques that can determine or confirm cell status and reveal potential divergences from the culture optimum. We modeled both intrinsic and extrinsic changes in human embryonic stem cell (hESC) states using different experimental strategies, and addressed the changes in cell status by intact cell mass spectrometry fingerprinting. The analysis of spectral fingerprints by methods routinely used in analytical chemistry, such as principal component analysis and machine learning approaches, clearly distinguished the morphologically and biochemically similar populations of hESCs and provided a biomarker-independent tool for the quality control of cell culture

DOI: 10.1002/sctm.17-0107
Impact factor (WOS, 2017): 4.929
Number of citations (WOS, 2018): not cited yet
Contribution of the author: 1st author. Collection and/or assembly of data, data analysis and interpretation, manuscript writing.

Publication was highlighted and reviewed on STEM CELLS Portal on January 6, 2018

[\(<http://stemcellportal.com>\)](http://stemcellportal.com)



Intact Cell Mass Spectrometry as a Quality Control Tool for Revealing Minute Phenotypic Changes of Cultured Human Embryonic Stem Cells

PETR VAŇHARA ^{a,b} LUKÁŠ KUČERA,^{a,b} LUBOMÍR PROKEŠ,^c LUCIE JUREČKOVÁ,^a
ELADIA MARÍA PEÑA-MÉNDEZ,^d JOSEF HAVEL,^c ALEŠ HAMPL^{a,b}

Key Words. Embryonic stem cells • Cell culture • Differentiation • Technology • Tissue engineering

^aFaculty of Medicine, Department of Histology and Embryology and ^cFaculty of Science, Department of Chemistry, Masaryk University, Brno, Czech Republic; ^bInternational Clinical Research Center, St. Anne's University Hospital, Brno, Czech Republic; ^dDepartamento de Química, Unidad Departamental de Química Analítica, Facultad de Ciencias, Universidad de La Laguna (ULL), Avda. Astrofísico Fco. Sánchez, s/n, 38206 La Laguna, Spain

Correspondence: Aleš Hampl, D.V.M., Ph.D., Faculty of Medicine, Department of Histology and Embryology, Masaryk University, 62500 Brno, Czech Republic. Telephone: +420 549 493 514; e-mail: ahampl@mail.muni.cz

Received April 26, 2017; accepted for publication October 6, 2017; first published December 16, 2017.

<http://dx.doi.org/10.1002/sctm.17-0107>

This is an open access article under the terms of the Creative Commons Attribution-NonCommercial-NoDerivs License, which permits use and distribution in any medium, provided the original work is properly cited, the use is non-commercial and no modifications or adaptations are made.

ABSTRACT

The stability of *in vitro* cell cultures is an important issue for any clinical, bio-industrial, or pharmaceutical use. Embryonic stem cells are pluripotent; consequently, they possess the ability to differentiate into all three germ layers and are inherently prone to respond to differentiation stimuli. However, long-term culture inevitably yields clones that are best adapted to the culture conditions, passaging regimes, or differentiation sensitivity. This cellular plasticity is a major obstacle in the development of bio-industrial or clinical-grade cultures. At present, the quality control of cell cultures is limited by the lack of reliable (epi)genetic or molecular markers or by the focus on a particular type of instability such as karyotype abnormalities or adverse phenotypic traits. Therefore, there is an ongoing need for robust, feasible, and sensitive methods of determining or confirming cell status and for revealing potential divergences from the optimal state. We modeled both intrinsic and extrinsic changes in human embryonic stem cell (hESC) states using different experimental strategies and addressed the changes in cell status by intact cell mass spectrometry fingerprinting. The analysis of spectral fingerprints by methods routinely used in analytical chemistry clearly distinguished the morphologically and biochemically similar populations of hESCs and provided a biomarker-independent tool for the quality control of cell culture. *STEM CELLS TRANSLATIONAL MEDICINE* 2018;7:109–114

SIGNIFICANCE STATEMENT

Safe biomedical applications of cells require predictable and well-defined cell populations. This study describes intact cell mass spectrometry combined with chemometric and artificial intelligence approaches as a simple, robust, and hypothesis-free quality control tool for determining induced and spontaneous alterations in genetically and morphologically uniform embryonic stem cell populations in routine cell cultures.

INTRODUCTION

Cell-based applications are dependent on rigorous conditions including predictable and stable cell populations. Human embryonic stem cells (hESCs) paved the road for the development of state-of-the-art technologies for regenerative medicine and bio-industry applications. Derived from the pluripotent inner cell mass of a pre-implantation blastocyst, hESCs are inherently unstable and prone to rapid, spontaneous differentiation *in vitro*. Current culture protocols are focused on maintaining the pluripotent character of hESCs by repressing their differentiation and supporting sustained self-renewal. In culture, hESCs cumulatively acquire various alterations on both the genetic and non-genetic levels [1] and despite sophisticated culture techniques, culture-adapted clones are inevitably selected during long-term *in vitro* cultures [2].

However, these changes could remain unnoticed until they substantially alter the cell karyotype or cell phenotype, even in case of the stable expression of stemness-associated transcription factors including c-Myc, Sox-2, Klf4, Nanog, or Oct3/4, or their differentiation capacity or typical morphology. Further, molecular, genetic, and/or light-microscopy analyses can fail in the case of the genetically or karyotypically silent changes that arise in cultured cells.

Matrix-assisted laser desorption/ionization time-of-flight mass spectrometry (MALDI-TOF MS) and its derivatives have diverse applications in classic analytical and structural chemistry and, thanks to their universality, have been adapted for analysis and determination of complex biological samples, including bacteria, yeasts, or mammalian cells [3, 4]. For monitoring of cell cultures, two possible approaches for analyzing mass

spectra are available. The “top-down” approach is based on revealing and identifying individual unique peaks and their use as biomarkers that are correlated with phenotypes or cell states, such as pluripotency, reprogramming events, or differentiation cues [5]. However, despite the precise identification of specific biomarkers that could be statistically associated with cell parameters, their applicability is often based on a random correlation among myriads of other dynamically changing molecules in a cell- or culture-dependent context. Also, we have recently documented that using one or two dominant peaks for quantitative analysis of a cell type reveals non-linear relationships that can be easily influenced by the technical or biological variability in the measurement or the sample itself [6]. The alternative approach assumes that a full spectral fingerprint is sufficiently robust to eliminate any undesired variability but contains enough information to discriminate species, cell types, or even cell states differing in chemical composition, even without the identification of individual molecules. Thus, the analysis without a preceding subjective reduction to several major peaks and their identification can eliminate the bias of the random correlation of individual molecules to a phenotypic change or a cell status and avoid potential misinterpretation. Avoiding the fractionation of cells also helps to reduce the unwanted variability while improving the overall consistency of the mass spectra and their reproducibility.

In addition to MS-based quantitative cell line authentication that we reported recently [6], here we demonstrate that the whole mass spectrum acquired from intact hESCs contains sufficient information to provide an unambiguous fingerprint also of a cell state in an otherwise uniform cell population and offers a simple tool for the monitoring and quality control of pluripotent stem cells in culture.

MATERIALS AND METHODS

Cell Culture

Undifferentiated CCTL-14 hESCs (hPSCreg: MUNIe007-A, RRID: CVCL_C860), passage numbers 29, 72, and 269) were maintained in 6-cm Petri dishes (TPP, Trasadingen, Switzerland) on mitotically inactivated mouse embryonic fibroblasts (MEFs) in Dulbecco’s modified Eagle’s medium/F12 supplemented with 15% knockout serum replacement (both from Invitrogen, Life Technologies, Carlsbad, CA), L-glutamine, minimum essential medium, nonessential amino acids, 0.5% penicillin-streptomycin (both from PAA Laboratories, Pasching, Austria), 2-mercaptoethanol (Sigma-Aldrich, Prague, Czech Republic), and 10 ng/ml fibroblast growth factor-2 (PeproTech, Rocky Hill, NJ). The hESCs were maintained in an incubator at 37°C in a humidified atmosphere containing 5% CO₂ and the media was exchanged daily. Retinoic acid was purchased from Sigma-Aldrich (Prague, Czech Republic) and added to the fresh culture medium to the final concentration of 10⁻⁸ M.

Isolation of RNA, Reverse Transcription, and Quantitative PCR

Total RNA from hESCs was extracted using an RNeasy Mini Kit (Qiagen) and quantified using a NanoDrop (Thermo Scientific). cDNA was synthesized from 1 µg DNase I-treated total RNA using a First Strand Reverse Transcription Kit (Roche, Prague, Czech Republic). Relative expression was quantified using exon-spanning primers and UPL probes specific for *SOX2*, *NANOG*, *OCT4*, *PAX6*, *SOX1*, *GATA4*, and *BRACHYURY*. Glyceraldehyde 3-phosphate

dehydrogenase was used as the housekeeping gene control (Roche, Prague, Czech Republic). Results were expressed as relative ratio units. All PCR reactions were performed in triplicate from three independent experiments, and reverse transcriptase-negative and template-negative controls were included.

Immunofluorescent Microscopy

The hESC colonies were manually harvested under visual control, washed in 1× phosphate-buffered saline (PBS), fixed in 4% formaldehyde for 15 minutes, washed three times in 1× PBS, permeabilized in 0.1% Triton-X100 in PBS for 10 minutes/RT, blocked in 3% BSA in PBS for 1 hour. Then, cells were incubated with anti-Sox2 (AB5603, Merck Millipore, Prague, Czech Republic, dilution 1:500) or anti-Oct3/4 (sc-5279, Santa Cruz Biotechnology, Heidelberg, Germany, dilution 1:100) primary antibodies overnight at 4°C. The cells were then washed three times in 1× PBS and incubated for 60 minutes room temperature with secondary antibody conjugated with AlexaFluor 568 (Sox2) or 488 (Oct3/4) and diluted 1:1,000 (Life Technologies/ThermoFisher Scientific, Prague, Czech Republic, A11004 or A11008, respectively), followed by additional wash in 1× PBS. Hoechst 33342 stain was added to the final concentration 5 µg/ml. Images were acquired using an automated microscope with ×10 objective (Image Xpress MicroXL, Molecular Devices).

Flow Cytometry

The hESC colonies were manually harvested under visual control, disaggregated using TryPLE Express (1×) for 2 minutes at 37°C, cells counted and resuspended in FACS buffer (5 mM EDTA, 2% FBS in 1× PBS). Prior staining of intracellular Sox2, cells were fixed using 3.7% formaldehyde in 1× PBS and permeabilized in BD Phosflow Perm Buffer III (BD Biosciences, Prague, Czech Republic). For blocking, 10% mouse serum in 1× PBS was used. Sox2 was stained using anti-Sox2 antibody (Abcam, Cambridge, UK, Ab97959), diluted 1:200 and incubated at 4°C/overnight and anti-rabbit IgG conjugated with Alexa Fluor 488 (Life Technologies/ThermoFisher Scientific, Prague, Czech Republic, A11008).

Sample Preparation for Mass Spectrometry

The hESC colonies were manually harvested under visual control, disaggregated using TryPLE Express (1×) for 2 minutes at 37°C, washed in 1× PBS and cells counted. To eliminate traces of PBS, the cells were centrifuged (200g, 2 minutes) and washed three times in 1 ml of 150 mM ammonium bicarbonate buffer. The cell numbers were determined using a Cedex XS cell counter operated with Cedex Control Center software v. 1.0.3. (Innovatis AG, Roche Life Sciences, Prague, Czech Republic). Finally, the cells were resuspended in 150 mM ammonium bicarbonate buffer to the final concentration of 100 × 10⁶ cells per ml. The cell suspension was then mixed with an acidified matrix containing sinapinic acid (30 mg ml⁻¹) and 2,2,2-trifluoroacetic acid (7.5% vol/vol) in a 2:1 sample to matrix ratio and applied to a target plate that was purified in an ultrasonic bath before spotting the samples.

Mass Spectrometry

The mass spectra were recorded in linear positive ion mode over the 2,000–12,000 m/z range using an AXIMA-CFR mass spectrometer from Shimadzu Biotech (Kratos, U.K.) equipped with a nitrogen laser (337 nm). The time pulse length of the laser was 3 ns. The maximum laser fluency was 60 mJ per pulse. The full laser power was indicated on the instrument as 180 arbitrary units

(a.u.; 6 mW). The irradiated spot size was approximately 150 μm in diameter. An external calibration was performed using standard mixtures of peptides and proteins (ToFMix, PepMix, LaserBio, France) and standard bacterial extracts (BTS standard) from Bruker BioSpin AG (Fällanden, Switzerland).

Processing of Mass Spectra

The spectral data (Supporting Information Figs. S1, S4) were exported using Launchpad software and imported into MATLAB 2014 Student edition from The MathWorks Inc. (Natick, Massachusetts, USA). The mass spectra in the complete data matrix were reduced to a uniform distribution of the 10,000 data points over the 2,000–12,000 m/z range and aligned using the peak alignment by the fast Fourier transform method. The baseline was subtracted, negative values were set to zero, and an average spectrum was calculated. Afterward, the normalization to the area under the curve or to the total ion count was performed.

Statistical Analysis

Pearson's correlation and principal component analysis (PCA) were performed in STATISTICA 12 (StatSoft Inc., Tulsa). For the artificial neural network (ANN) analysis, Trajan Neural Network Simulator, Release 3.0 D 1996–1998 from Trajan Software Ltd. (Durham, U.K.) was used. We constructed an ANN containing four neurons in one hidden layer. The intensities of the processed mass spectra served as the input, whereas the sample categories represented the output. The "learning" of the ANN was performed using the back-propagation training algorithm as previously described [7, 8]. The back-propagation was achieved by iteratively adjusting the values of the connection weights in order to minimize the difference between the ANN calculated output value and the experimental value. The optimal ANN architecture was confirmed by plotting the root mean square of the sum of residuals value against the number of neurons in the hidden layer(s) and the number of training cycles (epochs). The ANN input variables (peaks) were selected upon PCA analysis as the peaks covering more than 95% of the variability in the dataset.

RESULTS

First, we investigated if intact cell MALDI-TOF MS, without any previous sample fractionation or identification of dominant peaks, could discriminate between morphologically uniform, but inherently different hESCs. As a well characterized model, we employed hESC line CCTL-14 cultured on CF-1 MEFs [9]. During long-term culture, CCTL-14 line developed chromosomal abnormalities and also showed increased expression of CD44 and CD30 surface markers (Supporting Information Fig. S2), previously associated with culture adaptation and genomic instability, respectively [10, 11]. In parallel, expression of Sox2, marker associated with undifferentiated phenotype, remained constant (data not shown). To test our hypothesis, low (P29), medium (P72), and high (P269) passage number CCTL-14 hESCs were cultured under identical conditions, harvested 48 hours after seeding, and processed immediately for MS. The final normalized spectral dataset contained 255 m/z values with assigned peak intensities, which were subjected to statistical analyses. Pearson's correlation of the average mass spectra obtained from the low, medium, and high passage hESCs indicated disparities in the spectral fingerprints (Fig. 1A). Using PCA, the correctly clustered P29-hESC and P269-hESC populations were clearly identified, with the p72-hESCs

represented a transition population (Fig. 1B). To exclude potential contribution of MEFs to overall spectral heterogeneity, otherwise identical hESCs were seeded on different MEF batches and had their mass spectra recorded. No significant alterations in their mass spectra were detected due to this manipulation, documenting no distortion due to MEFs (data not shown). Thus, the complex mass spectral fingerprint based on a large number of non-dominant peaks provided sufficient information to discriminate the hidden phenotypes associated with long-term culture adaptation.

Next, we were curious if we could determine shifts in the hESC phenotypes shortly after induction of differentiation. We designed a hESC model using retinoic acid (RA) as a potent inducer of differentiation. It has been well documented in vitro that RA induces the differentiation of hESCs to the ectodermal phenotype, including neural lineages and keratinocytes or extra-embryonic tissues [12–14]. Thus, we picked the RA-driven differentiation model to evaluate the subtle changes that occur in hESC populations during early differentiation. We stimulated the CCTL-14 hESCs with 10^{-8} M RA for a period of 12, 24, or 48 hours (Supporting Information Fig. S3A).

We found that the mass spectra from the RA-treated and control cells were highly correlated and lacked obvious specific peaks that would allow a straightforward search for biomarkers (Fig. 2A). Interestingly, the Pearson's correlation matrix obtained from the average mass spectra revealed a decreased correlation within RA-treated P269-hESCs when compared to RA-treated P29-hESCs and P72-hESCs (Fig. 2B). We then performed the PCA of the control and RA-treated P29-hESCs and compared them with the P269-hESCs. The results revealed that the hESCs without any apparent morphological or molecular alterations were clearly clustered based only on the mass spectral fingerprint (Fig. 2C). Although the cluster analysis only allows for the analysis of an enclosed dataset, we wanted to test whether MS data could be used to predict and correctly categorize an unknown spectral sample. Thus, we constructed and trained a back-propagation ANN [7] based on a reduced dataset containing 23 peak intensities revealed by variable selection approaches (Fig. 2D). Critically, within these time intervals, the hESCs that were induced by RA to differentiate still possessed a typical uniform morphology, maintained high levels of Sox-2, Oct-4, and Nanog, and were completely indistinguishable from the untreated controls. Still, increased level of neuroectodermal determinant Pax6 and downregulation of mesodermal marker Brachyury, as determined by qRT-PCR, clearly spoke for RA-driven entry into differentiation pathway (Fig. 2E, Supporting Information Fig. S3B). The ANN correctly assigned the unknown spectrum to the appropriate sample. On the other hand, using the intensities of only 23 input peaks, the PCA failed to correctly cluster the samples (data not shown). This suggests that non-linear, self-learning approaches are suitable for handling complex data, allowing simple application for the monitoring of routine cultures or for quality control in current good manufacturing practice (CGMP) facilities.

DISCUSSION

The quality of stem cell cultures is an essential prerequisite for applications in which the product variability, lot-to-lot consistency, composition, contamination, or phenotype stability are significant. Here, we present a quality control tool based on the combination of intact cell MS (MALDI-TOF MS) and sophisticated statistical analysis that revealed the hidden variability in hESCs. Current approaches for routine cell identification or characterization use either DNA-based techniques, such as short tandem repeat (STR) profiling or the analysis of the expression of a defined set of

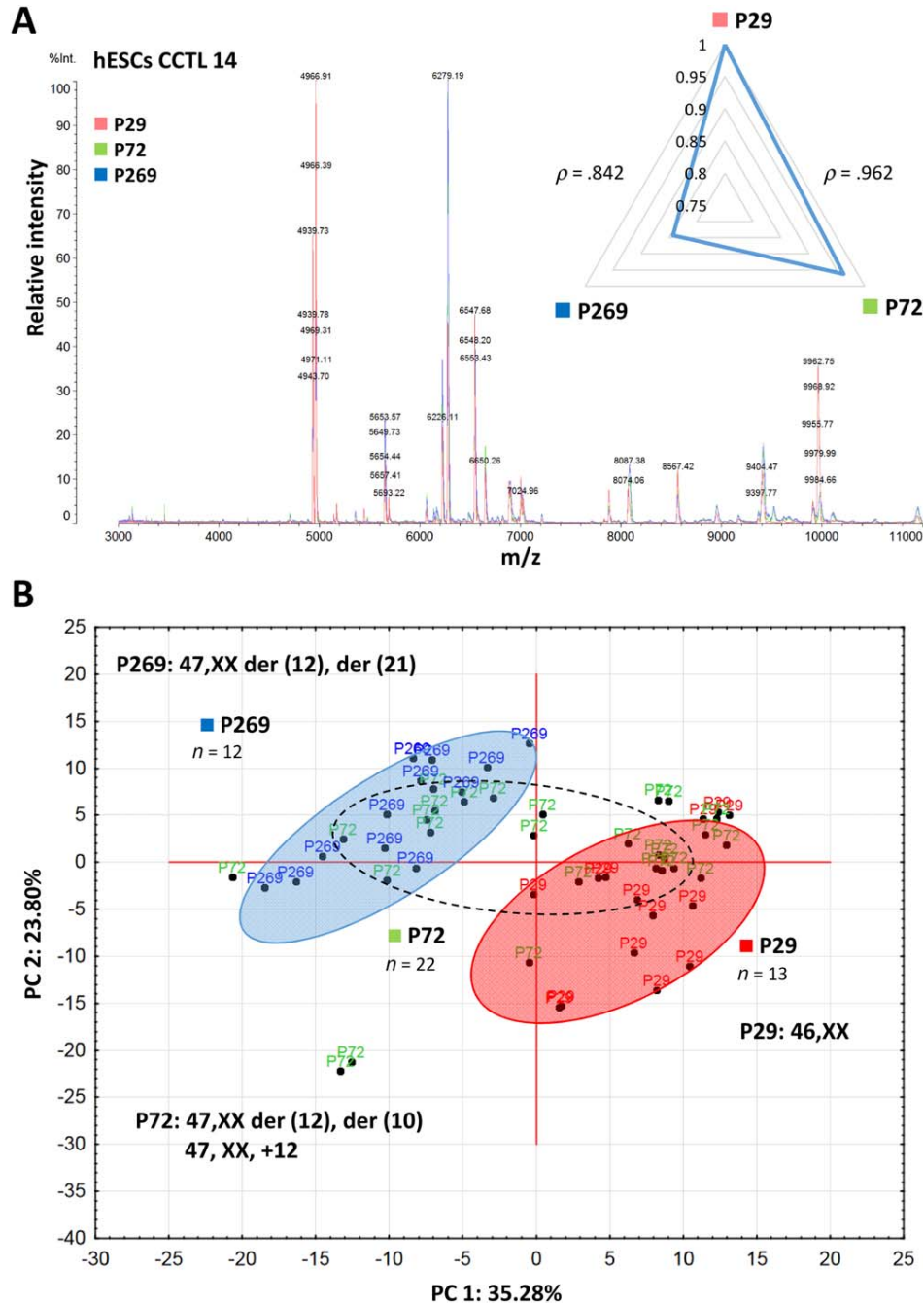


Figure 1. (A): Matrix-assisted laser desorption/ionization time-of-flight mass spectrometry mass spectra obtained from intact hESCs of different passage numbers (P29, P72, and P269). The inset shows the Pearson's correlation of the peak intensities in the average spectra between the P29, P72, and P269 experimental groups. (B): PCA of spectral datasets. Each point in the PCA plot represents a unique biological sample. Abbreviations: hESCs, human embryonic stem cell; PCA, principal component analysis.

marker genes [15], or molecular and functional characterization of phenotype alterations [16]. However, both approaches focus on a limited set of variables (e.g., gene expression or STR profiling), or in theory do not cover unknown or uncharacterized parameters. The identification of individual biomarkers in large, high-dimensional datasets can also be biased by the formulation of an initial hypothesis, the biological background, or the selection of candidate biomarkers, or can be limited to a particular experimental scenario. For instance, a recent comparison of mouse induced

pluripotent cells (miPSCs) and mouse ESCs using high-throughput lectin arrays coupled with surface plasmon resonance imaging revealed specific metabolomic profiles unique to miPSCs and mESCs, indicating differences in the global metabolism of cultured stem cells [17].

Recently, multiple reaction monitoring-mass spectrometry (MRM-MS) was introduced by Baud et al. for the rapid determination and quantitation of pluripotency markers in iPSCs [18]. MRM-MS precisely determined proteotypic peptides generated by

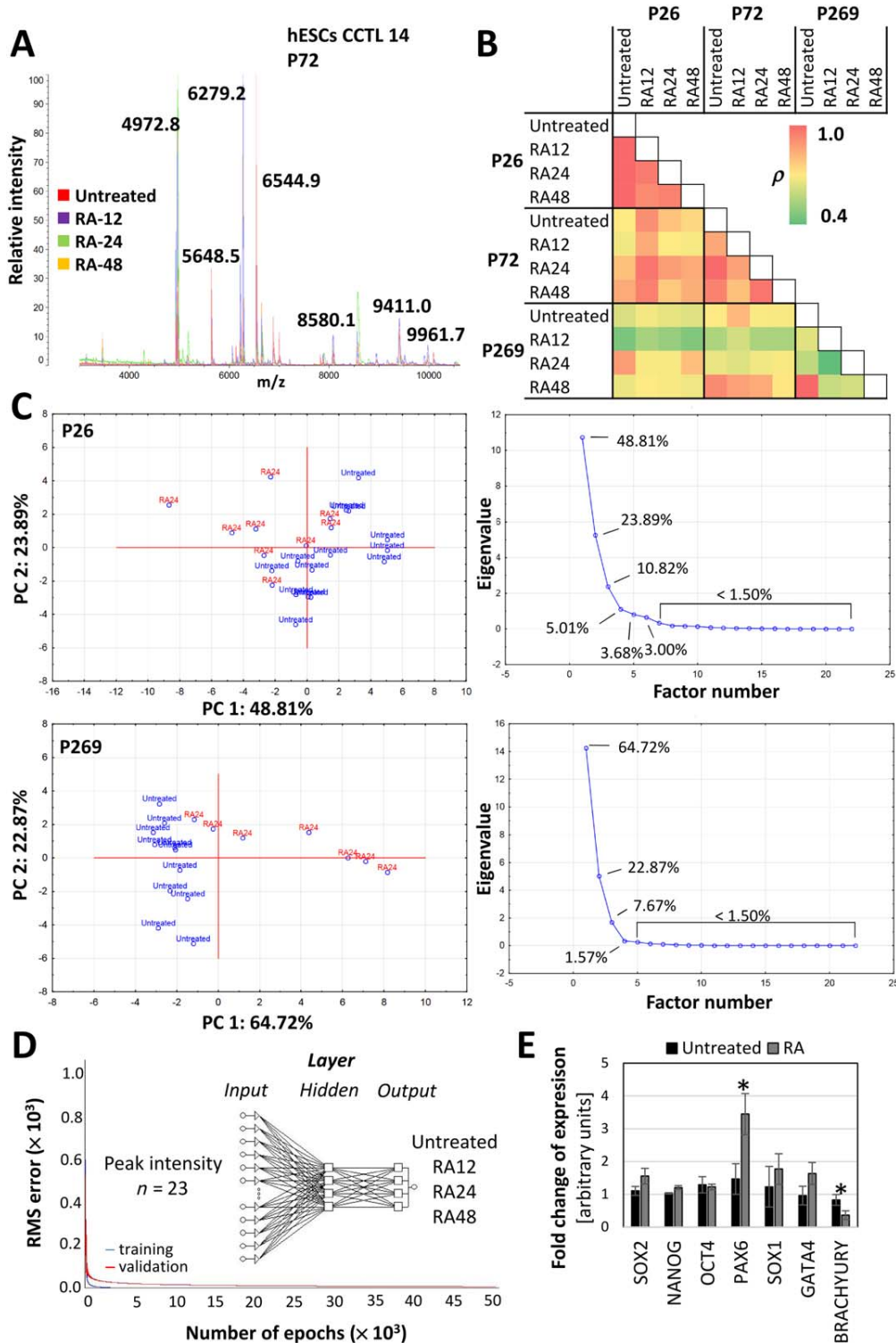


Figure 2. (A): Representative matrix-assisted laser desorption/ionization time-of-flight mass spectrometry mass spectra recorded from intact hESCs (P72) treated with RA for 12, 24, or 48 hours. (B): Heat map depicting the Pearson's correlation matrix of the peak intensities obtained from the average mass spectra. (C): PCA plots of the control and RA-treated P29 or P269 hESCs. Scree plots documenting the contribution of individual factors to the overall variability. (D): Training and leave-one-out verification plots of the RMS versus the number of training cycles (epochs). The first 50,000 iterations are shown. The inset shows the architecture of the artificial neural network used for the prediction of the sample category. (E): Relative normalized expression of stemness (Sox-2, Nanog, Oct-4), neuroectoderm (Pax-6, Sox-1), endoderm (GATA-4), and mesoderm markers (Brachyury) as determined by qRT-PCR. hESCs were cultured with 10^{-8} M RA for 48 hours, or left untreated. The asterisk indicates statistically significant changes in gene expression ($p < .05$). Abbreviations: hESCs, human embryonic stem cell; PC, principal component; PCA, principal component analysis; RA, retinoic acid; RMS, root mean square.

tryptic digestion of 15 marker proteins associated with self-renewal of reprogrammed cells constituting a pluripotency fingerprint. The intact cell MS approach we propose, employs rather a global mass spectrum as the classification input instead of searching for individual biomarkers, and might represent an independent technique that reflects the rational scale of the intrinsic heterogeneity of the cells and is likewise sensitive enough to reveal small changes that are below the detection limits of other techniques. Interestingly, using this technique we visualized the potential phenotypic drifts that occurred during long-term culture that might contribute to the phenomena of culture adaptation [19]. The intact cell MS, followed by the straightforward multivariate analysis, could therefore discriminate unapparent but critical alterations in stem/progenitor cells that are not detected by other techniques, which has clear application for quality control in routine cell cultures or CGMP.

CONCLUSION

In summary, we introduced a simple, robust, and hypothesis-free quality control tool for determining induced and spontaneous alterations in genetically and morphologically uniform embryonic stem cell populations in routine cell cultures.

ACKNOWLEDGMENTS

This study was supported by the Grant Agency of the Czech Republic (GA15-11707S), the Grant Agency of Masaryk

University [MUNI/A/1369/2016], the project COST CZ LD15144 by MEYS CR, the National Program of Sustainability II (project no. LQ1605, MEYS CR), and by funds from the Faculty of Medicine MU to junior researcher (P.V.).

AUTHOR CONTRIBUTIONS

P.V.: conception and design, collection and/or assembly of data, data analysis and interpretation, manuscript writing; L.K. and L.J.: collection and/or assembly of data; L.P. and E.M.P.-M.: data analysis and interpretation; J.H. and A.H.: conception and design, data analysis and interpretation, financial support, final approval of manuscript.

DISCLOSURE OF POTENTIAL CONFLICTS OF INTEREST

The authors indicated no potential conflicts of interest.

NOTE ADDED IN PROOF

This article was published online on 16 December 2017. Minor edits have been made that do not affect data. This notice is included in the online and print versions to indicate that both have been corrected 28 December 2017.

REFERENCES

- 1 Amps K, Andrews PW, Anyfantis G et al. Screening ethnically diverse human embryonic stem cells identifies a chromosome 20 minimal amplicon conferring growth advantage. *Nat Biotechnol* 2011;29:1132–U1113.
- 2 Canham MA, Sharov AA, Ko MS et al. Functional heterogeneity of embryonic stem cells revealed through translational amplification of an early endodermal transcript. *PLoS Biol* 2010;8:e1000379.
- 3 Croxatto A, Prod'hom G, Greub G. Applications of MALDI-TOF mass spectrometry in clinical diagnostic microbiology. *FEMS Microbiol Rev* 2012;36:380–407.
- 4 Munteanu B, von Reitzenstein C, Hansch GM et al. Sensitive, robust and automated protein analysis of cell differentiation and of primary human blood cells by intact cell MALDI mass spectrometry biotyping. *Anal Bioanal Chem* 2012;404:2277–2286.
- 5 Frisz JF, Choi JS, Wilson RL et al. Identifying differentiation stage of individual primary hematopoietic cells from mouse bone marrow by multivariate analysis of TOF-secondary ion mass spectrometry data. *Anal Chem* 2012;84:4307–4313.
- 6 Valletta E, Kučera L, Prokeš L et al. Multivariate calibration approach for quantitative determination of cell-line cross contamination by intact cell mass spectrometry and artificial neural networks. *PLoS One* 2016;11:e0147414.
- 7 Amato F, Lopez A, Pena-Mendez EM et al. Artificial neural networks in medical diagnosis. *J Appl Biomed* 2013;11:47–58.
- 8 Houska J, Pena-Mendez EM, Hernandez-Fernaund JR et al. Tissue profiling by nanogold-mediated mass spectrometry and artificial neural networks in the mouse model of human primary hyperoxaluria 1. *J Appl Biomed* 2014;12:119–125.
- 9 International Stem Cell Initiative. Characterization of human embryonic stem cell lines by the International Stem Cell Initiative. *Nat Biotechnol* 2007;25:803–816.
- 10 Harrison NJ, Barnes J, Jones M et al. CD30 expression reveals that culture adaptation of human embryonic stem cells can occur through differing routes. *STEM CELLS* 2009;27:1057–1065.
- 11 Nguyen HT, Geens M, Spits C. Genetic and epigenetic instability in human pluripotent stem cells. *Hum Reprod Update* 2013;19:187–205.
- 12 Baharvand H, Mehrjardi NZ, Hatami M et al. Neural differentiation from human embryonic stem cells in a defined adherent culture condition. *Int J Dev Biol* 2007;51:371–378.
- 13 Jagtap S, Meganathan K, Wagh V et al. All-trans retinoic acid and basic fibroblast growth factor synergistically direct pluripotent human embryonic stem cells to extraembryonic lineages. *Stem Cell Res* 2013;10:228–240.
- 14 Metallo CM, Ji L, De Pablo JJ et al. Retinoic acid and bone morphogenetic protein signaling synergize to efficiently direct epithelial differentiation of human embryonic stem cells. *STEM CELLS* 2008;26:372–380.
- 15 Masters JR, Thomson JA, Daly-Burns B et al. Short tandem repeat profiling provides an international reference standard for human cell lines. *Proc Natl Acad Sci USA* 2001;98:8012–8017.
- 16 Irelan JT, Wu MJ, Morgan J et al. Rapid and quantitative assessment of cell quality, identity, and functionality for cell-based assays using real-time cellular analysis. *J Biomol Screen* 2011;16:313–322.
- 17 Nand A, Singh V, Wang PZ et al. Glycoprotein profiling of stem cells using lectin microarray based on surface plasmon resonance imaging. *Anal Biochem* 2014;465:114–120.
- 18 Baud A, Wessely F, Mazzacuva F et al. Multiplex high-throughput targeted proteomic assay to identify induced pluripotent stem cells. *Anal Chem* 2017;89:2440–2448.
- 19 Harrison NJ, Baker D, Andrews PW. The significance of culture adaptation of embryonic stem cells for regenerative medicine. In: Baharvand H, Aghdami N, eds. *Advances in Stem Cell Research*. 1st ed. Totowa, NJ: Humana Press, 2012:398.



See www.StemCellsTM.com for supporting information available online.

18. Porokh V, Vaňhara P, Bárta T, Jurečková L, Bohačiaková D, Pospíšilová V, Mináriková D, Holubcová Z, Pelková V, Souček K, Hampl A. **Soluble Cripto-1 induces accumulation of supernumerary centrosomes and formation of aberrant mitoses in human embryonic stem cells.** *Stem Cells and Development* 2018; **27**(16): 1077-1084. doi: 10.1089/scd.2018.0017.

Commentary:

Here we report the molecular mechanism of centrosomal instability induced by protein Cripto-1 in human embryonic stem cells. Aberrant numbers of centrosomes in pristine hESCs were reported previously and represented a risk factor for development of abnormalities in chromosomal numbers due to multicentrosomal mitotic divisions. We have also documented previously that this phenomenon diminished with prolonged time in culture and with induction of differentiation, and it is strongly affected by the culture microenvironment, especially cues coming from the culture substratum. In this work, we report for the first time that Cripto-1 protein (or teratocarcinoma-derived growth factor 1, epidermal growth factor-CFC, EGF-CFC) is produced by hESC and represents a molecular factor capable of inducing frequency of supernumerary centrosomes in cultured hESC. Downregulation of Cripto-1 signaling by chemical inhibitors restored the normal number of centrosomes in hESC. Knowledge of the secretory phenotype of hESC under various culture conditions or associated with a particular cell state contribute to improved cell culture protocols for clinical grade cultures of hESC, pharmacology or bioindustry, as well for understanding early events of embryonic development.

DOI: 10.1089/scd.2018.0017

Impact factor (WOS, 2017): 3.315

Number of citations (WOS, 2018): not cited yet

Contribution of the author: 1st co-author. Collection and/or assembly of data, data analysis and interpretation, manuscript writing.

Publication was selected to be highlighted on Journal cover page.

Soluble Cripto-1 Induces Accumulation of Supernumerary Centrosomes and Formation of Aberrant Mitoses in Human Embryonic Stem Cells

Volodymyr Porokh,^{1,*} Petr Vaňhara,^{1,2,*} Tomáš Bárta,¹ Lucie Jurečková,¹ Dáša Boháčiková,¹
Veronika Pospíšilová,¹ Daniela Mináriková,¹ Zuzana Holubcová,¹ Vendula Pelková,¹
Karel Souček,^{2,3} and Aleš Hampel^{1,2}

Chromosomal instability evoked by abnormalities in centrosome numbers has been traditionally considered as a hallmark of aberrant, typically cancerous or senescent cells. We have reported previously that pristine human embryonic stem cells (hESC) suffer from high frequency of supernumerary centrosomes and hence may be prone to undergo abnormal mitotic divisions. We have also unraveled that this phenomenon of multi-centrosomal mitoses vanishes with prolonged time in culture and with initiation of differentiation, and it is strongly affected by the culture substratum. In this study, we report for the first time that Cripto-1 protein (teratocarcinoma-derived growth factor 1, epidermal growth factor-Cripto/FRL-1/Cryptic) produced by hESC represents a factor capable of inducing formation of supernumerary centrosomes in cultured hESC. Elimination of Cripto-1 signaling on the other hand restores the normal number of centrosomes in hESC. Linking the secretory phenotype of hESC to the centrosomal metabolism may help to develop better strategies for propagation of stable and safe bioindustrial and clinical grade cultures of hESC. From a broader point of view, it may lead to unravelling Cripto-1 as a micro-environmental factor contributing to adverse cell behaviors in vivo.

Keywords: embryonic stem cells, centrosomes, multipolar mitoses, Cripto-1, culture adaptation

Introduction

HUMAN EMBRYONIC STEM CELLS (hESC) are self-renewing pluripotent cells that originate from ephemeral cells constituting the embryoblast of the human blastocyst. Although hESC can be indefinitely propagated in culture without losing their defining properties, they still suffer from various forms of cell stress affecting their pristine phenotype. A likely reason is an absence of unique embryoblast micro-environment that inevitably results in a disturbance of fine regulatory networks normally coordinating cell behaviors. In accordance with this fact, culture propagation of hESC often leads to harboring of structural and numerical chromosomal abnormalities, such as aneuploidy or chromatin rearrangements [1]; expression of atypical surface markers, such as CD30 [2]; and/or acquisition of a phenotype best adapted to in vitro conditions [3].

We have previously reported the unusually high incidence of supernumerary centrosomes in pristine early passage hESC, which may represent a risk factor contributing to

chromosomal instability [4]. Frequency of mitoses with supernumerary centrosomes decreased in culture-adapted hESC and/or after induction of differentiation, and it was also strongly affected by culture substratum. Our findings suggested that increased number of centrosomes is an inherent hallmark of pristine hESC restricted to their pluripotent state, as documented on several independent hESC lines. Gu et al. [5] also reported supernumerary centrosomes in developing human zygotes, early embryos, and hESC; however, the mechanism that drives over-amplification of centrosomes remains unexplained.

Centrosomes are small unbound organelles that provide cells with two microtubule organizing centers (MTOC), typically during assembly of the bipolar mitotic spindle. Deregulation of centrosome numbers may thus produce abnormal spindle, leading to unequal distribution of chromosomes during mitosis, and finally to structural or numerical abnormalities of chromosomes. Abnormalities in centrosome number or structure are linked to various pathological states, including cancer, ciliopathies, and developmental disorders

¹Department of Histology and Embryology, Faculty of Medicine, Masaryk University, Brno, Czech Republic.

²Center of Biomolecular and Cellular Engineering (CBCE), International Clinical Research Center, St. Anne's University Hospital, Brno, Czech Republic.

³Department of Cytokinetics, Institute of Biophysics of the Czech Academy of Sciences, Brno, Czech Republic.

*These authors contributed equally to this work.

[6]. Generally, supernumerary centrosomes may develop by: (1) inordinate cycles of centrosomal duplication, (2) failure of cytokinesis but not karyokinesis, (3) disintegration of centriolar pair and breaking up of the centrosome, or (4) development of foci of pericentriolar matrix (PCM), providing the cell surrogate MTOC [6].

We have shown in our initial study that in hESC, high frequency of supernumerary centrosomes was not associated with detectable structural defects to centrioles and/or PCM [4]. Also, on average, 40% of cells with supernumerary centrosomes contained the proper number of kinetochores documenting euploidy of such cells [4]. Rather, activities of cell cycle regulators CDK2 and Aurora A were linked to the over-amplification of centrosomes. In hESC, cell cycle regulating machinery undergoes changes as the cells adapt to culture conditions (reviewed in Ref. [7]), and these changes may possibly imprint into regulation of centrosomal cycle. Still, this is only hypothetical since no specific molecules or circuitries involved in development of supernumerary centrosomes in hESC were unraveled.

In this study, we searched for factors that are responsible for induction of the multicentrosomal phenotype observed in hESC. We found that hESC secrete Cripto-1 protein, with low-passage cells producing more Cripto-1 than high-passage cells. Inhibition of Cripto-1 signaling either by blocking antibody or by chemical disruption significantly decreased frequency of supernumerary centrosomes in hESC. Taken together, we revealed Cripto-1 as the candidate factor affecting genomic stability of cultured hESC.

Materials and Methods

Cell lines, cell culture, and treatments

Two independent lines of hESC, both derived in our laboratory, were used: (1) well established line CCTL14 (hPSCreg: MUNIe007-A, RRID: CVCL_C860 [8]) and (2) newly derived line MUES1 (registered under no. 23 by Ministry of Education, Youth and Sport of the Czech Republic, MSMT-15983/2017-3, June 6, 2017). The Faculty of Medicine of Masaryk University and its Department of Histology and Embryology are fully accredited for experimenting with hESC (No. MSMT-14648/2016-5). The cells were maintained undifferentiated by culturing in 6-cm Petri dishes (TPP, Trasadingen, Switzerland) on mitotically inactivated mouse embryonic fibroblasts (MEFs) in Dulbecco's modified Eagle's medium/F12 supplemented with 15% KnockOut Serum Replacement (Invitrogen, Life Technologies, Carlsbad, CA), 1% L-glutamine, 1% minimum essential medium (MEM) nonessential amino acids, 0.5% penicillin-streptomycin (all from Invitrogen, Life Technologies), 100 μ M β -mercaptoethanol (Sigma-Aldrich, Prague, Czech Republic) and 4 ng/mL fibroblast growth factor (FGF)-2 (PeproTech, Rocky Hill, NJ).

Cells were maintained in an incubator at 37°C in a humidified atmosphere containing 5% CO₂ and the media was exchanged daily. Recombinant human Cripto-1 (R&D Systems, Minneapolis, MN; cat. no. 145-CR) was reconstituted at 10 μ g/mL in sterile phosphate buffered saline (PBS) containing 0.1% bovine serum albumin and added directly to the culture media at the final concentration of 100 ng/mL. Anti-Cripto-1 polyclonal antibody at the final concentration of

10 μ g/mL (Novus Biologicals, Littleton, CO; cat. no. NB100-1598) and alantolactone at the final concentration of 5 μ M (Sigma-Aldrich; cat. no. SML0415), respectively, were added directly to the culture media.

Specificity of Cripto-1 protein and anti-Cripto-1 antibody was validated by treatment of hESC with different concentrations of Cripto-1 (Supplementary Fig. S1A; Supplementary Data are available online at www.liebertpub.com/scd), and by neutralization of Cripto-1 by anti-Cripto-1 antibody for 30 min. at 37°C in vitro before adding to culture medium, respectively (Supplementary Fig. S1B). The Aurora A chemical inhibitor, MLN8054 (Selleckchem, Munich, Germany; cat. no. S1100), and the CDK2 inhibitor olomoucine II (provided by Dr. Miroslav Strnad, Palacký University Olomouc, Olomouc, Czech Republic), were prepared as 1,000 \times stocks in dimethyl sulfoxide (DMSO) and were directly added to the culture media at the final concentration 1 μ M, with DMSO (0.1%) serving as vehicle control.

Indirect immunofluorescence and microscopy

For assessing centrosome numbers, hESC were cultured on MEF feeders on ibidi μ Dish (ibidi GmbH, Martinsried, Germany; cat. no. 81156) coated with 0.1% gelatin (Sigma-Aldrich; cat. no. G1890). For immunofluorescence, hESC were fixed with 4% paraformaldehyde at room temperature for 10 min and then they were permeabilized with PBS/Triton 0.1% solution for 5 min. Then the cells were incubated overnight at 4°C with a rabbit polyclonal antibody against human pericentrin (Abcam, Cambridge, UK; cat. no. A11008) diluted 1:10,000 in PBS/Tween 0.05% pH 7.4. Finally, they were incubated for 1 h at room temperature with goat anti-rabbit secondary antibody conjugated with AlexaFluor 488 (ThermoFisher Scientific, Rockford, IL; cat. no. A-11034) diluted 1:1,000 in PBS pH 7.4. Cell nuclei were counterstained with 2-(4-amidinophenyl)-1H-indole-6-carboxamide (DAPI; Sigma-Aldrich). Cells were then mounted in Mowiol (Sigma-Aldrich). Images were acquired using Olympus FluoView 500 laser scanning microscope (Olympus C&S Ltd., Prague, Czech Republic) with a 60 \times objective. Sequential excitation at 488 and 405 nm was provided by argon gas laser and laser diode, respectively.

Isolation of RNA, reverse transcription, and quantitative PCR

Total RNA was isolated from hESC using an RNeasy Mini Kit (Qiagen, Germany; cat. no. 74106) and quantified using a NanoDrop (Thermo Scientific). Complementary DNA was synthesized from 1 μ g DNase I-treated total RNA using a First Strand Reverse Transcription Kit (Roche, Basel, Switzerland). Relative expression of *CRIPTO-1* gene was quantified using exon-spanning primers (forward: CTT CAGAGATGACAGCATTGG, reverse: CAGCAGGTTC TGTTTAGCTCCT) and UPL probe no. 79 (Roche, Prague, Czech Republic). Glyceraldehyde 3-phosphate dehydrogenase (*GAPDH*) was used as the housekeeping gene control (forward: CCCCAGTTTCTATAAATTGAGC, reverse: CACCTTCCCCATGGTGTCT, UPL probe no. 63). Results were expressed as normalized relative ratio units. All PCR reactions were performed in triplicate from three independent experiments, and reverse transcriptase-negative and template-negative controls were included.

Flow cytometry

Colonies of hESC were manually harvested under visual control and disaggregated using TryPLE™ Express (1×) for 2 min at 37°C. The cells were then counted and resuspended in fluorescent activated cell sorting (FACS) buffer (0.5 mM ethylenediaminetetraacetic acid, 0.5% fetal bovine serum in PBS pH 7.4). To detect Cripto-1, 500×10^3 cells were incubated for 30 min at 4°C with anti-Cripto-1 antibody (Novus Biologicals; cat. no. NB100-1589) diluted 1:500 in FACS buffer. After washing twice in FACS buffer, the cells were incubated for 30 min at 4°C with anti-rabbit secondary immunoglobulin G conjugated with Alexa Fluor 488 (Life Technologies/ThermoFisher Scientific, Prague, Czech Republic; cat. no. A11008) diluted 1:100 in FACS buffer. After washing twice in FACS buffer, the cells were measured using BD FACSCanto II (BD Biosciences) with negative control included. Fluorescence data were analyzed using FlowJo X (FlowJo, LLC, Ashland, OR) and the expression expressed as median fluorescence intensity relative to a negative control.

Immunoaffinity analysis of cytokines in conditioned medium

The presence and quantity of cytokines and chemokines secreted by hESC into culture media were determined using a membrane-based sandwich immunoassay (Proteome Profiler Human XL Cytokine Array Kit; Bio-Techne R&D Systems, Prague, Czech Republic; cat. no. ARY022B) according to manufacturer's instructions. Briefly, culture media conditioned for 24 h were collected from cells of high and low passage, filtered through 0.22 μ m low protein binding filter (TPP; cat. no. #99722), concentrated using Amicon Ultra-4 Centrifugal Filter with 10 kDa cutoff (Merck, Darmstadt, Germany; cat. no. UFC801096), diluted to total protein concentration 30 mg/mL, and analyzed by the given immunoassay. Chemiluminescent signals were recorded on film, scanned and analyzed using ImageJ software [9].

Quantification of Cripto-1 by enzyme-linked immunosorbent assay

Culture media conditioned for 24 h were collected as described above for immunoaffinity analysis of cytokines. Cripto-1 protein was then quantified using Human Cripto-1 DuoSet ELISA (enzyme-linked immunosorbent assay) (R&D Systems; cat. no. DY145) according to manufacturer's instruction.

Statistical analysis

Where applicable, data were analyzed using Student's *t*-test.

Results and Discussion

Previously, we have shown on a large sample of independent lines of hESC (12 lines in total) that in vitro cultured hESC suffer from increased centrosome numbers and develop aberrant multipolar mitoses [4]. Interestingly, prolonged passaging of hESC, entry into differentiation, "improved" culture substratum, and downregulation of CDK2 and Aurora A, all have led to cessation of these centrosome over-amplifications, indicating nonrandom basis of such abnormal centrosome behavior.

Here we have accomplished a series of experiments aimed at unravelling the molecular mechanisms underlying these phenomena. We have built on the well-characterized line of hESC-CCTL-14 that we also used in our original study by Holubcova et al. [4]. In the current study, the cells in passage P21-60 represented low-passage cells, while the cells in passage P280-310 represented high-passage cells. As shown in Figure 1, cultured hESC followed the scenario described by Holubcova et al. [4] and produced supernumerary centrosomes (with multipolar mitoses) as determined by visualization of centrosomal protein pericentrin. Also, as expected, the frequency of mitoses with supernumerary centrosomes was higher in low-passage cells (~11.4%) and lower in high-passage cells (~5.4%). Based on these findings we were confident about the functionality of the cellular system to be used here.

First, we tested whether some soluble factor, differently produced by low- and high-passage hESC, may contribute to deregulation of numbers of centrosomes. To address this question, we simply exposed, for 24 h, low-passage hESC to media conditioned by high-passage hESC and *vice versa* and then determined the number of centrosomes by standard pericentrin staining (schematized in Fig. 2A). As shown in Figure 2B, while adding high-passage conditioned media to low-passage hESC did not cause significant change in the frequency of multicentrosomal mitoses, adding low-passage conditioned media to the high-passage hESC dramatically increased the frequency of multicentrosomal mitoses to almost the level typical for low-passage cells. This finding indicated that low-passage hESC produce in the media some

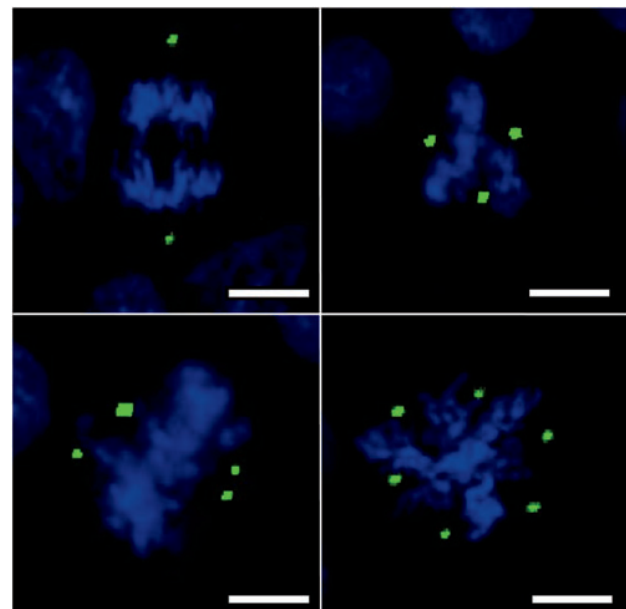


FIG. 1. Examples of hESC (CCTL14 line of hESC) with normal (two) and supernumerary centrosomes (three, four, six), as observed at metaphase. Chromatin was stained with DAPI (blue) and centrosomes were labeled with anti-pericentrin antibody (green). Scale bar 150 μ m. DAPI, 2-(4-amidinophenyl)-1H-indole-6-carboxamide; hESC, human embryonic stem cell. Color images available online at www.liebertpub.com/scd

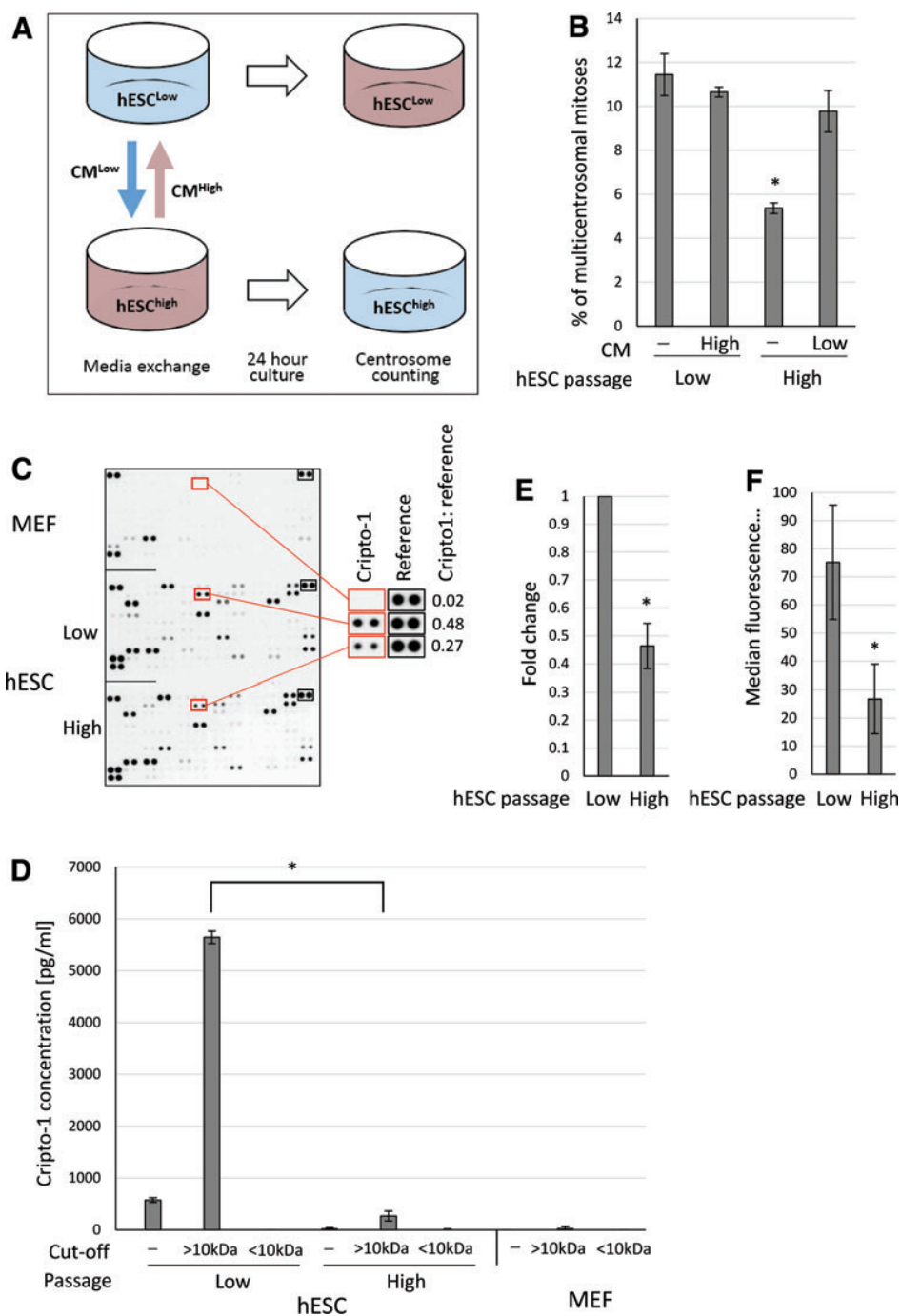


FIG. 2. (A) Schematic showing the experimental design for testing the effect of media conditioned by low- and high-passage hESC on the frequency of multicentrosomal mitoses. (B) The effect of CM harvested from low- and high-passage hESC on the percentage of multicentrosomal mitoses. Low-passage hESC were exposed for 24 h to high-passage CM and vice versa. The numbers of centrosomes were counted as visualized by anti-pericentrin antibody. Data are expressed as mean \pm SD. * $P < 0.05$. (C) Expression of signaling molecules in conditioned media collected from low- and high-passage hESC, as determined by Proteome Profiler™ immunoaffinity array. Media collected from only MEF is included for comparison. Red rectangles indicate spots representing Cripto-1. Density of Cripto-1 spots are normalized to the reference spot. The array is representative to two independent experiments. (D) The quantity of Cripto-1 protein in media conditioned by low- and high-passage hESC. Both complete and concentrated media were measured. Media collected from only MEF are included for comparison. Data are expressed as mean \pm SD. * $P < 0.05$. (E) Expression of *CRIPTO-1* mRNA in low- and high-passage hESC as determined by quantitative real-time PCR. Expression of Cripto-1 was normalized to GAPDH. Data are expressed as mean \pm SD. Asterisk indicates statistical significance at $P < 0.05$. (F) Expression of Cripto-1 protein in low- and high-passage hESC as determined by flow cytometry. Data are expressed as the mean \pm SD. * $P < 0.05$. CM, conditioned media; GAPDH, glyceraldehyde 3-phosphate dehydrogenase; MEF, mouse embryonic fibroblast; mRNA, messenger RNA; SD, standard deviation. Color images available online at www.liebertpub.com/scd

soluble factor that contributes to deregulation of centrosome numbers. To identify this factor (or factors) we started by fractionating the culture media collected from low-passage hESC using columns with cutoffs of 5 and 50 kDa, which separated the media into three molecular weight (MW) fractions: (1) MW <5 kDa, (2) MW 5–50 kDa, (3) MW >50 kDa. Importantly, from all these three media fractions, only the second fraction containing molecules with MW ranging from 5 to 50 kDa produced significant increase in the frequency of multicentrosomal mitoses when applied onto high-passage hESC (data not shown). This effect was similar to that of relevant complete conditioned media and suggested that molecule(s) of a protein nature, rather than low mass compound(s), are responsible for the centrosome over-amplification.

The above-described findings draw our attention to cytokines and chemokines; therefore, we applied commercially available immunoassay to screen for the presence and quantity of 102 different signaling molecules. For such screening we have used “active fraction” (MW 5–50 kDa) prepared from conditioned media harvested from both low- and high-passage hESC. The media harvested from only feeder cells (MEF) was used to discriminate between hESC-specific and MEF-specific molecules. As shown in Figure 2C and Supplementary Table S1, out of 120 molecules assayed, 18 molecules that were specifically produced by hESC (and not by MEF) were produced at higher levels by low-passage hESC, and 7 molecules were produced at higher levels by high-passage hESC. Among these molecules, there were some offering tangible logic for their involvement in modulation of centrosomal metabolism.

We have focused our attention to Cripto-1 that is linked by multiple means to processes taking place in early development [10]. To confirm and more precisely determine the levels of Cripto-1 in culture media, we applied ELISA on complete (unfractionated) media and also on media concentrates, which we obtained using spin columns with 10 kDa cutoff. Measurements on both complete media and their concentrated counterparts documented over 10-fold higher levels of soluble Cripto-1 in “low-passage conditioned media” compared with “high-passage conditioned media” (Fig. 2D). We have also used quantitative real-time PCR and flow cytometry to confirm the decrease of Cripto-1 production that takes place during prolonged culture of hESC. As shown in Figure 2E and F, both *CRIPTO-1* messenger RNA (mRNA) and Cripto-1 protein become downregulated by at least two-fold in high-passage hESC compared with their low-passage counterparts.

To further investigate the link between Cripto-1 and occurrence of supernumerary centrosomes, we have increased and decreased Cripto-1 signaling by recombinant Cripto-1 protein and by anti-Cripto-1 blocking antibody, respectively, with each one being separately added to both low- and high-passage hESC. In accordance with our hypothesis, increased Cripto-1 signaling resulted in a dramatically increased percentage of multicentrosomal mitoses (Fig. 3A). Specifically, this increase was about 1.6-fold in low-passage hESC and about 2.0-fold in high-passage hESC. Correspondingly, inhibition of Cripto-1 signaling decreased the percentage of multicentrosomal mitoses by about 1.5-fold in low-passage hESC. No significant decrease was observed in high-passage hESC, most likely because these cells already

reached the basal level of multicentrosomal mitoses typical for this hESC line. Still, when the multicentrosomal mitoses were induced in high-passage hESC by conditioned media harvested from low-passage hESC, then such increase could be eliminated by blocking of Cripto-1 (Fig. 3A). This finding further points to Cripto-1 as the molecule that is responsible for centrosome over-amplification in hESC.

We have demonstrated in our previous study [4] that chemical inhibition of activities of Aurora A and CDK2, which are typically high in pristine hESC, decreases the frequency of supernumerary centrosomes. Here, we observed analogous suppression of multicentrosomal mitoses by inhibitor of Aurora A (MLN8059) and CDK2 (olomoucine II), respectively, in hESC that were driven to produce supernumerary centrosomes by their exposure to Cripto-1 protein (Fig. 3B). This finding, applicable to both low- and high-passage hESC, further strengthens a functional relevance of centrosomal amplifications induced in hESC by recombinant Cripto-1.

Cripto-1 is known to interact with activin receptor type IIA [11]. This interaction, and possibly also interaction of Cripto-1 with other major canonical signaling pathways (Nodal, Notch, Wnt/ β -catenin), can be disrupted by alantolactone [12]. When hESC were here exposed to this chemical, in case of low-passage hESC but not high passage hESC, it has led to a dramatic dose-dependent decrease of the percentage of multicentrosomal mitoses (Fig. 3C). We attempted to support the role of transforming growth factor- β signaling in this phenomenon by demonstrating changes to phosphorylation status of downstream molecules, but we did not find any substantial changes to Smad2/3, PI3K p110 gamma, PI3K p110 alpha, PI3K beta, PI3K p85, and p-AKT, respectively (data not shown). Still, although at this stage we were not able to position Cripto-1 into defined a signaling pathway, the effects of alantolactone has further supported the notion that Cripto-1 signaling is essential for development of a multicentrosomal phenotype.

All of the experiments described above were accomplished on the CCTL14 line of hESC that is being routinely used in our lab as the gold standard, mainly because of its detailed characterization in the worldwide comparative studies [1,8]. Still, to exclude cell line-specific bias, we have confirmed the validity of the data on low-passage cells (P35) using newly a established line of hESC–MUES1. As shown in Figure 4A, the given hESC produced high quantities of Cripto-1 protein in culture media, similar to that produced by the low-passage hESC of CCTL14 line (see Fig. 2D for comparison). Furthermore, these cells produced supernumerary centrosomes with a frequency of about 5% that became (1) significantly increased by recombinant Cripto-1 protein and (2) reduced by antibody- and alantolactone-mediated blocking of Cripto-1 signaling to 1% and 2%, respectively (Fig. 4B).

Cripto-1, a member of the epidermal growth factor-cripto-1-FRL-1-cryptic family of cytokines, functions in early embryonic development by mediating major signaling pathways that are involved in maintenance of pluripotency and stem-like phenotype, as well as in driving differentiation to principal germ layers [13,14]. Cripto-1 was reported as a noncompetitive activin antagonist [15], interacting with activin type II (ActRII and ActRIIB) and type I (ALK4) receptors. Moreover, Cripto-1 is capable of interacting with

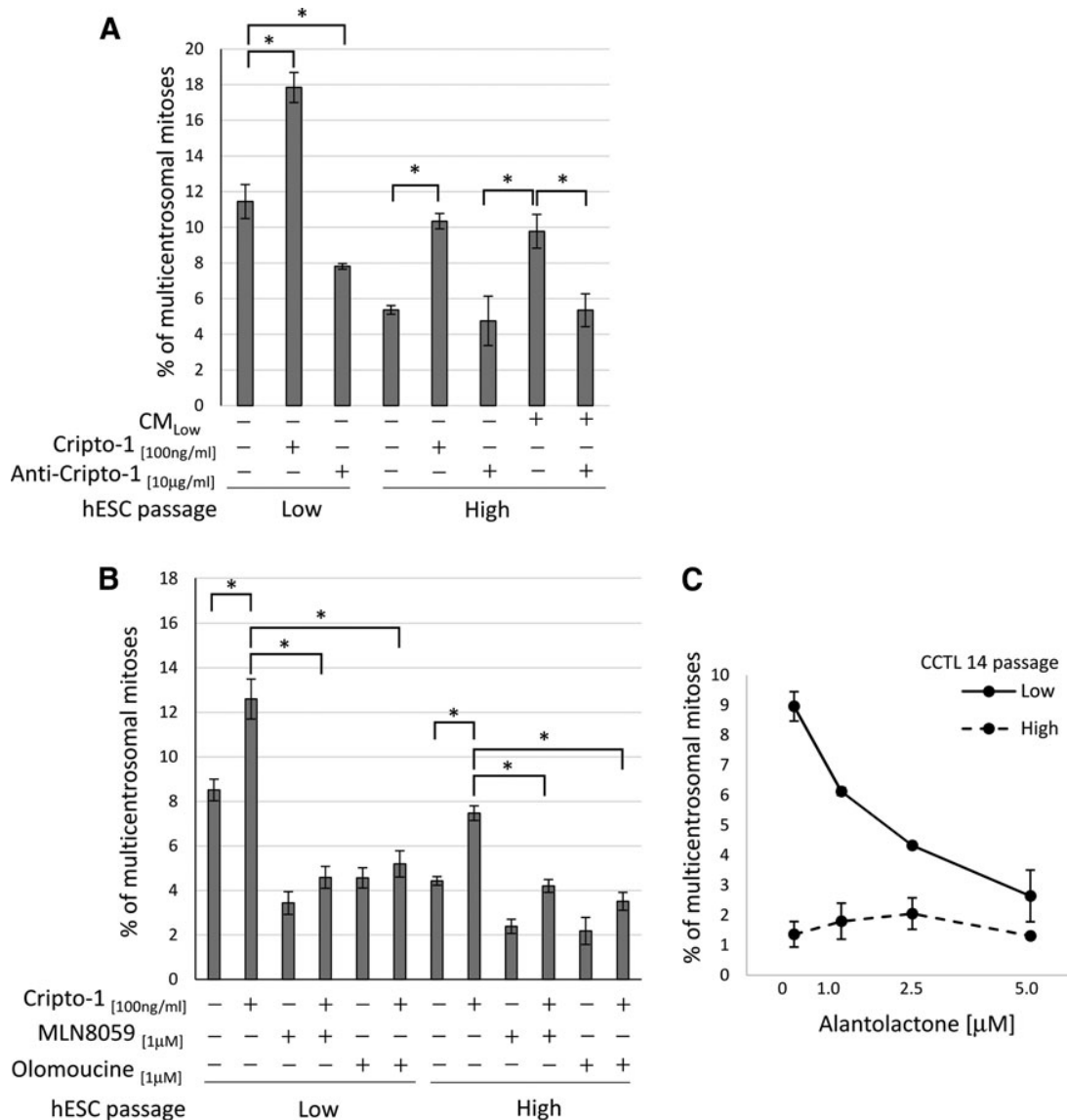


FIG. 3. (A) The effect of recombinant Cripto-1 protein and anti-Cripto-1 blocking antibody, respectively, on the percentage of multicentrosomal mitoses in low- and high-passage hESC. The two columns on far right represent high-passage hESC that were exposed to low-passage CM at the time of treatment with anti-Cripto-1 antibody. The numbers of centrosomes were counted as visualized by anti-pericentrin antibody. Data are expressed as mean \pm SD. * $P < 0.05$. (B) The effect of inhibitors of Aurora A (MLN 8054) and CDK2 (olomoucine), respectively, on the percentage of multicentrosomal mitoses in low- and high-passage hESC. The cells were exposed for 24 h to either inhibitor, with or without simultaneous exposure to Cripto-1. The numbers of centrosomes were counted as visualized by anti-pericentrin antibody. Data are expressed as mean \pm SD. * $P < 0.05$. (C) The effect of alantolactone on the percentage of multicentrosomal mitoses in low- and high-passage hESC. The cells were exposed for 24 h to alantolactone at concentration of 1.0, 2.5, and 5.0 μ M, respectively. The numbers of centrosomes were counted as visualized by anti-pericentrin antibody. Data are expressed as mean \pm SD.

also other ligands of AcrRII, such as Nodal, growth differentiation factor (GDF)-1, or GDF-3 [16]. When binding of Cripto-1 to ActRII was disrupted in human colon adenocarcinoma HCT-8 cells by alantolactone, the activin/SMAD3 signaling became activated and the cells stopped dividing [11]. In our study on hESC, exposure of cells to alantolactone as well as blocking of Cripto-1 by neutralizing antibody caused reduction of supernumerary centrosomes. Based on this we may conclude that Cripto-1 influences certain molecular circuitry (or circuitries) that,

at least in hESC, coregulate metabolism of centrosomes, although the detailed mechanism remains unresolved. Indeed, since activin signaling in itself integrates both extracellular signaling cues (eg, Wnts [17]), and intracellular regulators (eg, p53-p21^{Waf1/Cip1} [18]), the effect of Cripto-1 observed here on hESC may involve a variety of different molecular pathways.

Initiation of centrosome duplication requires phosphorylation of nucleophosmin/B23 by CDK2/cyclin E complex [19]. We have previously demonstrated that inhibition of

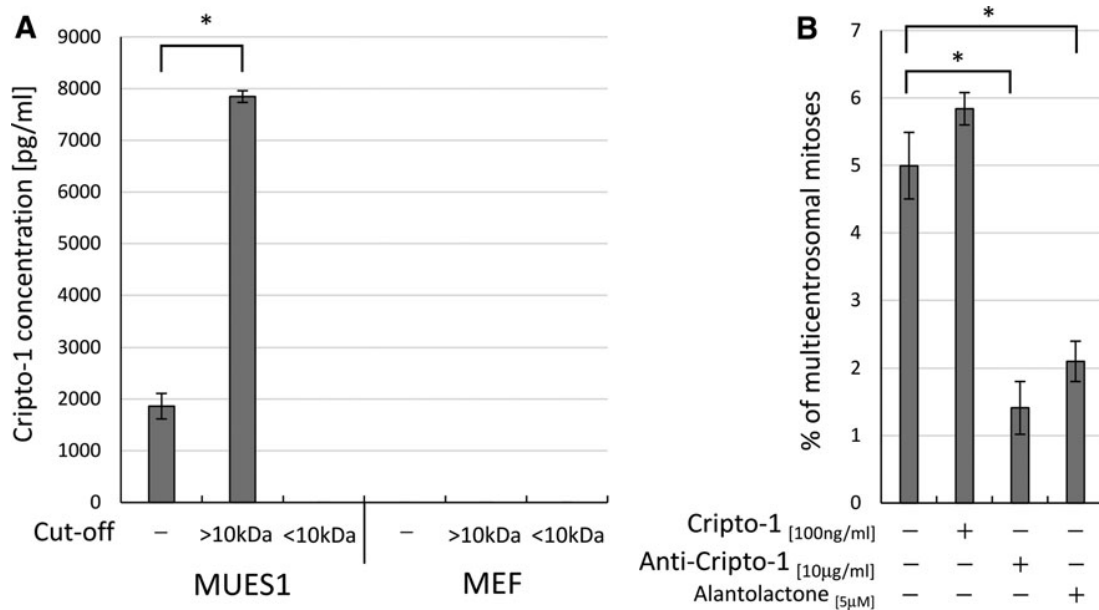


FIG. 4. (A) The quantity of Cripto-1 protein in media conditioned by low- and high-passage hESC (MUES1 line of hESC). Both complete and concentrated media were measured. Media collected from only MEF is included for comparison. Data are expressed as the mean \pm SD. * $P < 0.05$. (B) The effect of recombinant Cripto-1 protein, anti-Cripto-1 blocking antibody, and alantolactone on the percentage of multicentrosomal mitoses in hESC (MUES1 line of hESC). Data are expressed as the mean \pm SD. * $P < 0.05$.

CDK2 and Aurora A by small molecule inhibitors resulted in decreased frequency of supernumerary centrosomes in hESC [4]. Here, we have observed the same effect of Aurora A and CDK2 inhibition in hESC, in which the frequency of supernumerary centrosomes was elevated by their exposure to Cripto-1 protein. In somatic cells, signaling via activin leads to inhibition of G1-specific CDK that then produces arrest of cell cycle progression. In hESC, instead, activin signaling, together with signaling by Nodal and FGF, seem to be indispensable for their self-renewal at pluripotent state [20]. Thus, one may speculate that occurrence of supernumerary centrosomes in hESC results “simply” from inadequate intracellular integration of Cripto-1 signals.

Here we show that abnormal metabolism of centrosomes is typical for pristine hESC in their low passage and becomes eliminated as these cell cultures progress into higher passage. This may sound contradictory with the fact that hESC tend to harbor chromosomal abnormalities with prolonged cultivation. This controversy, however, is only seeming. In reality, prolonged culture leads to a selection of cells that are best proficient (due to genetic and/or metabolic modifications) in realizing their vital functions. We think that normal karyokinesis supported by “bi-centrosomal” spindles observed here in hESC is also reached by such selection process, irrespective of the karyotype status of the cells.

Taken together, although we may only hypothesize about underlying molecular mechanisms, this study still for the first time reveals Cripto-1 as the signaling molecule that (1) is produced by hESC, (2) is active constituent of the hESC culture microenvironment, (3) undergoes changes during propagation of hESC, and (4) mediates behaviors of hESC, which are highly relevant from both a biological and the practical points of view. Based on this, we propose that

manipulating Cripto-1 signaling may contribute to development of more effective and safer clinical application scenarios involving hESC. From the broader perspective, we hypothesize that the link between Cripto-1 signaling and the regulation of mitotic events, demonstrated here in vitro on hESC, may be operative also in vivo and Cripto-1 thus may act as oncogenic factor emanating from tissue microenvironment.

Acknowledgments

This study was supported by funds from the Czech Science Foundation (GA15-11707S), Masaryk University (MUNI/A/1369/2016, MUNI/C/1418/2017), and the National Program of Sustainability II (project no. LQ1605, MEYS CR). We acknowledge Dr. Milan Ešner and the core facility Cellular Imaging (CELLIM) of Central European Institute of Technology (CEITEC), Brno, Czech Republic, supported by the MEYS CR (LM2015062 Czech-BioImaging) for support with obtaining image data presented in this paper. We are also grateful to Dr. Klára Koudelková for her excellent technical assistance.

Author Disclosure Statement

No competing financial interests exist.

References

1. Amps K, PW Andrews, G Anyfantis, L Armstrong, S Avery, H Baharvand, J Baker, D Baker, MB Munoz, et al. (2011). Screening ethnically diverse human embryonic stem cells identifies a chromosome 20 minimal amplicon conferring growth advantage. *Nat Biotechnol* 29:1132–1144.

2. Harrison NJ, J Barnes, M Jones, D Baker, PJ Gokhale and PW Andrews. (2009). CD30 expression reveals that culture adaptation of human embryonic stem cells can occur through differing routes. *Stem Cells* 27:1057–1065.
3. Baker DE, NJ Harrison, E Maltby, K Smith, HD Moore, PJ Shaw, PR Heath, H Holden and PW Andrews. (2007). Adaptation to culture of human embryonic stem cells and oncogenesis in vivo. *Nat Biotechnol* 25:207–215.
4. Holubcova Z, P Matula, M Sedlackova, V Vinarsky, D Dolezalova, T Barta, P Dvorak and A Hampl. (2011). Human embryonic stem cells suffer from centrosomal amplification. *Stem Cells* 29:46–56.
5. Gu YF, Q OuYang, C Dai, CF Lu, G Lin, F Gong and GX Lu. (2016). Abnormalities in centrosome number in human embryos and embryonic stem cells. *Mol Reprod Dev* 83:392–404.
6. Nigg EA, L Cajanek and C Arquint. (2014). The centrosome duplication cycle in health and disease. *FEBS Lett* 588:2366–2372.
7. Barta T, D Dolezalova, Z Holubcova and A Hampl. (2013). Cell cycle regulation in human embryonic stem cells: links to adaptation to cell culture. *Exp Biol Med (Maywood)* 238:271–275.
8. International Stem Cell Initiative, Adewumi O, B Aflatoonian, L Ahrlund-Richter, M Amit, PW Andrews, G Beighton, PA Bello, N Benvenisty, et al. (2007). Characterization of human embryonic stem cell lines by the International Stem Cell Initiative. *Nat Biotechnol* 25: 803–816.
9. Rueden CT, J Schindelin, MC Hiner, BE DeZonia, AE Walter, ET Arena and KW Eliceiri. (2017). ImageJ2: ImageJ for the next generation of scientific image data. *BMC Bioinformatics* 18:529.
10. Strizzi L, C Bianco, N Normanno and D Salomon. (2005). Cripto-1: a multifunctional modulator during embryogenesis and oncogenesis. *Oncogene* 24:5731–5741.
11. Shi Y, YL Bao, Y Wu, CL Yu, YX Huang, Y Sun, LH Zheng and YX Li. (2011). Alantolactone inhibits cell proliferation by interrupting the interaction between Cripto-1 and activin receptor type II A in activin signaling pathway. *J Biomol Screen* 16:525–535.
12. Klauzinska M, NP Castro, MC Rangel, BT Spike, PC Gray, D Bertolette, F Cuttitta and D Salomon. (2014). The multifaceted role of the embryonic gene Cripto-1 in cancer, stem cells and epithelial-mesenchymal transition. *Semin Cancer Biol* 29:51–58.
13. Fiorenzano A, E Pascale, C D'Aniello, D Acampora, C Bassalert, F Russo, G Andolfi, M Biffoni, F Francescangeli, et al. (2016). Cripto is essential to capture mouse epiblast stem cell and human embryonic stem cell pluripotency. *Nat Commun* 7:12589.
14. Yan YT, JJ Liu, Y Luo, E Chaosu, RS Haltiwanger, C Abate-Shen and MM Shen. (2002). Dual roles of Cripto as a ligand and coreceptor in the nodal signaling pathway. *Mol Cell Biol* 22:4439–4449.
15. Kelber JA, G Shani, EC Booker, WW Vale and PC Gray. (2008). Cripto is a noncompetitive activin antagonist that forms analogous signaling complexes with activin and nodal. *J Biol Chem* 283:4490–4500.
16. Bianco C, MC Rangel, NP Castro, T Nagaoka, K Rollman, M Gonzales and DS Salomon. (2010). Role of Cripto-1 in stem cell maintenance and malignant progression. *Am J Pathol* 177:532–540.
17. Bryja V, I Cervenka and L Cajanek. (2017). The connections of Wnt pathway components with cell cycle and centrosome: side effects or a hidden logic? *Crit Rev Biochem Mol Biol* 52:614–637.
18. Tarapore P, HF Horn, Y Tokuyama and K Fukasawa. (2001). Direct regulation of the centrosome duplication cycle by the p53-p21Waf1/Cip1 pathway. *Oncogene* 20: 3173–3184.
19. Okuda M, HF Horn, P Tarapore, Y Tokuyama, AG Smulian, PK Chan, ES Knudsen, IA Hofmann, JD Snyder, KE Bove and K Fukasawa. (2000). Nucleophosmin/B23 is a target of CDK2/Cyclin E in centrosome duplication. *Cell* 103:127–140.
20. Vallier L, M Alexander and RA Pedersen. (2005). Activin/Nodal and FGF pathways cooperate to maintain pluripotency of human embryonic stem cells. *J Cell Sci* 118:4495–4509.

Address correspondence to:

*Assoc. Prof. Aleš Hampl
Department of Histology and Embryology
Faculty of Medicine
Masaryk University
Kamenice 3, Building A1
Brno 62500
Czech Republic*

E-mail: ahampl@med.muni.cz

Received for publication January 18, 2018

Accepted after revision June 7, 2018

Prepublished on Liebert Instant Online June 8, 2018

VIII. FULL LIST OF PUBLICATIONS 2006-2018

1. Vašíčková K, Moráň L, Gurín D, Vaňhara P. **Alleviation of endoplasmic reticulum stress by tauroursodeoxycholic acid delays senescence of mouse ovarian surface epithelium.** *Cell and Tissue Research* 2018; **374**(3):643-652.
2. Vašíčková K, Horák P, Vaňhara P. **TUSC3: functional duality of a cancer gene.** *Cellular and Molecular Life Sciences : CMLS* 2018; **75**(5):849-857.
3. Vaňhara P, Kučera L, Prokeš L, Jurečková L, Pena-Mendez EM, Havel J, Hampl A. **Intact cell mass spectrometry as a quality control tool for revealing minute phenotypic changes of cultured human embryonic stem cells.** *Stem Cells Translational Medicine* 2018; **7**(1):109-114.
4. Porokh V, Vaňhara P, Bárta T, Jurečková L, Bohačiaková D, Pospíšilová V, Holubcová Z, Pelková V, Souček K, Hampl A. **Soluble Cripto-1 induces accumulation of supernumerary centrosomes and formation of aberrant mitoses in human embryonic stem cells.** *Stem Cells and Development* 2018; **27**(16):1077-1084.
5. Cadoni E, Vaňhara P, Valletta E, Pinna E, Vascellari S, Caddeo G, Isaia F, Pani A, Havel J, Pivetta T. **Mass spectrometry discrimination of phospholipid patterns in cisplatin-resistant and sensitive cancer cells.** *Rapid Communications in Mass Spectrometry : RCM* 2018. doi: 10.1002/rcm.8320. [Epub ahead of print]
6. Samadder P, Suchankova T, Hylse O, Khirsariya P, Nikulenkov F, Drapela S, Straková N, Vaňhara P, Vašíčková K, Kolářová H, Binó L, Bittová M, Ovesná P, Kollár P, Fedr R, Ešner M, Jaroš J, Hampl A, Krejčí L, Paruch K, Souček K. **Synthesis and profiling of a novel potent selective inhibitor of CHK1 kinase possessing unusual N-trifluoromethylpyrazole pharmacophore resistant to metabolic N-dealkylation.** *Molecular Cancer Therapeutics* 2017; **16**(9):1831-1842.
7. Kolářová L, Prokeš L, Kučera L, Hampl A, Pena-Mendez E, Vaňhara P, Havel J. **Clusters of monoisotopic elements for calibration in (TOF) mass spectrometry.** *Journal of the American Society for Mass Spectrometry* 2017; **28**(3):419-427.
8. Valletta E, Kučera L, Prokeš L, Amato F, Pivetta T, Hampl A, Havel J, Vaňhara P. **Multivariate calibration approach for quantitative determination of cell-line cross contamination by intact cell mass spectrometry and artificial neural networks.** *PLoS ONE* 2016; **11**(1):e0147414.

9. Kratochvílová K, Moráň L, Paďourová S, Stejskal S, Tesařová L, Šimara P, Hampl A, Koutná I, Vaňhara P. **The role of the endoplasmic reticulum stress in stemness, pluripotency and development.** *European Journal of Cell Biology* 2016; **95**(3-5):115-23.
10. Trudu F, Amato F, Vaňhara P, Pivetta T, Pena-Mendez EM, Havel J. **Coordination compounds in cancer: Past, present and perspectives.** *Journal of Applied Biomedicine* 2015; **13**(2):79-103.
11. Kratochvílová K, Horák P, Ešner M, Souček K, Pils D, Anees M, Tomasich E, Dráfi F, Jurtíková V, Hampl A, Krainer M, Vaňhara P. **Tumor suppressor candidate 3 (TUSC3) prevents the epithelial-to-mesenchymal transition and inhibits tumor growth by modulating the endoplasmic reticulum stress response in ovarian cancer cells.** *International Journal of Cancer* 2015; **137**(6):1330-1340.
12. Kolářová L, Kučera L, Vaňhara P, Hampl A, Havel J. **Use of flower-like gold nanoparticles in time-of-flight mass spectrometry.** *Rapid Communications in Mass Spectrometry* 2015; **29**(17):1585-1595.
13. Ahmed IS, M. Sultan, A. Murtaza, I. Yousaf, S. Maqsood, B. Vaňhara, P. Anees, M. **The erratic antibiotic susceptibility patterns of bacterial pathogens causing urinary tract infections.** *EXCLI Journal* 2015;(14):916-925.
14. Ručka Z, Koutná I, Tesařová L, Potěšilová M, Stejskal S, Šimara P, Vaňhara P, Doležel J, Zvoníček V, Coufal O, Čapov I. **Intravenous insulin therapy during lung resection does not affect lung function or surfactant proteins.** *BMC Pulmonary Medicine* 2014; **14**(1): 155.
15. Kolářová L, Vaňhara P, Pena-Mendez EM, Hampl A, Havel J. **Tissue visualization mediated by nanoparticles: from tissue staining to mass spectrometry tissue profiling and imaging.** In: Seifalian A (ed). *Nanomedicine*. One Central Press: Manchester, UK, 2014, pp 468-482.
16. Houška J, Pena-Mendez EM, Hernandez-Fernaund JR, Salido E, Hampl A, Havel J, Vaňhara P. **Tissue profiling by nanogold-mediated mass spectrometry and artificial neural networks in the mouse model of human primary hyperoxaluria 1.** *Journal of Applied Biomedicine* 2014; **12**(2):119-125.
17. Horak P, Tomasich E, Vaňhara P, Kratochvílová K, Anees M, Marhold M, Lemberger CE, Gerschpacher M, Horvat R, Sibilija M, Pils D, Krainer M. **TUSC3 loss alters the ER stress response and accelerates prostate cancer growth in vivo.** *Scientific Reports* 2014; **4**:3739.
18. Anees M, Horak P, Schiefer AI, Vanhara P, El-Gazzar A, Perco P, Kiesewetter B, Müllauer L, Streubel B, Raderer M, Krainer M. **The potential evasion of immune surveillance in MALT lymphoma by DcR2-mediated upregulation of NF-kappaB.** *Leukemia & Lymphoma* 2015; **56**(5):1440-9.

19. Vaňhara P, Souček P. **Mutual cytokine crosstalk between colon cancer cells and microenvironment initiates development of distant metastases.** *JAK-STAT* 2013; **2**(2):1-4.
20. Vaňhara P, Horak P, Pils D, Anees M, Petz M, Gregor W, Zeillinger R, Krainer M. **Loss of the oligosaccharyl transferase subunit TUSC3 promotes proliferation and migration of ovarian cancer cells.** *International Journal of Oncology* 2013; **42**(4):1383-1389.
21. Ručka Z, Vaňhara P, Koutná I, Tesařová L, Potěšilová M, Stejskal S, Šimara P, Doležel J, Zvoníček V, Coufal O, Čapov I. **Differential effects of insulin and dexamethasone on pulmonary surfactant-associated genes and proteins in A549 and H441 cells and lung tissue.** *International Journal of Molecular Medicine* 2013; **32**(1):211-8.
22. Pils D, Horak P, Vaňhara P, Anees M, Petz M, Alfan A, Gugerell A, Wittinger M, Gleiss A, Auner V, Tong D, Zeillinger R, Braicu EI, Sehoul J, Krainer M. **Methylation status of TUSC3 is a prognostic factor in ovarian cancer.** *Cancer* 2013; **119**(5):946-954.
23. Pernicová Z, Vaňhara P, Souček K. **Formation of secretory senescent cells in prostate tumors: the role of androgen receptor activity and cell cycle regulation.** In: Hayat MA (ed). *Tumor Dormancy, Quiescence, and Senescence, Volume 1*, vol. 1. Springer Netherlands, 2013, pp 303-316.
24. Amato F, Lopez A, Pena-Mendez E, Vaňhara P, Hampl A, Havel J. **Artificial neural networks in medical diagnosis.** *Journal of Applied Biomedicine* 2013; **11**(2):47-58.
25. Vaňhara P, Hampl A, Kozubík A, Souček K. **Growth/differentiation factor-15: prostate cancer suppressor or promoter?** *Prostate Cancer and Prostatic Diseases* 2012; **15**(4):320-328.
26. Wittinger M, Vaňhara P, El-Gazzar A, Savarese-Brenner B, Pils D, Anees M, Grunt TW, Sibilia M, Holcman M, Horvat R, Schemper M, Zeillinger R, Schöfer C, Dolznig H, Horak P, Krainer M. **hVps37A Status affects prognosis and cetuximab sensitivity in ovarian cancer.** *Clinical Cancer Research: an official journal of the American Association for Cancer Research* 2011; **17**(24):7816-7827.
27. Křen L, Slabý O, Múčková K, Lžičarová E, Sova M, Vybíhal V, Svoboda T, Fadrus P, Lakomý R, Vaňhara P, Křenová Z, Štěrba J, Smrčka M, Michálek J. **Expression of immune-modulatory molecules HLA-G and HLA-E by tumor cells in glioblastomas: an unexpected prognostic significance?** *Neuropathology : official journal of the Japanese Society of Neuropathology* 2011; **31**(2):129-134.
28. Křen L, Múčková K, Lžičarová E, Sova M, Vybíhal V, Svoboda T, Fadrus P, Smrčka M, Slabý O, Lakomý R, Vaňhara P, Křenová Z, Michálek J. **Production of immune-modulatory**

- nonclassical molecules HLA-G and HLA-E by tumor infiltrating ameboid microglia/macrophages in glioblastomas: a role in innate immunity?** *Journal of Neuroimmunology* 2010; **220**(1-2):131-135.
29. Vaňhara P, Lincová E, Kozubík A, Jurdic P, Souček K, Šmarda J. **Growth/differentiation factor-15 inhibits differentiation into osteoclasts--a novel factor involved in control of osteoclast differentiation.** *Differentiation; research in biological diversity* 2009; **78**(4):213-222.
30. Navrátilová J, Jungová P, Vaňhara P, Preisler J, Kanický V, Šmarda J. **Copper ions regulate cytotoxicity of disulfiram to myeloid leukemia cells.** *International Journal of Molecular Medicine* 2009; **24**(5):661-670.
31. Vaňhara P, Bryja V, Horváth V, Kozubík A, Hampl A, Šmarda J. **c-Jun induces apoptosis of starved BM2 monoblasts by activating cyclin A-CDK2.** *Biochemical and Biophysical Research Communications* 2007; **353**(1):92-97.
32. Vaňhara P, Šmarda J. **Jun: the master regulator in healthy and cancer cells.** *Journal of Applied Biomedicine* 2006; **4**(4):163-170.
33. Vaňhara P, Šmarda J. **[Regulation of osteoclast activity: a new approach in the therapy of bone diseases].** *Casopis Lekarů Ceských* 2006; **145**(8):606-610.
34. Pekár S, Vaňhara P. **Geographical sexual size dimorphism in an ant-eating spider, Zodarion rubidum (Araneae: Zodariidae).** *Journal of Natural History* 2006; **40**(21-22):1343-1350.